AD-A111 783   NAVY AEROBALLISTICS ADVISORY COMMITTEE   F/G 20/4
               PROCEEDINGS OF THE NAVY SYMPOSIUM ON AEROBALLISTICS (12TH) HELD--ETC(U)
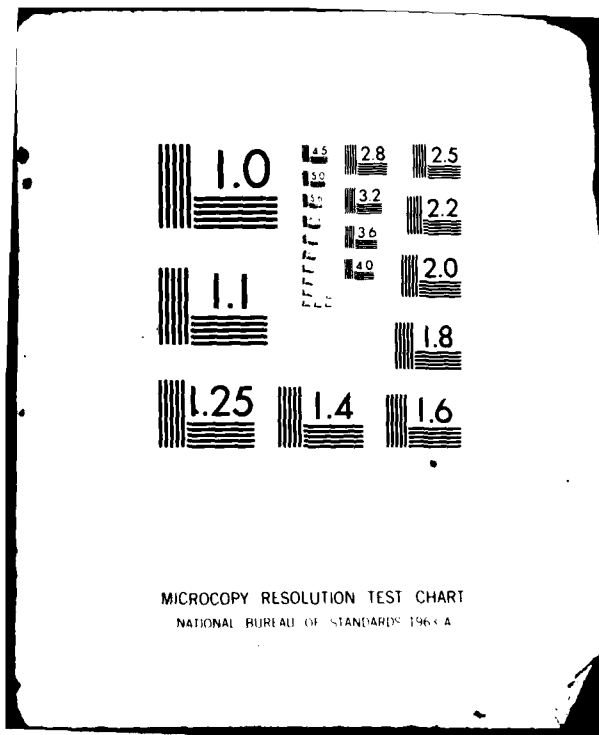   MAY 81
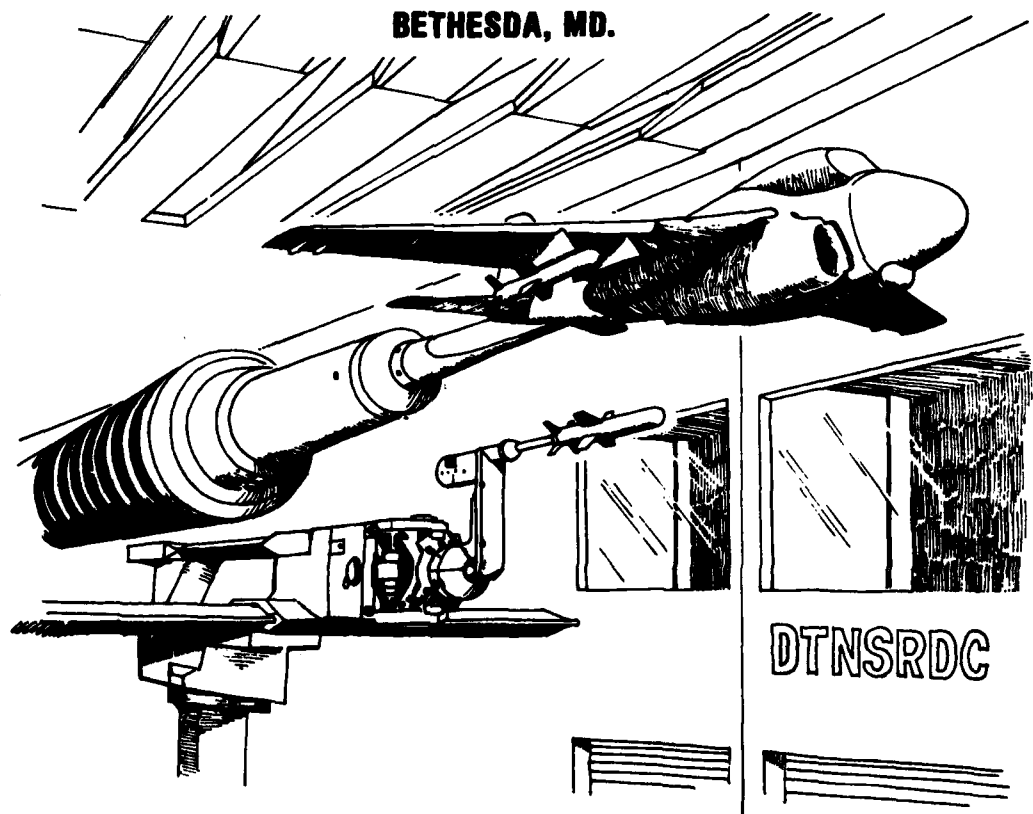
UNCLASSIFIED   NL

MICROCOPY RESOLUTION TEST CHART

NATIONAL BUREAU OF STANDARDS 1963 A

12th NAVY
SYMPOSIUM on
AEROBALLISTICS

12 - 13 - 14 MAY 1981

HOSTED BY THE
DAVID TAYLOR NAVAL SHIP R&D CENTER
BETHESDA, MD.

DTNSRDC

VOLUME II

SPONSORED BY THE
NAVAL AIR SYSTEMS COMMAND

82 03 08 001

**PROCEEDINGS OF THE TWELFTH
NAVY SYMPOSIUM ON AEROBALLISTICS**

VOLUME II

12-13-14 MAY 1981

**HELD AT THE DAVID TAYLOR NAVAL SHIP R&D CENTER
BETHESDA, MARYLAND**

**SPONSORED BY THE
NAVAL AIR SYSTEMS COMMAND**

TABLE OF CONTENTS

FOREWORD

S. de los Santos
Chairman
Navy Aeroballistics Committee

It is a great pleasure and privilege for me, on behalf of the Navy Aeroballistics Committee to welcome you to the 12th U.S. Navy Symposium on Aeroballistics.

This Symposium is being held for the purpose of presenting the results of recent work associated with aeroballistics. As indicated in the program included in your registration package, the Symposium will consist of 45 papers presented in 5 technical sessions. A banquet, preceded by cocktails will be held this evening at the Kenwood Club, and for those who are interested, there will be a Center Facility tour on Thursday afternoon. The first four sessions of the Symposium are unclassified. For security reasons, all classified papers will be presented in the fifth session on Thursday. The Proceedings will include the unclassified papers in Volumes I and II and the classified papers in Volume III.

The papers accepted for presentation come from the NAC activity members, Air Force, NASA, the universities, and industry. To round out the program, we have invited several prominent speakers to share with us their knowledge and experience that would be of interest in aeroballistics. These speakers include Jack Nielsen of Nielsen Engineering & Research, Inc. who will review missile aerodynamics; Art Maddox of NWC, now visiting Professor at the Naval Academy, who will review store separation; G.C. Paynter of Boeing Military who will give us the current status of inlet flow prediction methods; J.W. Stultz of McDonnell Douglas who will speak on heating methods used to determine structural temperatures; and W. Ballhaus of NASA Ames who will talk on the numerical aerodynamic simulator. Our afterdinner speaker will be Colonel John Boyd (USAF, retired) who will talk on energy maneuverability.

This is the second time around for DTNSRDC to host the Navy Aeroballistics Symposium, and, perhaps, it would be appropriate here to share with you some observations. The first Center hosting (Sixth Symposium) was held at Fort McNair in 1963 for lack of an auditorium facility at the Center. It is recalled that 28 40-minute papers were presented by the participants (Navy, Air Force, Army, NASA, the universities, and industry). Since then, the committee decided to limit the presentation time without limiting the length of the written manuscripts. It comes as no surprise then that for the same duration, more papers could be presented without loss of essential detail. Accordingly, the last 5 symposia have averaged 45 papers.

Although the number of papers has remained the same, the contributions of various activities have changed considerably. Since 1975, for instance, there has been a 50-percent reduction in Navy contributions; this has been offset by a several-fold increase from the universities. The decline in Navy participation is not surprising. It is the result of DOD's policy (promulgated in 1975) of seeking constant growth in its program to strengthen and revitalize its research base and ties with the external research community — a policy that resulted in increasing external research funding while maintaining reduced levels of research at the inhouse laboratories! Data indicate that the services, particularly the Air Force, took a beating (70-percent decline in inhouse research funds).

Laboratory heads and other knowledgeable individuals have expressed concern for this state of affairs. Allowing the laboratories to remain at the current level of research performance could, if it hasn't already, erode their long-term ability to perform those functions which are basic to supporting their missions.

A recent General Accounting Office (GAO) study recognized the predicament of the laboratories and has requested DOD to give the same careful consideration to the research base represented by the inhouse laboratories as has been given the needs of the external research community. How DOD will respond to this GAO recommendation is not yet known, but the feeling is that it would be better to accomplish the true increase in inhouse research by an overall increase in research funding rather than through a corresponding reduction of the planned growth in extramural research.

Already we seem pressed for time. The scheduling shown in the program was based on the cafeteria renovation being completed in April and having lunch on station. Unfortunately, the scheduled completion date has slipped, and now we'll have to go off station for lunch — some think this to be a blessing in disguise. I have accordingly requested each speaker to streamline their presentation or take no more time than has been allotted them.

Again, welcome and I hope you have a very profitable and enjoyable Symposium.

PAPERS PRESENTED

VOLUME I

*Invited Speaker

PAGE

*Invited Speaker

PAGE

*Invited Speaker

PAGE

*Invited Speaker

VOLUME III
(CLASSIFIED PAPERS)

PAGE

AUTHORS

	Paper	Volume	Page
ANDERSON, ARVID A.	36	II	II-331
BALLHAUS, WILLIAM S., Jr.	28	II	II-129
BALTAKIS, FRANK P.	3	I	I-73
BARNES, G.A.	41	III	III-187
BAUER, RALPH L.	5	I	Withdrawn
BRADDOCK, WILLIAM F.	16	I	I-347
BURKE, GERALD L.	39	III	III-103
CALIANNO, CARL T.	20	I	I-417
CENKO, ALEXIS	15	I	I-331
CUADROS, JAIME H.	18	I	I-377
DAILEY, G.	35	II	II-309
DANIEL, DONALD C.	9	I	I-181
DENYSYK, BO	31	II	II-241
DEVAN, LEROY	2	I	I-39
FOTIEO, GEORGE	17	I	I-371
FOX, HAROLD G.	27	II	II-101
GILLIES, D.S.	34	III	III-21
GOODWIN, FREDERICK K.	12	I	I-251
GRIFFIN, MICHAEL D.	22	III	III-1
HACKERMAN, L.B.	3	I	I-73
HARDY, SAMUEL R.	44	III	III-275
HAYES, CLYDE	24	II	II-53
HEMSCH, MICHAEL J.	4, 14	I	I-107, 313
HSIEH, CARL T.	33	II	II-297
JISCHKE, MARTIN C.	9	I	I-181
KEIRSEY, JAMES L.	22	III	III-1
KIM, IN-KUN	19	I	I-395
KIM, MOO DO	25, 30	II	II-63, 191

AUTHORS

	Paper	Volume	Page
LAMB, MILTON	6	I	I-117
LEWIS, CLARK H.	25, 29, 30, 31	II	II-63, 165, 191, 241
LUCAS, BILLY F.	18	I	I-377
LUCERO, EDDIE F.	8	I	I-149
LUNDY, THOMAS E.	16	I	I-347
MADDOX, ARTHUR R.	11	I	I-239
MALLALIEU, R.C.	35	II	II-309
MARLEY, E.T.	40	III	III-171
MASON, L.A.	2	I	I-39
McMILLAN, O.J.	45	III	III-311
MEEKER, RICHARD E.	43	III	III-235
MEYER, RUDOLPH	15	I	I-331
MOORE, F.G.	2	I	I-39
NEWMAN, ROBB W.	27	II	II-101
NIELSEN, JACK N.	1, 4, 12	I	I-1, 107, 251
NORTH, B.F.	19	I	I-395
NTONE, FRANCOIS	23	II	II-37
PAYNTER, G.C.	21	II	II-1
PEPITONE, THOMAS R.	42	III	III-199
PERKINS, S.C., Jr.	45	III	III-311
PHILLIPS, KENNETH A.	13	I	I-295
RASMUSSEN, MAURICE L.	9	I	I-181
RIVELLO, ROBERT M.	37	III	III-47
RUNCIMAN, WILLIAM J.	5	I	Withdrawn
SAWYER, WALLACE C.	6	I	I-117
SCAGGS, NORMAN E.	34	III	III-21
SOLOMON, JAY M.	3	I	I-73

AUTHORS

ATTENDEES

NAME	AFFILIATION
ANDERSON, Arvid A.	Pacific Missile Test Center
BAKER, William B.	CALSPAN
BALLHAUS, William F.	NASA Ames Research Center
BALTAKIS, F.P.	NSWC, White Oak Laboratory
BELLASCHI, Jules J.	NAVSEA
BENARD, Irvin J.	United Technologies Corporation
BOYD, John	Air Force (Retired)
BRADDOCK, Bill F.	Lockheed Missiles & Space Company
BURKE, Gerald L.	AF Wright Aeronautical Laboratories
CALIANNO, Carl T.	Naval Air Development Center
CARTER, Stephen K.	Naval Weapons Center
CAYWOOD, William C.	JHU/APL
CENKO, Alexis	Grumman Aerospace Corporation
CHALK, Joseph B.	Naval Intelligence Support Center
CLANCY, Tom M.	DTNSRDC
CLARK, W.H.	Naval Weapons Center
COBB, Kenneth K.	Air Force Armament Laboratory
CRONVICH, L.L.	JHU/APL
CUADROS, Jaime H.	General Dynamics Pomona Division
DAILEY, George	JHU/APL
DE LOS SANTOS, S.	DTNSRDC
DEVAN, Leroy	NSWC, Dahlgren Laboratory
DRIFTMYER, Richard T.	NSWC, White Oak Laboratory
ESTES, Robert H.	Naval Weapons Center
FORTUNATO, Enrico	NSWC, White Oak Laboratory
FOTIEO, George	Martin Marietta Aerospace
FRIEDMAN, Eugene M.	U.S. Army ARRADCOM

NAME	AFFILIATION
GILBERT, Lee N.	Naval Weapons Center
GLEASON, Larry L.	Naval Weapons Center
HACKERMAN, Louis B.	NSWC, White Oak Laboratory
HALL, Darryl W.	Science Applications, Inc.
HARDY, Samuel R.	NSWC, Dahlgren Laboratory
HAYES, Clyde	NASA Langley Research Center
HEMSCH, Michael J.	Nielsen Engineering & Research, Inc.
HOPPS, Jack C.	Honeywell, Minneapolis
HSIEH, Tsuying	NSWC, White Oak Laboratory
HUDGINS, Henry E.	U.S. Army ARRADCOM
JOHNSON, Arne (LCDR, USN)	DTNSRDC
JOHNSON, Lloyd	NSWC, Dahlgren Laboratory
KANURI, Ravi	General Electric Company
KAUTZ, Frederick A.	Central Intelligence Agency
KIM, Moo Do	Virginia Polytechnic Institute
KRAUSE, David L.	Naval Ordnance Station
KREMZIER, Emil J.	The Marquardt Company
KRUMINS, M.V.	NSWC, White Oak Laboratory
LAMB, Milton	NASA Langley Research Center
LARSEN, Kenneth A.	Pacific Missile Test Center
LEHMAN, Larry O.	Naval Air Development Center
LESLIE, David L.	General Dynamics, Pomona Division
LEWIS, Clark H.	Virginia Polytechnic Institute
LOEZOS, Stavros	Naval Air Systems Command
LUCERO, Eddie F.	JHU/APL
MacALLISTER, Leonard C.	Ballistic Research Laboratory
MADDOX, Arthur R.	U.S. Naval Academy
MAGUIRE, Bill	DTNSRDC
MARLEY, Edward T.	JHU/APL

NAME	AFFILIATION
MARSHALL, James R.	Hughes Aircraft Company
MASON, Lawrence A.	NSWC, Dahlgren Laboratory
MATTHEWS, R.K.	CALSPAN
McKAY, D.W.	Eglin AFB
McMILLAN, Oden J.	Nielsen Engineering & Research, Inc.
MEYER, Rudolph C.	Grumman Aerospace Corporation
MILLER, Robert A.	Rockwell International Corporation
MILLER, Richard J. (CAPT, USN)	Naval Air Systems Command
MOORE, Frank G.	NSWC, Dahlgren Laboratory
MORRIS, George W.	Lockheed Missiles & Space Company
NEWMAN, Robb W.	JHU/APL
NIELSEN, Jack N.	Nielsen Engineering & Research, Inc.
NORTH, Bob F.	General Dynamics Convair Division
OHRENBERGER, John T.	TRW, California
OSTROWSKI, Paul P.	Naval Ordnance Station
PAPADOPOULOS, James	MBD Advanced Technology Center
PASIUK, Lionel	Naval Sea Systems Command
PAYNTER, Gerald C.	The Boeing Company, Seattle
PEPITONE, Thomas R.	NSWC, Dahlgren Laboratory
PHILLIPS, Kenneth A.	DTNSRDC
POLLIN, Irvin	Harry Diamond Laboratories
POPHAM, Edgar R.	McDonnell Douglas Corporation
POWELL, Alan	DTNSRDC Technical Director
PRILLMAN, Floyd W.	Vought Corporation
RACHNER, Jerome E.	Rockwell International Corporation
RAGSDALE, W.C.	NSWC, White Oak Laboratory
RASMUSSEN, Maurice L.	University of Oklahoma
RIVELLO, Robert M.	JHU/APL
RUTLEDGE, Walter H.	NSWC, Dahlgren Laboratory

NAME	AFFILIATION
RYAN, Bertha	Naval Weapons Center
SCAGGS, Norman E.	AF Wright Aeronautical Laboratories
SCHINDEL, Leon H.	NSWC, White Oak Laboratory
SCHMIDT, L.V.	Naval Post Graduate School
SEARS, Edward S.	Air Force Armament Laboratory
SIMPERS, Glen	Naval Ordnance Station
SMITH, Lloyd H.	Naval Weapons Center
SMITH, Renard E.	Naval Weapons Center
SMITH, Stephen D.	McDonnell Douglas Astronautics
SMITHEY, W.J.H. (CAPT, USN)	Pacific Missile Test Center
SOLIS, Ricardo	NSWC, Dahlgren Laboratory
SOLOMON, Jay M.	NSWC, White Oak Laboratory
STAHARA, Stephen S.	Nielsen Engineering & Research, Inc.
STANDARD, Charles M.	Vought Corporation
STEVENS, J.R.	JHU/APL
STRUTZ, Larry W.	Naval Weapons Center
STULTZ, J. Warren	McDonnell Douglas Corporation
STUREK, Walter B.	U.S. Army Ballistic Research Lab
SUN, John	Hughes Aircraft Company
SWAMINATHAN, S.	Virginia Polytechnic Institute
SZEMA, K.Y.	Virginia Polytechnic Institute
TAI, Tsze C.	DTNSRDC
TAYLOR, Robert M.	DTNSRDC
THAREJA, Rajiv R.	Virginia Polytechnic Institute
TIBBITTS, B.F. (CAPT, USN)	Commander, DTNSRDC
TISSERAND, Lawrence E.	JHU/APL
TESSITORE, Frank A.	Grumman Aerospace Corporation
UTREJA, Lajpat Rai	Lockheed Missiles & Space Company
VAN AKEN, Ray W.	Naval Weapons Center

NAME	AFFILIATION
VAN TUYL, Andrew H.	NSWC, White Oak Laboratory
VOLZ, William C.	NAVAIR
WARDLAW, Andrew B.	NSWC, White Oak Laboratory
WASICKO, Richard J.	NASA, Washington, D.C.
WAUGH, Charles E.	Martin Marietta Corporation
WECKESSER, Louis B.	JHU/APL
WEISEL, John S.	NSWC, Dahlgren Laboratory
WERBACK, Bill	Naval Weapons Center
XERIKOS, James	McDonnell Douglas Astronautics
YANG, Tah-Teh	Clemson University
ZARLINGO, Frederick C.	Naval Weapons Center
ZIEN, Tse-Fou	NSWC, White Oak Laboratory

CURRENT STATUS OF INLET FLOW PREDICTION METHODS

Gerald C. Paynter
Boeing Military Airplane Company
Seattle, Washington 98124

ABSTRACT

The increasing availability of large computers, advances in numerical fluid mechanics, and the rapidly escalating cost of wind tunnel testing are responsible for a trend toward the use of parametric analysis rather than parametric testing to support the design of inlet systems. With an emphasis on the transonic and supersonic speed regimes, current approaches to inlet flow analysis are discussed in the context of the inlet design process. Results from typical procedures now under development for supersonic inlet flows are presented along with a discussion of the advantages and disadvantages of each for design. The requirements for experimental validation of a procedure and analysis problem areas are reviewed. Recent developments which may lead to an improved inlet flow analysis capability are discussed.

INTRODUCTION

Inlet performance may be defined in terms of inlet recovery, distortion, drag, weight, maneuverability, controllability, stability, starting characteristics, etc. The function of the inlet is to prepare the flow for the engine by capturing and compressing a desired weight flow rate to a chosen state while minimizing losses associated with the compression process and the inlet installation. Inlet performance is usually closely related to the boundary layer development through and around the inlet. A boundary layer developing through the adverse pressure gradients associated with an inlet will thicken more rapidly and have a velocity profile distribution which is less "full" than a boundary layer developing through a constant pressure region. For high adverse pressure gradients, boundary layer separation may occur with high loss of inlet total pressure and high distortion.

In a typical design problem, the losses associated with the compression process are minimized by limiting the thickening and distortion of the boundary layer as the flow develops through the inlet. This is done by contouring the inlet surfaces to control the local gradients in static pressure and by the use of boundary layer control. Constraints on the design are typically the weight, length, location, and drag of the installation. The radar cross-section of an inlet installation is also a constraint for certain military aircraft.

The traditional approach to inlet design is illustrated in Figure 1. In this approach, the geometry of a design concept is varied parametrically and tested at model scale. Configurations are selected on the basis of the model scale test results for full scale validation and optimization. Problems with this approach are the rising cost of wind tunnel testing, uncertain scaling of

test results, and the constraints imposed on new designs by the existing test data base. Advanced aircraft. for example, those shown in Figure 2, require inlet systems of a type not in the present data base. Test based *design of new inlet systems implies high development cost, high design risk or both.*

An alternative to test based design is to replace parametric model scale testing with parametric analysis. This "analysis based" approach is also illustrated in Figure 1. The increasing availability of large computers and advances in numerical fluid mechanics have made possible the use of analysis based design. Major advantages of this approach are lower development cost, a better understanding of the inlet flow processes, and the removal of the existing test data base as a design constraint.

In practice, a design study is usually a composite of both the test and analysis based approaches. The available analysis is used to reduce the required test matrix to the smallest possible number of configurations. Testing is used to evaluate configurations in flow regimes outside the range of the available analyses. As computer size and speed increase and analyses become more powerful, less and less testing is required to achieve a successful design. This trend is illustrated in Figure 3 for the design of conventional subsonic inlets for commercial aircraft.

The goals of inlet flow analyses for design include:
    o analysis of all important flow phenomena
    o programs which are easy to use and understand
    o low computer cost per case
    o easy modification of inlet geometry and flow boundary conditions
    o easy identification of cause and effect relationships

In the sections which follow, the historical development of numerical fluid mechanics and the current status of inlet flow analysis are reviewed. Analysis problem areas are discussed and current approaches toward extending the present capability are described. Promising developments which may lead to significant improvements in capability are briefly discussed.

HISTORICAL DEVELOPMENT

Inlet design prior to 1970 was based on one-dimensional analysis and parametric model scale testing. Key events which led to the use of more powerful flow analyses in the design process were:
    o 1968 Stanford Conference on Computation of Turbulent Boundary Layers
    o The availability of powerful digital computers
    o The American SST program.

The 1968 Stanford Conference produced a set of checked-out standard test cases for a wide range of 2-D or axisymmetric turbulent boundary layer flows. This quickly led to accurate and widely available boundary layer methods. As noted above, accurate prediction of the boundary layer development through an inlet is essential for inlet performance prediction.

The American SST effort started about 1960 and ended in 1971 with the decision by the U.S. Congress to discontinue the project. This effort was

significant because of the major involvement by both Government and Industry to develop SST technology. Commercially viable aircraft required inlets with very high performance. The aerospace industry, faced with this difficult design task, successfully applied the available flow analysis capability including the boundary layer methods which resulted from the 1968 Stanford Conference to the design of the SST inlets. This was the first application of a primarily analysis based design philosophy to the development of a complex inlet system. The striking success of this approach for the development of the SST inlet system was widely recognized.[1]

With the cancellation of the SST program, the technology and the design philosophy were infused into other projects through the transfer of people from the program. As illustrated in Figure 3, this has led to major revisions in inlet design practice in the last decade.

The growth in the use of Computational Fluid Dynamics, CFD, for inlet design over the last decade or so paralleled development of CFD technology. This development is illustrated in Figure 4. CFD technology for design has only existed since the early 1960's. Progress, in terms of the number and range of flows predicted, has been slow but steady over the last two decades.

CURRENT STATUS

In the context of the design process, we can at present predict many 2-D or axisymmetric inlet flows and some 3-D inlet flows with sufficient accuracy for many engineering purposes. It is worth noting that the lead time for analysis development is very long. Most methods developed over the last decade are still in use and still under development. Experience has shown that the impact of a new analysis on the design process is to reduce the amount of wind tunnel testing required. New analyses usually do not displace previously useful analyses, which is a point usually not well understood by the research community. The designer will invariably use the simplest and least costly analysis applicable for a given flow. The availability of a powerful but expensive and difficult-to-implement Navier-Stokes procedure, for example, does not negate the usefulness of simpler procedures for design.

The current inlet flow analysis capability is illustrated below through several example flow predictions. These example flows include a subsonic V/STOL inlet at high angle-of-attack, a subsonic diffuser with a rectangular-to-round geometry transition and supersonic axisymmetric inlets operating at low speed, at transonic speed, and at cruise speed.

Example - Subsonic V/STOL Inlet - An asymmetric V/STOL inlet shown in Figure 5 was tested through a range of free stream Mach numbers, angles-of-attack and compressor face Mach numbers.[2] In the example flow selected, M_∞ = .19, the angle-of-attack was 60° and the compressor face Mach number was .39. This example illustrates that inviscid flow properties characteristic of a 3-D inlet geometry operating at high angle of attack with local regions of transonic flow can be accurately predicted. The 3-D full potential flow analysis of Forester[3] was used to compute the surface static pressure distribution through the inlet for the selected test case. This analysis features a body fitted mesh system, solution by SLOR and solution acceleration by Lyusternik extrapolation.

The computational mesh, Figure 6, was generated using a cubic connecting function mesh generator by Kowalski.[4] A number of grid densities and domain dimensions were investigated to ensure that the computed results were independent of the mesh and the solution domain. Note that the body fitted mesh system allows high mesh density to be focused in regions where high solution accuracy is required. Since the computational cost is a function of the total number of computational cells used, the ability to use a dense mesh in regions of interest and a sparse mesh where desired, results in a very efficient computational procedure. Computed results for the local surface Mach number in axial planes at three circumferential locations are shown in Figure 7. The results shown required about 30 min. CPU time on a Cyber 175 computer.

Example - Subsonic Diffuser with a Geometry Transition - Subsonic diffusers with geometry transitions were tested by MacMiller[5] to simulate the subsonic diffusers of supersonic aircraft with rectangular external compression inlets. In the selected example flow, the free stream Mach number at the diffuser entrance was .605 and the boundary layer thickness on all four surfaces of the rectangular diffuser entrance was .5 inches. This example illustrates that a diffuser flow with a geometry transition can be at least qualitatively predicted. A detailed evaluation of this (or any) procedure for this type of flow is not possible because suitable data is not available.

The 3-D parabolized Navier-Stokes procedure of Roberts and Forester[6] was used to compute this example flow. The analysis features a body fitted mesh system and simulation of turbulent stresses with a k-ε turbulent model. The solution is "marched" down the duct using an iterative ADI procedure. The computational mesh for the example problem was generated with a Thompson et al[7] mesh generator.

The duct geometry and computed results for the diffuser flow are shown in Figure 8. Again, mesh refinement was done to ensure the computed results were independent of the mesh. Agreement between predicted and measured static pressure distributions on the duct surface along the plane of symmetry is very good. Separation was observed experimentally about two thirds of the way along the duct and this was accurately predicted. Good agreement was obtained between computed and measured boundary layer pitot profiles along the plane of symmetry. This calculation required about 20 minutes CPU time on a Cyber 175 computer.

Example - Supersonic Inlet at Low Speed - An axisymmetric mixed compresion inlet, Figure 9, designed for a cruise Mach number of 2.65, will be tested at low speed in early 1982 as part of the NASA Supersonic Cruise Research program.[8] This low speed test program, to be conductd at the NASA Lewis 9x15 low speed wind tunnel, will be used to provide data on the noise, performance and aerodynamic characteristics of the inlet under low speed operating conditions. The inlet features a translating centerbody, traveling bleed system and take-off doors. In preparation for the low speed test, the inlet flow was analyzed at a number of free stream Mach numbers, inlet flow rates, and centerbody positions to determine the throat Mach number in the inlet as a function of these parameters. This example illustrates that a Navier-Stokes procedure can be practically applied to the analysis of low speed inlet flows.

The 2-D/axisymmetric Navier-Stokes procedure of Peery and Forester[9] was used to compute the desired inlet flows. Steady state solutions are obtained to the Navier-Stokes equations using an explicit time marching relaxation procedure. The analysis features the use of wall functions and zonal algebraic turbulence modeling for computational efficiency. Computed results for the Mach number distribution through the inlet with the centerbody fully retracted are shown in Figure 10 for free stream Mach numbers of 0. and 0.3. Note that with a static free stream Mach number the analysis predicts a lip separation and high throat flow distortion. At a free stream Mach number of 0.3, the lip separation has nearly disappeared and the throat flow is much more uniform. Work is underway on a mesh refinement study and the inclusion of a two equation turbulence model in the analysis. Detailed comparison of computed and measured flow properties through the inlet are planned when the test data becomes available.

Example - Supersonic Inlet at Transonic Speed - Flow interference between engine nacelles and an airframe has an important effect on the aerodynamic efficiency of an aircraft operating in the transonic speed regime. NASA conducted an extensive wind tunnel test program[10] to evaluate aerodynamic performance penalties associated with the propulsion system installation in the NASA Ames 11x11 foot wind tunnel. The model used, Figure 11, is a .024 scale model of the 1971 U.S. SST. The model selected for the present example had sharp-lip flow-through nacelles. The mass flow through each nacelle could be controlled by means of a variable position exit plug.

In the low supersonic speed regime and with inlet capture mass flow ratios less than one (spillage), it was found that a panel potential flow method alone provides a poor simulation of the wing surface pressure distribution and thus a poor simulation of nacelle interference effects on lift, drag and pitching moments. An example flow was selected at a Mach number of 1.4 and a mass flow ratio of 0.8 to illustrate that a Navier-Stokes procedure can be used with a panel method to provide an improved simulation.

Kulfan[11] simulated the model flow field with the PANAIR panel method. As shown in Figure 12, Kulfan used the Navier-Stokes procedure of Peery and Forester[9] in a small region near the inlet to predict the shock shape and location, local Mach number distribution and streamline pattern about the nacelle as a function of free stream Mach number and mass flow ratio through the inlet. The Navier-Stokes procedure was found to give an accurate simulation of the shock shape and stand-off distance for the range of upstream Mach numbers and mass flow ratios of interest, as shown in Figure 12. Kulfan then used the Navier-Stokes results to locate a stream tube about the nacelle where the flow on the stream tube surface was everywhere supersonic. As shown in Figure 13, Kulfan modified the PANAIR paneling to treat this stream tube as an inlet of larger diameter positioned further forward. The results of the PANAIR simulation, modified by the use of the Navier-Stokes procedure, are shown in Figure 14 for a Mach number of 1.4 and a capture mass flow ratio of 0.8. The new simulation gives a much improved prediction of the under surface pressure distribution.

Example - Supersonic Inlet at Cruise Speed - An axisymmetric mixed compression inlet similar to that shown in Figure 9 was tested at a Mach number of 2.65 as part of a NASA inlet technology development.[12] The inlet features a translating centerbody and a traveling bleed system. This

example was selected to show that a very accurate simulation of at least some high speed inlet flows is possible and that this capability has been available for at least a decade.

Reyhner and Hickcox[13] simulated this inlet flow with a procedure that uses method-of-characteristics to compute the core flow, a finite difference solution for the boundary layer development, and control volume analyses for the shock/boundary layer interactions. Boundary layer bleed is accounted for in the analysis as well as the displacement of the shock system due to viscous effects. With reference to the Historical Development section above, it should be noted that this analysis procedure was developed to support design of the inlet system for the American SST.

Comparisons between computed results and test data for the static pressure distributions on the cowl and centerbody are shown in Figure 15. Note that the combined flowfield solution procedure of Reyhner and Hickcox provides a very accurate simulation of the inlet static pressure distribution. The forward translation of the shock system due to viscous effects is also shown.

Comparisons between computed results and test data for boundary layer pitot profiles on cowl and centerbody surfaces at a number of axial locations are shown in Figure 16. The simulation accounted for boundary layer bleed and for shock/boundary layer interactions and agreement between computed results and test data is excellent. This good agreement is not accidental, as an extensive validation of each component of the overall analysis procedure was conducted before any attempt was made to construct the overall inlet analysis procedure.

PROBLEM AREAS

We are now progressively acquiring the capability to predict 3-D flows associated with inlets and with propulsion system installations in the subsonic, transonic and supersonic speed regimes. Geometry description has been and continues to be a problem in all speed regimes. Highly integrated blended installations imply geometries for which it is very difficult to obtain either an analytic description of the surface or the coordinates of points on the surfaces. The acquisition of an analytic surface representation or the surface coordinates are an essential step in the analysis of almost every flow of interest. Experience has shown that a substantial portion of the time spent in completing a given flow analysis is spent dealing with geometry.

Viscous flow phenomena are important in all speed regimes. With only a few exceptions, available turbulence models were developed for 2-D flow phenomena.[14] These models are currently being used to simulate 3-D flows without adequate validation and thus achieving only a mixed degree of success. Data for modeling or validation of 3-D viscous phenomena are generally not available or are to a large degree inadequate. Detailed experimental investigations of the following flows are essential if we are to extend our present inlet flow analysis capability in the supersonic regime to include inlets at angle-of-attack and 3-D inlet geometries:

o Glancing (3-D) shock/boundary layer interactions
o Swept shock/boundary layer or shear layer interactions
o BLC (bleed, V.G.'s, etc.) for 3-D boundary layers
o Separation
o Pressure driven secondary flows in ducts with offsets, diffusion and
  geometry variation

The final flow on this list is, of course, that of a subsonic diffuser with geometry variation and offset. This particular flow cries for a definitive experimental study because it is of current interest for many new military arcraft — especially those with an RCS constraint. As was shown above, procedures[6] exist which will qualitatively predict such flows. Effective use of these procedures for design is impeded by the current lack of detailed data.

Great care must be taken in the interpretation of computed results for viscous flows. Turbulence modeling has in many instances become a catch-all for numerical truncation errors (inadequate mesh density and/or a bad mesh-algorithm interaction), residual errors (inadequate convergence) or a poor selection of boundary conditions. In too many instances, a mesh is selected on the basis of the available computer storage, the maximum number of iterations selected to satisfy a budget constraint, and any differences between computed and measured results attributed to the turbulence modeling. The high cost of computing 3-D flows with adequate numerics make the use of such erroneous procedures very attractive. We should be careful not to buy the "fools gold" of carelessly conducted and interpreted studies.

In the numerics area, although large class 6 computers are now becoming widely available, the high cost of computing many flows of practical interest impedes the use of CFD for inlet design. Experience indicates that the cost of acquiring design information analytically must be less than about 10% of the cost of an equivalent wind tunnel simulation if parametric analysis is to be considered for a design study. Formal methods need to be developed to define automatically the residual and truncation errors associated with a numerical procedure for a given mesh. The process of acquiring such information is at present very tedious and as noted above, the failure to conduct such studies has led to problems in the interpretation of computed results. Methods should be developed to adjust the grid adaptively to satisfy input limits on residual and truncation error.

Interest in computing aircraft/inlet flow interactions has focused attention on the use of zonal modeling techniques since such flows are generally beyond the capacity of the largest available computers with a single procedure. While zonal modeling makes the calculation of such flows possible by dividing the flow field of interest into subdomains each with an appropriate analysis (the PANAIR/Navier-Stokes coupling used in the nacelle interference example above), much work needs to be done to develop zonal modeling techniques for design. For many flows, solution domains must overlap and the solutions in the various subdomains must be iterated. The selection of subdomain boundaries, the handling of boundary conditions, mesh generation, interpolation of properties between non-coincident meshes in regions of overlap, and the acquisition of numerical error information as the solution progresses are all important questions to be answered if zonal strategies are to be utilized.

In many instances, the designer is not able to apply the available analysis capability effectively in a design study. Many flows that can be computed are difficult for even the experienced fluid analyst. How can a designer hope to compute such flows in the context of a design study? One possible method is to make available the analysis capability through a group of expert users. The designer doesn't expect the keys to the wind tunnel when he wants design information from an experimental study. He should also not expect the keys to the computer building when design information is wanted from an analysis study.

Another problem is that computer codes useful for design have not proven to be very portable as noted in a March 9, 1981 article in Business Week. Flow codes developed for industry by government or university researchers unfamiliar with the intended application are invariably deficient for design studies. Experience indicates that the intended user should work very closely with the code developer to ensure the code developed satisfies the user's needs. Progress in the use of analysis for design has been much slower than necessary because of the general failure of industry, government and university researchers to cooperate effectively to produce flow codes for design. Computer system differences and code requirements which vary from user-to-user contribute to the problem.

SUPERSONIC INLET FLOWS - CURRENT APPROACHES

A review of current analysis approaches to inlet flows in all speed regimes is beyond the scope of the present paper. Because inlets operating in the supersonic speed regime are of high current interest, a brief discussion of the more popular approaches to the analysis of these flows is included in the present article. Current approaches can be grouped into three categories:
- o Zonal modeling
- o Navier-Stokes
- o Space marching

Because these approaches are at different stages of development, conclusions as to the relative merits of the approaches are not drawn. An example and a discussion of each of these approaches follows below.

Zonal Modeling - As noted above, a zonal modeling strategy was used very successfully to develop an inlet system for the American SST. This procedure has been further developed and refined over the last decade as shown in Figure 17. The procedure was applied to the design of a Mach 3.5 axisymmetric mixed compression inlet and bleed system in the mid-1970's.[15] The application of this procedure resulted in a detail definition of the bleed system geometry, such as number of bleed holes, hole size, hole spacing, and bleed exit area, for each individual bleed region. The bleed mass flows, bleed plenum pressures and the effect of the individual bleed regions on the boundary layer development were also predicted. These predictions were made not only at the design Mach number but across the entire started Mach number range. A wind tunnel test of a 1/3 scale model of the analytically designed inlet showed excellent agreement with the theoretical predictions, thus validating the analytical design procedure. Work is underway at Boeing to extend this analysis procedure to predict the flow of an axisymmetric mixed

compression inlet at angle-of-attack. This work, part of the NASA Supersonic Cruise Research program, was selected as an example of a zonal approach to a difficult supersonic inlet flow. The improved analysis will provide flow properties for inlet design, instrumentation definition and digital control system using a detailed inlet simulation in a model following controller concept and for control signal synthesis. It will also improve the inlet design and control procedures by allowing inlet performance to be computed at off design conditions.

The planned analysis for the inlet at angle-of-attack is illustrated in Figure 18. A 3-D method-of-characteristics program[16] will be used for the core flow. Boundary layer and shock/boundary layer interaction programs are being developed for the viscous flow development through the supersonic diffuser. The 3-D parabolized Navier-Stokes procedure of Roberts and Forester[6] will be used for the subsonic diffuser.

The NASA Mach 2.65 "P" inlet bleed system has been redesigned and the inlet instrumented and tested at a number of Mach number and angle of attack conditions to provide validation data for the overall analysis procedure, when complete. Detailed experimental studies of the swept and normal shock/boundary layer interactions have been proposed to NASA and a detailed experimental study of the subsonic diffuser will be proposed.

The asymmetry of the shock structure in an axisymmetric mixed compression inlet at angle-of-attack is shown in Figure 19. Note the substantial modification of the shock structure induced by a small (3^0) angle-of-attack at Mach 3.0. The shock structure at angle-of-attack was computed with the 3-D method-of-characteristics program.[16]

Navier-Stokes - A numerical procedure under development by Knight[17] for the simulation of 2-D mixed compression inlet flows for the Air Force was selected as an example of a Navier-Stokes approach. Knight's analysis solves the compressible Navier-Stokes equations using the explicit finite difference operator of MacCormack. The method features an algebraic eddy viscosity turbulence model and a body fitted mesh system. Boundary layer bleed is accounted for in the analysis. The method has been validated for flat plate boundary layer and 2-D shock/boundary layer interaction flows.

Knight[18] applied this two-dimensional procedure to a rectangular high speed inlet investigated experimentally by Carter and Spong.[19] As shown in Figure 20, the model consisted of a supersonic diffuser formed by two plates at an angle to one another followed by a constant area throat. The upper and lower surfaces were considered analogous to ramp and cowl surfaces of a high speed inlet. The "cowl" plate was hinged to permit variation of the cowl angle, δ_c. Boundary layer bleed was used on the ramp and cowl surfaces and on the inlet sideplates to control the boundary layer development on these surfaces.

A comparison between computed results and experimental data for the cowl and ramp surface pressure distributions is presented in Figure 20. For this case, the free stream Mach number was 3.5 and δ_c was 6^0. Good agreement was obtained between computed and measured static pressure for the first shock interactions on both the ramp and cowl surfaces. The analysis substantially underpredicts the static pressure rise through the second and third shock

interactions on the ramp and through the second shock interaction on the cowl. The analysis also appears to "smear" the static pressure distribution in the vicinity of these interactions.

A comparison between computed and measured pitot profiles on the ramp and cowl surfaces is presented in Figure 21. Good agreement was obtained for the stations reported.

This analysis required several hours CPU time on a Cyber 175 computer. Work is underway to vectorize the algorithm for the NASA Langley STAR computer which should substantially reduce the cost of the analysis.

Space Marching - A 3-D numerical procedure by Buggeln et al[20] was selected as an example of a space marching analysis. In this analysis, a primary flow direction is assumed and diffusion in that direction is neglected. The simplified equations which retain the viscous stress terms are solved using a marching procedure. The analysis features the use of a curvilinear orthogonal coordinate system and a mixing length turbulence model. The total enthalpy is assumed constant through the solution region to avoid solving an energy equation.

Anderson and Towne[21] applied the analysis to a two-dimensional (rectangular) inlet configuration, Figure 22, at Mach 3.0. This inlet flow, at a high Reynolds number, had a complex internal shock structure and a large "core" of inviscid flow. Anderson ran three mesh densities for the inlet. The finest mesh had over 70,000 grid point, however, only six mesh planes were used between the sidewall and the symmetry plane. The total computing time on a UNIVAC 1100/42 was about 3 hours for the finest mesh.

Computed Mach number profiles for coarse and medium mesh solutions are shown in Figure 22. The predicted shock system appears to move forward as the mesh is refined. A comparison between computed and measured cowl and ramp static pressure distributions is shown in Figure 23. Good agreement was obtained for both meshes with the experimental data.

Each of the above procedures under development for analysis of supersonic inlet flows offers advantages and disadvantages. The advantages of the zonal approach are that it is well understood, very efficient, and it is usually easy to sort out cause and effect relationships in a design study. This usually means deciding whether to change the contours or the bleed system for optimum performance. Disadvantages are that a complex coupling of the component analyses is required, the analysis is restricted in application to only a few types of geometries, and a number of flow phenomena of practical interest cannot typically be predicted (local separation or a local subsonic pockets).

The advantages of the Navier-Stokes procedures are that modeling of complex viscous-inviscid interactions is unnecessary and that no restrictions (theoretically) are placed on the flow phenomena or geometries which can be computed. Major disadvantages are the high cost, difficulty in recognizing and controlling numerical errors, the difficulty of applying the analysis successfully, and the difficulty in making "bleed vs geometry" modification decisions.

The potential advantages of space marching procedures are that complex viscous inviscid interactions don't have to be modeled and that only a few restrictions (no separation) are placed on flows or geometries which can be analyzed. While this approach is less developed than the others, the computing costs reported are disappointing. The method also appears to position the shocks at shock/boundary layer interactions too far downstream. Whether this can be corrected by mesh refinement (or other means) remains to be determined.

PROMISING DEVELOPMENTS

Events which should lead to a significant improvement in our present inlet flow analysis capability are:
- o 1980-81 AFOSR-HTTM-Stanford Conference on Complex Turbulent Flows
- o New schemes to improve the efficiency of numerical solution procedures
- o Wide availability of Class 6 computers

The Stanford Conference will make available a number of data sets reviewed and selected by the leading experimentalists to support either improved modeling or code validation. Current numerical procedures and turbulence models will be applied to these data. The computed results will be evaluated to gain insight into where further modeling or experimental work is required. The Stanford Conference could be a significant step toward improved modeling of 3-D viscous flow phenomena. A strategy should, however, be developed so that improved modeling of 3-D flows of interest is not left to chance.

Tremendous progress has been reported recently toward the development of algorithms which could reduce the cost of computing difficult flows down to a level practical for design. These include implicit algorithms, self adaptive meshes, and multigrid schemes. Automated numerical error assessment is essential if we are to make much of the present analysis capability available for design.

Class 6 computers are now commercially available. Vectorization of existing algorithms on these computers has resulted in about an order-of-magnitude reduction in the CPU time necessary for a given problem. The large fast core available on these machines implies that greater mesh densities or larger flow regions can be computed than before. The combination of the new large computers and improved numerical algorithms should lead to a substantial improvement in the range of flows which can be computed as well as a marked reduction in the cost of computing a given flow.

CONCLUSIONS AND RECOMMENDATIONS

There is an increasing trend toward the use of parametric analysis rather than parametric testing for inlet design. This trend, driven by the high cost of wind tunnel testing, is expected to continue. We can, at present analyze many 2-D and some 3-D inlet flows. Many of the available flow analyses are, however, not being utilized for design. The high skill level required to successfully apply many existing flow analyses effectively blocks their use for design.

Greater care must be taken to ensure that computed flow properties are not contaminated with numerical errors. Analyses should be applied only to those flow phenomena for which they have been validated. Adequate experimental validation data for many flows (especially 3D flows) of current interest is not available.

REFERENCES

1. Tjonneland, E., "The Design, Development and Testing of a Supersonic Transport Inlet System,"

2. Syberg, J. and Koncsek, J. L., "Low Speed Tests of a Fixed Geometry Inlet for a Tilt Nacelle V/STOL Airplane," NASA Contract Report NASA CR-151922, January 1977.

3. Forester, C. K., "Body Fitted 3-D Full Potential Flow Analysis of Complex Ducts and Inlets," AIAA Paper 81-0002, presented to the 19th Aerospace Sciences Meeting, January 12-15, 1981.

4. Kowalski, E. J., "Boundary Fitted Coordinate Systems For Arbitrary Computational Regions," Workshop on Grid Generation, NASA Langley Research Center, October 6-7, 1980.

5. MacMiller, C. J., "Investigation of Subsonic Duct Distortion," AFFDL-TR-69-21, 1969, pp. 218-221.

6. Roberts, D. W., and Forester, C. K., "Parabolic Procedure for Flow in Ducts with Arbitrary Cross-Sections," AIAA J., V. 17, No. 1, pp. 33-40, January 1979.

7. Thompson, J. F., Thames, F. C., and Mastin, C. W., "Automatic Numerical Generation of Body Fitted Curvilinear Coordinate System for Field Containing Any Number of Two-Dimensional Bodies," J. of Computational Physics, V. 15, 1974, pp. 299-319.

8. Syberg, J. and Turner, L., "Supersonic Test of a Mixed Compression Axisymmetric Inlet at Angles of Incidence," NASA CR 165686, April 1981.

9. Peery, K. M. and Forester, C. K., "Numerical Simulation of Multi-Stream Nozzle Flows," AIAA J., V. 18, No. 9, September 1980, pp. 1088-1093.

10. Bencze, D. P., "Wind Tunnel Investigation of Nacelle Airframe Interference of Mach Numbers of 0.9 to 1.4", NASA TMX-62, 489, 73, 147, 088, 3321; 1976-1977.

11. Kulfan, R. M. and Sigalla, A., "Airframe Propulsion System Aerodynamic Interference Predictions at High Transonic Mach Numbers Including Off-Design Engine Airflow Effects," AGARD Symposium on Aerodyamics of Power Plant Installation, Toulouse, France, May 1981.

12. Koncsek, J. L. and Syberg, J., "Transonic and Supersonic Test of a Mach 2.65 Mixed Compression Axisymmetric Intake," NASA CR-1977, March 1972.

13. Reyhner, T. A. and Hickcox, T. E., "Combined Viscous-Inviscid Analysis of Supersonic Inlet Flowfields," AIAA J. of Aircraft, V. 9, No. 8, August 1972, pp. 589-595.

14. Birch, S. F., "Turbulence Models - Progress and Problems," Computer Methods in Fluids, Pentech Press Ltd., 1980, pp. 285-307.

15. Syberg, J. and Koncsek, J. L., "Experimental Evaluation of a Mach 3.5 Inlet," NASA Cr-2563, July 1975.

16. Vadyak, J. and Hoffman, J. D., "Calculation of the Flowfield in Supersonic Mixed-Compression Inlets at Angle-of-Attack using the Three-Dimensional Method of Characteristics with Discrete Shock Wave Fitting," NASA CR-135425, June 1978.

17. Knight, D. D., "Improved Calculation of High Speed Inlet Flows. Part 1: Numerical Algorithm," AIAA J., V. 19, No. 1, January 1981, pp. 34-41.

18. Knight, D. D., "Improved Calculation of High Speed Inlet Flows. Part II: Results," AIAA J., V. 19, No. 2, February 1981, pp. 172-179.

19. Carter, T. D. and Spong, E. D., "High Speed Inlet Investigation. Vol. I: Description of Program and Results. Vol. II: Data Summary," AFFDL-TR-77-105, November 1977.

20. Buggeln, R. C., Kreskovsky, J. P. and McDonald, H., "Computation of Three-Dimensional Viscous Supersonic Flow in Inlets," AIAA paper 80-0194, January 1980.

21. Anderson, B. H. and Towne, C. E., "Numerical Simulation of Supersonic Inlets Using a Three-Dimensional Viscous Flow Analysis," AIAA Paper 80-0384

DESIGN PROCEDURES FOR PROPULSION INSTALLATIONS

TO DEVELOP A GIVEN DESIGN CONCEPT . . . .

TRADITIONAL APPROACH

- DESIGN CONCEPT
- PARAMETRIC MODEL TESTS
- SELECT CONFIG. FOR FULL SCALE VALIDATION AND OPTIMIZATION
- FULL SCALE TESTS
- FINAL DESIGN

ITERATE IF REQ'D

ANALYSIS BASED APPROACH

- DESIGN CONCEPT
- PARAMETRIC ANALYSIS
- SELECT CONFIG. FOR VALIDATION
- MODEL SCALE ANALYSIS AND TEST TO VALIDATE USE OF ANALYSIS (OPTIONAL)
- FULL SCALE VALIDATION TEST
- FINAL DESIGN

ITERATE IF REQ'D

$\neq$
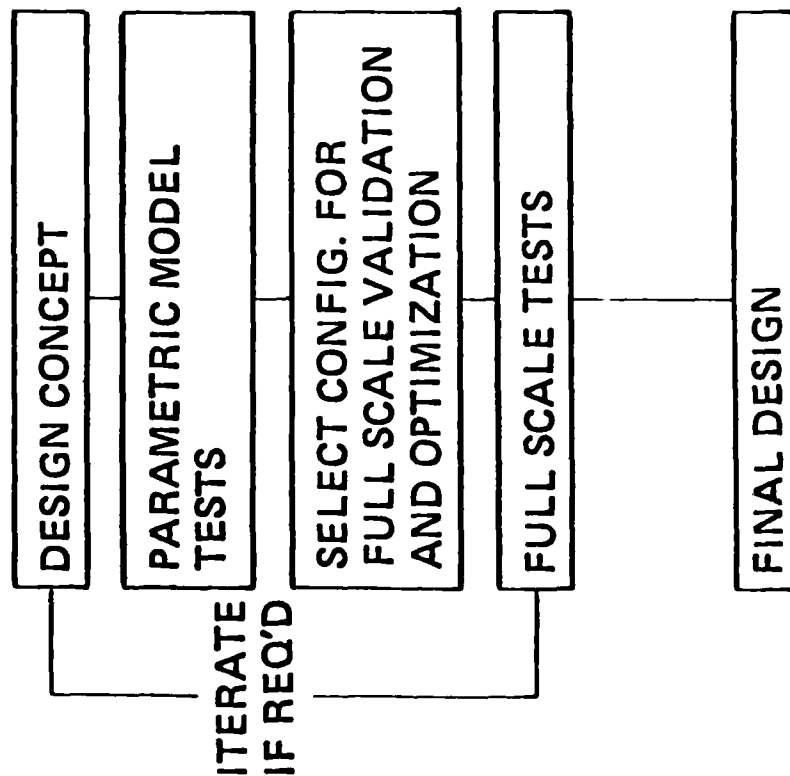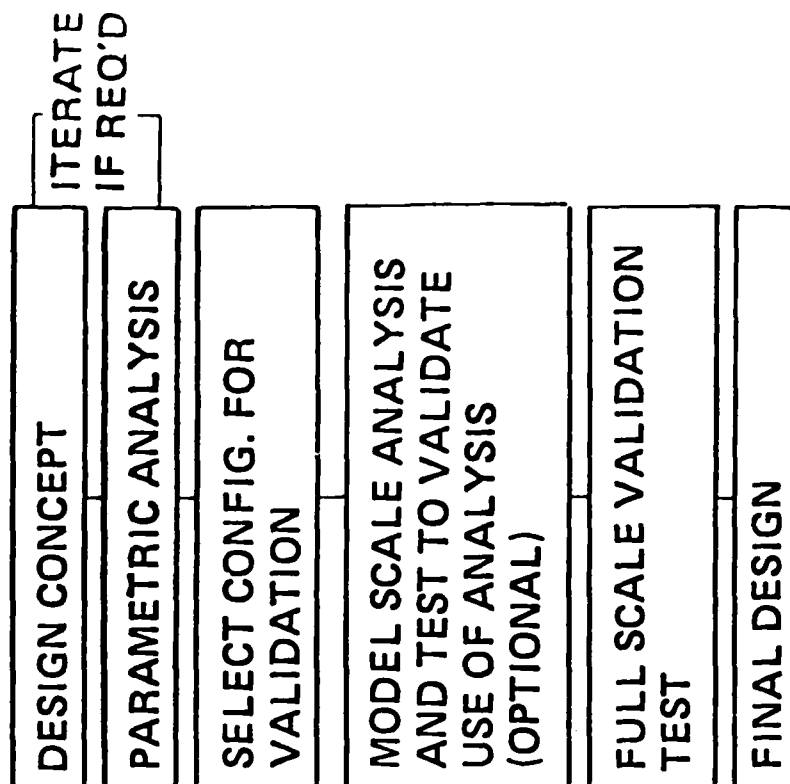
PERFORMANCE + COST

FIGURE 1.

II-14

FIGURE 2. ADVANCED AIRCRAFT CONCEPTS

EVOLUTION OF THE INLET
DESIGN PROCEDURE

USED
- 1-D ANALYSIS
- 2-D INCOMP. POTENTIAL FLOW
- PARAMETRIC MODEL AND FULL SCALE VALIDATION TESTS

1965

INITIAL DESIGN

USED
- 1-D ANALYSIS
- 2-D SUBSONIC POTENTIAL FLOW ANALYSIS
- 2-D BOUNDARY LAYER ANALYSIS
- PARAMETRIC MODEL AND FULL SCALE VALIDATION TESTS

1971

REDESIGN FOR NOISE SUPPRESSION

WOULD USE
- 1-D ANALYSIS
- 2-D COUPLED B.L. AND POTENTIAL FLOW ANALYSIS (TRANSONIC)
- 3-D B.L. AND TRANSONIC POTENTIAL FLOW ANALYSIS
- COMPUTER GRAPHICS FOR RAPID DISPLAY OF PREDICTED INLET FLOW AND PERFORMANCE CHARACTERISTICS
- FULL SCALE VALIDATION TEST

1981

IF INLET WAS TO BE REDESIGNED

FIGURE 3.

II-16

Historical Development
Numerical Fluid Mechanics
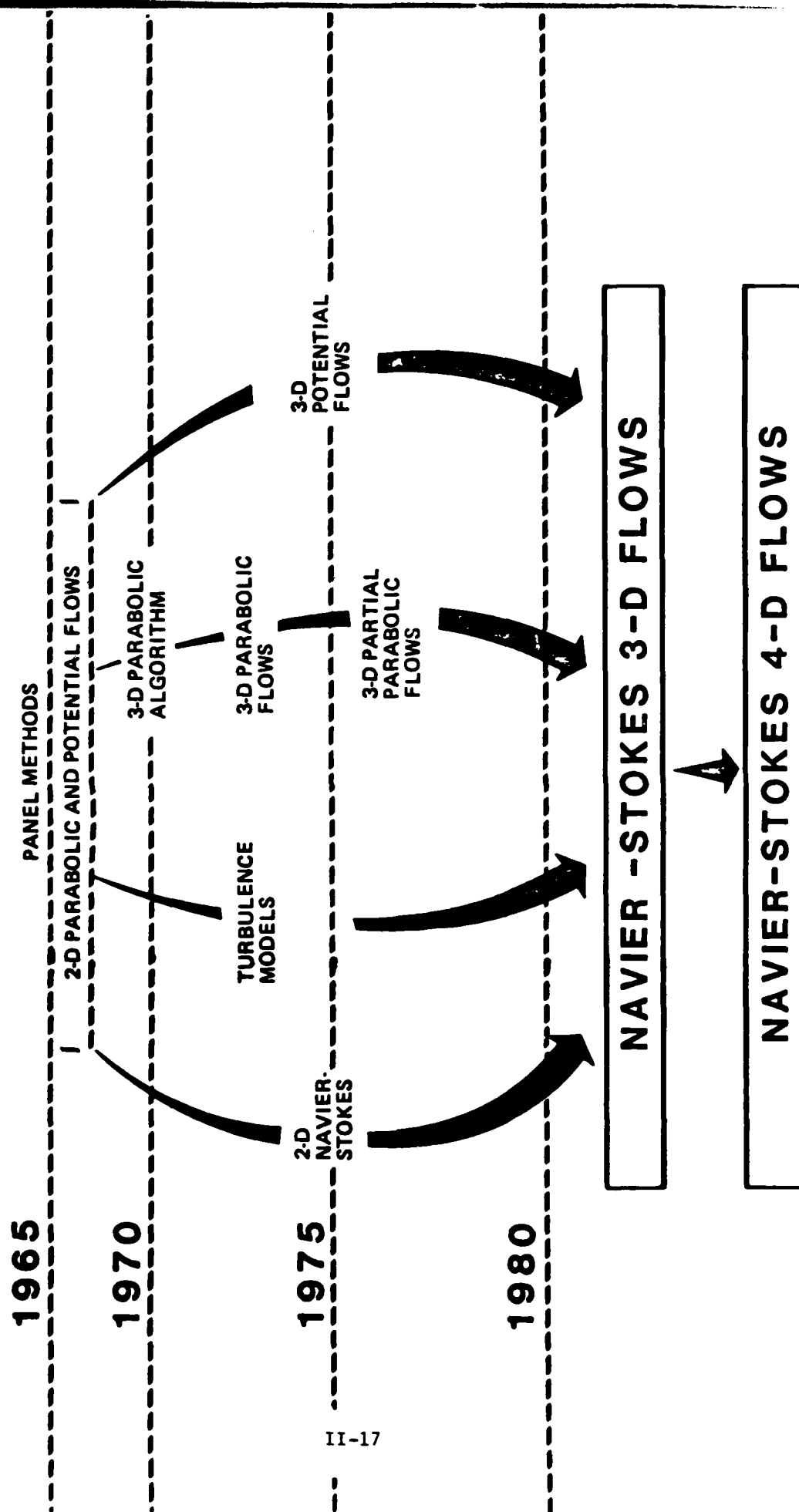
FIGURE 4.
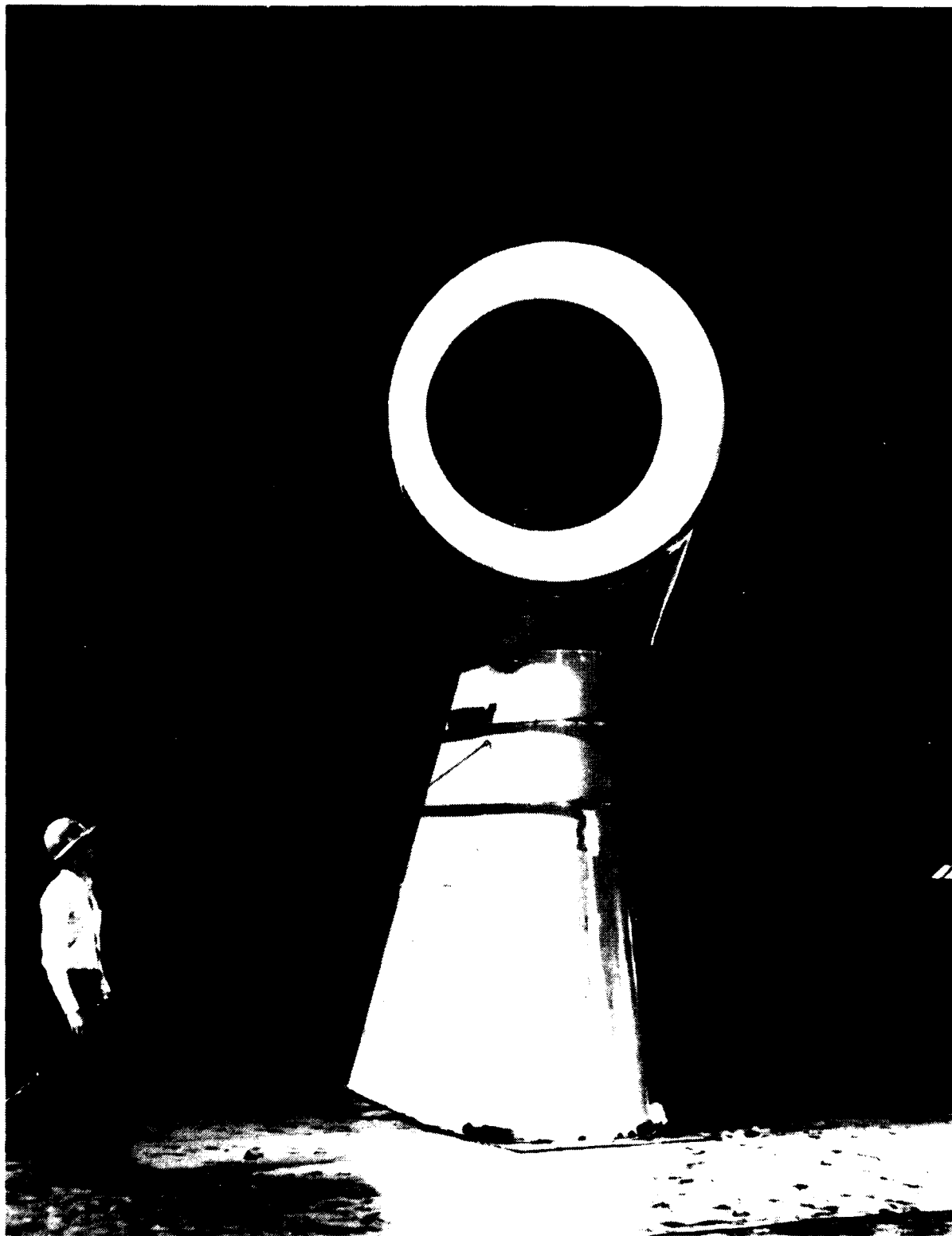
FIGURE 5. **Asymmetric V/STOL Inlet Model**

0° 180°
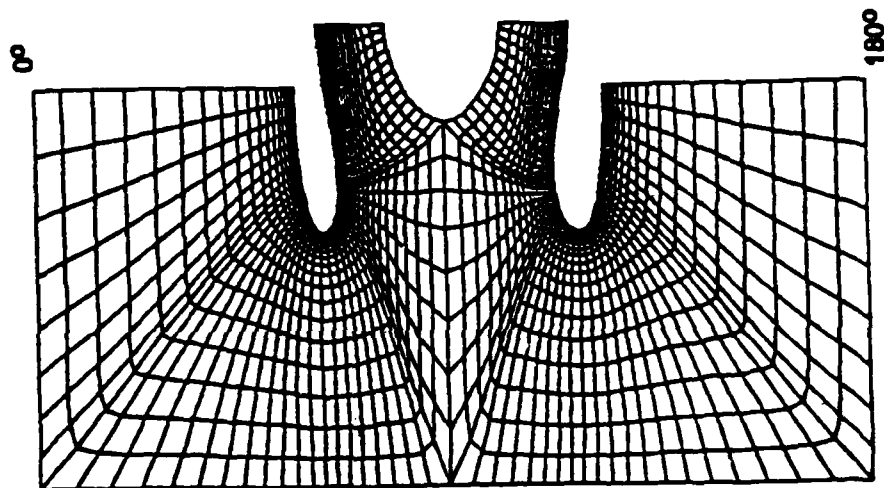
FIGURE 6. THE COMPUTATIONAL MESH

Cowl Surface Mach Number Distribution for an Asymmetric V/STOL Airplane Inlet.

FIGURE 7.

STATIC PRESSURE RISE
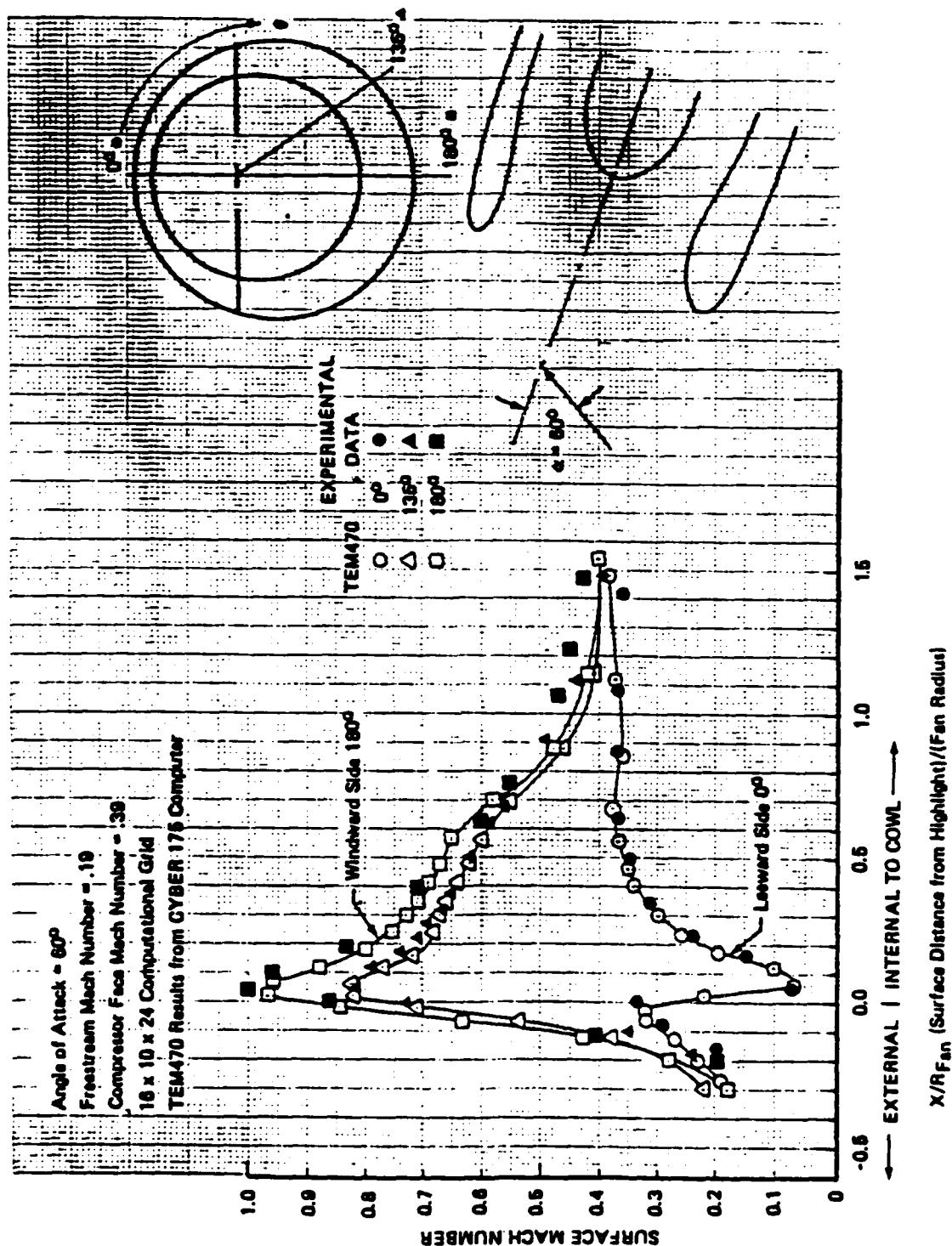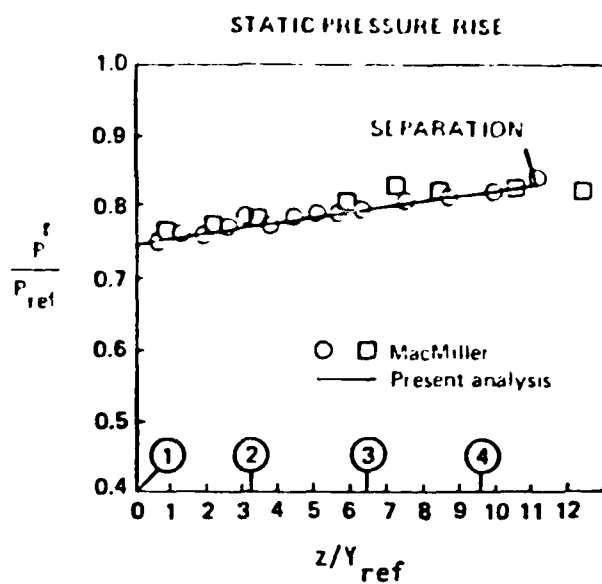
RECTANGULAR TO ROUND DIFFUSER

TOTAL PRESSURE PROFILES
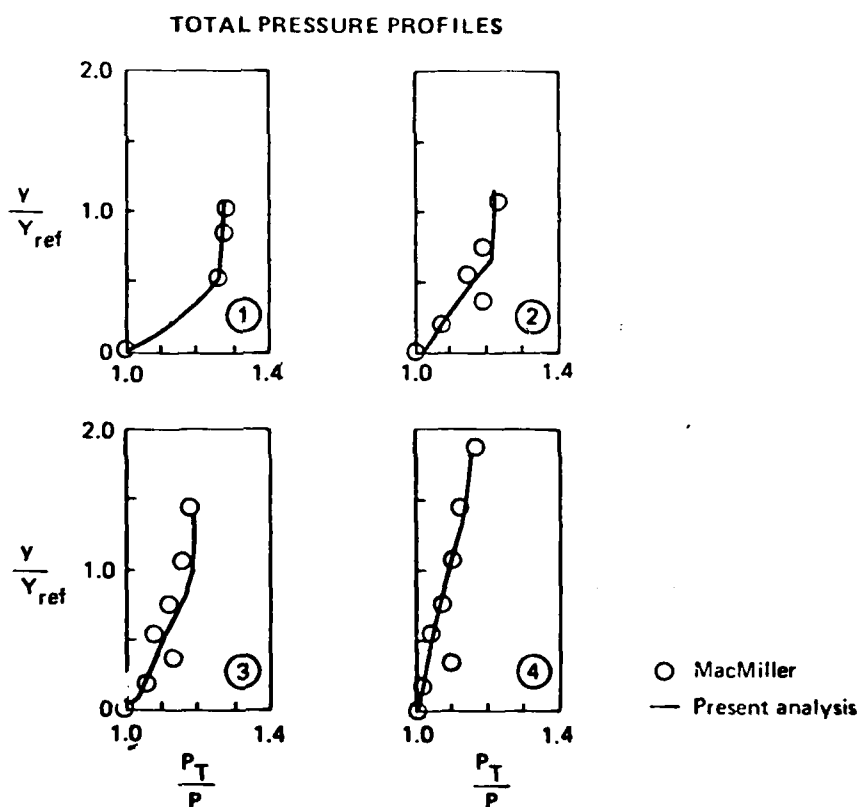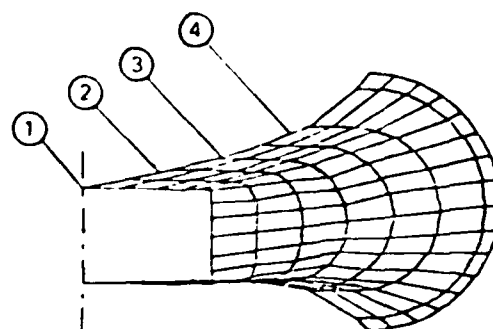
Figure 8.   Analysis Results for a Diffuser With a Cross-Section
             Geometry Transition
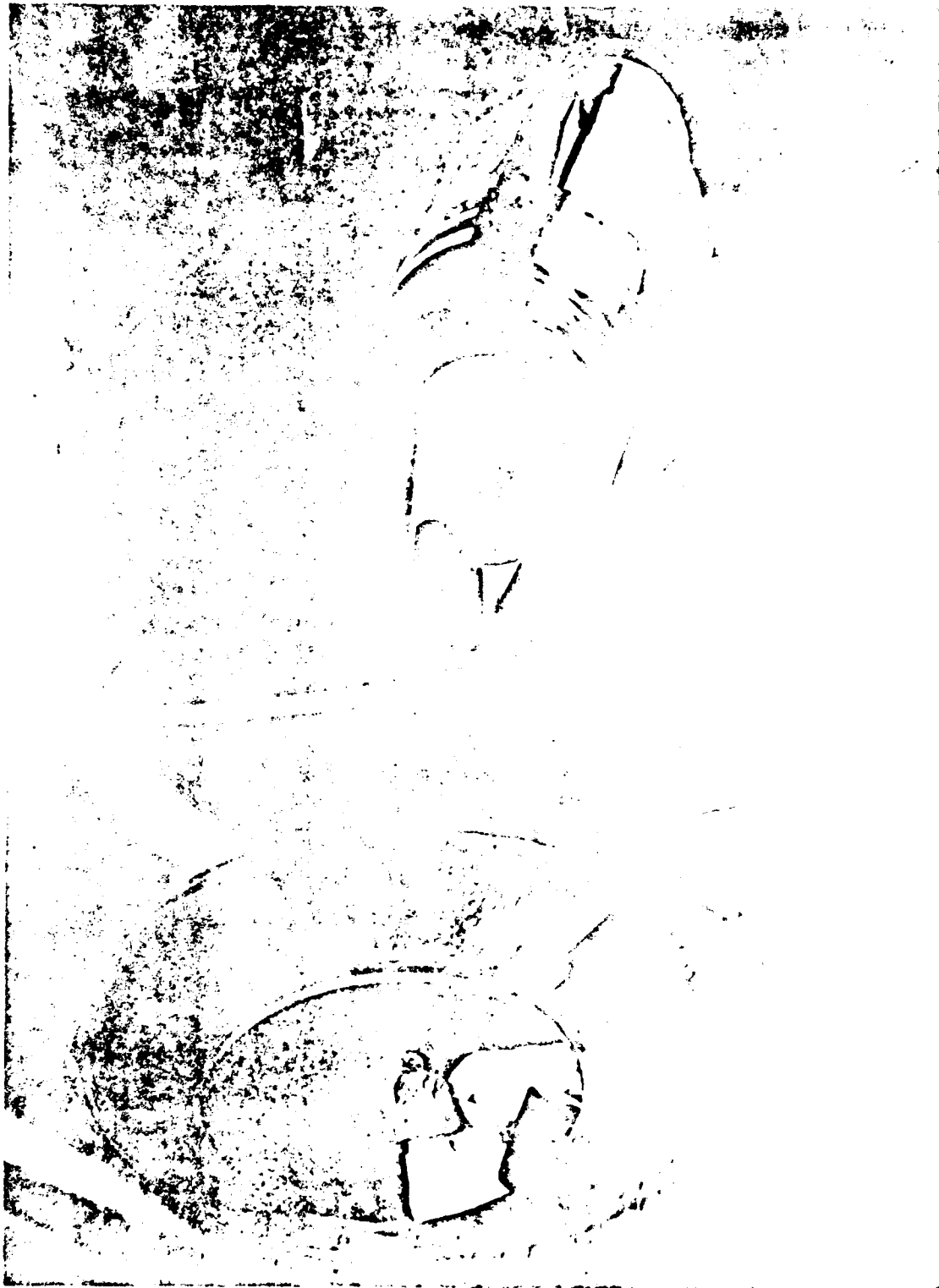
Figure 9. P-Inlet Installed in NASA-Lewis 10- by 10-ft Supersonic Wind Tunnel

Supersonic Cruise Inlet Mach Number Profiles
Noise Abatement Mode—Spike Fully Retracted

MACH = 0.3
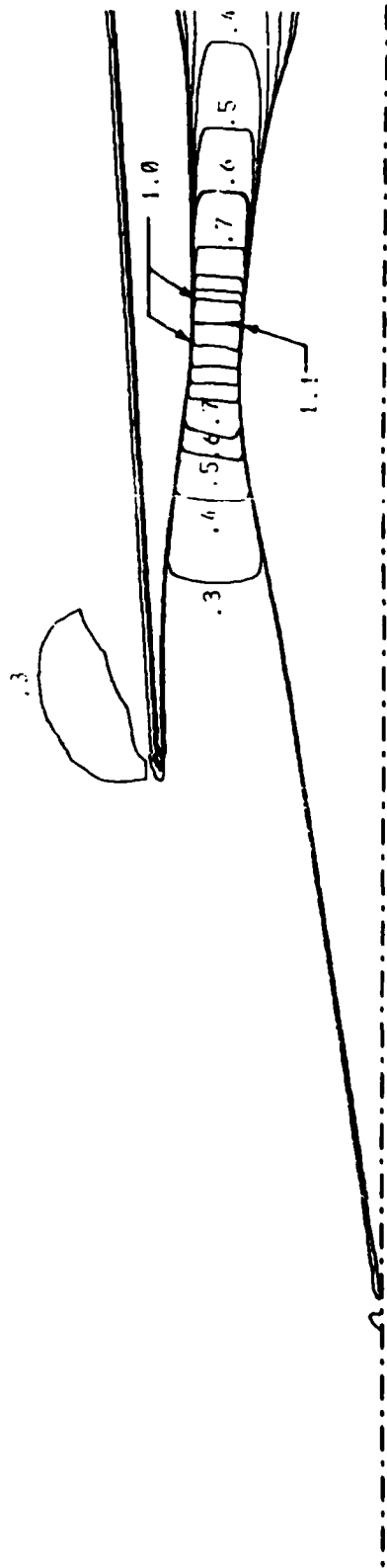
MACH = 0.0
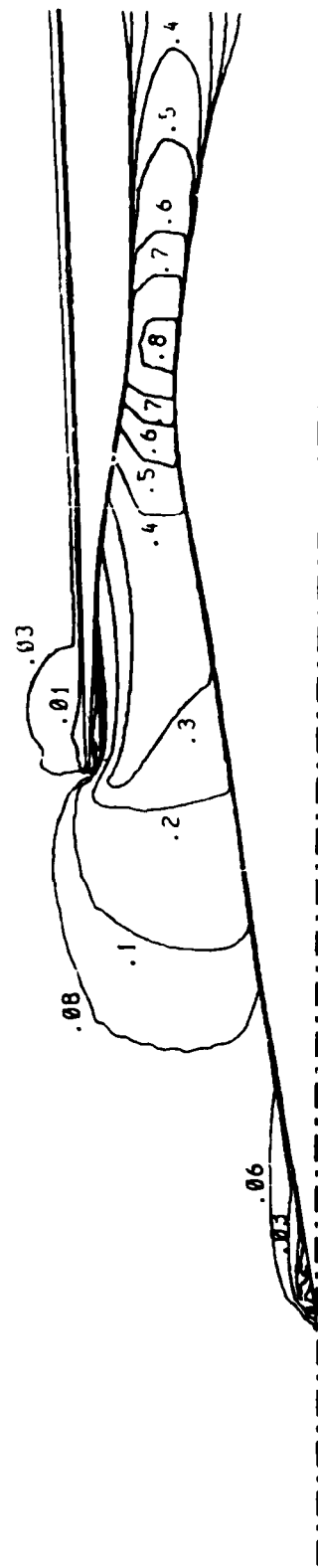
BOEING

FIGURE 10.

NASA NACELLE AIRFRAME INTERFERENCE
WIND TUNNEL MODEL

FIGURE 11.

VERIFICATION OF THE MIXED-FLOW THEORY

REGION OF INLET FLOW FIELD ANALYSES

5 deg

R_1

Date reference: ● NACA RM L56C28

Theory: ● Boeing Mixed-Flow Axisymmetric Flow Program (TEM-367)

FIGURE 12.

COMPARSION OF PREDICTED BOW-SHOCK SHAPES FOR MASS-FLOW RATIOS OF 0.7 AND 0.8 AT MACH 1.4
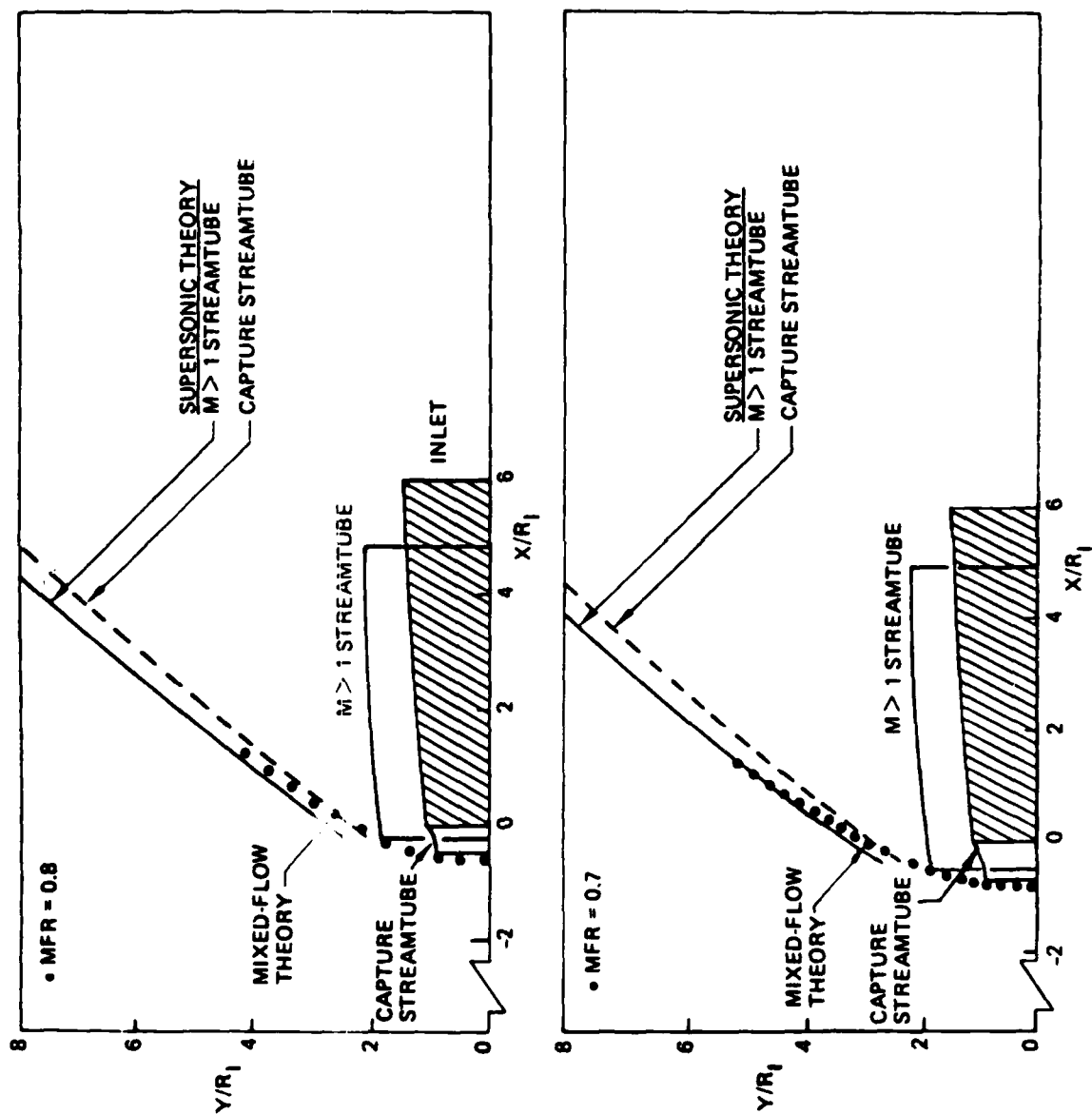
FIGURE 13.

EFFECT OF NORMAL-SHOCK SPILLAGE ON ISOLATED NACELLE PRESSURES &WING LOWER SURFACE PRESSURES AT MACH 1.4, ZERO ANGLE OF ATTACK, & A MASS FLOW RATIO OF 0.8

THEORY: SUPERSONIC THEORY WITH
CAPTURE STREAMTUBE
PSEUDO-NACELLE GEOMETRY
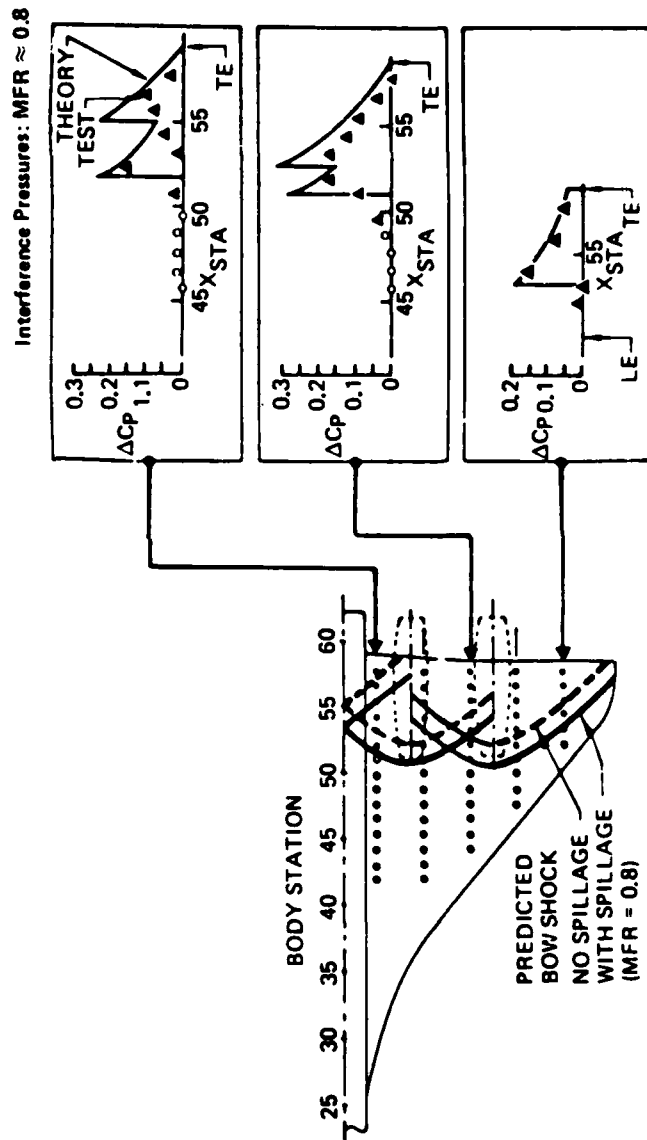
FIGURE 14.

Comparison of analytic predictions with experiment for cowl static pressure distribution (Ref. 6, $M_\infty = 2.65,$)
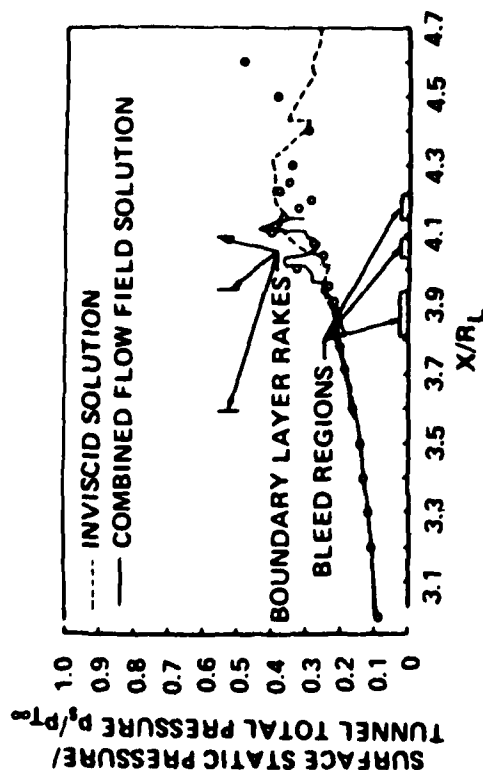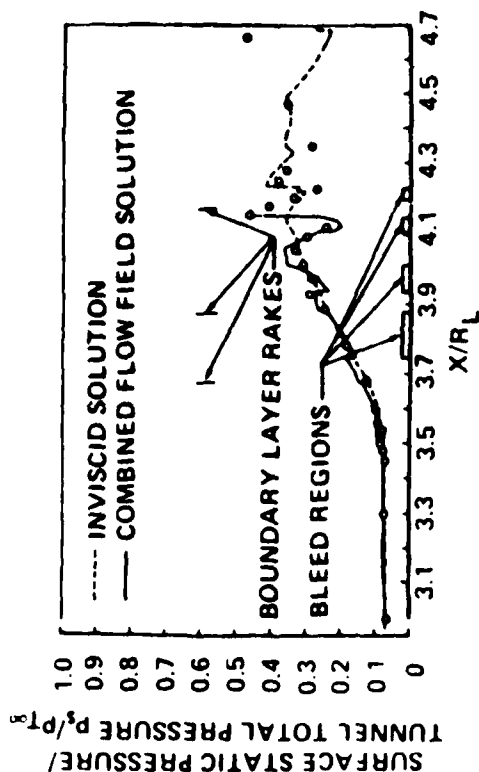
Comparison of analytic predictions with experiment for centerbody static pressure distribution (Ref. $M_\infty = 2.65,$)
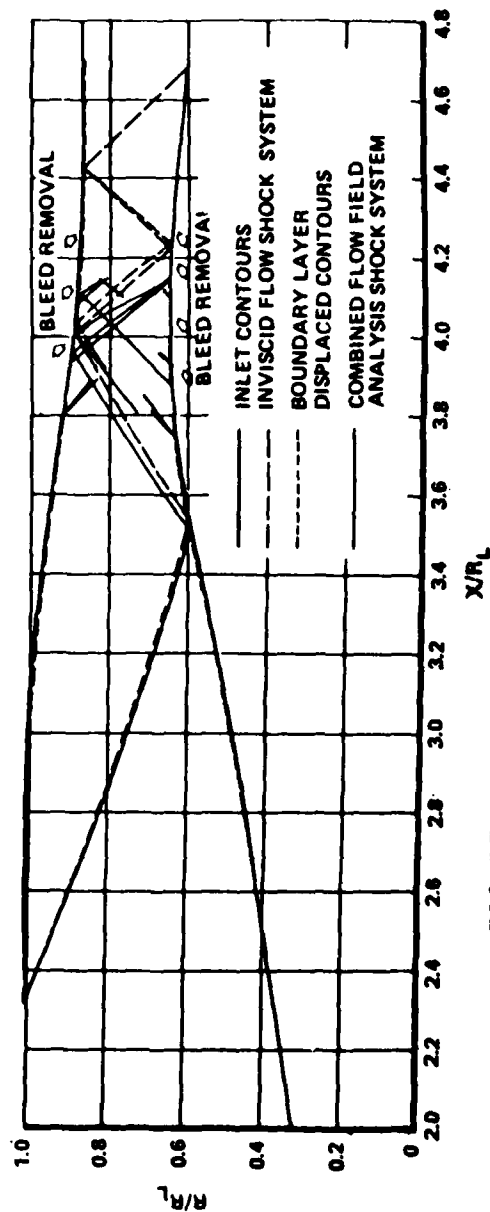
Comparison between inviscid flow and Combined Flowfield Analysis predictions for shock and expansion wave locations (Ref. $M_\infty = 2.65,$)

FIGURE 15. COWL AND CENTERBODY PRESSURE DISTRIBUTIONS FOR A MACH 2.65 AXISYMMETRIC INLET

Comparison of predicted boundary layer with experimental
results (Ref. $M_c = 2.65$.
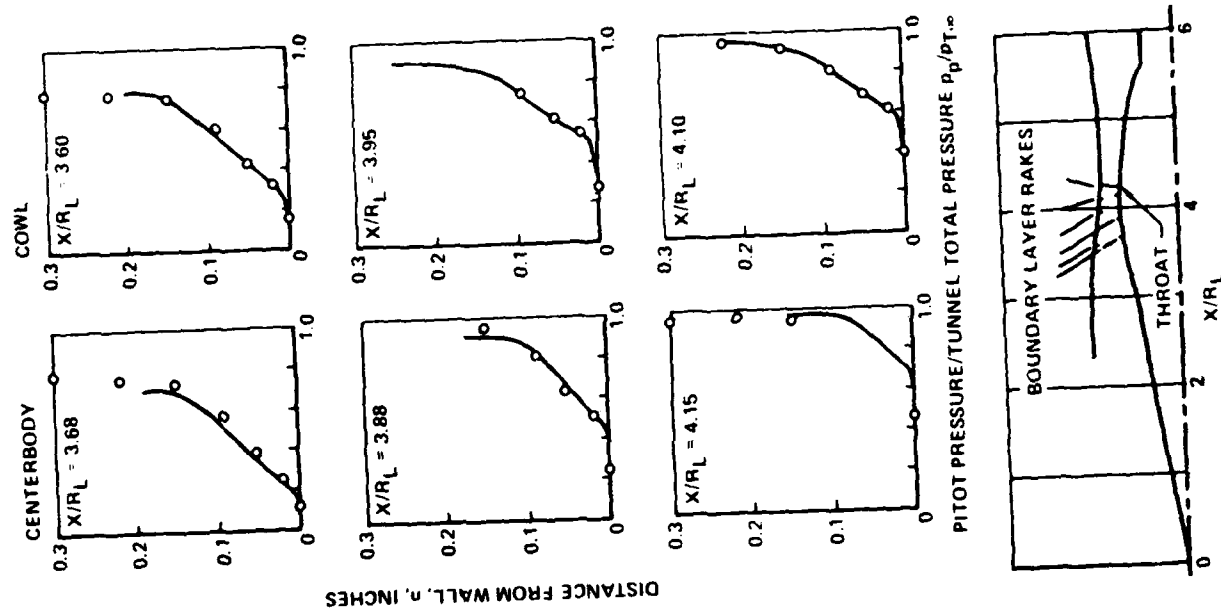
FIGURE 16.

Boeing Supersonic Inlet Technology Programs

	1967	1968	1969	1970	1971	1972	1973	1974	1975	1976	1977
SST INTAKE DEVELOPMENT											
JOINT AMES-BOEING INLET PROGRAM				'P' INLET							
DOT SST FOLLOW-ON PROGRAM											
NASA-AMES MACH 3.5 INLET PROGRAM											
BLEED SYSTEM DESIGN FOR HIGH MACH INLETS											
AST INLET ANALYTICAL DESIGN											

FIGURE 17.

BOEING

II-30
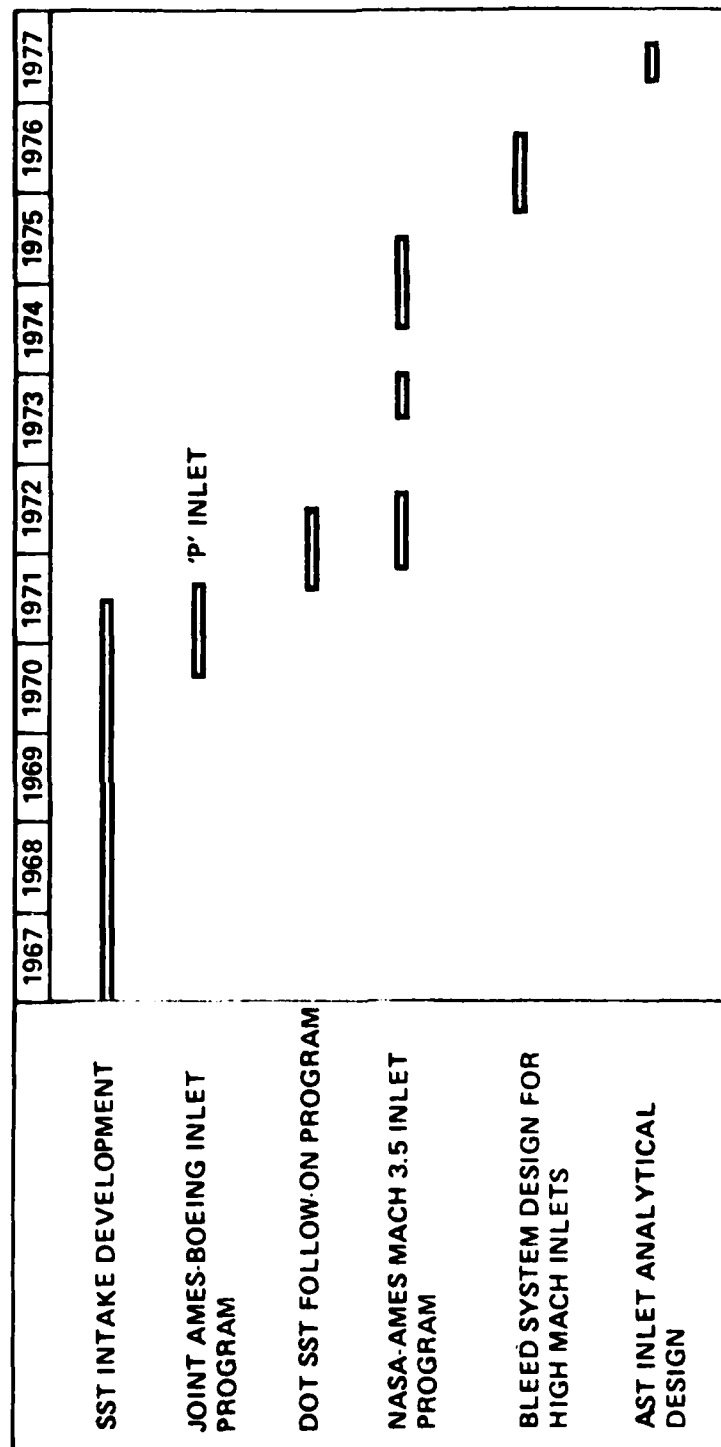
Analysis of Inlet Flow at Off-Design

NASA·SCR

3-D SHOCK/BOUNDARY LAYER INTERACTIONS

3-D SUBSONIC DIFFUSER FLOW

3-D INVISCID CORE FLOW

3-D BOUNDARY LAYERS

α

BOEING

FIGURE 18.

$M = 2.5, \alpha = 3$ deg

Freestream flow

Offset caused by angle of attack
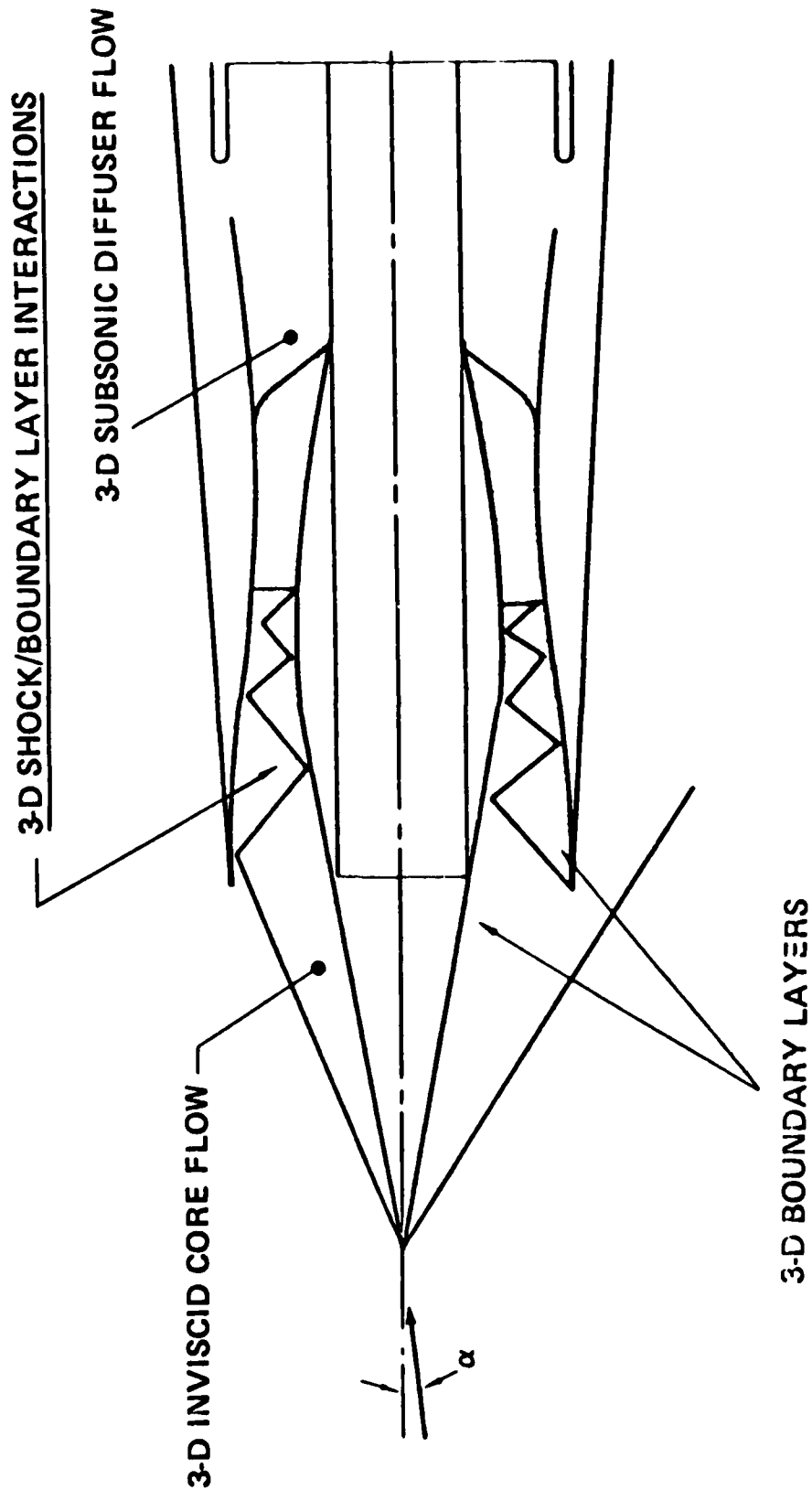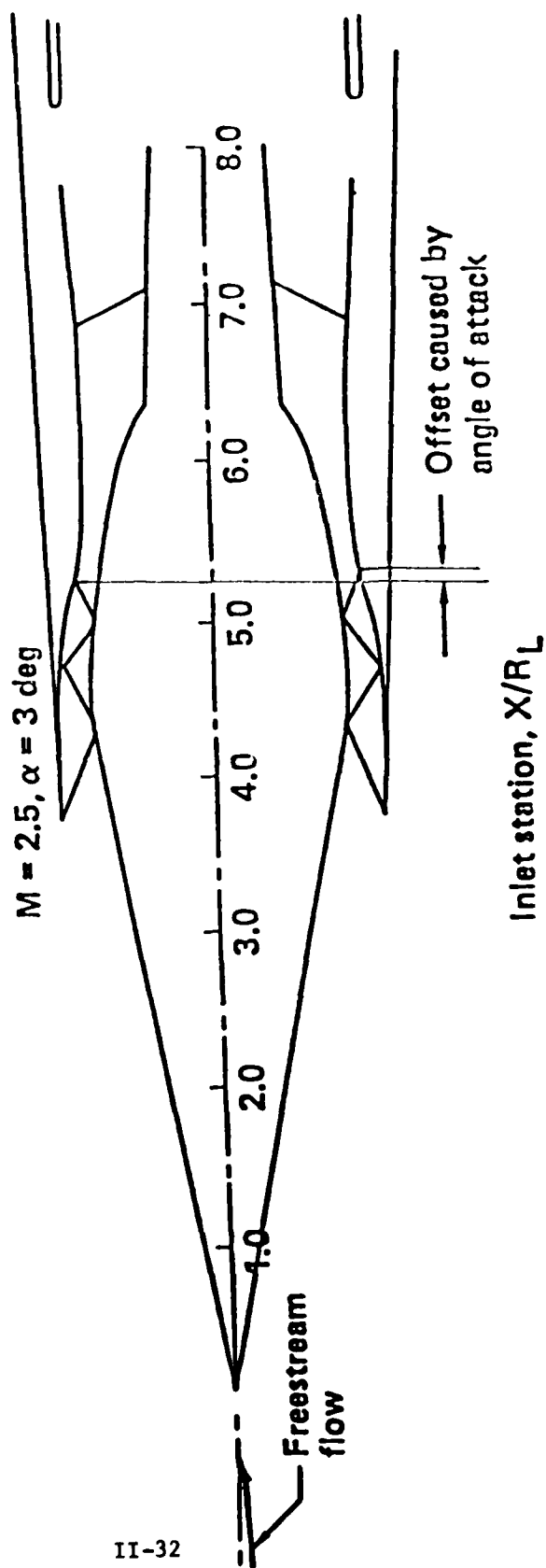
Inlet station, X/R_L

BOEING

FIGURE 19. SHOCK LOCATION PREDICTION-METHOD OF CHARCTERISTICS
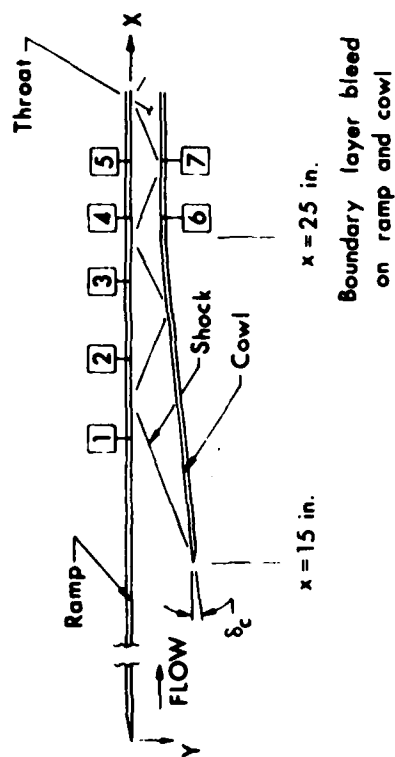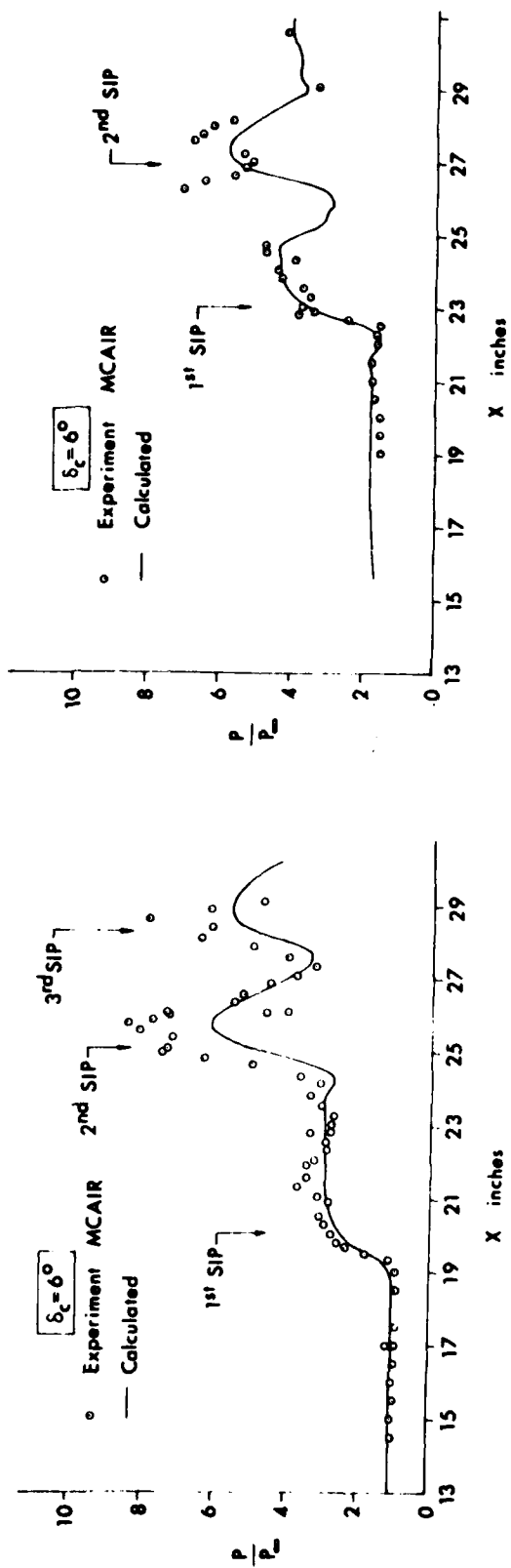
FIGURE 20. INLET STATIC PRESSURE DISTRIBUTIONS USING A NAVIER-STOKES ANALYSIS
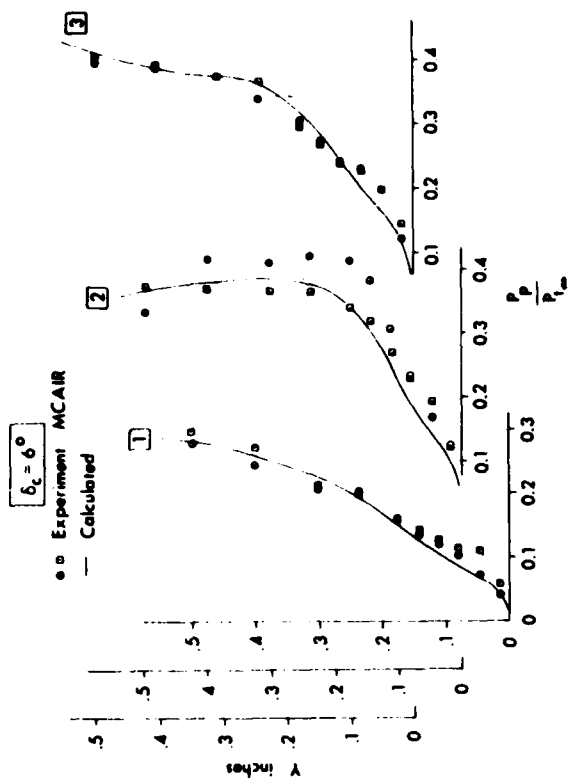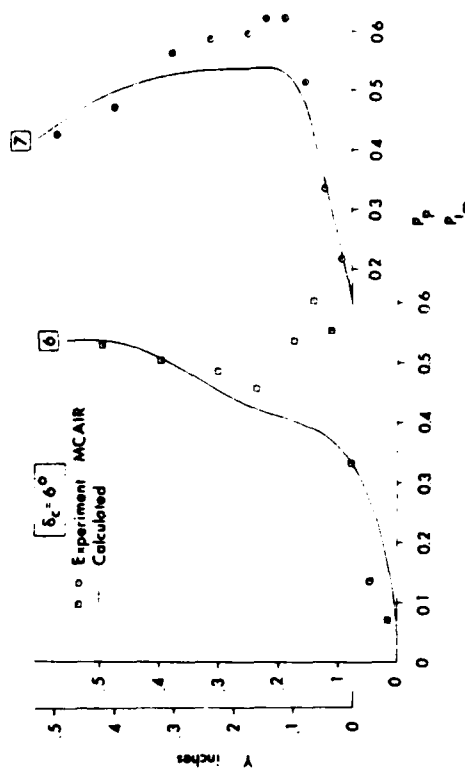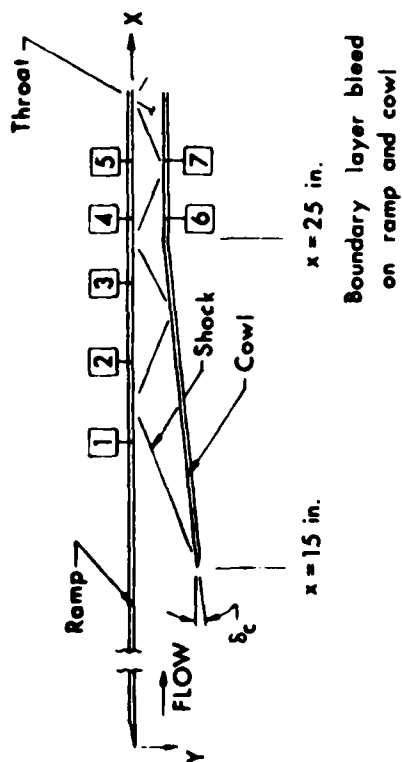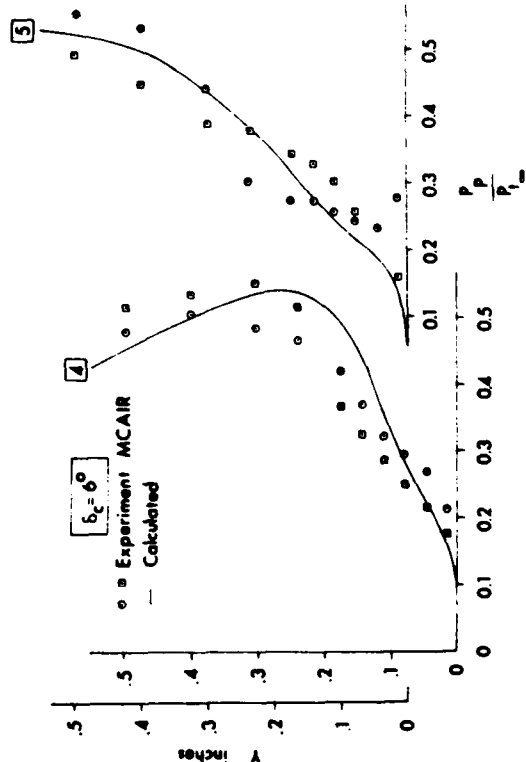
FIGURE 21.
INLET BOUNDARY LAYER DEVELOPMENT USING A NAVIER-STOKES PROCEDURE

FIGURE 22. - Schematic diagram of M3 inlet configuration showing inviscid shock structure.

M_∞
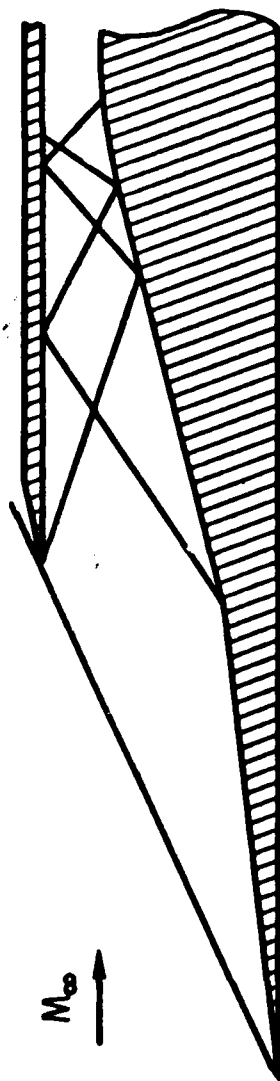
MACH NO. PROFILES IN CENTER PLANE OF M3 INLET CONFIGURATIN $M_\infty=3.0$, RE=7.2X10^6/m (2.2X10^6/ft)

(a) COARSE MESH.

(b) MEDIUM MESH.

COMPARSION OF COARSE AND MEDIUM MESH USED IN COMPUTATION OF M3 INLET FLOW FIELD
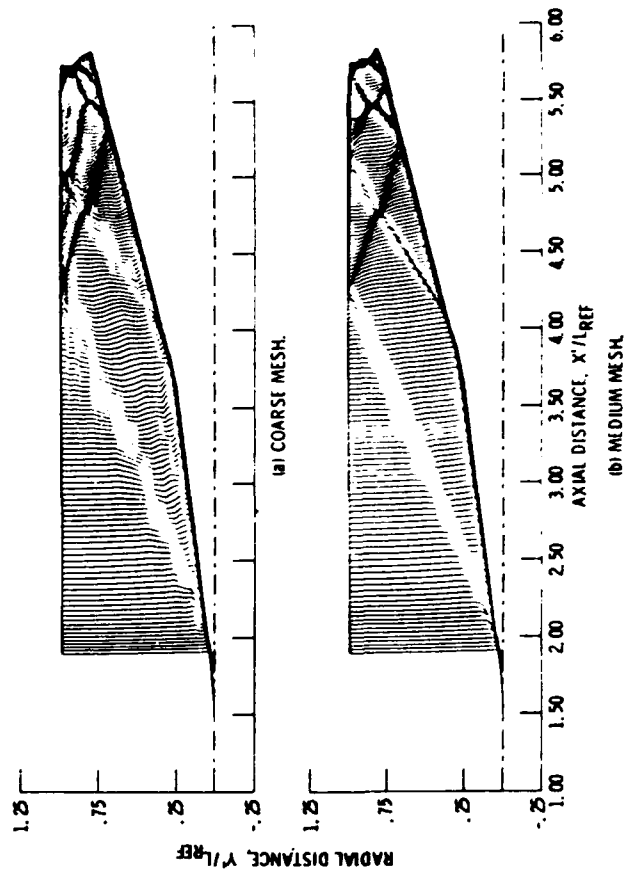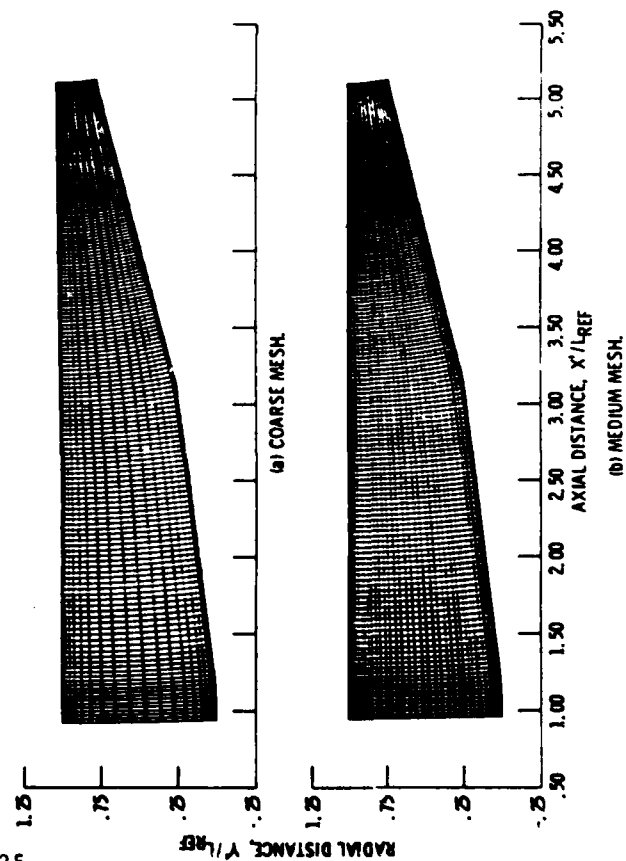
(a) COARSE MESH.

(b) MEDIUM MESH.

- Schematic diagram of M3 inlet configuration showing inviscid shock structure.

M_∞

ANALYSIS
—— MEDIUM MESH
- - - COARSE MESH
○ DATA, REF. 12

STATIC PRESSURE, p/p_{REF}

(a) COWL SURFACE

(b) RAMP SURFACE

AXIAL DISTANCE, X'/l_{REF}
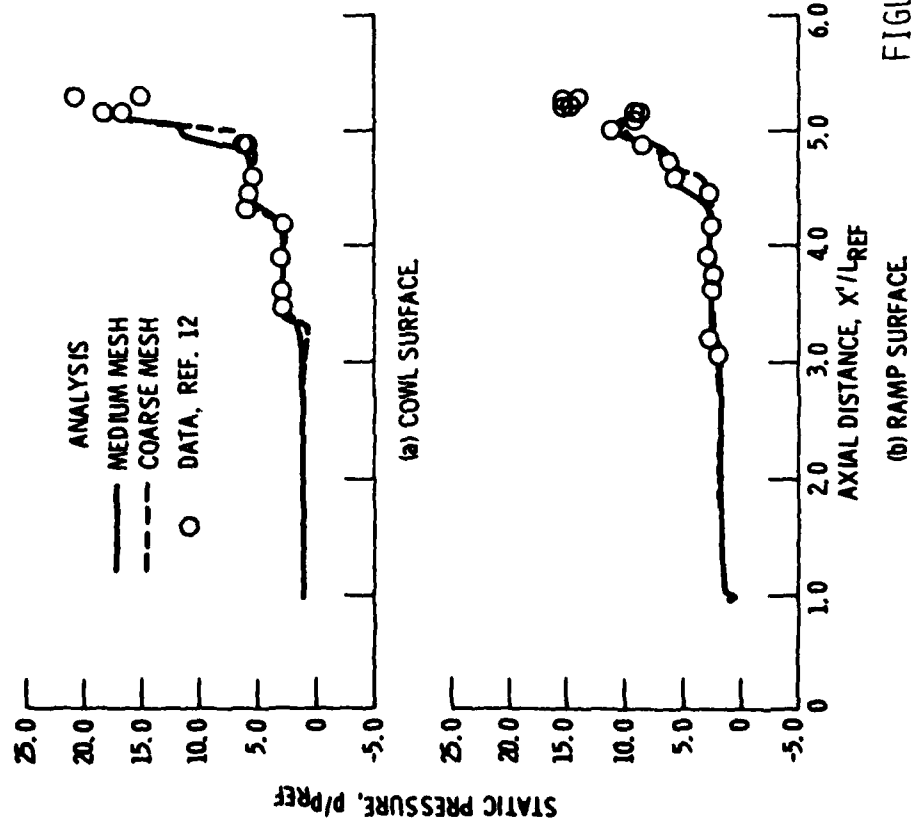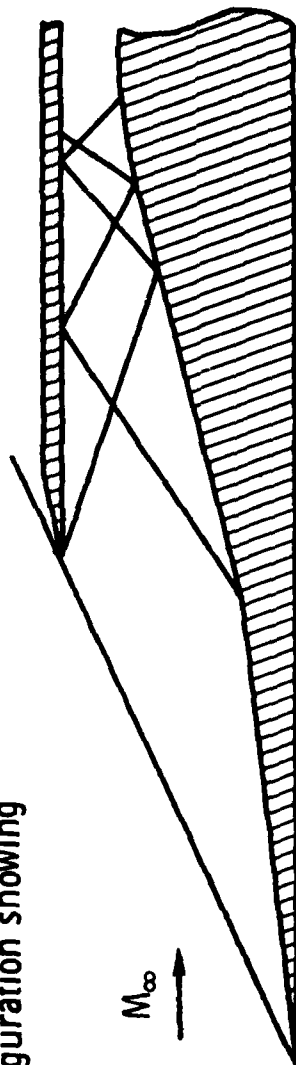
- Effect of mesh on the wall static pressure distribution in center plane of M3 inlet configuration.

FIGURE 23.

ROTATIONAL FLOW IN A CURVED-WALL DIFFUSER DESIGNED BY USING THE INVERSE METHOD OF SOLUTION OF POTENTIAL FLOW THEORY

Tah-teh Yang and Francois Ntone
Mechanical Engineering Department, Clemson University
Clemson, South Carolina

ABSTRACT

Curved wall diffusers designed by using an inverse method of solution of potential flow theory have been shown to be both short and highly efficient. These features make this type of diffuser attractive in thrust ejector applications. In ejectors, however, the flow at the diffuser inlet is nearly a uniform shear flow. This paper presents a method used in examining the flow velocity along the diffuser wall and some of the analytical results for diffusers designed with potential flow theory and receiving a rotational flow. The inlet flow vorticity and the diffuser area ratios prescribed in the inverse solution of the irrotational flow are the parameters of the study. The geometry of a sample ejector using such a diffuser and its estimated thrust augmentation ratio are also presented.

INTRODUCTION

The existing "Clemson Inverse Design Program for Short Curved Wall Diffusers"[1] is based on irrotational flow theory. Much experimental data have been examined for inlet flows having thin boundary layers with core flows well represented by potential flow theory. In such cases, experimentally obtained wall pressure distributions agree with the theoretically prescribed distributions very well. In ejectors, however, the diffuser inlet flow is significantly different from irrotational flow.

Based on the inlet velocity measurements reported by Hill and Gilbert[2] it appears that diffuser inlet flow should be represented by a shear flow of uniform vorticity. Under this condition (admitting a shear flow) the wall pressure distribution could be significantly different from that which was prescribed for the particular diffuser inlet design. Specifically, this raises a concern about the presence of an adverse pressure gradient or a deceleration in diffuser wall velocity which may result from the inlet shear flow. A moderate deceleration upstream of the suction slot may be overcome by increasing the suction flow rate. A strong deceleration will result in flow separation. A combination of large design area ratio and inlet vorticity could also result in a flow reversal at the diffuser exit because of the shear flow requirement, even in an inviscid flow. It becomes apparent, therefore that a method of calculating the wall velocity of a shear flow in this type curved diffuser is necessary to assure no adverse pressure gradient along the diffuser wall. And this will allow us to obtain the high thrust augmentation benefit afforded by using a short, curved wall diffuser section in the ejector design.

METHOD OF SOLUTION

1. Equations of Motion

The coordinate system is defined by Figure 1. For axisymmetric flow, the continuity equation is:

$$\frac{\partial u}{\partial r} + \frac{\partial w}{\partial x} + \frac{u}{r} = 0 \tag{1}$$

Define the stream function $\Psi(r,x)$ such that:

$$w = \frac{1}{r} \frac{\partial \Psi}{\partial r} \quad \text{and} \quad u = -\frac{1}{r} \frac{\partial \Psi}{\partial x} \tag{2a,b}$$

Then equation (1) becomes:

$$\frac{1}{r^2} \frac{\partial \Psi}{\partial x} - \frac{1}{r} \frac{\partial^2 \Psi}{\partial r \partial x} + \frac{1}{r} \frac{\partial^2 \Psi}{\partial x \partial r} - \frac{1}{r} (\frac{1}{r} \frac{\partial \Psi}{\partial x}) = 0$$

In addition, Ψ satisfies the vorticity equation which in cylindrical coordinates for an axisymmetric shear flow is:

$$\frac{\partial u}{\partial x} - \frac{\partial w}{\partial r} = B \tag{3}$$

Substituting equations (2a,b) into equation (3) yields the following

$$\frac{\partial^2 \Psi}{\partial x^2} + \frac{\partial^2 \Psi}{\partial r^2} = \frac{1}{r} \frac{\partial \Psi}{\partial r} - Br \tag{4}$$

which is an elliptic partial differential equation.

2. Boundary Conditions

In the numerical solution of equation (4) for shear flow, we used the same grid network as for irrotational flow. The boundary conditions used are as follows.

(1) Inlet
At the diffuser inlet, there is a parallel flow in the x-direction, and consequently u = 0. The Ψ's are obtained from equations (2a,b) as follows

$$\frac{1}{r} \frac{\partial \Psi}{\partial r} = w \quad \text{and} \quad -\frac{1}{r} \frac{\partial \Psi}{\partial x} = 0$$

Therefore ψ only changes with r, hence

$$\frac{d\Psi}{dr} = wr$$

For shear flow,

$$w = w_{o,in} - Br$$

therefore

$$\Psi = \int_0^r r(w_{o,in} - Br)dr$$

II-38

Which yields

$$\Psi = \frac{1}{2} r^2 w_{o,in} - \frac{1}{3} Br^3 \tag{5}$$

From equation (5), we have:

$$\Psi_{wall} = \frac{1}{2} R_{in}^2 w_{o,in} - \frac{1}{3} BR_{in}^3 \tag{6}$$

where $R = r(\Psi_{wall})$

For irrotational flow and uniform parallel inlet velocity q_{irr}, we have:

$$\Psi_{irr} = \int_0^{R_{in}} rq_{irr} \, dr$$

At the wall:

$$(\Psi_{irr})_{wall} = \frac{1}{2} q_{irr} R_{in}^2 \tag{7}$$

However, Ψ_{wall} may not necessarily be equal to $(\Psi_{irr})_{wall}$, which means that for the same diffuser geometry, flow rates for the irrotational and rotational (shear) cases may not be the same.

Define γ such that

$$(\Psi_{irr})_{wall} = \gamma \Psi_{wall}$$

and then

$$q_{irr} = \gamma (w_{o,in} - \frac{2}{3} BR_{in}) \tag{8}$$

For the shear flow solution, we will need to (i) specify, for the inlet boundary condition, the values of $w_{o,in}$ and γ; (ii) obtain B from equation (8); and (iii) specify the streamline according to equation (5).

Another possibility is that both B and $w_{o,in}$ are specified, and γ is to be calculated from equation (8).

In the inverse design program if we have prescribed parallel but non-uniform irrotational flows at the inlet and the exit, then the boundary condition at the inlet would be as follows:

$$(\Psi_{irr})_{wall} = \gamma \left[\frac{1}{2} R_{in}^2 w_{o,in} - \frac{1}{3} BR_{in}^3 \right]$$

For known B and $w_{o,in}$, γ can be calculated from the following

$$\gamma = \frac{(\Psi_{irr})_{wall}}{\frac{1}{2} R_{in}^2 w_{o,in} - \frac{1}{3} BR_{in}^3} \tag{9}$$

and the streamlines can be calculated from equation (5).

(2) Centerline

Along the centerline, we have $\Psi = 0$.

(3) Wall, upstream of slot

Along the wall, upstream of the slot, we have $\Psi = \Psi_{wall}$, where Ψ_{wall} is the same as the one calculated at the inlet.

(4) Wall, downstream of slot and inside of slot

Let β and β_{irr} be the fractions of the flow into the slot for the rotational and irrotational cases respectively. These β's are related to the stream functions as shown in the following expressions.

$$\beta_{irr} = 1 - \frac{\Psi_{irr,st}}{\Psi_{irr,wall}} \tag{10}$$

and

$$\beta = \frac{\Psi_{wall} - \Psi_{st}}{\Psi_{wall}}$$

or

$$\Psi_{st} = \Psi_{wall}(1 - \beta) \tag{11}$$

β is specified as an input to the analysis. The Ψ values for lines AB and AC in Figure 2 are determined from equation (10).

(5) Diffuser Exit

Letting Q_{irr} = Volumetric flow rate at the diffuser exit for irrotational flow and

Q = Volumetric flow rate at diffuser exit for shear flow

results in:

$$Q_{irr}/(1 - \beta_{irr}) = \gamma Q/(1 - \beta) \tag{12}$$

It can be shown that for parallel flow

$$w_{o,e} = \frac{2}{3} BR_{NSTAGU} + \frac{2(\Psi_{irr})_{wall}(1 - \beta)}{\gamma R_{NSTAGU}^2}. \tag{13}$$

II-40

Here B is specified, Ψ_{irr} and R_{NSTAGU} are obtained from the Clemson Inverse Solution Computer Program, and $w_{o,e}$ is the center line velocity at the diffuser exit. (R_{NSTAGU} is the radius at the stagnation point A of Figure 2.)

(6) Exit of Slot

At the slot exit, a shear flow having vorticity B is assumed.

Referring to Figure 4:

$$R - R_o = y \sin(90^o - \alpha) = y \cos \alpha$$

or

$$R = R_o + y \cos \alpha \tag{14}$$

The following development is to determine the stream function in the slot.

$$\Psi_y - \Psi_{st} = \int_o^y qRdy \tag{15}$$

But from Figure 3 we see that, $q = q_{o,sl} - By$

and therefore

$$\Psi_y = \Psi_{st} + R_o q_{o,sl} y + \frac{1}{2}(q_{o,sl} \cos \alpha - R_o B)y^2 - \frac{1}{3} By^3 \cos \alpha \tag{16}$$

The Ψ's at the exit of the slot can be prescribed using equation (15) where y is replaced by $\dfrac{(R-R_o)}{\cos \alpha}$, viz.

$$q_{o,sl} = \frac{B\Psi_{wall} + \frac{1}{2} R_o B \left(\frac{R_{w,sl}-R_o}{\cos \alpha}\right)^2 + \frac{1}{3} B \left(\frac{R_{w,sl}-R_o}{\cos \alpha}\right)^3 \cos \alpha}{R_o \frac{R_{w,sl}-R_o}{\cos \alpha} + \frac{1}{2} \frac{R_{w,sl}-R_o}{\cos \alpha}^2 \cos \alpha} \tag{17}$$

3. Computational Procedures

(1) For irrotational flow, prescribe q_{irr} parallel at inlet and exit of diffuser. Prescribe a slightly increasing velocity distribution at wall, upstream and downstream of the slot, with desired deceleration across the slot region.

(2) Solve the inverse problem for irrotational flow. The grid work in terms of x's and r's and the velocity distributions at inlet and exit of the diffuser and at the slot exit are then obtained.

(3) Solve the rotational flow equation for Ψ using the previously discussed boundary conditions.

(4) Solve for the velocity distribution at the wall. If the velocity distribution at the wall is slightly increasing with an abrupt deceleration across the slot, the diffuser geometry is satisfactory. If there is a deceleration along the wall, change the irrotational wall velocity distribution and go back to (2).

Using equations (2a,b) we may compute the velocity distribution along the wall from the Ψ distribution, i.e., with

$$q = \sqrt{(\frac{1}{r}\frac{\partial \Psi}{\partial r})^2 + (\frac{1}{r}\frac{\partial \Psi}{\partial x})^2} \tag{18}$$

In the wall velocity computation, the vorticity is to be specified as one of the parameters at the diffuser inlet, and in ejector application this parameter is determined from the mass ratio of the primary and the secondary flow rates and the geometry of the mixing chamber. Using this method, computations were carried out on the University's IBM 370/3033 digital computer. Before a more generalized inverse design program is formulated, the method outlined above will be used to examine the wall velocity distribution to assure the absence of any adverse pressure gradient in ejector design. A more detailed version of the analysis will be published as Mr. Francois Ntone's thesis for a Master of Science Degree in Mechanical Engineering at Clemson University, which is expected to be completed by May 1981. Results of the sample computations using the above outlined analysis are presented in the next section.

ANALYTICAL RESULTS

Figure 5 represents an axisymmetric diffuser having an area ratio of 2.5 to 1. Figure 6 shows the velocity distributions along the diffuser walls. The circles denote the velocity distribution prescribed to the "Inverse Design Program" for irrotational flow, and the triangles represent the velocity distribution along the diffusers depicted in Figure 5. The second velocity distributions were computed for inlet shear flow having a nondimensional vorticity value of 0.33 where velocity and length are normalized by inlet center line velocity and inlet width respectively. It is apparent that even though the prescribed diffuser wall velocity distribution upstream of the slot has a strong acceleration, the wall velocity distributions may experience deceleration in the diffuser when a shear flow is admitted. In actual operation a flow separation would most likely take place.

Figure 7 shows three velocity distributions for the diffuser depicted in Figure 5; these are specifically for inlet vorticity values of 0.33, 0.5, and 0.65. There is a significant change in the magnitude of the velocities, but their gradients vary only slightly. As expected, larger vorticity results in more deceleration. The larger change of wall velocity magnitude results from the assumption in our analysis that the diffuser center line velocity is kept constant, therefore the wall velocity decreases more when the inlet shear flow vorticity increases more. Judging from the distributions of this figure, a flow separation would likely take place in all three cases. Figure 8 shows the wall velocity distributions for the diffuser depicted in Figure 5, under the conditions of (i) admitting an inlet shear flow with a vorticity of 0.5 and (ii) three different slot suction rates. A suction rate Of 5.6% was the design value. At a suction rate of 8.5%, the velocity gradient upstream of the slot has not improved significantly in comparison to the distribution resulting from the 5.6% suction flow. Perhaps none of these distributions will yield a fully attached flow throughout the diffuser.

Figure 9 shows a diffuser designed for irrotational flow and having an area ratio of 2.5 to 1 with its suction slot slightly modified. Figure 10 shows the rotational velocity distribution along the walls of diffusers depicted in Figures 1 and 5 with inlet vorticity of 0.5. Apparently, there is no significant difference in wall velocity distribution for these two shear flow inlet cases. Figure 11 shows a diffuser designed for irrotational flow and having an area ratio of 2 to 1. Figure 12 shows wall velocity distributions for the diffuser depicted in Figure 11. The velocity distribution represented by circles is for irrotational flow, and that represented by triangles is for shear flow with velocity of 0.5. In this case hardly any deceleration is detected for the rotational flow, therefore, one should expect a highly effective diffuser even when a shear flow inlet condition is imposed at the curved wall diffuser inlet. Figures 13 and 14 are similar to Figure 12 and are for an area ratio of 1.5 to 1.

SAMPLE EJECTOR

Now the variation of wall velocity distribution due to vorticity is understood, and one may select ejector design parameters in such a way that no deceleration takes place along the diffuser wall and the diffuser flow can be maintained attached without excessive boundary layer suction.

Figure 15 shows an example of an air-to-air ejector for thrust augmentation with the area ratio of the secondary flow to the primary flow at the mixing chamber inlet of 40 to 1, and the mass ratio of the secondary flow to primary flow of 12 to 1. This ejector has a static pressure of $-1.25/psig$ at the exit of a mixing chamber. From this pressure level one may use a highly effective short diffuser with an area ratio of 2.2 to achieve an exit pressure of the ambient level.

Based on the conventional definition of thrust augmentation ratio ϕ , namely; the momentum of the mixture of the primary and secondary flows at the ejector exit to the momentum of the primary flow at the mixing chamber inlet, this sample ejector has a vlaue of ϕ of 2.182. Since the short diffuser of the sample ejector uses boundary layer control, an auxilliary ejector will be used to achieve the necessary boundary layer suction. The removed air will be discharged in the same direction as the thrust ejector and thus contributes to the overall thrust. Therefore a modified thrust augmentation ratio ϕ_2 , defined as the total momentum at the ejector exit to the sum of the momentum of the primary flows at the mixing chamber inlet and the suction chamber, must be used for this type of ejector. We found that for the sample ejector, ϕ_2 has a value of 1.830 provided that a suction fraction of 10% is adequate for the boundary layer control, and the mass ratio of the auxilliary ejector of 4 to 1 can be accomplished. These assumptions are considered to be reasonable. It is noteworthy that the overall length of the ejector is much reduced relative to the ones having diffusers designed by using the concept of incipient separation. The performance level in thrust augmentation ratio compared favorably to those reported in reference 3.

REFERENCES

1. Nelson, C.D. and T. Yang, "Design of Bounded and Unbounded Axially Symmetrical Ducts with Specified Distributions", AIAA Journal, Vol. 15, No. 9, Sept. 1977.

2. Gilbert, G.B. and P.G. Hill, "Analysis and Testing of Two-Dimensional Slot Nozzle Ejectors with Variable Area Mixing Sections", NASA CR 2251, Nov. 1972.

3. Tai, T.C., "Optimization of Axisymmetric Thrust Augmenting Ejectors", Proceedings of AIAA 10th Fluid and Plasmadynamics Conference, Alberquerque, New Mexico, June 27-29 1977, paper 77-707.
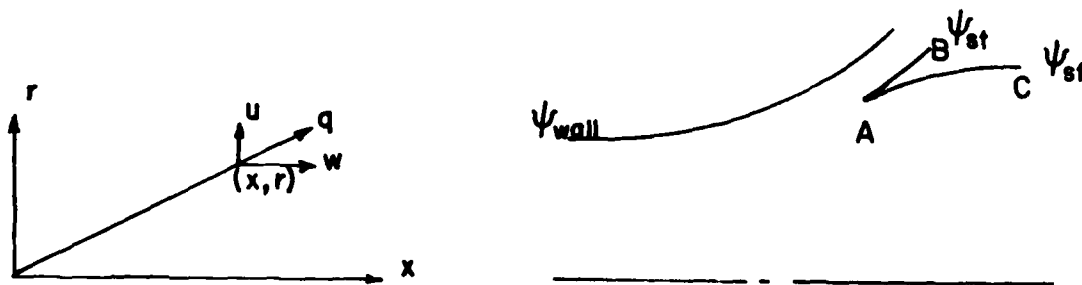
Figure 1. Coordinate System and
Velocity Components
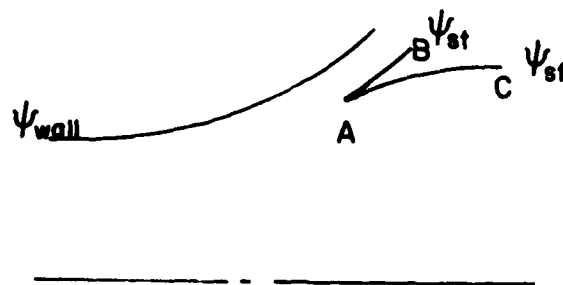
Figure 2. Wall Streamlines and
the Branching Point
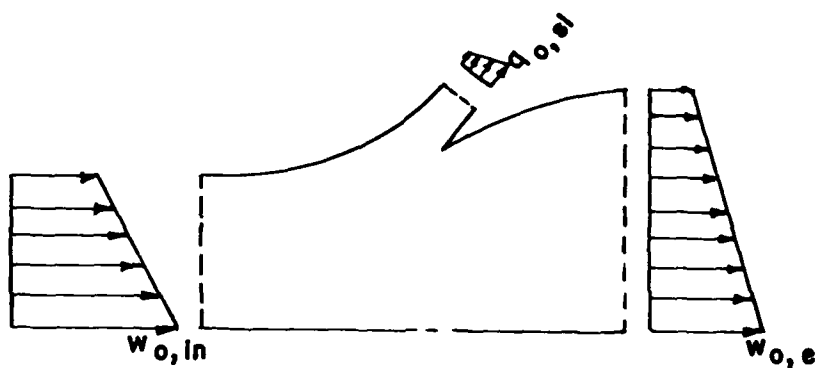
Figure 3. Velocity Distributions for Shear Flow
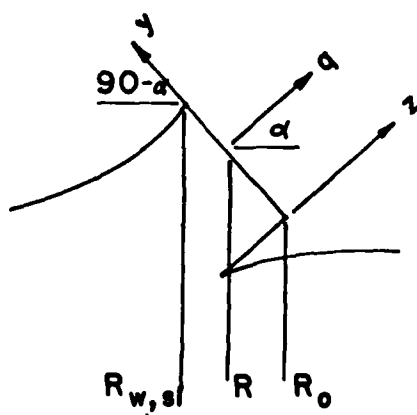
Figure 4. Coordinate System at Slot Exit
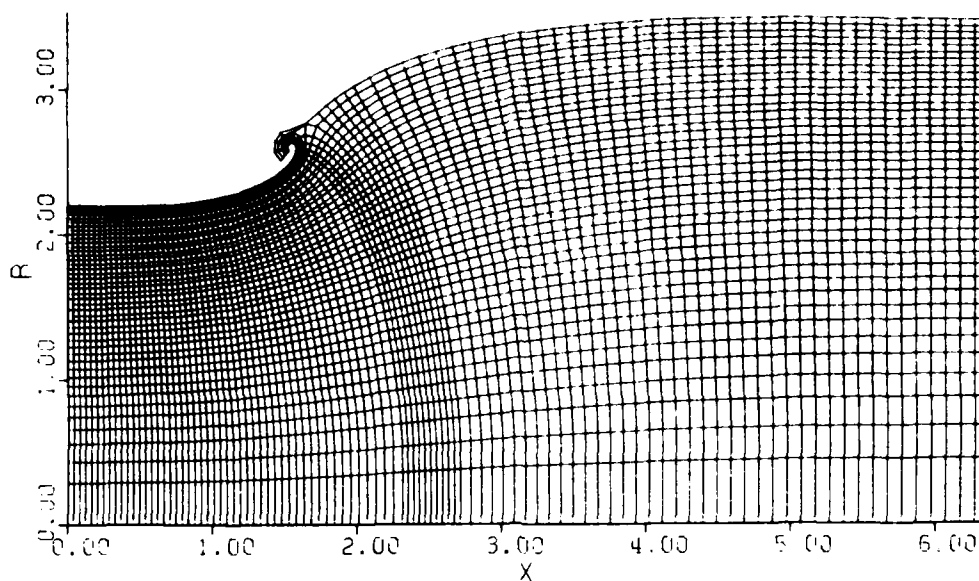
Figure 5. Computer Plot of $\phi - \Psi$ Grid for an Axisymmetric Diffuser, AR = 2.5, Suction Rate = 5.6%
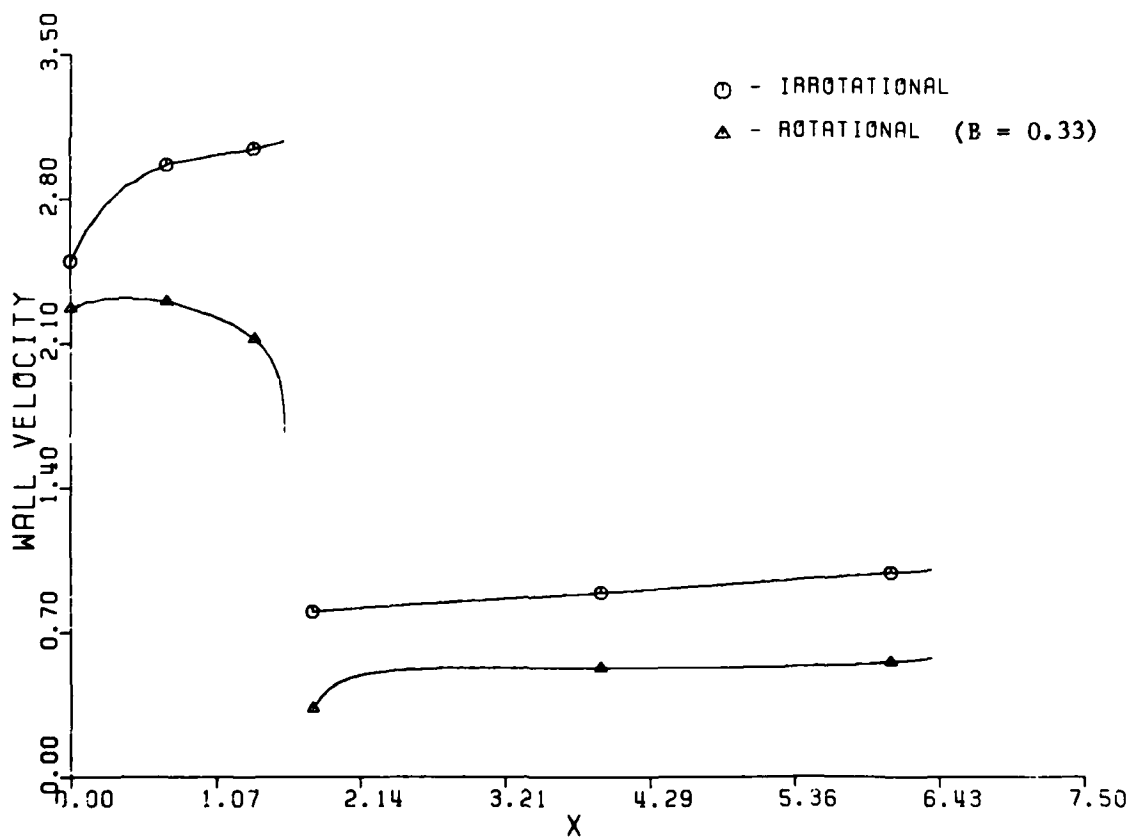
Figure 6. Velocity Distributions for Rotational and Irrotational Flow
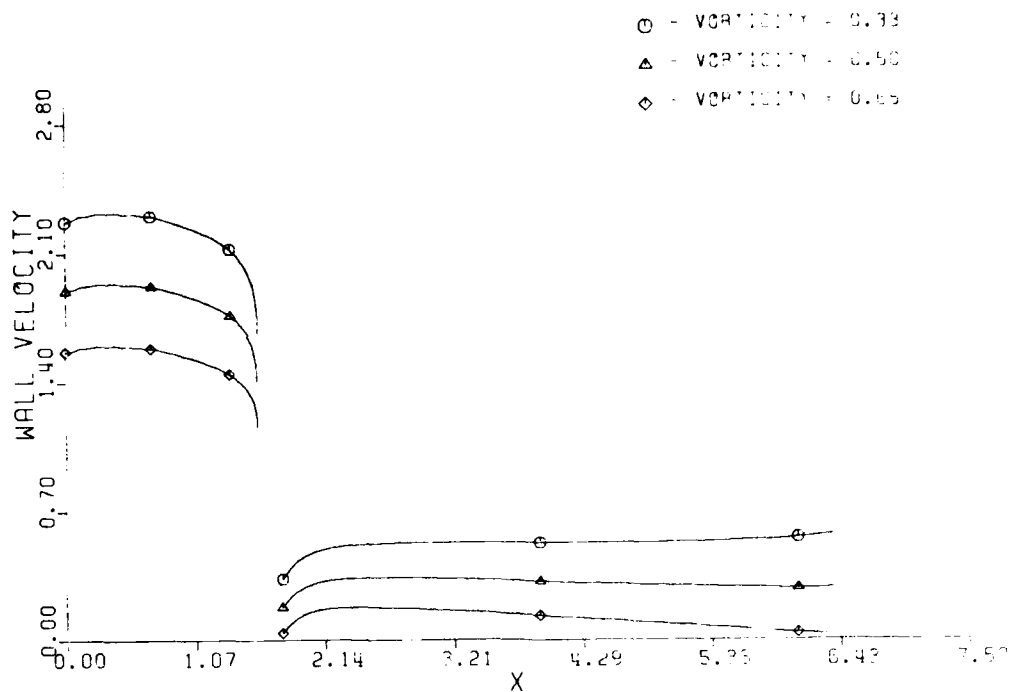
Figure 7. Velocity Distributions for Three Rotational Flows with Suction Rate of 5.6%
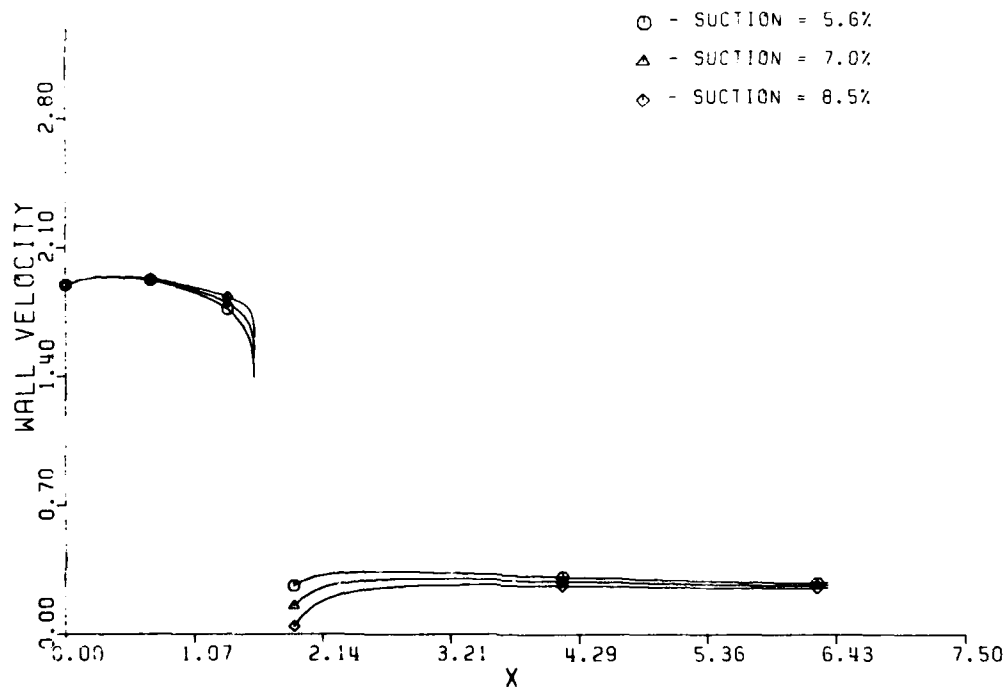
Figure 8. Velocity Distributions for Rotational Flow with B = 0.5 and Three Suction Rates
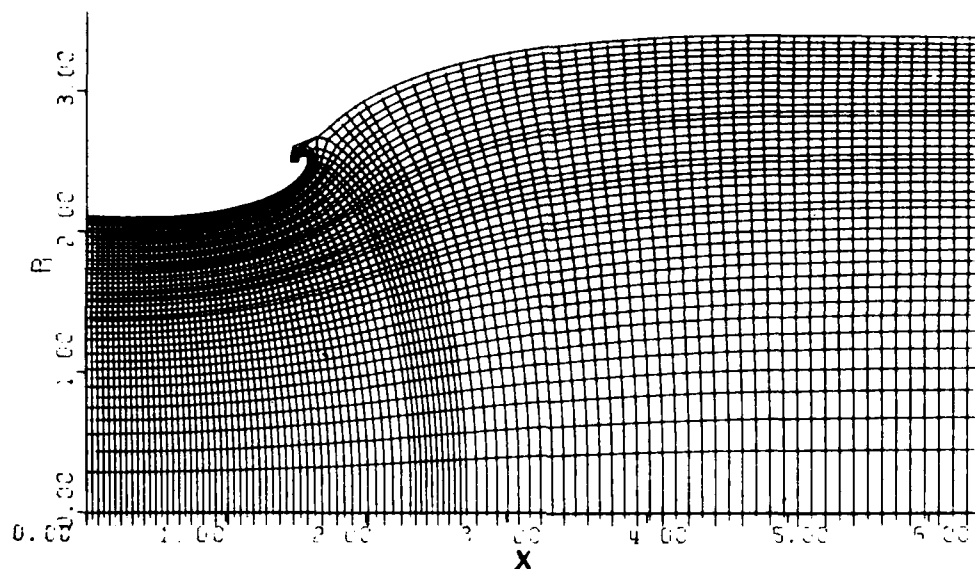
Figure 9. Computer Plot of φ-Ψ Grid for an Axisymmetric Diffuser, AR = 2.5, Suction Rate = 5.6% (Change in Suction Slot)

⊙ – ROTATIONAL 1
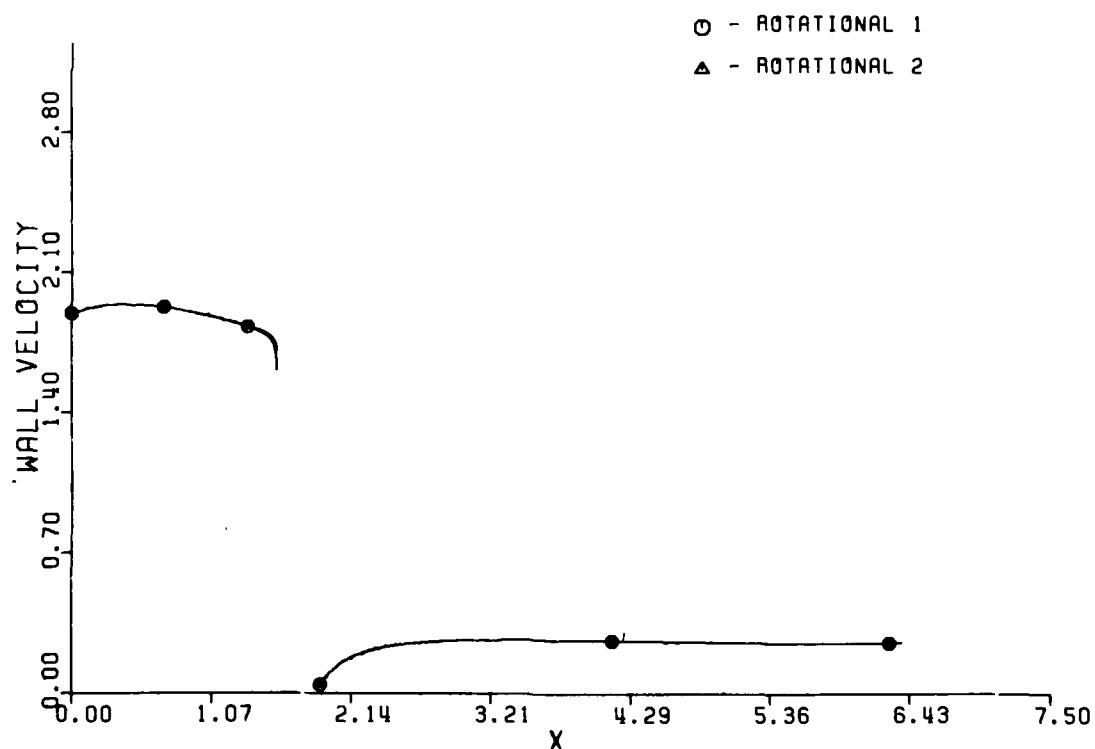
△ – ROTATIONAL 2

Figure 10. Velocity Distributions for Diffusers Represented in Figures 5 and 9 (B = 0.5, Suction Rate = 8.5%)
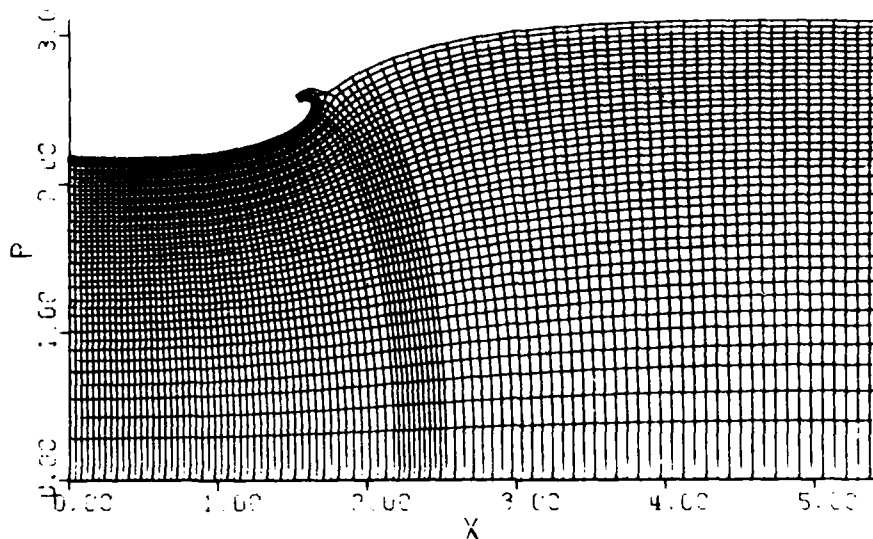
Figure 11. Computer Plot of ϕ-Ψ Grid for an Axisymmetric Diffuser, AR = 2.0, Suction Rate = 5.6%
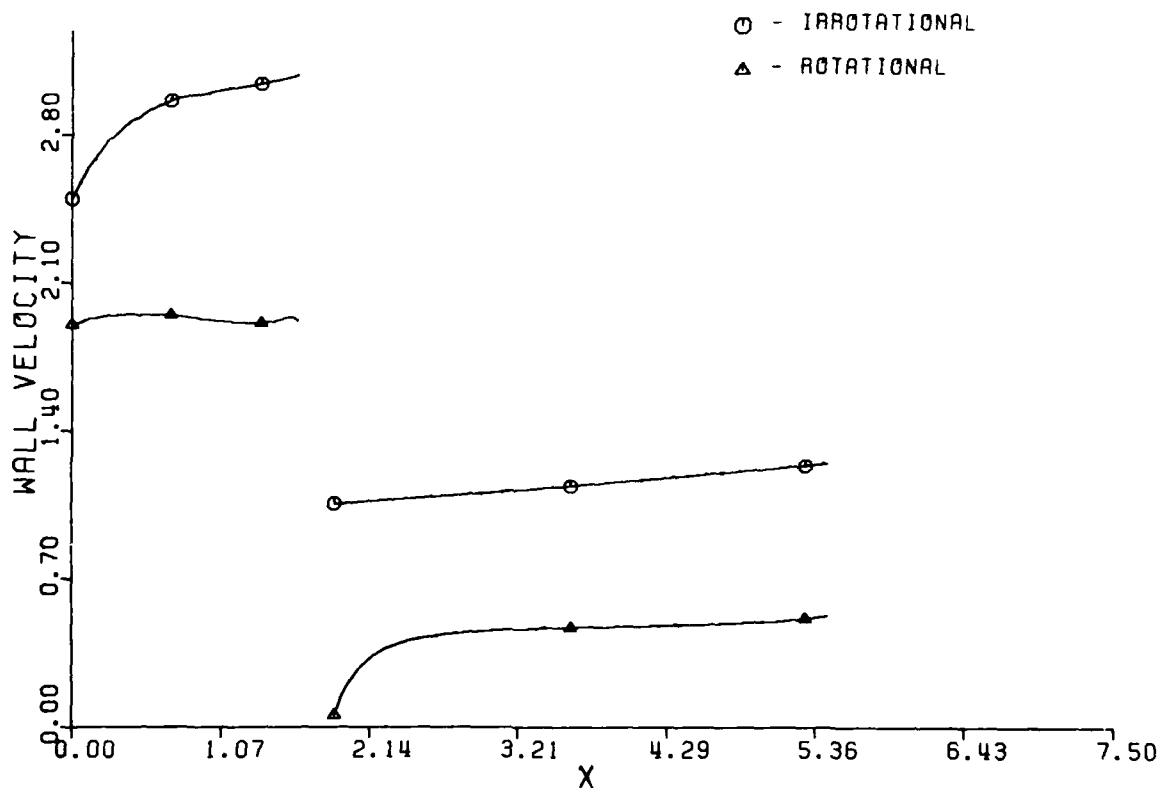
Figure 12. Velocity Distributions for Rotational and Irrotational Flows, B = 0.5, Suction Rate = 8.5%

II-49
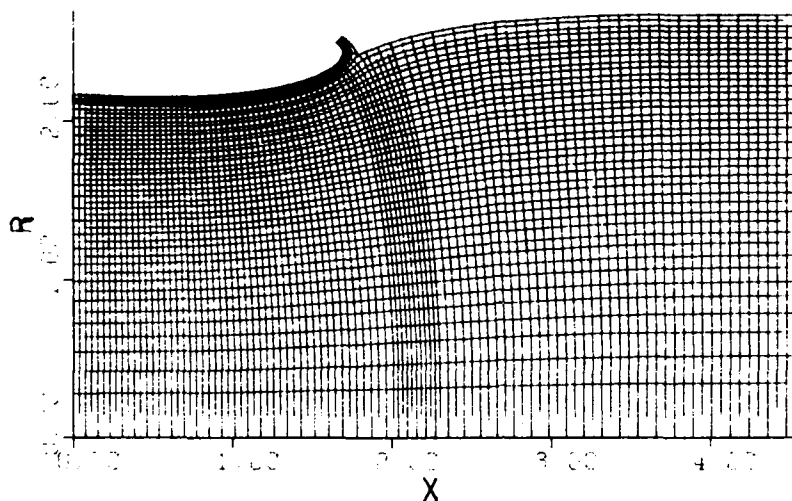
Figure 13. Computer Plot of ϕ-ψ Grid for an Axisymmetric Diffuser, AR = 1.5, Suction Rate = 8.5%
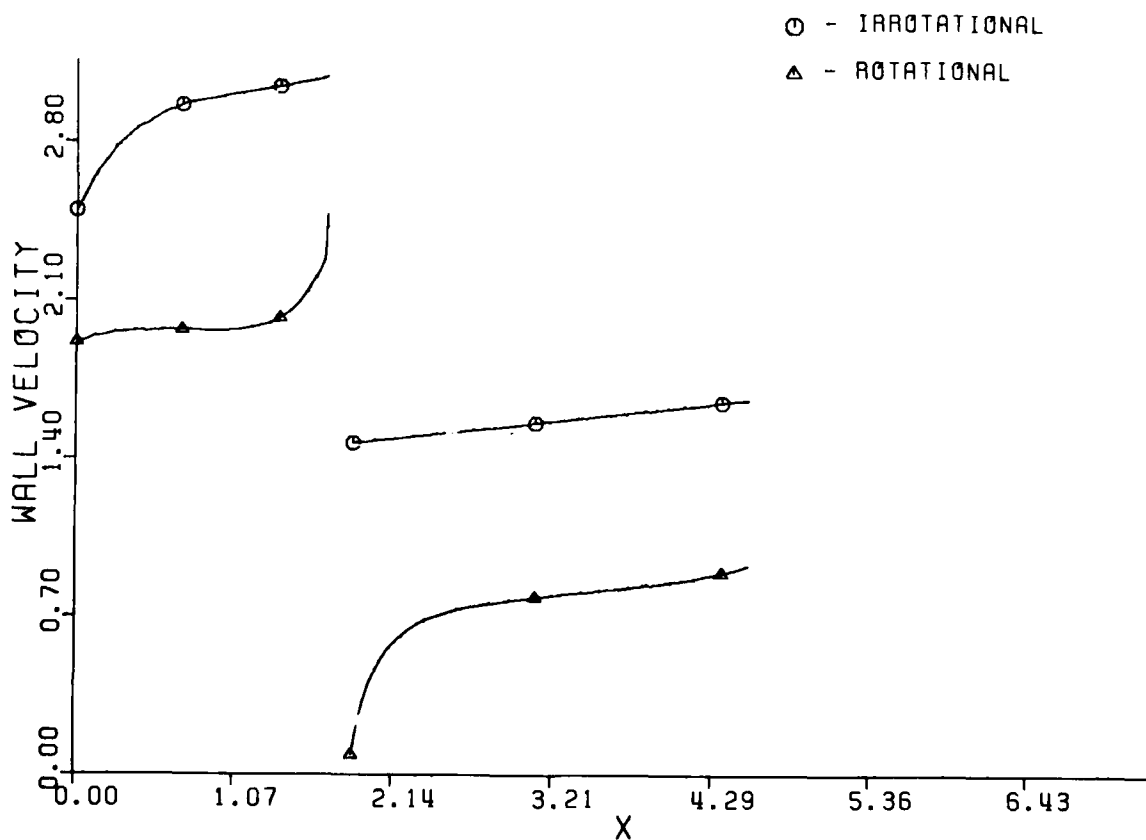
Figure 14. Velocity Distributions for Rotational and Irrotational Flows, B = 0.5, Suction Rate = 8.5%
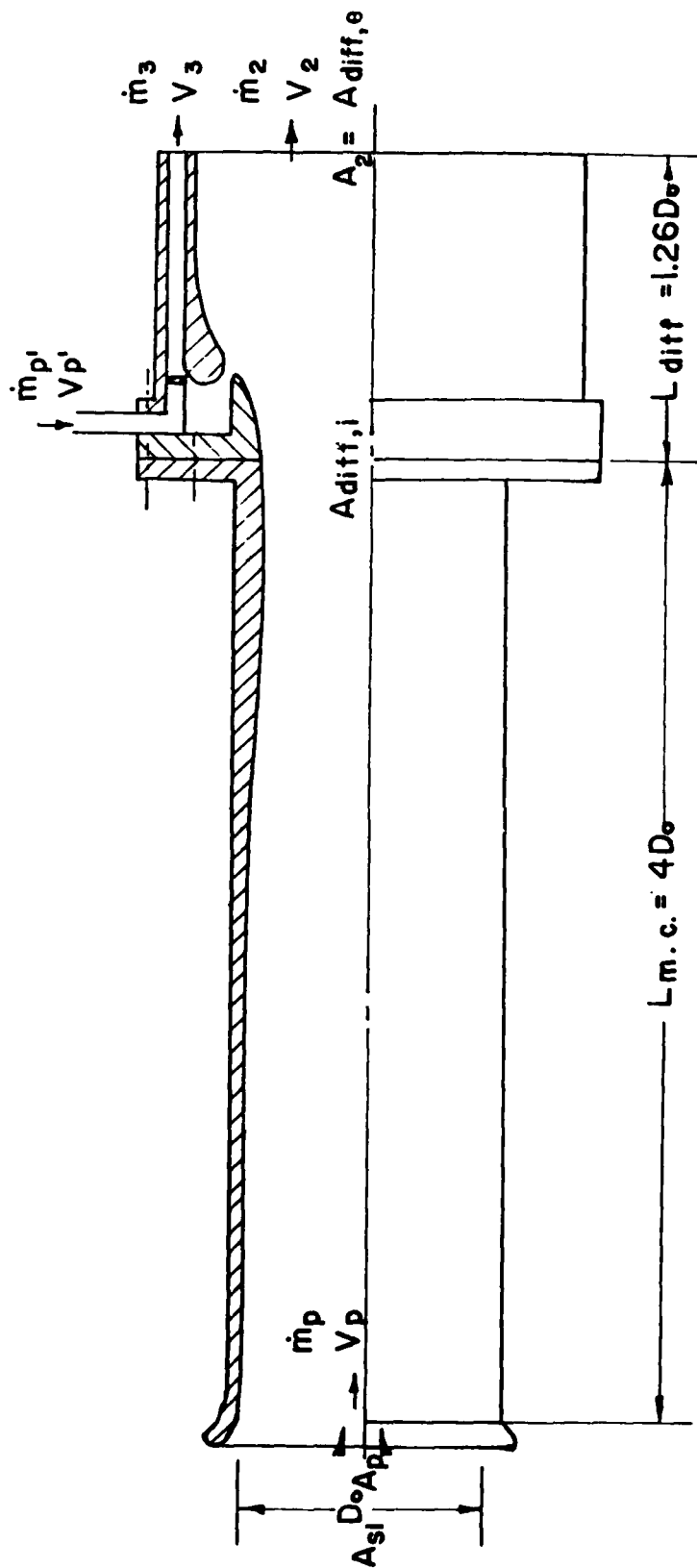
$$\frac{A_2}{A_{s1}} = AR = 2 \qquad \frac{A_{diff,e}}{A_{diff,i}} = AR_2 = 2.2 \qquad \phi_2 = \frac{\dot{m}_2 V_2 + \dot{m}_3 V_3}{\dot{m}_p V_p + \dot{m}_{p'} V_{p'}} = 1.83$$

Figure 15. A Sample Air-to-Air Ejector with 10% Contraction for Mixing Chamber, No Deceleration Along Diffuser Wall

AERODYNAMIC CHARACTERISTICS OF A SERIES OF AIRBREATHING MISSILE CONFIGURATIONS

Clyde Hayes
NASA Langley Research Center
Hampton, Virginia

ABSTRACT

Due to the interest in the application of airbreathing propulsion to missiles and the lack of a suitable data base, an experimental program has been conducted to contribute to such a data base. The configurations investigated were with twin-inlets, either two-dimensional or axisymmetric, each located at three circumferential locations. The effects of a wing located above the inlets and of tail configuration were investigated. Longitudinal stability and control and lateral-directional stability were included in the data obtained.

This paper will present a summary of the program and some of the results obtained. Certain trends of the data, as well as problem areas, will be discussed. Due to the large volume of data obtained, a detailed analysis will not be presented.

INTRODUCTION

Since 1972, the National Aeronautics and Space Administration has participated in several airbreathing missile research programs. These programs have included the MORASS[1], ALRAAM[2], SASS[3], AIAAM[4-5], and the ASALM[6] configurations. The results from these studies indicated that a more comprehensive data base would be required to advance and develop new design techniques for airbreathing missile configurations.

In 1977, Langley Research Center developed a parametric model series that could be configured to cover a wide range of airbreathing missile configurations (figure 1). The model components, shown schematically in figure 1, included single and twin axisymmetric and two-dimensional inlets. The twin-inlets could be rotated about half the body centerline from 0° to 45° from horizontal. Various wing and tail configurations could be installed.

This model series has been tested with internal flow in the Langley Unitary Plan Wind Tunnel and in the David W. Taylor Naval Ship Research & Development Center (DTNSRDC) 7' x 10' Transonic Tunnel without internal flow. Figure 2 shows the extent of this investigation. In addition to the variables shown in figure 2, a series of tests at both Langley and DTNSRDC have been run with single tail surfaces deflected for pitch, yaw, and roll control.

This paper will present only a small portion of the findings of this investigation. A comparison will be shown between the twin axisymmetrical and two-dimensional inlet configuration, and the effect of various variables in the twin axisymmetric inlet configuration.

The aerodynamic characteristics are referred to the body axis system. The moment reference center was located at 50.0 percent of the body length.

A   maximum cross-sectional area of body

C_{l_β} effective dihedral parameter (roll stability), $\left(\dfrac{\Delta C_l}{\Delta \beta}\right)_{\beta = 0°, 3°}$, where

$$C_l = \frac{\text{rolling moment}}{qAd}$$

C_{n_β} directional-stability parameter, $\left(\dfrac{\Delta C_n}{\Delta \beta}\right)_{\beta = 0°, 3°}$, where

$$C_n = \frac{\text{yawing moment}}{qA}$$

d   maximum body diameter

M   free-stream Mach number

q   free-stream dynamic pressure

α angle of attack

β angle of sideslip

ϕ_I angle of inlet orientation

DISCUSSION

The twin-inlet configurations are shown in figure 3. The geometries of the axisymmetric and two-dimensional configuration are compared and the wing and tail arrangements are shown. The wing could not be attached to the model when the inlets were located at $\phi_I = 90°$. Two vertical wing locations are shown for the two circumferential positions for which the wing was used. A tri-tail configuration was used for all the inlet circumferential positions. For inlets in the 45° position, in addition to the tri-tail, an x-tail and inverted tri-tail configuration were tested and are shown in figure 4.

Figure 5 shows the effect of inlet orientation angle on the longitudinal aerodynamics for both the axisymmetric and two-dimensional inlets. The body-inlet-tail (tri-tail) configuration shows a variation of pitching moment with angle of attack that tends to be a characteristic of this type of configuration--very stable at high angles of attack with little or no margin of stability near 0° angle of attack. The effect of inlet orientation was to decrease the longitudinal stability as the inlets were rotated downward. The difference between the two inlet types was generally an overall lower stability level for the two-dimensional inlet as compared to the axisymmetric inlet. The effect of the decrease in stability as the inlets were rotated downward is due largely to the decrease in planform area at the aft end of the model. This should also affect the directional stability, since the lateral area of the model at the aft end is also changed.

Figure 6 shows the affect on the directional stability to be about as expected at low angle of attack (up to about α = 6°). It should be noted that the change of inlet orientation angle from 90° to 115° showed little affect on pitching moment with a large change between 115° and 135°, while the variation of directional stability varied more directly with inlet orientation angle. Above about α = 6°, the vertical tail surface becomes ineffective and the model is directionally unstable at angle of attack above about 12°. The change in lateral area also affects the lateral stability and the model was laterally unstable with the 135° inlet orientation angle.

Figure 7 shows the longitudinal aerodynamic characteristics of the body-inlet-tail and body-inlet-wing-tail compared for three different tail configurations. These configurations are with the axisymmetric inlets at 135° orientation angle. While the configuration with the tri-tail shows rather nonlinear pitching moment characteristics, the x-tail configuration provides a much more linear variation, in fact, without the wing the curve is essentially a straight line for the range of angle of attack of the tests. With the wing added, the curve is somewhat less linear, but the configuration remained stable for the range of angle of attack. The third tail configuration, an inverted tri-tail has unsatisfactory stability characteristics.

Figure 8 shows the effect of pitch control deflection for the winged configuration. The left half of the figure is from the previous figure. The right side shows the effect of -10° pitch control deflection. The tri-tail configuration would trim at an angle of attack above 20°, but has an unstable range of angle of attack. The x-tail, despite its stability level, trims at 20° angle of attack and has a more linear pitching-moment variation. The inverted tri-tail shows a straightening of the pitching-moment curve apparently due to the loss of effectiveness at high angle of attack.

Figure 9 shows the lateral-directional stability of the tail winged configuration. Generally, the x-tail and inverted tri-tail show lateral-directional stability throughout the angle-of-attack range. The tri-tail became laterally unstable at high angles of attack and was generally unstable laterally throughout the angle-of-attack range.

CONCLUDING REMARKS

Due to the interest in the application of airbreathing propulsion to missiles and the lack of a suitable data base, an experimental program has been conducted to contribute to such a data base. The configurations investigated were with twin-inlets, either two-dimensional or axisymmetric, each located at three circumferential locations. The effects of a wing located above the inlets and of tail configurations were also investigated. Longitudinal stability and control and lateral-directional stability characteristics were obtained as part of the experimental program. Some of the more general observations regarding the aerodynamic characteristics of the model can be made:

(1) The configuration tested showed a trend which consisted of a variation of pitching moment with angle of attack, that the model was very stable at high angles of attack and with little or no margin of stability near 0° angle of attack.

(2) Rotating the inlets downward tended to decrease the longitudinal stability, while increasing the directional stability, and decreasing the lateral stabilty.

(3) Of the three tails tested, the x-tail configuration provided the best performance, the most linear pitching-moment curve, sufficient pitch control effectiveness and positive lateral-directional stability.

REFERENCES

1. Hayes, Clyde, and Monta, William J.: Aerodynamic Characteristics of a 1/4-Scale Model of MORASS Missile Configurations at Supersonic Speeds. NASA TM X-3354, 1976.

2. Hayes, Clyde: Aerodynamic Characteristics of 1/4-Scale Model of ALRAAM Missile Configuration at Supersonic Speeds. NASA TM 74075, 1977.

3. Hayes, Clyde; and Sawyer, Wallace C.: Aerodynamic Characteristics of a Series of Air-Breathing Missile Configurations Investigated as Part of the SASS Program. NASA TM 80139, 1979.

4. Hayes, Clyde: Aerodynamic Characteristics of Twin-Inlet Missile Configurations Tested as Part of the AIAAM Program. Proposed NASA TM.

5. Hayes, Clyde: Aerodynamic Characteristics of a Single-Inlet Missile Configuration Tested as Part of the AIAAM Program. Proposed NASA TM.

6. Sawyer, Wallace C.; and Hayes, Clyde: Stability and Control Characterisitcs of an Air-Breathing Missile Configuration Having a Forward Located Inlet. NASA TM X-3391, 1976.

TWIN INLETS

INLET CIRCUMFERENTIAL
POSITION

SINGLE INLETS

INLET LONGITUDINAL
POSITION

INLET LONGITUDINAL
POSITION

WING AND FOREBODY POSITION
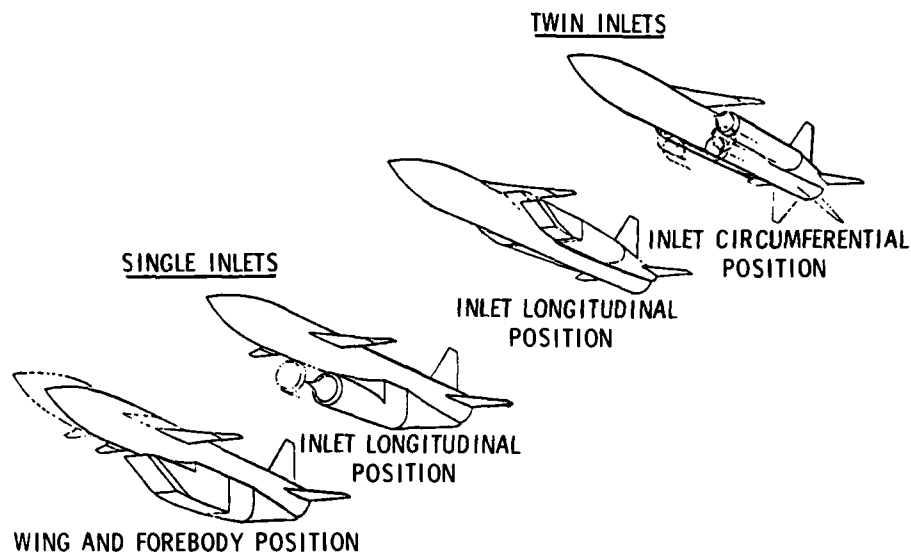
Figure 1. - Configuration variables.

Model Drawing		Angle Of Attack		Mach Number		Control Deflection		Configuration Inlets Included			
Planform	Inlet/Tail	α	β	Subsonic	Supersonic	δ_{pitch}	δ_{yaw}	Body	Body-Wing	Body-Tail	Body-Wing-Tail
		-2° to 12°	0°, 5°	.60, .80, .95		-10° 0° +10°		90° 115° 135°	115° 135°	90° 115° 135°	115° 135°
		-5° to 20°	0°, 3°		2.50, 2.95 3.50, 3.95	0° -10° -20°		90° 115° 135°	115° 135°	90° 115° 135°	115° 135°
		-2° to 12°	0°, 5°	.60, .80, .95		-10° 0° +10°		135°	135°	135°	135°
		-5° to 20°	0°, 3°		2.50, 2.95 3.50, 3.95	+10° 0° -10° -20°		135°	135°	135°	135°
		-2° to 12°	0°, 5°	.60, .80, .95		0° +10°		135°	135°	135°	135°
		-5° to 20°	0°, 3°		2.50, 2.95 3.50, 3.95	0° -10° -20°		135°	135°	135°	135°
		-2° to 12°	0°, 5°	.60, .80, .95		0° +10° -10°		90° 115° 135°	115° 135°	90° 115° 135°	115° 135°
		-5° to 20°	0°, 3°		2.50, 2.95 3.50, 3.95	0° -10° -20°		90° 115° 135°	115° 135°	90° 115° 135°	115° 135°
				.60, .80, .95		0°		135°		135	
		-5° to 20°	0°, 3°		2.50, 2.95 3.50, 3.95	0° -10° -20°		135°		135°	
				.60, .80, .95		0°				90° 115° 135	
		-5° to 20°	0°, 3°		2.50, 2.95 3.50, 3.95	0° -10° -20°		90° 115° 135°		90° 115° 135°	
	8			.60, .80, .95		0° +10° -10°		Tested	Tested	T_1 T_2	T_1 T_2
		-5° to 20°	0°, 3°		2.50, 2.95 3.50, 3.95	0° -10° -20°		Tested	Tested	T_1 T_2	T_1 T_2
	ℓ			.60, .80, .95		0° +10° -10°		Tested	Tested	T_1	T_1
		-5° to 20°	0°, 3°		2.50, 2.95 3.50, 3.95	0° -10° -20°		Tested	Tested	T_1 T_2	T_1 T_2
		-5° to 20°	0°, 3°		2.50, 2.95 3.50, 3.95	0° -10° 20°				135°	135°

Figure 2. - Test matrix of UPWT airbreathing
missile model tests.

WING LOCATION FOR
Φ_I = 115° AND 135° ONLY

MODEL REFERENCE CENTER
50 % BODY LENGTH

90° 115° 135°
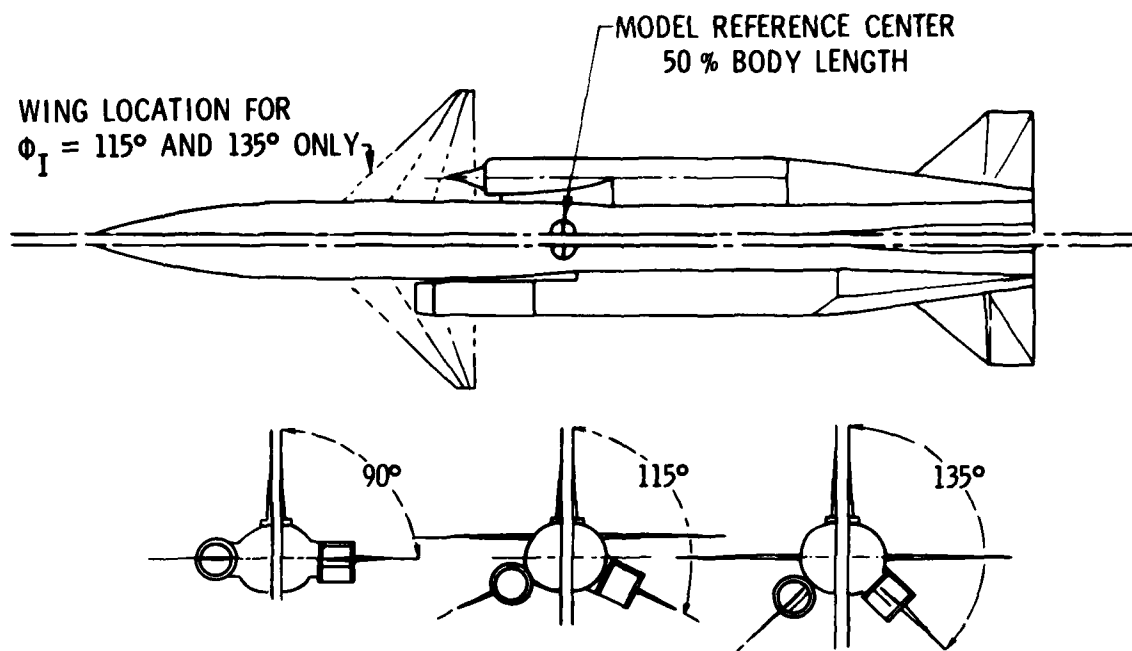
Figure 3. - Twin-inlet model configurations.

TRI-TAIL, T_1 X-TAIL, T_2 INVERTED TRI-TAIL, T_3
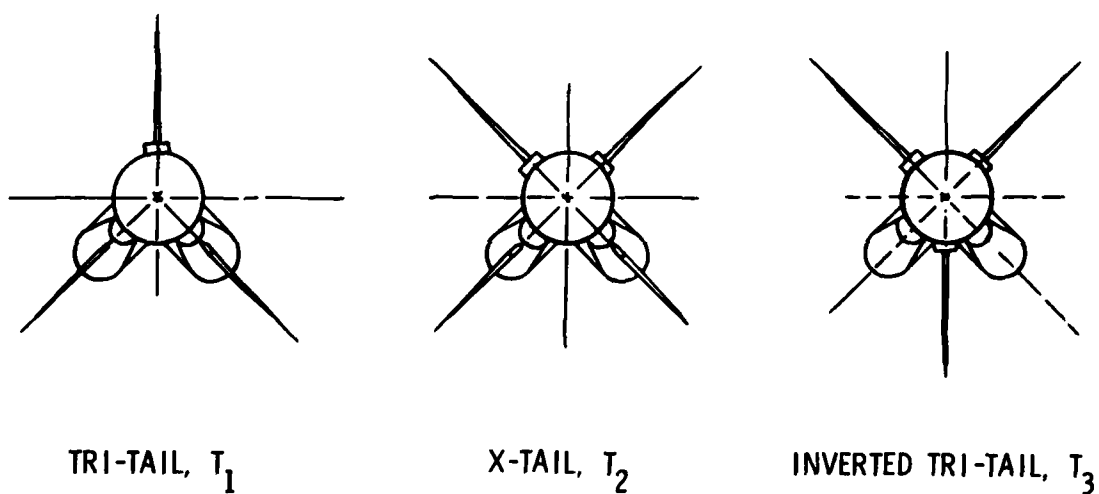
Figure 4. - Tail configurations.
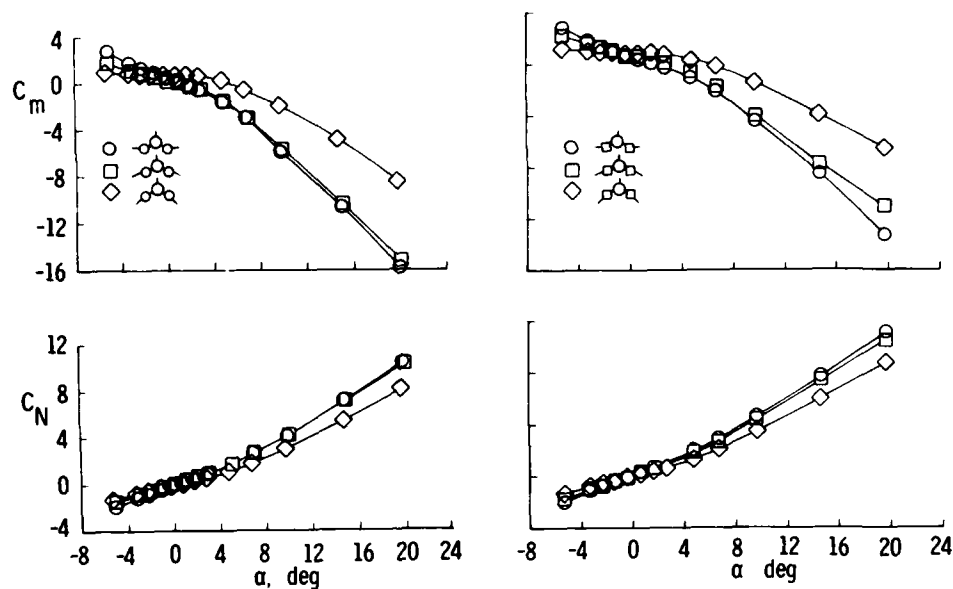
Figure 5. - Effect of inlet orientation on
longitudinal aerodynamic charac-
teristics. M = 2.95.
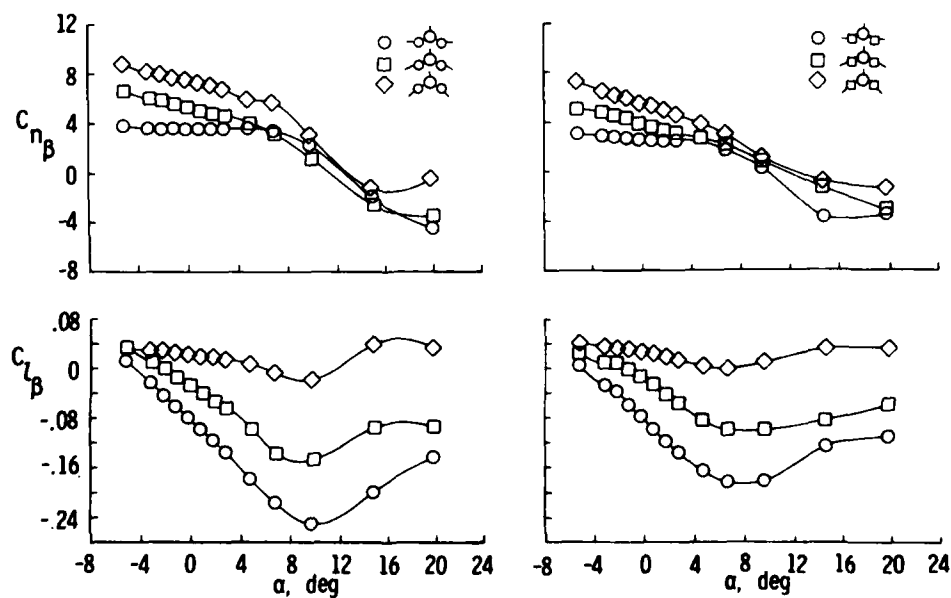
Figure 6. - Effect of inlet orientation on
lateral-directional stability.
M = 2.95
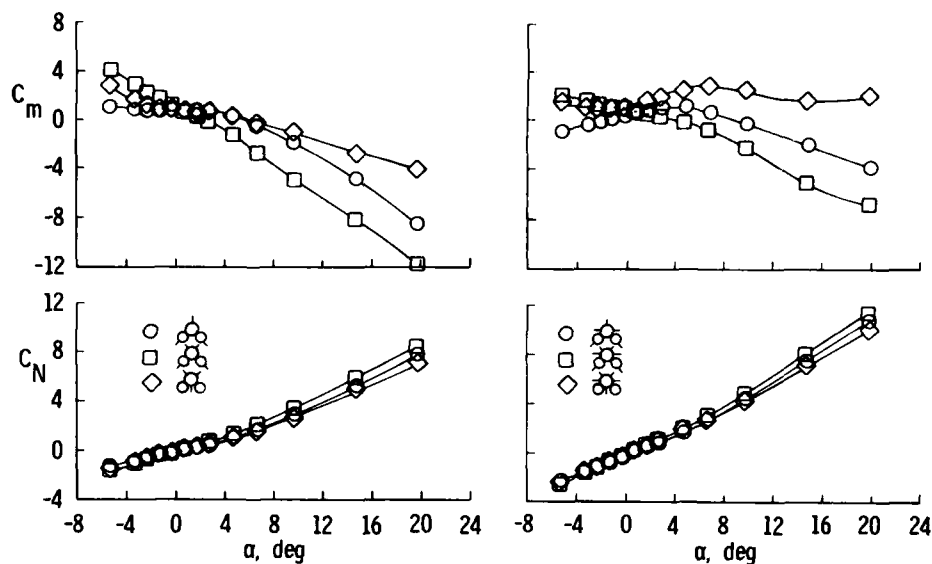
Figure 7. - Effect of tail configuration on longi-
tudinal aerodynamic characteristics
with and without wing. M = 2.95.
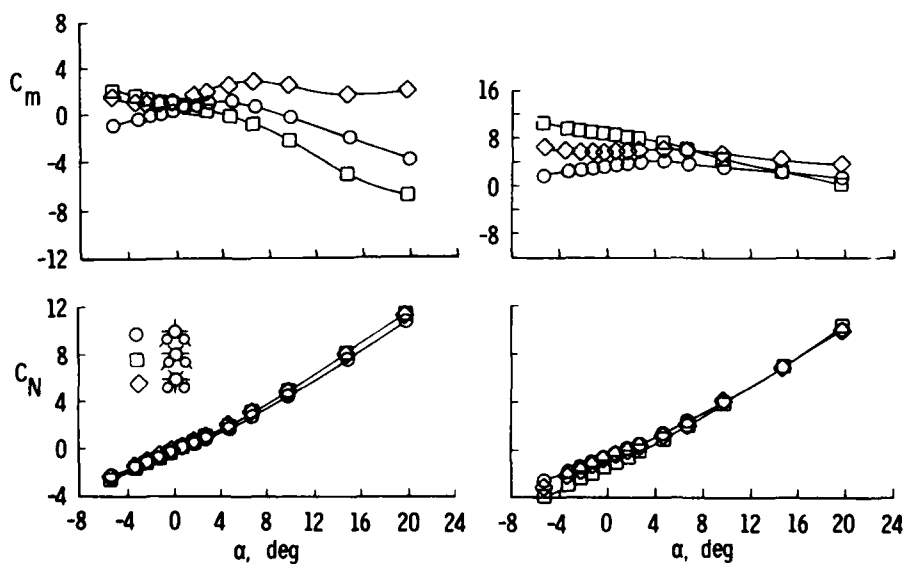
Figure 8. - Effect of -10° pitch control deflection
on three tail configurations. M = 2.95.
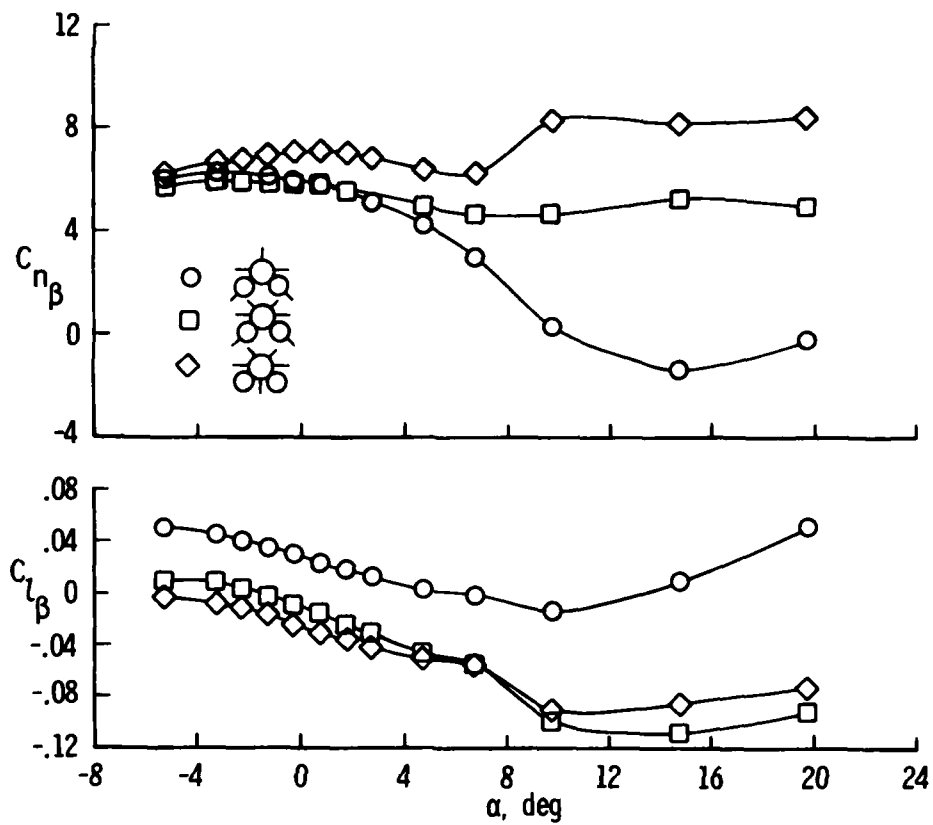
Figure 9. - Effect of tail configuration on lateral-
directional stability.   M = 2.95.

PARABOLIZED NAVIER-STOKES PREDICTIONS FOR

THREE-DIMENSIONAL VISCOUS SUPERSONIC FLOWS

S. Swaminathan,* M. D. Kim,*

R. A. Thompson,** and C. H. Lewis[†]

Virginia Polytechnic Institute and State University
Aerospace and Ocean Engineering Department
Blacksburg, Virginia

ABSTRACT

A parabolized Navier-Stokes Code (HYTAC) is used to pre-
dict the supersonic, laminar or turbulent viscous flow about arbi-
trary geometries at moderate angles of attack, and the results are
compared with those from other viscous and inviscid codes. The test
cases presented in this paper include the external flow over a su-
personic, blunt nosed inlet, a slab delta wing and an elliptic body
at various Mach numbers. The results for the inlet are compared
with the results from a viscous shock-layer code (VSL3D) and they
show good agreement. The slab delta wing surface pressure compares
well with the results from an inviscid code (STEIN) and with experi-
mental results. The surface heat transfer for this case is in good
agreement with the results from a boundary layer code using stream-
line tracing (TRACE) and with experimental results.

INTRODUCTION

The design and successful flight of high speed inlets and complex lift-
ing and reentry vehicles can be aided by the use of accurate and efficient
computational fluid dynamics. In this paper, results of computer analyses
of three bodies of complex shapes are given. The first body considered is a
supersonic blunt nosed inlet, designed to operate at Mach numbers from 4 to 7
and at angles of attack up to 10 degrees (Figure 1). The inlet is a sphere-
cone with an afterbody of smooth curvature. The second body is a slab delta
wing with 80 degree sweep angle (Figure 2). This wing has a nose radius of
0.5 inch and is designed to operate at a Mach number of 9.6 at various angles
of attack. The third geometry is an elliptic body, which has a spherical
nose of 0.3 feet radius and an afterbody with elliptical cross section
(Figure 3). The change from spherical to elliptical cross section is gradual,
and the final cross section of 2:3 ellipse is achieved within 8 to 10 nose
radii. This body is designed to operate at Mach numbers of about 20. Flight

---

*Graduate Student
**Senior Undergraduate Student
†Professor

performance under all the above conditions requires a thorough understanding of the aerodynamic forces and the surface heat transfer and of their influence on the vehicle trajectory and structure.

The flowfield over such general bodies can be quite complicated. The blunt nose generates a bow shock and within the shock layer, depending on the body geometry, imbedded shocks and expansion waves may exist. At moderate angles of attack there could be a large region of crossflow separation. The flowfield over these bodies under such flow conditions can be numerically predicted by solving the steady, three-dimensional Parabolized Navier-Stokes (PNS) equations. This method has a great savings in computer time compared to the solution of full Navier-Stokes equations. The PNS equations are parabolic in the streamwise direction and elliptic in the crossflow direction which makes it possible for this method to solve the crossflow separated region. The derivatives are written in the conservative form which makes it possible to capture the imbedded shocks in the flowfield.

In recent years the three-dimensional viscous shock-layer approach (VSL3D)[1] and the Parabolized Navier Stokes method (PNS)[2-4] have been applied to various problems. The VSL3D equations are parabolic in both streamwise and crossflow directions and are solved by efficient methods which require substantially less computing time than the PNS method. The VSL3D[1] method can be applied to general geometries to obtain the flowfield solution over the entire body when the angle of attack is not too high. For high angles of attack, the PNS methods are more efficient in handling crossflow separation.

In this paper, the general bodies noted above have been analyzed by different methods and the results are compared. The HYTAC code, developed by Helliwell and coworkers,[4,5] has been used to analyze all three bodies. The inlet has been analyzed by HYTAC, and the results are compared with those from VSL3D[1]. The results for the slab delta wing are compared with those from an inviscid plus streamline heat-transfer code (BLUNT-STEIN-TRACE)[6-9] and experimental results.[10]

The HYTAC code uses a body-normal, shock-normal nonorthogonal coordinate system (Figure 4). In this coordinate system the body and the bow shock are ξ-ζ coordinate surfaces. The second coordinate η is body-normal and shock-normal and always orthogonal to the ξ and ζ coordinates. At the body no-slip boundary conditions are used and the enthalpy is specified. At the shock, the freestream velocity vector is transformed into the computational coordinate direction, and then the Rankine-Hugoniot jump conditions are used. The governing equations are solved by implicit differencing in the η-ζ plane. A Gauss-Seidel iteration procedure is used in solving the equation.

ANALYSIS

Generation of a suitable computational grid is one of the important steps in the numerical solution of flowfields. In the present study, a body-oriented nonorthogonal coordinate system (ξ,η,ζ) has been used. The first coordinate, ξ is along the body in the primary flow direction (Figure 4). The third coordinate lines (ζ) are constructed to be normal to the ξ coordinate on the body surface, and this facilitates easy calculation of body forces and

moments and easy introduction of surface boundary condition. The second co-ordinate (η) is constructed normal to both ξ and ζ -coordinate lines in the region between the body and the shock surfaces. The shock surface is taken as a ξ-ζ coordinate surface (η=1) and the η-coordinate lines are both body-normal and shock normal. A body-oriented cylindrical coordinate system is used as the reference coordinate system for the interpretation of the body geometry, shock shape and every grid point. In this sytem, the ξ and ζ coordinates will not be orthogonal to each other in the region between the body and shock surfaces.

The steady three-dimensional parabolized Navier-Stokes equations are written in nondimensional form in a general curvilinear coordinate system. In the equations for the stress tensor components, all the derivatives with respect to ξ were neglected. The resulting equations are parabolic in the ξ coordinate direction and elliptic in the crossflow direction. The governing equations are solved by implicit differencing in the η-ζ plane. The ξ de-rivatives are approximated by a backward difference, while the η and ζ derivatives are written in terms of an unequally spaced three-point dif-ference scheme. The equations were linearized by the Newton-Raphson method and subsequently solved by Gauss-Seidel iteration.

At the surface boundary, no-slip conditions are used and the enthalpy is specified. Pressure on the body surface is obtained from the v-momentum e-quations. At the plane of symmetry, ζ = 0 and 180 degrees, w and g_{13} are antisymmetric while all the other variables and metrics are symmetric. At the shock Rankine-Hugoniot jump conditions are used as the boundary condition. Since the shock standoff distance is also an unknown, the continuity equa-tion is used as a sixth equation.

For a numerical procedure using a marching scheme, the construction of an accurate initial data plane is important in obtaining the correct solution of the whole flowfield. The entire flowfield, coordinate and metrics at the initial data plane have been generated using a viscous shock-layer method. The coordinate and metrics for the body-normal, shock-normal coordinate sys-tem have been generated from the two-step body-normal data of the shock-layer solution by the method described in References 4 and 5.

DESCRIPTION OF GEOMETRY AND FREESTREAM CONDITIONS

The various geometries included in this study are blunt nosed supersonic inlets, an 80-deg swept slab delta wing and an elliptic body. In this section the details of the geometries and the freestream conditions under which they are analyzed are explained.

The inlet is a blunt sphere-cone with an afterbody of smooth curvature. The blunt nose has a radius of 0.5 inch and the cone angle is 12.5 degrees. The afterbody is expressed in analytical form and the complete inlet is shown in Figure 1. In the present study, the external flowfield up to the cowl lip has been analyzed. The analysis of the inlet is done for a free-stream Mach number of 7 at 0 and 5 degrees angles of attack. Although the program has a capability to analyze a laminar flowfield, in this case turbu-lent flow is assumed and a two-layer eddy-viscosity model is used. The wall temperature is assumed to be constant, and the analysis is done for two

different temperatures. The details of the freestream conditions are given in Table 1.

Surface heat-transfer and pressure distribution over an 80-deg swept slab delta wing have been studied for a Mach number of 9.6 at zero and 10 degrees angles of attack. The wing has cylindrical leading edges, and a hemispherical nose of 0.5-inch radius. The length of the body is about 15 nose radii. The details of the geometry are given in Figure 2. In this case the laminar flow regime has been considered, and the surface temperature is about 540R.

The elliptic body has a spherical nose of radius 0.3 feet and an after-body with elliptical cross section. The change from spherical cross section to the elliptical cross section is gradual and is finally achieved after 8 to 10 nose radii. The final cross section obtained is a two by three ellipse. This body has been analyzed for a freestream Mach number of 20. The analysis is done for laminar flow and for a surface temperature of 800R. The details of the geometry are given in Figure 3, and the freestream conditions are given in Table 1.

RESULTS AND DISCUSSION

INLET GEOMETRY

Figures 5 and 6 show the variation of surface pressure and heat transfer for the inlet geometry at zero angle of attack. The surface pressure predictions agree very well with results from a viscous shock-layer code (VSL3D).[1] The surface heat-transfer predictions by HYTAC is higher than those from VSL3D by about 30 percent. Figures 7, 8 and 9 show the axial velocity, static pressure and enthalpy profiles for this case. From these profiles it can be seen that the HYTAC code is capable of capturing the imbedded shocks.

Figures 10 and 11 show the variation of surface pressure and heat transfer for angle of attack 5 degrees for various ζ angles. The solution could be obtained only up to 61 nose radii, and it was found that at this point axial separation occurred. This can be verified from the plot of axial shear stress variations as shown in Figure 12. At this point the surface slope of the body is about 20 degrees.

SLAB DELTA WING

The computed surface pressure from HYTAC and STEIN are compared with experimental results for both $\zeta = 0$ and 90 deg (Figures 13 and 14). For both cases the results are in good agreement. Figures 15 and 16 show the comparison of surface heat-transfer results from TRACE and HYTAC with the experimental results for $\zeta = 0$ and 90 deg. The predictions are good in the nose regions for both the cases. For the downstream region, HYTAC predicts a lower heat transfer for both cases. The predictions by TRACE seem to be in error in the far downstream region at $\zeta = 90$ deg. This may be due to the fact that the computed streamlines diverge from leading edge.

Figures 17 and 18 show the surface pressure results from STEIN and HYTAC for $\alpha = 10$ deg for both $\zeta = 0$ and 90 degree planes. For $\zeta = 0$, the results are compared with the experimental values, and both HYTAC and STEIN underpredict

the surface pressure. Experimental results are not available for ζ = 90 degree plane; however, the results from HYTAC and STEIN agree very well.

Figures 19 and 20 show the surface heat-transfer results from HYTAC and TRACE for α = 10 deg for both ζ = 0 and 90 degree planes. The results for the nose region agree well with the experimental values; however, both codes underpredict the surface heat transfer in the downstream region.

ELLIPTIC BODY

Figures 21 and 22 show the variation of surface pressure and heat transfer for various ζ planes for the elliptic body. Both the surface pressure and heat transfer are higher at the windward plane. Since the sphere-cone tangent locations depend on ζ, a patching is needed to obtain a smooth variation. This procedure resulted in a slightly concave region for ζ = 0 and 30 deg (Figure 31). The increase in surface pressure between s = 1.5 and 2.5 is due to this concavity in the geometry.

CONCLUDING REMARKS

The capability of HYTAC in predicting the three-dimensional viscous-supersonic flows over three geometries has been shown by comparison with experimental results and results from a viscous shock-layer code indicates that HYTAC can accurately solve the flowfield over axisymmetirc and nonaxisymmetric geometries. Although HYTAC requires more computing time, it is capable of solving the crossflow separated region. However, by looking at the results for the inlet geometry, it can be seen that HYTAC is unable to solve flow-fields with axial separation. In this particular case, even though the flow is attached for zero angle of attack, at moderate angles of attack like 5 degrees, the flow separates on the leeward side. In order to solve the separated flowfields, the time dependent Navier-Stokes equations must be solved.

Comparing the results for the inlet for zero angle of attack, with those from VSL3D shows that the VSL3D is able to solve the flowfield in less time. Although the surface pressure results are in good agreement, the surface heat-transfer results from HYTAC is higher by 30 percent. Due to lack of experimental data, the computational results could not be verified.

Both HYTAC and STEIN predicted the surface pressure over the slab delta wing reasonably accurately. The results for zero angle of attack agree very well with the experimental results. Both HYTAC and STEIN underpredict the surface pressure for 10 degree angle of attack. For the nose region the surface heat-transfer results from TRACE and HYTAC agree very well with the experimental results. For the downstream region, the prediction by TRACE seems to be in error, and this is due to the fact that the computed streamlines diverge from leading edge.

The results for the elliptic body could not be compared with other results due to a lack of data. HYTAC predicts higher heat transfer and surface pressure at the windward plane. Because of the presence of a concavity in the geometry near the sphere-cone tangent point for ζ = 0 and 30 degrees, the surface pressure results are higher at these locations.

In summary, methods have been shown which can predict supersonic viscous flowfield over complex three-dimensional bodies at angles of attack up to about 15 degrees.

NOMENCLATURE

g_{ij}	coordinate metric tensor i, j = 1,2,3
H	total enthalpy, H^*/h_∞
h	static enthalpy, h^*/h_∞
M_∞	freestream Mach number
p	pressure, $p^*/\rho_\infty U_\infty^2$
P_{ref}	reference pressure, $\rho_\infty U_\infty^2$
$\dot{q}^*$	dimensional heat-transfer rate
Re_∞, R_n	freestream Reynolds number
R_n	nose radius of curvature
STINF	Stanton number, $\dot{q}^*/\rho_\infty U_\infty (H_0^* - H_w^*)$
s	surface distance coordinate measured along the body, s^*/R_n^*
T	temperature, T^*/T_∞
U_∞	dimensional freestream velocity
u	velocity component along ξ coordinate, u^*/U_∞
v	velocity component along η coordinate, v^*/U_∞
w	velocity component along ζ coordinate, w^*/U_∞
z,r,ϕ	body-oriented cylindrical coordinate system
α	angle of attack, degree
θ_c	cone half angle, degree
μ	coefficient of viscosity, μ^*/μ_∞
ρ	density, ρ^*/ρ_∞
η	coordinate, body-normal, shock-normal direction
ξ	coordinate, along the body
ζ	coordinate, normal to ξ and η on the body surface

Subscript

w   wall value

0   stagnation condition

∞   freestream condition (dimensional quantity)

Superscript

*   dimensional quantity

REFERENCES

1. Szema, K. Y. and Lewis, C. H.: "Three-Dimensional Hypersonic Laminar, Transitional and/or Turbulent Shock-Layer Flows." AIAA Paper No. 80-1457. AIAA 15th Thermophysics Conference, Snowmass, Colorado, July 14-16, 1980.

2. Lubard, S. C. and Helliwell, W. S.: "Calculation of the Flow on a Cone at High Angle of Attack," AIAA J., Vol. 12, No. 7, July 1974, pp. 965-974.

3. Agopian, K., Collins, J., Helliwell, W., Lubard, S. C. and Swan, J.: "NASA Viscous 3-D Flowfield Calculations," R&D Associates, RDA-TR-6100-007, October 1975.

4. Helliwell, S. W., Dickinson, R. P. and Lubard, S. C.: "HYTAC Phase 1 Report: Viscous Flow over Arbitrary Geometries at High Angle of Attack," Arete Associates Technical Report, AR-79-046-TR, April 24, 1979.

5. Helliwell, W. S., Dickinson, R. P. and Lubard, S. C.: "HYTAC User's Manual," Arete Associates Technical Report, AR-80-207-TR, July 31, 1980.

6. Moretti, G. and Bleich, G.: "Three-Dimensional Flow Around Blunt Bodies," AIAA J., Vol. 5, 1966.

7. Marconi, F., Salas, M. and Yaeger, L.: "Development of a Computer Code for Calculating the Steady Super/Hypersonic Inviscid Flow Around Real Configurations." Volume I - Computational Technique, NASA-CR-2675, April 1976.

8. Marconi, F., Salas, M. and Yaeger, L.: "Development of a Computer Code for Calculating the Steady Super/Hypersonic Inviscid Flow Around Real Configurations." Volume II - Code Description, NASA-CR-2676, April 1976.

9. Hamilton, H. Harris: "Calculation of Heating Rates on Three-Dimensional Configurations," thesis for Degree of Engineer, School of Engineering and Applied Science of the George Washington University, December 1978.

10. Whitehead, A. H. Jr. and Dunavant, J. C.: "A study of Pressure and Heat Transfer over an 80° Sweep Slab Delta Wing in Hypersonic Flow," NASA-TN-D2708, Langley Research Center, November 9, 1964.

TABLE I. TEST CASE CONDITIONS

Geometry	Flow Type	Nose Radius (ft)	α (deg)	M_∞	FREESTREAM CONDITIONS					WALL CONDITIONS	
					Altitude (ft)	T_∞ (°R)	Re_∞, R_n	ρ_∞ (lbm/ft³)	υ_∞ (ft/sec)	T_w/T_0	T_w/T_∞
INLET	TURB	0.04167	0	7	80,000	394.69	81781.4	2.78×10^{-3}	6816.3	0.1877	2.027
INLET	TURB	0.04167	0	7	80,000	394.69	81781.4	2.78×10^{-3}	6816.3	0.821	8.867
INLET	TURB	0.04167	5	7	80,000	394.69	81781.4	2.78×10^{-3}	6816.4	0.821	8.88
ELLIPTIC	LAM	0.3	0	20		392.59	542841	4.76×10^{-3}	19423.3	0.02516	2.0378
SLAB DELTA	LAM	0.04167	0	9.6		84.4	57701.3	6.46×10^{-4}	4348.5	0.33	6.413
SLAB DELTA	LAM	0.04167	10	9.6		84.4	57701.3	6.40×10^{-4}	4348.5	0.33	6.413

TABLE II. TEST CASE COMPUTING TIMES*

	α (degrees)	Method of Solution	ξ range	ξ steps	η points	ζ planes	Time min:sec
INLET	0	HYTAC	1.22-69	137	50	3	9:20
INLET	0	VSL3D	0-69.7	135	101	1	3:44
INLET	5	HYTAC	1.14-61	96	50	19	57:47
SLAB DELTA	0	HYTAC	1.22-14.2	50	50	19	39:22
	10	HYTAC	1.22-9.64	33	50	19	27:35
ELLIPTIC	0	HYTAC	1.22-8.18	28	50	19	20:01

*CPU time on IBM 3032 H=OPT2 compiler.
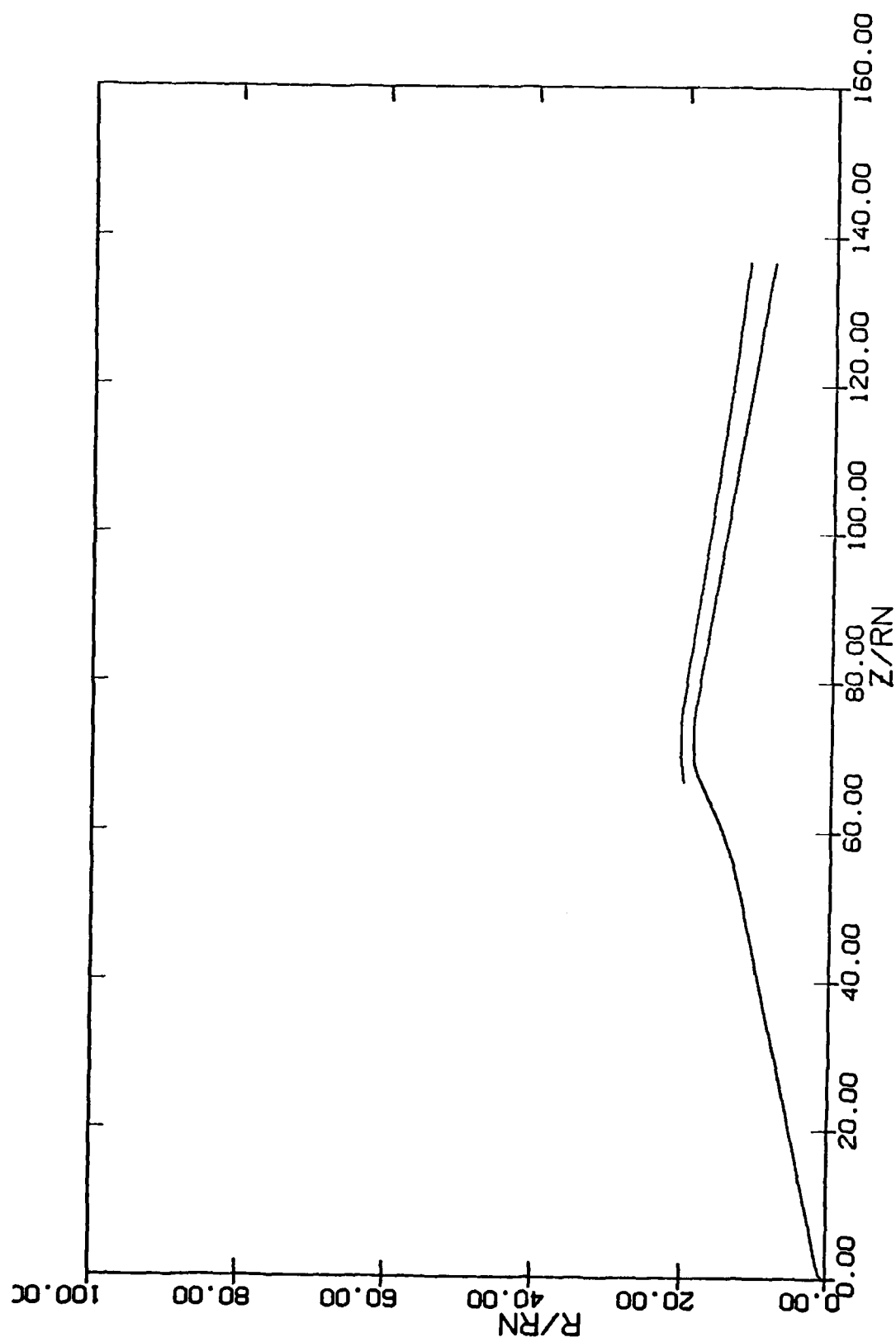
Figure 1. Inlet Geometry

7.06R

10°

1.0R

2.0R

15.26R

1.0R
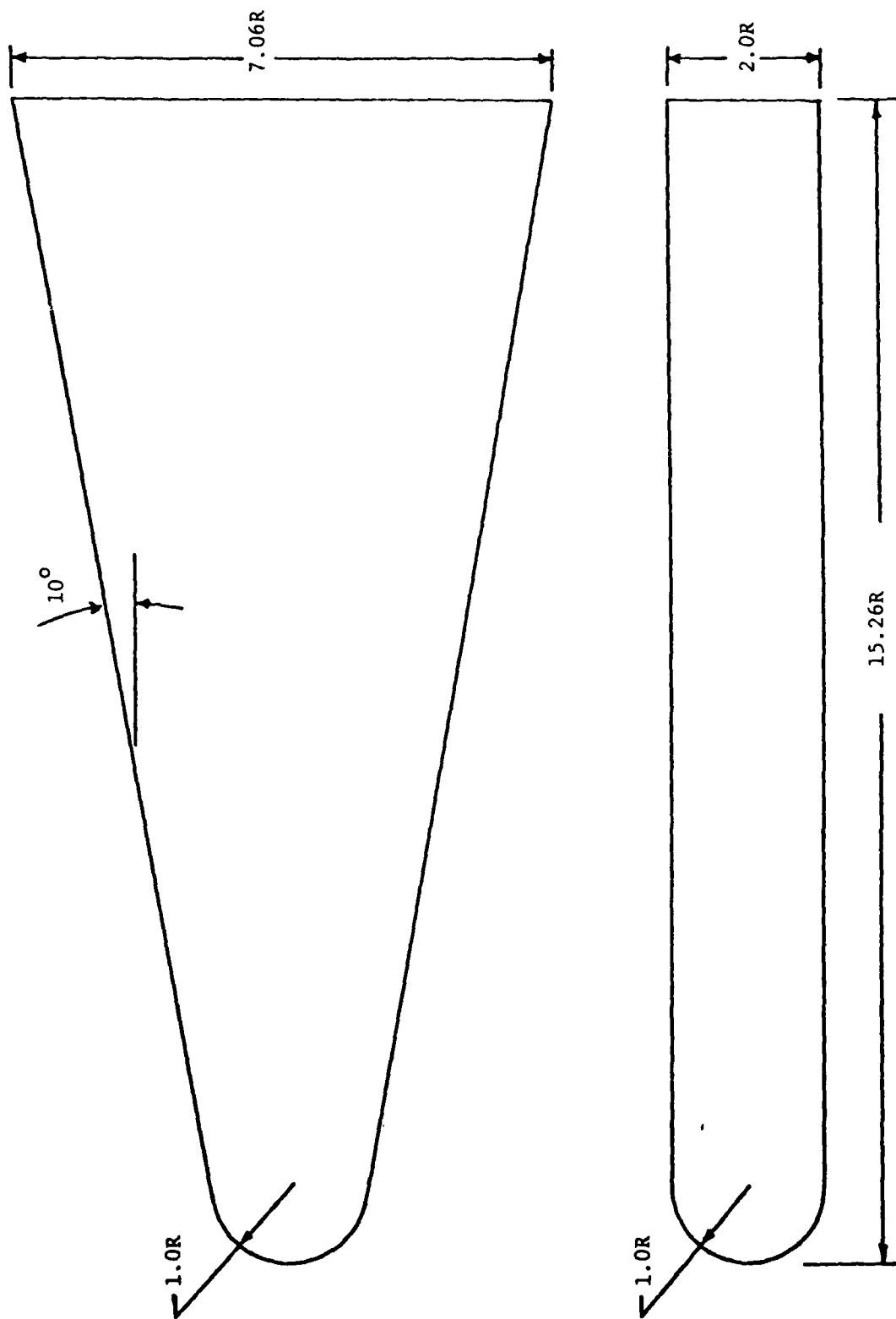
Figure 2. Slab Delta Wing

II-73
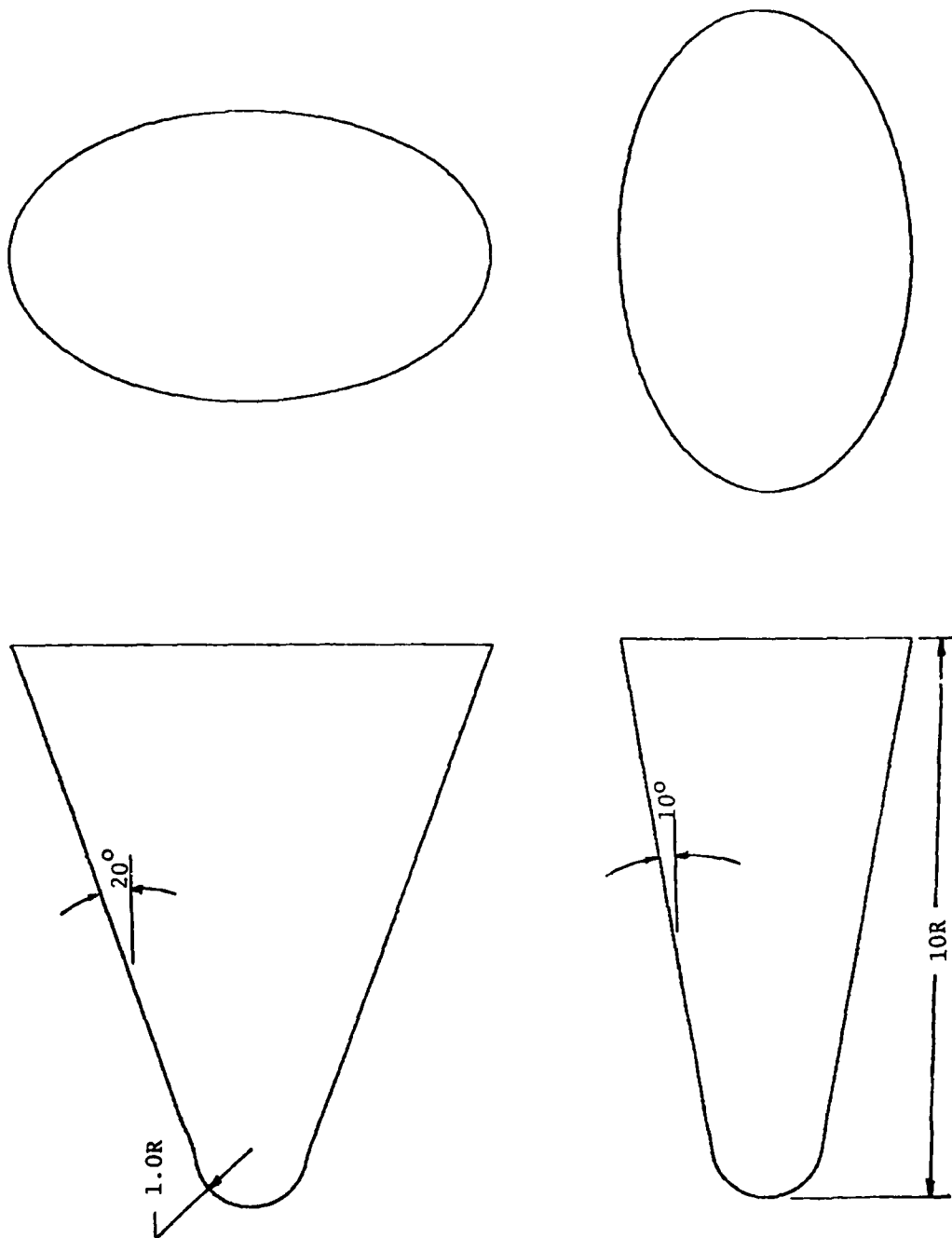
Figure 3. Blunt Elliptic Cone Geometry
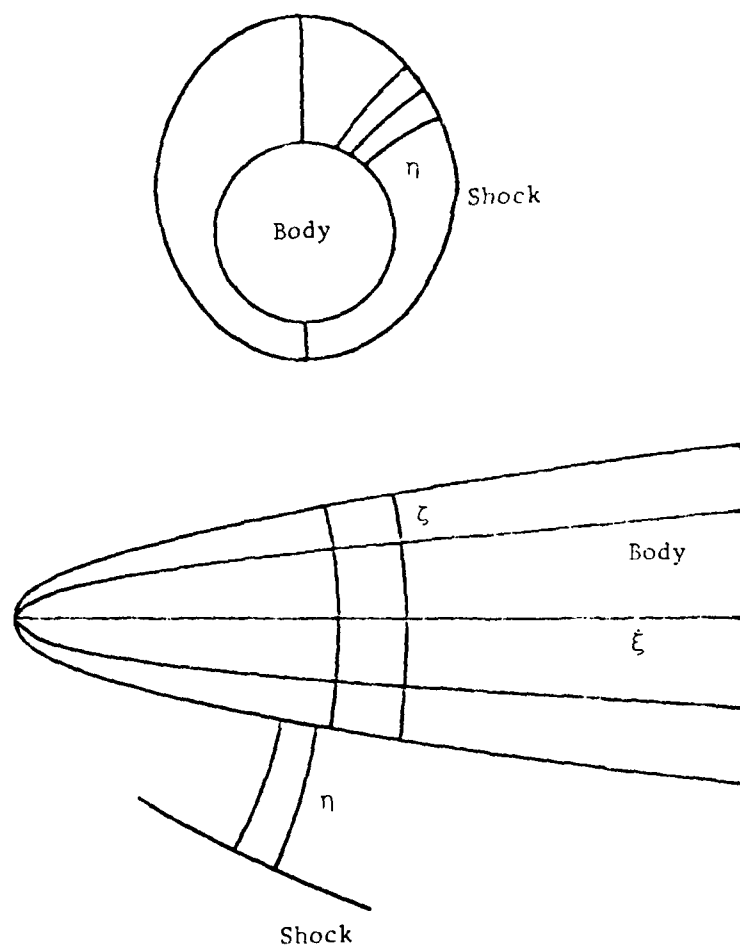
Figure 4. Coordinate System for HYTAC
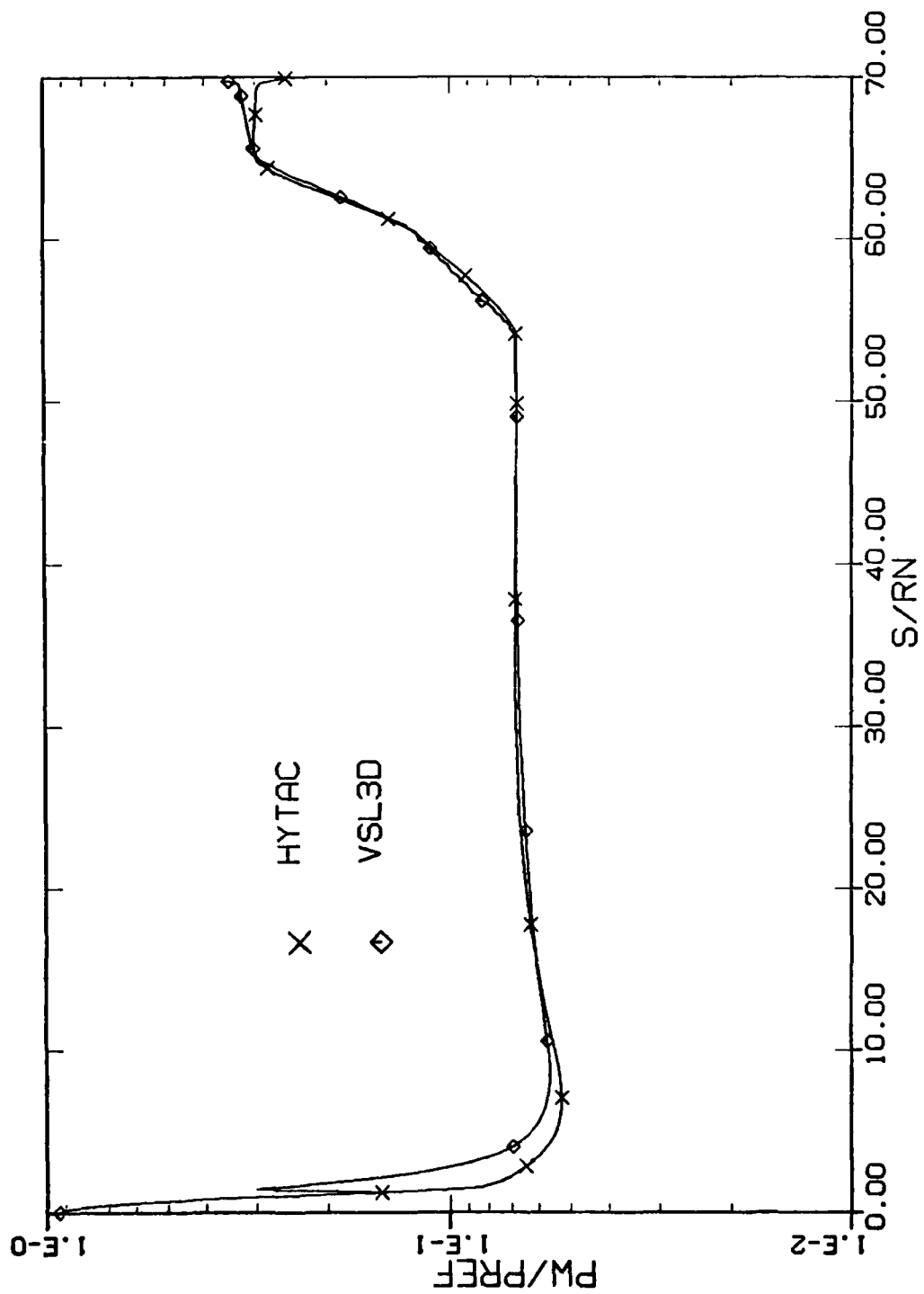
Figure 5. Surface Pressure Distribution for Inlet Geometry at α = 0
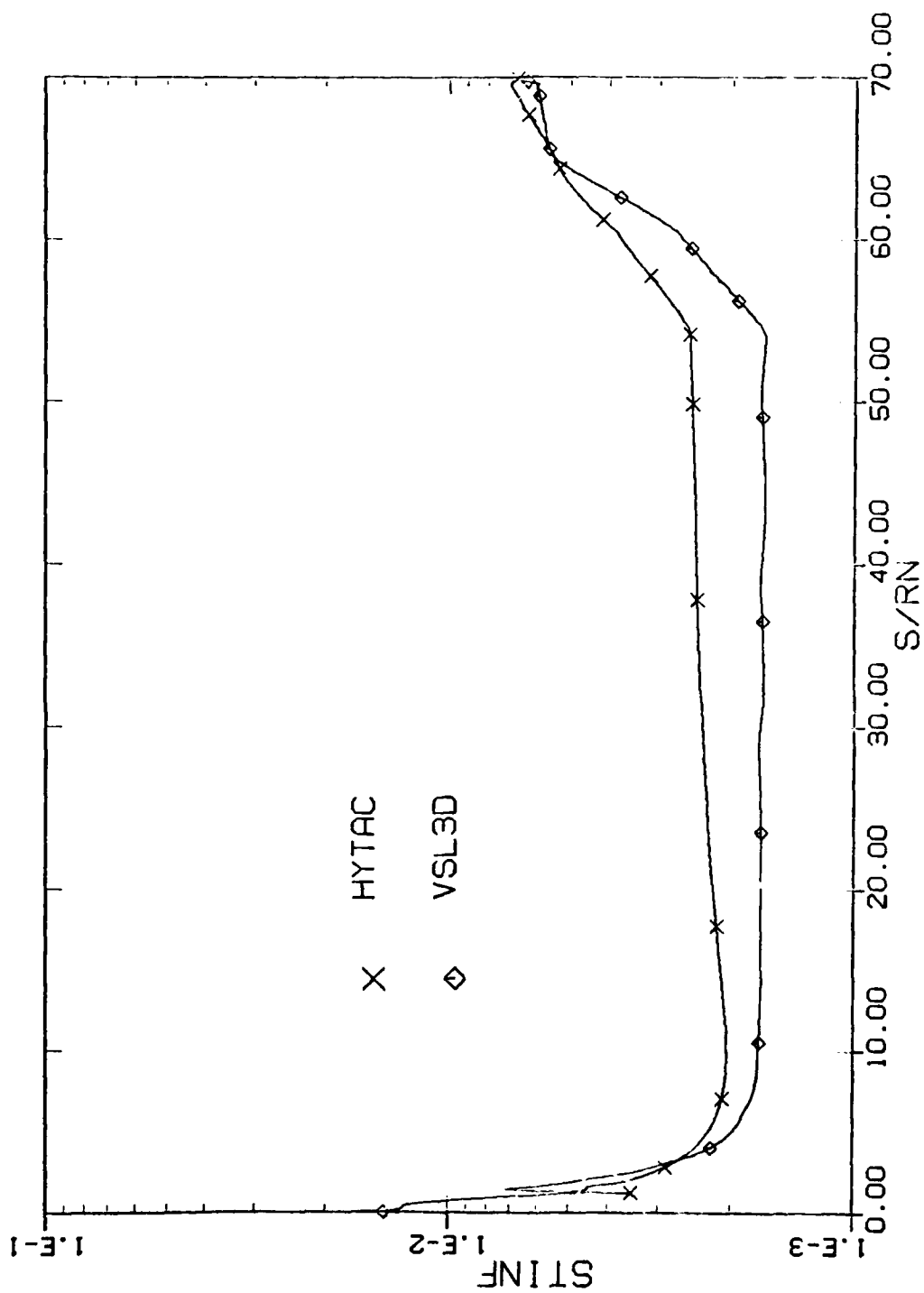
Figure 6. Surface Heat-Transfer Distribution for Inlet Geometry at $\alpha = 0$
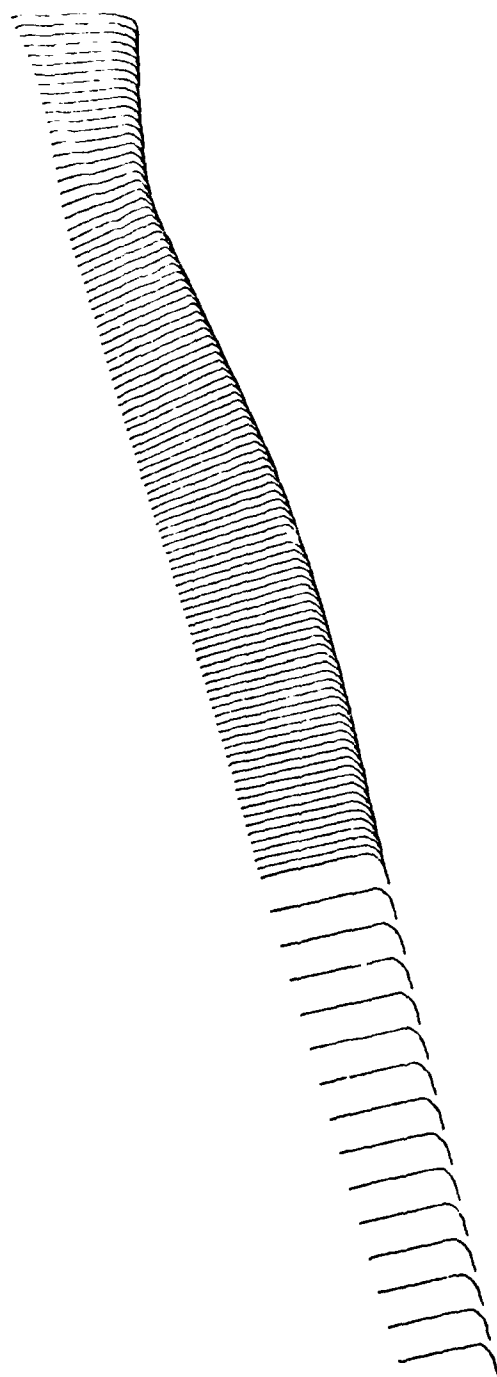
Figure 7. Axial Velocity Profiles for Inlet Geometry at $\alpha = 0$

1.0

1.1

1.25

4.5
5.0
5.6

2.8
3.2
3.6
4.0

4.5 2.5

2.2

2.0

1.8

1.4 1.6
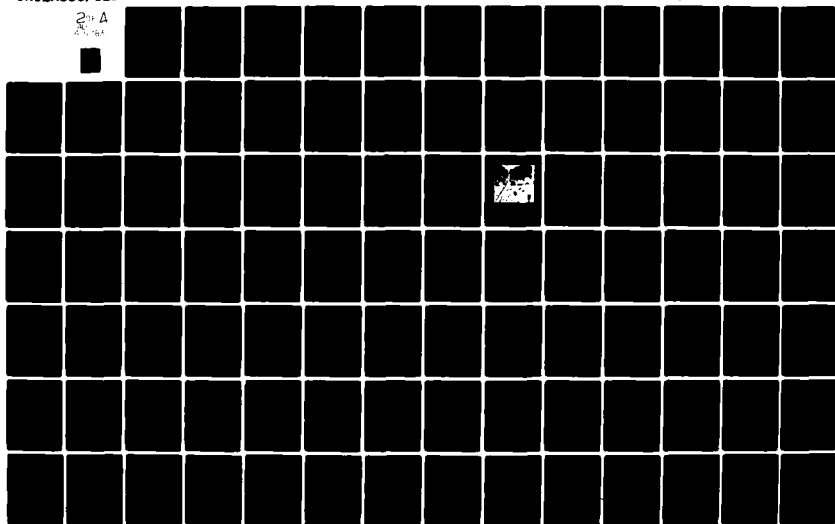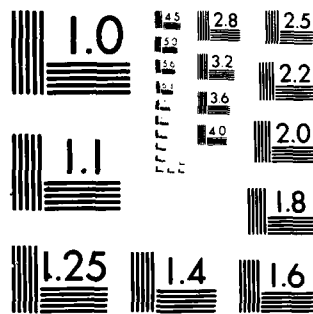
MICROCOPY RESOLUTION TEST CHART
NATIONAL BUREAU OF STANDARDS 1963 A
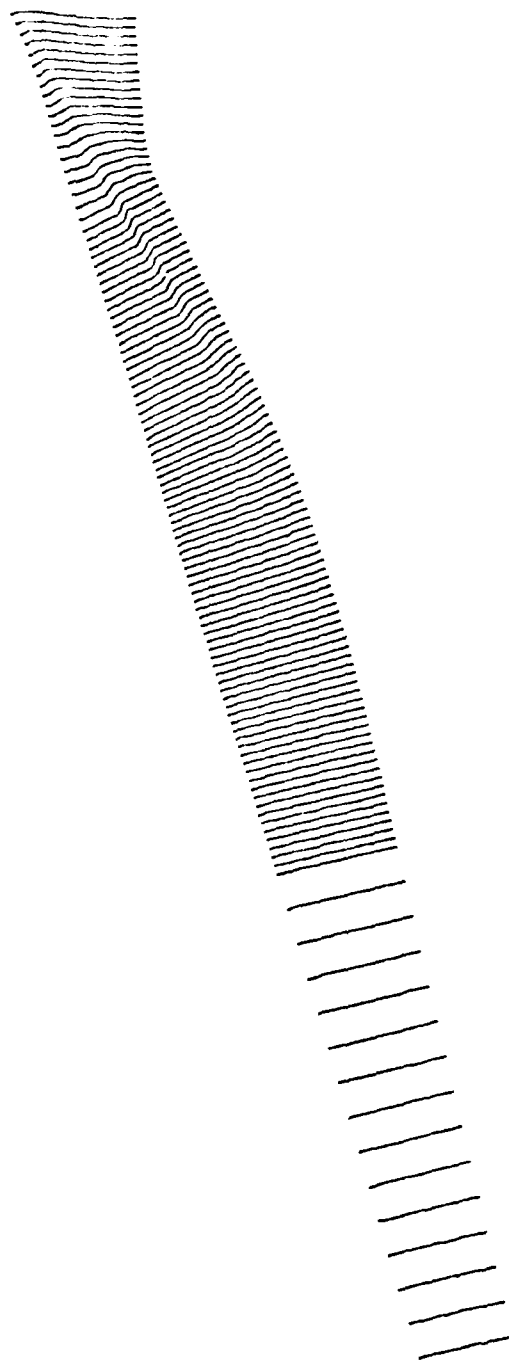
Figure 8. Static Pressure Profiles for Inlet Geometry at $\alpha = 0$
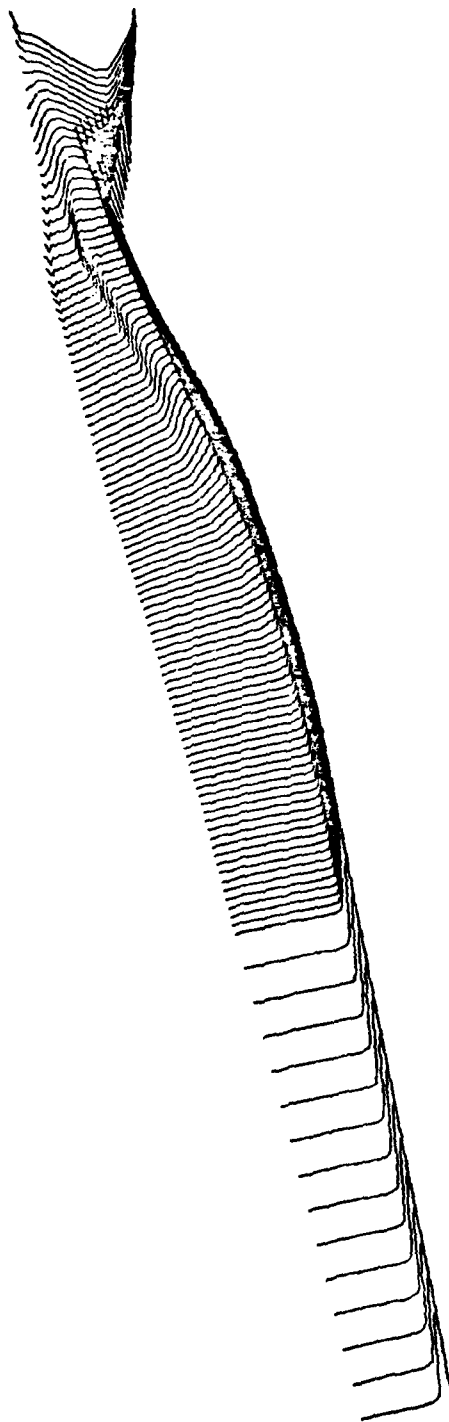
Figure 9.   Static Enthalpy Profiles for Inlet Geometry at $\alpha = 0$
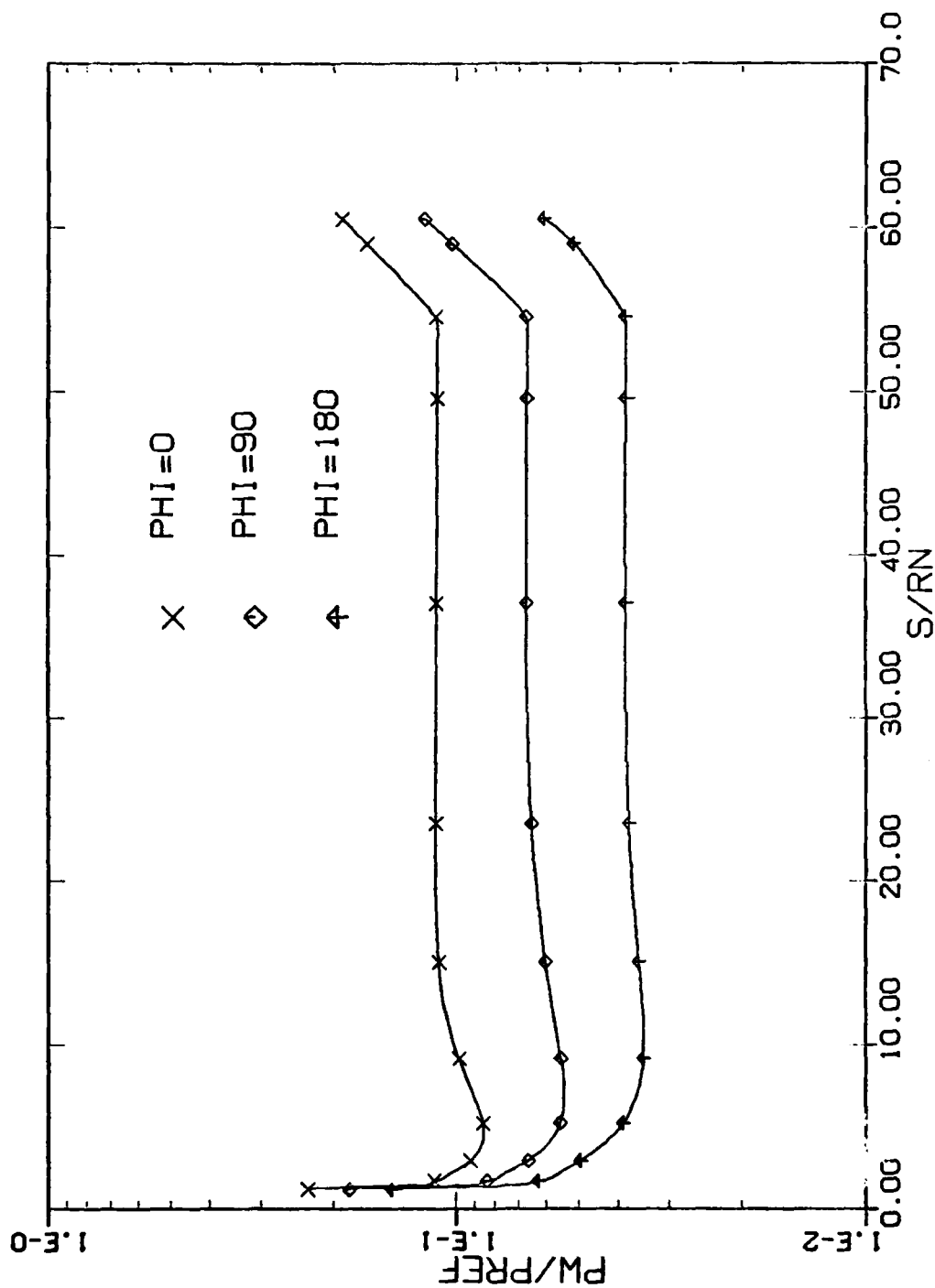
Figure 10. Surface Pressure Distribution for Inlet Geometry at $\alpha = 5^{\circ}$
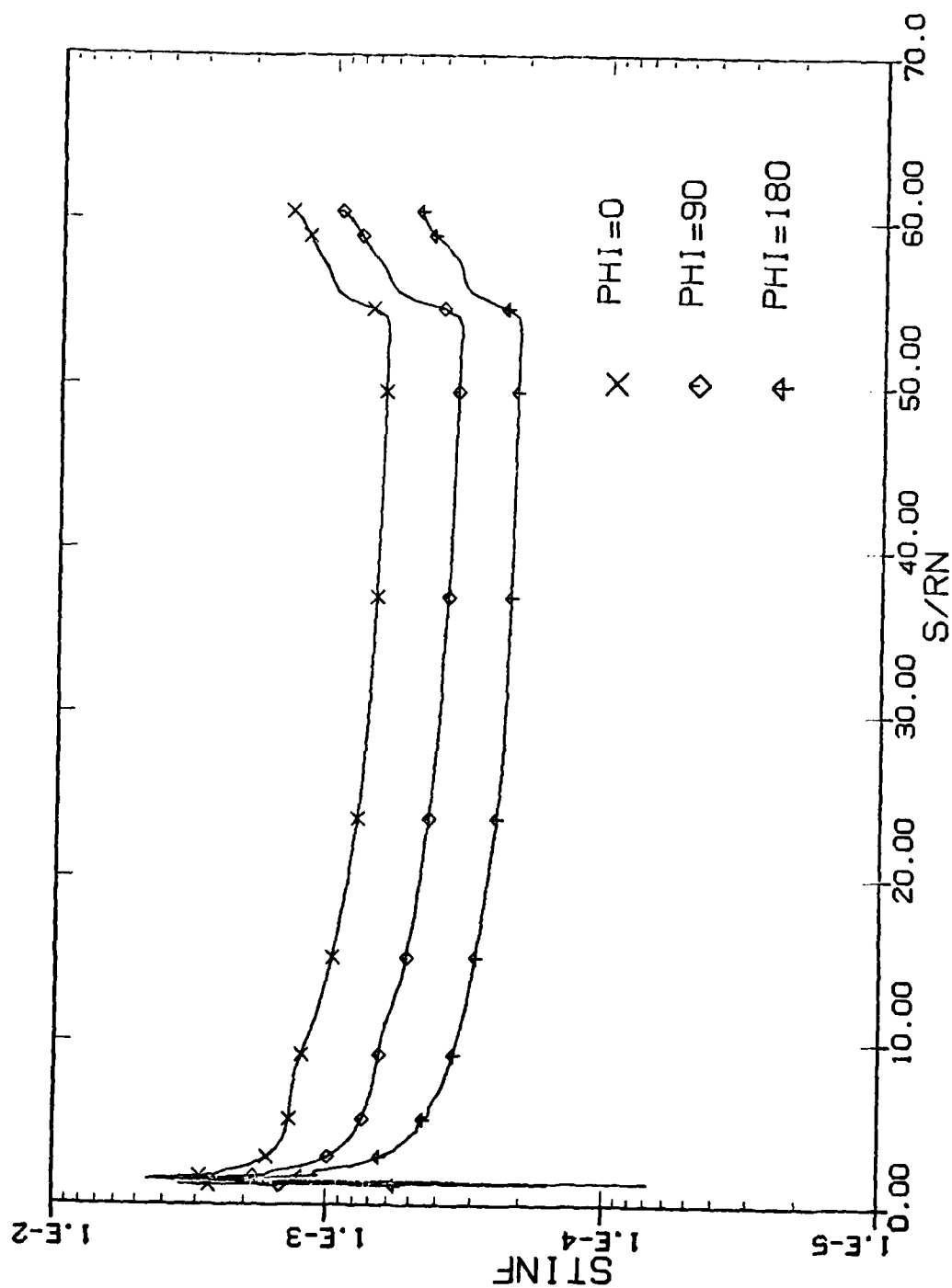
Figure 11. Surface Heat-Transfer Distribution for Inlet Geometry at $\alpha = 5°$
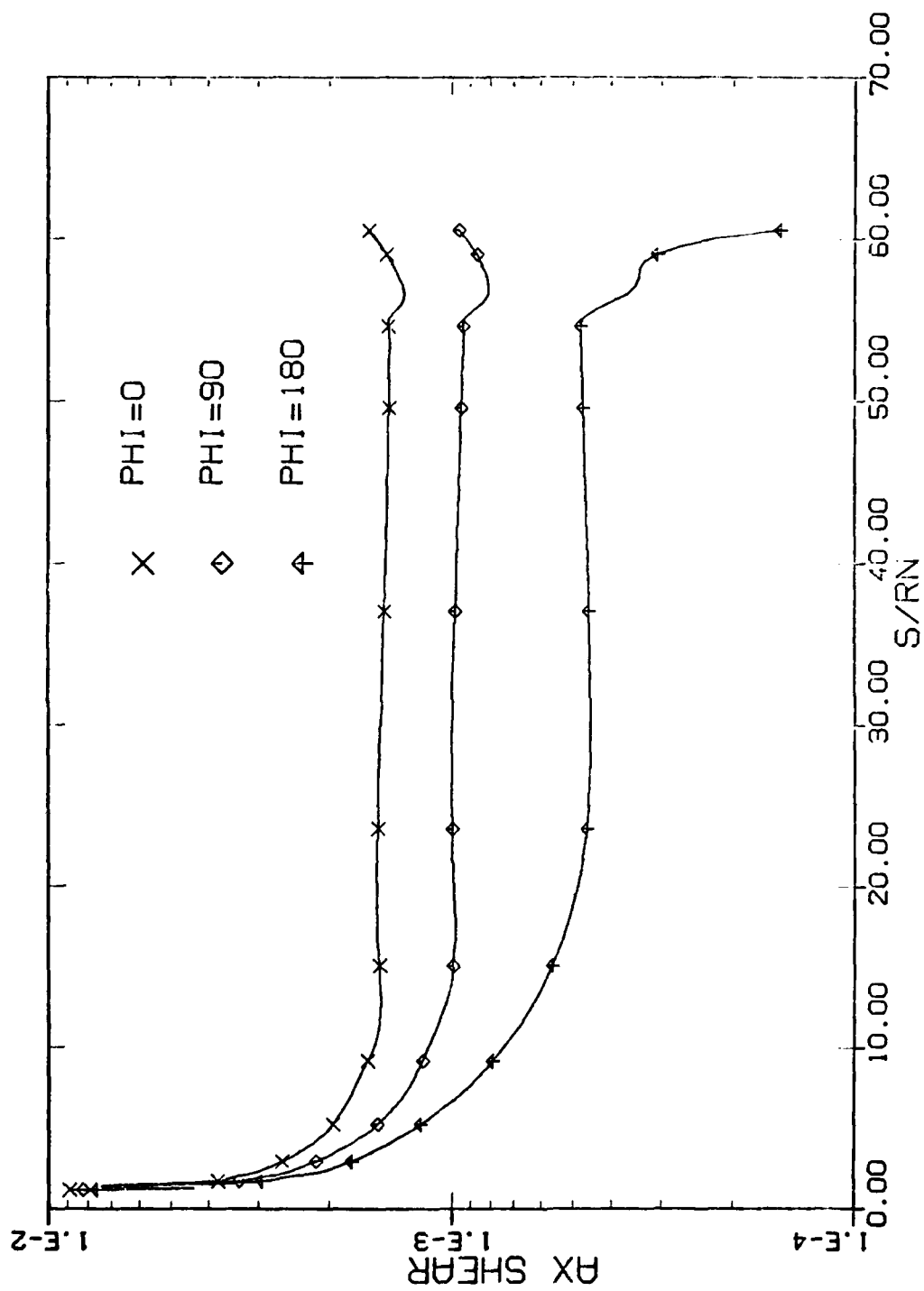
Figure 12. Axial Shear-Force Distribution for Inlet Geometry at $\alpha = 5^\circ$
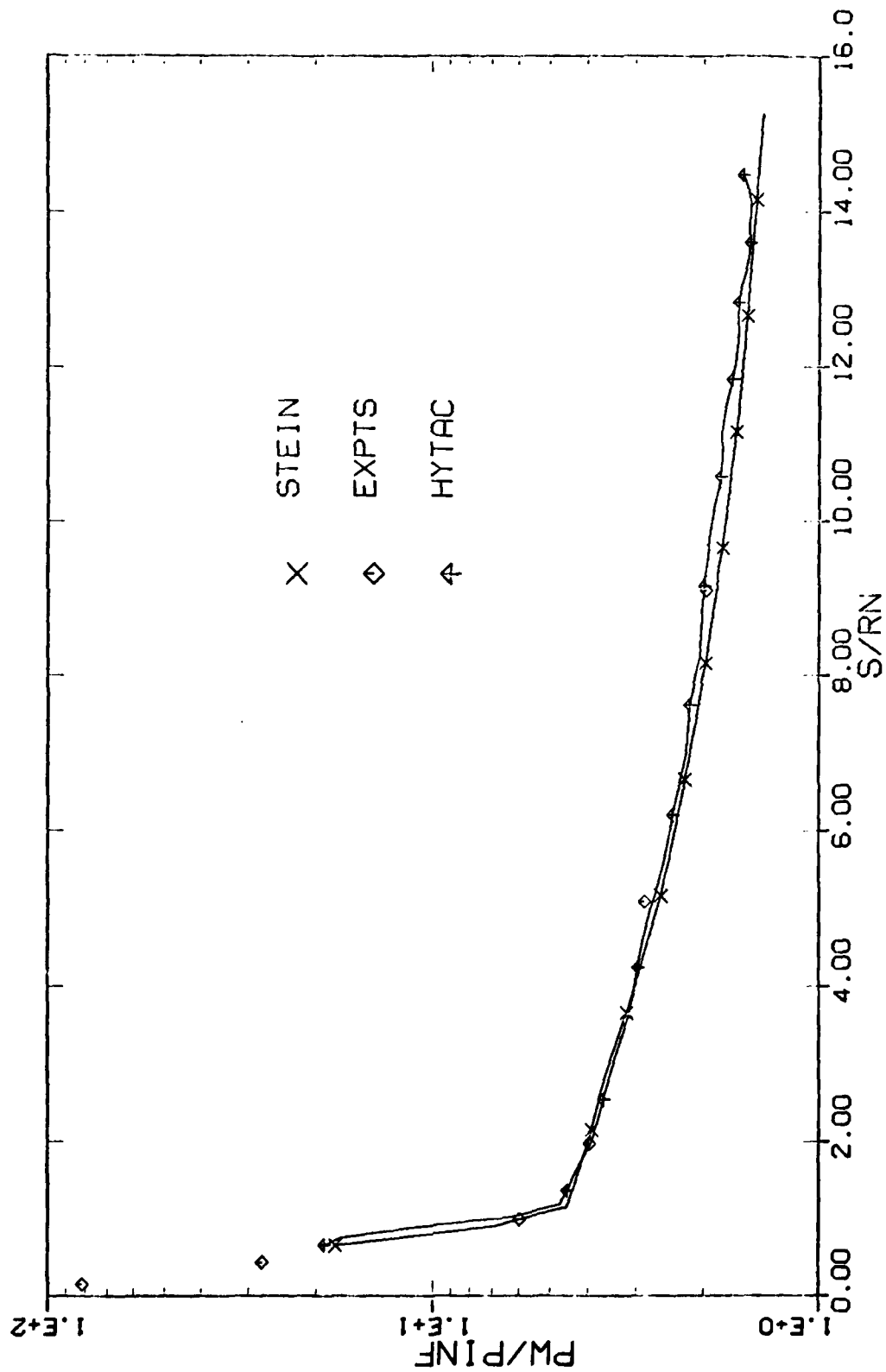
Figure 13. Surface Pressure Distribution for Slab Delta Wing at $\alpha = 0$ and $\zeta = 0$
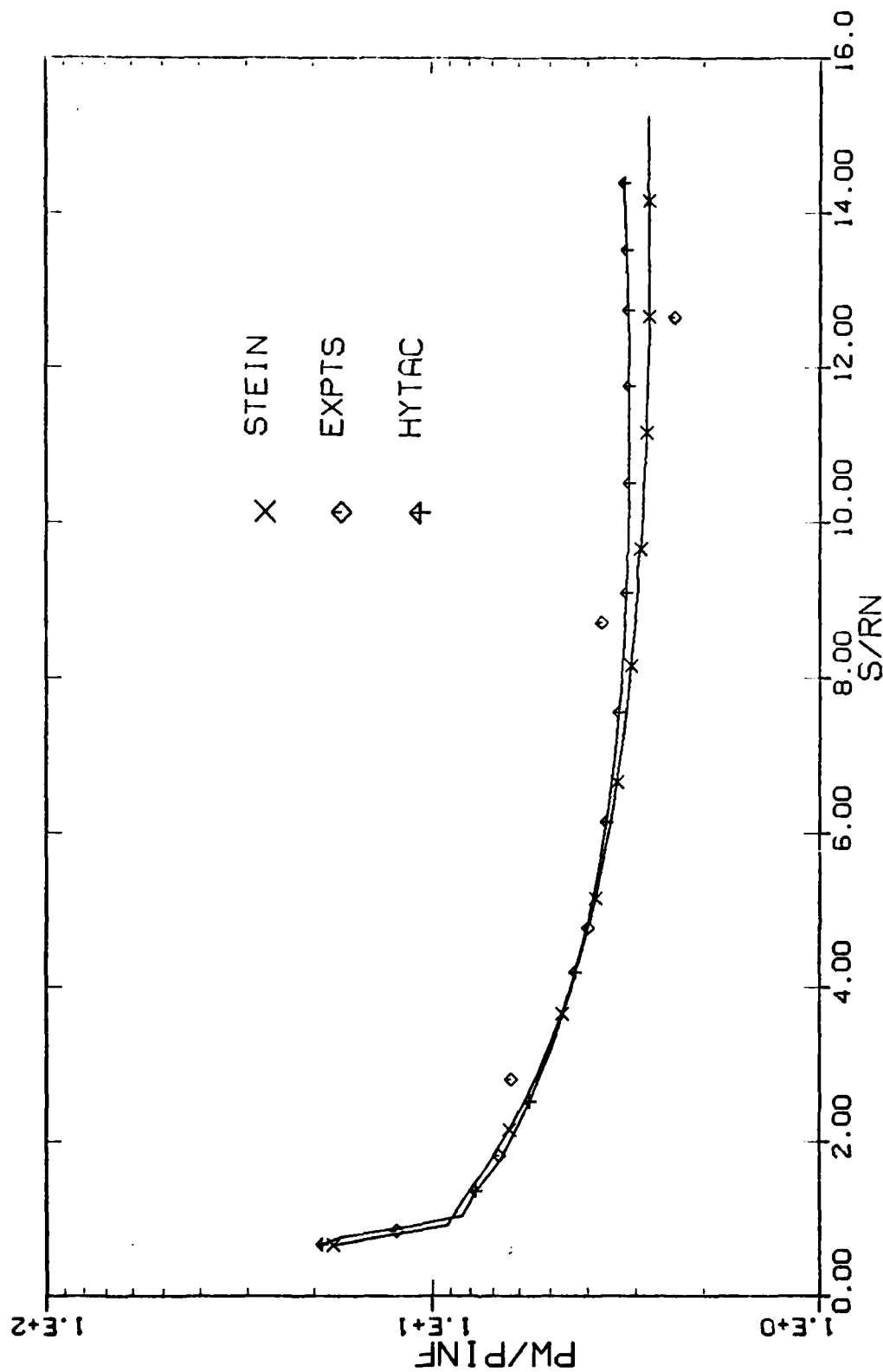
Figure 14. Surface Pressure Distribution for Slab Delta Wing at $\alpha = 0$ and $\zeta = 90$ deg
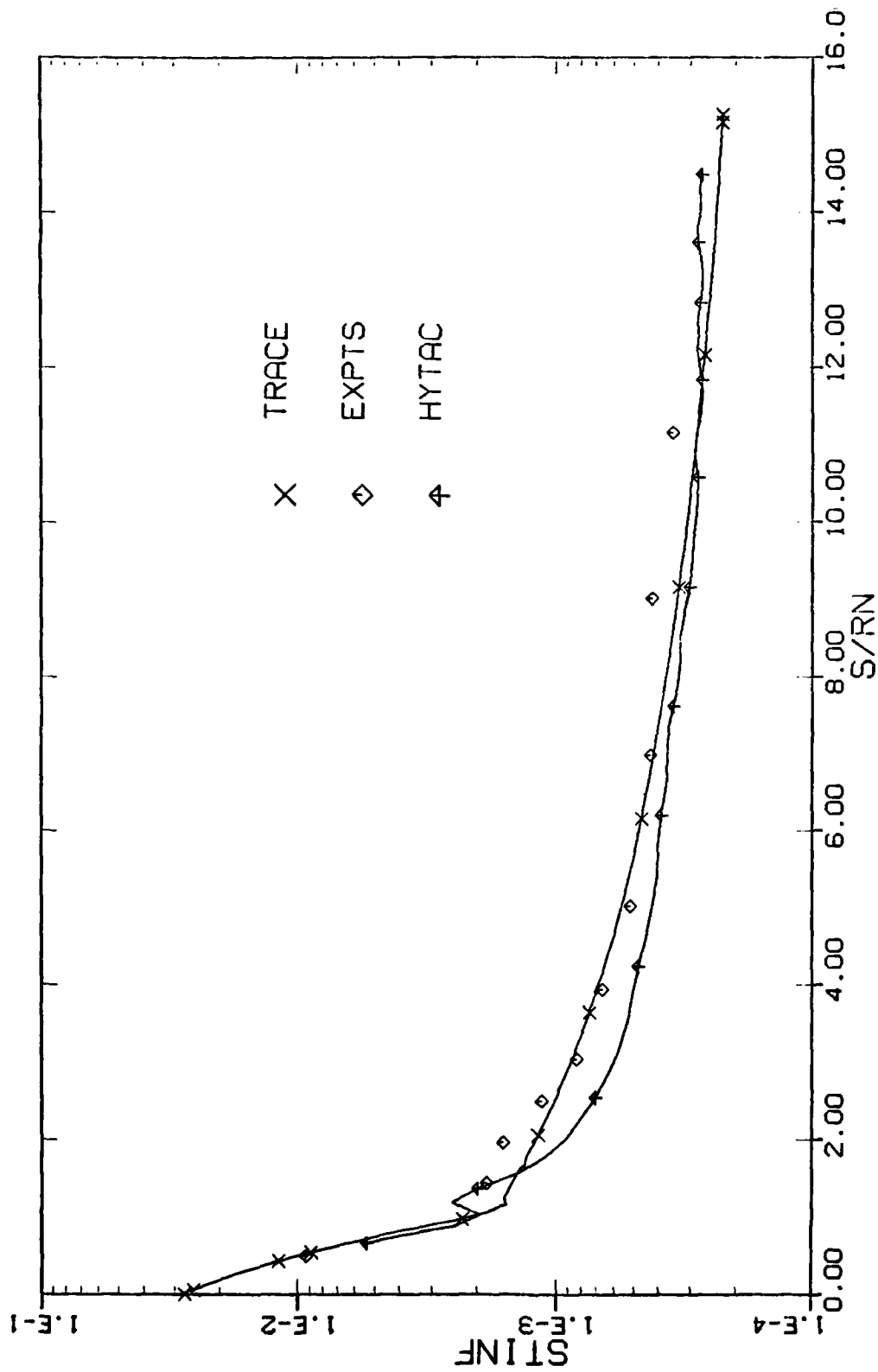
Figure 15. Surface Heat-Transfer Distribution for Slab Delta Wing at $\alpha = 0$ and $\zeta = 0$ deg
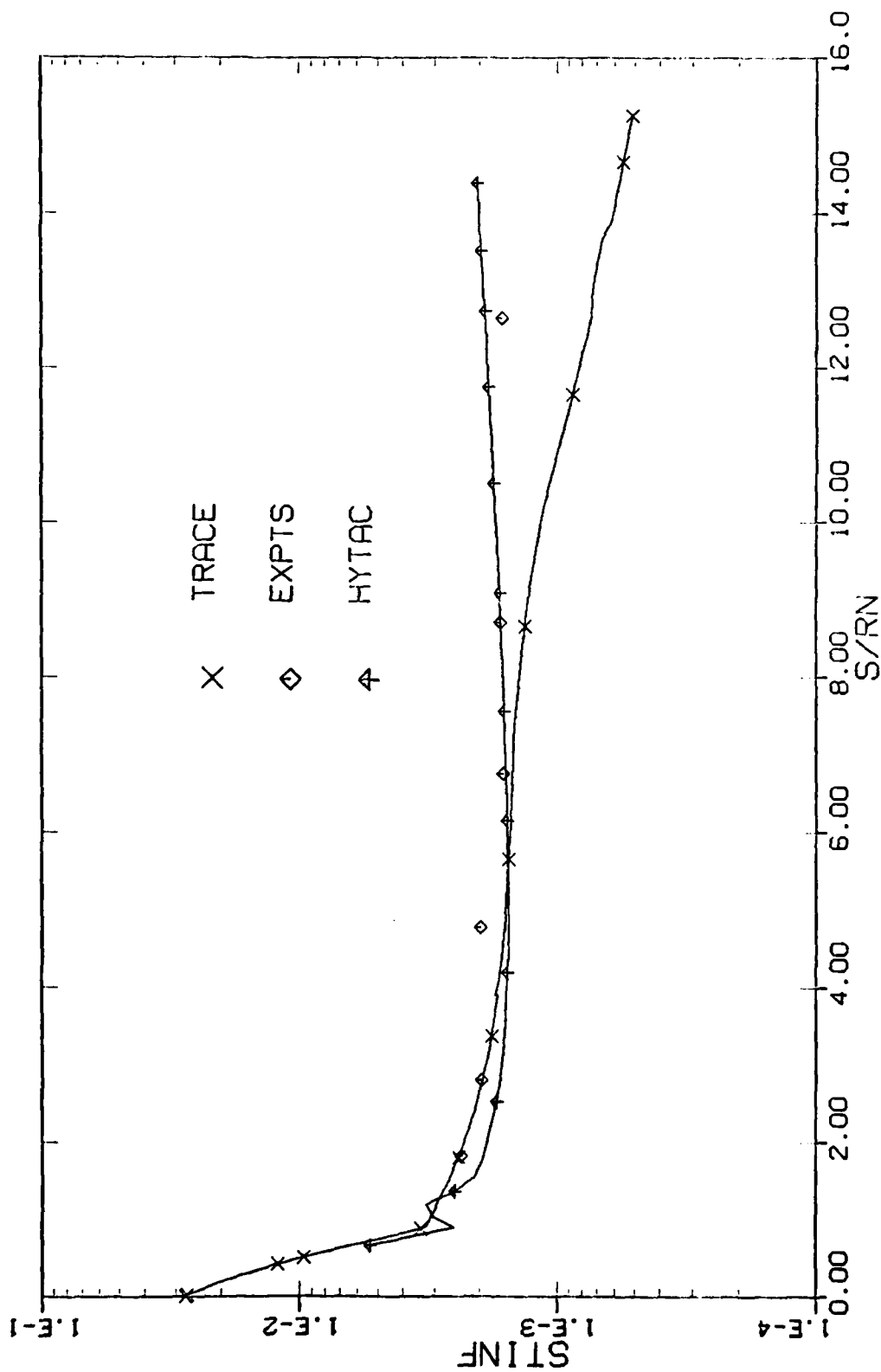
Figure 16. Surface Heat-Transfer Distribution for Slab Delta Wing at α = 0 and ζ = 90 deg
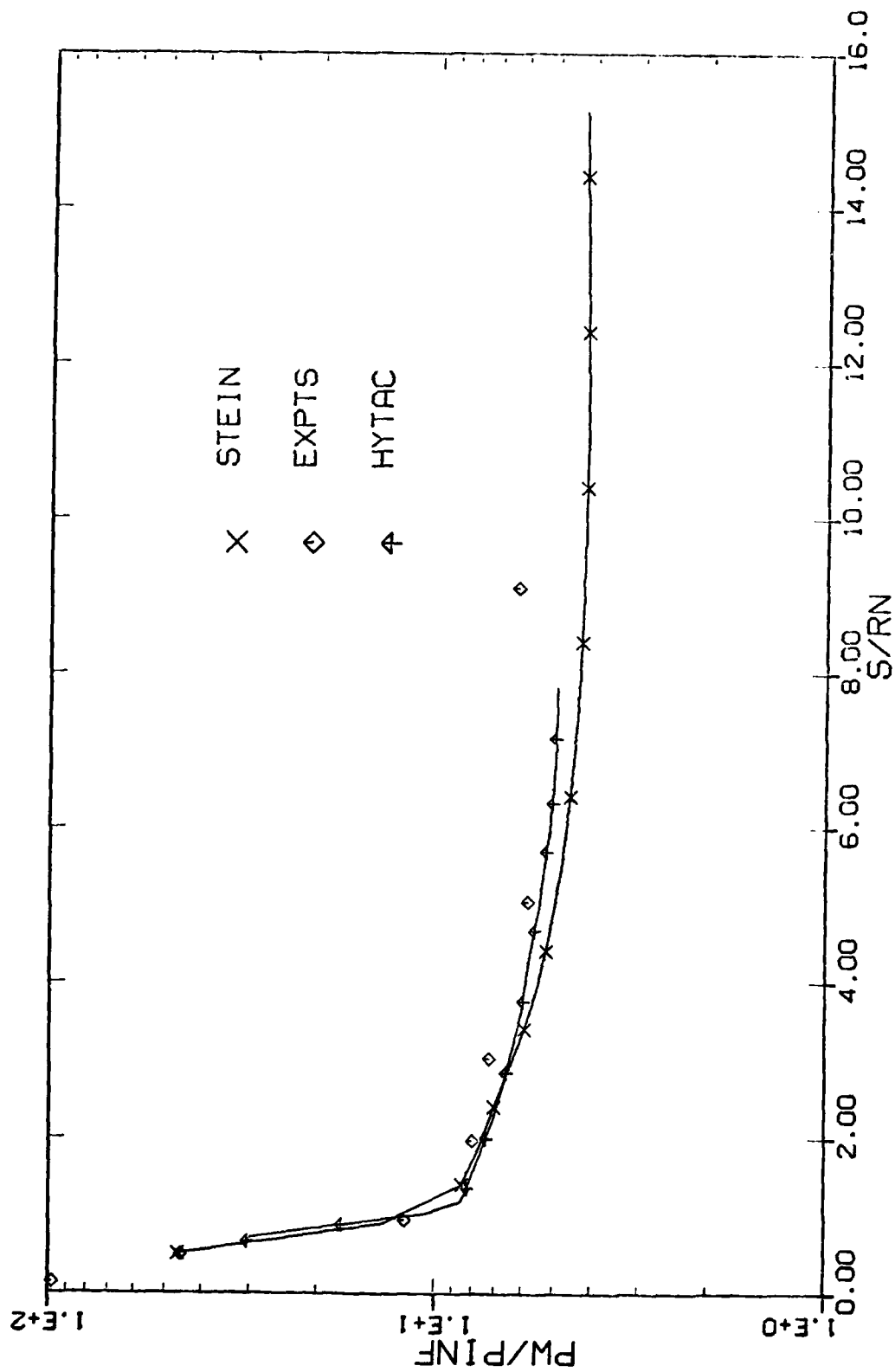
Figure 17.   Surface Pressure Distribution for Slab Delta Wing at $\alpha = 10$ and $\zeta = 0$ deg
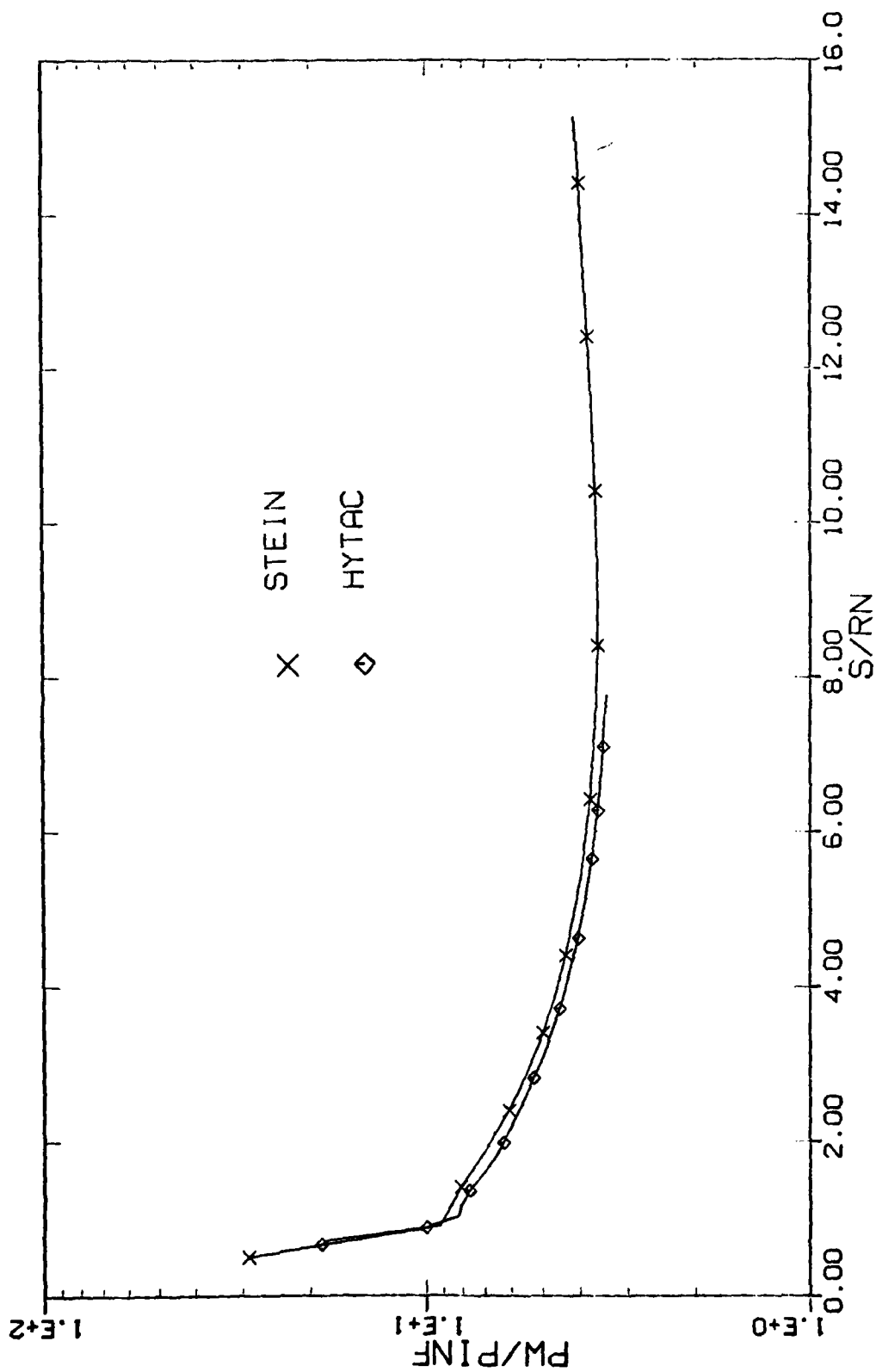
Figure 18. Surface Pressure Distribution for Slab Delta Wing at α = 10 and ζ = 90 deg
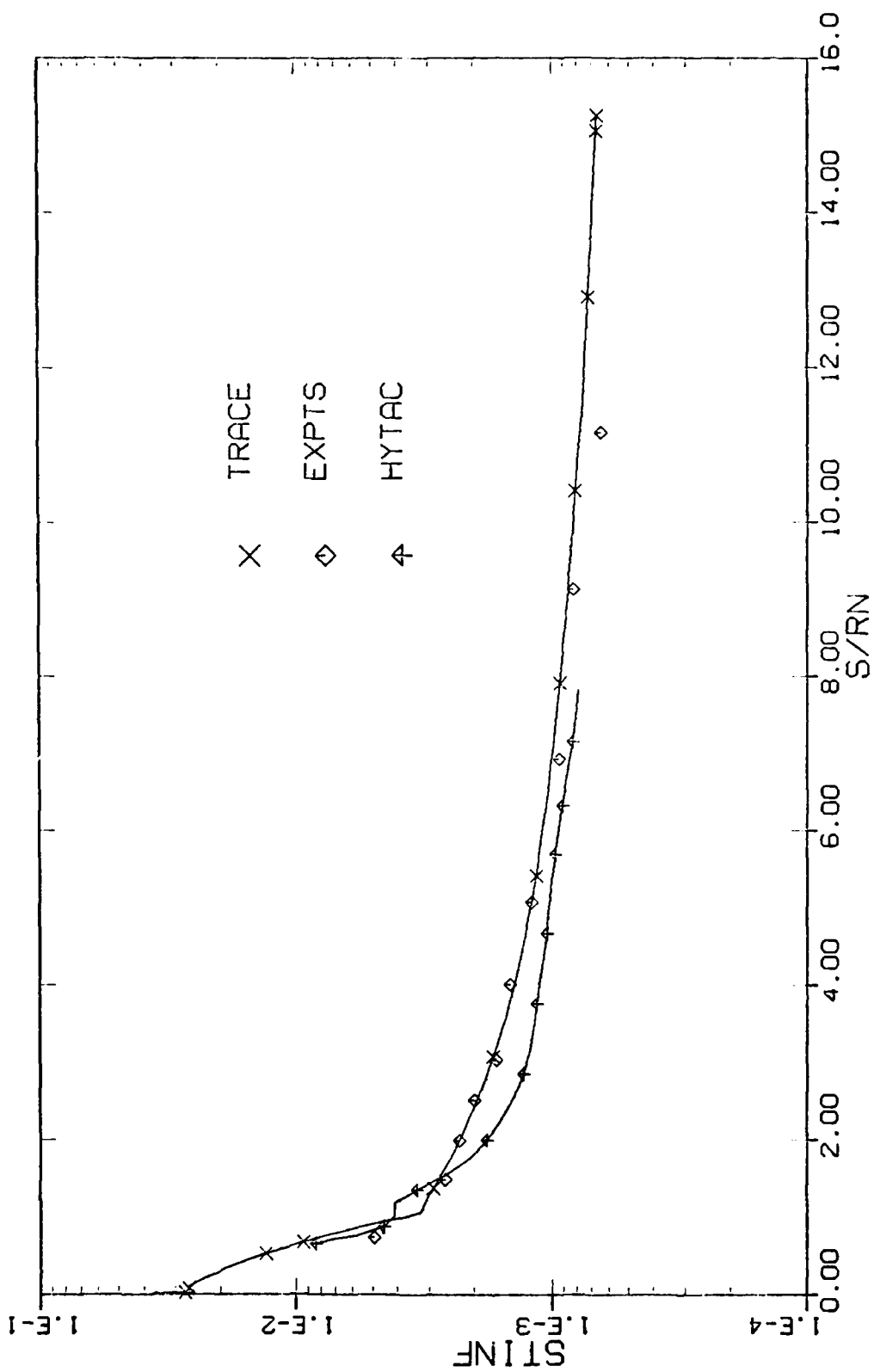
Figure 19. Surface Heat-Transfer Distribution for Slab Delta Wing at $\alpha = 10$ and $\zeta = 0$ deg
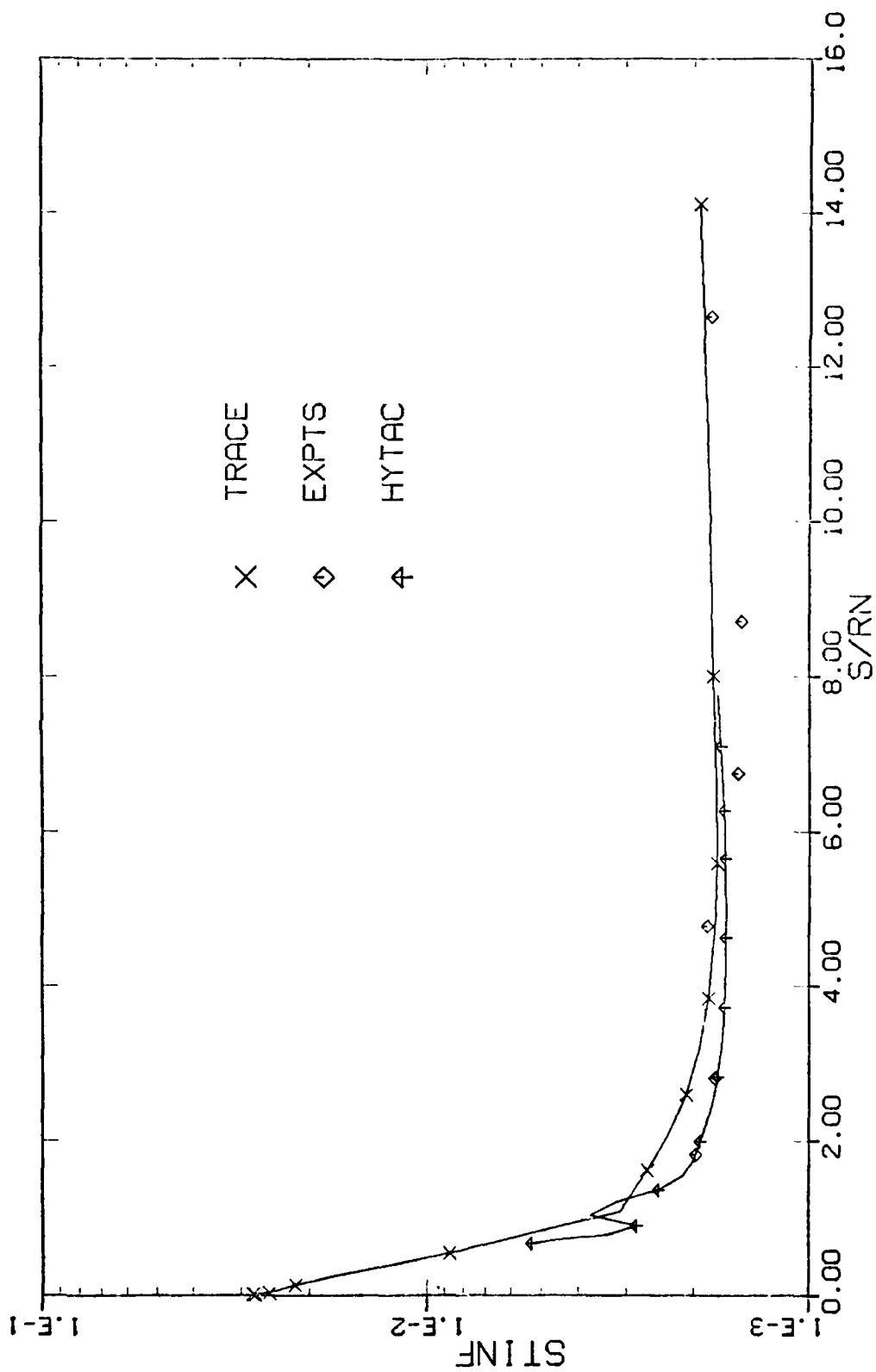
Figure 20. Surface Heat-Transfer Distribution for Slab Delta Wing at $\alpha = 10$ and $\zeta = 90$ deg
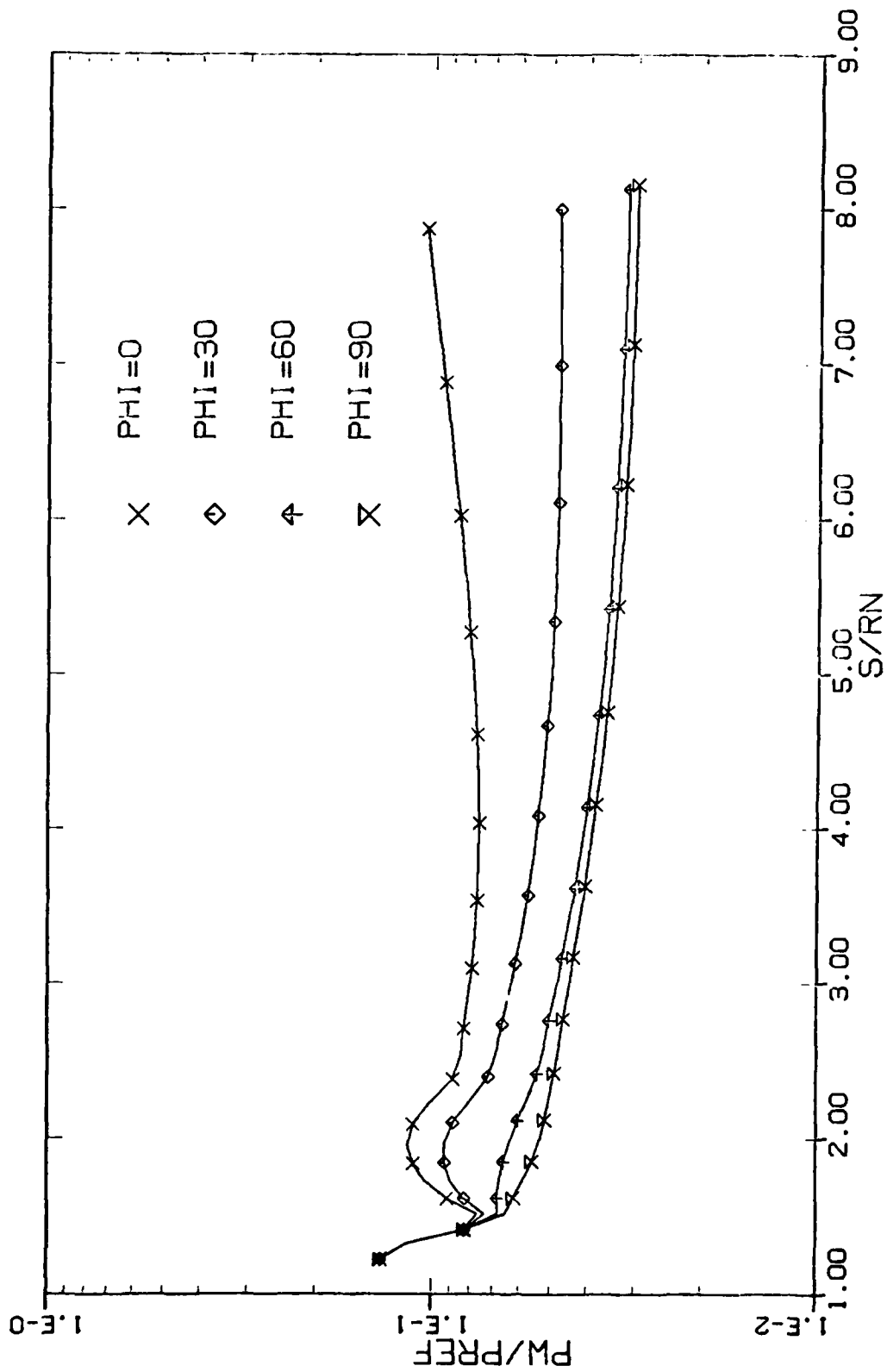
Figure 21. Surface Pressure Distribution for Elliptic Body at $\alpha = 0$
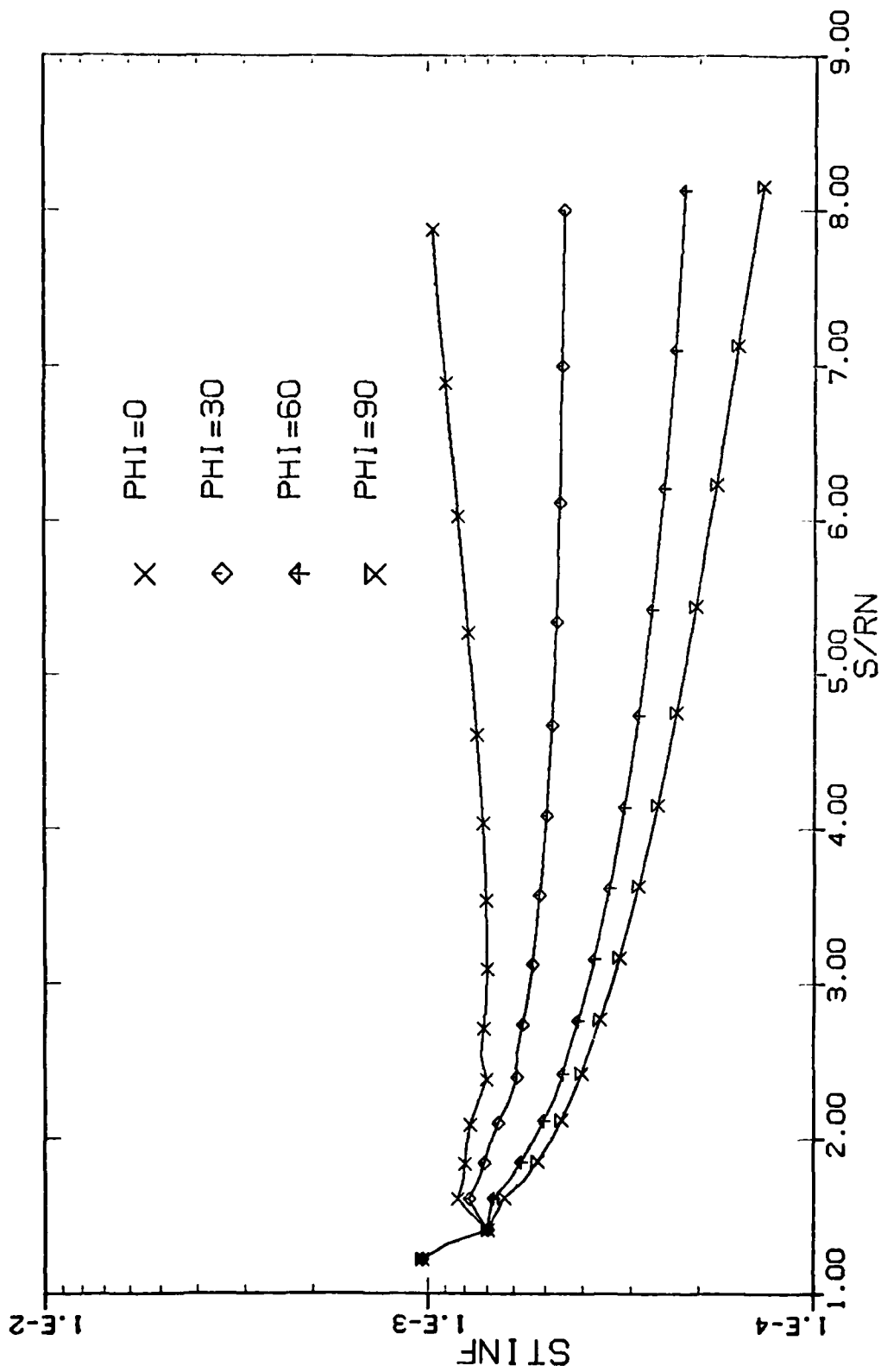
Figure 22. Surface Heat-Transfer Distribution for Elliptic Body at $\alpha = 0$

Results of a Government and Industry Survey of the Heating Methods Used to Determine Missile Structural Temperatures

The design and development of missile structures in an elevated temperature environment (Mach 2 to 6) has been demonstrated on many flight test and production programs. The approaches to structural design at elevated temperature were varied; each tailored to the unique, immediate technical challenges and schedule milestones facing the program manager. A conservative formulation was evolved to deal with elevated temperature effects and configuration complexities associated with the project at hand. A good structural design requires the expertise of many specialists and cuts across several technologies. A government and industry survey on structural design criteria and heat transfer analysis procedures to account for the effects of elevated temperatures was completed. This paper presents a summary of the results of the heating methods currently used.

J. W. Stultz

Lead Engineer-Thermodynamics,
MDAC-St. Louis.
St. Louis, Mo.

D. B. Paul

AFWAL/FIBE,
Criteria and Applications Group,
Dayton, Ohio

INTRODUCTION

Future missile systems designed to operate in the supersonic/hypersonic flight regime will encounter high structural temperatures due to the combination of aerodynamic heating on the external surface and combustion heating within the vehicle. Accurate prediction of the thermal environments and resultant structural temperatures is important for the selection of materials and the design of the vehicle structure. In the past three decades significant advances have been made in the development of heat transfer methods and experimental procedures for hypersonic vehicles. Some of these methods and procedures are being used to design current and future missile systems.

A government and industry survey (questionnaire plus selected field trips) was completed to provide a better understanding of how these methods and procedures are used in missile design criteria. The survey was organized according to the various involved disciplines. It was distributed to 37 government and industry organizations actively working in the design of missile systems. Twenty-seven completed or partially completed responses were returned. This paper presents a summary of the results for aerodynamic heating, convective heating and structural temperature analysis.

AERODYNAMIC HEATING

A better understanding of the aerodynamic heating methods used to predict missile structural temperatures is a key factor in developing sound design criteria. A typical missile flow field structure and related aerodynamic heating region is presented in Figure 1. Aerodynamic heating is the primary input that determines the missile skin temperatures,

internal structural temperatures and temperature gradients. The subject has been studied both experimentally and analytically over several decades with most of the effort devoted to high supersonic and hypersonic flight regimes. With the advent of computers and high speed flight heat-transfer data, substantial improvements have been made in the technology. Current missile program plans require improvements in the methodology for missiles operating in the Mach 2 to 6 flight regime.
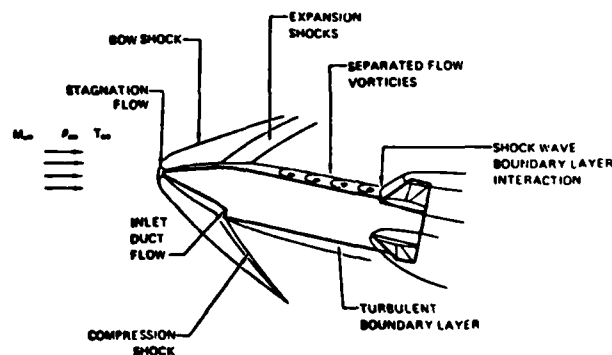
Fig. 1 Typical Missile Flow Field Structure

Fundamentally, a rigorous heating method should apply across the entire speed regime. This is true for the classical heat transfer methods; however, the semiempirical techniques used by industry for rapid and economical predictions require calibration for the specific flow regimes and/or vehicle configu-

rations. The aerodynamic heating portion of the survey was designed to provide an updated understanding of the principal methods used by government and industry personnel. Results of the survey have been organized into selected flow regions to provide a clear picture of the methods employed. Table 1 contains the questions included in the survey together with brief summaries of the answers.

Windward Region

The windward region discussed herein is defined as the main body of the vehicle that has a positive flow deflection angle. The methods used to predict temperatures in these regions are very important. The temperatures are used to help select materials that will meet the design requirements with a minimum penalty on vehicle performance and cost. Perhaps the most severe structural temperature gradients (both in-board and peripheral), and therefore thermal stresses, are produced in this region. To calculate the heating the engineer must choose a flow field method that properly defines the inviscid flow. The choice is often difficult because of flow discontinuities created by the engine inlet. Elaborate computer codes have been developed to solve for the flow fields, but they are cumbersome and expensive. For engineering analyses the most useful solutions are based on simple body shapes such as flat plates (wedges), cones, hemispheres and cylinders. Several heating methods exist for these shapes and are used throughout the industry.

Participants were asked to identify (Table 1, Questions 1.1 and 1.2) which flat plate and cone heating method they use for laminar and turbulent flow. A majority of those surveyed use Eckerts reference enthalpy method (Reference 1) for both laminar and turbulent flow on a flat plate. The second and third choices for turbulent flow were Spalding-Chi (Reference 2) and Van Driest (Reference 3) respectively. For heating on a cone the respondents selected Eckerts reference enthalpy method on a flat plate with corrections for cross flow. The second and third choices were Lees and Reshotko (Reference 4) respectively.

Stagnation Region

The stagnation region discussed below is divided into two flow regimes: (1) stagnation point and (2) stagnation line. The stagnation point generally experiences the highest heating of any location on the missile. Fortunately, however, the high heating is limited to a small region near the stagnation point. Materials selected for use in this region must be capable of operating at or very near the peak recovery temperature which is determined by the missiles Mach-altitude trajectory. Perhaps more experimental heat transfer data have been obtained for the stagnation point and immediate region than any other flow regime. Excellent correlations exist between theory and experiment. The stagnation line includes the leading edge region of wings, fins, engine inlets and other lifting or control surface that protrude from the main body. Viscous flow over these surfaces can be laminar, transitional or turbulent depending on the freestream conditions. The similarity of flow between the stagnation line and the stagnation point, together with, the large amount of test data, have provided an excellent correlation between theory and data.

Participants in the questionnaire were asked to identify which stagnation heating method they used (Questions 1.3 and 1.4). For laminar flow at the stagnation point the method defined by Fay-Riddell (Reference 5) was the overwhelming choice. For laminar flow on the stagnation line the participants were evenly divided between Lees and Fay-Riddell. For turbulent flow, a majority use the method of Beckwith and Gallagher (Reference 7) followed closely by the method of Detra and Hidalgo (Reference 8). A small number of participants use flat plate methods such as $\rho_R u_R$, Van Driest or Colburn with corrections for cross flow.

Boundary Layer Transition

Boundary layer transition has been, perhaps, the most studied and least understood viscous flow phenomenon. For over 70 years the subject has been studied both analytically and experimentally. vast amounts of data have been generated, evaluated and correlated. Correlations have been made with practically every known parameter. However, it appears that a solution is no closer than the early work by Tollmien (Reference 9) or Schlicting (Reference 10). It has been suggested (B.M. Ryan, Reference 11) that today's transition criteria are subject to change based on tomorrow's data-- until a basic understanding of the phenomena is achieved.

The choice of a transition criterion is important for the successful design of the missile radomes. Thermal stress levels can exceed the structural capabilities of current domes and an incorrect choice of the transition criteria can lead to unacceptable design margins. Respondents were asked in the questionnaire to identify which transition criteria they use for heat transfer calculations (Question 1.5). A majority of those surveyed use the *local Reynolds number* method. The second most commonly used is the momentum thickness Reynolds number method. The two methods are basic approaches to estimating transition and usually produce a conservative design. The survey did not uncover any participants using a complex correlation parameter such as those developed during the Shuttle program. Also, in a number of the responses the participants stated that they assume all turbulent flow. In summary, it appears that most of the participants choose to follow a conservative approach to the thermal design of a radome.

Design Heating Methods

Design heating methods discussed below refer to the methods and procedures used to obtain aerodynamic heating for three levels of design (preliminary, detailed and final). The missile engineer has several options available to assist him in predicting aerodynamic heating: (1) computer programs, (2) wind tunnel data, (3) flight data, and (4) handbook charts or curves. Experience has shown that the use of a specific option in the preliminary design phase can significantly influence the final design. For example, preliminary design calculations are often used well into the design phase. Changes are allowed during the detailed design phase and are usually based on test data. If planned tests cannot be accomplished on time and the data reduced, the preliminary design calculations become final. It is therefore important to understand the level of detail the engineer uses to predict aerodynamic heating for preliminary, detailed and final design analysis.

Respondents to the questionnaire were asked to identify their preferred methods for predicting

heating for preliminary, detailed and final design (Questions 1.6, 1.7 and 1.8). For preliminary design a majority use a computer to predict heating while a significant minority indicated that they use parametric curves or design charts. For detailed design, a majority indicated that they use a computer to predict heating and wind tunnel data to verify their theoretical model. Nearly all participants indicated that they use a computer model for the final design phase. In summary, the evolution of thermal analysis for a missile design is as follows: (1) a rough computer model using basic shapes to estimate the configuration for preliminary design, (2) a refined computer model which has been verified and/or modified with wind tunnel data, and (3) a final computer model for design verification and any off nominal trajectory calculations.

Secondary Heating

The questionnaire included two aerodynamic heating topics normally considered of secondary importance in missile design heating analysis. The topics which are discussed below are: (1) entropy layer effects and (2) surface roughness effects. Entropy layer effects on aerodynamic heating have been shown to be most important for the supersonic/hypersonic flight regime (see Figure 2). In the nose region a normal or near normal shock must be crossed and the loss of total pressure in the inviscid flow combined with variable surface pressures create a complex analytic problem. The prediction of heating in this region requires a complex computer solution that can be expensive. A simple flow model can be used if the surface pressure is known. The approach consists of calculating the heating based on properties obtained from a specified shock angle followed by an expansion to the local pressure. The questionnaire addressed this subject (Question 1.9) to determine in what phase of the design the participant considers entropy effects important. The majority indicated that they consider entropy effects during the detailed design phase. A large number indicated that they did not consider entropy effects until final or the verification phase. Also, a significant number did not include entropy effects at any point in their analysis.
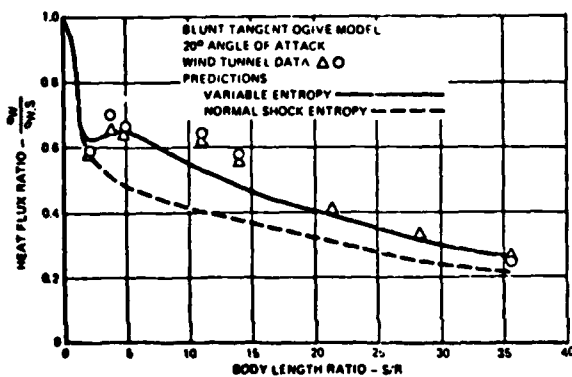
Fig. 2 Entropy Effects Increase Windward Heating Rates

Surface roughness effects become increasingly important as the missile flight speed is increased. Ablation from the radome surface increases the surface roughness thereby promoting boundary layer transition. The participants were asked to identify the design phase in which they give consideration to surface roughness (Questions 1.10). The majority consider roughness effects during the detailed design phase. A much smaller group considers roughness effects only during the final design. A significant group did not consider roughness effects important.

Methodology Work

Substantial improvements have been made in aerodynamic heating technology through the use of high speed flight data. The major emphasis has been in the hypersonic flight regime (re-entry vehicles). Missiles under current development in the Mach 2 to 6 flight regime (and potentially higher) could benefit significantly from improvements in heat transfer methodologies. The improvements are needed to reduce the uncertainty in predicting skin and structural temperatures to provide a payoff in design margins. To assess the current level of methodology work throughout the industry, the participants were asked to identify any work currently in progress or recently completed by their organizations (Question 1.11). A majority of participants indicated that their organizations were not currently working on and had not recently completed any heat transfer methodology development. A small number indicated that their methodology work consisted of updating existing in-house computer programs. Although a number of participants responded with brief abstracts of methodology work from their organizations, only a small number were identified as applicable to the Mach 2 to 6 missile flight regime.

Flow Fields

A typical missile flow field structure can be complex and the engineer must choose the proper method to define the shock layer and downstream flow properties. From these properties, the recovery temperature and the aerodynamic heat transfer coefficients are calculated. Although elaborate computer codes, such as the Method of Characteristics, have been developed to solve the flow field problem, they are cumbersome and expensive to apply. For engineering analysis, the most expedient flow field solutions are often based on simple body shapes such as flat plates, cones, hemispheres and cylinders. The engineer must choose which basic shape best approximates the flight vehicle configuration. The engineer must also choose which analysis tool (elaborate computer code, computer code with basic shapes or parametric curves) to use for preliminary, detailed or final design analysis. The participants were asked to identify in what phase of design (preliminary, detailed or final) they use a computer program to solve for the flow field structure (Question 1.13). A majority use a computer program during the detailed design phase. The second choice was a tie between the preliminary and final design phases. In summary, it appears that the participants consider a good description of the flow field structure essential for all phases of design analysis.

Special Areas

The special areas of aerodynamic heating that require an increasing amount of attention due to the higher Mach number regimes are: (1) leeward side (separated, reattached and vortex flow), (2) inter-

ference regions (fins, wings and duct inlets), and (3) protuberances and gaps.

Leeward Side. The flow on the leeward surface can be attached, separated or under the influence of strong vortices. Attached and separated flow heating rates are relatively low due to the low pressure expansion region. Heating predictions in these regions are extremely difficult due to the complex flow structure. Vortices can start in the boundary layer and extend into the inviscid flow region depending on vehicle geometry and stream parameters. Associated with vortex flow is a reattachment region which has significantly high heating rates. Both the onset of vortex flow and the increase in heating are very difficult to predict.

Participants in the questionnaire were asked to define the methods they use to predict heating in these regions (Question 1.14). A majority indicated that they prefer to use wind tunnel data. If no data are available for their particular configuration, they search the literature for applicable correlations. Several participants use multiplying factors which are applied to an equivalent flat plate heating value.

Interference Regions. Interference regions discussed below refer to heating on fins, wings and duct inlets and the region near their attachment to the missile body. Substantial experimental work has yielded several semiempirical techniques that can be used to estimate the heating (see Figure 3). The heating is principally due to higher local pressures induced by the shock boundary-layer interaction. These regions are very important to structural design engineer due to the increased temperatures.

Participants were asked to identify their preferred methods for predicting heating in these regions (Question 1.15). The majority prefer to use wind tunnel data supported by, or compared with, data correlations published in literature.
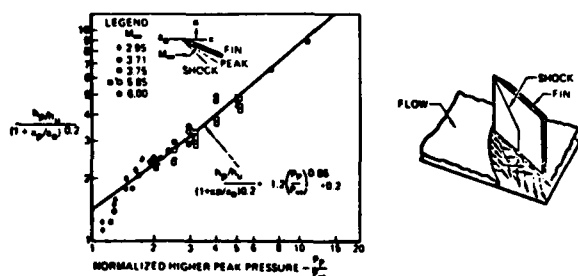
Fig. 3   Interference Heating Correlation

Protuberances and Gaps. Missile surfaces are usually smooth with minimum flow disturbances. However, as the flight Mach number increases, local heating becomes more severe and protuberances and gaps can become increasingly important. Protuberances (forward and aft facing) can be created when two materials with different thermal expansion coefficients are joined. A protuberance can increase the local heating and produce a higher temperature region on the structure. Also, to allow for thermal

growth at these higher Mach numbers, gaps in joints must be incorporated. The gaps can increase the heating in the joint and affect the structural design.

Participants were asked to define their preferred methods for heating in protuberances and gaps (Question 1.16). A majority prefer to use wind tunnel data compared with data from the literature. The second most used method is to apply a safety factor to the undisturbed value in the region of the disturbance.

In summary, for the special areas of aerodynamic heating where complex flow over the missile cannot be evaluated analytically, the participants prefer to use wind tunnel data augmented by or compared with empirical correlations from literature.

INTERNAL FORCED AND FREE CONVECTION

Internal forced and free convection can have a large influence on missile structural and component temperatures. In many cases, heating from internal flow and combustion is the dominant heat source.

Inlet and Ducts

Inlet and duct flow can usually be characterized as an internal boundary layer developing under both adverse and favorable pressure gradients. While much research has been done in the general area and computer programs are available for performing these calculations, rarely is a detailed boundary layer analysis used in predicting design temperatures. Correlations such as Bartz (Reference 12) and pipe flow were found to be the most popular methods among the participants (Question 1.17). These methods are generally applied with some conservatism early in the design process with the predicted structural design temperatures being modified to correlate with experimental data as they become available.

Combustor and Nozzle

Prediction of structural temperatures in the combustor and nozzle regions may involve the consideration of forced convection, wall radiation, gas/particle radiation, and thermochemical reactions. Due to the complexity of the forced convection in these regions, recourse is usually made to turbulent pipe flow and correlations such as Bartz. A majority of participants in the survey use the Bartz correlation (Question 1.18). Analyses in these regions are usually conservative with the degree of conservatism decreasing when design verification testing is performed. Conservatism is generally applied in the heat flux calculation and/or in sizing the insulation/ablative material or cooling system.

Free Convection

Where free convection is considered important, the majority of participants use the classical textbook analysis for horizontal and vertical surfaces. A large number of those surveyed do not consider free convection important in most structural areas (Question 1.19).

STRUCTURAL TEMPERATURE ANALYSIS

Thermal Models

Methods and procedures used to calculate missile structural temperatures are additional factors in developing sound design criteria. It is important to understand the following: (1) how thermal models are formulated, (2) how node size and spacing are determined, (3) what method is used to

analyze heat transfer across interfaces, and (4) how uncertainties in material properties are included in the analysis. For thermal modeling, the participants were asked to identify the design phases (preliminary, detailed or final) during which they use two and three dimensional models (Question 2.1). The preferred approach is to use two-dimensional models for preliminary and detailed design and three-dimensional models for detailed and final design calculations. Engineering judgement is used for selecting node size and node spacing (Question 2.2). For interface conductance (Question 2.3), the results indicate that most engineers prefer using test data. Generally, most engineers have a variety of computer programs available to perform conduction calculations. Most of these programs are based on the finite difference method. The finite element method is being used mostly in large analyses, particularly when a transfer of temperature data to a structural finite element program is necessary.

Major uncertainties in computing conduction within structural members are the material properties (conductivity, density and specific heat). The survey indicated (Question 2.4) that the majority of engineers use conservative values for material property data. A significant number evaluate the sensitivity to material properties to arrive at a safety factor. The way in which the material properties are factored depends on what condition is critical to the structural component (i.e., maximum temperature or maximum temperature gradient).

Radiation Heat Transfer

Radiation heat transfer between structural members becomes more important as the flight Mach number increases. The participants were asked to identify the methods they use to calculate internal radiation exchange factors (Question 2.5). Most participants use a computerized detailed view factor modeling analysis; such as the Thermal Radiation System Analyzer (TRASYS) computer program. A significant number use handbooks or standard textbooks to determine the view factors.

Heating Uncertainties

Procedures used to include heating uncertainties in structural temperature analysis were investigated. Participants were asked to describe their method or procedure for including heating uncertainties in the detailed design structural temperature analysis (Question 2.6). A majority indicated that heating uncertainties are included within their thermal models (use conservative assumptions) and the results are used as limit requirements. The second most used approach is to apply a constant factor to the calculated heating rate. The third choice selected is to use the most severe trajectory for detailed temperature analysis.

SUMMARY

Results of the questionnaire survey indicate that uncertainties are frequently not specifically accounted for in structural temperature analysis. Most engineers surveyed prefer using a computer during all phases of design (preliminary, detailed and final). Depending upon the complexity of the problem they use two and three dimensional models and use engineering judgement to determine node size and node distribution. The thermal models incorporate conservative values for material property data. Heating inputs to the models use conservative assumptions

and are often based on a sensitivity analysis. Most analyst prefer using test data for all areas of thermal uncertainties.

REFERENCES

1 Eckert, E.R.G., "Survey of Heat Transfer at High Speeds," WADC TR 54-70, April 1954.

2 Spalding, D.B., and Chi, S.W., "The Drag of Compressible Turbulent Boundary Layer on a Smooth Flat Plate With and Without Heat Transfer," Journal of Fluid Mechanics, Janaury 1964.

3 Van Driest, E.R., Journal of Aeronautical Science, Vol. 18, No. 3, pp. 145-160, 1951.

4 Reshotko, E., and Cohen, C.B., "Heat Transfer at the Forward Stagnation Point of Blunt Bodies," NACA Report 3513, 1955.

5 Fay, J.A., and Roddell, F.R., "Theory of Stagnation Point Heat Transfer in Dissociated Air," Journal of the Aeronautical Sciences, February 1958, pp. 73-75, 121.

6 Lees, L., "Similarity Parameters for Surface Melting of a Blunted Nose Body in a High Velocity Gas Stream," Journal of American Rocket Society, Vol. 29, 1959, pp. 345-54.

7 Beckwith, I.E., and Gallagher, J.J., "Local Heat Transfer and Recovery Temperatures on a Yawed Cylinder at a Mach Number of 4.15 and High Reynolds Numbers," NASA Memo 2-27-59L, April 1959.

8 Detra, R.W., and Hidalgo, H., "Generalized Heat Transfer Formulas and Graphs for Nose Cone Reentry into Atmosphere", Journal of American Rocket Society, Vol. 31, 1961, p. 318.

9 Tollmien, W. Uber die Entstehung der Turbulenz. Rep. of the Ges. Wiss. Göttingen, Math. Phys. Klasse, 21, 1929.

10 Schlichting, H. Amplitudenverteilung und Energiebilanz der kleinen Storungen bei der Plattenstromung. Nachr. Ges. Wiss. Göttinger, Math. Phys. Klasse, Fachgruppe I, Vol. 1, 1935.

11 Ryan, B.M., "Boundary Layer Transition Data with Emphasis on Application to Missile Seeker Domes," NWC Technical Note 4061-178, December 1975.

12 Bartz, D.R., "A Simplified Equation for Rapid Estimation of Rocket Nozzle Convective Heat Transfer Coefficients," Jet Propulsion Technical Note, January 1957, pp. 49-51.

TABLE 1

SUMMARY OF SURVEY QUESTIONNAIRE

QUESTION		RANKING OF ANSWERS		
		CONSENSUS	SECOND	THIRD
1.1 IDENTIFY WHICH FLAT PLATE HEATING METHOD YOU USE?	LAMINAR	ECKERTS REFERENCE ENTHALPY	*	*
	TURBULENT	ECKERTS REFERENCE ENTHALPY	SPALDING-CHI	VAN DRIEST
1.2 IDENTIFY WHICH CONE HEATING METHOD YOU USE?	LAMINAR	FLAT PLATE/CROSS FLOW CORRECTIONS	LEES	RESHOTKO
	TURBULENT	FLAT PLATE/CROSS FLOW CORRECTIONS	LEES	*
1.3 IDENTIFY WHICH STAGNATION POINT HEATING METHOD YOU USE?		FAY-RIDDELL	*	*
1.4 IDENTIFY WHICH STAGNATION REGION HEATING METHOD YOU USE?	LAMINAR	FAY-RIDDELL /LEES	*	PR METHOD
	TURBULENT	BECKWITH-GALLAGHER	DETRA-HIDALGO	*
1.5 WHICH BOUNDARY LAYER TRANSITION CRITERION DO YOU USE FOR AERODYNAMIC HEATING?		LOCAL REYNOLDS NUMBER	MOMENTUM THICKNESS REYNOLDS NUMBER	*
1.6 WHAT ARE YOUR PREFERRED METHODS FOR PRELIMINARY DESIGN HEATING PREDICTIONS?		COMPUTER ANALYSIS	PARAMETRIC CURVES	*
1.7 WHAT ARE YOUR PREFERRED METHODS FOR DETAILED DESIGN HEATING PREDICTIONS?		COMPUTER ANALYSIS *	WIND TUNNEL DATA	*
1.8 WHAT ARE YOUR PREFERRED METHODS FOR FINAL DESIGN HEATING PREDICTIONS?		COMPUTER ANALYSIS	WIND TUNNEL DATA	*
1.9 AT WHICH LEVEL OF THE DESIGN DO YOU CONSIDER ENTROPY LAYER EFFECTS?		DETAILED	FINAL OR VERIFICATION	PRELIMINARY/NOT CONSIDERED
1.10 AT WHAT LEVEL OF DESIGN DO YOU CONSIDER SURFACE ROUGHNESS EFFECTS?		DETAILED	FINAL	NOT CONSIDERED
1.11 WHAT AERO HEATING METHODOLOGY IS YOUR COMPANY WORKING ON?		NO COMPANY METHODS WORK	UP-DATING INHOUSE COMPUTER PROGRAMS	*
1.12 AT WHAT LEVEL OF DESIGN DO YOU USE A COMPUTER PROGRAM TO SOLVE FOR THE MISSILE FLOWFIELD STRUCTURE?		DETAILED	FINAL	PRELIMINARY
1.13 WHAT ARE YOUR PREFERRED METHODS FOR PREDICTING HEATING IN THE FOLLOWING REGIONS? (1) SEPARATED FLOW, (2) REATTACHMENT, (3) VORTEX		WIND TUNNEL TEST DATA	CORRELATIONS FROM LITERATURE	*
1.14 WHAT ARE YOUR PREFERRED METHODS FOR PREDICTING INTERFERENCE HEATING IN REGIONS SUCH AS FINS, WINGS, AND DUCT INLETS?		WIND TUNNEL TEST DATA	CORRELATIONS FROM LITERATURE	*
1.15 WHAT ARE YOUR PREFERRED METHODS FOR PREDICTING HEATING IN AREAS SUCH AS PROTUBERANCES AND GAPS?		WIND TUNNEL TEST DATA	SAFETY FACTOR APPLIED TO UNDISTURBED VALUE	*
1.16 WHAT ARE YOUR PREFERRED METHODS FOR PREDICTING HEATING IN INLETS AND DUCTS?		TIE: ① BARTZ AND ② SUB-SONIC FLOW ANALYSIS		TEST DATA
1.17 HOW DO YOU CALCULATE INTERNAL HEATING FOR THE COMBUSTOR AND NOZZLE REGIONS?		BARTZ	BOUNDARY LAYER HEATING ANALYSIS	*
1.18 WHAT METHOD DO YOU USE TO CALCULATE INTERNAL CONVECTION FOR STRUCTURAL TEMPERATURE ANALYSIS?		CLASSICAL TEXT BOOK APPROACH	DO NOT CONSIDER IMPORTANT	*
2.1 AT WHAT LEVEL OF DESIGN DO YOU USE TWO AND THREE DIMENSIONAL HEAT TRANSFER MODELS FOR STRUCTURAL TEMPERATURE ANALYSIS?	2D	PRELIMINARY	DETAILED	FINAL
	3D	DETAILED	FINAL	PRELIMINARY
2.2 HOW DO YOU ACCOUNT FOR THERMAL MODEL SIZE (NUMBER OF NODES AND SPACING) WHEN PREDICTING DETAILED STRUCTURAL TEMPERATURES?		ENGINEERING EXPERIENCE	*	*
2.3 HOW DO YOU ACCOUNT FOR INTERFACE CONDUCTANCE IN STRUCTURAL TEMPERATURE ANALYSIS?		TEST DATA	LITERATURE/HANDBOOK	*
2.4 HOW DO YOU ACCOUNT FOR UNCERTAINTY IN MATERIAL PROPERTIES WHEN ASSESSING STRUCTURAL TEMPERATURES FOR DESIGN?		CONSERVATIVE VALUE/EVALUATE SENSITIVITY OF TEMPERATURES	APPLY A FACTOR TO NOMINAL VALUES	*
2.5 WHAT METHOD DO YOU USE TO CALCULATE RADIATION EXCHANGE FACTORS FOR INTERNAL RADIATION?		DETAILED CALCULATION PRO-CEDURE **	HANDBOOK/TEXT BOOK APPROACH	
2.6 FOR DETAILED DESIGN STRUCTURAL TEMPERATURE ANALYSIS HOW DO YOU ACCOUNT FOR HEATING UNCERTAINTIES?		INCLUDED WITHIN THERMAL CALCULATION AND RESULTS USED AS LIMIT REQUIREMENTS	APPLY CONSTANT FACTOR ON CALCULATED HEATING RATE	USE MOST SEVERE TRAJECTORY

* NOT ENOUGH RESPONSES TO SELECT SECOND AND THIRD RANKINGS   ** TRASYS USED BY TWO RESPONDENTS

CONVECTIVE HEATING

STRUCTURAL TEMPERATURE ANALYSIS

SUPERSONIC COMBUSTOR INSULATION
ABLATION ANALYSIS AND TESTS

Robb W. Newman and Harold G. Fox
Johns Hopkins/Applied Physics Laboratory, Laurel, Maryland

ABSTRACT

The design of passively cooled, hypersonic tactical missiles poses many severe structural problems whose solutions are beyond the current state-of-the-art. Specifically, the heating conditions in the supersonic combustor of such a missile approach those in the throat section of rocket motors but are more damaging to most materials because the flow is oxidizing rather than reducing.

Carbon-carbon materials are being considered for the supersonic combustor wall structure because they have attractive strength-weight characteristics at elevated temperatures. Since these materials have poor oxidation resistance, metal loaded carbon-carbon materials which form an oxidation resistant layer are also being considered. In order to design such a combustor, the designer must be able to accurately predict the erosion rate of candidate materials so that a realistic balance can be achieved between weight and performance. This paper addresses the problem of thermochemical erosion of graphitic materials, the development of procedures for the analytic prediction of these erosion rates in a combustor environment, and experimental procedures used to validate the analytical model and evaluate candidate combustor liner materials.

INTRODUCTION

Previous reviews and evaluations of graphite ablation theory and experimental data[1,2] have been conducted for blunt body atmospheric reentry analyses as part of the Aerospace Nuclear Safety Program. Although these references are slanted to environmental conditions and configurations entirely different than those under consideration herein, the basic theory and simplified model are applicable. Therefore, it was the objective of this study to modify the existing model in order to consider the oxidation of graphite wall materials in the presence of a supersonic combustor environment during a flight profile.

During the powered flight portion of the ramjet trajectory, the fuel is burned in varying mass ratios with air, releasing heat and by-products in the combustor chamber. The resulting high temperature gas mixture flows through this pipe-like configuration at supersonic velocities while transferring heat to the combustor wall. The heat transfer rate at this interface has been determined from an empirical correlation which will be discussed later.

In review, the basic ablation process occurs as follows:

When the wall temperature reaches a certain level, which depends on the surface material's reactivity, a heterogeneous chemical reaction (oxidation) between the hot boundary layer and the surface material ensues. In this first "reaction-rate controlled" regime, the surface oxidation rate increases exponentially with surface temperature (e.g., by an Arrhenius kinetic mechanism). Reaction-rate control

II-101

persists with increasing surface temperature until the diffusional transport of oxident to the surface becomes too slow to maintain the exponential increase in reaction rate. This "transition regime" extends to the temperature level where the surface reaction becomes completely diffusion controlled. At this condition, the reaction is said to be in the diffusion-limited regime and is characterized by surface oxidation occurring in stoichiometric proportions (the stoichiometry depending on the products formed). As the surface temperature continues to increase, the oxidation rate remains diffusion-limited until a critical temperature/pressure condition is reached at which the graphitic material also begins to sublime. In this sublimation regime the mass loss rate again increases exponentially with surface temperature as dictated by the partial pressure of the vaporizing carbon species.

For our combustor ablation model, the sublimation regime has been neglected. This simplification has been assumed because sublimation of graphite materials have been observed to begin at approximately $5500^\circ R$, which is a temperature well above the maximum expected surface temperature under consideration for the trajectories presently being evaluated.

THE REACTION-RATE CONTROLLED (KINETIC) REGIME

Experimental surface reaction rate data are normally presented in the Arrhenius plane, i.e., $\log m_r$ vs $1/T$, in an attempt to correlate the data with the empirical Arrhenius rate equation,

$$m_r = P_{O_w}^n k_o \exp(-E/RT_w) \qquad (1)$$

where m_r is the carbon mass loss rate, k_o is the "frequency factor" or "reaction rate constant", n is the order of the reaction, E is the activation energy, and P_{O_w} is the partial pressure of the oxidant at the surface.

Scala[3] in an attempt to bracket the available data on graphite, utilized a set of "slow" and "fast" values for E and k_o with $n = 1/2$. Subsequently Metzger[4], based on the experimental arc-jet data on ATJ, formulated a third set that resulted in rates between the "fast" and "slow" values of Scala and labeled as the 'moderate' rates. The resulting values are:

$k_o = 9.65 \times 10^5 \ lb/(ft^2 - sec\text{-}atm^{1/2})$

$E = 44,000 \ cal/mol$

$R = 1.98718 \ cal/mole - {}^\circ K$ (universal gas constant)

$T_w = $ wall temperature, $^\circ K$

Presently, there are no reported experimental data on carbon-carbon to arrive at similar reaction constant values for this material. Therefore, the above values for ATJ graphite are employed as the first approximation for the E and k_o of carbon-carbon for our present model.

Nagle[5] and Strickland-Constable[6] have reported rate constants for the oxidation of pyrolytic graphite (PG). They fit their experimental data to a surface reaction mechanism proposed by Blyholder, Binford, and Eyring[7]. The mechanism was developed to explain the observation that the oxidation of PG appears to follow at

least two different rate equations. At temperatures below $1000^O K$ ($1340^O F$), the oxidation can be described by a rate equation with an activation energy of 25 to 30 kcal/gmole. The rate of oxidation reaches a maximum in the region between 1000 and 1700 K (1340 to $2600^O F$), then decreases, and at still higher temperatures again increases with an activation energy from 70 to 90 kcal/gmole.

It is assumed that two types of surface active sites are present on PG. Type A sites, the more reactive sites, support the oxidation reaction at low temperatures. At higher temperatures some Type A sites are converted to less reactive type B sites, accounting for the temporary decrease in the oxidation rate in the intermediate range of temperatures. This mechanism is described by a set of three elementary reactions wherein CO is assumed to be the only product:

(i) $A + O_2 \rightarrow A + 2CO$ $\qquad \dot{m}_r \ (i) \qquad = k_A P_{O_w} X / \left(1 + k_z P_{O_w}\right)$

(ii) $B + O_2 \rightarrow A + 2CO$ $\qquad \dot{m}_r \ (ii) \qquad = k_B P_{O_w} (1-X)$

(iii) $A \rightarrow B$ $\qquad\qquad\qquad \dot{m}_r \ (iii) \qquad = k_T X$
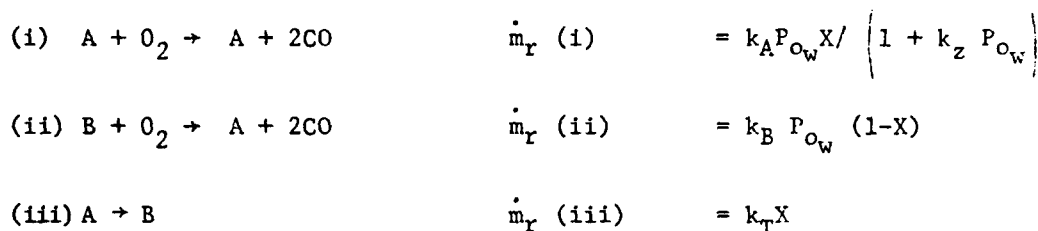
where

X = Fraction of surface covered with Type A sites

$(1-X)$ = Fraction of surface covered with Type B sites

P_{O_w} = Partial pressure of oxygen, atm ($= P_w \cdot \Phi_{O_2}$)

Φ_{O_2} = Mole fraction of oxygen

k_A, k_B, k_z, k_T = constants

where

$$ X = \frac{k_B P_{O_w}}{k_B' P_{O_w} + k_T} \tag{2} $$

The total rate of reaction is

$$ \dot{m}_r = \frac{k_A P_{O_w}}{1 + k_z P_{O_w}} \ X + k_B P_{O_w} (1-X) \tag{3} $$

in gram atoms carbon/cm^2-sec. Values for the reaction rate constants were obtained by finding those values which best fit the experimental data:

$\qquad k_A \qquad = \qquad 20 \exp (-30,000/RT)$ gram-atoms/(cm^2-sec-atm)

$\qquad k_B \qquad = \qquad 4.46 \times 10^{-3} \exp (-15,200/RT)$ gram-atom/(cm^2-sec-atm)

$\qquad k_T \qquad = \qquad 1.51 \times 10^5 \exp (-97,000/RT)$ gram-atom/(cm^2-sec)

$\qquad k_z \qquad = \qquad 21.3 \exp (+4,100/RT)$ 1/atm

TRANSITION AND DIFFUSION LIMITED REGIMES

In the transition regime the mass loss rate is computed from,

$$\frac{\dot{m}}{\dot{m}_D} = \frac{1}{2} + \left[\frac{1}{4} + \frac{\dot{m}_D}{\dot{m}_r}\right]^{1/2} \quad^{-1} \tag{4}$$

which is for a 1/2-order reaction (Reference 1) and where $\dot{m}_D$ is the mass loss rate in the diffusion-limited regime.

The evaluation of graphite surface ablation throughout all the thermo-chemical regimes is summarized by the non-dimensional oxidation term called the "mass transfer parameter", β, which is defined as

$$\beta' = \dot{m}/\rho u C_h \tag{5}$$

where

$$\dot{m} = \text{the mass loss rate}$$

$$\rho u C_h = \text{heat transfer coefficient}$$

$$C_h = \text{Stanton Number}$$

and for the diffusion limited regime

$$\beta'_D = \dot{m}_D / (\rho u C_h) \tag{6}$$

Equation (6) can be re-arranged to obtain the $\dot{m}_D$ from the "diffusion limited mass transfer parameter", β'_D

$$\dot{m}_D = (\rho u C_h) \beta'_D \tag{7}$$

where $(\rho u C_h)$ and β'_D can be independently determined, which will be discussed later.

The mass loss rate equations for each of the thermochemical regimes are combined by means of the Mickley-Spalding blowing relation[8] to form the following equation to determine β' (which is essentially the solid carbon to free stream gas mixture mass ratio),

$$\beta' = (1 + \beta'_D)^{\dot{m}/\dot{m}_D} - 1 \tag{8}$$

REACTIVITY OF CARBON

At elevated temperatures, and, to a first approximation, irrespective of the nature of the carbon, the reactivity is the greatest in oxygen and least in hydrogen, as summarized in Table 1 (Reference 9). This table also reveals that the $C + O_2$ reaction is roughly 10^5 times as fast as the $C + CO_2$ reaction at around $1900°R$. Based on this finding, our model assumes that the carbon wall reacts only with the O_2 remaining in the by-products of the Shelldyne-H/air* mixture and CO

*Shelldyne-H is the fuel under consideration. See Appendix A for properties.

is the only by-product of the solid carbon reaction according to

$$2C + O_2 \rightarrow 2CO \tag{9}$$

Table 1

Approximate Relative Rates of Carbon + Gas Reactions at $1931^\circ R$ and 0.1 Atm

Reaction	Relative Rates
$C + CO_2$	1
$C + O_2$	1×10^5
$C + H_2O$	3
$C + H_2$	3×10^{-3}

DIFFUSION-LIMITED MASS TRANSFER PARAMETER (β_D')

The diffusion-limited mass transfer parameter, β_D', is essentially the solid carbon to free stream gas mixture mass ratio at stoichiometric proportions. With the assumption that the solid carbon only reacts with the O_2 in the free stream and CO is the only by-product, the basic reaction equation is

$$C + \frac{1}{2(0.21 - 0.198ER)} \frac{M_a}{M_f} \cdot f_s \cdot ER \cdot C_{14} H_{18} + 0.198 \cdot ER \cdot O_2 + 0.79 \cdot N_2 +$$

$$(0.21 - 0.198 \cdot ER) \, O_2 \rightarrow CO + (\text{Shelldyne H/air less } O_2) \tag{10}$$
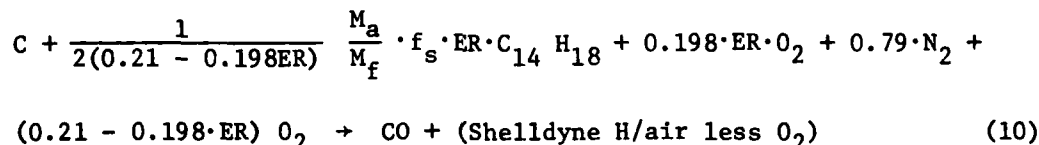
The relationship defining β_D' as a function of the fuel/air equivalence ratio (ER) can be derived with the utilization of this reaction equation. After further rearrangement of terms and the substitution of molecular weights, the β_D' equation reduces to

$$\beta_D' = \frac{(0.1748 - 0.1648 \, ER)}{(1.0 + 0.0730 \, ER)} \tag{11}$$

Figure 1 presents the variation of β_D' versus ER per equation (11). When the ER equals zero, the β_D' is essentially equal to the diffusion limited value for air (0.1748).

COMBUSTOR HEAT TRANSFER CORRELATION

Over many years of combustor testing at APL, heat transfer measurements have been taken for varied geometries and different fuels. It has been the intent of this data gathering exercise to correlate the average heat flux values from these tests against a heat release parameter which is proportional to the effective equivalence ratio (ER_{eff}) for any given fuel. This heat release parameter is

Fig. 1 Diffusion limited mass transfer parameter.

In the figure, the vertical axis is labeled "Diffusion limited mass transfer parameter β'_D" with values 0, 0.05, 0.10, 0.15, 0.20. The horizontal axis is labeled "Equivalence ratio, ER" with values 0, 0.20, 0.40, 0.60, 0.80, 1.00. The equation shown is:
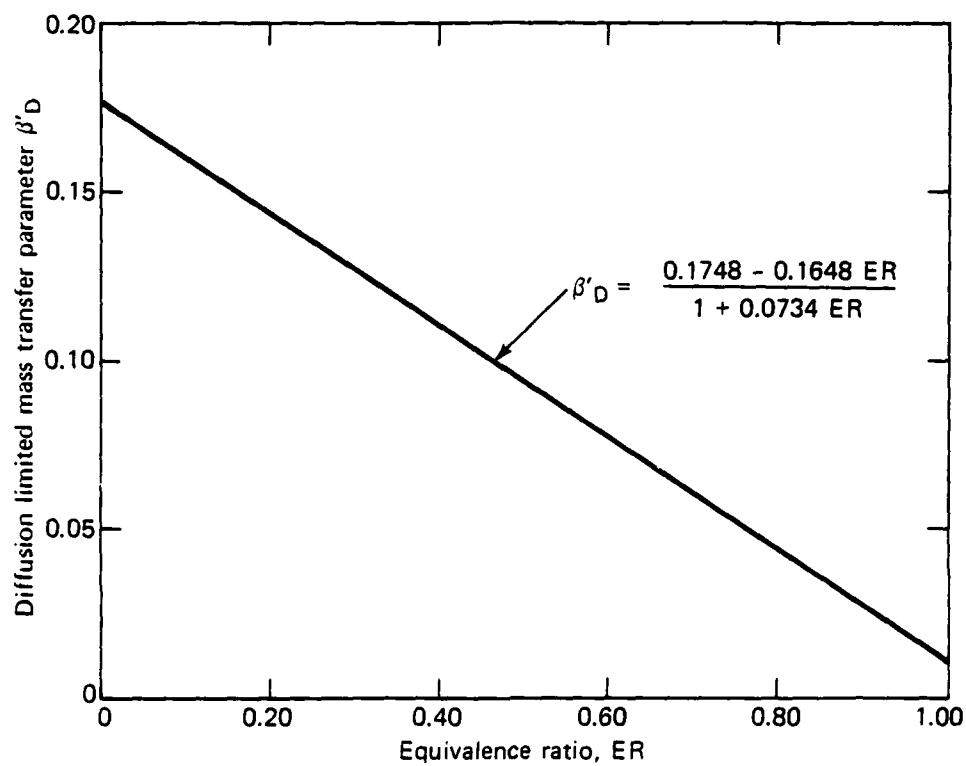
$$\beta'_D = \frac{0.1748 - 0.1648\ ER}{1 + 0.0734\ ER}$$

equal to the product of the fuel-air ratio (f), the lower heating value of the fuel (h_f), and the combustor efficiency (η).

Figure 2 (from Reference 10) presents the correlation of the normalized wall heat flux parameter as a function of the heat release parameter (the ER_{eff} scale for Shelldyne-H is also included.) The normalized wall heat flux parameter is equal to

$$(q_w/A_w) / \left[\frac{\dot{w}_a \Delta h}{A_{c_i}} \right]$$

where:

q_w = Wall heat flux

A_w = Wall area

A_{c_i} = Combustor inlet area

$\dot{w}_a$ = Air mass flow rate

Δh = Average gas to wall enthalpy difference

Noting that by definition

$$\rho u C_h \simeq (q_w/A_w)/\Delta h \tag{12}$$

the combustor heat transfer coefficient can be determined for any air mass flow rate ($\dot{w}_a$) and a specific combustor geometry cross sectional area (A_{c_i}) from this empirical correlation instead of an analytical approximation such as Bartz[11].

The air mass flow rate in the supersonic combustor is determined from the continuity equation in the following form,

$$w_a = P_w A_c M \left(\frac{g\gamma}{RT_g} \right)^{1/2}$$

where

P_w = Pressure at the wall

A_c = Cross-sectional area of combustor

M = Mach Number

R = Air mixture gas constant

T_g = Average total temperature of the air mixture
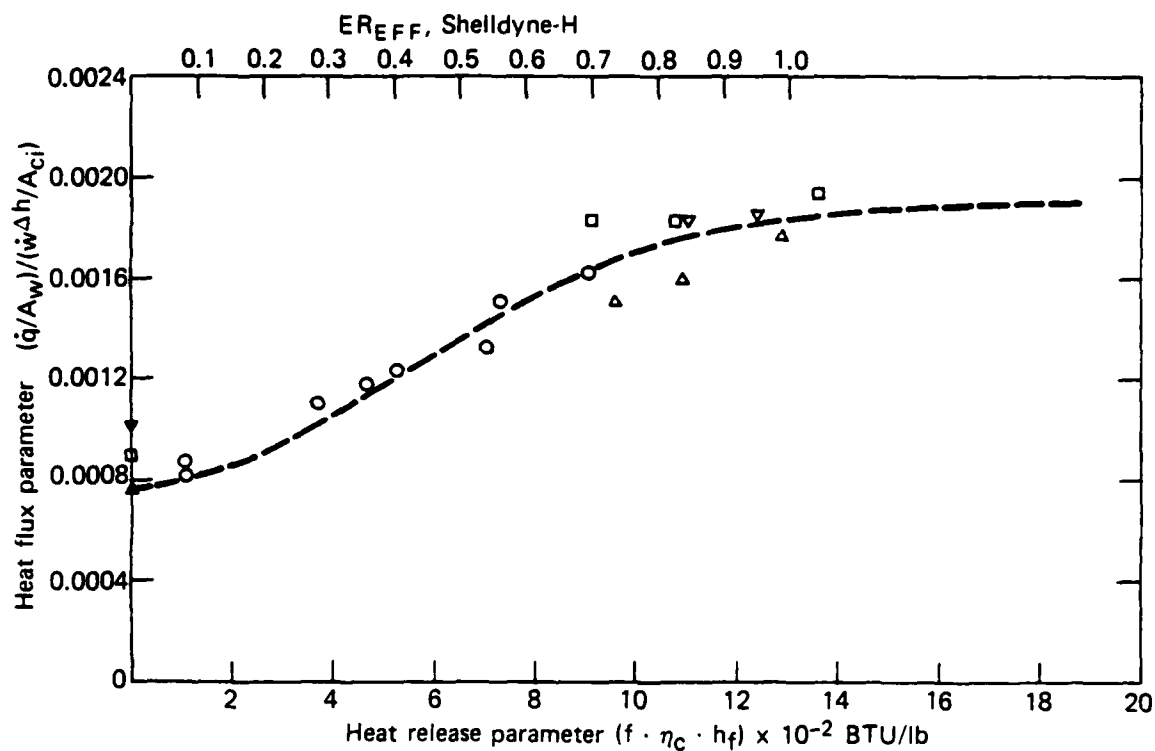
Fig. 2   Correlations of wall heat-flux parameter with heat-release parameter.

THERMOCHEMISTRY DATA DETERMINATION

The thermochemical erosion of graphite materials is dependent on information denoted as thermochemistry data. This data consists of the mass transfer parameter (β') and the enthalpy of the gas mixture at the graphite wall interface (h_w) tabulated for different wall temperatures (T_w) and pressures (P_w). The ablation model reviewed in the previous sections is now utilized to calculate the β' for varying T_w and P_w for a specific supersonic combustor design and fuel equivalence ratio (ER).

A basic procedure leading to the calculated β' is:

1. For the desired ER, the β'_D and the oxygen mole fraction of the by-products mixture can be determined for the Shelldyne-H/air fuel mixture (See Appendix A for Shelldyne-H properties);

2. For the specific combustor design (A, M, T_g), the air mass flow rate can be determined for varying P_w;

3. The heat transfer coefficient between the free stream gas mixture and the combustor wall can then be determined from the heat flux correlation for the ER and w_a;

4. The mass loss rates for each of the thermochemical regimes (depending on PG or C/C) is determined for varying T_w and P_w;

5. β' can be determined.

The relationship between β', h_w, T_w, P_w is generated by means of a thermochemical computer code (NOTS)[12]. The calculations are based on equilibrium thermochemistry where solid carbon is the fuel reacting with the hydrogen, carbon, nitrogen, and oxygen constituents of the gas mixture. Twenty-one species have been considered in the equilibrium calculation in which their thermochemical data are from the JANNAF tabulations where all enthalpies are referred to the base at 298.16°K, 1 atm and the elements in their natural state.

COMPUTER PROGRAM

The above procedure has been incorporated into a computer program. A new version of the NOTS (NOTS-CMA)[12] code has been created with modifications and the addition of a subroutine for the sole purpose of generating the thermochemistry data in the proper input format for the heat transfer analysis computer program CMA[13].

Figure 3 presents the calculated β' for various Shelldyne-H ER's over carbon-carbon material. In each case, the β' levels off at the diffusion limited value. For any specific ER, the effect of P_w on β' is negligible above 2500°R. However, for the case of Shelldyne-H over PG, its an entirely different result. Figure 4 presents the β' for the ER = 0.5 case showing, not only a variation with wall pressure, but, more importantly, the mass transfer parameter reaches a maximum in the temperature range of $3500-4000^\circ$R then drops. The oxidation of PG is kinetically controlled (not diffusion limited) and behaves in a peculiar manner per the previous discussion. Since CMA requires that the
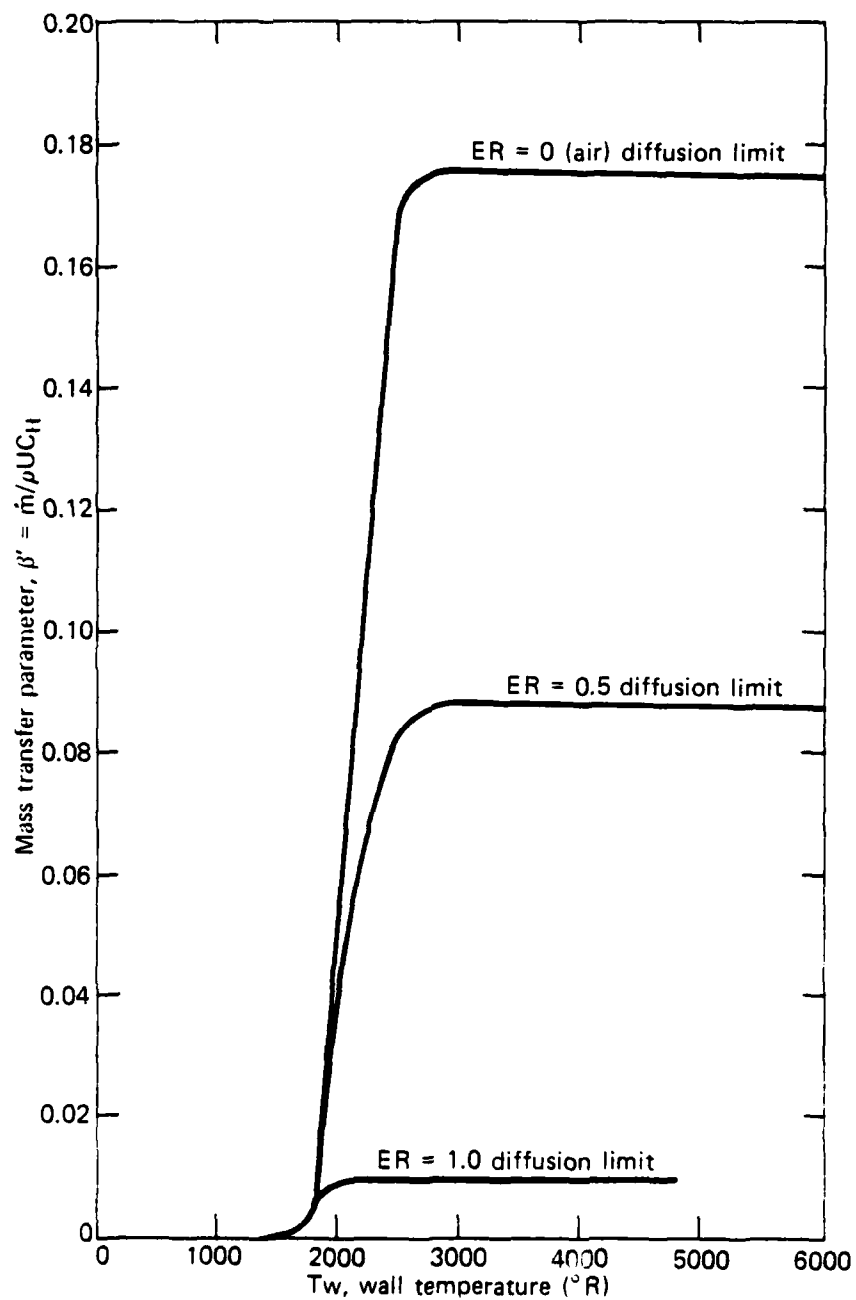
Fig. 3   Carbon oxidation comparison of transition region, 1 atm pipe configuration, 0.795 ft dia., carbon-carbon, Shelldyne - H/air.
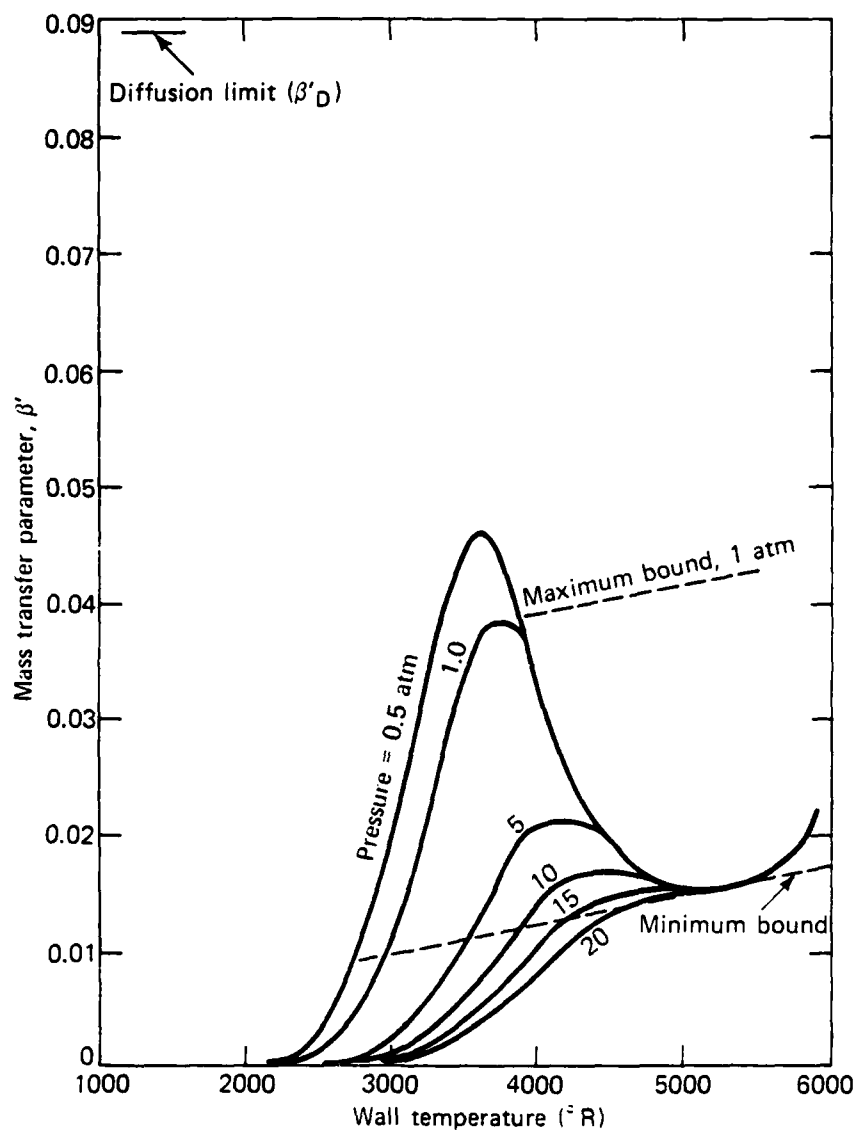
Fig. 4   Mass-transfer parameter versus wall temperature for various pressures.
Shelldyne - H, ER = 0.50, PG wall.

β' versus T_w be monatonically increasing, β' is bounded at a maximum and minimum slope as shown in Figure 4 and a range of surface ablation is calculated.

EXPERIMENTAL RESULTS

The development of high performance supersonic combustor materials requires an understanding of the mechanical and chemical processes taking place at the ablating surface of various materials. This is impossible to obtain from analysis alone and requires some experimentation. Consequently a series of tests were performed at the McDonnell Douglas High Impact Pressure (HIP)[14] arc heater facility to simulate sea level and high altitude cruise conditions in a supersonic combustor.

The purposes of these tests were to evaluate candidate supersonic combustor materials and to obtain mass loss and surface temperature data for comparison with analysis. A total of 40 models were tested, with each model nominally 0.5 inches wide by 0.5 inches thick by 1.25 inches long. A model was placed on each arm of an eight arm turret (Figures 5 and 6) and injected into the arc jet. Thirty-two of the models were tested at a 10° angle-of-attack for 75 s each at a nominal brightness temperature of $5000^\circ R$ ($\epsilon=1$) using a similated Shelldyne – air mixture to approximate high altitude cruise conditions. Eight models were tested for 40 s at a 25° angle-of-attack using a Shelldyne – air mixture to simulate sea-level conditions. Surface brightness temperature was measured at four locations along the model centerline (0.25, 0.55, 0.85 and 1.15 inches from the leading edge) using optical pyrometers. The model backface temperature history was measured at the 0.85 inch position using a tungsten-rhenium thermocouple. Model recession histories were obtained from 16 mm movie films of the model profile.

Several materials were used to determine which were best suited for scramjet engine combustors. Particular interest was given to metal impregnated carbon-carbon (C-C) materials which in theory form protective metal oxide layers, retained at the surface by high viscosity silica compounds also added to the specimens. A summary of the processing treatments and composition of metal and silica additives for each specimen is presented in Table 2. In addition, some reference materials including virgin C-C, pyrolytic graphite (PG) coated C-C, pyrolytic graphite/silicon carbide (PG/S-C) coated ATJ graphite, and ATJ-S graphite were also used.

A summary of the mass recession loss rate results is presented in Figure 7 for the long-range, high altitude tests and Figure 8 for the sea-level test. In the high-altitude tests there is no particular trend in the metal additive corposition or process and there appears to be no benefit from metal additives. On the contrary, the limited data suggests metal additives have increased the recession rate. Except for model #21 (ZR(.6) – Si(.2) – B(.2)/RH), the pyrolytic graphite is clearly superior.

The recession rates for materials tested at the sea-level condition show that the metalized C-C samples (24, 14 and 2) are the same or worse than the plain C-C sample number 45. Moreover, PG and PG/SiC had much lower recession rates. Although it appears that the metalized C-C materials offer no significant improvement over other combustor materials, shear stresses on the surface were slightly higher than desired and may have altered the performance that these materials would experience in a real combustor application.
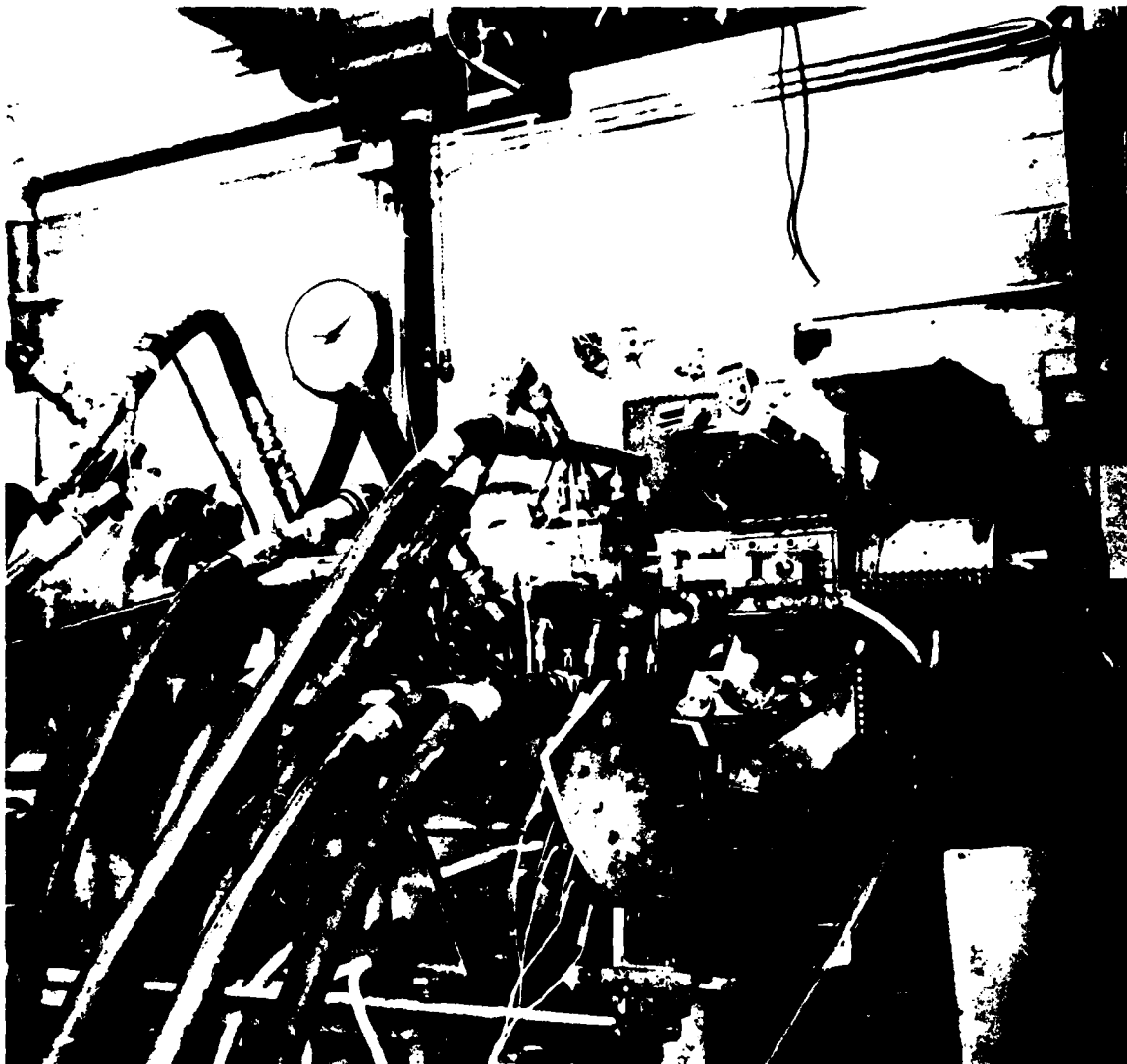
Fig. 5   Typical arc heater and wedge model set-up.

Run No.	A (in.)	B (in.)	α (deg)
1554	0.050	0.100	10
1555	0.050	0.100	10
1558	0.020	0.100	10
1559	0.020	0.100	10
1564	0.050	0.000	25
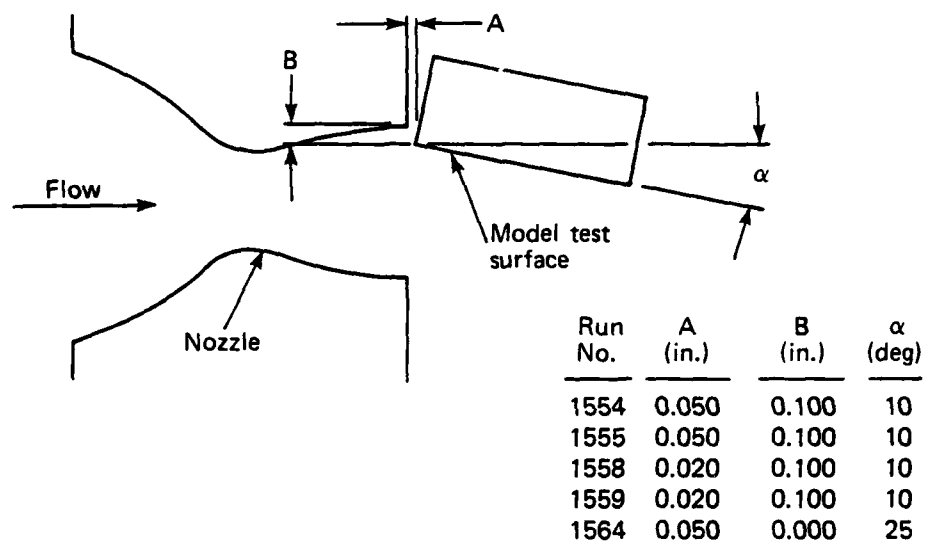
Fig. 6   Profile view of model (top camera).

Table 2 Material Specimen Number Identifications for HIP Tests

Metallic Additives Composition[+,++]	AH	Processing Precursor and Phase				
		AL	RH	RL	RO	AO
Zr(.6)-Si(.2)-B(.2)	15	(16)	(21)	(23)	(37)	(39)
		17	22	[24]	38	40
Zr(.8)-Si(.1)-B(.1)	(13)					
	[14]					
Zr(.6)-Si(.2)-Ti(.2)	(25)					
Zr(.8)-Si(.1)-Ti(.1)	(18)					
	19					
Hf(.6)-Si(.2)-B(.2)						
Hf(.8)-Si(.1)-B(.1)	(1)					
	[2]					
Hf(.6)-Si(.2)-Ti(.2)	(9)					
Hf(.8)-Si(.1)-Ti(.1)	(7)					

Non-metallized specimens (pitch only) are [45] , (47) , ⬡48

Code

AH = Alkoxy - HiC
AL = Alkoxy - LoC
RH = Resinate - HiC
RL = Resinate - LoC
RO = Resinate - Oxide
AO = Alkoxy - Oxide

◯ - Runs 1554 & 1555
⬡ - Runs 1558 & 1559
▢ - Run 1564

[+] Numbers in parentheses refer to mole fraction of the metal additive.
[++] Materials are listed from top to bottom in order of increasing theoretical refractoriness.
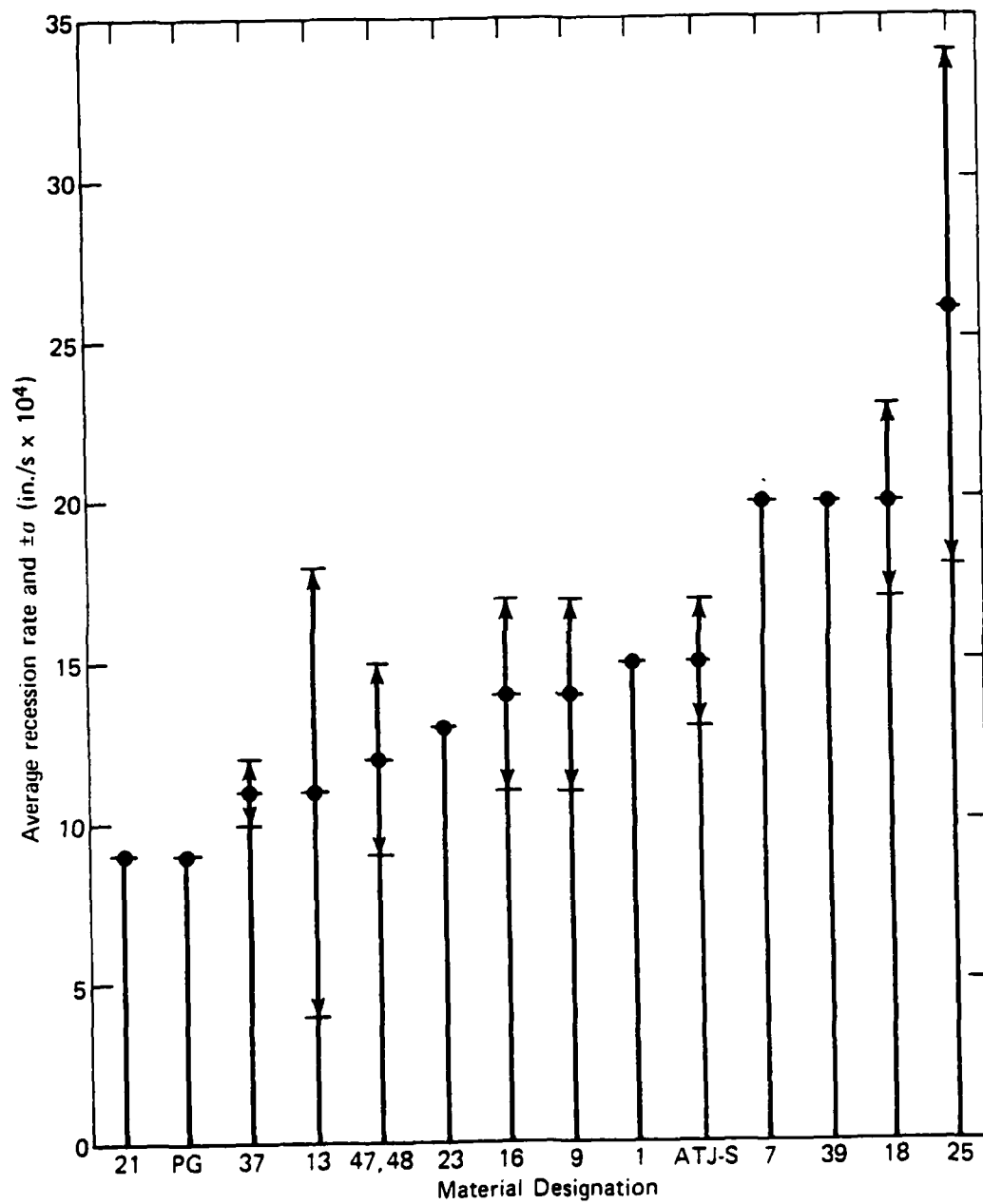
Fig. 7   Material recession rate performance for high-altitude tests.
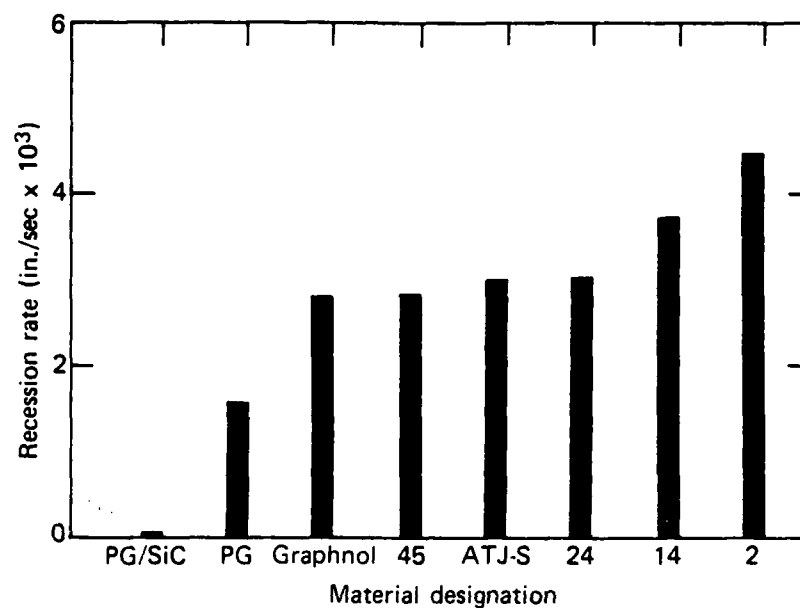
Fig. 8   Material recession rate performance for sea-level tests.

COMPARISON OF MEASURED AND PREDICTED MATERIAL RECESSION

Results from the HIP tests have been compared with predicted analytical values of recession and surface temperature and agree to within 25%. The test conditions analyzed were for an ATJ-S specimen placed at a 3.5° angle of attack in air at 5620°R at simulated high altitude cruise conditions. Thermochemical properties of carbon-carbon were obtained from the EST computer code[15] assuming no CO_2 in the chemically reacting products near the ablating surface. The rational for this assumption is based on the fact that the $(2C + O_2 \rightarrow 2CO)$ reaction rate is much faster than the $(2CO + O_2 \rightarrow 2CO)$ reaction rate which in turn, is much faster than the $(2CO + O_2 \rightarrow 2CO)$ rate. Consequently, CO is produced and then swept away from the reacting surface before it has a chance to react with O_2, to form CO_2.

The analytical model consists of a 0.5 inch thick piece of ATJ-S, insulated from a 0.5" steel support by a 0.02" layer of zirconium dioxide (Figure 9). Measured surface temperatures were obtained from black body optical pyrometer temperatures assuming an ATJ-S surface emissivity of 0.78 at 0.9μ.

Predicted surface temperatures compare favorably with optically measured temperatures during the first 20 to 30 seconds of the test (Figure 10). After this time however, measured temperatures decrease sharply and are no longer in good agreement with predicted temperatures which continue to increase. The reason for this is that as the specimen ablates it recedes out of the freejet main stream and into the cooler boundary layer. Therefore, only the first 20 to 30 seconds of the test are a valid simulation of actual combustor conditions, and data taken after that should be ignored.

Surface ablation rates measured during this test, compare well with predicted recession rates throughout the test (Figure 11). Both experiment and analysis indicate ablation begins between 6 and 11 seconds and continues at a constant rate throughout the test. Constant recession rates of 0.0027 and 0.0024 inches/sec have been measured and compare with a slightly higher predicted rate of 0.0033 inches/sec. The somewhat surprising aspect of this data is that measured recession rates remain constant even at times greater than 30 seconds, when the surface temperature is decreasing and the heated surface is moving into the freejet boundary layer. This seemingly inconsistent behavior can be explained as follows: In general, ablation rate is expressed as $\beta' \cdot \rho u C_h$ (Equation 7), where β' is the diffusion mass flux ratio expressed as a function of the material, its surface temperature and pressure, while $\rho u C_h$ is the enthalpy based heat transfer coefficient. For ATJ-S the ablation rate is diffusion limited at temperatures above 2400°R, which means β' is constant about 2400°R. Since surface temperatures remain above 2400°k for most of the test (Figure 10), β' is a constant. However, in order to have a constant recession rate, $\rho u C_h$ must also be constant. Apparently, as the surface recedes into the cool thermal boundary layer, the effect of decreasing stream velocity (u) is offset by a decrease in the reference length, since the effective distance to the leading edge is decreasing as the leading edge leaves the freejet main stream. The good agreement between experimental and analytical surface temperatures and ablation rates give us added confidence in our analytical model.
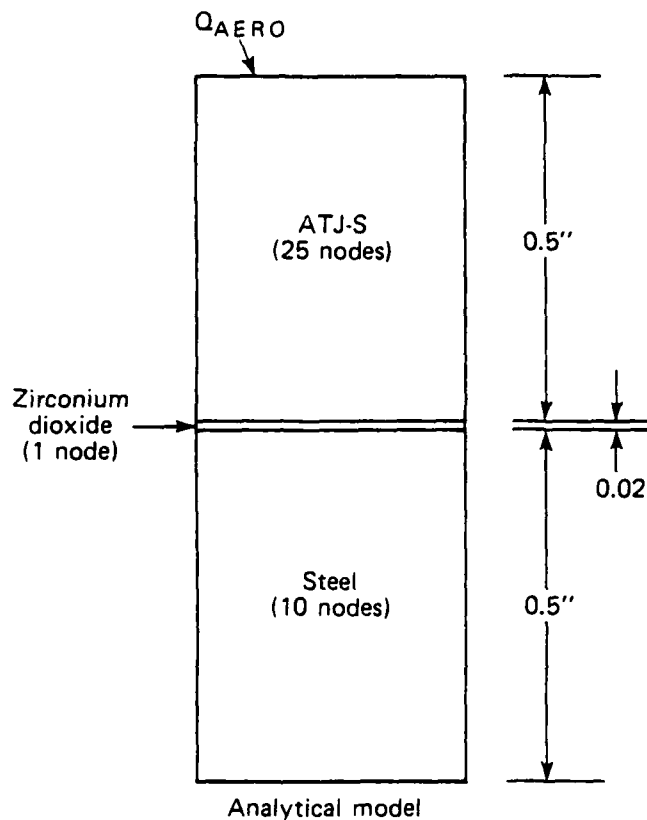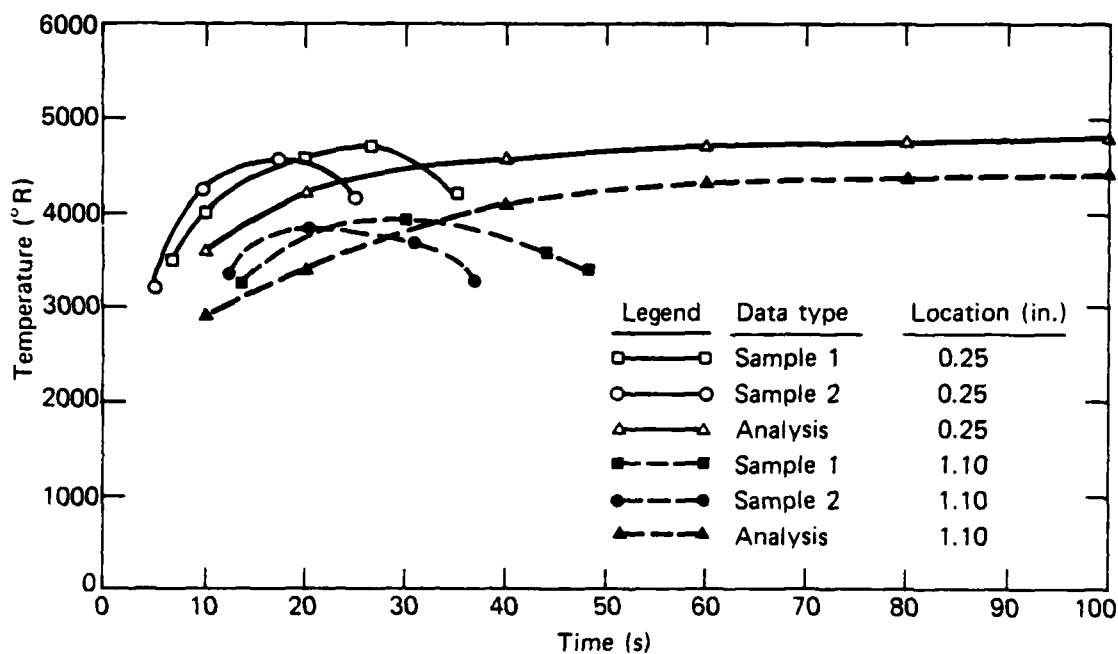
Fig. 9   HIP test specimen.

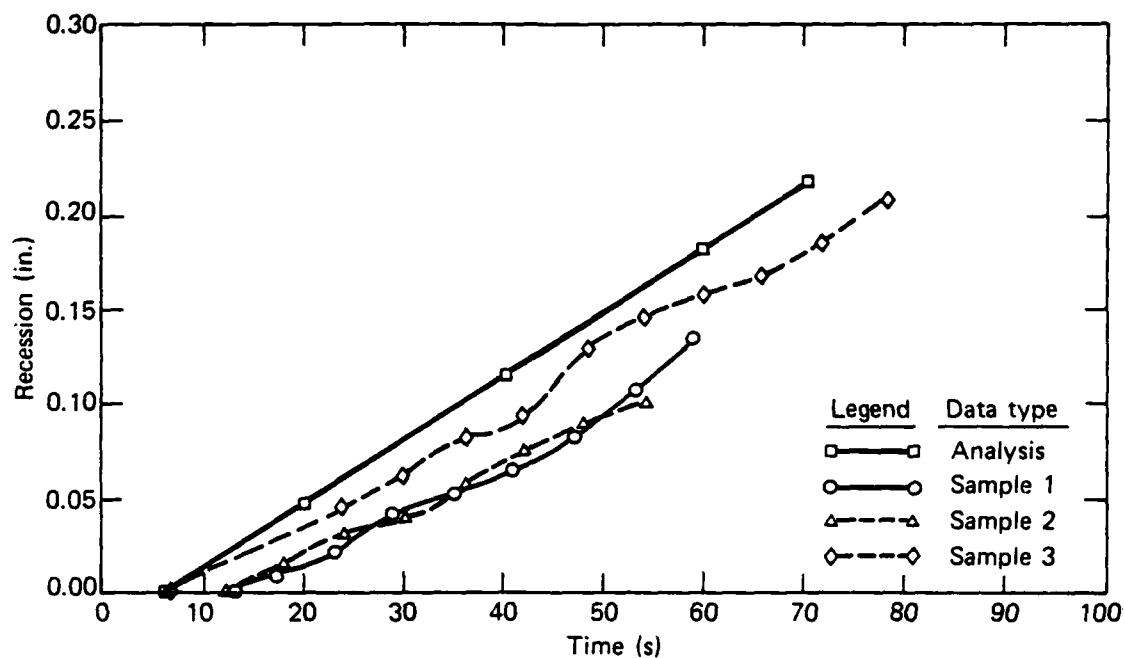Fig. 10   Comparison of test and analysis surface temperature histories ATJ-S.

Fig. 11 Comparison of test and analysis ablation histories ATJ-S, 0.85 in. location.

ACKNOWLEDGEMENTS

REFERENCES

1. Perini, L. L., "Review of Graphite Ablation Theory and Experimental Data", APL/JHU ANSP-M, Dec. 1971.

2. Perini, L. I.., "Graphite Oxidation Modeling in Subsonic Flow", APL/JHU ANSP-111, Aug. 1977.

3. Scala, S. M. and Gilbert, L. M., "Aerothermal Behavior of Graphite at Elevated Temperatures", GE Report No. R635D81, Nov. 1963.

4. Metzger, J. W., Engel, M. J., and Diaconis, N. S., "The Oxidation and Sublimation of Graphite in Simulated Re-entry Environments", AIAA No. 65-643, 1965.

5. Nagle, J. and Strickland-Constable, R. F., "Oxidation of Carbon Between 1000-2000°C", Proc. Fifth Conference on Carbon, 1961.

6. Strickland-Constable, R. F., "Theory and the Reaction of Graphite with Oxygen in the Temperature Range 1000-2400°C", 2nd Conference on Industrial Carbon and Graphite, Soc. Chem. Ind. (London), 1966.

7. Blyholder, G., Binford, J. S. and Eyring, H., "A Kinetic Theory for the Oxidation of Carbonized Filaments", J. Phys. Chem., pp. 62, 263, 1958.

8. Mickley, H. S., Ross, R. C., Squyers, A. L., and Stewart, W. E., "Heat, Mass, and Momentum Transfer for Flow Over a Hot Plate with Blowing or Suction", NACA TN-3208, July 1954.

9. Thomas, J. M., "Reactivity of Carbon: Some Current Problems and Trends", Carbon 1970, Vol. 8, pp. 413-421, Pergamon Press.

10. Funk, J. A. Waltrup, P. J., "Wall Heat Flux Correlations for Scram Combustion and Nozzles", Section 11 (U) Quarterly Report, April-June 1977, APL/JHU C-RQR/77-2 (Confidential).

11. Bartz, D. R., "A Simple Equation for Rapid Estimation of Rocket-Nozzle Convective Heat Transfer Coefficients", Jet Prop., pp. 99, Jan. 1957.

12. D. R. Cruise, "Notes on the Rapid Computation of Chemical Equilibria", Journal of Physics and Chemistry, Vol. 68 No. 12 (Dec 1964), pp. 3797-3802.

13. "User's Manual, Aerotherm Charring Material Thermal Response and Ablation Program, Version 3", (CMA), Vol. I and Vol. II, Aerotherm Report No. UM 70-14, April 1970.

14. W. A. Rinehart, R. A. Williamson and J. A. Grace, "Supersonic Combustor Materials Screening in the HIP Arc Heater Facility", McDonnell Douglas Company, St. Louis Division, MDC E2216.

15. "User's Manual, Aerotherm Equilibrium Surface Thermochemistry Program", Version 3, Aerotherm Corporation, Mountain View, California, Report UM-70-13, May 1970.

Appendix A

Shelldyne-H Fuel Properties

The ramjet fuel under consideration for the hypersonic missile is the hydrocarbon fuel, Shelldyne-H ($C_{14} H_{18}$). Some of its basic properties are:

Density	=	67.5 #/ft^3
Stoichiometric fuel-air ratio (f_s)	=	0.072832
Lower heating value	=	17,890 Btu/#

Table A-1 presents a tabulation of the mole percent of various by-products of combustion for varying equivalence ratio (ER) of the Shelldyne-H/air mixture. The mole percent of O_2 by-product versus ER is plotted for two different free stream air total temperatures of 1080°R and 3780°R in Figure A-1. The approximate curve fit of oxygen mole function for use in our analytical model is

$$(\phi O_2) \text{moles} = 0.21 - 0.198 \text{ ER}$$

which is also plotted in Figure A-1 for comparison.

Figure A-2 presents the variation of combustor total gas temperature versus free stream air total temperature for varying equivalence ratio.

Table A-1

Mole Percent of Products of Combustion
Shelldyne-H + Air

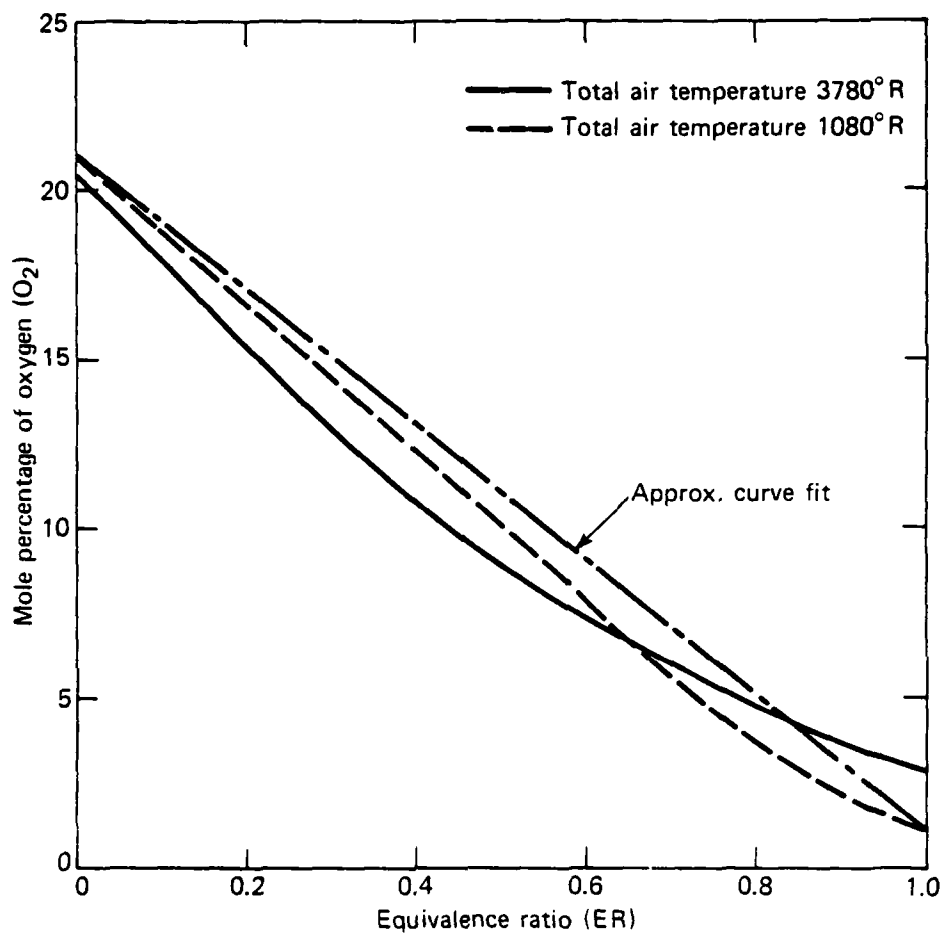| ER	0	.3	.4	.5	.6	.7	.8	.9	1.0
$T^{\circ}R$	1080	2438	2830	3197	3539	3845	4098	4281	4392
O_2	21.0	14.45	12.28	10.1	7.9	5.8	3.9	2.32	1.20
N_2	79.0	77.78	77.35	76.9	76.4	75.8	75.2	74.4	73.5
CO_2	0	4.70	6.23	7.74	9.2	10.6	11.6	12.1	11.96
CO	0	0	0	0	.03	.17	.58	1.46	2.87
H_2O	0	3.02	4.0	4.96	5.9	6.8	7.54	8.25	8.85
H	0	0	0	0	0	.01	.02	.06	.11
HO	0	0	0	.034	.10	.22	.37	.50	.54
O	0	0	0	0	.01	.04	.09	.12	.12
NO	0	.05	.14	.28	.45	.59	.66	.63	.50
H_2	0	0	0	0	0	.02	.07	.17	.36

Fig. A-1   Mole percentage of oxygen in Shelldyne - H/air mixture.
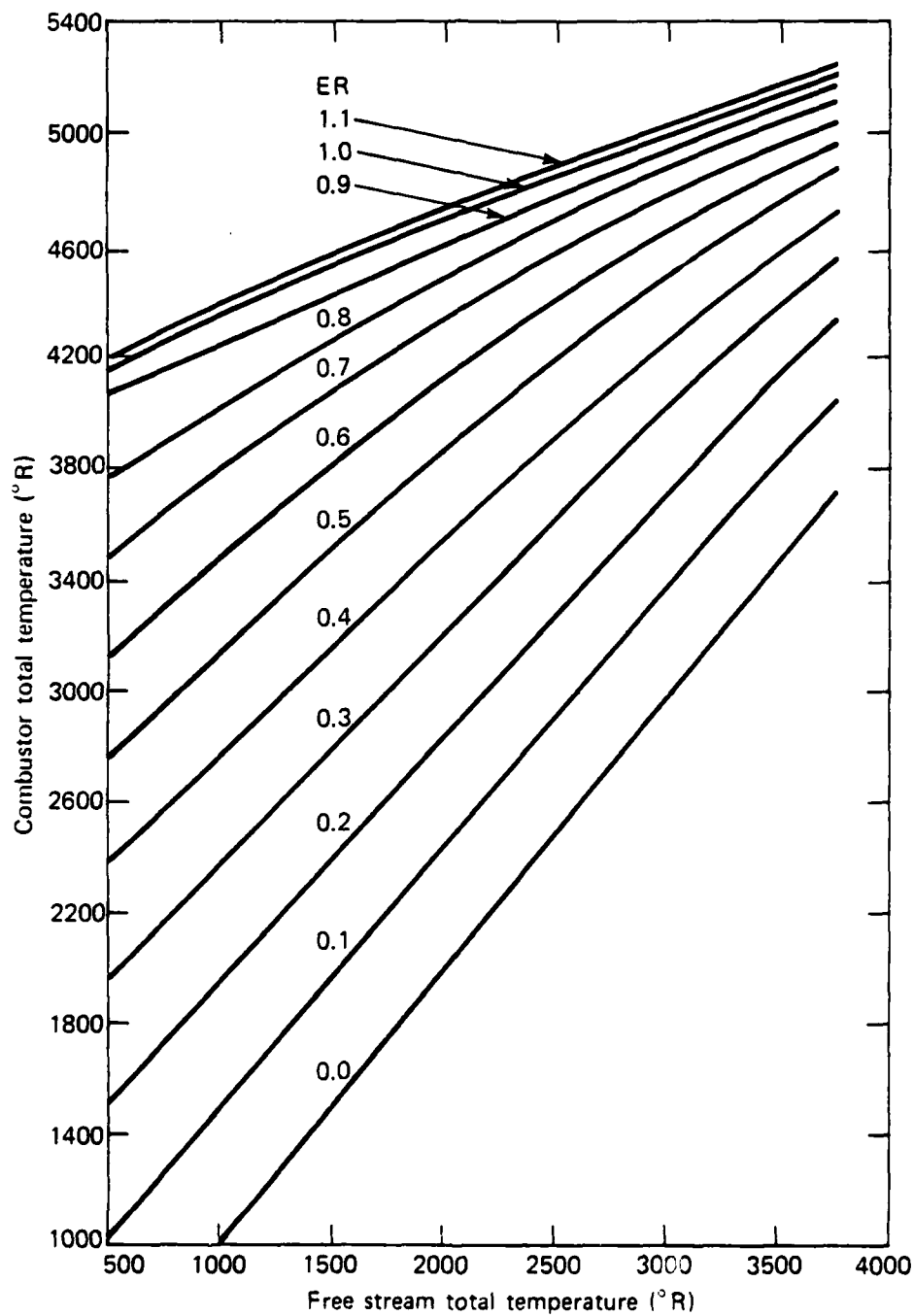
Fig. A-2   Combustor T_t versus free stream T_t, Shelldyne - H.

NUMERICAL AERODYNAMIC SIMULATOR:

BACKGROUND, REQUIREMENTS, AND JUSTIFICATION

AMES RESEARCH CENTER
National Aeronautics and Space Administration

Pages II-129 through II-164 withdrawn at request of author.
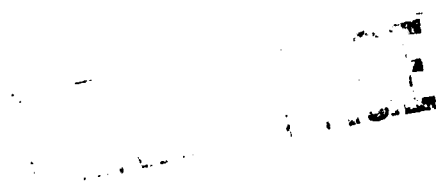
COMPUTATION OF THREE-DIMENSIONAL VISCOUS FLOW OVER

BLUNT LIFTING BODIES AT HIGH ANGLE OF ATTACK

K. Y. Szema* and C. H. Lewis**

Virginia Polytechnic Institute and State University
Aerospace and Ocean Engineering Department
Blacksburg, Virginia

ABSTRACT

The viscous shock-layer equations for three-dimensional
hypersonic flows of a perfect gas or equilibrium air over lifting
bodies at high angles of attack have been developed. For the complex
three-dimensional reentry vehicle geometries of interest, the re-
sulting equations are written in a nonorthogonal, body-oriented
coordinate system, and the three velocity components are defined
in the nonorthogonal coordinate directions. Since the viscous
shock-layer governing equations are parabolic in both the stream-
wise and crossflow directions, the equations are solved by a highly
efficient finite-difference scheme. The principal advantages of
this technique are (i) the numerical method can be used to predict
the flowfield about arbitrary geometries in both subsonic and super-
sonic regions, (ii) the solution is direct, and (iii) the effects of
inviscid-viscous interactions are uniformly valid throughout the
shock layer. Numerical solutions have been obtained for a 1:1.4
(perfect gas), 1:2 ellipsoid in a perfect gas or equilibrium air
and the nose portion of the shuttle orbiter at zero, 10 and 25-deg
angles of attack. Comparisons were made with inviscid solutions
and existing experimental data, and the agreement is good for all
the cases.

INTRODUCTION

Various analyses are available to investigate the flowfields and wall-
measurable quantities for hypersonic flow past an axisymmetric blunt body at
different angles of attack. However, the effects of the noncircular body
geometry can be significant, and the main purpose of this study is to develop
a technique to predict hypersonic viscous flows over a noncircular body at
typical planetary entry conditions.

Recently a numerical method for 3-D laminar, transitional and/or turbu-
lent hypersonic flows of perfect gas over a blunt body, used for planetary
probes, has been investigated[1] at different angles of attack by using an

*Research Associate
**Professor

implicit finite-difference viscous shock-layer analysis. However, that analysis is valid for axisymmetric bodies only. For the complex three-dimensional lifting reentry vehicle geometries of interest, the resulting equations are written in a nonorthogonal body-oriented coordinate system, and the three velocity components are defined in the nonorthogonal coordinate directions. This procedure is different from writing the equations in an orthogonal coordinate system and explicitly performing a coordinate transformation. Since the viscous shock-layer equations are parabolic in both the streamwise and crossflow directions, the equations were solved by a highly efficient finite-difference scheme[1,2]. The principle advantages of this technique are (i) the numerical method can be used to predict the flowfield about arbitrary geometries in both subsonic and supersonic regions, (ii) the solution is direct, and (iii) the effects of inviscid-viscous interactions are included within a single set of governing equations which are uniformly valid throughout the shock layer.

The basic formulation of the problem is presented in Section 2. Boundary conditions at the body surface and immediately behind the shock are given in Section 3. Coordinates and method of solution are presented in Sections 4 and 5, respectively. The results are discussed in Section 6, and the conclusions are presented in Section 7.

BASIC FORMULATION

The basic equations are derived from the steady Navier-Stokes equations in general body-oriented tensor form (Figure 1). One of the coordinates, $\xi 1$, is chosen in the general axial direction, and another, $\xi 2$, in a direction normal to the body, and the third, $\xi 3$, around the body. The coordinate system requires orthognality only at the body surface. The normal velocity v and normal coordinate $\xi 2$ are assumed to be of order ε, and all terms which are of higher order than ε are neglected. The methods of obtaining these equations are discussed in detail elsewhere[2,3]. The nondimensional form of the viscous shock-layer equations that are applicable in the present case can be written as follows:

Continuity Equation:

$$\frac{\partial}{\partial \xi_1} (\rho u g^{\frac{1}{2}}) + \frac{\partial}{\partial \xi_2} (\rho v g^{\frac{1}{2}}) + \frac{\partial}{\partial \xi_3} (\rho w g^{\frac{1}{2}}) = 0 \tag{1}$$

ξ_1-Momentum:

$$\rho u \frac{\partial u}{\partial \xi_1} + \rho v \frac{\partial u}{\partial \xi_2} + \rho w \frac{\partial}{\partial \xi_3} + \rho \left[u^2 \left\{ \begin{matrix} 1 \\ 1\ 1 \end{matrix} \right\} + 2uv \left\{ \begin{matrix} 1 \\ 1\ 2 \end{matrix} \right\} \right.$$

$$\left. + 2uw \left\{ \begin{matrix} 1 \\ 1\ 3 \end{matrix} \right\} + v^2 \left\{ \begin{matrix} 1 \\ 2\ 2 \end{matrix} \right\} + 2vw \left\{ \begin{matrix} 1 \\ 2\ 3 \end{matrix} \right\} + w^2 \left\{ \begin{matrix} 1 \\ 3\ 3 \end{matrix} \right\} \right]$$

II-166

$$+ \frac{g_{22}}{g} \left[g_{33} \frac{\partial P}{\partial \xi_1} - g_{13} \frac{\partial P}{\partial \xi_3} \right]$$

$$= \varepsilon^2 \left[\frac{1}{g_{22}} \left(\frac{\partial \mu}{\partial \xi_2} \frac{\partial u}{\partial \xi_2} + \mu \frac{\partial^2 u}{\partial \xi_2^2} \right) \right] \tag{2}$$

ξ_2-Momentum:

$$\rho u \frac{\partial v}{\partial \xi_1} + \rho v \frac{\partial v}{\partial \xi_2} + \rho w \frac{\partial v}{\partial \xi_3} + \rho \left[u^2 \left\{ {2 \atop 1 \; 1} \right\} + 2uv \left\{ {2 \atop 1 \; 2} \right\} \right.$$

$$\left. + 2uw \left\{ {2 \atop 1 \; 3} \right\} + v^2 \left\{ {2 \atop 2 \; 2} \right\} + 2vw \left\{ {2 \atop 2 \; 3} \right\} + w^2 \left\{ {2 \atop 3 \; 3} \right\} \right]$$

$$+ \frac{1}{g_{22}} \frac{\partial P}{\partial \xi_2} = 0 \tag{3}$$

ξ_3-Momentum:

$$\rho u \frac{\partial w}{\partial \xi_1} + \rho v \frac{\partial w}{\partial \xi_2} + \delta w \frac{\partial w}{\partial \xi_3} + \rho \left[u^2 \left\{ {3 \atop 1 \; 1} \right\} + 2uv \left\{ {3 \atop 1 \; 2} \right\} + 2uw \left\{ {3 \atop 1 \; 3} \right\} \right.$$

$$\left. + v^2 \left\{ {3 \atop 2 \; 2} \right\} + 2vw \left\{ {3 \atop 2 \; 3} \right\} + w^2 \left\{ {3 \atop 3 \; 3} \right\} \right] + \frac{g_{22}}{g} \left[g_{11} \frac{\partial P}{\partial \xi_3} \right.$$

$$\left. - g_{13} \frac{\partial P}{\partial \xi_1} \right] = \varepsilon^2 \left[\frac{1}{g_{22}} \left(\frac{\partial \mu}{\partial \xi_2} \frac{\partial w}{\partial \xi_2} + \mu \frac{\partial^2 w}{\partial \xi_2^2} \right) \right] \tag{4}$$

Energy Equation:

$$\rho u \frac{\partial h}{\partial \xi_1} + \rho v \frac{\partial h}{\partial \xi_2} + \rho w \frac{\partial h}{\partial \xi_3} - \left[u \frac{\partial P}{\partial \xi_1} + v \frac{\partial P}{\partial \xi_2} \right.$$

$$\left. + w \frac{\partial P}{\partial \xi_3} \right] = \varepsilon^2 \left[\frac{1}{g_{22}} \left(\frac{\partial}{\partial \xi_2} \left(\frac{\mu}{Pr} \right) \frac{\partial h}{\partial \xi_2} + \frac{\mu}{Pr} \frac{\partial^2 h}{\partial \xi_2^2} \right) \right]$$

$$+ \varepsilon^2 \left\{ \mu \left[\frac{g_{11}}{g_{22}} \left(\frac{\partial u}{\partial \xi_2} \right)^2 + 2 \frac{g_{13}}{g_{22}} \frac{\partial u}{\partial \xi_2} \frac{\partial w}{\partial \xi_2} + \frac{g_{33}}{g_{22}} \left(\frac{\partial w}{\partial \xi_2} \right)^2 \right] \right\} \tag{5}$$

II-167

It should be noted that the Prandtl number is assumed constant for a perfect gas and is a function of pressure and temperature for a gas in chemical equilibrium.

Equation of State

$$\rho = \rho(p, h) \tag{6}$$

For a perfect gas, Equation (6) has the analytical form

$$\rho = \gamma p/[(\gamma-1)RT]$$

where γ is the ratio of specific heats. For the chemical equilibrium assumption, the functional relation may be given by a table or an approximate analytical expression (curve fits) which are given in detail in Reference 4.

In the governing equations $\left\{ {}_j{}^i{}_k \right\}$ are Christoffel symbols of the second kind, and the matrix g_{ij} can be obtained numerically from the grid generation procedure.

BOUNDARY CONDITION

In order to solve the above set of governing equations, it is essential to specify appropriate boundary conditions at the body surface and at the shock. At the body surface (wall), no-slip and no-temperature-jump conditions were used. Consequently, $u_w = v_w = w_w = 0$, and the wall temperature or heat-transfer rate was specified. The conditions immediately behind the shock were obtained by using the Rankine-Hugoniot relations. However, before those equations may be applied, the tangential and normal components of the velocity must be found. These components are obtained by the method of Rakich[5]. An orthogonal set of vectors with $\vec{N}$ a unit vector normal to the shock surface and $\vec{T}$ a tangent vector is considered. The N-T plane is parallel to the direction of freestream $\vec{U}_\infty$. Then the two-dimensional Rankine-Hugoniot relations are used to calculate the conditions behind the shock. The total velocity can be written as

$$\vec{U} = U_T \vec{T} + U_N \vec{N}$$

$$= \left[U_T \left(\frac{U_z - bN_z}{a} \right) - U_N \left(\frac{\sin\sigma}{c} \right) \right] \hat{e}_z$$

$$+ \left[U_T \left(\frac{U_r - bN_r}{a} \right) + U_N \left(\frac{\cos\sigma}{c} \right) \right] \hat{e}_r$$

$$+ \left[U_T \left(\frac{U_\phi - bN_\phi}{a} \right) - U_N \left(\frac{\cos\sigma \, \mathrm{Tan}\delta}{c} \right) \right] \hat{e}_\phi \tag{7}$$

where a, b, c, σ and δ are given by Rakich[5]. After the velocity behind the
shock has been calculated, it is necessary to rotate these components into a
body-normal nonorthogonal coordinate system. This is done by expressing the
vectors $\hat{e}_z$, $\hat{e}_r$, $\hat{e}_\phi$ in terms of $\vec{g}_1$, $\vec{g}_2$, $\vec{g}_3$ in the ξ_1, ξ_2, ξ_3 directions

$$
\begin{bmatrix} \hat{e}_z \\[6pt] \hat{e}_r \\[6pt] \hat{e}_\phi \end{bmatrix} = \begin{bmatrix} \dfrac{\partial z}{\partial \xi_1} & \dfrac{\partial r}{\partial \xi_1} & r\,\dfrac{\partial \phi}{\partial \xi_1} \\[6pt] \dfrac{\partial z}{\partial \xi_2} & \dfrac{\partial r}{\partial \xi_2} & r\,\dfrac{\partial \phi}{\partial \xi_2} \\[6pt] \dfrac{\partial z}{\partial \xi_3} & \dfrac{\partial r}{\partial \xi_3} & r\,\dfrac{\partial \phi}{\partial \xi_3} \end{bmatrix}^{-1} \begin{bmatrix} \vec{g}_1 \\[6pt] \vec{g}_2 \\[6pt] \vec{g}_3 \end{bmatrix} \tag{8}
$$

Using Equation 8, the shock velocity components in the body-normal non-
orthogonal coordinate system are determined.

COORDINATE GENERATION

Based on the general curvilinear coordinate governing equations, a body-
oriented nonorthogonal coordinate system is constructed. This is first done
on the surface of the body, where $\xi_2 = 0$, and then extended to the points
away from the surface of the body. The coordinate system requires ortho-
gonality only at the body surface, and the ξ_2 coordinate is always orthogonal
to ξ_1 and ξ_3. The approach used is an extension of that presented by Blottner[6]
and a detailed discussion of a similar procedure can be found in Reference 3.

METHOD OF SOLUTION

Davis[7] presented an implicit finite-difference method to solve the
viscous shock-layer equations for axially symmetric flows. Murray and Lewis[2]
extended the method of solution to three-dimensional high angle of attack
conditions. The present method of solution is identical to that of Murray
and Lewis. Therefore, only an overview of the solution procedure is presented.

The solution begins on the blunt nose by obtaining an approximate stag-
nation solution in the wind-fixed coordinate system. The 3-D solution begins
on the windward plane and marches around the body obtaining a converged so-
lution in each ϕ sweep. After completing a sweep in the ϕ direction, the
procedure then steps downstream in ξ_1 and begins the next ϕ sweep. At each
point the equations are solved in the following order (i) ϕ-momentum, (ii)
energy, (iii) ξ_1-momentum, (iv) integration of continuity for Y_s, and (v)
coupled continuity and normal momentum equations.

RESULTS AND DISCUSSION

Numerical solutions of the three-dimensional nonorthogonal shock-layer
equations were obtained for a 1:1.4, 1:2 ellipsoid and the nose portion of

the shuttle orbiter at different angles of attack. It should be mentioned here that the wind-fixed coordinate system is used in the 1:2 ellipsoid 10-deg angle of attack case. The freestream conditions for these cases are given in Table 1. Comparisons are made for shock standoff distance, surface pressure distribution and heat-transfer rate with inviscid results and existing experimental data.

Shock-standoff distance as a function of the coordinate along the body surface in different ϕ-planes is illustrated in Figures 2 and 3. The inviscid solutions from Marconi and Yaeger[8] are also presented and are in very good agreement with the present nonorthogonal viscous shock-layer calculations. It is noted that the shock standoff distance increases more rapidly between $\phi = 0$ and 30-deg for the 1:2 ellipsoid case than for the 1:1.4 case. However, this would be expected because the body curvature in the transverse direction is smaller for the 1:2 ellipsoid case in this region.

Figures 4 and 5 present the surface pressure distribution along the body at different ϕ-planes for these two cases. Some inviscid pressure results are also presented. It is noted that the inviscid data are in very good agreement with present results.

Figures 6 and 7 show the convective heating rate in several ϕ-planes along the body surface. The solution for Case 1 is compared with the experimental data given by Hillsamer and Rhudy[9]. The results show that the present prediction is in excellent agreement with the experimental data. Because of the streamwise body curvature effects, the heating rate is higher at $\phi = 90$ and 30-deg than $\phi = 0$ deg near the stagnation region for the 1:2 ellipsoid case. Except in the stagnation region, as was expected, the convective heat-transfer rate decreases with increasing ϕ.

Figures 8, 9 and 10 present the modified 1:2 ellipsoid geometry, surface pressure and convective heating rate for an equilibrium air calculation. As shown in Figure 9, the surface pressure is in reasonably good agreement with the inviscid solution. Since the geometry near the stagnation region is very flat and narrow, the convective heating rate decreased rapidly between $\phi = 0$ and 30-deg. After $\phi = 30$ deg, a much smaller heating rate change is noticed in Figure 10.

Figures 11 to 16 are the body geometry and results of the space shuttle orbiter nose portion up to seven nose radii. The cross section and longitudinal slope of the shuttle orbiter are given in Figure 11. It is noted that on the windward side, the body is relatively flat and the transverse direction curvature changes rapidly at about $\phi = 65$-deg. The shock standoff distance in different planes along the body is shown in Figure 12. Because of the flat windward side, the shock standoff distance decreased slightly on the windward side and then increased rapidly on the leeward side. The inviscid results are also presented, and the agreement is very good. Figure 13 presents the surface pressure distribution around the body at the s = 5.32 station. A very small pressure change was detected on the windward side ($\phi \le 50^\circ$). However, a rapidly decreasing surface pressure was noticed in the region $50 < \phi < 90$ due to the transverse curvature effect. On the leeward side ($\phi > 90^\circ$), the pressure tends to stabilize and the change is small once again. Figure 14 shows that the same trend is followed for all stations along the body surface. Finally, the temperature profiles normal to the body

surface at $s = 0$ (stagnation point) and $s = 5.325$ and the convective heating rate along the body surface are plotted in Figures 15 and 16. Since no other data are available for this case, only the present results are presented here. For the same reason discussed earlier, the temperature and heating rate jump in the region $60 < \phi < 90$ was also noticed.

CONCLUSIONS

The main objective of this study is to investigate the influence of the noncircular body on the shock-layer flow phenomena within reasonable computing times. A general nonorthogonal shock-layer analysis is used. The present surface pressure, shock standoff distance and convective heating rate predictions are in good agreement with inviscid solutions and existing experimental data. The viscous shock-layer technique requires much less computing time than the time-dependent method[10] (Table 1). In the future we plan to include the transitional and/or turbulent flow in the technique.

LIST OF SYMBOLS

C_p^* specific heat at constant pressure

$\hat{e}_i$ unit vector of a general orthogonal coordinate system

$\vec{g}_1, \vec{g}_2, \vec{g}_3$ vectors in ξ_1 (streamwise), ξ_2 (normal) and ξ_3 (circumferential) directions

g_{ij} metrics $g_{ij} = \dfrac{\partial z}{\partial \xi_i} \dfrac{\partial z}{\partial \xi_j} + \dfrac{\partial r}{\partial \xi_i} \dfrac{\partial r}{\partial \xi_j} + r^2 \dfrac{\partial \phi}{\partial \xi_i} \dfrac{\partial \phi}{\partial \xi_j}$

g $\det (g_{ij}) = g_{11} g_{22} g_{33} - g_{22} g_{13}^2$

h static enthalpy, h^*/U_∞^{*2}

$\vec{N}$ shock-normal vector

p pressure

Pr Prandtl number

R_n body nose radius

T temperature

T_{ref}^* reference temperature, U_∞^{*2}/C_p^*

$\vec{T}$ shock-tangent vector

u, v, w streamwise, normal and crossflow velocity components nondimensionalized by the freestream velocity U_∞^*

U_N velocity component normal to the shock

U_T velocity component tangent to the shock

z, r, ϕ cylindrical coordinates

Y_s shock standoff distance

α angle of attack

γ ratio of specific heats

ϵ Reynolds number parameter $\epsilon^2 = \mu^*_{ref}/\rho^*_\alpha U^*_\infty R^*_n$

μ viscosity, μ^*/μ^*_{ref}

μ_{ref} reference viscosity, $\mu^*(T_{ref})$

ξ_1, ξ_2, ξ_3 computational coordinates

ρ density, ρ^*/ρ^*_∞

$\left\{ \begin{matrix} i \\ j \ k \end{matrix} \right\}$ Christoffel symbol of the 2nd kind, $\dfrac{1}{2} \displaystyle\sum_m g^{im} \left[\dfrac{\partial g_{mk}}{\partial \xi_j} + \dfrac{\partial g_{mj}}{\partial \xi_k} - \dfrac{\partial g_{jk}}{\partial \xi_m} \right]$

Subscript

∞ dimensional freestream conditions

Superscript

$*$ dimensional quantity

REFERENCES

1. Szema, K. Y. and Lewis, C. H.: "Three-Dimensional Hypersonic Laminar, Transitional and/or Turbulent Shock Layer Flow." AIAA Paper No. 80-1457, July 1980.

2. Murray, A. L. and Lewis, C. H.: "Hypersonic Three-Dimensional Viscous Shock-Layer Flow over Blunt Bodies," AIAA J., Vol. 16, No. 12, pp. 1279-1286, December 1978.

3. Helliwell, W. S., Dickinson, R. P. and Lubard, S. C.: "Viscous Flow over Arbitrary Geometries at High Angle of Attack." AIAA Paper No. 80-0064, January 1980.

4. Thareja, R. R., Szema, K. Y. and Lewis, C. H.: "Three-Dimensional Viscous Shock-Layer Analysis of Laminar and/or Turbulent Flows in Chemical Equilibrium," 12th Navy Symposium on Aeroballistics, DTNSRDC, Maryland, May 1981.

5. Rakich, J. V.: "A Method of Characteristics for Steady 3-D Supersonic
    Flow with Application to Inclined Bodies of Revolution." NASA TN D-5341,
    October 1969.

6. Blottner, F. G. and Ellis, M.: "Three-Dimensional Incompressible Boundary
    Layer on Blunt Bodies." Sandia Laboratories, SLA-73-0366, April 1973.

7. Davis, R. T.: "Numerical Solution of the Hypersonic Viscous Shock Layer
    Equations." AIAA J., Vol. 8, No. 5, pp. 843-851, May 1970.

8. Marconi, F. and Yaeger, L.: "Development of a Computer Code for Calcu-
    lating the Steady Super/Hypersonic Inviscid Flow Around Real Configura-
    tions." NASA CR-2675, April 1976.

9. Hillsamer, M. E. and Rhudy, J. P.: "Heat Transfer and Shadowgraph Tests
    of Several Elliptical Lifting Bodies at Mach 10," AEDC-TDR-64, February
    1964, AD429931.

10. Kutler, P., Pedelty, J. A. and Pulliam, T. H.: "Supersonic Flow over
    Three Dimensional Ablated Nosetips Using an Unsteady Implicit Numerical
    Procedure. AIAA Paper No. 80-0063, January 1980.

TABLE 1. Test Case Conditions

Case	1	2	3	4
Body Geometry	1:1.4 (ellipsoid)	1:2 (ellipsoid)	1:2 (modified ellipsoid)	Shuttle
T_∞ ($^\circ$R)	81.5	203.5	540.0	94.87
ρ_∞, slug/ft^3	4.118E-6	2.340E-4	7.99E-4	1.0528E-3
P_∞, psia	0.041	0.567	5.145	0.0119
T_w ($^\circ$R)	470	366	3139	540
Re_∞ (1/ft)	2.38E+6	4.993E+6	3.3058E+7	5.5696E+5
α, deg	0°	10°	0°	25°
Gas Model	perfect gas	perfect gas	equilibrium air	perfect gas
Computational Time*(Min) IBM 370/3032	6	12	16	12

*It takes approximately two hours CDC 7600 time for a sphere nose when using time dependent method of Reference 10.
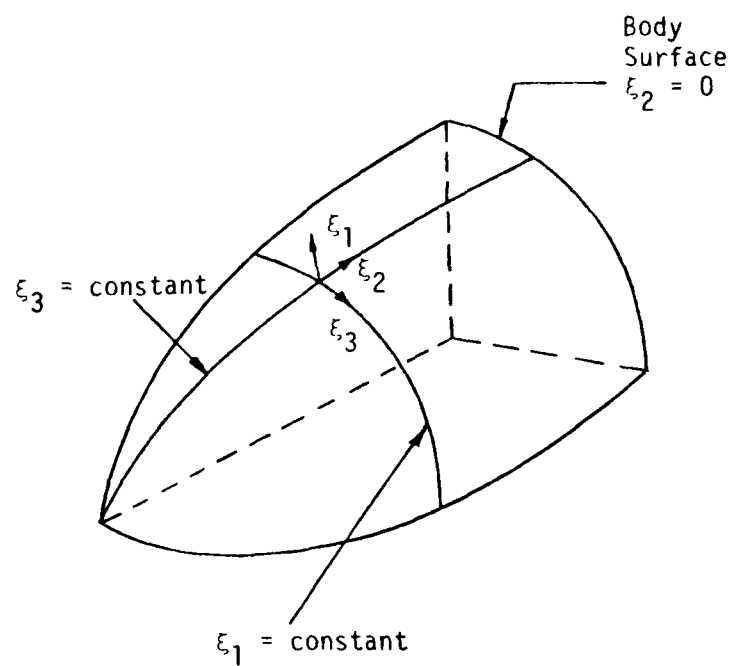
Figure 1. Coordinate System
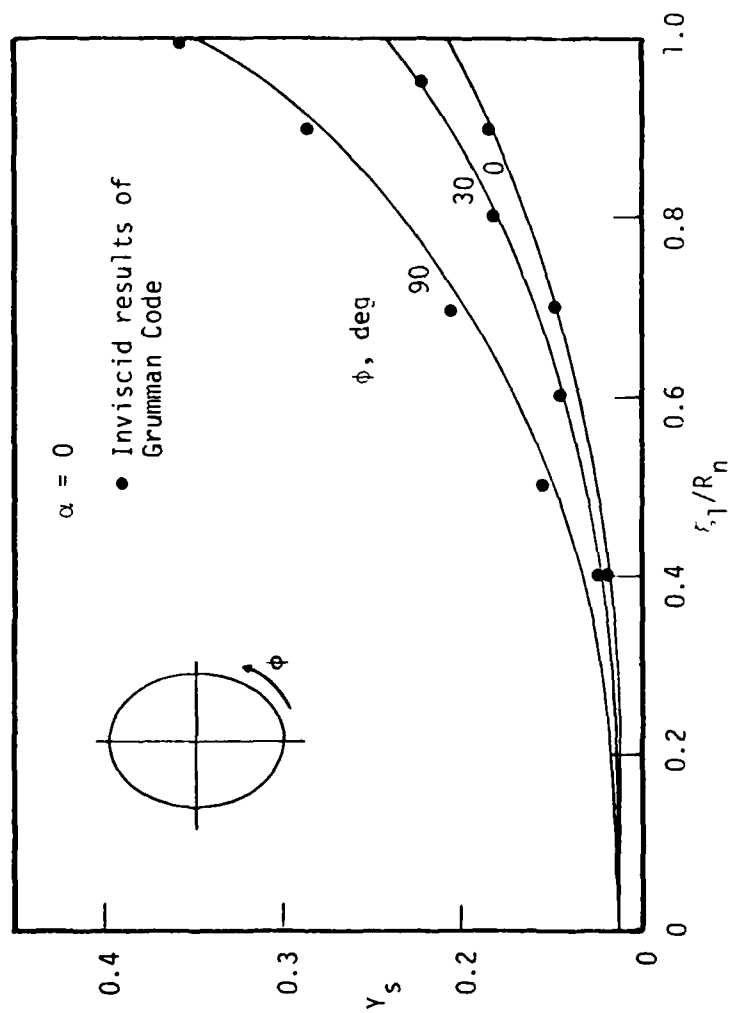
Figure 2. Shock Standoff Distance of 1:1.4 Ellipsoid
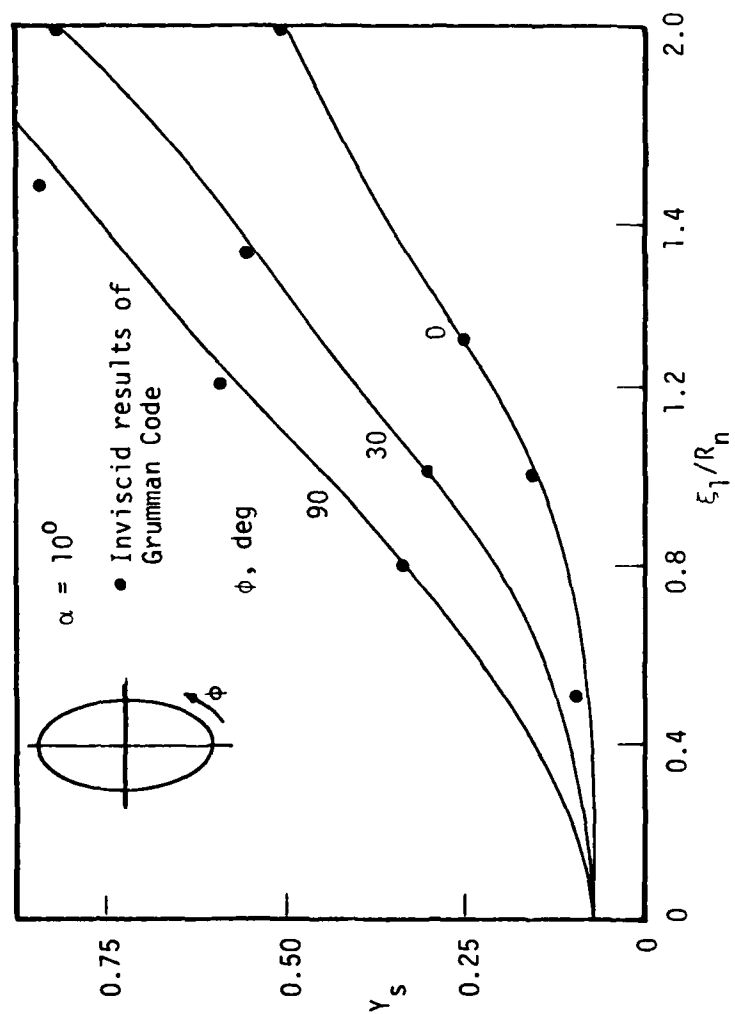
Figure 3. Shock Standoff Distance for 1:2 Ellipsoid
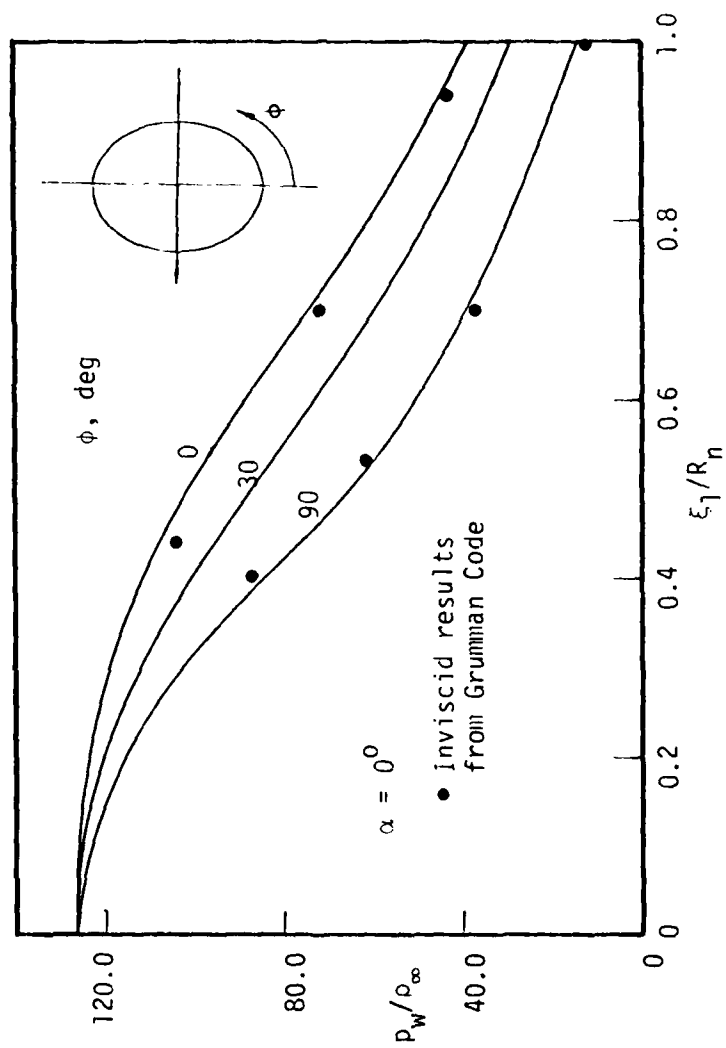
Figure 4. Surface pressure for 1:1.4 Ellipsoid
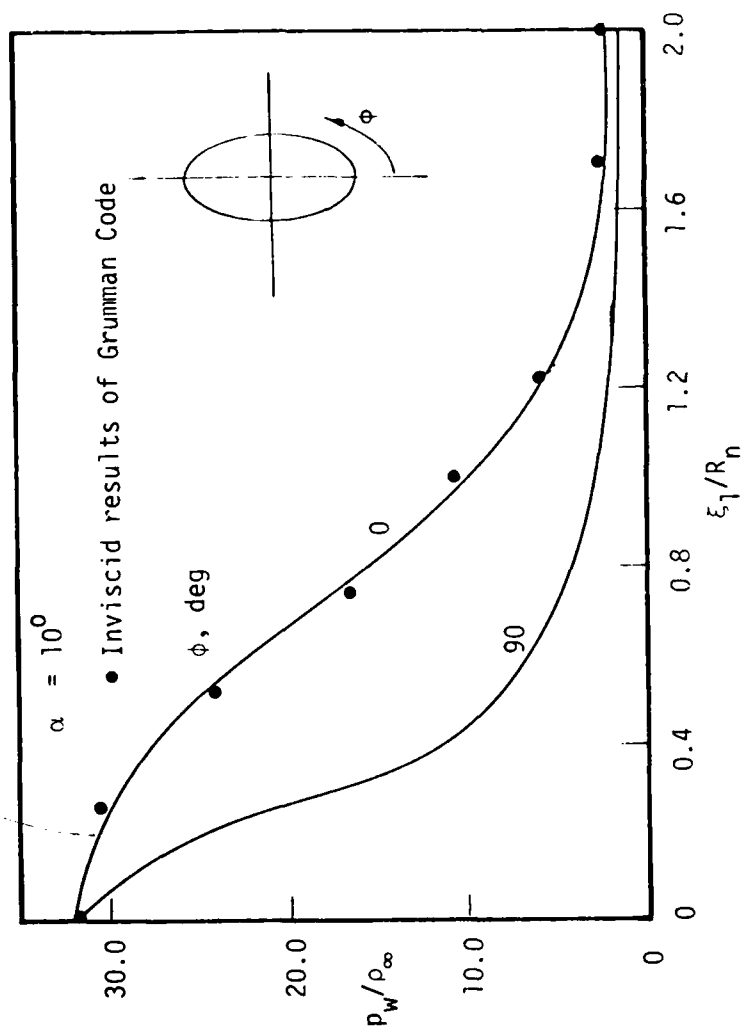
Figure 5. Surface Pressure for 1:2 Ellipsoid
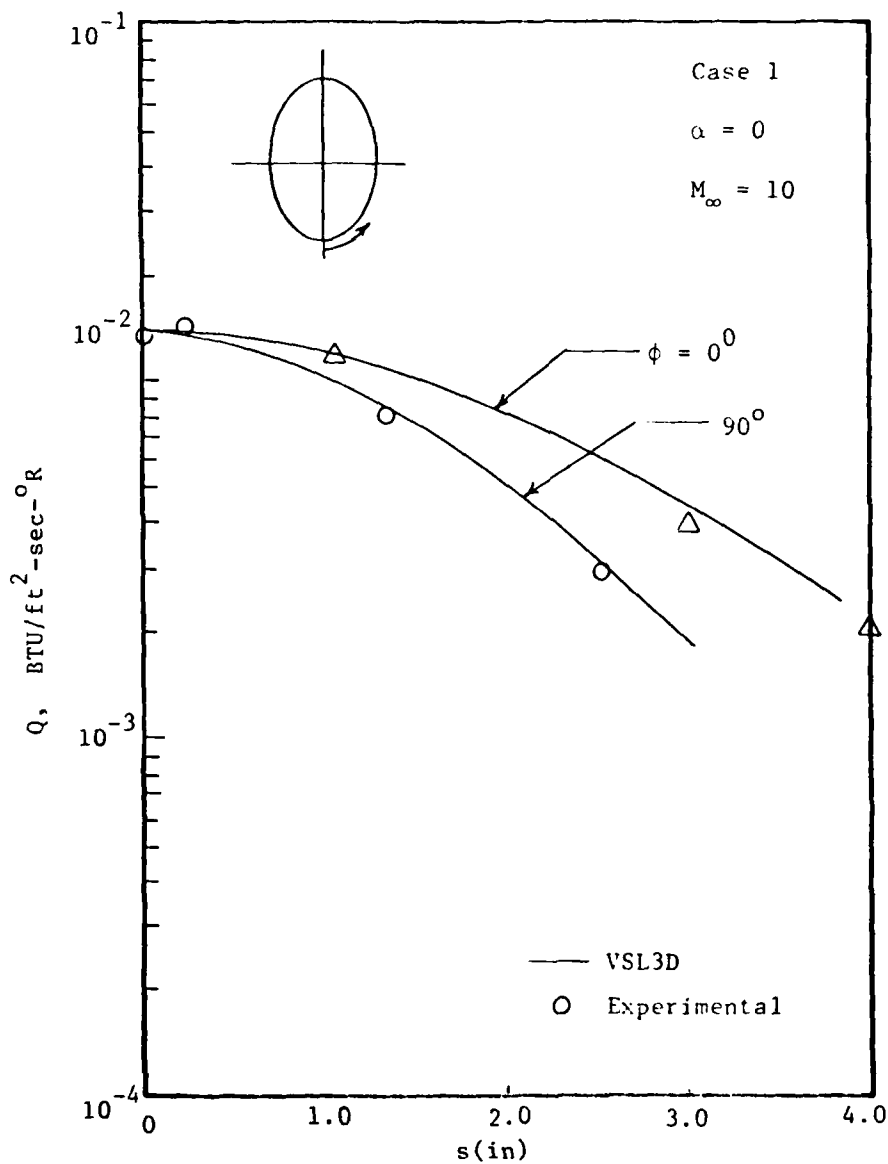
Figure 6. Convective Heat Transfer to 1:43 Ellipsoid.
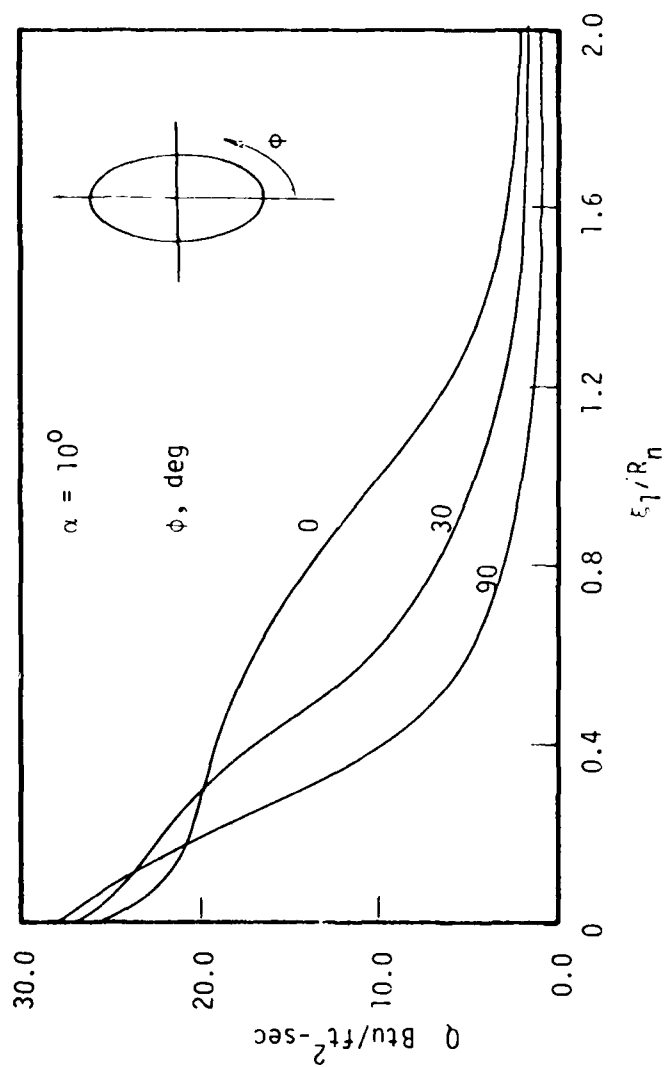
Figure 7. Convective Heat Transfer to 1:2 Ellipsoid
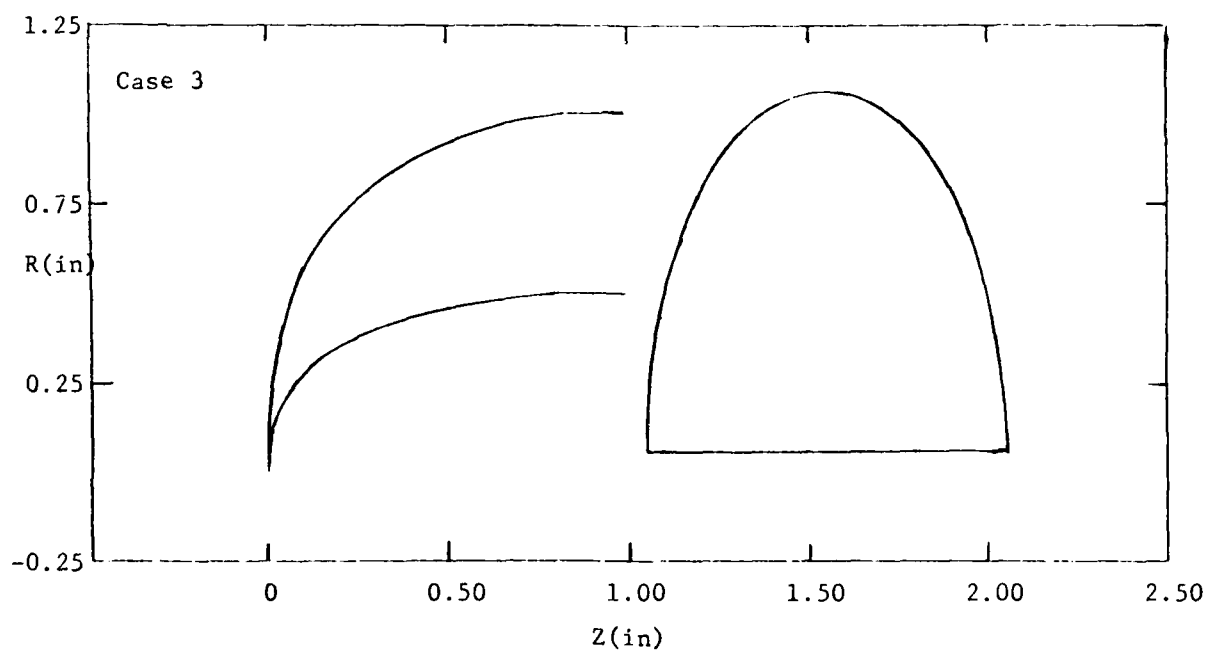
Figure 8.   The Geometry of Modified 1:2 Ellipsoid.

Case 3

Equilibrium Air

$\alpha = 0$

$M_\infty = 14$

$P_\infty = 5.145$ psia

$\triangle \odot$ inviscid results from
Grumman Code

$\phi = 0^\circ$

90°

p/p_0
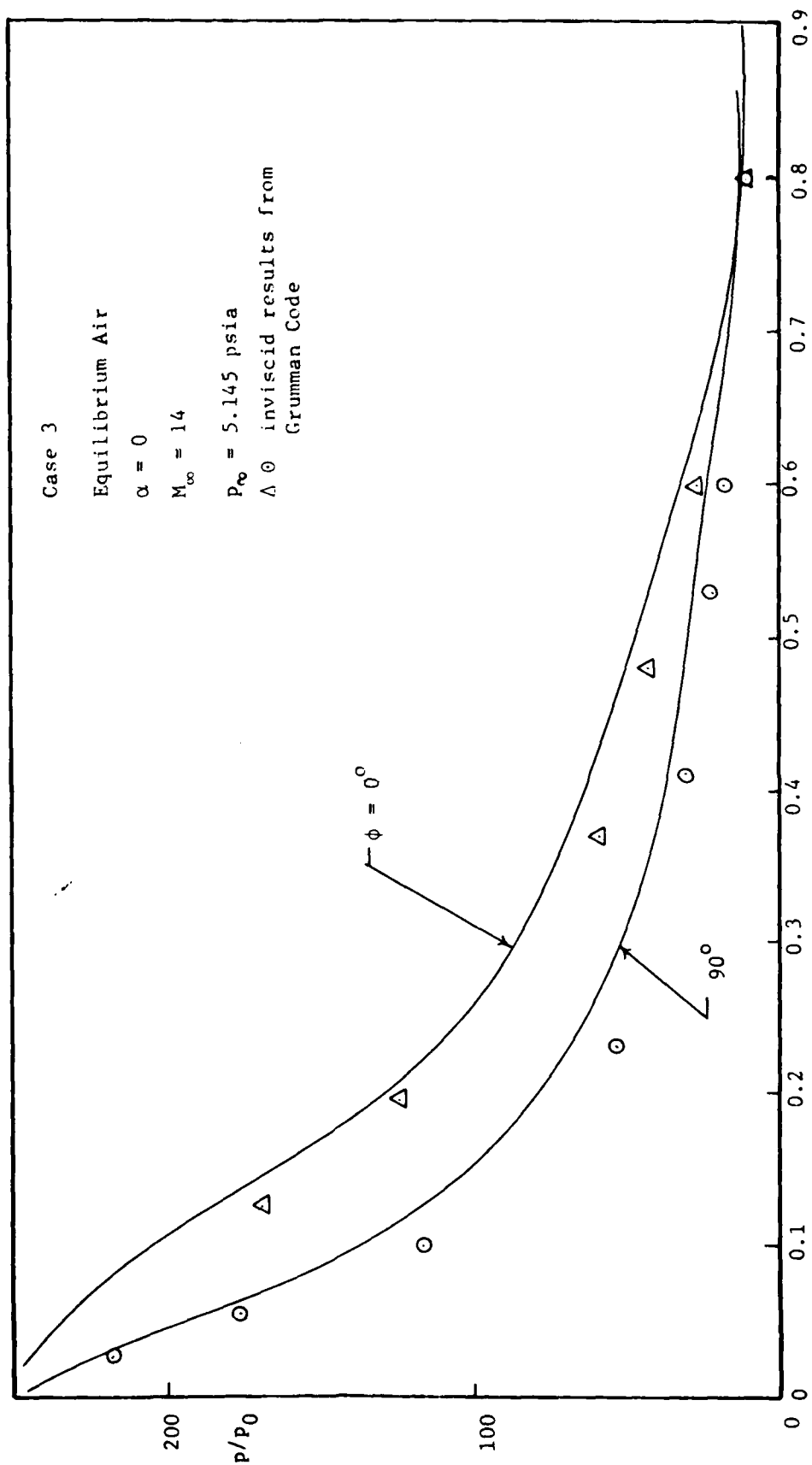
Figure 9. Surface Pressure for 1:2 Ellipsoid.

II-183
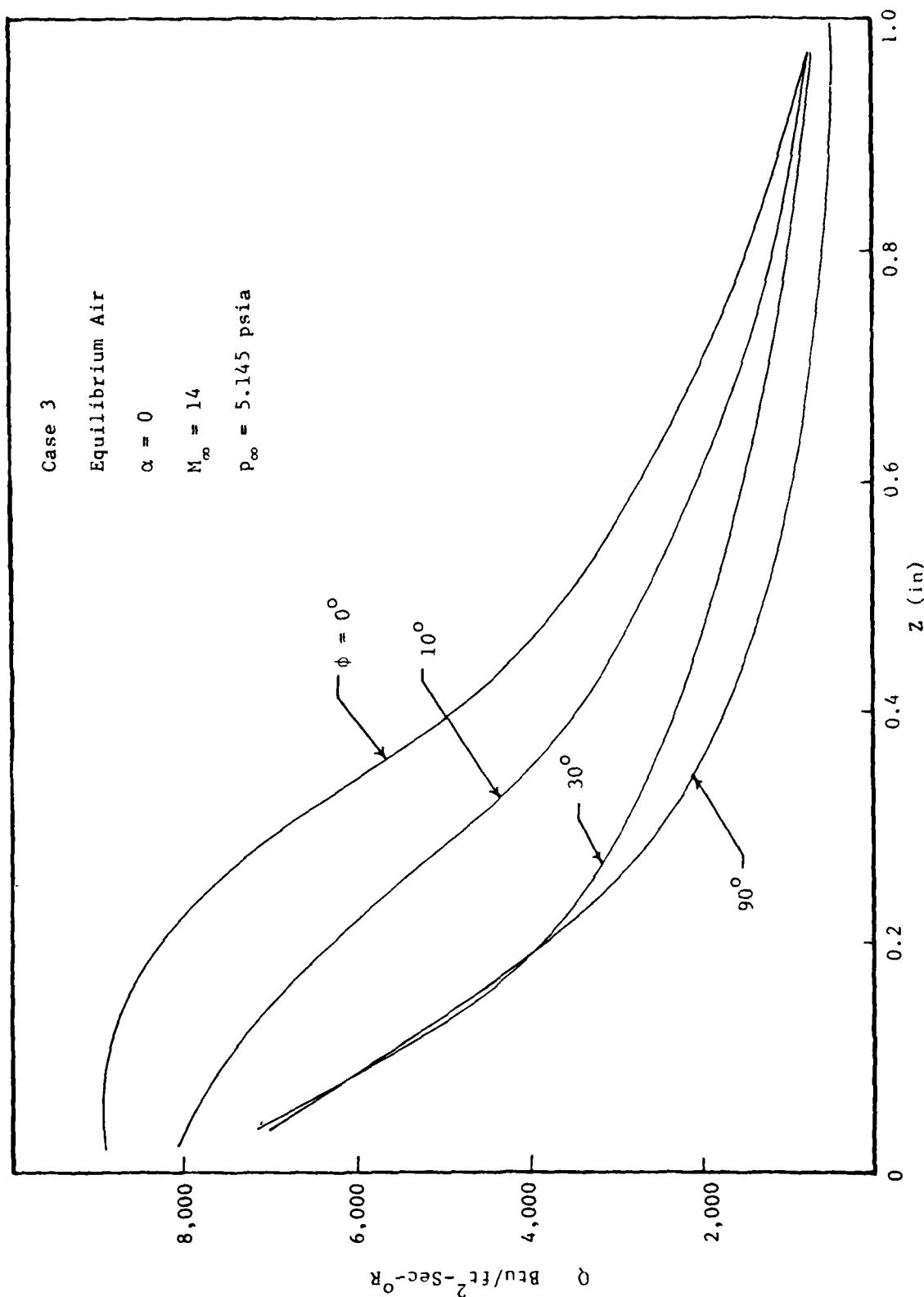
Figure 10.   Convective Heat Transfer to 1:2 Ellipsoid.
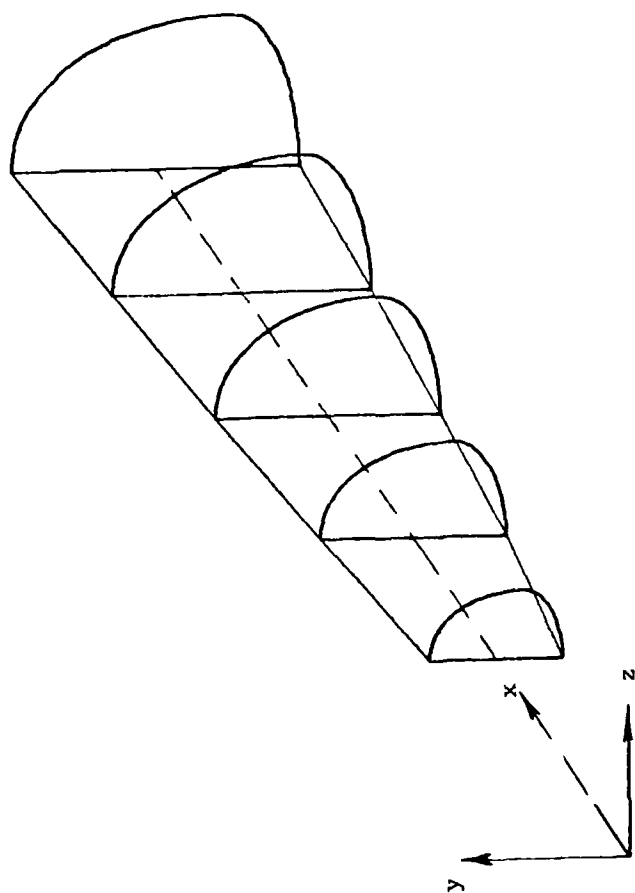
Figure 11. The Geometry of Shuttle Orbiter
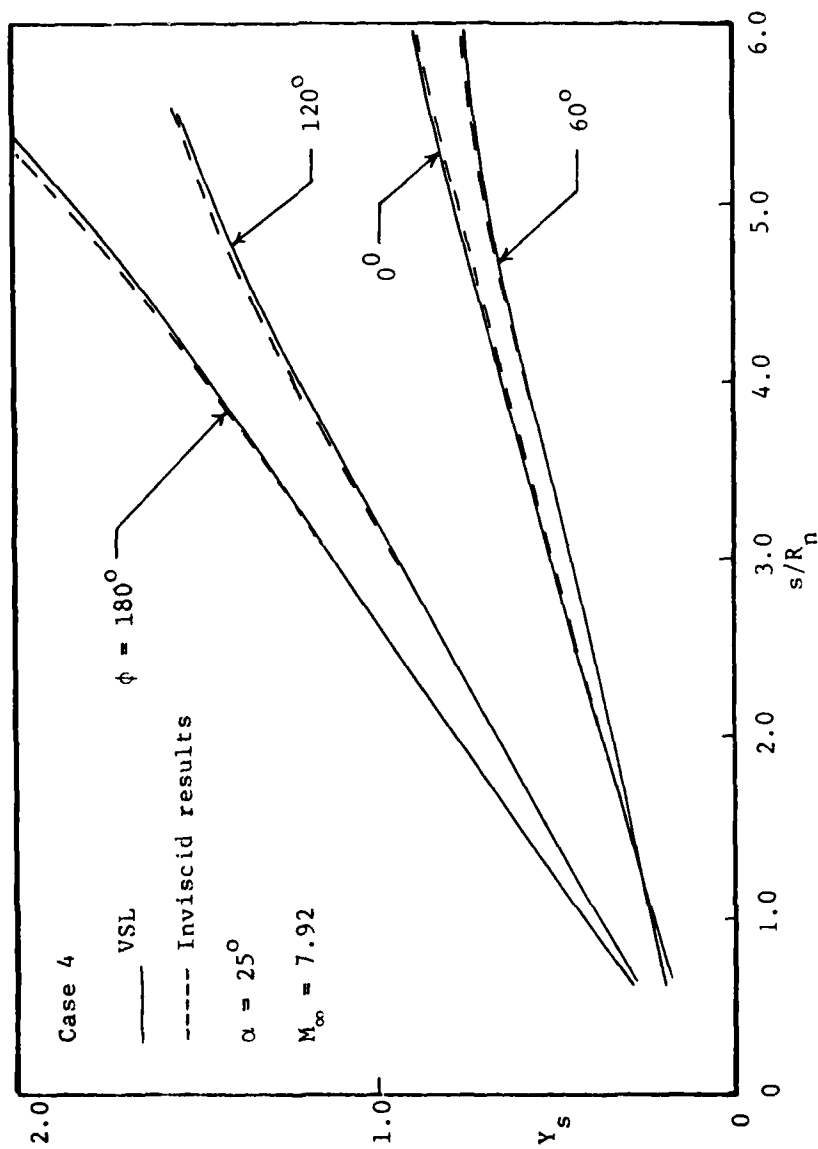
Figure 12. Shock Standoff Distance for Space Shuttle.
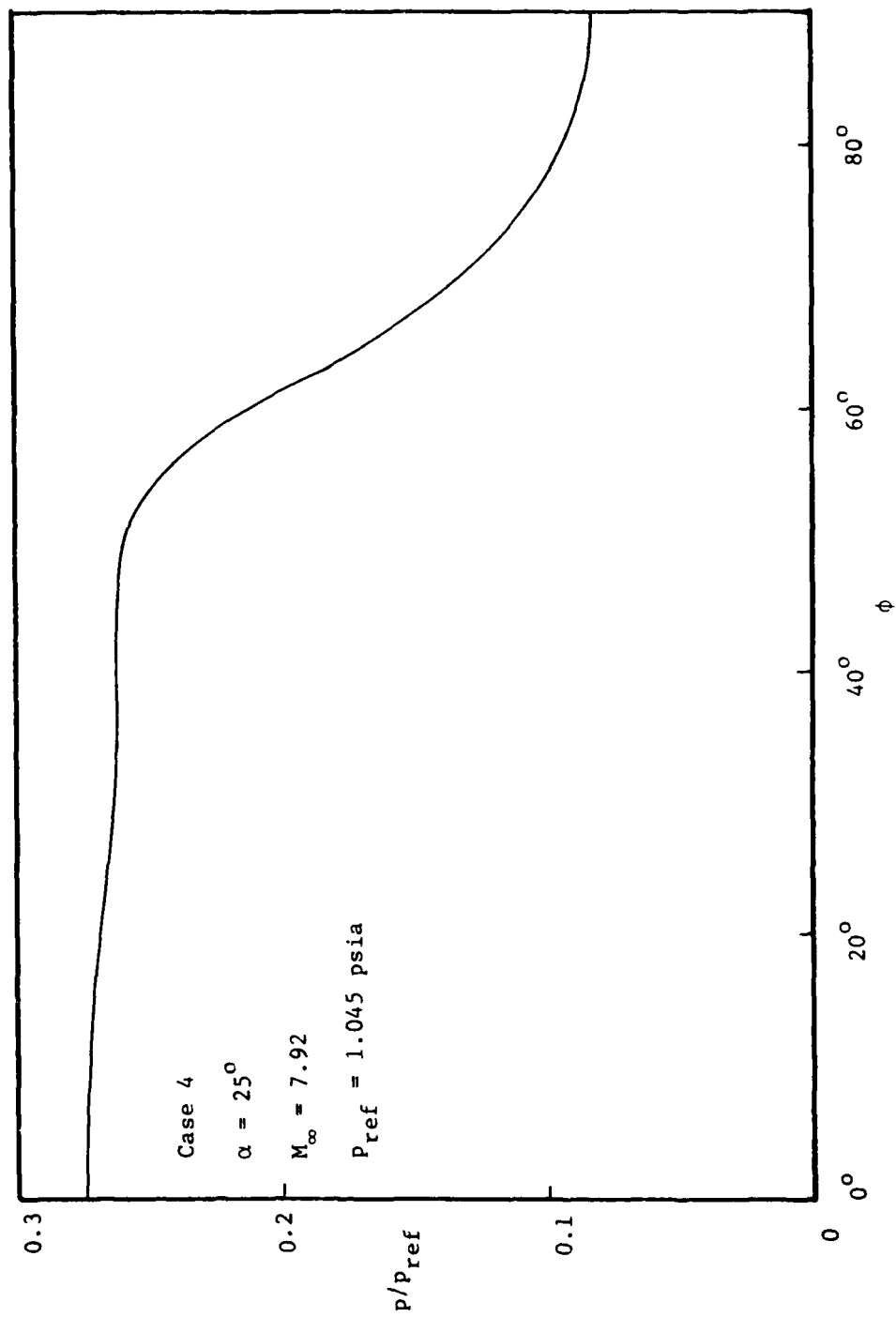
Figure 13. Space Pressure Profile for Space Shuttle at s = 5.32

Case 4

$\alpha = 25^{o}$

$M_{\infty} = 7.92$

$P_{ref} = 1.045$ psia
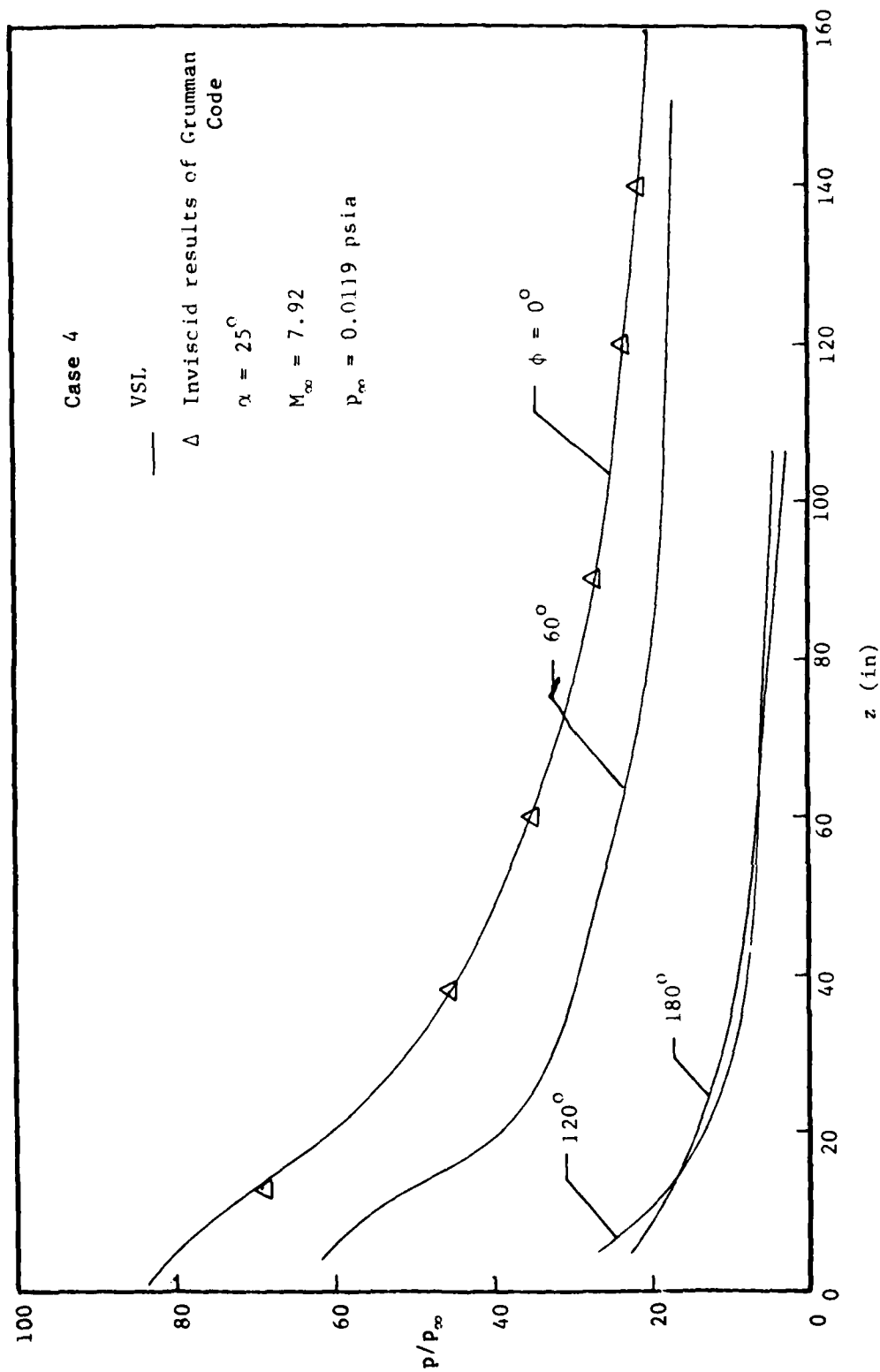
Figure 14. Space Shuttle Surface Pressure Distribution
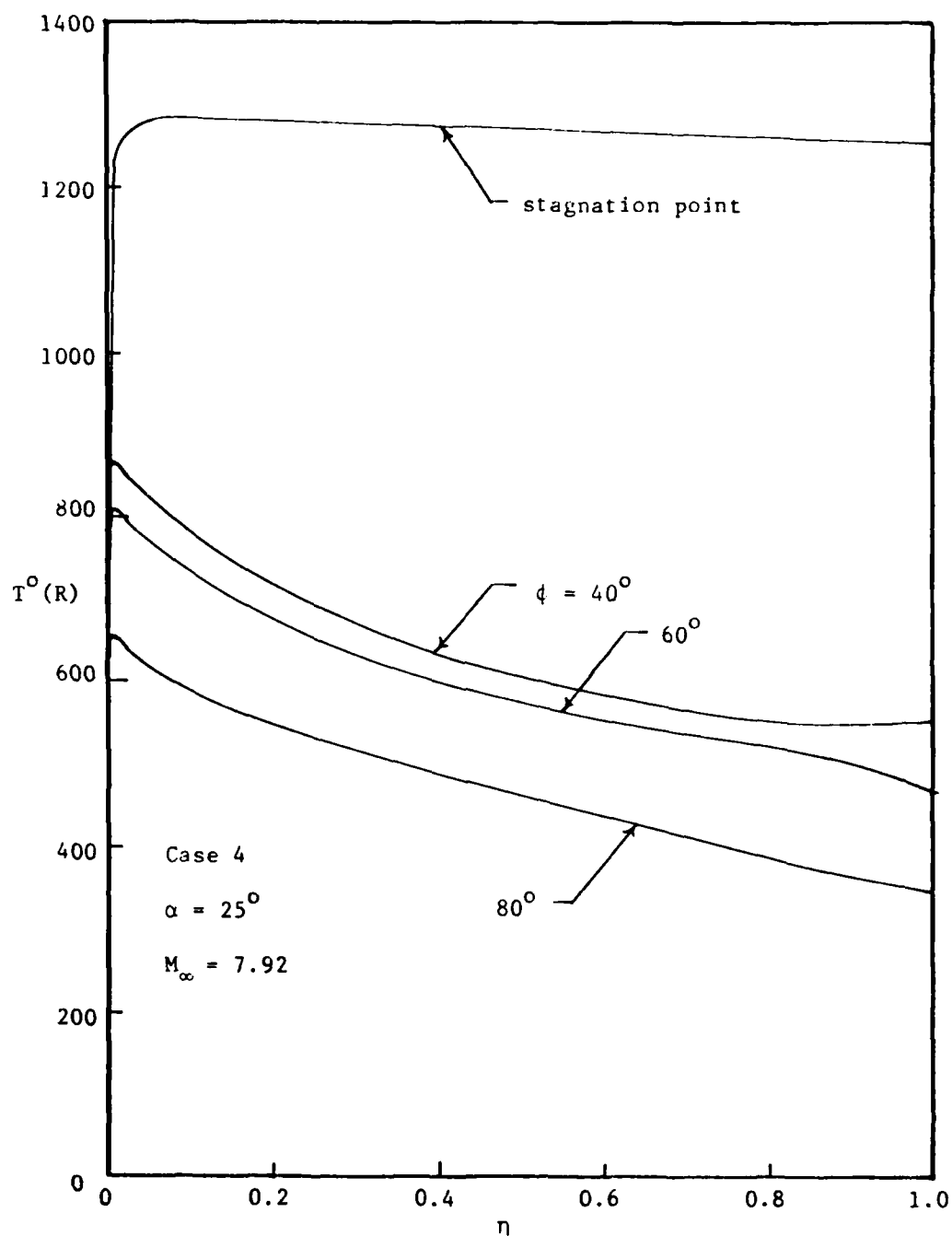
Figure 15. Space Shuttle Temperature Profile at Stagnation
Point and s = 5.32
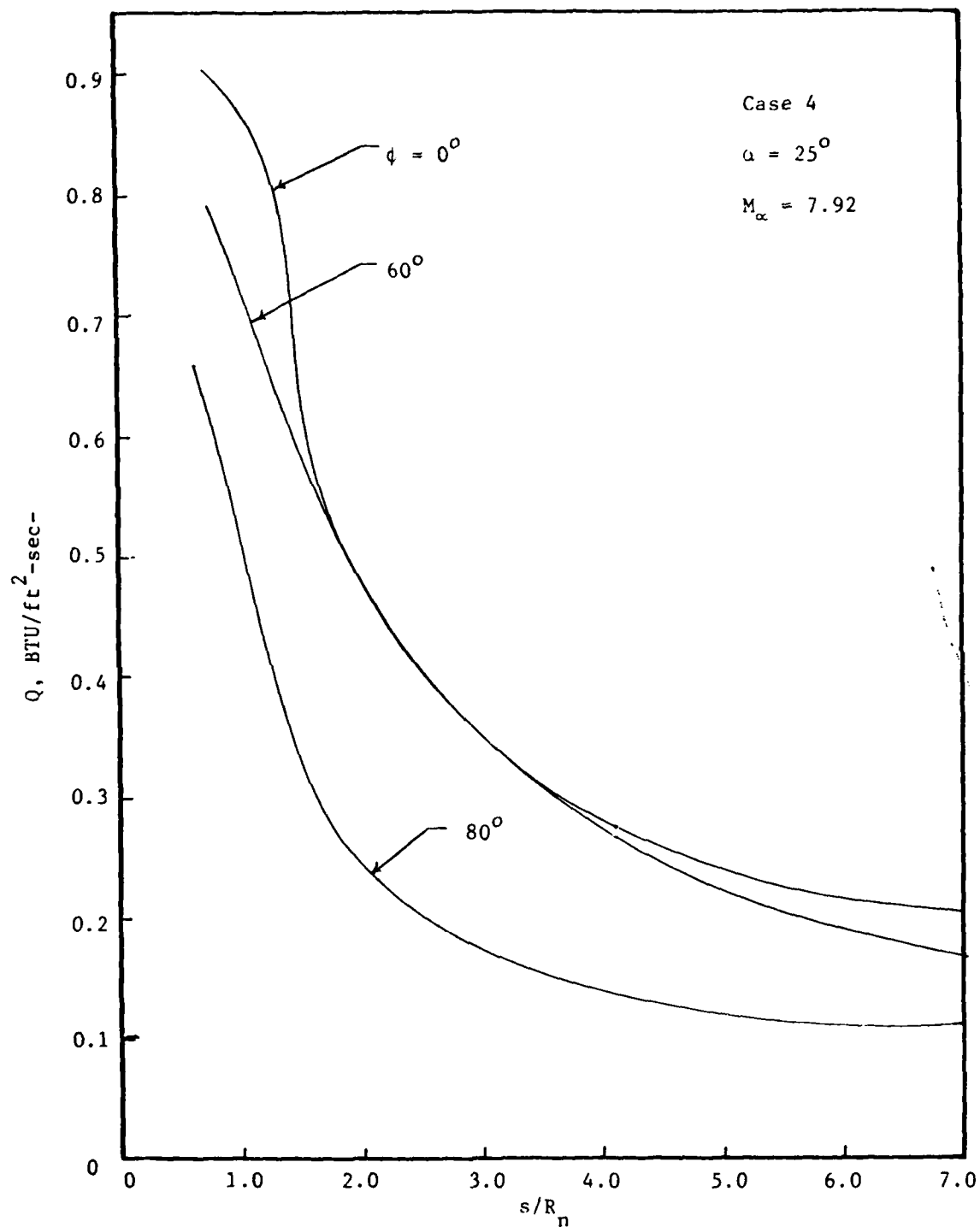
Figure 16. Convective Heat Transfer for Space Shuttle.

COMPUTATION OF HYPERSONIC LAMINAR VISCOUS FLOW OVER A BODY

WITH MASS TRANSFER AND/OR SPIN AT ANGLE OF ATTACK

M. D. KIM[*] and C. H. LEWIS[**]

Aerospace and Ocean Engineering Department

Virginia Polytechnic Institute and State University

Blacksburg, Virginia 24061

ABSTRACT

Computational results of hypersonic laminar viscous flow over blunt-nosed bodies with mass transfer and/or spin are presented. An implicit-iterative numerical scheme at each marching step is used to solve the parabolized Navier-Stokes equations. The code takes into account the mass-transfer and spin effects in the boundary condition at the body surface and the periodic effect in the boundary condition around the body. To facilitate convergence, the v-momentum equation has been used rather than the continuity equation to provide the pressure at the body boundary. The coupling effects of mass transfer and spin on the integrated forces and moments as well as the surface properties are presented and discussed.

INTRODUCTION

In recent years the analysis of hypersonic viscous flow past reentry vehicles with mass transfer and/or spin has been a problem of considerable interest in ballistics because of its relevance in slowly spinning planetary entry. Previously a numerical method (VSL3D)[1] based on a viscous shock-layer approach was applied to the computation of heat- and mass-transfer effects on three-dimensional viscous shock-layer flows by Murray and Lewis.[2] The VSL3D method was found to give accurate predictions even at very high altitude because the code takes into account wall and shock slip effects. Another numerical analysis for the mass-transfer effect using the viscous shock-layer theory was given by Whitehead and Davis.[3] The VSL3D method has a restriction on the angle of attack for the entire solution around the body. In other words, since the numerical scheme used is parabolic in the circumferential direction, it cannot treat the crossflow separated region. In the above studies, spin effects on the flowfield were not treated.

Recently a numerical approach for the hypersonic viscous flowfield solution was developed by Lubard and Helliwell[4] using the parabolized Navier-Stokes equations (PNS). The PNS method has been applied to the various

---

problems predicting hypersonic viscous flows over bodies at high angles of at-
tack. For instance, Waskiewicz and Lewis[5] applied the method to a variety
of freestream conditions and investigated the limit and applicability of the
method. They found that the PNS method could produce accurate predictions of
the flowfield during reentry up to at least 38-deg angle of attack. They also
discussed the following effects of axial pressure gradient models. For
problems involving high Mach number and Reynolds numbers, the implicit gradient
model provided unique solutions regardless of the stepsize with no noticeable
increase in the number of iterations required for convergence. Problems in-
volving large adverse streamwise pressure gradients due to high angle of at-
tack, large mass transfer, or small Mach and Reynolds numbers can cause dif-
ficulties in convergence for the implicit pressure gradient model. In such
cases an explicit or zero formulation was needed, and the accuracy of the so-
lution was dependent on the streamwise stepsize. In their work, the VPI VSL3D
code was satisfactory for the preparation of an initial plane data which was
used to start the PNS solution. In other works, Gogineni and Lewis[6] reduced
the computing times required for an entire solution by combining the VSL3D
and PNS methods and also by using a fast implicit-iterative technique known as
the Pseudo Elimination Method. The PNS method has been further developed by
Helliwell et al.[7,8] by introducing a more general body-generator coordinate
system, thus extending the applicability to more complex bodies. A stream-
line coordinate system also has been incorporated in the PNS method by Kim
and Lewis[9] in an effort to extend the capability to treat extremely high
angles of attack.

Spin effects on the hypersonic viscous flowfields past conical bodies
have been computed and analyzed by Agarwal and Rakich.[10] A PNS code has been
modified to include the periodic condition for the flow profiles in the wind-
ward plane to account for the asymmetry in the flow due to spin. They also
introduced a new criterion for defining crossflow separation behind spinning
bodies which generalizes the Moore-Rott-Sears criterion for two-dimensional
unsteady separation. The onset of separation in the flowfield is characterized
by the condition $\partial w/\partial y = 0$ at $w = 0$ where w is the circumferential component
of velocity and y the coordinate normal to the body. In their work, detail
analyses were made concerning the effects of angle of attack, freestream
Reynolds number, nose bluntness, and finally spin rate on the Magnus force
components and various flow properties. Coning motion also was considered by
Agarwal and Rakich[11] using a PNS method further modified. Another study of
the spin effects for cones or ogive-cylinder-boattailed bodies has been re-
ported by Sturek and Schiff[12] using another PNS approach. None of the fore-
going investigations considered the coupling effects of mass transfer and spin.

In the present study, computational results and discussion are presented
for the parametric effects of mass transfer and/or spin together with the
reasonable computing times consumed for each test case. The original PNS
code used the continuity equation to obtain the wall pressure at the body
boundary in the case of mass transfer. Theoretically this method appears
quite reasonable because it can provide a finite value of the wall pressure
when the normal velocity at wall does not vanish, and moreover it is a
relatively simple equation. However, by numerical experiment it has been
found that a solution is hardly obtainable by this method in the case of mass
transfer. Therefore, in the present work, the v-momentum equation is dif-
ferenced to provide the wall pressure at the body boundary. In most cases,

the flowfield solution has been obtained without convergence problems by the current method.

In the next section, the theoretical background and procedure will be presented which includes a discussion of the governing equations, coordinate system, boundary conditions, and numerical solution. A few methods to provide initial plane data are also introduced, and the effect of initial plane data for a starting solution is discussed. In the present work, the zero pressure gradient model has been used for all the test cases in order to obtain a solution in the case of high angles of attack with mass transfer and/or spin.

Two sets of freestream conditions are considered. The first case is Mach = 5, α = 2 and Re_∞/ft = 6.21 x 10^5. The second case is Mach = 18, α = 15 and Re_∞/ft = 5.45 x 10^5. For both cases, the body geometry is a spherically blunted 7-deg half-angle cone 0.817-ft long. Spin rates considered are 2000 and 8000 rev/min and mass-transfer rates 0.00125 and 0.00250. For Case 1, an asymmetric sinusoidal distribution of mass transfer around body as well as a constant distribution has been considered. For each freestream condition, computational results were obtained for four parametric cases, i.e., basic case, spin only case, mass transfer only case, and finally mass transfer and spin case. Parametric comparisons are presented to study the effect of mass transfer and/or spin on the Magnus force components as well as all the surface properties. It will be noted that a significant coupling effect on the Magnus force can result from mass transfer and spin. Reasonable computing times required for the solutions are also presented.

<center>ANALYSIS</center>

GOVERNING EQUATIONS

The governing equations are the laminar, steady parabolized Navier-Stokes equations derived by Lubard and Helliwell[4] under the assumption that the gradients of the shear stress in the streamwise direction are negligibly small compared with the gradients in the direction of normal and circumferential directions. The resulting equations are parabolic in the streamwise direction and elliptic in the crossflow direction. The governing equations include the continuity, three momentum, and energy equations. The fluid density is given by the equation of state for a perfect gas. Prandtl number and specific heat are assumed constant and Sutherland's viscosity law is used.

In addition to the usual boundary-layer order of magnitude terms, $d\phi$ is assumed to be $O(\varepsilon)$ to include the crossflow separation and the normal velocity v is taken as $O(1)$. The flow variables are nondimensionalized by their freestream values. The normal coordinate is normalized by the shock-layer thickness to facilitate the computation of the shock location. The complete set of governing equations together with the derivation procedure can be found in Reference 4.

In the development of these equations, a body-oriented coordinate system is used (Figure 1), with x taken along the body generator, y normal to the body surface, and ϕ the circumferential coordinate where ϕ = 0 represents the windward ray. The coordinate system does not rotate with the body.

<center>II-193</center>

BOUNDARY CONDITIONS

The following equations are used for the boundary conditions at the body surface with mass transfer and spin.

$u = 0$

$v = $ specified distribution (mass transfer)

$w = $ specified distribution (spin)

$h = $ specified distribution

$$\left(\frac{\partial p}{\partial y}\right)_w = -\frac{1}{r}\frac{\partial(\rho v^2 r)}{\partial y} - \frac{1}{r}\frac{\partial(\rho vw)}{\partial \phi} + \frac{\rho w^2 \cos\theta_c}{r}$$

$$+ \frac{1}{Re}\left(\frac{4}{3}\mu\frac{\partial^2 v}{\partial y^2} + \frac{\partial v}{\partial y}\frac{\partial\left(\frac{4}{3}\mu\right)}{\partial y} + \frac{\mu}{r^2}\frac{\partial^2 v}{\partial\phi^2} + \frac{1}{r^2}\frac{\partial v}{\partial\phi}\frac{\partial\mu}{\partial\phi}\right.$$

$$\left.+ \frac{1}{r}(\mu + \lambda)\frac{\partial^2 w}{\partial\phi\partial y} + \frac{1}{r}\frac{\partial\mu}{\partial\phi}\frac{\partial w}{\partial y} - \frac{1}{r\xi}(\mu + \lambda)\frac{\partial w}{\partial y}\frac{\partial\xi}{\partial\phi}\right)$$

To obtain the wall pressure for the mass-transfer and spin case, the original code utilized the continuity equation; however, the method turned out to be inefficient for the convergence of a solution by a numerical experiment. It has been found that the employment of the v-momentum equation gives a more stable solution. Thus, for the present analysis the v-momentum equation has been taken and differenced using a one-sided differencing scheme to provide the pressure at the body boundary.

In order to obtain the outer boundary conditions, Rankine-Hugoniot jump conditions are utilized at the shock. The components of freestream velocity in the body oriented coordinate system are:

$u = \cos\theta_c \cos\alpha - \sin\theta_c \sin\alpha \cos\phi$

$v = -\sin\theta_c \cos\alpha - \cos\theta_c \sin\alpha \cos\phi$

$w = \sin\phi \sin\alpha$

From the freestream components and jump conditions, five conservation equations are obtained which can be used to determine the aftershock properties. To uniquely determine the six unknowns ξ, u, v, w, p, h at the shock boundary, one more equation is required. Thus, the one-sided differencing of the continuity equation provides the sixth equation.

Since the windward and leeward surfaces are not symmetry planes for the spinning cone, a periodic condition for the flow profiles in the windward plane is specified, thus providing the boundary conditions in the ϕ-coordinate direction.

In a rectangular y-ϕ grid, the shock may not fall on a mesh point. To resolve this difficulty, a coordinate transformation, $\eta = y/\xi$ (x,ϕ) is made, where $\xi(x,\phi)$ is local shock-layer thickness. Due to the coordinate transformation, the shock-layer thickness ξ appears in all the governing equations, thus requiring one more governing equation, $\partial\xi/\partial y = 0$ to be differenced.

INITIAL CONDITIONS

For a numerical flowfield solution which utilizes a marching scheme, preparation of an accurate initial data plane (IDP) is one of the most crucial conditions for a successful start of solution. By previous investigations[5,6] the viscous shock-layer method (VSL3D)[1] for blunt bodies was found to be able to generate a satisfactory initial data plane to start the PNS solution. Thus, the entire flow properties including the shock shape must be supplied at an initial data plane to get the PNS code started.

Three different methods have been used to generate an initial data plane. The first method is to construct a one-step IDP using the VSL3D method at the sphere-cone juncture. In most cases, the one-step IDP constructed by the VSL3D code was satisfactory to start the PNS solution. The one-step IDP is obtained by an axisymmetric VSL solution and necessary rotations of the solution. In this case, a few initial marching stepsizes should be small to start a solution.

The second method is to prepare a two-step IDP using VSL3D code at any desired axial station of the body. This method is better than the first one for the convergence of the starting solutions, and hence the initial marching step-sizes can be taken larger. The third method is to prepare a two-step IDP using LUB2 code which is another PNS code developed by Agopian et al.[7] for more general bodies. In this method, an axisymmetric VSL solution provides an IDP at the blunt nose for the LUB2 solution, and then the LUB2 code again prepares an IDP at a desired axial station by the necessary three-dimensional calculations. This method is somewhat tedious but can produce an accurate IDP even when the angle of attack is over 30 degrees. In the preparation of IDP for the test cases, the spherical nose tips of the bodies were considered to have neither spin nor mass transfer.

NUMERICAL SOLUTION

The equations are solved by implicit differencing in the y, ϕ-plane. The x derivatives are approximated by a backward difference while y and ϕ derivatives use an unequally spaced three-point difference formula, e.g.,

$$\frac{\partial f}{\partial x} = \frac{f_j - f_{j-1}}{\Delta x}$$

and

$$\frac{\partial f}{\partial y} = \alpha_{k-1} f_{k-1} + \alpha_k f_k + \alpha_{k+1} f_{k+1}$$

where the α_i are determined from the Taylor series expansions of f_{k-1} and f_{k+1} around the k-th location, and hence they are functions of the stepsize between the grid points.

The PNS equations and the perturbation equations during the iterations can be written in the matrix form

$$\underline{F}(\underline{U}) = 0$$

$$\underline{\Delta}^n = \underline{U}^{n+1} - \underline{U}^n$$

where $\underline{F}$ denotes the governing equations for the unknowns $\underline{U}$, and $\underline{\Delta}^n$ is the column matrix of perturbation properties at n-th iteration.

After differencing, the equations are linearized by the Newton-Raphson method. Thus, all the nonlinear terms of perturbation properties are dropped. This results in an equation of the form

$$\underline{\underline{M}} (\underline{U}^n) \underline{\Delta}^n = - \underline{F}(\underline{U}^n) \quad ; \qquad n = 0, 1, 2, \ldots$$

with $\underline{U}^0$ an initial guess to the solution of the governing equations, and $\underline{\underline{M}}$ the Jacobian of $\underline{F}$. Because of the size of the system, instead of solving the above equation directly, the Gauss-Seidel iteration method is used. In the ϕ-direction, an implicit-iterative scheme[8] is used, but after convergence, the solution obtained is a fully implicit one. After convergence, another step in the marching direction is taken and the whole procedure is repeated.

Convergence problems often occur when the marching solution encounters a strongly separated region due to crossflow. To reduce the problem, either zero or explicit pressure gradient model may be used. Smaller marching stepsizes and/or pressure smoothing in the y coordinate direction also can help the convergence. When the angle of attack is very high, more careful selection of grid sizes and preparation of more accurate initial plane data are required in order to start a solution.

Mass transfer and spin add more disturbances in the viscous flowfield, thus deteriorating the convergence of the solution. A large mass-transfer distribution along the body can cause an axial flow separation at some downstream station which causes the marching solution to fail. To reduce the marching stepsize problem in a solution, the marching stepsizes are controlled internally by the code considering the number of iterations taken for the solution at the previous step.

RESULTS AND DISCUSSION

For the present study, a body-generator coordinate system is used with x along the body, y normal to the body and ϕ around the body, and it does not rotate with the body. Figure 1 shows the coordinate system and the sign conventions for aerodynamic coefficients. Since this sign convention is not a universal one, it is recommended to be used only for the interpretation of the directions of the forces and moments reported in this paper.

The initial plane data for the test cases have been obtained using a perfect gas viscous shock-layer approach (VSL) at the sphere-cone tangency point, and all the flow properties together with forces and moments are transferred to the PNS solution. To start the PNS solution, an initial marching stepsize of less than one-tenth of the nose radius has been used, and it was increased internally in the code, considering the number of iterations taken and the maximum permissible marching stepsize for a meaningful solution. In the present calculations, 101 grid-points in the normal direction and 19 planes around the body are used for all cases.

The original PNS code utilized the continuity equation in order to predict the wall pressure at the body boundary when the body had mass transfer. However, by numerical experiment, it has been found that the method is likely to give an unstable and divergent solution even in the case of very small mass transfer. Therefore, in the present work the v-momentum equation is taken and differenced at the body boundary. By this method, stable solutions have been obtained in most cases with moderate mass transfer. A large mass transfer at the wall can cause an axial flow separation at some downstream station. In such a case, it should be noted that the PNS method cannot treat the primary flow separated region.

In the case of high angle of attack with large mass transfer and spin, a relatively large amount of perturbations can occur in the viscous flowfield. These perturbations have an adverse effect on the convergence of a solution. For this reason, in the present computations, the zero pressure gradient model in the marching direction was used to improve the convergence. The effect of the three different kinds of axial pressure gradient models has been discussed in detail by Waskiewicz and Lewis.[7]

To investigate the effect of mass transfer and/or spin on the viscous flow past a sphere-cone geometry, two sets of freestream conditions have been chosen and parametric computations have been made. Case 1 considers a freestream condition of $M = 5$, $\alpha = 2$ and $Re_\infty/ft = 6.21 \times 10^5$. Case 2 considers a freestream condition of $M = 18$, $\alpha = 15$ and $Re_\infty/ft = 5.45 \times 10^5$. The body geometry is a spherically blunted 7-deg half-angle cone 0.817 ft long. For both cases, a parametric comparison is presented to study the effect of spin, the effect of mass transfer, and the coupling effect of mass transfer and spin. For Case 1, the effect of the asymmetric mass-transfer distribution around the body as well as constant mass-transfer distribution will be analyzed in detail. Spin rates considered are 2000 and 8000 rev/min. Case 1a has a sinusoidal mass-transfer distribution around the body, and the maximum value of mass-transfer rate is 0.0025. Case 1b and Case 2 have a mass transfer rate of 0.00125, which is constant along and around the body. Details of the freestream conditions are given in Table 1.

For Case 1, the flowfield solution over the body with mass transfer could not be obtained up to the body end. For Case 1a with mass transfer only, the solution was obtained up to $s = 24.8$ where axial flow separation occurred due to the mass-transfer effect. For Case 1a with both mass transfer and spin, the solution was obtained up to $s = 23.3$ before axial flow separation occurred. The effect of mass transfer on axial flow separation will be further discussed later.

Figure 2 shows a sinusoidal distribution of mass transfer for Case 1a, which is designed to exert a relatively large side force in the minus direction. In Figure 3, the Magnus force due to the sinusoidal mass-transfer distribution is shown, and also it can be observed that the coupling effect of mass transfer and spin on the Magnus force is remarkable. Figure 4 shows the Magnus force components distribution along the body for Case 1a, where it is noted that the Magnus force component due to the wall pressure distribution constitutes the largest part of the total Magnus force, while the components due to the axial and the circumferential shear stresses are negligible.

For Case 1b, we have constant mass transfer around the body. Hence in this case, the Magnus force due to mass transfer should be negligible. In Figure 5, it is noted that the Magnus force due to the coupling effect of the mass transfer and spin is substantial, and the effect is over three times as much as the spin-only effect on the Magnus force. The Magnus force component due to the wall pressure prevails over the others due to the wall shear stresses for this case as shown in Figure 6.

Figure 7 shows the effect of mass transfer and spin on the Magnus force for Case 2 which has relatively large Mach number and high angle of attack. For this case, it is noted that the coupling effect of mass transfer and spin is again remarkable. Therefore, on the basis of the present computational results, it is concluded that this coupling effect should not be neglected in a flight dynamics analysis of slow-spin reentry vehicle with mass transfer. Figure 8 shows that the Magnus force component due to the crossflow shear stress is not negligible, and it has a different direction from the F_{p_w} for the Case 2.

The effect of mass transfer and spin on the wall pressure is shown in Figure 9, where the spin effect was almost negligible. Hence, the differences shown are largely due to mass transfer. It is noted that the mass-transfer effect increases the wall pressure because the thickening of the viscous layer increases the displacement-induced pressure interaction. In this figure, an unstable solution due to axial flow separation can be seen at $s = 24$ and $\phi = 180$ deg.

Figure 10 shows the effect of asymmetric mass transfer and spin on the wall pressure at $s = 23$. In fact, the pressure difference between the two cases is due mostly to the mass-transfer effect. Since Case 1a has maximum mass transfer in the $\phi = 270$-deg plane of the body, the pressure difference is larger on this plane of the body, as can be seen in the figure. Figure 11 shows the effect of mass transfer and spin on the shock-layer thickness which slightly increases the shock-layer thickness. Figure 12 shows the effect of mass transfer and spin on the shock-layer thickness around the body at $s = 23$ where the slight increase in the shock-layer thickness is due mostly to the mass transfer effect, not the spin effect.

The effect of mass transfer and spin on the surface heat transfer along the body is shown in Figure 13. Mass-transfer effect decreases the wall heat transfer, and the effect is more sizable on the windward side. Figure 14 shows the effect of asymmetric mass transfer and spin on the heat transfer at $s = 23$ for Case 1a. The big asymmetric difference between the two cases is largely due to the mass-transfer effect. Figures 15 and 16 show the effects

of mass transfer and spin on the streamwise wall shear, and the effects are quite similar to the effects on the heat transfer. Figure 17 shows the effects of asymmetric mass transfer and spin on the crossflow wall shear at s = 23. The effect is to decrease the shear stress in absolute value on both sides of the body. As previously mentioned, for Case 1 the spin effects on wall pressure, shock-layer thickness, heat transfer, and wall shear were very small compared to the mass-transfer effects. However, for Case 2 which has a larger spin rate than Case 1, the spin effect was not negligible, which will be shown later.

Figure 18 shows the effect of mass transfer on axial flow separation for Case 1a. In the figure it can be observed that the mass transfer retards the axial flow velocity in the boundary layer. The effect becomes larger further downstream, and finally the axial flow separates at s = 24 as can be seen in the figure. The PNS method cannot treat the axial-flow separated region, hence the solution diverged at this station. In the downstream region before axial flow separation, the numerical solution took a relatively large number of iterations and small marching stepsizes. This effect resulted in the relatively large computing time for this case as can be seen in Table 3.

Case 2 had a spin rate of 8000 rpm and constant mass-transfer rate of 0.00125. The computational results for this case showed more sizable effects of spin on the wall pressure and other surface properties. Hence, parametric comparisons will be presented for this case. Figures 19 and 20 show the wall pressure in case of mass transfer and spin. Acutally it was hard to distinguish each effect separately in this kind of figure. Hence, it was desirable to compare the ratios of each pressure to its basic value. Here, the basic value means the computed wall pressure for the body with neither mass transfer nor spin. Thus, Figure 21 shows the coupling effect as well as the separate effects of mass transfer and/or spin on the wall pressure. In this figure, the spin effect appears antisymmetric, while the mass-transfer effect is symmetric around the body. The coupling effect is quite clear, and it has nearly additive characteristic. The spin effect decreases the surface pressure in ϕ = 0 - 180-deg of the body, and increases the pressure in ϕ = 180 - 360-deg of the body, thus producing a negative Magnus force as can be expected. The symmetric mass transfer itself cannot produce a Magnus force, but it increases the wall pressure symmetrically. From Figures 20 and 21 it is observed that at station s = 30.06 a strongly separated flow is developed in the crossflow direction. For this case at α = 15-deg, the crossflow separation begins as early as s = 6, as can be seen in Figures 32 and 33.

Figures 22 and 23 show the shock-layer thicknesses along and around the body respectively where the effects of mass transfer and spin on the shock-layer thickness appear negligible. Figure 24 shows the effect of mass transfer and spin on the heat transfer in the windward and leeward planes. A parametric comparison of the effect of mass transfer and/or spin on the heat transfer around the body at s = 30.06 is presented in Figure 26, and it can be interpreted on the basis of the data given in Figure 25. The spin effect on the heat transfer around the body turns out quite complex due to the crossflow separation as shown in Figure 26. The mass-transfer effect is symmetric and decreases the wall heat transfer. The coupling effect is approximately additive of both effects. Figures 27 - 29 show the effects of mass transfer and/or spin on the streamwise wall shear, and the effects have similar trends to the effects on the heat transfer.

Figures 30 and 31 show the effects of mass transfer and/or spin on the crossflow wall shear around the body at s = 30.06. The effects frequently change their directions due to crossflow separation. The coupling effect is again additive of both effects. Since the current PNS method is elliptic in the crossflow direction, it can solve the crossflow separated region. But the crossflow separation produces more perturbations in the flowfield, and the perturbations have an adverse effect on the convergence of a solution. Therefore, generally smaller marching stepsizes are required to pass through the region where the crossflow separation begins. Mass transfer causes crossflow separation at an earlier station on the body while spin suppresses the crossflow separation. A definition of crossflow separation in the case of spinning body has been introduced by Agarwal and Rakich.[10] The criterion generalizes the Moore-Rott-Sears criterion for two-dimensional unsteady separation. The onset of separation in the flowfield is characterized by the condition $\partial w/\partial y = 0$ at $w = 0$ where w is the circumferential component of velocity and y is the coordinate normal to the body.

Figure 32 shows the effect of spin on crossflow separation at s = 6.4 and ϕ = 160-deg for Case 2. The basic case already has the separated crossflow profile at this station. But for the spin case, the profile is not separated yet at this station due to the definition introduced above. Figure 33 shows the effect of mass transfer on crossflow separation. It is observed that mass transfer causes crossflow separation at an earlier station on the body. As previously mentioned, mass transfer can cause axial flow separation also. In a numerical experiment, mass transfer of a few percent of $\rho_\infty U_\infty$ was found to easily cause an axial flow separation within a few nose radii downstream. In the case of low mass transfer as in Case 1a, the axial flow was separated at s = 24.

Table 2 summarizes all the force and moment coefficients obtained from the parametric computations for the two test cases. The effect of the spin on the axial and normal forces is found to be negligible while the effect on the Magnus side force is sizable. An asymmetric mass transfer also can produce a finite amount of side force. From the table, it is also observed that the mass transfer decreases the normal and axial forces. An important fact found in the present work is that mass transfer and spin have a measurable coupling effect on the Magnus side force, which is shown in Table 2 as well as in the figures. However, no experimental data are known to the authors at this time to validate the present results for the coupling effects.

Computing times for these cases are given in Table 3. These times were obtained on the IBM 3032 system at Virginia Polytechnic Institute and State University. Most cases consumed less than 40 minutes of CPU time for the entire solution, but the solutions for Case 1a and 1b with mass transfer took relatively longer computing times because of the small stepsizes taken before axial flow separation.

SUMMARY

The viscous flowfield over a sphere-cone undergoing mass transfer and/or spin at angle of attack has been calculated using the parabolized Navier-Stokes equations. In the mass-transfer case, the wall pressure is obtained using the v-momentum equation rather than continuity equation to facilitate

the convergence. The main results of the present work can be summarized as follows:

1. The coupling effect of mass transfer and spin on the Magnus force is remarkable, i.e., it is much more than the additive effect.

2. Mass transfer has a tendency to reduce the axial and normal forces, and it increases the wall pressure and decreases the heat transfer and wall shear stresses.

3. Mass transfer causes earlier axial and crossflow separations.

4. Spinning motion has negligibly small effect on the normal and axial forces, and it produces asymmetric effects on the wall pressure as well as the other surface properties around the body.

5. Spin has a tendency to suppress the appearance of crossflow separation at high angles of attack.

REFERENCES

1. Murray, A. L. and Lewis, C. H.: "Hypersonic Three-Dimensional Viscous Shock-Layer Flows over Blunt Bodies," AIAA J., Vol. 16, No. 12, December 1978, pp. 1279-1286.

2. Murray, A. L. and Lewis, C. H.: "Heat and Mass-Transfer Effects on Three-Dimensional Viscous Shock-Layer Flows," AIAA Paper 78-844, May 1978.

3. Whitehead, R. E. and Davis, R. T.: "Numerical Solutions to the Viscous Shock-Layer Blunt Body Problem with Inert Gas Injection," Sandia Laboratories, SC-CR-70-6162, January 1971.

4. Lubard, S. C. and Helliwell, W. S.: "Calculation of the Flow on a Cone at High Angle of Attack," AIAA J., Vol. 12, No. 7, July 1974, pp. 965-974.

5. Waskiewicz, J. D. and Lewis, C. H.: "Hypersonic Viscous Flows over Sphere-Cones at High Angles of Attack," AIAA Paper 78-64, AIAA 16th Aerospace Sciences Meeting, Huntsville, AL, January 1978.

6. Gogineni, P. R. and Lewis, C. H.: "Three-Dimensional Viscous Hypersonic Flows over General Bodies," AIAA Paper 80-0029, AIAA 18th Aerospace Sciences Meeting, Pasadena, CA, January 1980.

7. Agopian, K., Collins, J., Helliwell, W. S., Lubard, S.C., and Swan, J.: "NASA Viscous 3-D Flowfield Calculations," R&D Associates, RDA-TR-6100-007, October 1975.

8. Helliwell, W. S., Dickinson, R. P., and Lubard, S. C.: "HYTAC Phase I Report: Viscous Flow over Arbitrary Geometries at High Angle of Attack," Arete Associates Technical Report, AR-79-046-TR, April 24, 1979.

9. Kim, M. D., Thareja, R. R., and Lewis, C. H.: "Three-Dimensional Viscous Flowfield Computations in a Streamline Coordinate System," AIAA Paper 81-0401, AIAA 19th Aerospace Sciences Meeting, St. Louis, MO, January 1981.

10. Agarwal, R. and Rakich, J. V.: "Computation of Hypersonic Laminar Viscous Flow Past Spinning Sharp and Blunt Cones at High Angle of Attack," AIAA Paper 78-65, January 1978.

11. Agarwal, R. and Rakich, J. V.: "Computation of Supersonic Laminar Viscous Flow Past a Pointed Cone at Angle of Attack in Spinning and Coning Motion," AIAA Paper 78-1211, July 1978.

12. Sturek, W. B. and Schiff, L. B.: "Computations of the Magnus Effect for Slender Bodies in Supersonic Flow," AIAA Paper 80-1586, 1980.

NOMENCLATURE

c_p	constant pressure specific heat
CFS	streamwise skin-friction coefficient, $2\tau_x^*/(\rho_\infty U_\infty^2)$
CFW	crossflow skin-friction coefficient, $2\tau_\phi^*/(\rho_\infty U_\infty^2)$
C_A	axial force coefficient
C_N	normal force coefficient
C_Y	Magnus force coefficient
C_m	pitching moment coefficient about blunt nose-tip
C_n	Magnus moment coefficient about blunt nose-tip
F_{τ_x}	$\sin^2\theta_c \int_0^x \int_0^{2\pi} x \sin\phi\ \tau_x(x,\phi)\ d\phi\ dx$
F_{p_w}	$\frac{1}{2} \sin 2\theta_c \int_0^x \int_0^{2\pi} x \sin\phi\ p_w(x,\phi)\ d\phi\ dx$
F_{τ_ϕ}	$\sin\theta_c \int_0^x \int_0^{2\pi} x \cos\phi\ \tau_\phi(x,\phi)\ d\phi\ dx$
FY	total Magnus side force, $F_{\tau_x} + F_{p_w} + F_{\tau_\phi}$
H	total enthalpy, H^*/U_∞^2
h	static enthalpy, $h^*/(C_p^* T_\infty)$
L	reference length, equivalent cone slantwise length
M	freestream Mach number

$\dot{m}$ mass-transfer rate at wall, $\rho_w^* v_w^* / \rho_\infty U_\infty$

p nondimensional pressure, $p^*/(\rho_\infty U_\infty^2)$

p_w wall pressure, $p_w^*/\rho_\infty U_\infty^2$

Pr Prandtl number

q heat-transfer rate, $q^*/(\rho_\infty U_\infty^3)$

r local body radius, r^*/L

R_n dimensional body nose radius of curvature

Re_∞/ft freestream unit Reynolds number

STINF   Stanton number, $q^*/[\rho_\infty U_\infty (H_0^* - H_w^*)]$

s surface distance coordinate measured along the body from nose tip, s^*/R_n

T temperature, T^*/T_∞

T_0 freestream stagnation temperature

T_{ref} reference temperature, $(\gamma - 1) M^2 T_\infty$ or U_∞^2/C_p^*

T_w wall temperature, T_w^*/T_∞

U_∞ dimensional freestream velocity

u velocity in the x direction, u^*/U_∞

v velocity in the y direction, v^*/U_∞

w velocity in the ϕ direction, w^*/U_∞

x coordinate along the body surface with constant ϕ, x^*/L

y coordinate normal to the surface, y^*/L

YSH   bow-shock standoff distance divided by R_n

$Z_{c.p}$ center of pressure from blunt nosetip in percentage of the blunt body axial length

α angle of attack, degree

γ ratio of specific heats

η transformed normal coordinate, y/ξ

ε perturbation parameter, $\varepsilon^2 = \mu^*(T_{ref})/(\rho_\infty U_\infty R_n)$

θ_c cone half-angle, degree

μ coefficient of viscosity, μ^*/μ_∞

ξ bow-shock standoff distance divided by L

ρ density, ρ^*/ρ_∞

τ_x primary flow wall shear stress, $\tau_x^*/(\rho_\infty U_\infty^2)$

τ_ϕ crossflow wall shear stress, $\tau_\phi^*/(\rho_\infty U_\infty^2)$

ϕ circumferential coordinate

Ω angular velocity (rev/min)

Subscript

w   wall value

0   stagnation condition

∞ freestream condition (dimensional quantity)

Superscript

*   dimensional quantity

TABLE 1

Test Case Freestream Conditions and Body Geometries

Case	S U∞ (fps)	M T∞ (°R)	Re∞(1/ft) α (deg)	R_n (ft) θ_c (deg)	T_w (°R) T_w/T_0	ε	Ω(rpm)	ṁ(max)
1a	30.06 2341.	5. 91.247	621000. 2.	0.027917 7.	460. 0.84	0.0218	2000.	0.00250 dist.
1b	30.06 2341.	5. 91.247	621000. 2.	0.027917 7.	460. 0.84	0.0218	2000.	0.00125 const.
2	30.06 7223.	18. 64.80	544740. 15.	0.027917 7.	540. 0.1266	0.0545	8000.	0.00125 const.

Dist.: asymmetric distribution around body and constant along body.
Const.: constant around and along body.

TABLE 2

Aerodynamic Coefficients for Test Cases

Case	$\dot{m}$ (max)	Ω(rpm)	C_A	C_N	C_Y	C_m	C_n	Z_{cp}
1a basic	0.0	0.0	0.1880	0.0372	-0.0	-0.0214	0.0	0.577
1a Ω only	0.0	2000.	0.1880	0.0372	-0.1850E-3	-0.0214	0.1280E-3	0.577
1a $\dot{m}$ only	0.00250 dist.	0.0	0.1849	0.0285	-0.8471E-2	-0.0148	0.4902E-2	0.520
1a Ω + $\dot{m}$	0.00250 dist.	2000.	0.1849	0.0284	-0.9392E-2	-0.0147	0.5609E-2	0.517
1b Ω + $\dot{m}$	0.00125 const.	2000.	0.1840	0.0307	-0.5940E-3	-0.0166	0.4560E-3	0.538
2 basic	0.0	0.0	0.2070	0.4740	-0.0	-0.3075	0.0	0.649
2 Ω only	0.0	8000.	0.2070	0.4740	-0.5285E-3	-0.3075	0.3388E-3	0.649
2 $\dot{m}$ only	0.00125 const.	0.0	0.2005	0.4703	-0.0	-0.3050	0.0	0.648
2 Ω + $\dot{m}$	0.00125 const.	8000.	0.2005	0.4703	-0.8246E-3	-0.3050	0.5396E-3	0.648

Case 1a, case 1b: integrated up to s = 23.
Case 2: integrated up to s = 30.06
Reference area: body base area
Reference length: blunt body axial length
Moment: about blunt nosetip
Z_{cp}: percentage of the blunt body axial length

TABLE 3

Computing Times* for Test Cases

| Case | s | grid size of | | time(min) |
		s-steps	n-points	φ-planes	
1a, basic	30.06	45	101	19	37.
1a, Ω only	30.06	45	101	19	37.
1a, ṁ only	24.80	82	101	19	73.
1a, ṁ + Ω	23.33	70	101	19	65.
1b, ṁ + Ω	30.06	58	101	19	54.
2, basic	30.06	45	101	19	38.
2, Ω only	30.06	45	101	19	38.
2, ṁ only	30.06	45	101	19	40.
2, ṁ + Ω	30.06	45	101	19	40.

*CPU time on IBM 3032, H=OPT2 compiler
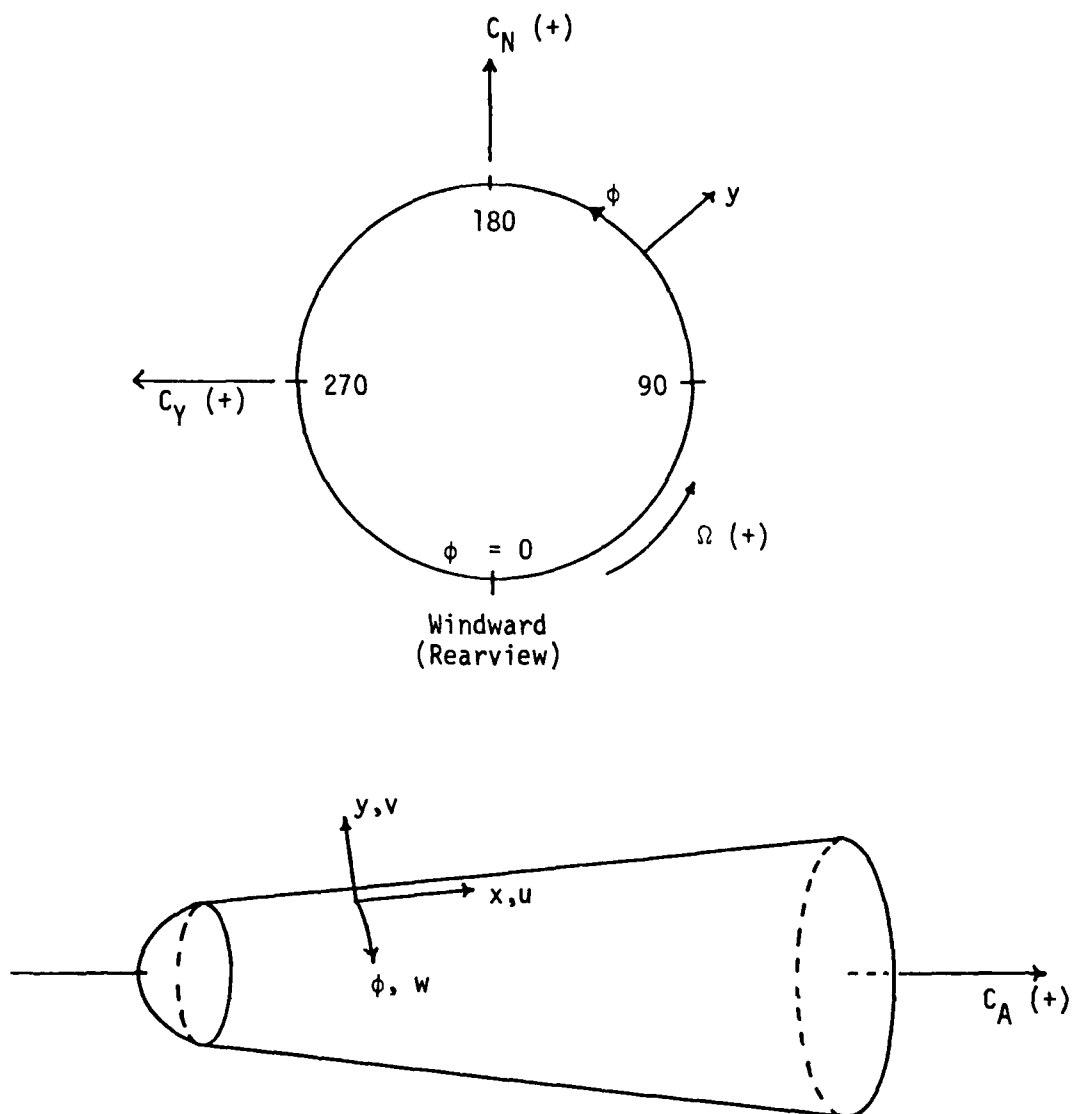
Figure 1. Body-generator coordinate system
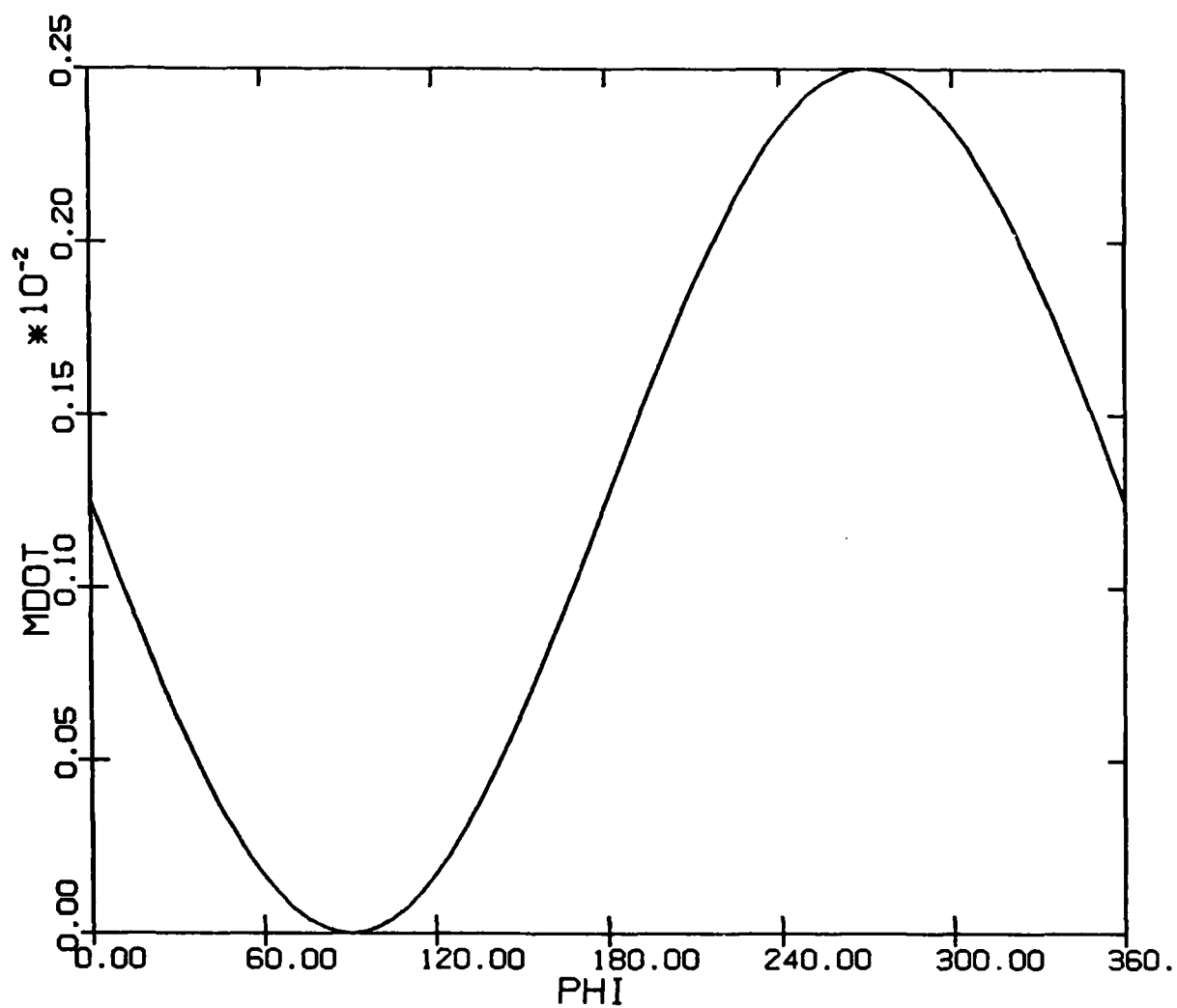
Figure 2: Case 1a Asymmetric mass-transfer distribution around the body.

1.0

1.1

1.25   1.4   1.6

2.8   2.5

3.2   2.2

2.0

1.8

MICROCOPY RESOLUTION TEST CHART
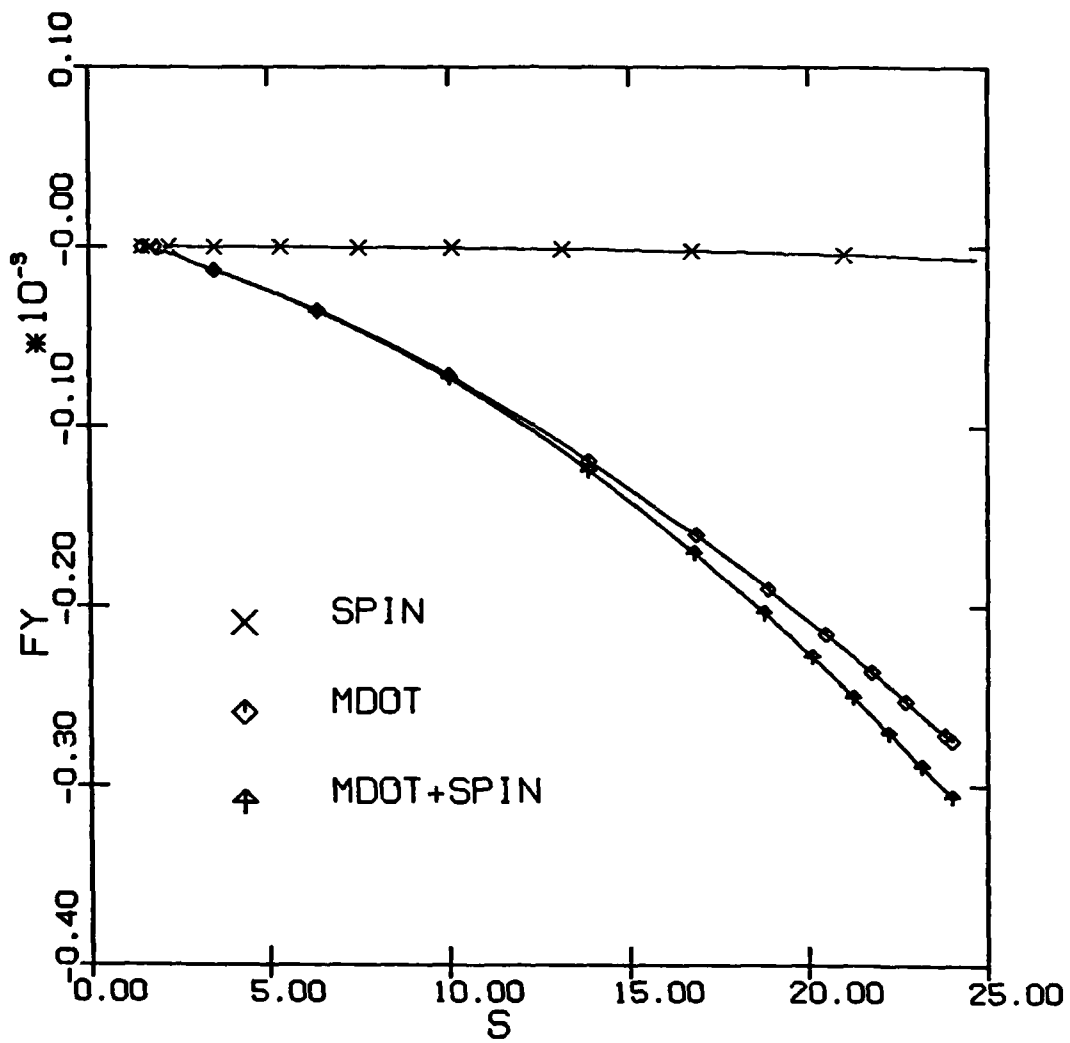
NATIONAL BUREAU OF STANDARDS 1963 A

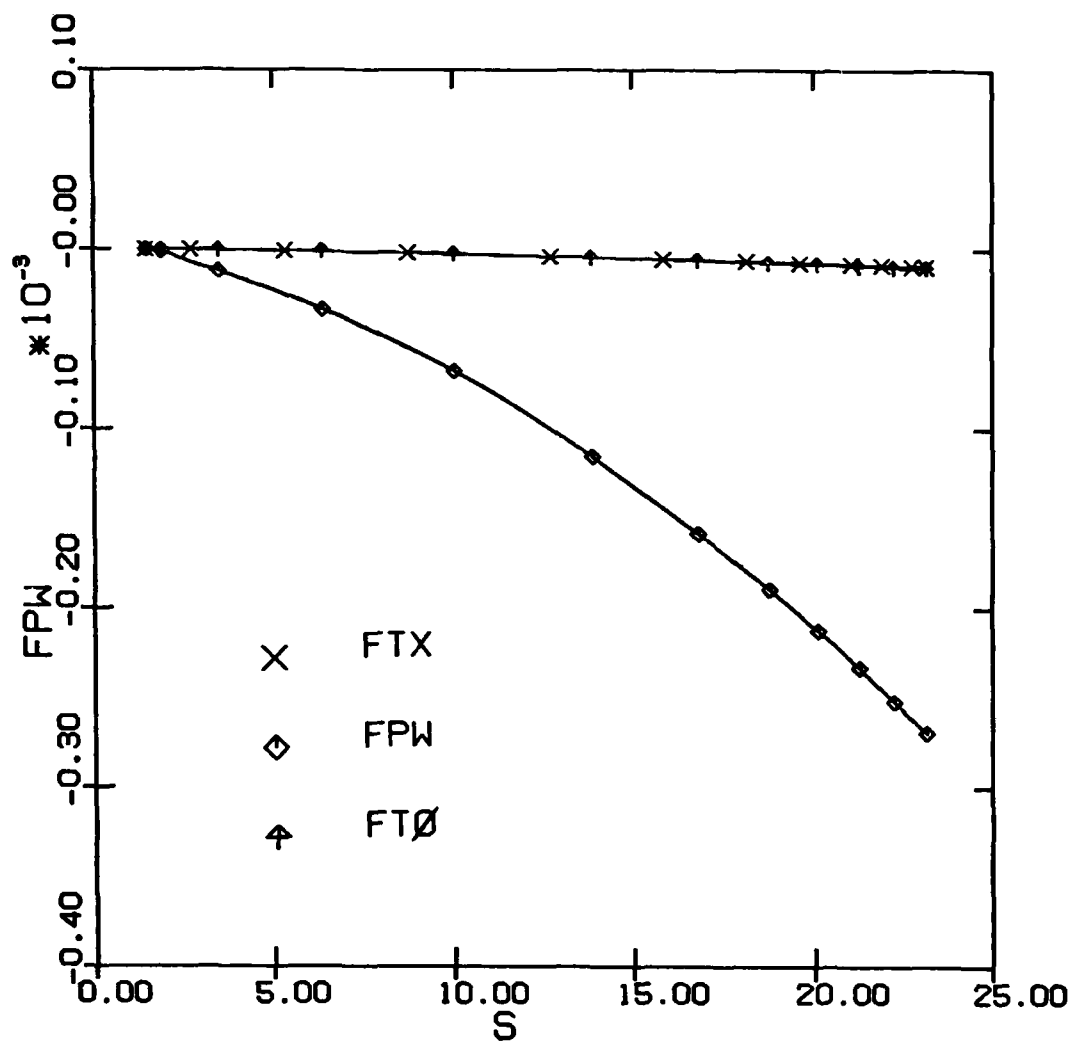Figure 3: Case 1a Effects of asymmetric mass transfer and spin on the
Magnus force along the body.

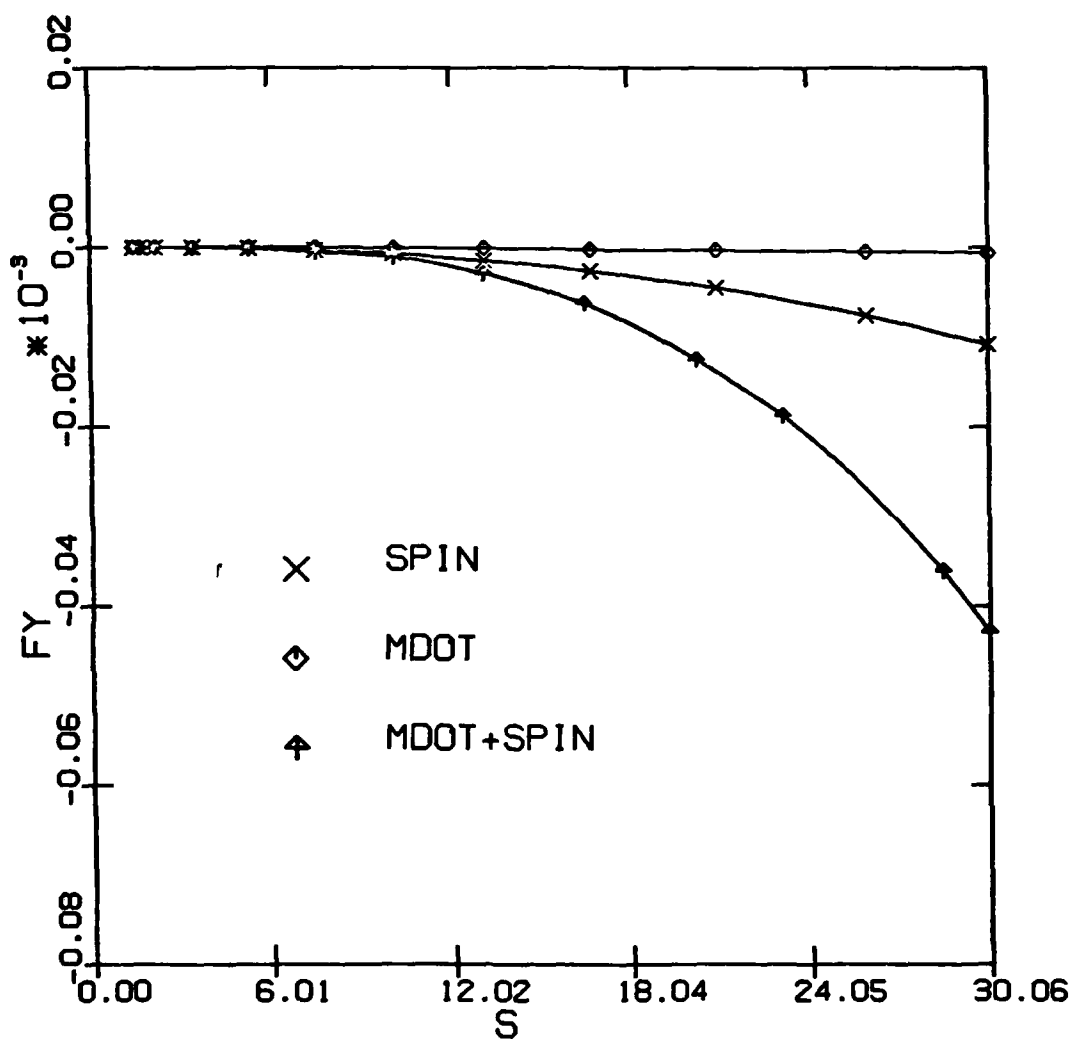**Figure 4:** Case 1a Magnus force components along the body with mass transfer and spin.

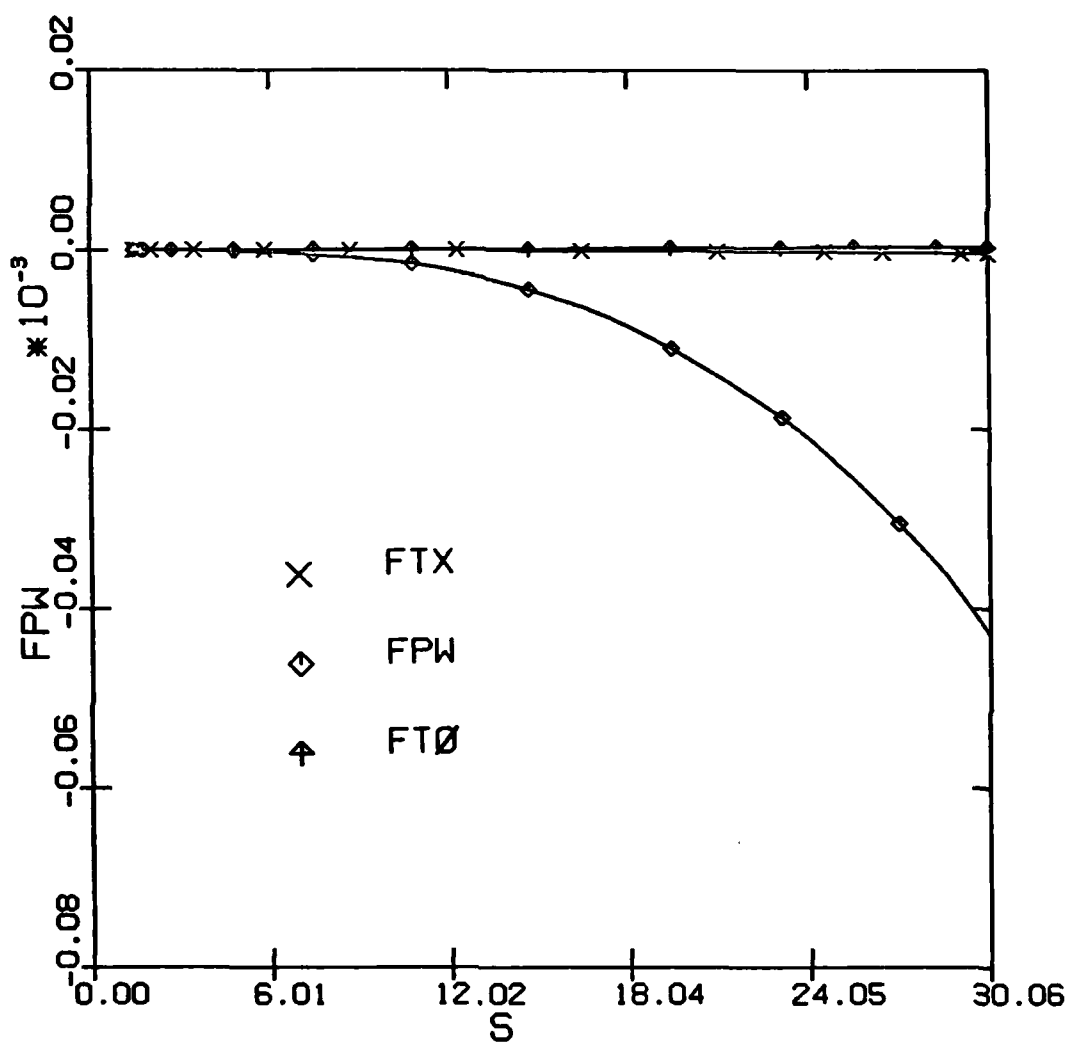Figure 5: Case 1b Effects of constant mass transfer and spin on the Magnus force along the body.

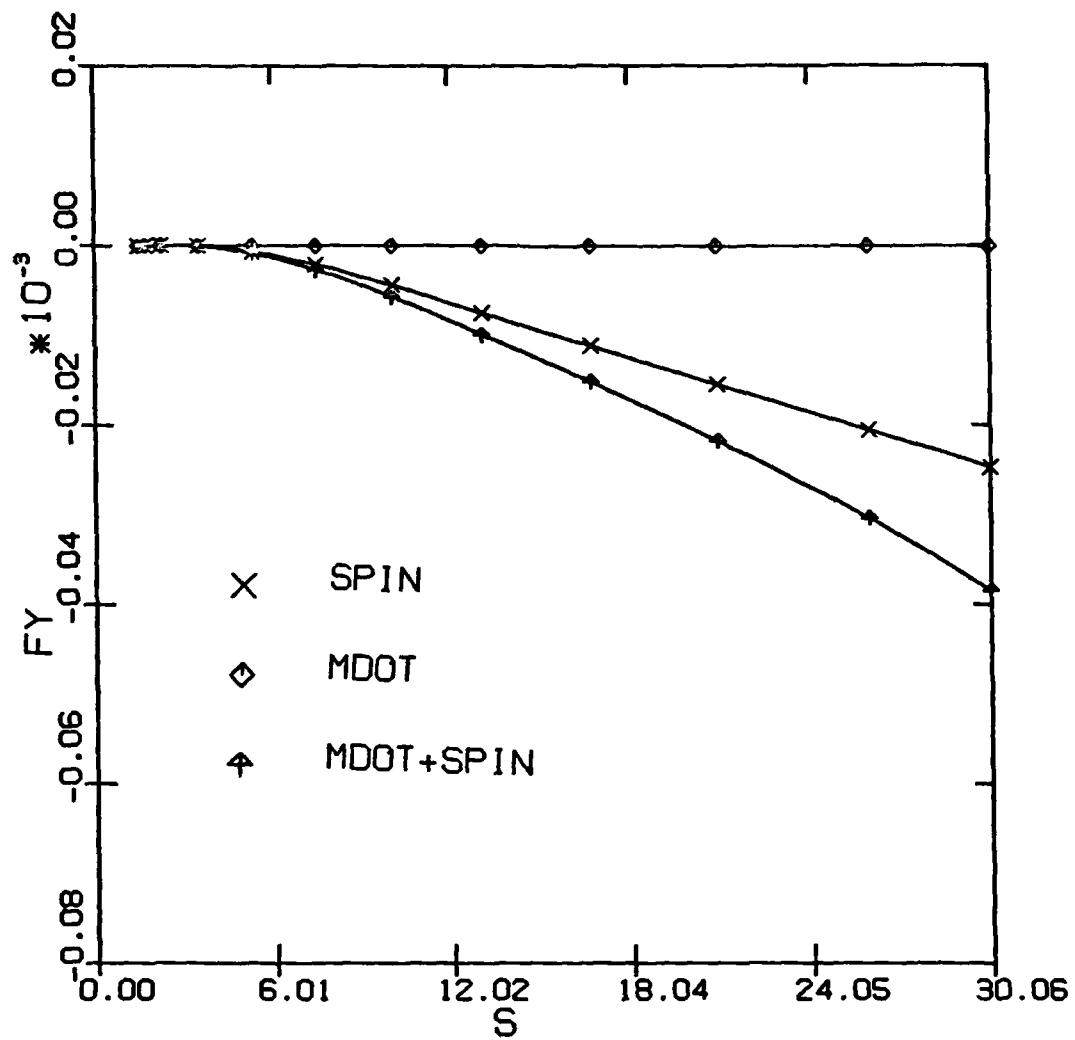Figure 6: Case 1b Magnus force components along the body with mass
transfer and spin.

Figure 7: Case 2 Effects of constant mass transfer and spin on the Magnus force along the body.
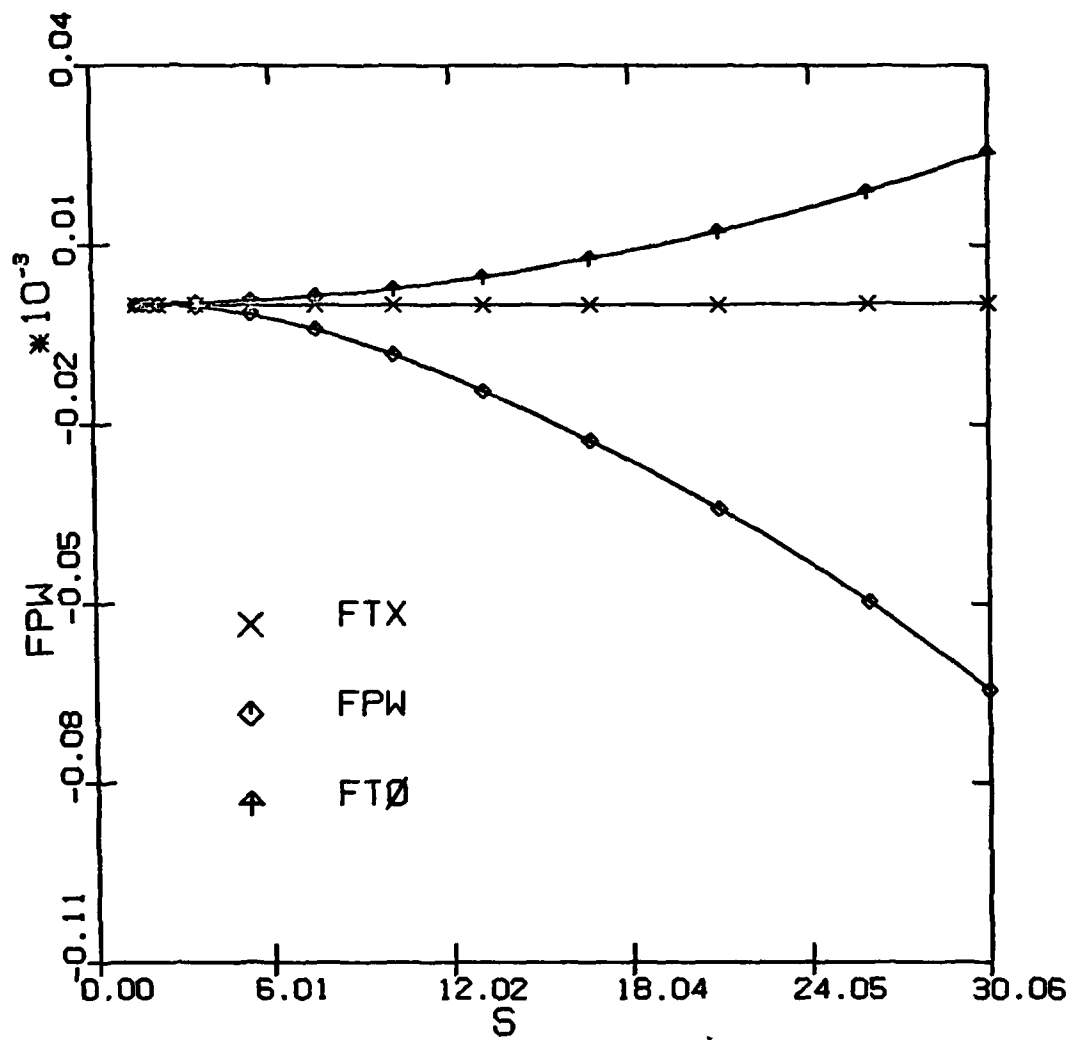
Figure 8: Case 2 Magnus force components along the body with mass transfer and spin.
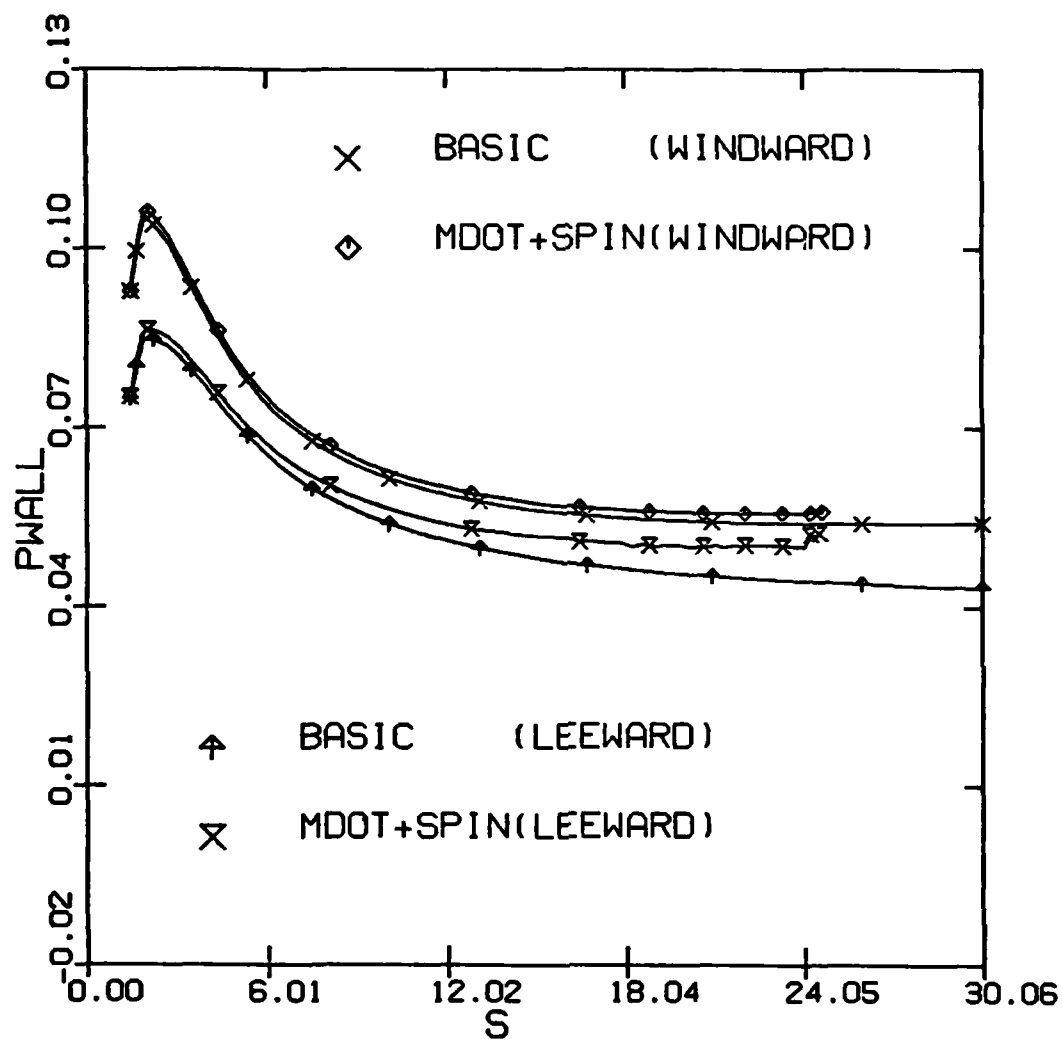
Figure 9: Case 1a Effects of mass transfer and spin on the surface pressure along the body.
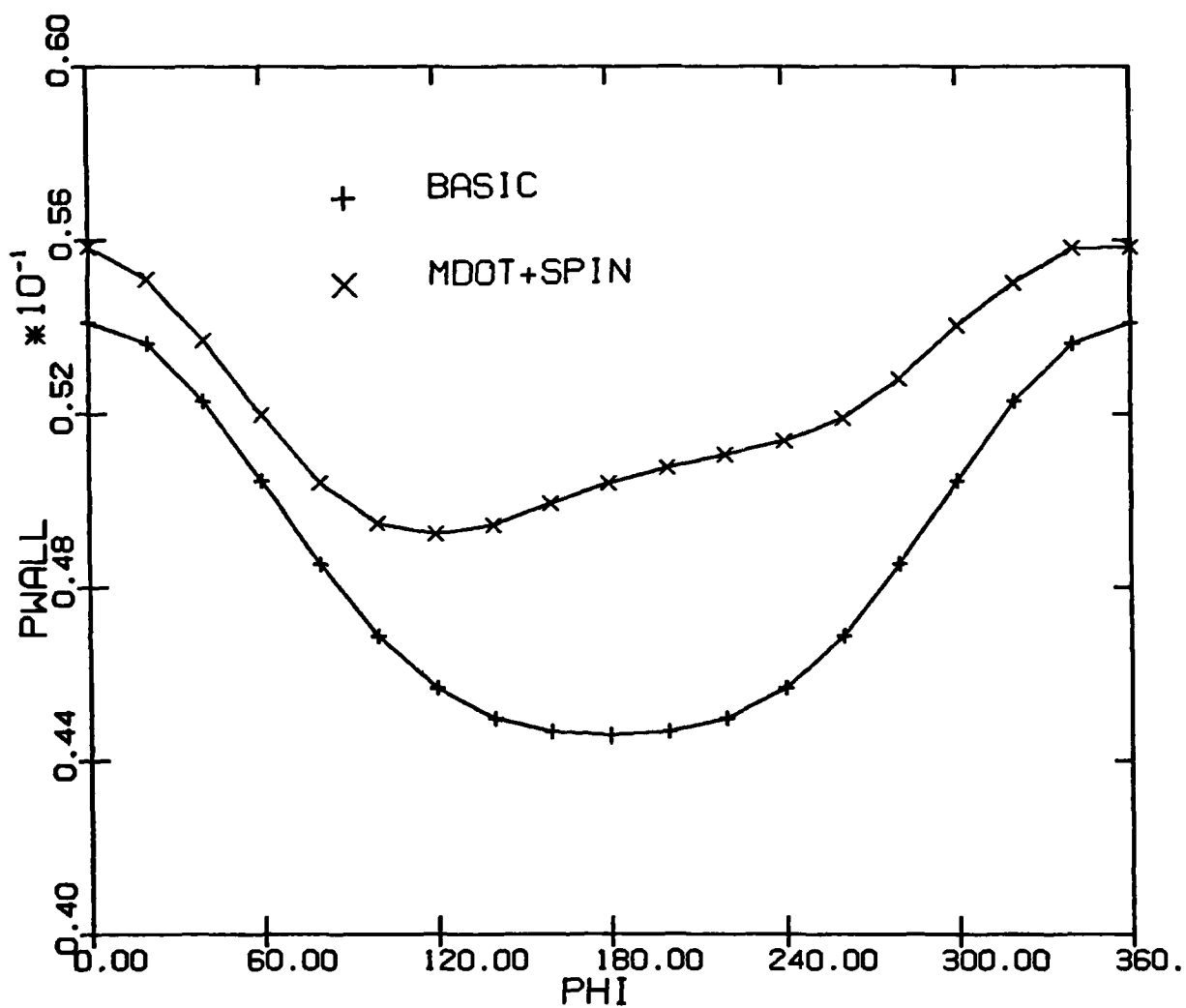
Figure 10: Case 1a Effects of asymmetric mass transfer and spin on the surface pressure around the body at s = 23.
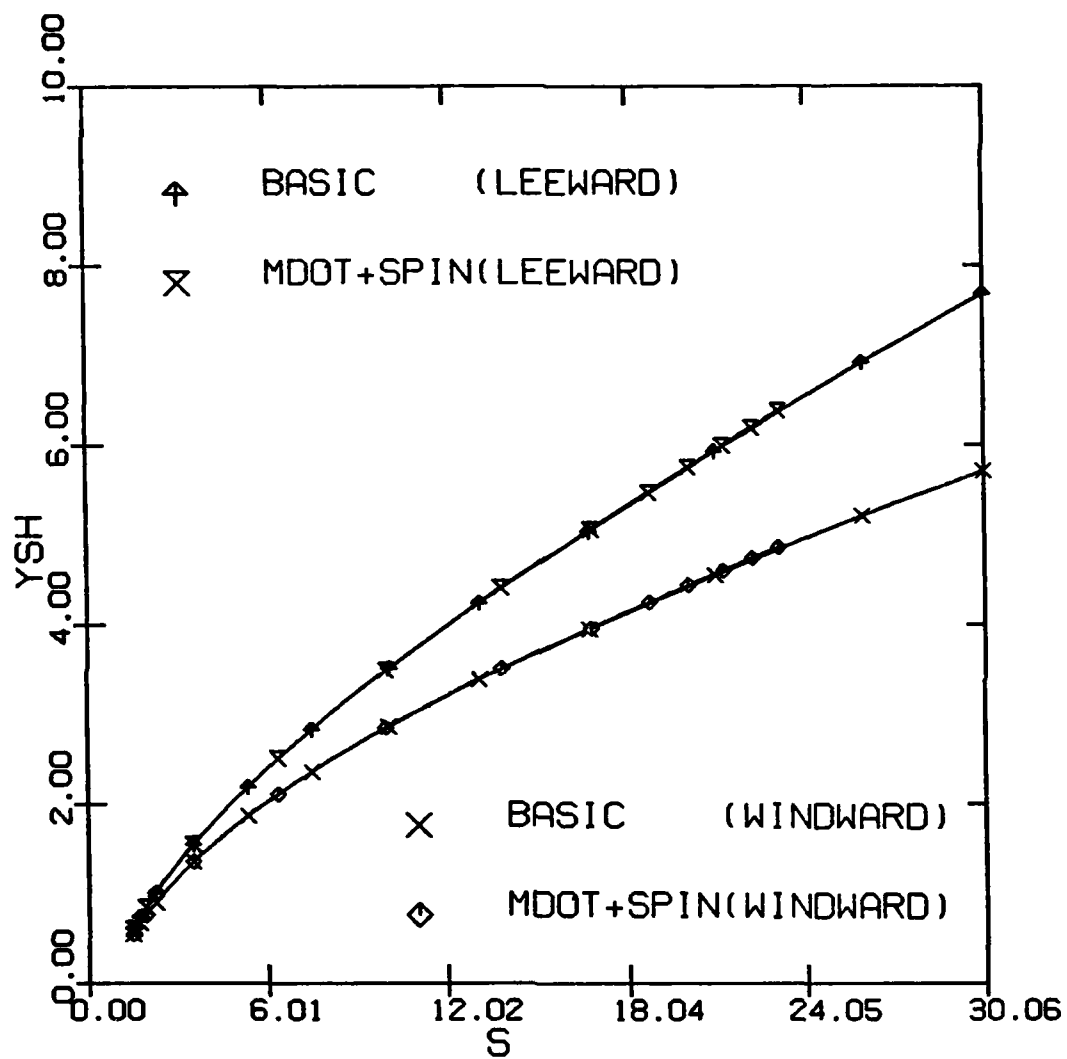
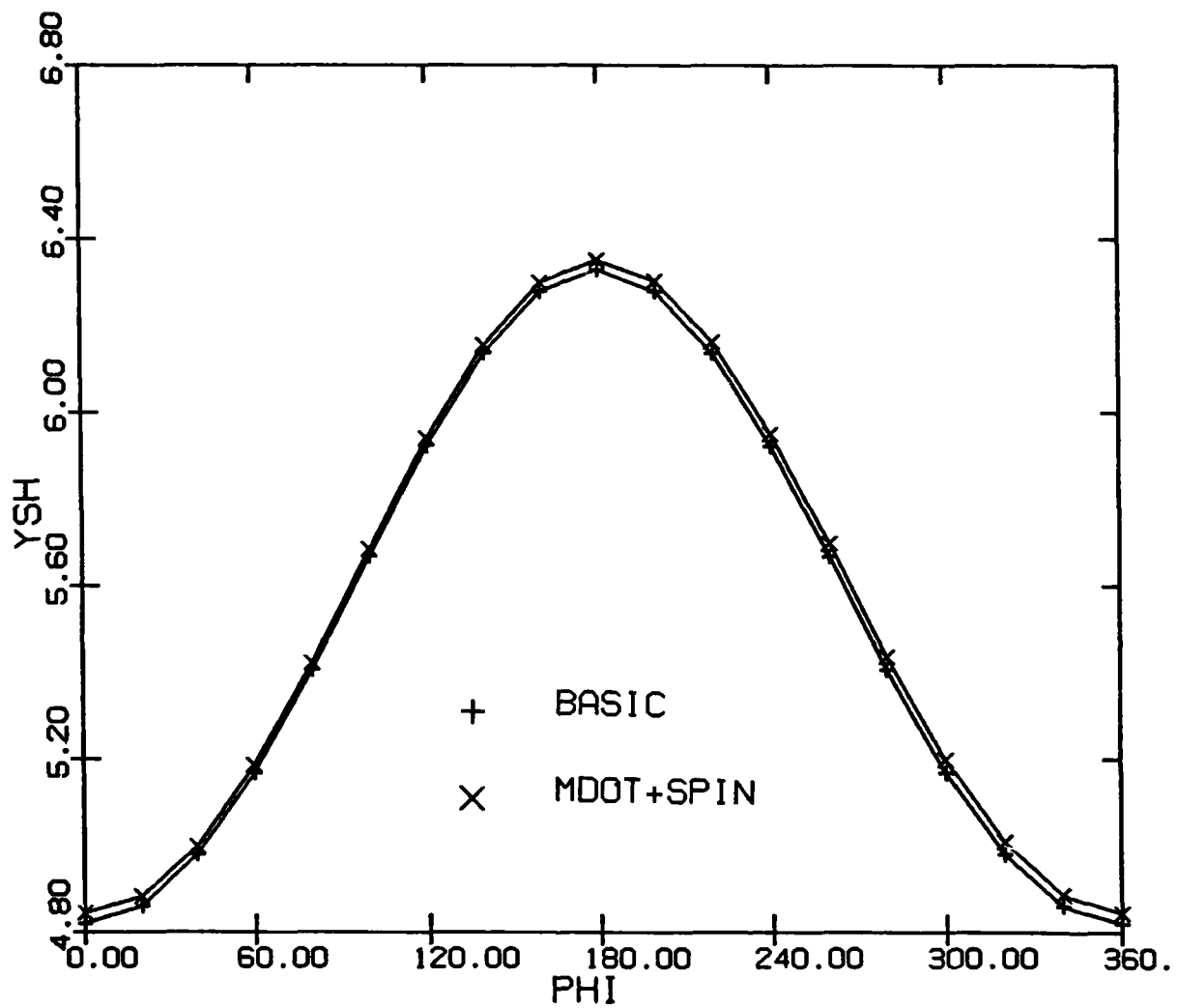Figure 11: Case 1a Effects of mass transfer and spin on the shock-layer thickness along the body.

Figure 12: Case 1a Effects of asymmetric mass transfer and spin on the shock-layer thickness around the body at s = 23.

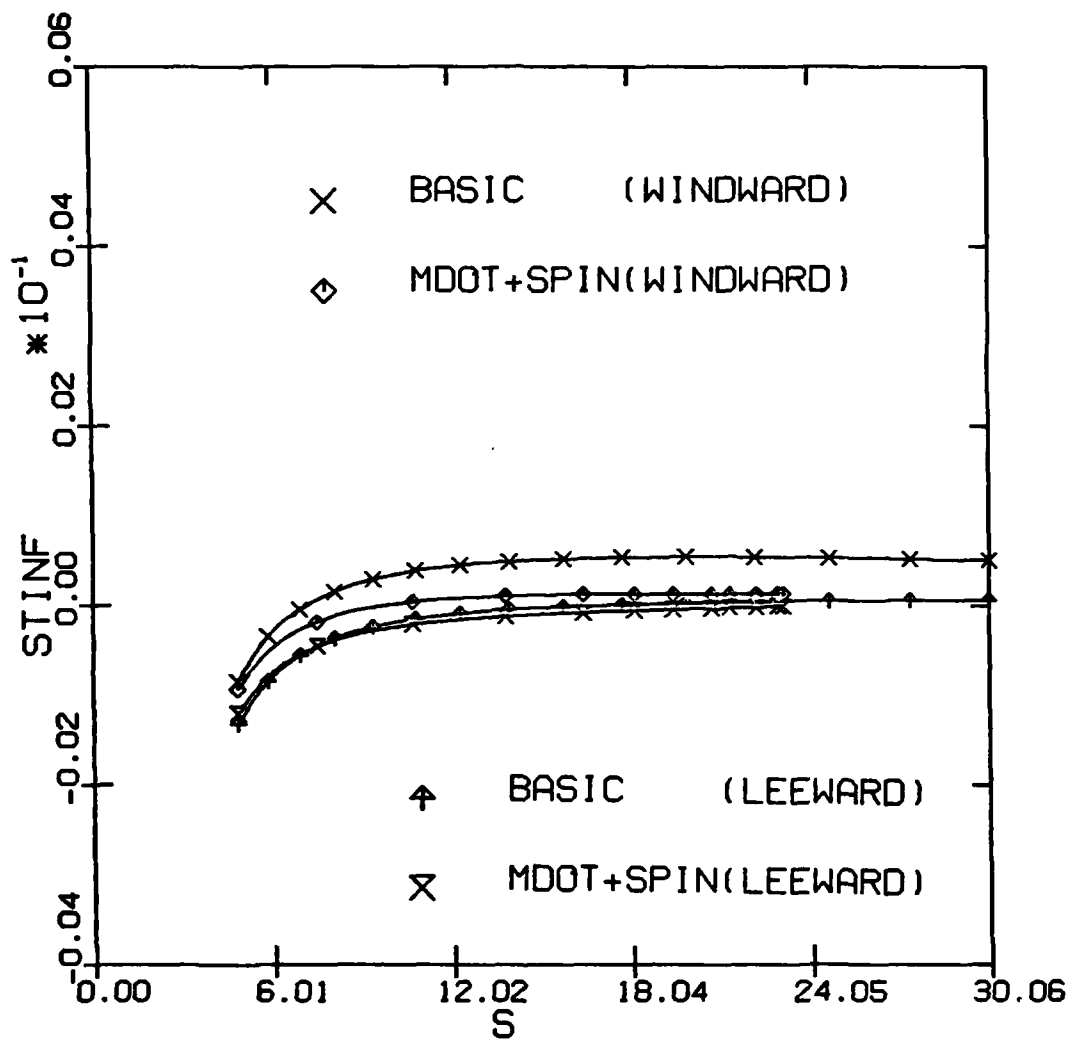Figure 13: Case 1a   Effects of mass transfer and spin on the heat transfer along the body.

Figure 14: Case 1a Effects of asymmetric mass transfer and spin on the heat transfer around the body at s = 23.

Figure 15: Case 1a Effects of mass transfer and spin on the streamwise shear along the body.

Figure 16: Case 1a Effects of asymmetric mass transfer and spin on the streamwise shear around the body at s = 23.

Figure 17: Case la Effects of asymmetric mass transfer and spin on
the crossflow sheár around the body at s = 23.

Figure 18: Case 1a Effect of mass transfer on the axial flow separation.
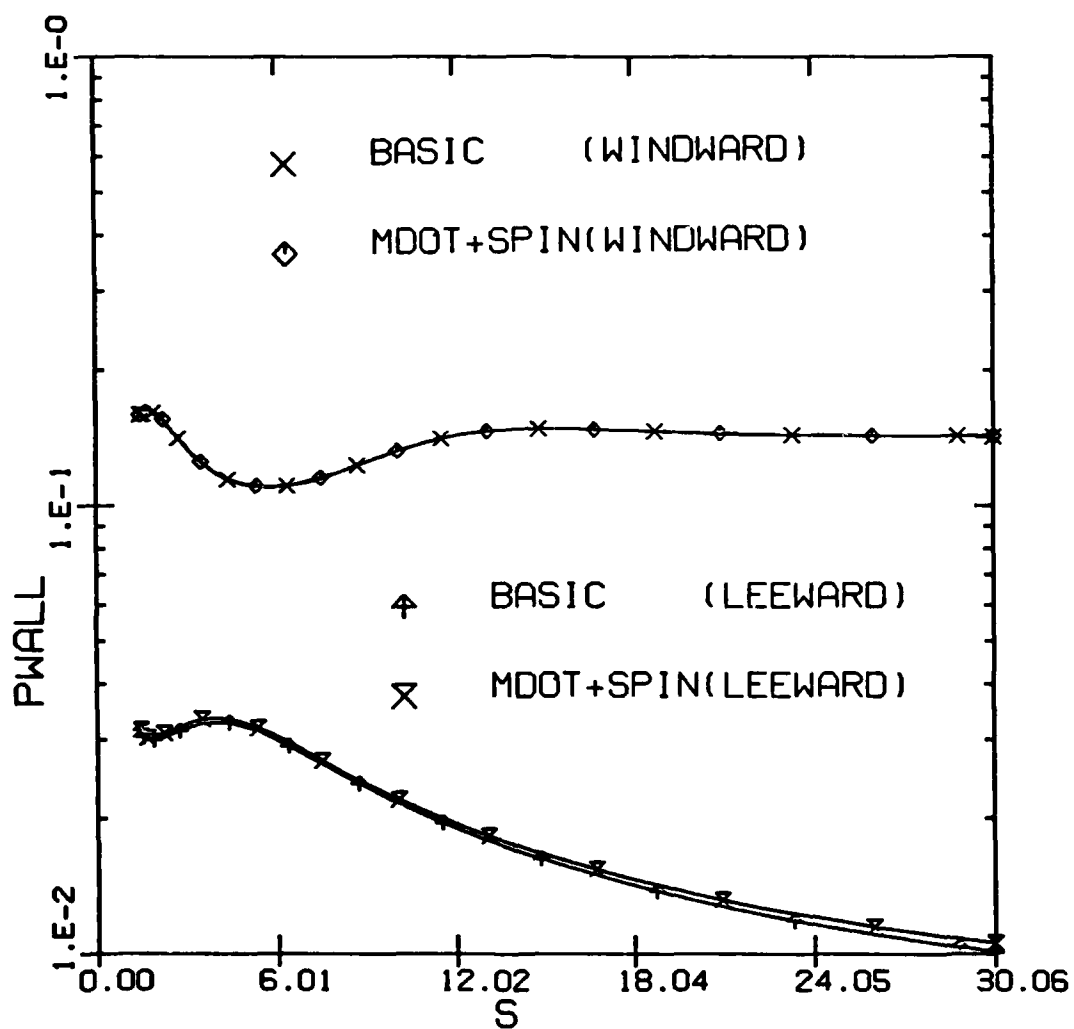
Figure 19: Case 2 Effects of mass transfer and spin on the surface pressure along the body.
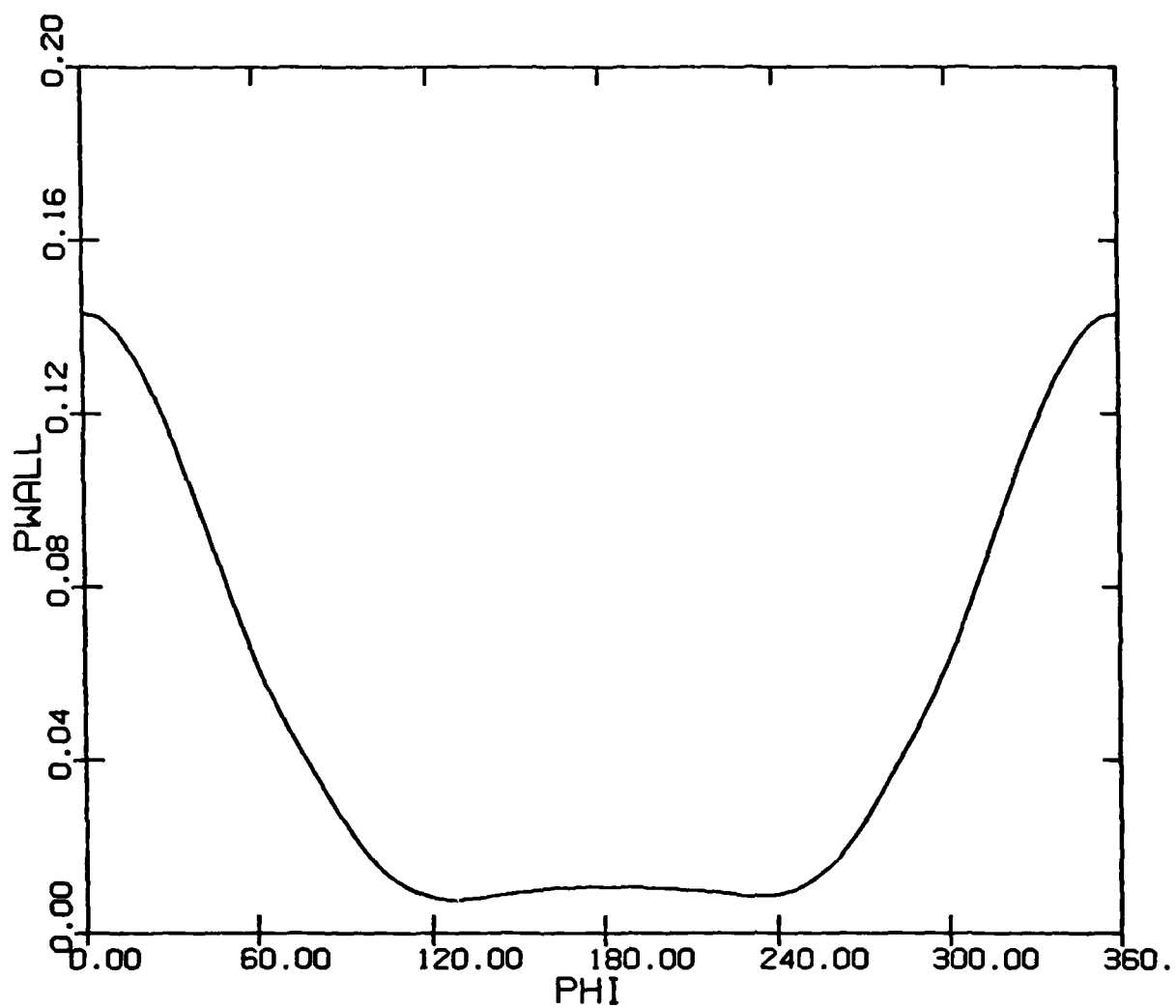
Figure 20: Case 2 Surface pressure around the body with mass transfer and spin at s = 30.06.
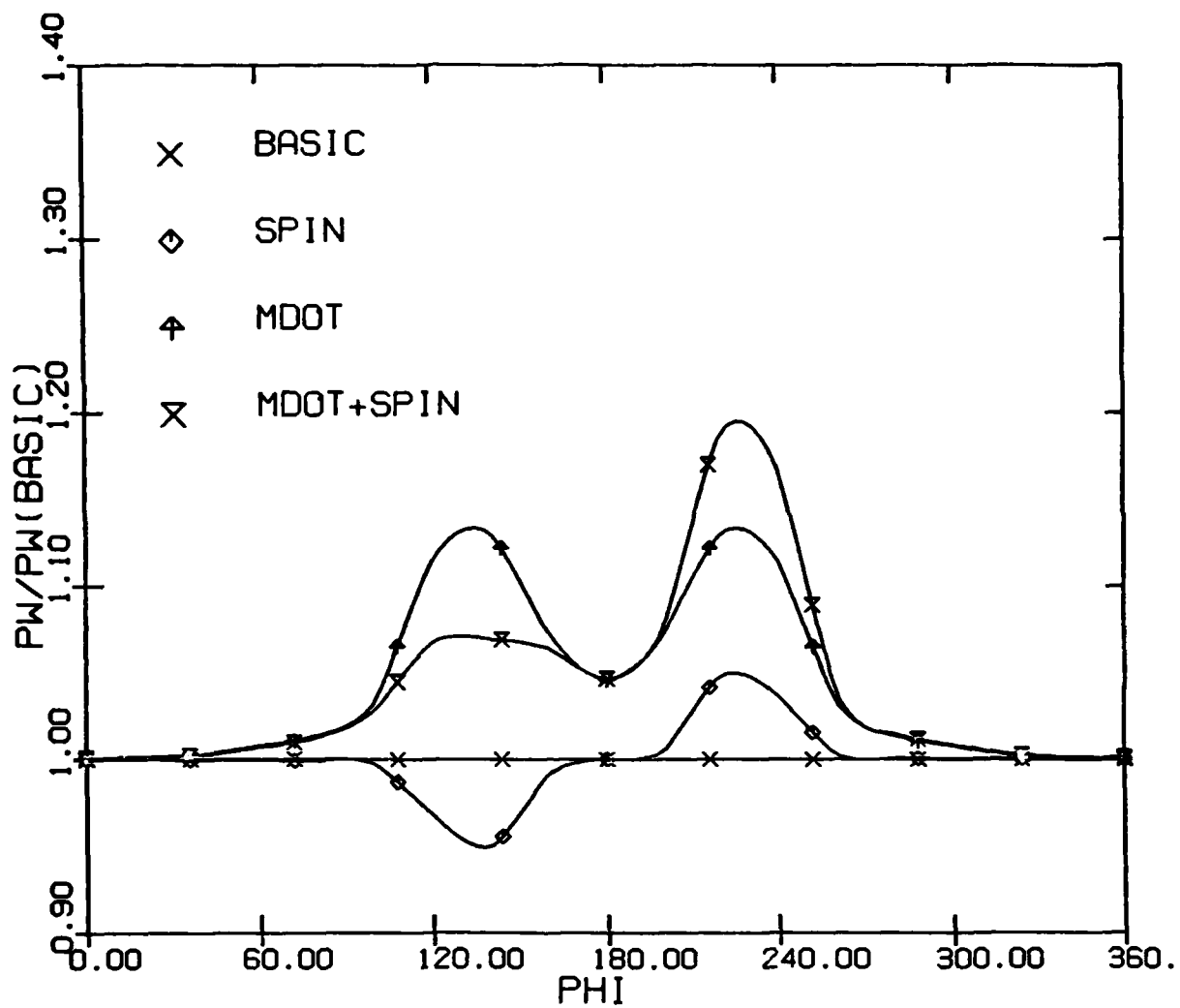
Figure 21: Case 2 Effects of mass transfer and/or spin on the surface pressure around the·body at s = 30.06.
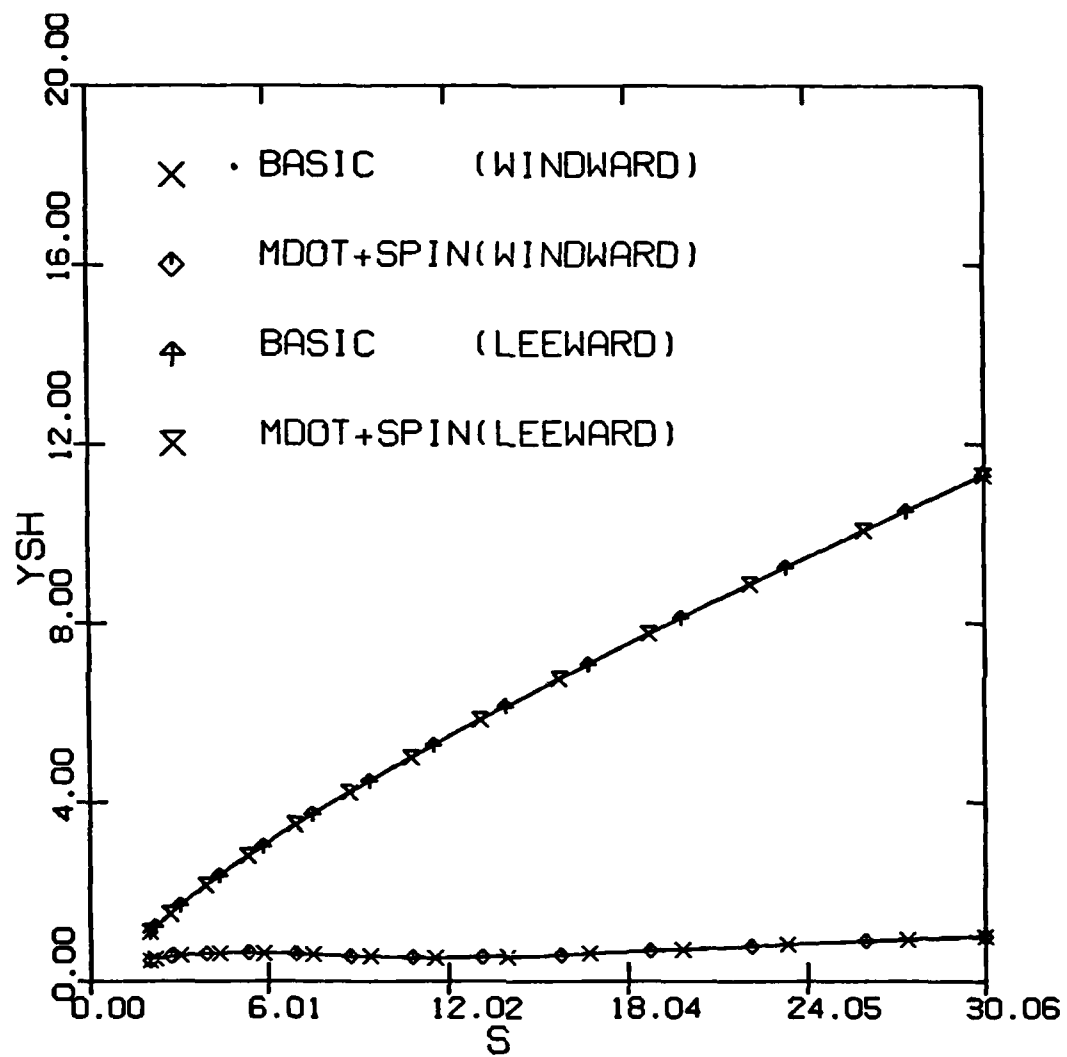
Figure 22: Case 2 Effects of mass transfer and spin on the shock-layer thickness along the body.
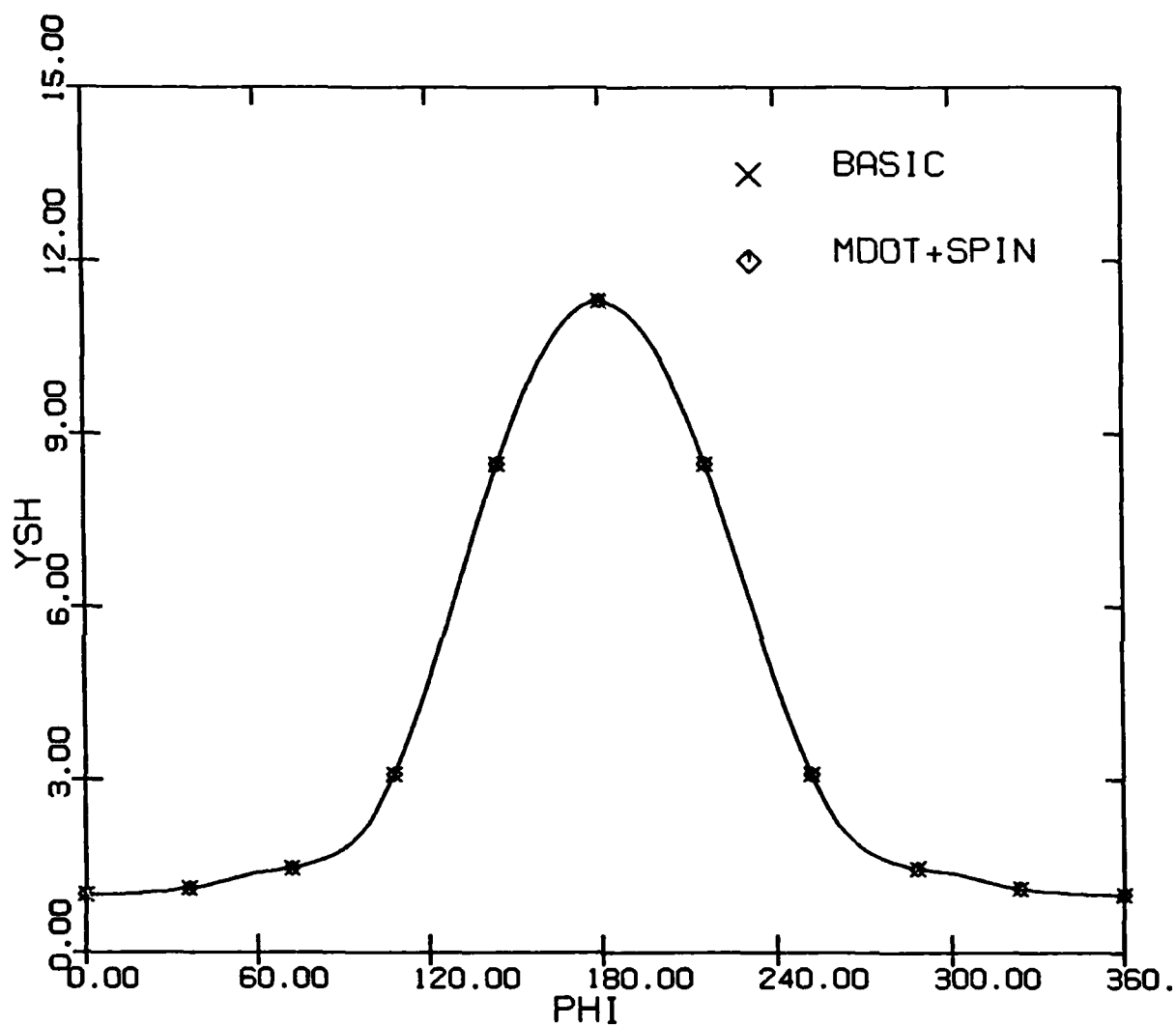
Figure 23: Case 2 Effects of mass transfer and spin on the shock-layer
thickness around the body at s = 30.06.
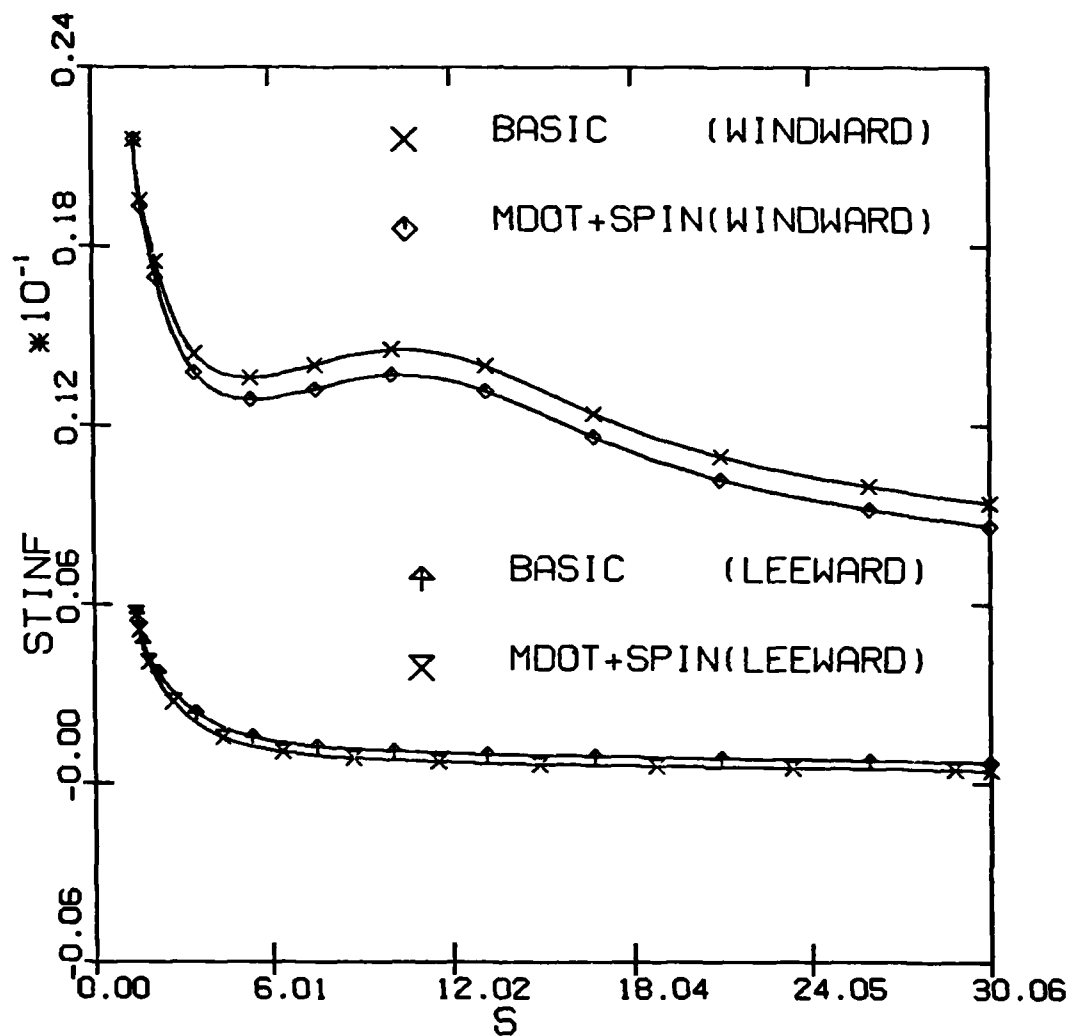
Figure 24: Case 2 Effects of mass transfer and spin on the heat
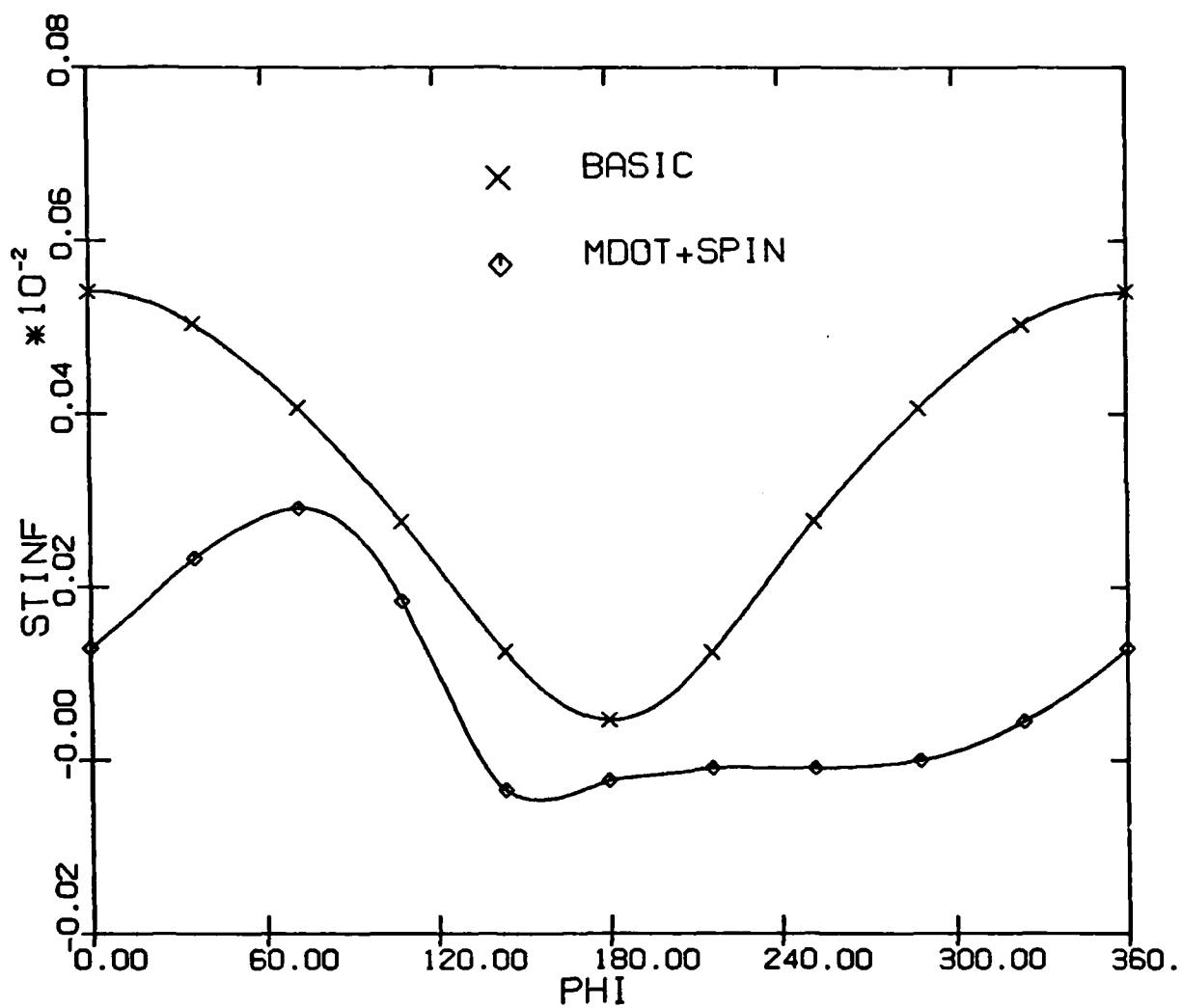transfer along the body.
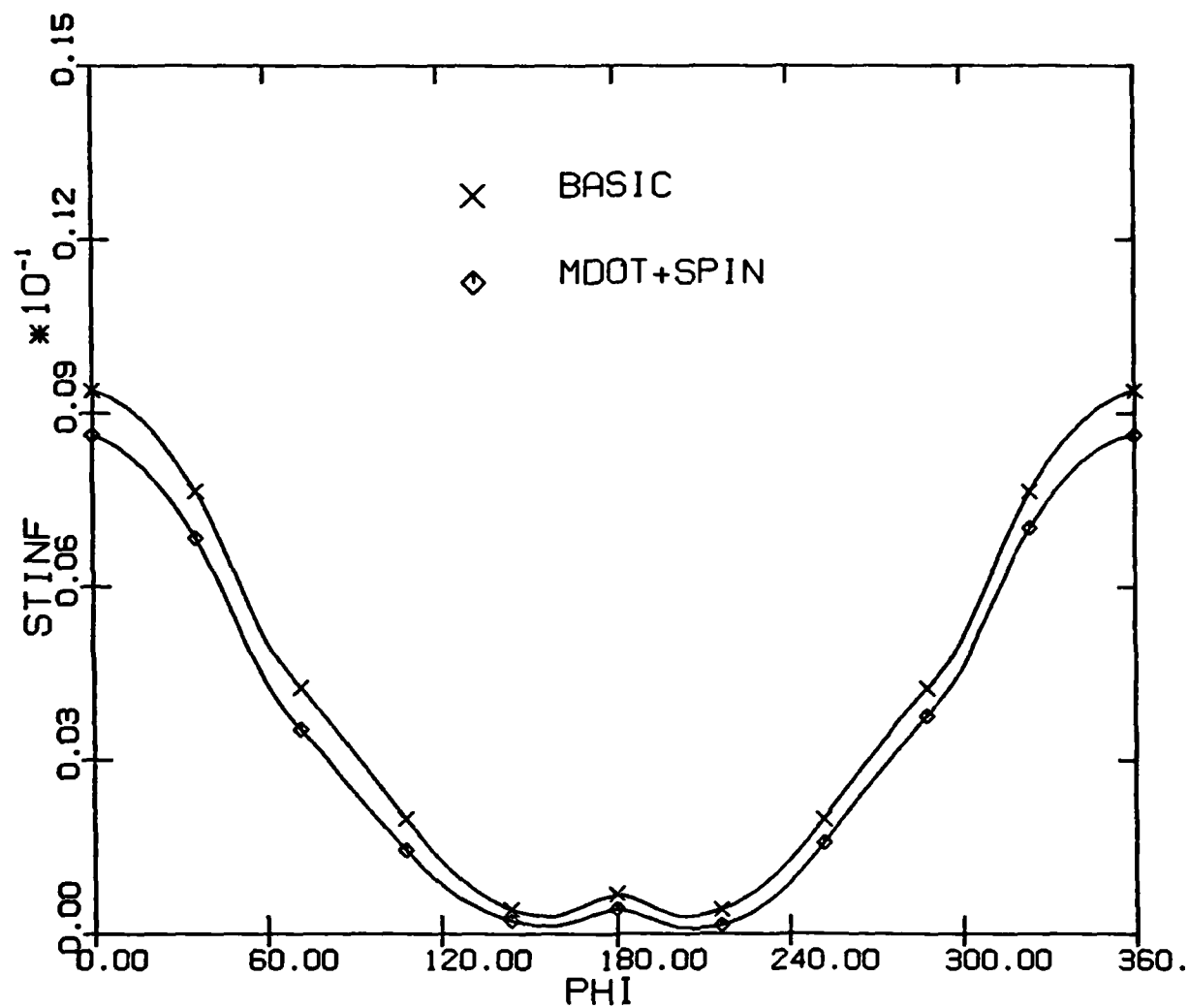
Figure 25: Case 2 Effects of mass transfer and spin on the heat transfer
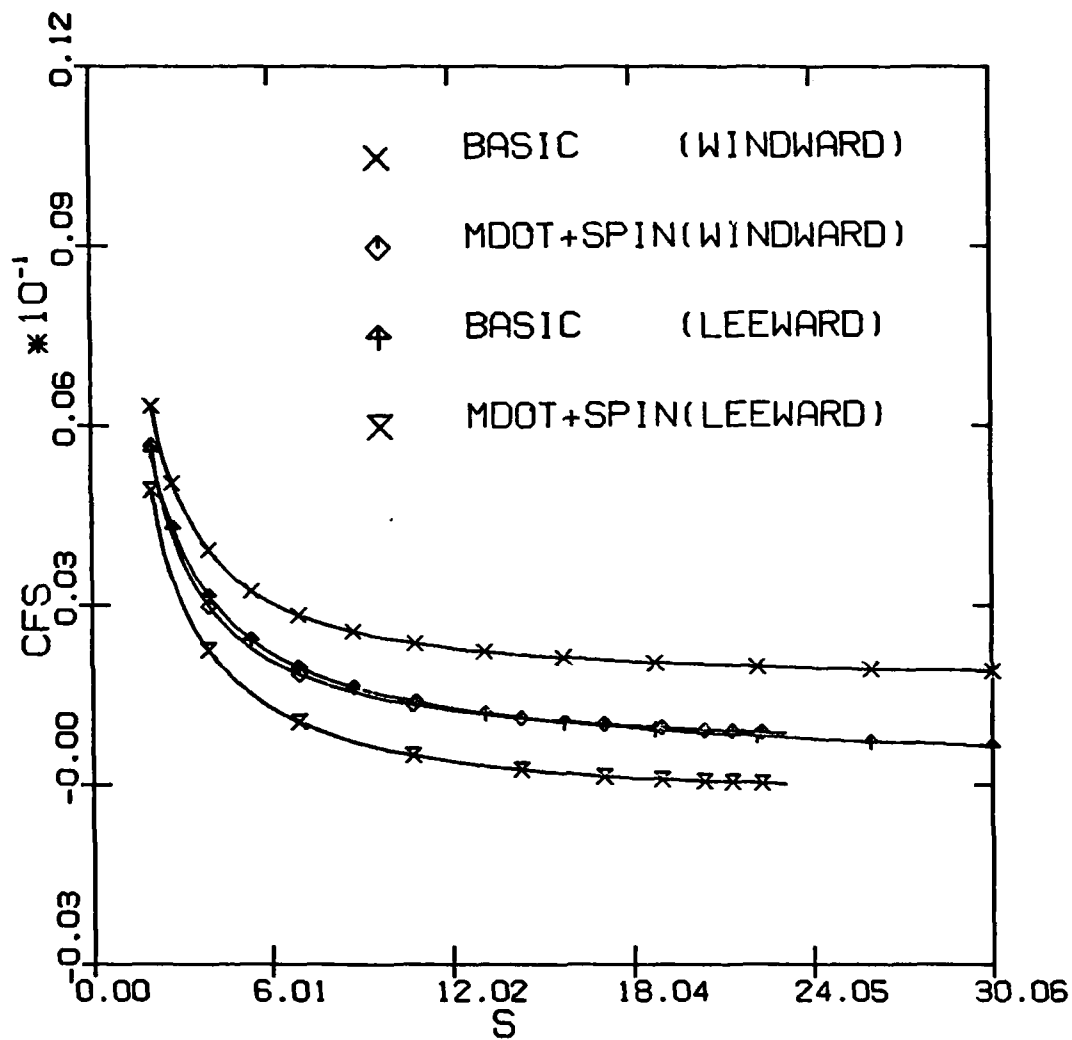around the body at $s = 30.06$.
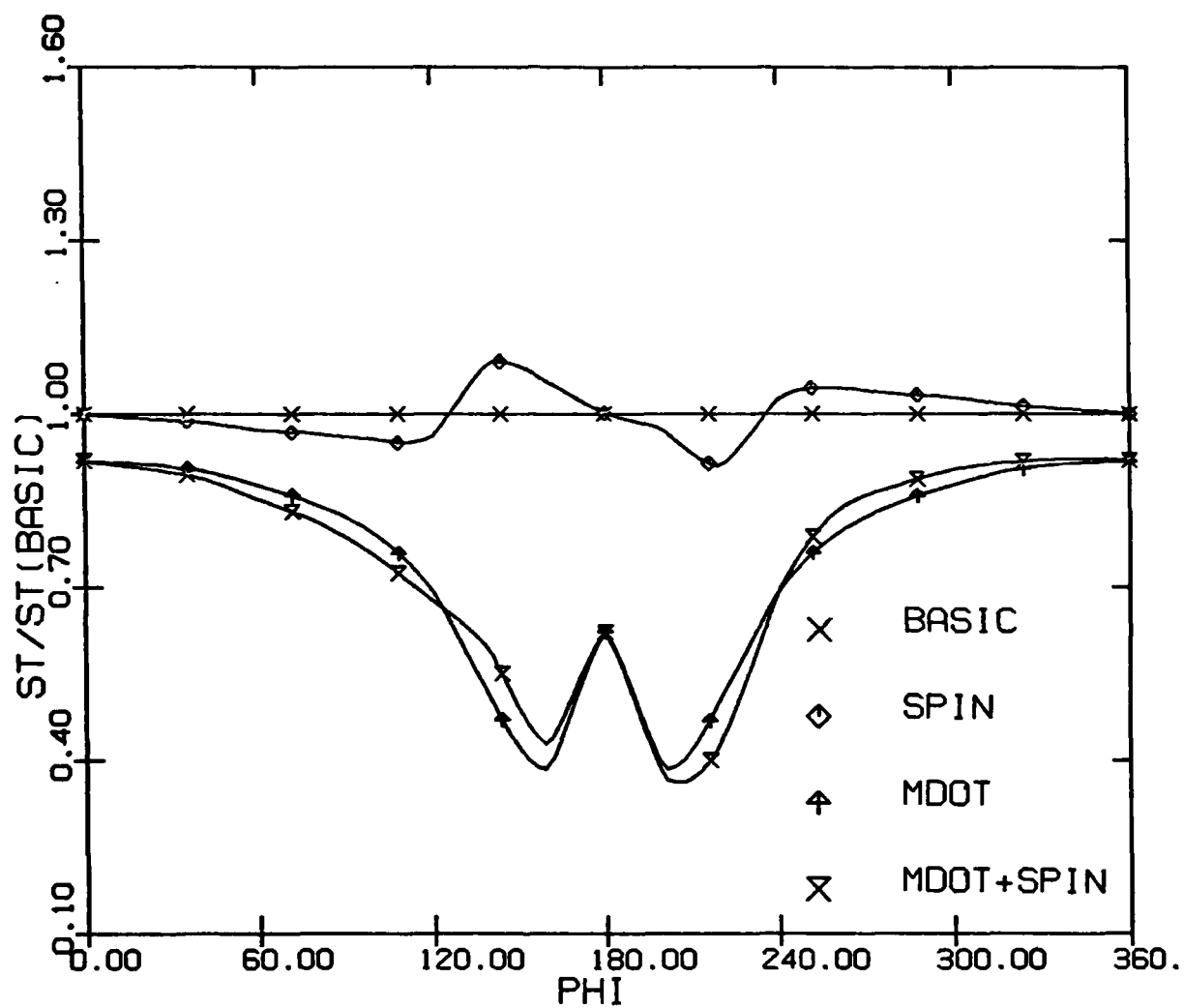
Figure 26: Case 2 Effects of mass transfer and/or spin on the heat transfer around the body at ' = 30.06.
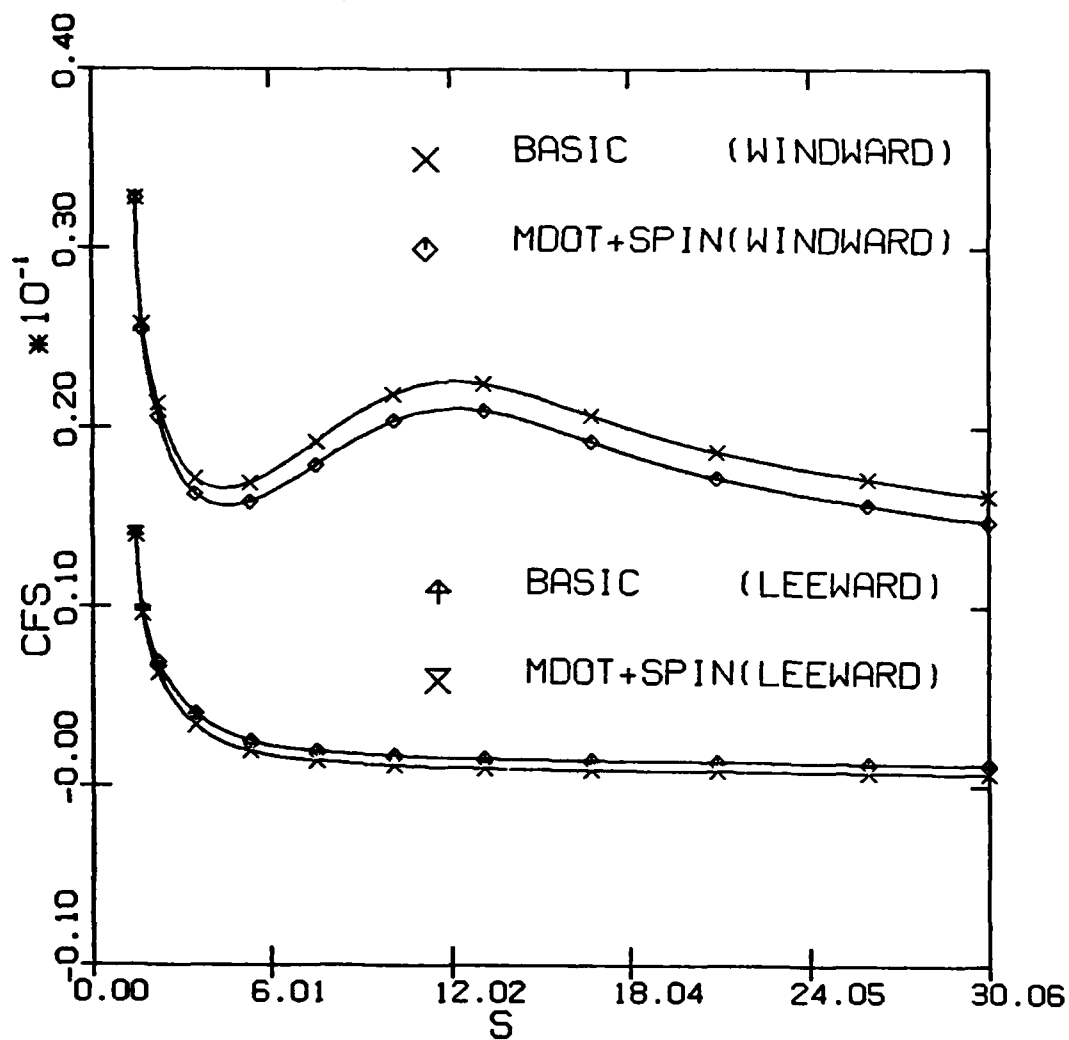
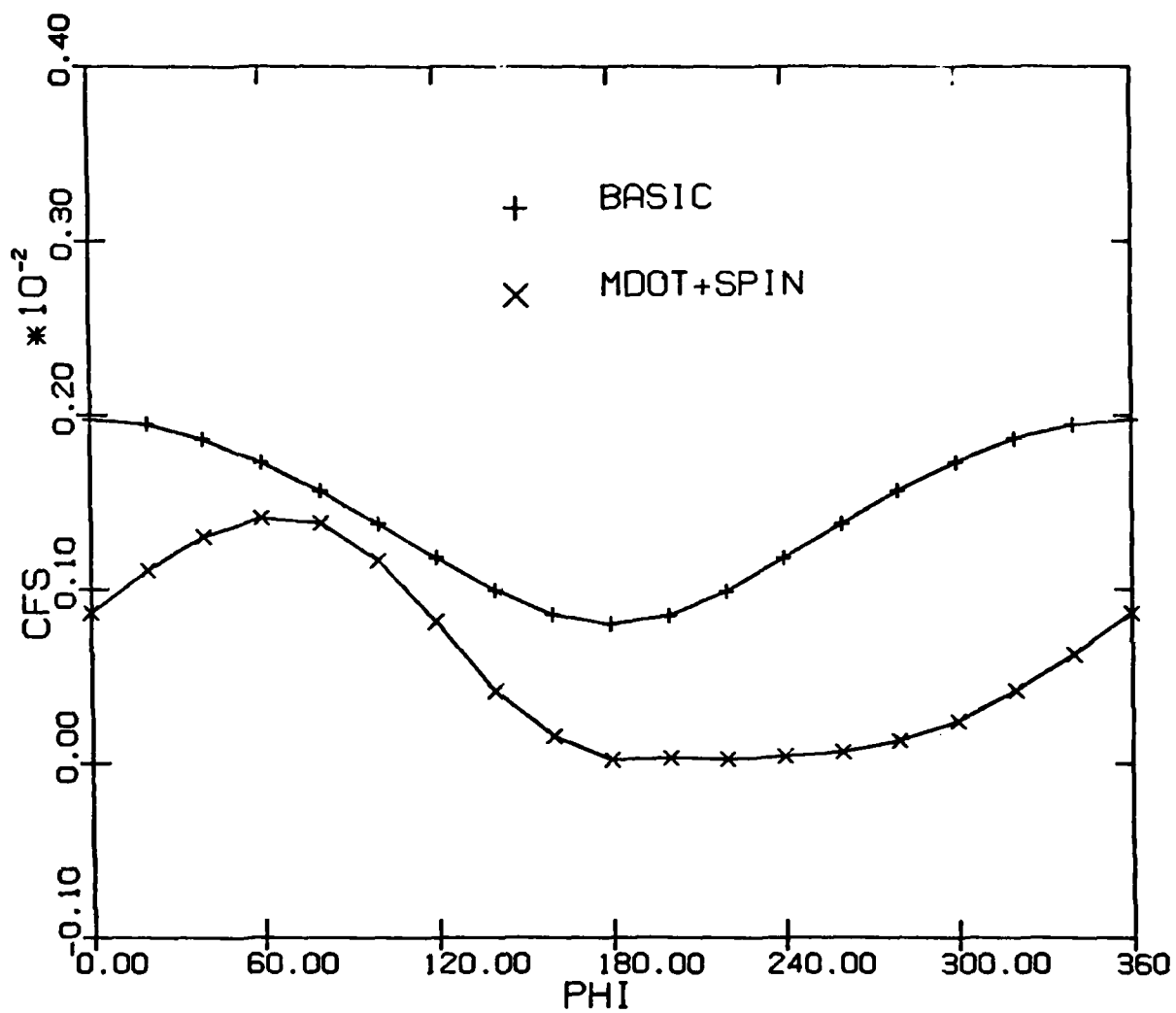Figure 27: Case 2 Effects of mass transfer and spin on the streamwise shear along the body.
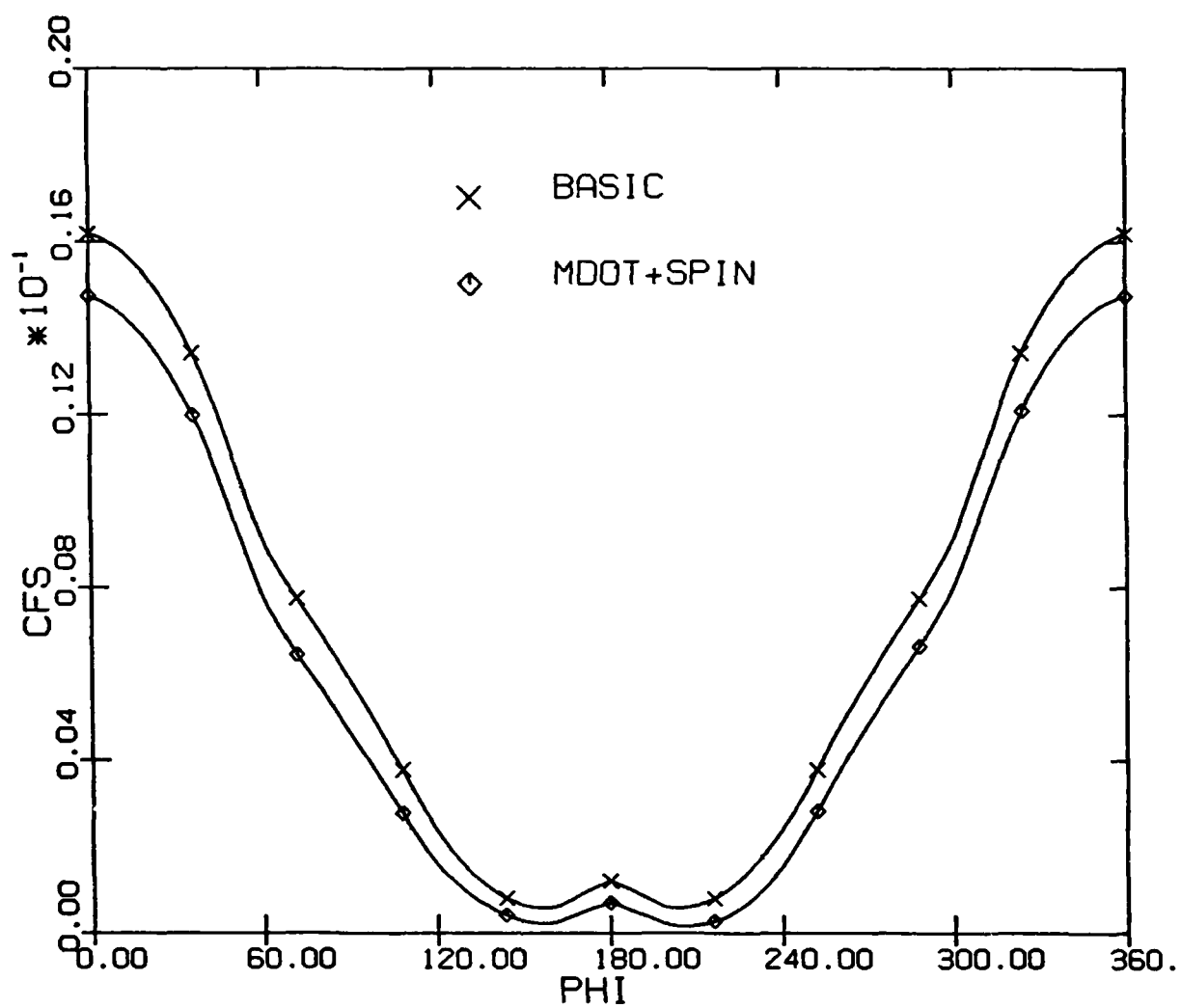
Figure 28: Case 2   Effects of mass transfer and spin on the streamwise
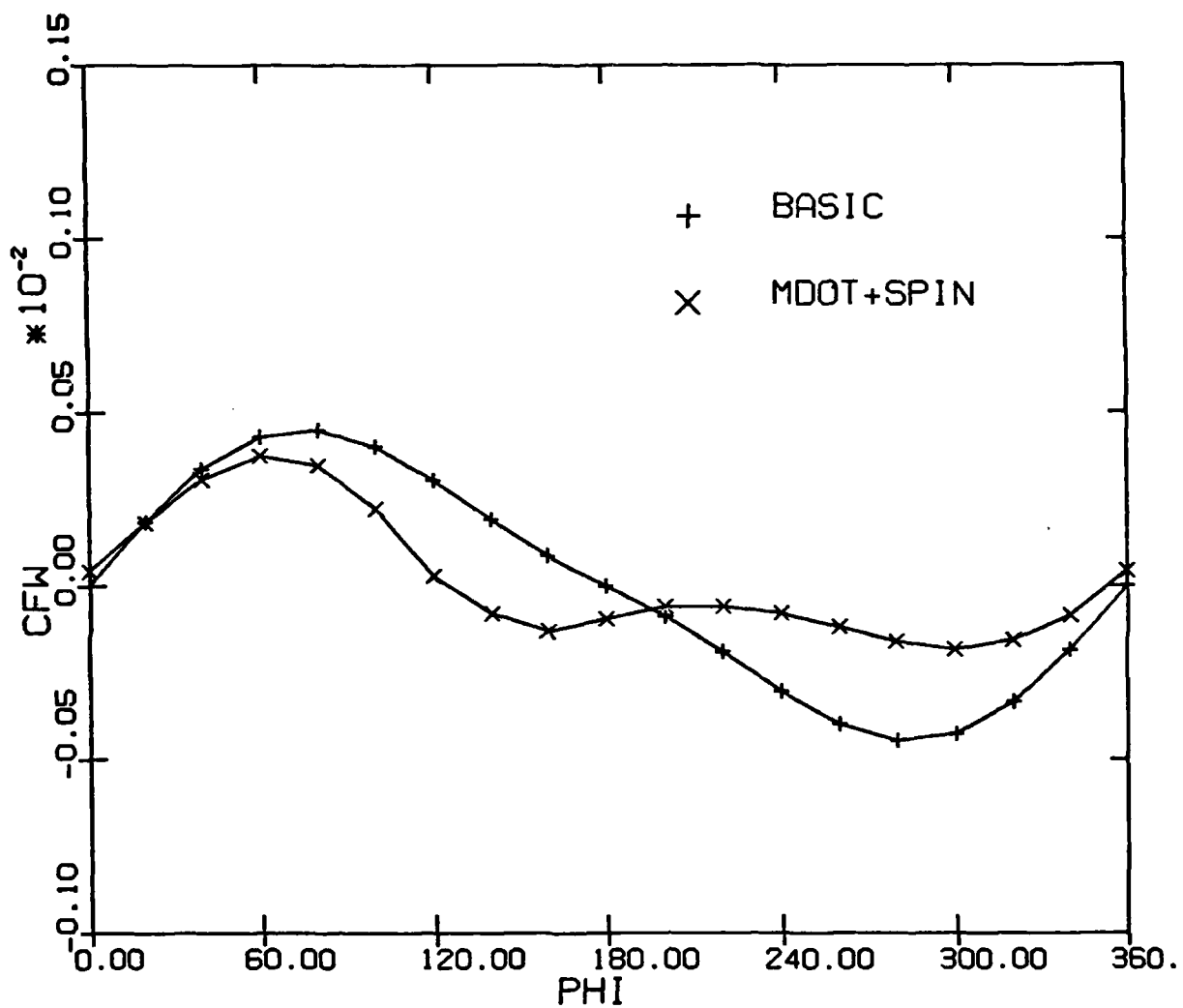sheat around the body at s = 30.06.
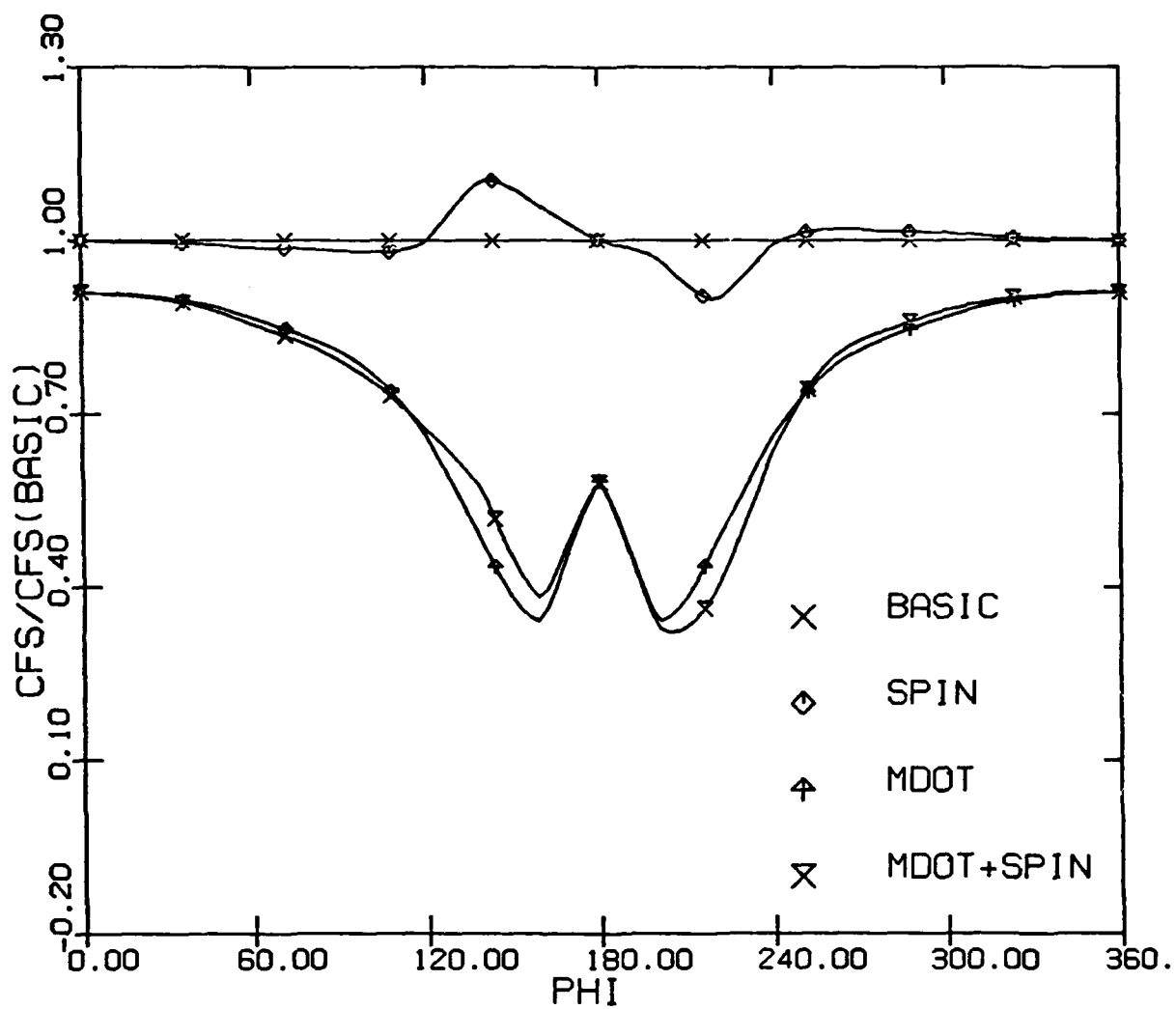
Figure 29: Case 2 Effects of mass transfer and/or spin on the
streamwise shear around the body at s = 30.06.
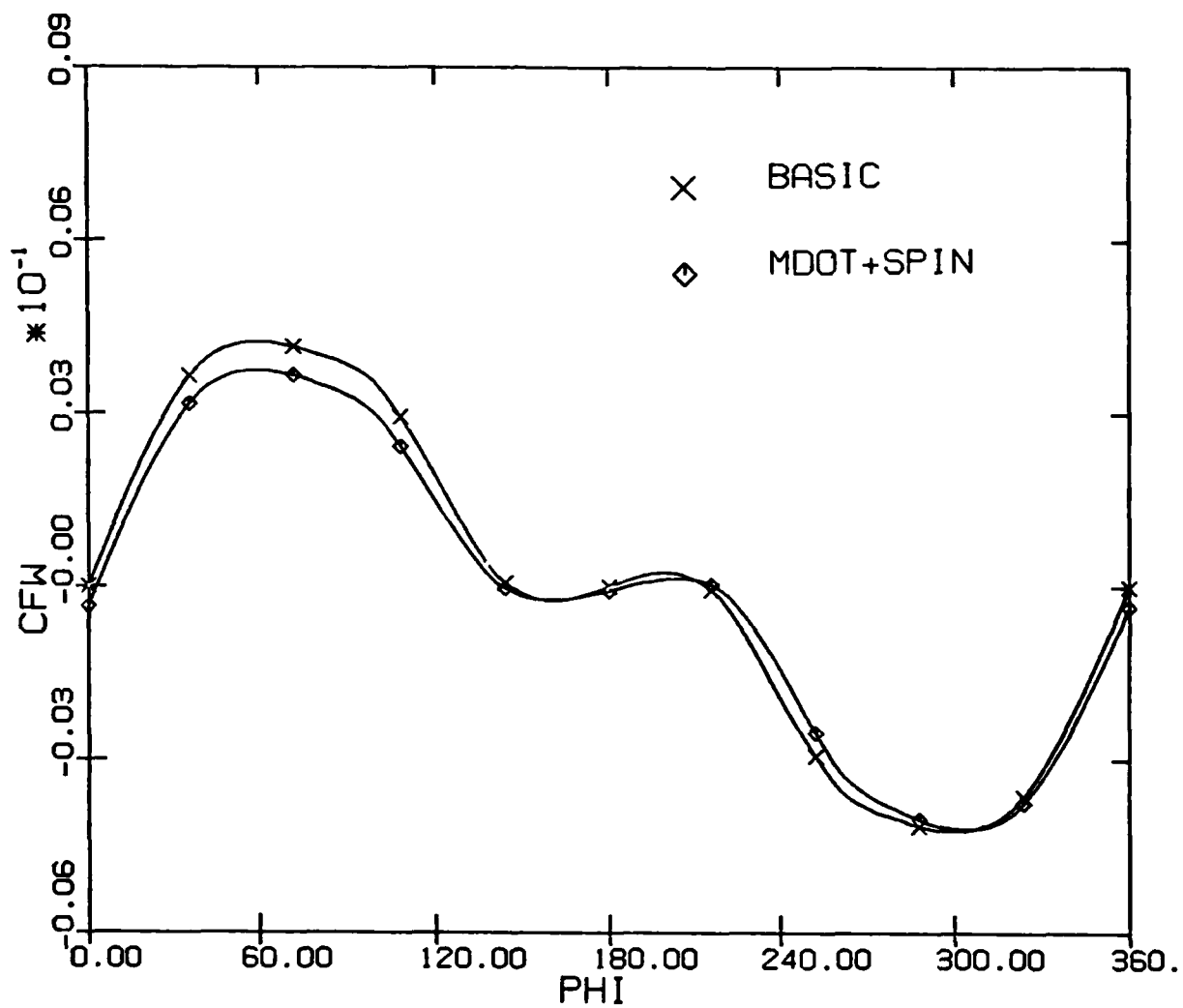
Figure 30: Case 2 Effects of mass transfer and spin on the crossflow shear around the body at s = 30.06.
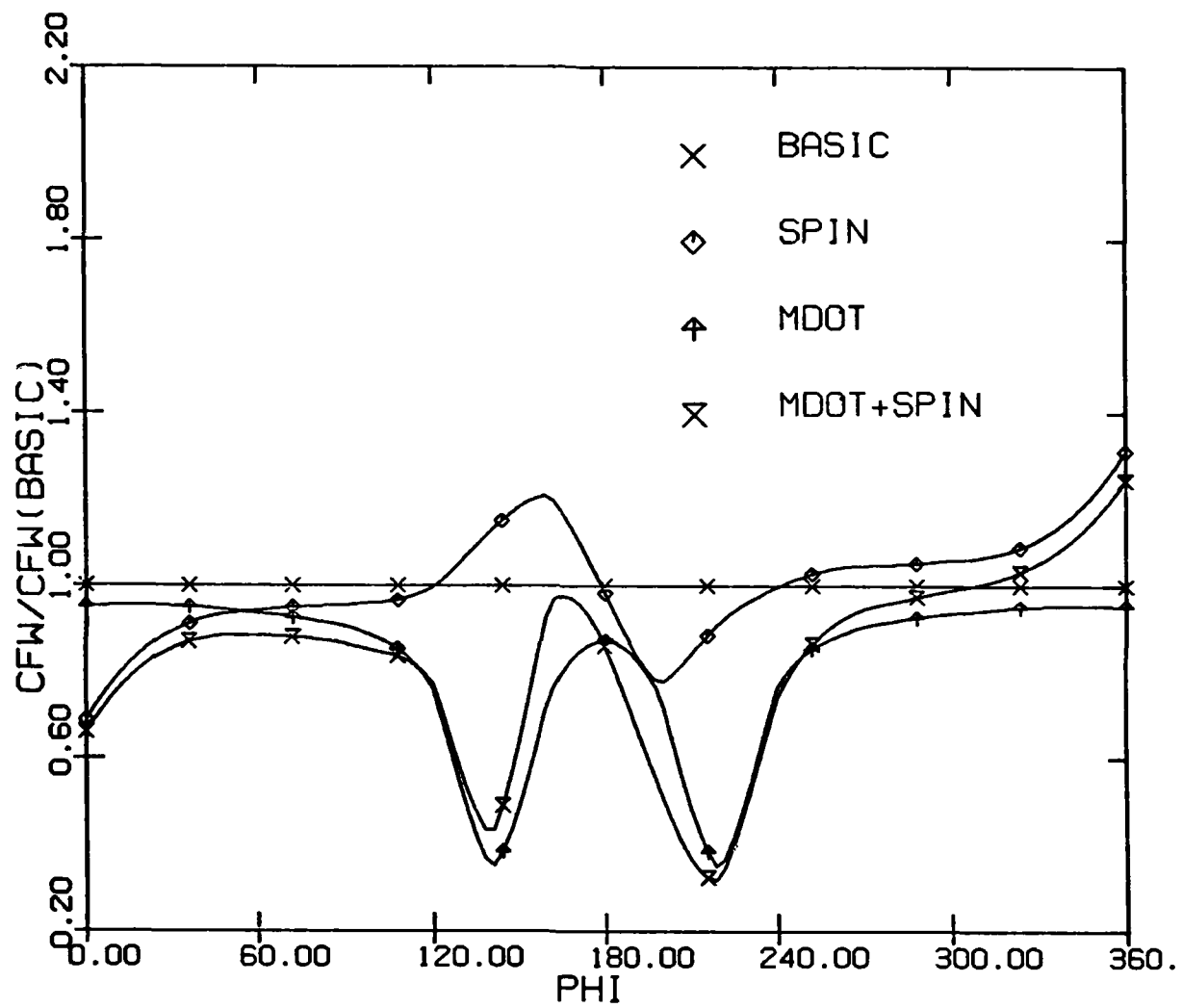
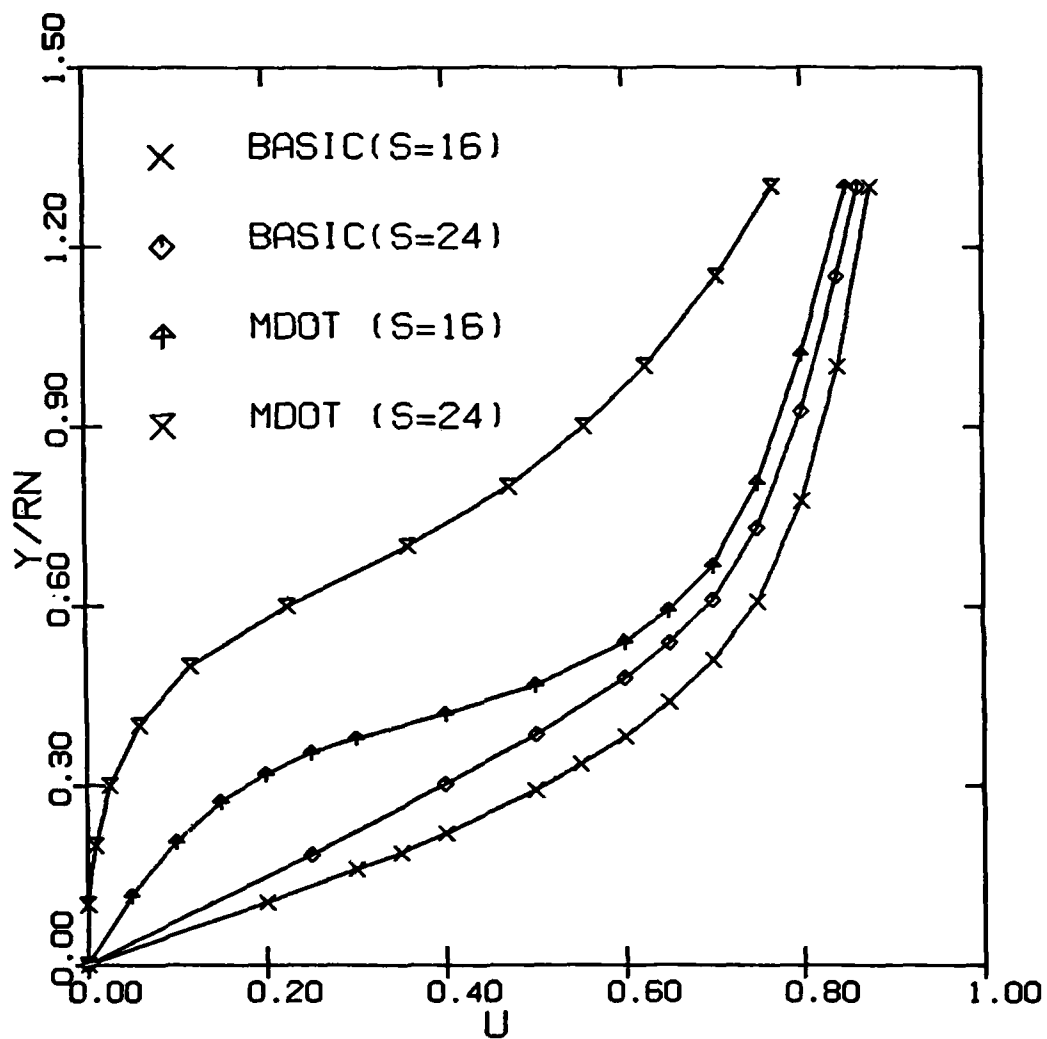Figure 31: Case 2 Effects of mass transfer and/or spin on the crossflow shear around the body at s = 30.06.
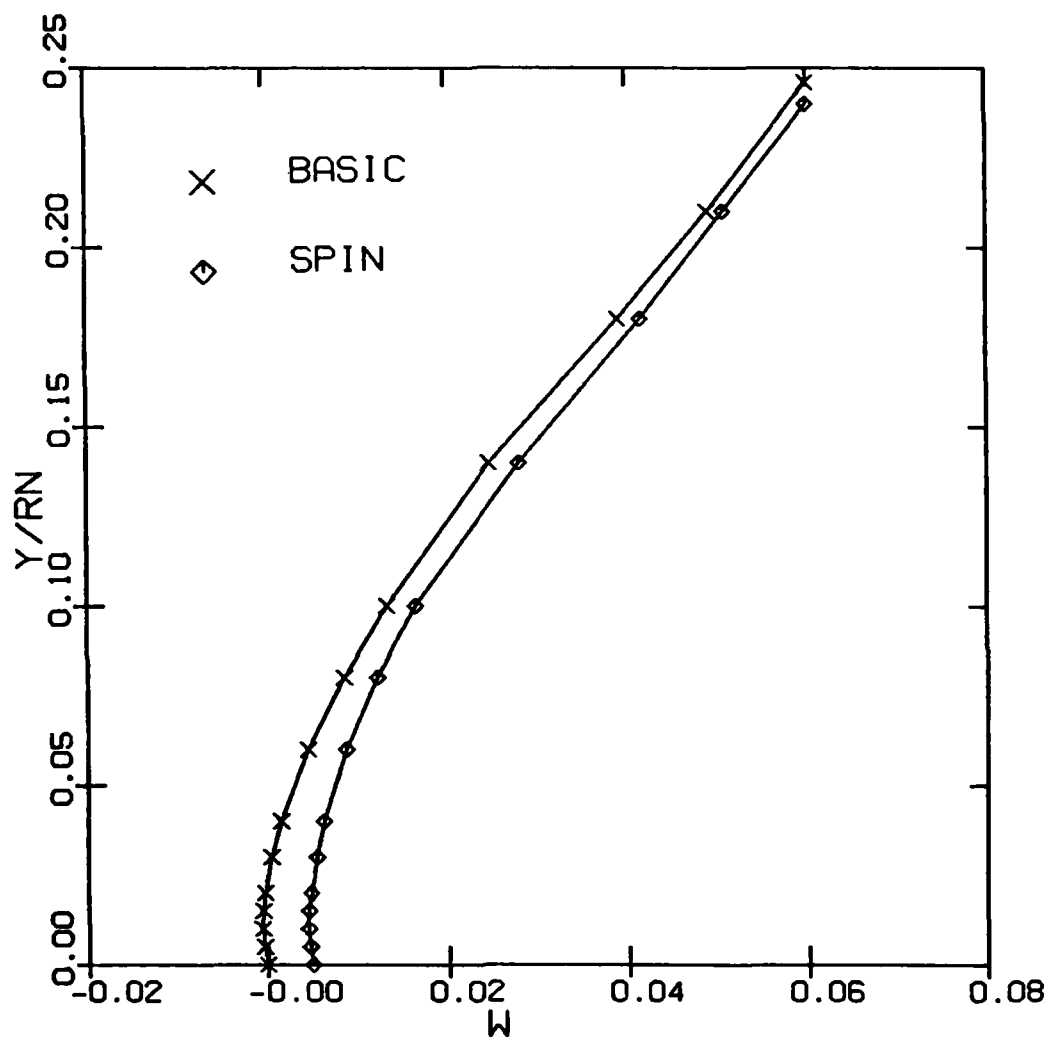
Figure 32: Case 2 Effect of spin on the crossflow velocity at
s = 6.40, ϕ = 160 deg
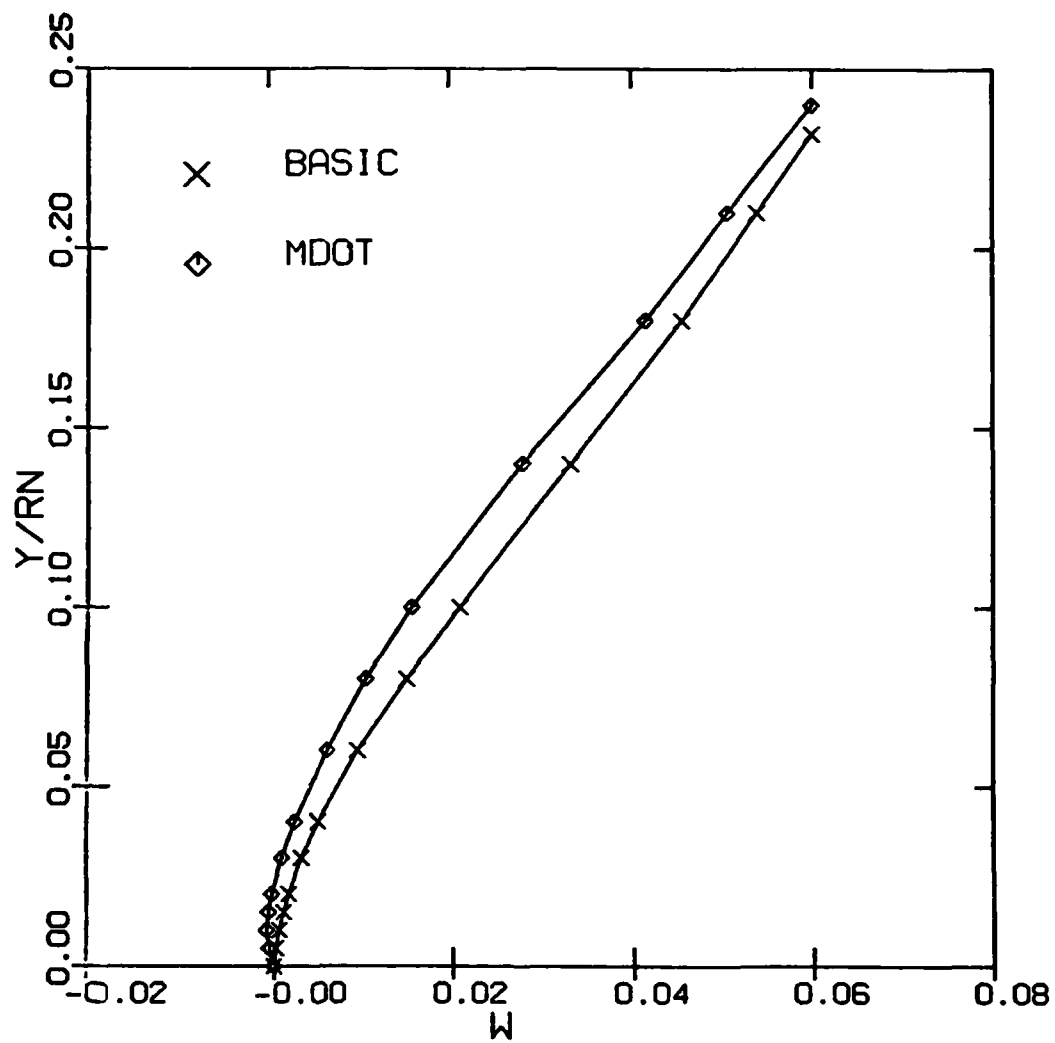
Figure 33: Case 2 Effect of mass transfer on the crossflow
velocity at s = 5.85, ϕ = 160 deg.

THREE-DIMENSIONAL VISCOUS SHOCK-LAYER ANALYSIS

OF LAMINAR OR TURBULENT FLOWS IN CHEMICAL EQUILIBRIUM

R. R. Thareja,[*] K. Y. Szema,[**] C. H. Lewis[†]

Virginia Polytechnic Institute and State University
Aerospace and Ocean Engineering Department
Blacksburg, Virginia

and

B. Denysyk[‡]

EG&G
Dahlgren, Virginia

ABSTRACT

A method has been developed to predict three-dimensional
hypersonic laminar or turbulent shock-layer flows for perfect
gas or equilibrium air. A two-layer eddy-viscosity model is
used for the turbulent regime. The thermodynamic and trans-
port properties for air are obtained by interpolation within
a two-dimensional table or from curve-fit data. Comparisons
are made for air in chemical equilibrium and perfect gas for
a seven-degree half-angle spherically blunted cone at various
flight altitudes with a cold, moderately cool and an adiabatic
wall for angles of attack up to twenty degrees. Wall heat
transfer, wall pressure, force and moment coefficients and ex-
ecution times are compared for some sample cases. This method
can be used to predict viscous flow in chemical equilibrium
over axisymmetric reentry vehicles at angles of attack up to
25 degrees.

INTRODUCTION

There is renewed interest in the problem of computing the hypersonic flow
past a blunt body under flight conditions. Due to the current interest in the
improved accuracy of ballistic and lifting reentry vehicles, a perfect gas
model can no longer accurately predict the thermodynamic and transport proper-
ties required for inviscid and viscous flowfield analyses. Earlier investigators

---

[*]Graduate Student
[**]Research Associate
[†]Professor
[‡]Department Head

used a table look-up procedure[1] or curve-fit data[2] to model the thermodynamic and transport properties of air in chemical equilibrium for viscous boundary-layer flows.

Reentry vehicles operate through a wide range of flow conditions. The complex flowfield is bounded by the body and the bow shock. Crossflow separation may be present, and the viscous effects may predominate over the entire flowfield. The full Navier-Stokes equations are elliptic in all three space directions, and a numerical solution is difficult and requires large computing times and storage. For moderately high values of Reynolds number, there is no need to solve the full Navier-Stokes equations.[3] The classical approach of dividing the flowfield into a viscous boundary-layer region and an outer inviscid region becomes inaccurate for reentry flowfields due to the presence of viscous effects throughout the entire flowfield. The parabolized Navier-Stokes (PNS) approach[3] uses a parabolic approximation in the streamwise direction. This involves large matrix solutions, and the computing times are still quite large. The viscous shock-layer (VSL) approach[4] developed by Murray and Lewis for three-dimensional flows is parabolic in both the stream-wise and crossflow directions. Since the crossflow momentum equation is parabolic, the crossflow separated region on the leeward side cannot be treated. The solution for the windward region up to crossflow separation is accurate, and the computing times are relatively small. In the viscous shock-layer solution, the entire flowfield from the body to the shock is treated with a uniform set of equations. The problems associated with the displacement thickness interaction and edge conditions are eliminated, with vorticity interaction present in the inviscid + boundary-layer approach. As a result, the viscous shock-layer method treats all higher-order boundary-layer effects (displacement, vorticity interaction, longitudinal and transverse curvature, including proper matching conditions) in a straight-forward and consistent manner, making the viscous shock-layer approach especially attractive for design studies.

Recently, a numerical method was developed to predict laminar, transitional and/or turbulent hypersonic flows for a perfect gas[5] over a blunt body at angle of attack. In that approach a two-layer eddy-viscosity model proposed by Cebeci[6] and the transition model developed by Dhawan and Narasimha[7] were used. This method has been extended to include the effect of air in chemical equilibrium. Results from a table look-up procedure and curve-fit methods have been compared with those from a perfect gas analysis. The table look-up procedure, described later, is known to model the thermodynamic properties of air quite accurately, while the transport properties are curve-fits of Hansen[8] data.

Numerical solutions are presented for a seven-degree half-angle spherically blunted cone at a flight velocity of 20,000 ft/sec at altitudes of 40,000, 80,000 and 160,000 ft with a cold (540R), moderately cool (3600R) and an adiabatic wall for angles of attack up to twenty degrees. Wall heat-transfer, wall pressure, force and moment coefficients, center of pressure locations and execution times are compared for perfect gas and air in chemical equilibrium for some sample cases.

ANALYSIS

The basic, three-dimensional, viscous shock-layer equations are derived from the steady Navier-Stokes equations in a surface-oriented coordinate system

(s,n,ϕ). The governing equations for turbulent flow are developed using methods analogous to those presented in References 9 and 10. The normal velocity v and normal coordinate n are assumed to be of order ϵ , and second-order terms are retained in the s-momentum, ϕ-momentum and energy equations. The nondimensional turbulent-conservative form of the equations in a body-oriented coordinate system can be found in Reference 5.

EQUATION OF STATE

$$\rho = \rho(p,h)$$

For a perfect gas, the above equation has the analytical form:

$$\rho = \gamma p/[(\gamma-1)T]$$

For a gas in chemical equilibrium, the functional relation may be given by a table or an approximating analytical expression (curve-fit) as discussed in the section on thermodynamic and transport properties.

The same equations are valid for laminar flow if the turbulent eddy-viscosity ϵ^+ is set to zero.

For perfect gas flows, since the Prandtl number is not a function of n, it can be taken out of the derivative in the energy equation. For flows in chemical equilibrium, the Prandtl number is a function of pressure and enthalpy and thus of n; therefore, it must be retained within the derivative term.

BOUNDARY CONDITIONS

Appropriate boundary conditions at the body surface and the shock must be specified for the set of governing equations. At the body surface or wall, no-slip and no temperature jump conditions are used. Thus, $u_w = v_w = w_w = 0$, and the wall temperature or heat-transfer rate is specified. The conditions immediately behind the shock are obtained from the Rankine-Hugoniot relations.

EDDY-VISCOSITY MODEL

For turbulent flow a two-layer eddy-viscosity model introduced by Cebeci[6] consisting of an inner law based upon Prandtl's mixing-length concept and the Klebanoff[11]-Clauser[12] expression for the outer law is used. Further details on the eddy-viscosity model can be found in Reference 5.

THERMODYNAMIC AND TRANSPORT PROPERTIES

For a perfect gas, the thermodynamic properties for specific heat and enthalpy can be expressed as

$$C_p = \gamma R/(\gamma-1)$$

$$h = C_p T$$

The viscosity is calculated from Sutherland's viscosity law:

$$\mu = 2.27 \text{ E-8 } T^{3/2}/(T + 198.6) \text{ slug/ft-sec}$$

The Prandtl number is assumed constant everywhere.

For air in chemical equilibrium a table look-up procedure or curve-fit data is used to provide the thermodynamic and transport properties as a function of the pressure and enthalpy.

TABLE LOOK-UP

A two-dimensional table was generated for the properties using the method developed by Miner, Anderson and Lewis.[1] For a given pressure and temperature, the enthalpy and density are determined using the reservoir calculations of Lordi.[14] The viscosity is obtained by curve-fits from the Wilke semi-emperical formula,[1] while the Prandtl number is obtained by interpolation of the Hansen data.[8]

COHEN CURVE-FITS

Curve-fit data are based on Cohen's fit[2] of Hansen's tables[8] for the transport properties and Moeckel tables[15] for the thermodynamic properties of equilibrium air.

Density: The enthalpy dependence of the density is given by the curve-fit:

$$\frac{\rho_E}{\rho} = 1.0 - 1.0477 \left[1.0 - \left(\frac{h}{h_E} \right)^{0.6123} \right]$$

This fit is reasonably good for the enthalpy range $0.0152 \leq h/h_E \leq 2.0$. The maximum deviation in this range is about 25 percent at low enthalpy, and the average deviation for all data is about six percent.

The pressure dependence is given by the following:

$$\frac{\rho_E}{\rho_C} = 0.0294 \left(\frac{p}{p_C} \right)^{0.965}$$

This fit has a deviation of less than one-half percent over the range of pressures $10^{-4} \leq p/p_C \leq 10$.

Viscosity: The enthalpy dependence for the viscosity-density product is given by the curve-fit:

$$\frac{\rho_E \mu_E}{\rho\mu} = 1.0 - 1.0213 \left[1.0 - \left(\frac{h}{h_E} \right)^{0.3329} \right]$$

This fit has better agreement than that for the density. The maximum deviation over the enthalpy range $0.0152 \leq h/h_E \leq 2.0$ is about 8 percent and the average deviation is about three percent.

For the pressure dependence the following was used:

$$\frac{\rho_E \mu_E}{\rho_C \mu_C} \approx 0.225 \left(\frac{p}{p_C}\right)^{0.992}$$

This fit too has a deviation of about one-half percent.

Prandtl Number: The dependence of Prandtl number on pressure is neglected, and its variation with enthalpy is assumed to be of the form shown in Figure 2, which is a fit of Hansen's data.[8] A pre-condition for the validity of an effective Prandtl number is that the gas must be in local thermodynamic equilibrium.

BADE CURVE-FITS

The density curve-fits from Cohen[2] are not in good agreement at low enthalpy. Better values of density are obtained using curve-fits suggested by Bade[16]

$$\frac{\rho}{\rho_B} = \left(\frac{p}{p_B}\right)\left(\frac{h}{h_B}\right)^{-x}$$

where,

$$x = 0.70 + 0.04 \log_{10} (p/p_B) \quad \text{if } 31.9 < h/RT_0 \leq 480$$

$$x = 0.94 \quad\quad\quad\quad\quad\quad \text{if } h/RT_0 \leq 31.9$$

The fits have a maximum deviation of seven percent.

The viscosity and Prandtl number are then evaluated as in the Cohen curve-fits.

REFERENCE QUANTITIES IN CURVE-FITS

The following reference quantities were used in the calculations:

$h_E = 2.119 \times 10^8 \text{ ft}^2/\text{sec}^2 = 8465 \text{ Btu/lbm}$

$p_C = 1.0 \text{ atm}$

$\mu_C = 3.584 \times 10^{-7} \text{ slugs/ft-sec}$

$\rho_C = 2.498 \times 10^{-3} \text{ slugs/ft}^3$

$\rho_B = 0.01 \text{ lb/ft}^3$

$h_B = 1080 \text{ Btu/lb} = 31.9 \text{ RT}_0$

$p_B = 1.0 \text{ atm}$

METHOD OF SOLUTION

Davis[17] presented an implicit finite-difference method to solve the viscous shock-layer equations for axially symmetric flows. Murray and Lewis[4] extended the method of solution to three-dimensional, high angle of attack conditions. The present method of solution is identical to that of Murray and Lewis. Therefore, only an overview of the solution procedure is presented here.

The equations are written in the standard form

$$A_0 \frac{\partial^2 W}{\partial \eta^2} + A_1 \frac{\partial W}{\partial \eta} + A_2 W + A_3 + A_4 \frac{\partial W}{\partial s} + A_5 \frac{\partial W}{\partial \phi} = 0$$

The derivatives are evaluated by the finite-difference expressions used by Frieders and Lewis[18] and substituted into the parabolic equation giving the standard finite-difference form. The difference equation can be solved by the method developed by Richtmyer.

The continuity and normal momentum equations are solved by a similar method, but they are coupled together. Finally, the shock-standoff distance is evaluated by integrating the continuity equation as discussed by Murray and Lewis.[4]

The solution begins on the spherically-blunted nose by obtaining an axi-symmetric solution in the wind-fixed coordinate system. At a specified location, the axisymmetric solution is rotated into the body-fixed coordinates and used as the initial profile for the three-dimensional solution. The three-dimensional solution begins on the windward plane and marches around the body obtaining a converged solution at each ϕ step. After completing a sweep in ϕ, the procedure then steps downstream in s and begins the next ϕ sweep. At each point the equations are solved in the following order: (i) ϕ-momentum, (ii) energy, (iii) s-momentum, (iv) integration of continuity for n_{sh} and (v) the coupled continuity and normal momentum equations.

RESULTS AND DISCUSSION

The freestream conditions used for the three altitudes are tabulated in Table 1, while the sample cases presented are shown in Table 2. The flow was assumed to be turbulent at 40,000 feet and laminar at 80,000 and 160,000 feet altitudes. The dimensions of the seven-degree half-angle spherically blunted cone are shown in Figure 1. The angles of attack considered were 0, 2, 10 and 20 degrees. The three wall conditions were a cold wall (540R), a cool wall (3600R) and an adiabatic wall.

TEST CASE RESULTS

A wide range of conditions was attempted, but since the variations were similar, only a few sample results are presented.

There is a significant change in the shock standoff distance for perfect gas and air in chemical equilibrium (Figure 3). The shock-layer thickness is

nearly the same for all options of the equilibrium properties.

Case A ($\alpha = 0$ degrees):

The streamwise variation of wall pressure with altitude shows very little differences (Figure 4) at 40,000 and 80,000 feet altitudes, but lower values are predicted for 160,000 feet. These values are nearly identical for all the gas models except within the nose region.

The streamwise variation of wall heat-transfer rate is shown in Figure 5 for all the cases. In general, the perfect gas and table look-up values are the lowest and highest respectively, with the Cohen and Bade values lying in between.

The variation of streamwise skin-friction coefficient shows trends similar to those for the wall heat-transfer rate. For some cases, the Cohen and Bade results do not lie within the band of perfect gas and table look-up values.

The force and moment data (Table 3) show a nine percent difference in the axial force coefficients from the perfect gas and table look-up results, while these differences are quite small for the Cohen and Bade results.

Case B ($\alpha = 2$ degrees)

The variation of the wall pressure for the windward plane is shown in Figure 7. The pressures from the table look-up and Bade options are nearly identical. On the spherical nose, the differences between perfect gas and table look-up are substantial, and after tending together for some distance, they again tend to diverge.

The wall heat-transfer rate for the windward plane from the perfect gas prediction is about ten percent less than the table look-up results (Figure 8) and diverges downstream. The difference between the table look-up and Bade data is fairly small (within two percent).

The streamwise skin-friction coefficient shows results similar to the wall heat-transfer rate (Figure 9) data.

The transverse variation of wall pressure (Figure 10), wall heat-transfer rate (Figure 11), streamwise (Figure 12) and transverse (Figure 13) skin-friction coefficients show similar trends.

The variations in the force and moment data for one case are shown in Table 4. The inviscid axial and normal force coefficients for perfect gas conditions are four and twelve percent less than the table look-up results, while the viscous axial and normal force coefficients are nine and sixteen percent less. The variation of the center of pressure is about two percent. The differences between the table look-up and Bade results are much smaller and quite acceptable.

Case C ($\alpha = 10$ degrees)

The variation of wall pressure for the windward plane does not show the

divergence noted earlier, but substantial differences are observed in the nose region (Figure 14).

The streamwise skin-friction coefficient (Figure 15) shows good agreement for this case.

The transverse variation of wall pressure (Figure 16) shows large differences on the leeward side. Due to crossflow separation, data are not available up to the leeward plane. The differences in streamwise skin-friction coefficient are nearly constant in the transverse direction at a downstream section (Figure 17). The transverse variation of the transverse skin-friction coefficient is shown in Figure 18.

The force and moment data for this case are shown in Table 5. The differences between perfect gas and the table look-up results are much smaller. The axial force coefficient for perfect gas conditions is seven percent less than the table look-up results, while the center of pressure locations are within about one percent.

Case D (α = 20 degrees)

The streamwise variations for all the quantities are similar to those for Case C. At the same section there is earlier crossflow separation due to the higher angle of attack.

The transverse variations of wall pressure (Figure 19), wall heat-transfer rate (Figure 20), streamwise (Figure 21) and transverse (Figure 22) skin-friction coefficients are also similar.

The axial force coefficient for perfect gas is six percent less than the table look-up results (Table 6), while the center of pressure location is nearly the same.

Computing Times Required

Computing times given in the tables are with the table look-up time as a reference of 100. Due to the absence of some input/output for the perfect gas model, the time for this condition is slightly lower than the Cohen and Bade options. If one omits the extra printout, the curve-fit of equilibrium properties and perfect gas computing times are very comparable and result in a sixty percent reduction in the computing time required for the table look-up model.

For low values of wall temperature, since all the equilibrium models essentially use Sutherland's viscosity and the density from the table look-up and Bade options is in good agreement, the differences in the wall heat-transfer rate are probably due to the differences in the Prandtl number.

CONCLUSIONS

In general, wall heat-transfer rate differences between the perfect gas and table look-up results are about ten percent, while the axial force coefficients differ by five to fifteen percent. Large pressure differences in the

nose region (which constitutes a significant percentage of the frontal area) probably cause the large differences in axial force.

Curve-fits can be effectively used to model the thermodynamic and transport properties of air in chemical equilibrium producing reasonably good force and moment coefficient predictions and with computing times that are comparable to the perfect gas model. The differences in wall heat-transfer rate for equilibrium flow are probably caused by the differences in Prandtl number.

Since there are considerable differences between the perfect gas and equilibrium air results, the viscous shock-layer method just developed should be used to predict viscous flows in chemical equilibrium, such as for reentry conditions, with good accuracy and within reasonable computing times.

NOMENCLATURE

C_{f_s}	skin-friction coefficient in the streamwise direction
C_{f_ϕ}	skin-friction coefficient in the transverse direction
C_p	constant pressure specific heat
h	static enthalpy, h^*/U_∞^2
H	total enthalpy, $h + (u^2 + v^2 + w^2)/2$
k_t	eddy thermal conductivity, $-\overline{(\rho v)'h'}/(\varepsilon^2 \partial h/\partial n)$
M	Mach number
n_{sh}	shock-standoff distance, n_{sh}^*/R^*
p	pressure, $p^*/\rho_\infty U_\infty^2$
Pr	Prandtl number
Pr_t	turbulent Prandtl number, $C_p \mu_t/k_t$
Q	convective heating rate, Btu/ft^2-sec
r	distance from and normal to the body axis, r^*/R^*
R^*	body nose radius
s, n, ϕ	general surface-normal coordinate system streamwise, normal and crossflow directions
T	temperature
T_{ref}^*	reference temperature, U_∞^2/C_p^*

u,v,w	streamwise, normal and crossflow velocity components nondimensionalized by the freestream velocity, U_∞^*
W	dependent variable
α	angle of attack
γ	ratio of specific heat
ϵ	Reynolds number parameter, $\epsilon^2 = \mu_{ref}^*/\rho_\infty U_\infty R^*$
ϵ^+	μ_t/μ
θ	body angle in the streamwise direction
μ	viscosity, μ^*/μ_{ref}^*
μ_{ref}^*	reference viscosity, $\mu^*(T_{ref})$
μ_t	eddy viscosity, $\overline{-(\rho v)' u'}/(\epsilon^2 \partial u/\partial n)$
ρ	density, ρ^*/ρ_∞

Subscripts

B	Bade
C	Cohen
INV	Inviscid
s	Streamwise
sh	conditions behind the bow shock wave
t	turbulent quantity
w	wall condition
∞	dimensional freestream conditions
ϕ	transverse

Superscripts

*	dimensional quantity
´	fluctuating value

REFERENCES

1. Miner, E. W., Anderson, E. C. and Lewis, C. H.: "A Computer Program for Two Dimensional and Axisymmetric Nonreacting Perfect Gas and Equilibrium Chemically Reacting Laminar Transitional and/or Turbulent Boundary-Layer Flows," VPI-E-71-8, May 1971.

2. Cohen, N. B.: "Correlation Formulas and Tables of Density and Some Thermodynamic Properties of Equilibrium Dissociating Air for Use in Solutions of the Boundary-Layer Equations," NASA TN D-194, February 1960.

3. Lubard, S. C. and Helliwell, W. S.: "Calculation of the Flow on a Cone at High Angle of Attack," AIAA J., Vol. 12, July 1974, pp. 965-974.

4. Murray, A. L. and Lewis, C. H.: "Hypersonic Three-Dimensional Viscous Shock-Layer Flow over Blunt Bodies," AIAA J., Vol. 16, No. 12, pp. 1279-1286, December 1978.

5. Szema, K. Y. and Lewis, C. H.: "Three-Dimensional Hypersonic Laminar, Transitional and/or Turbulent Shock-Layer Flows," AIAA Paper No. 80-1457, July 1980.

6. Cebeci, T.: "Behavior of Turbulent Flows near a Porous Wall with Pressure Gradient," AIAA J., Vol. 8, No. 12, pp. 2152-2156, December 1970.

7. Dhawan, S. and Narasimha, R.: "Some Properties of Boundary Layer Flow During the Transition from Laminar to Turbulent Motion," Journal of Fluid Mechanics, Vol. 3, pt. 4, pp. 418-436, January 1958.

8. Hansen, C. F.: "Approximations for the Thermodynamic and Transport Properties of High Temperature Air," NASA TR R-50, 1959.

9. Cebeci, T. and Smith, M. O.: Analysis of Turbulent Boundary Layers, Academic Press, 1974

10. Anderson, C., Moss, J. N. and Sutton, K.: "Turbulent Viscous Shock-Layer Solutions with Strong Vorticity Interaction," AIAA Paper No. 76-120, January 1976.

11. Klebanoff, P. S.: "Characteristics of Turbulence in a Boundary Layer with Zero Pressure Gradient," NASA Report 1247, 1955.

12. Clauser, F. H.: "The Turbulent Boundary Layer," Advances in Applied Mechanics, H. L. Dryden and Th. von Karman, Eds., Academic Press, 1956, pp. 1-15.

13. White, F. M.: Viscous Fluid Flow, McGraw-Hill Book Company, 1974.

14. Lordi, J. A., Mates, R. E. and Moselle, J. R.: "A Computer Program for the Numerical Solution of Non-equilibrium Expansions of Reacting Gas Mixtures," CAL RPT No. AD-K89-A-6, 1965.

15. Moeckel, W. E. and Weston, K. C.: "Composition and Thermodynamic Properties of Air in Chemical Equilibrium," NACA TN 4265, 1958.

16. Bade, W. L.: "Simple Analytical Approximation to the Equation of State of Dissociating Air," *ARS Journal*, Vol. 29, No. 4, April 1959.

17. Davis, R. T.: "Numerical Solution of the Hypersonic Viscous Shock Layer Equations," *AIAA J.*, Vol. 8, No. 5, pp. 843-851, May 1970.

18. Frieders, M. C. and Lewis, C. H.: "Effects of Mass Transfer into Laminar and Turbulent Boundary Layers over Cones at Angle of Attack," VPI-AERO-031, March 1975.

TABLE 1. Freestream Conditions

	40,000	80,000	160,000
Altitude, h(feet)	40,000	80,000	160,000
M_∞	20.6	20.4	18.4
Velocity, U_∞(ft/sec)	20,000	20,000	20,000
Pressure, p_∞(lb/ft^2)	393.085	58.505	1.942
Temperature, T_∞(R)	389.97	397.69	487.17
Density, ρ_∞ (slug/ft^3)	5.873E-4	8.571E-5	2.322E-6
Reynolds Number (per foot)	3.955E7	5.679E6	1.305E5

TABLE 2. Test Cases

Case	α (degrees)	Alt (feet)	T_w (R)	T_w/T_∞	Flow
A	0	80,000	540	1.36	Laminar
B	2	40,000	3600	9.16	Turbulent
C	10	80,000	Adiabatic	–	Laminar
D	20	80,000	540	1.36	Laminar

TABLE 3. Force and Moment Data (Case A)

$\alpha = 0$ deg, Alt = 80,000 feet, T_w = 540R, S/R = 30

| | Actual Values | | | |
	PG	TLU	COHEN	BADE
$C_{A_{INV}}$	0.070216	0.076465	0.076465	0.076465
C_{A_P}	0.06831	0.07538	0.07509	0.07557
$C_{A_{SF}}$	0.00251	0.00245	0.00209	0.00218
$C_{A_{TOT}}$	0.070824	0.077835	0.077176	0.077757
TIME* (Sec)	72	233	102	100

| | Percent Variation Based on TLU | | |
	PG	COHEN	BADE
$C_{A_{INV}}$	8.2	0.0	0.0
C_{A_P}	9.4	0.4	-0.3
$C_{A_{SF}}$	-2.4	14.7	11.0
$C_{A_{TOT}}$	9.0	0.8	0.1
TIME[†]	33	44	43

*IBM 370/3032 with FORTHX COMPILER (OPT2)

[†]Based on TLU=100

II-255

TABLE 4. Force and Moment Data (Case B)

$\alpha = 2$ deg, Alt = 40,000 feet, $T_w = 3600^\circ R$ S/R = 32

	Actual Values			Percent Variation Based on TLU	
	PG	TLU	BADE	PG	BADE
$c_{A_{INV}}$	0.06331120	0.0654952	0.0654952	3.3	0.0
$c_{N_{INV}}$	0.0345556	0.0392156	0.0392156	11.9	0.0
c_A	0.071163	0.078564	0.078414	9.4	0.2
c_N	0.032386	0.038607	0.038653	16.1	-0.1
c_M	-0.021207	-0.025800	-0.025856	17.8	-0.2
z_{cp}/L	0.654814	0.668288	0.668924	2.0	-0.1
$c_{A_{SF}}$	0.00595	0.00744	0.00710	20.0	4.6
c_{A_P}	0.06521	0.07112	0.07132	8.3	-0.3
TIME	1778*	5203*	2384*	34[+]	46[+]

*Seconds, IBM 370/3032 with FORTHX COMPILER (OPT2)

[+]Based on TLU=100

TABLE 5. Force and Moment Data (Case C)

α = 10 deg, Alt = 80,000 ft, T_w = Adiabatic, S/R = 32

| | Actual Values | | Percent Variation Based on TLU |
	PG	TLU	PG
$C_{A_{INV}}$	0.094359	0.097347	3.1
$C_{N_{INV}}$	0.296715	0.302710	2.0
C_A	0.099410	0.106954	7.1
C_N	0.302246	0.299984	-0.8
C_M	-0.198296	-0.194445	-2.0
Z_{cp}/L	0.656076	0.648185	-1.2
$C_{A_{SF}}$	0.00433	0.00482	10.2
C_{A_P}	0.09508	0.10214	6.9

TABLE 6. Force and Moment Data (Case D)

α = 20 deg, Alt = 80,000 ft, T_w = 540R, S/R = 32

| | Actual Values | | Percent Variation Based on TLU |
	PG	TLU	PG
$C_{A_{INV}}$	0.151591	0.155653	2.6
$C_{N_{INV}}$	0.716164	0.727595	1.6
C_A	0.159610	0.170116	6.2
C_N	0.719390	0.732410	1.8
C_M	-0.450558	-0.459907	2.0
Z_{cp}/L	0.626305	0.627937	0.3
$C_{A_{SF}}$	0.00613	0.00644	4.8
C_{A_P}	0.15348	0.16368	6.2
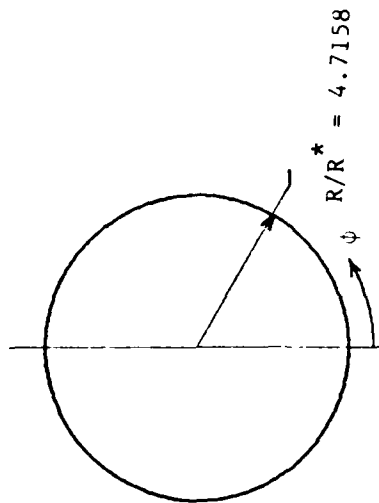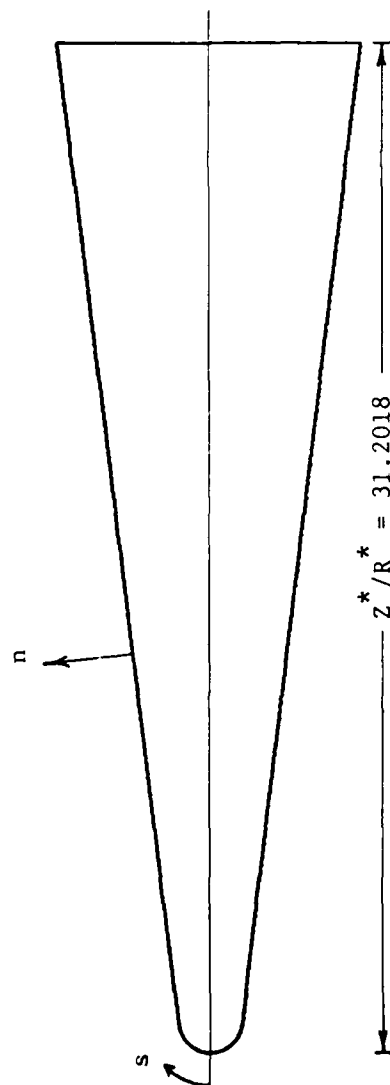
Figure 1. Non-Dimensional Body Geometry and Coordinate System

θ_c = 7 degrees

R/R^* = 4.7158

ϕ

z^*/R^* = 31.2018

n

s
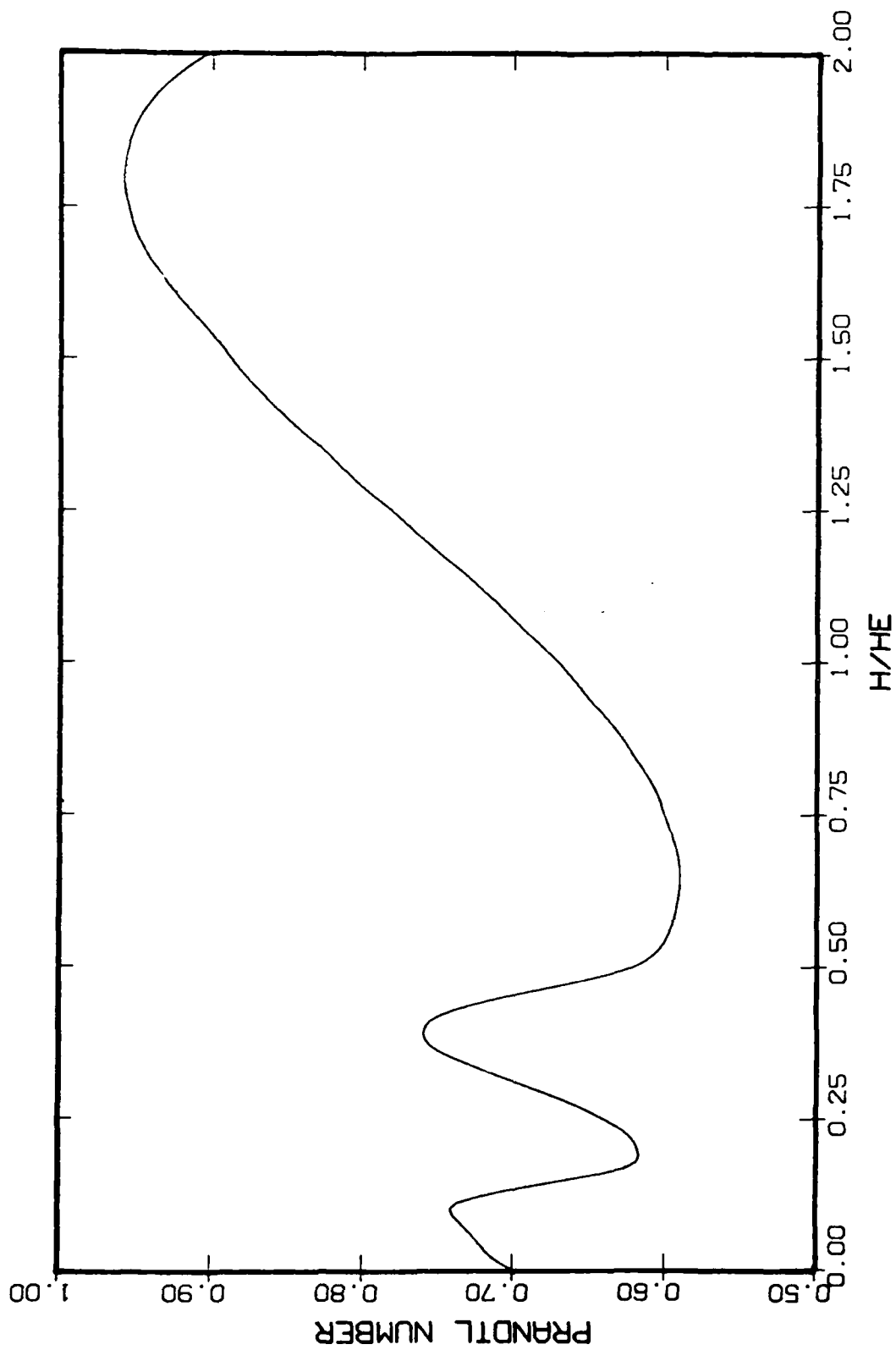
Figure 2. Prandtl Number Variation with Enthalpy Ratio (Cohen and Bade Options)
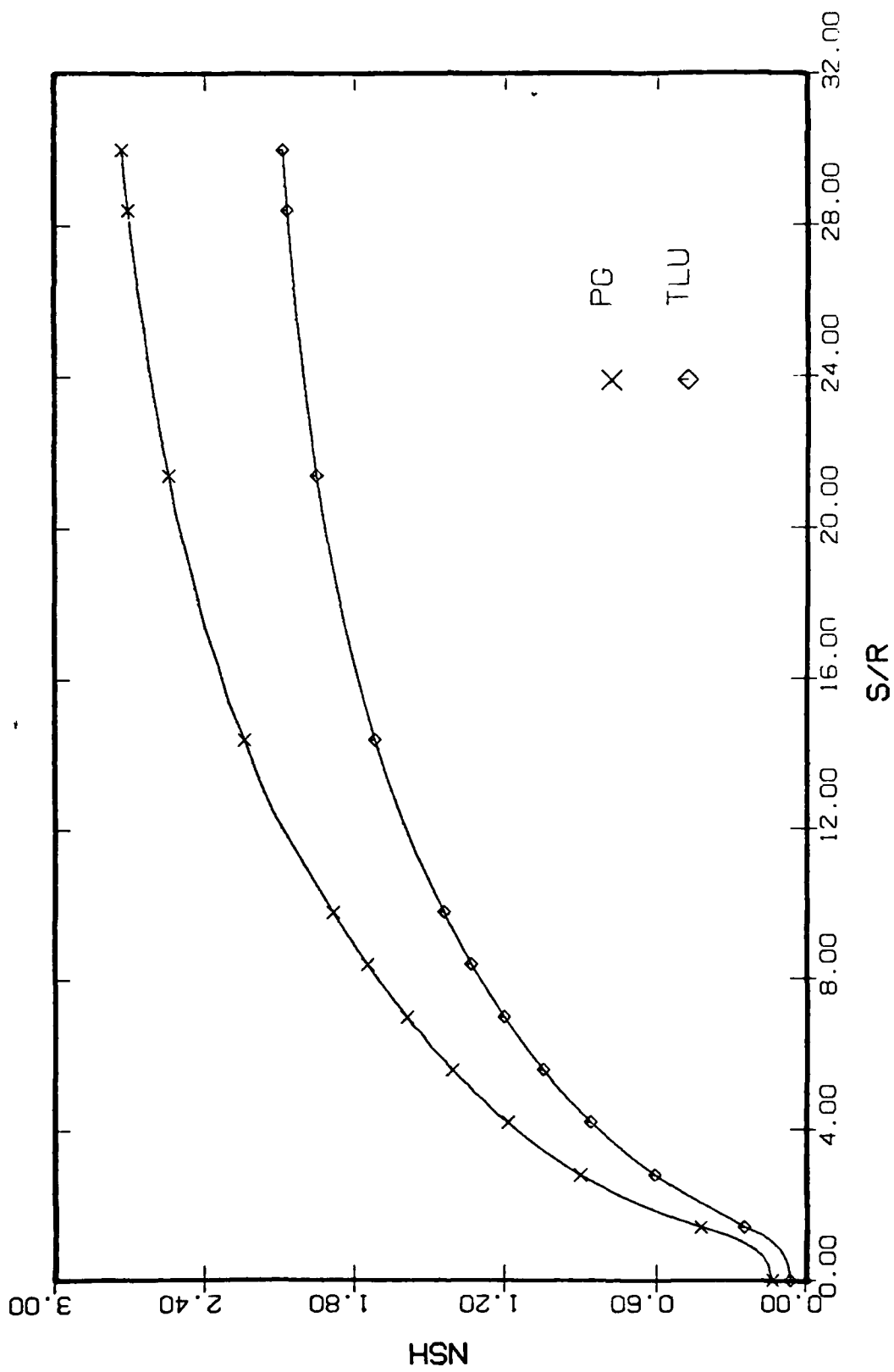
Figure 3. Streamwise Variation of Shock Standoff Distance (Case A, α = 0 deg, Alt = 160,000 ft, T_w = 3600R)
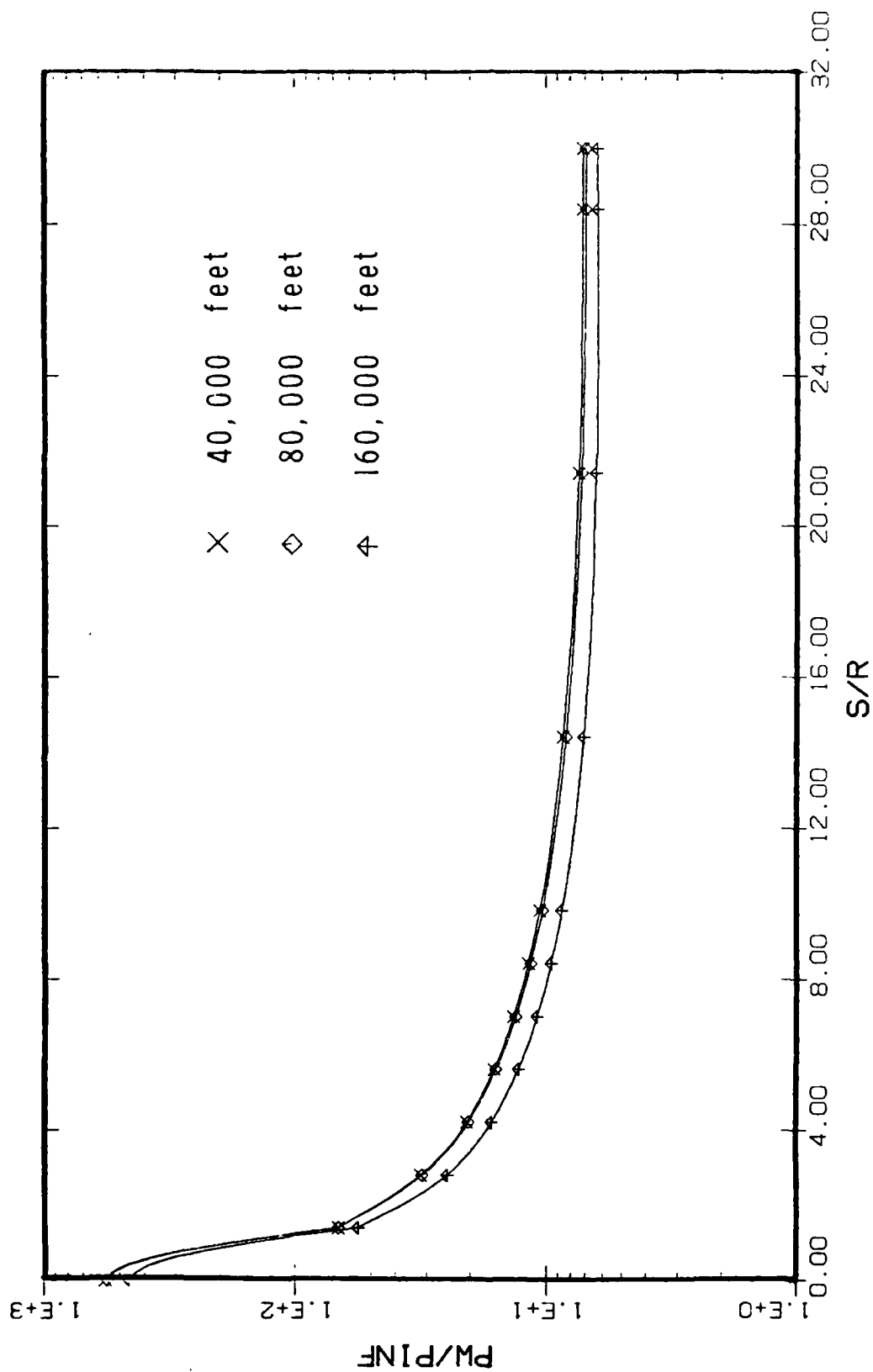
Figure 4. Streamwise Variation of Wall Pressure (Case A, α = 0 deg, Alt = 40,000, 80,000 and 160,000 ft, T_w = 540R)
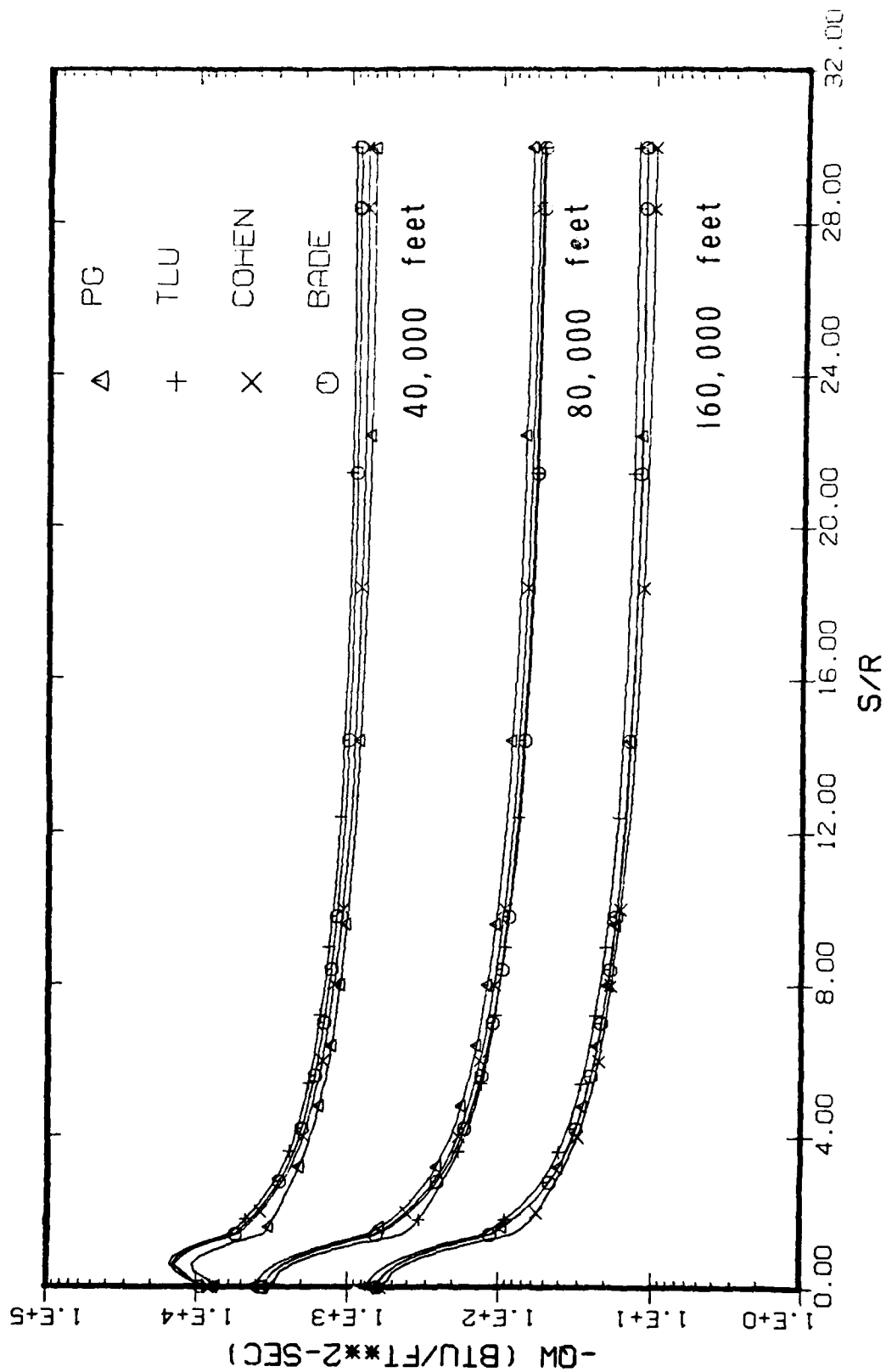
Figure 5. Streamwise Variation of Wall Heat-Transfer Rate (Case A, $\alpha = 0$ deg, Alt = 40,000, 80,000 and 160,000 ft, $T_w = 540R$)
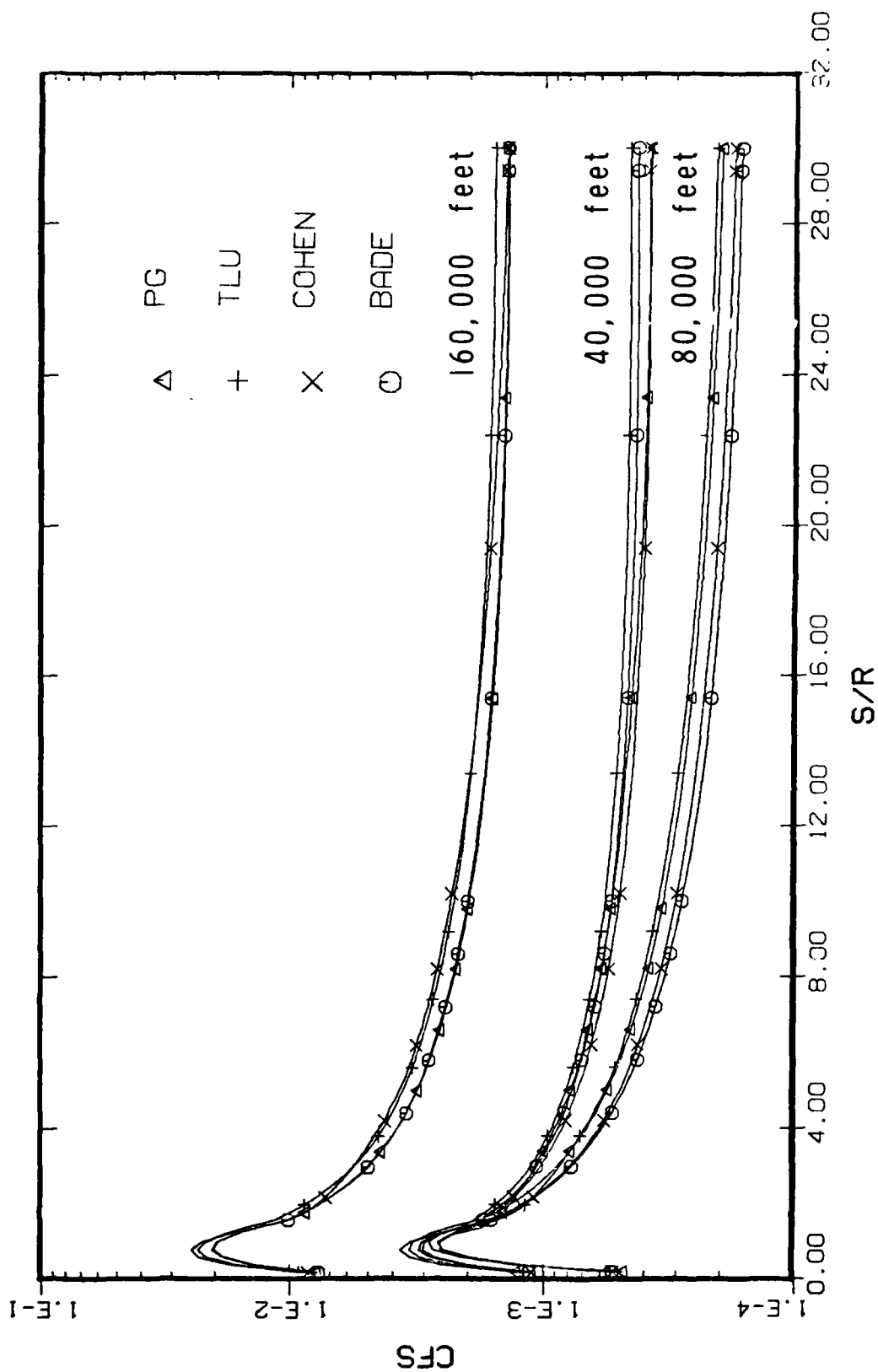
Figure 6. Streamwise Variation of C_{f_s} (Case A, $\alpha = 0$ deg, Alt = 40,000, 80,000 and 160,000 ft, $T_w = 540R$)
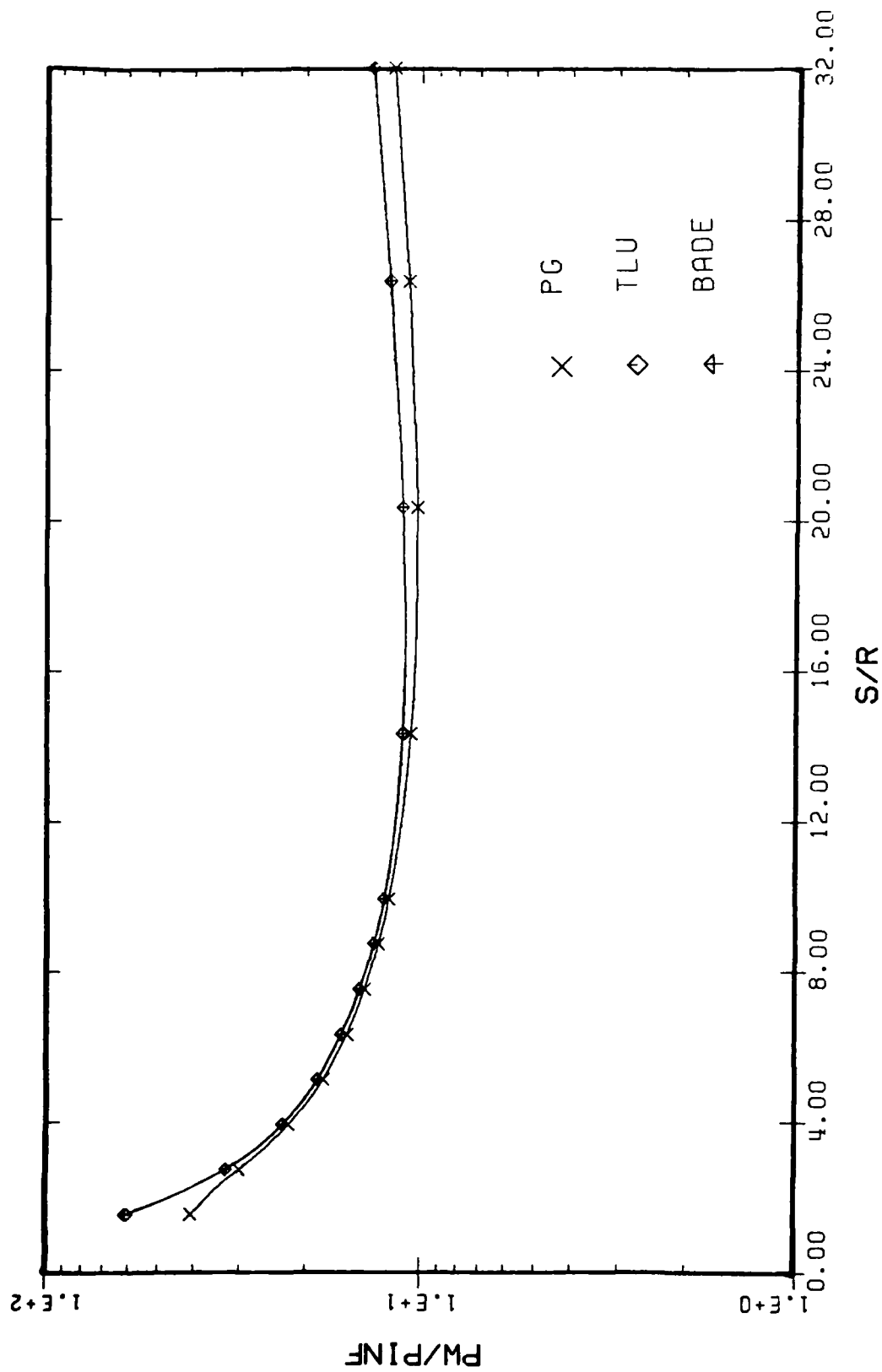
Figure 7. Streamwise Variation of Wall Pressure for $\phi = 0$ Plane
(Case B, $\alpha = 2$ deg, Alt $= 40,000$ ft, $T_w = 3600R$)
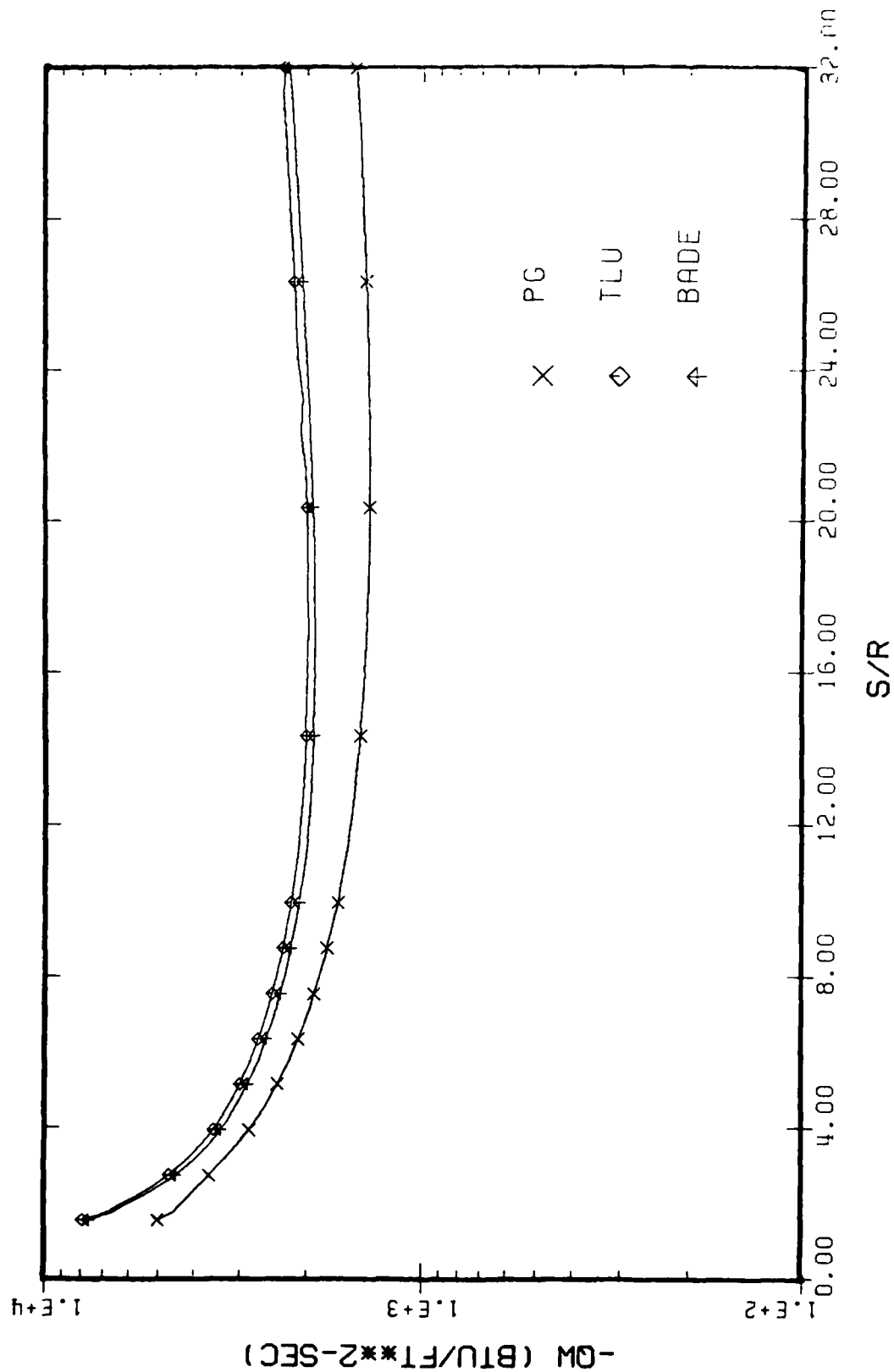
Figure 8. Streamwise Variation of Wall Heat-Transfer Rate for $\phi = 0$ Plane
(Case B, $\alpha = 2$ deg, Alt = 40,000 ft, $T_w = 3600R$)
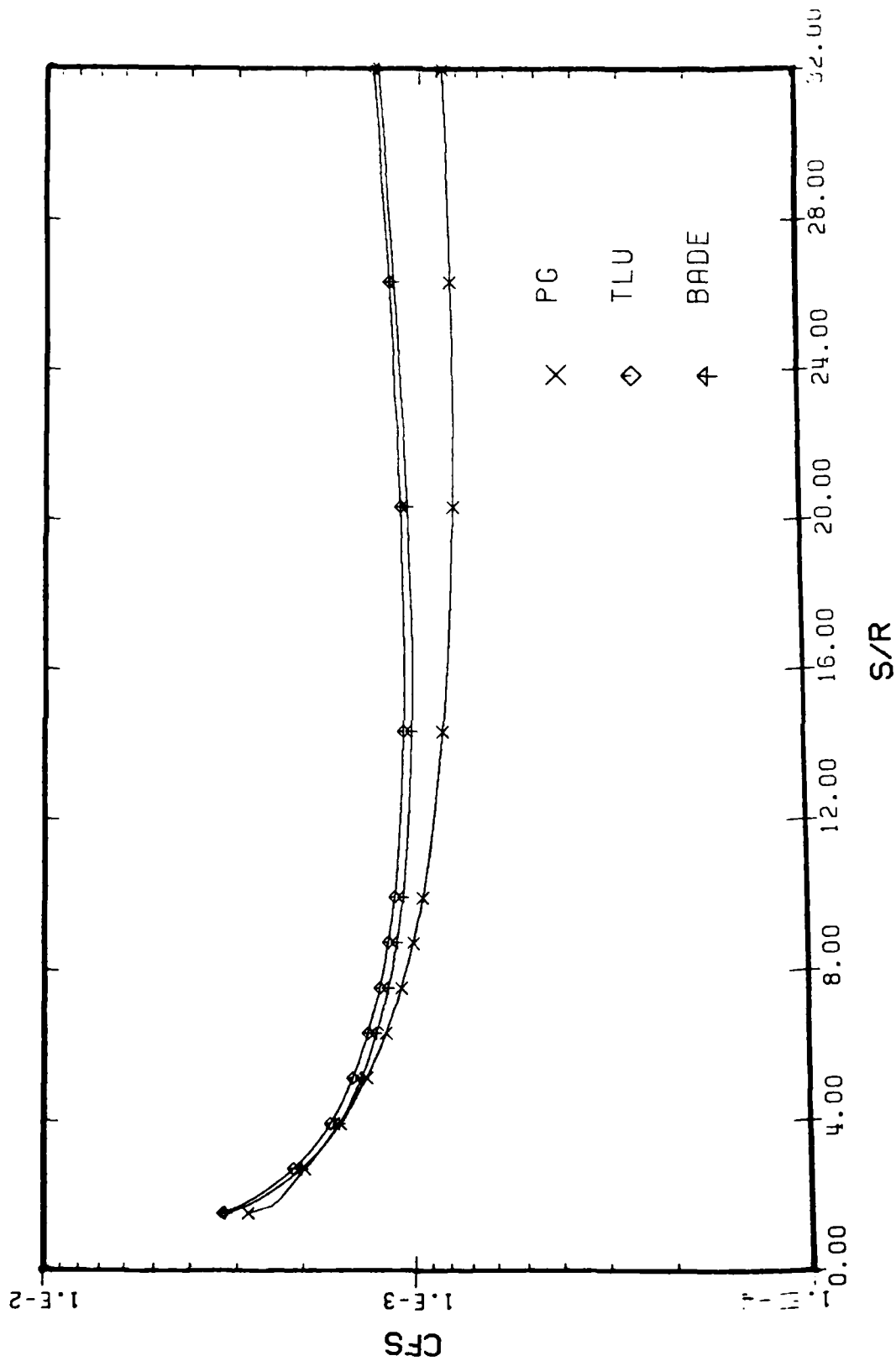
Figure 9. Streamwise Variation of Cf_s for $\phi = 0$ Plane (Case B, $\alpha = 2$ deg, Alt = 40,000 ft, $T_w = 3600R$)
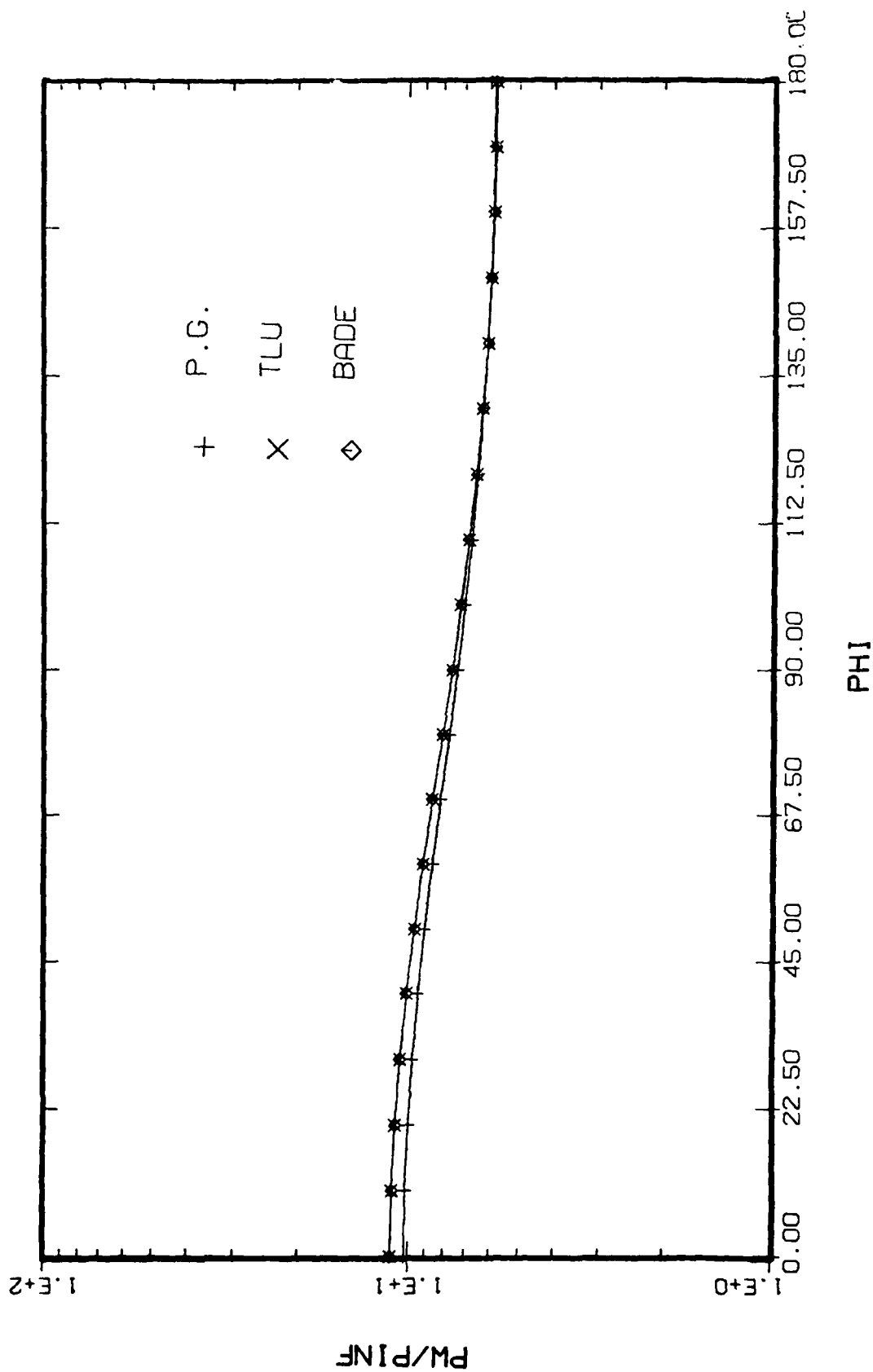
Figure 10. Transverse Variation of Wall Pressure at S/R = 20 (Case B, α = 2 deg, Alt = 40,000 ft, T_w = 3600R)
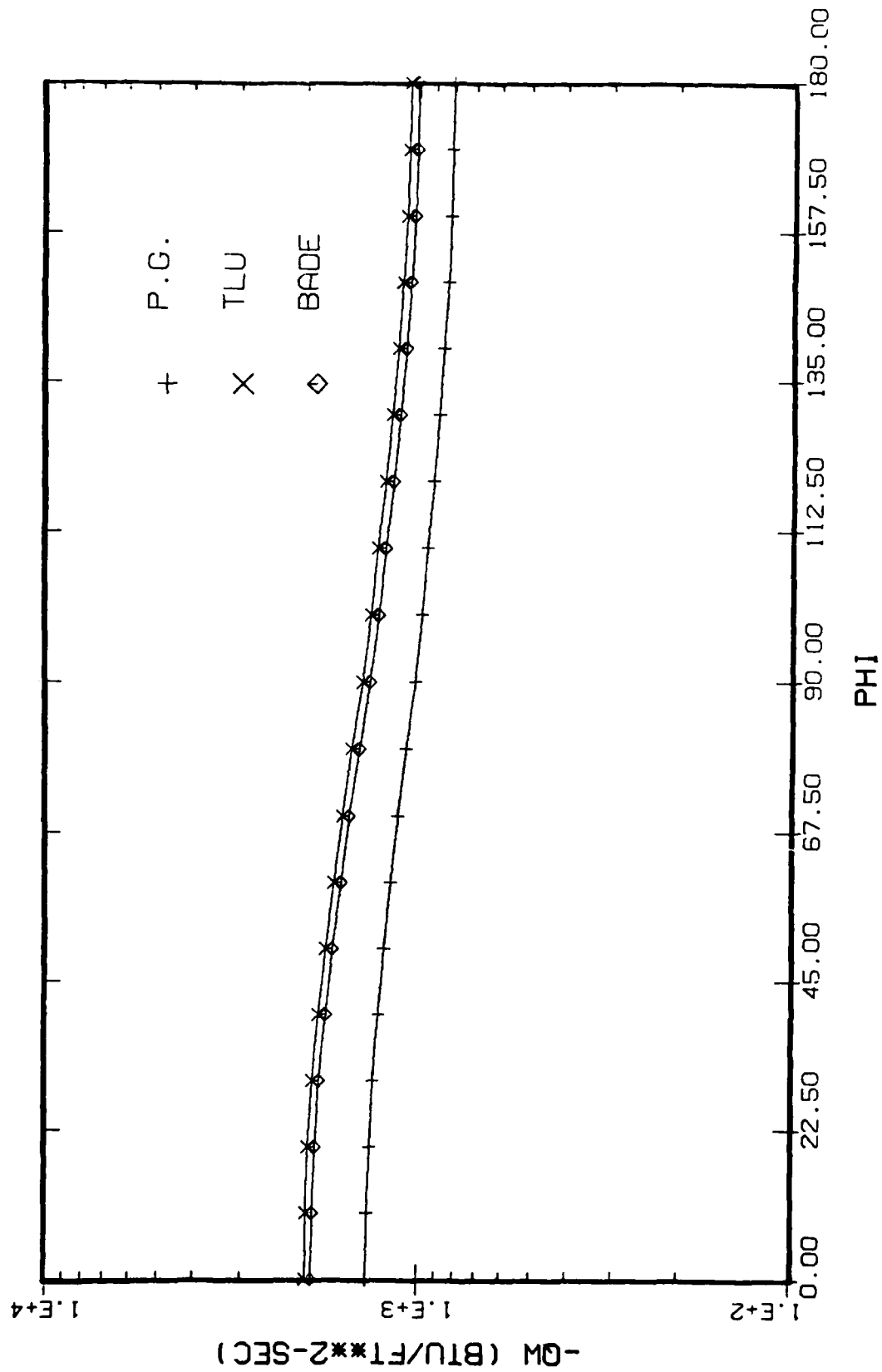
Figure 11. Transverse Variation of Wall Heat-Transfer Rate at S/R = 20 (Case B, α = 2 deg, Alt = 40,000 ft, T_w = 3600R)

Figure 12. Transverse Variation of C_{f} at $S/R = 20$
(Case B, α = 2 deg, Alt = 40,000 ft, T_{w} = 3600R)

Figure 13. Transverse Variation of $C_{f\phi}$ at S/R = 20
(Case B, α = 2 deg, Alt = 40,000 ft, T_w = 3600R)

Figure 14. Streamwise Variation of Wall Pressure for $\phi = 0$ Plane
(Case C, $\alpha = 10$ deg, Alt = 80,000 ft, T_w = Adiabatic)
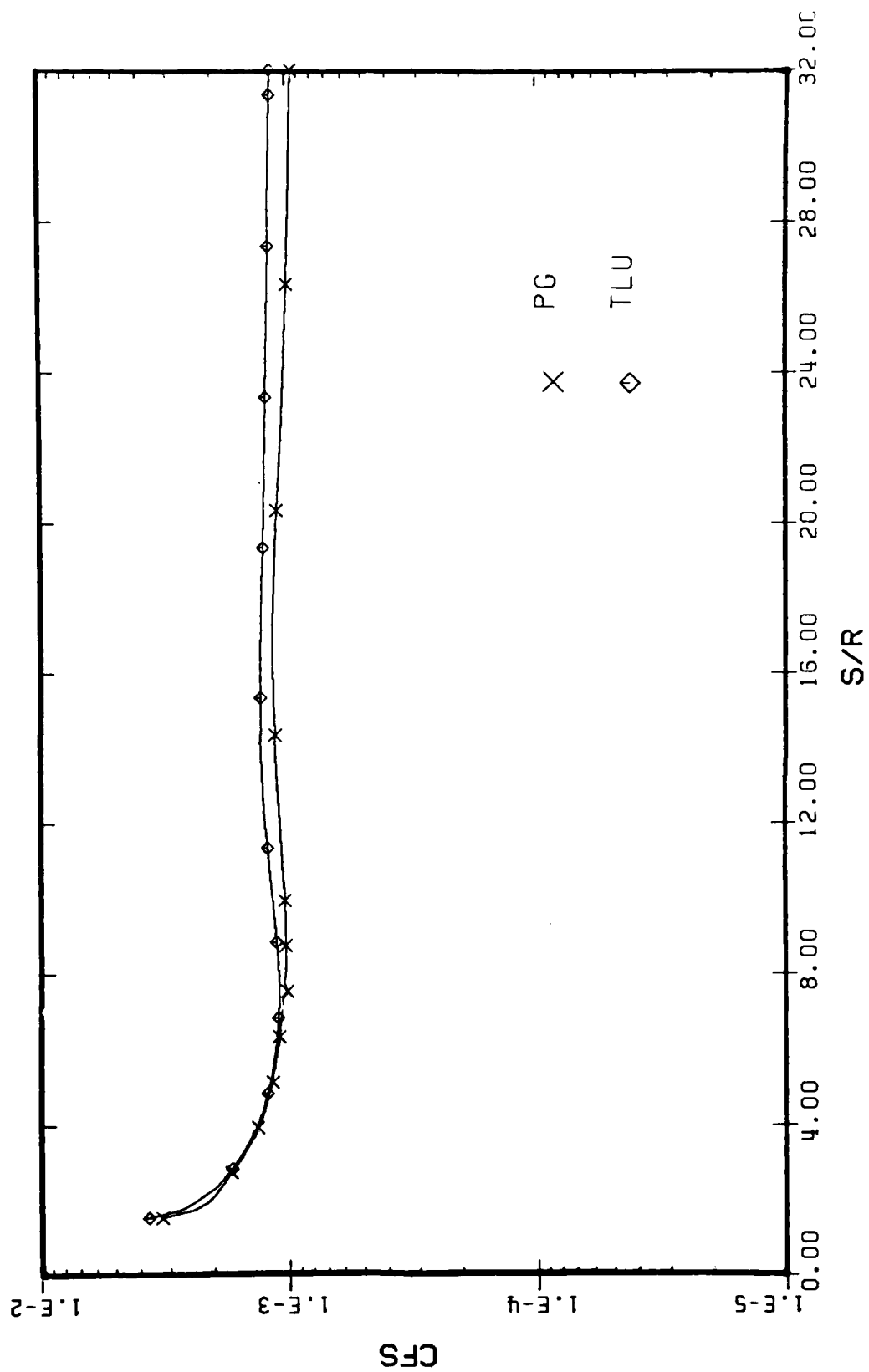
Figure 15. Streamwise Variation of C_{f_s} for $\phi = 0$ Plane (Case C, $\alpha = 10$ deg, Alt = 80,000 ft, T_w = Adiabatic)
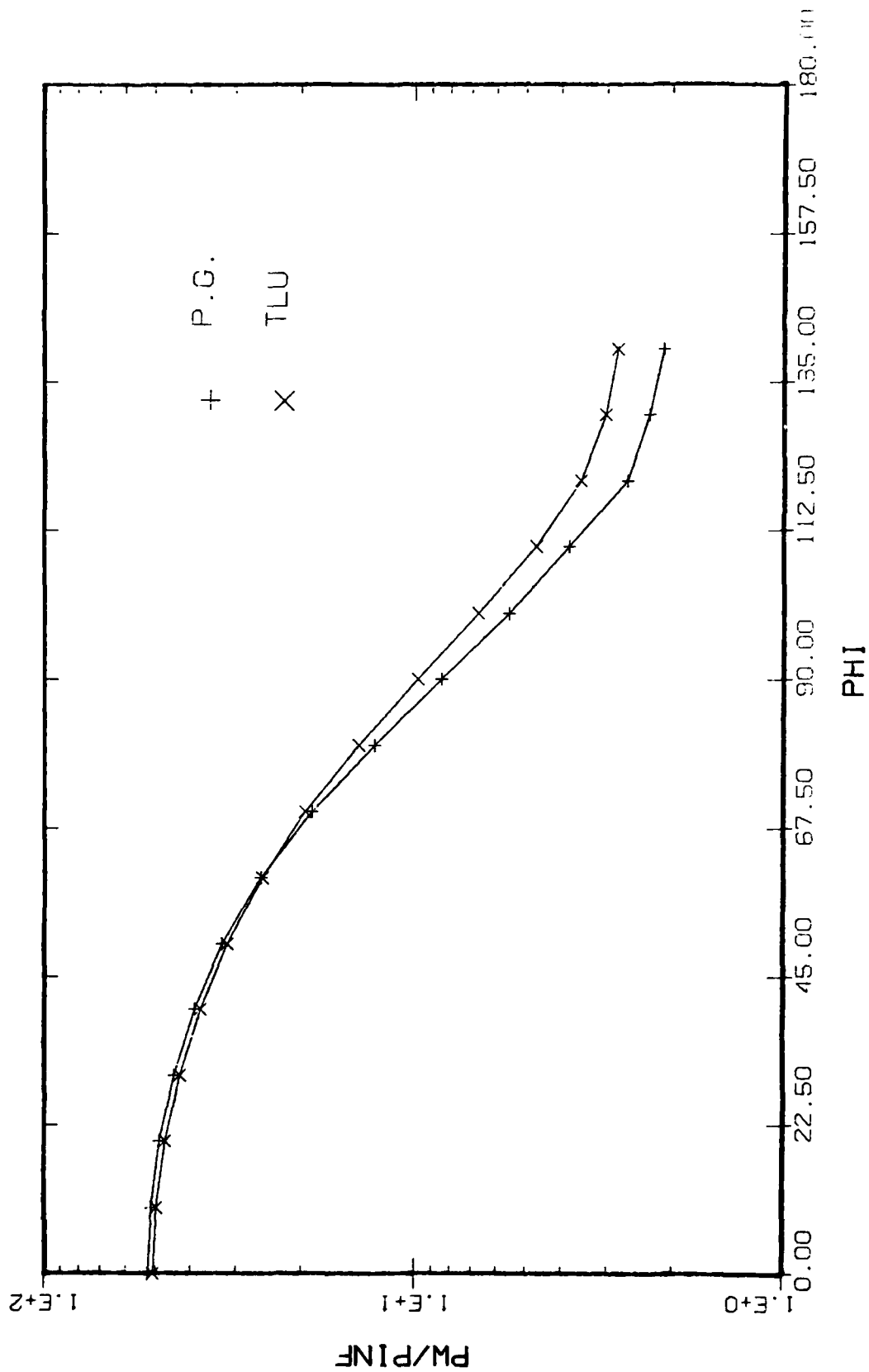
Figure 16.   Transverse Variation of Wall Pressure at S/R = 20
(Case C, α = 10 deg, Alt = 80,000 ft, T_w = Adiabatic)

Figure 17. Transverse Variation of C_{f_s} at S/R = 20
(Case C, α = 10 deg, Alt = 80,000 ft, T_w = Adiabatic)

II-275

Figure 18. Transverse Variation of C_{f_ϕ} at $S/R = 20$
(Case C, $\alpha = 10$ deg, Alt = 80,000 ft, T_w = Adiabatic)
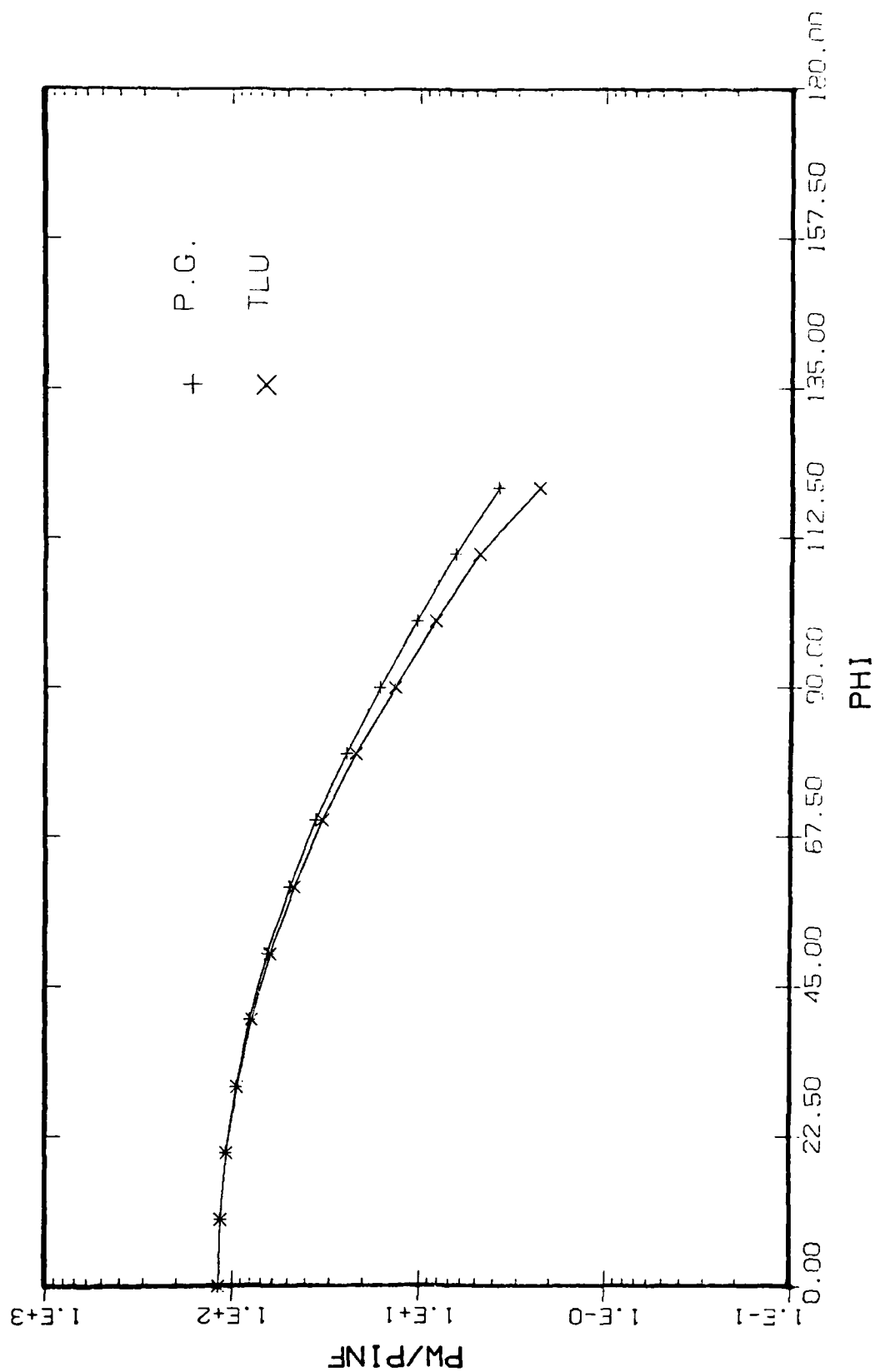
Figure 19. Transverse Variation of Wall Pressure at $S/R = 20$ (Case D, $\alpha = 20$ deg, Alt = 80,000 ft, $T_w = 540R$)
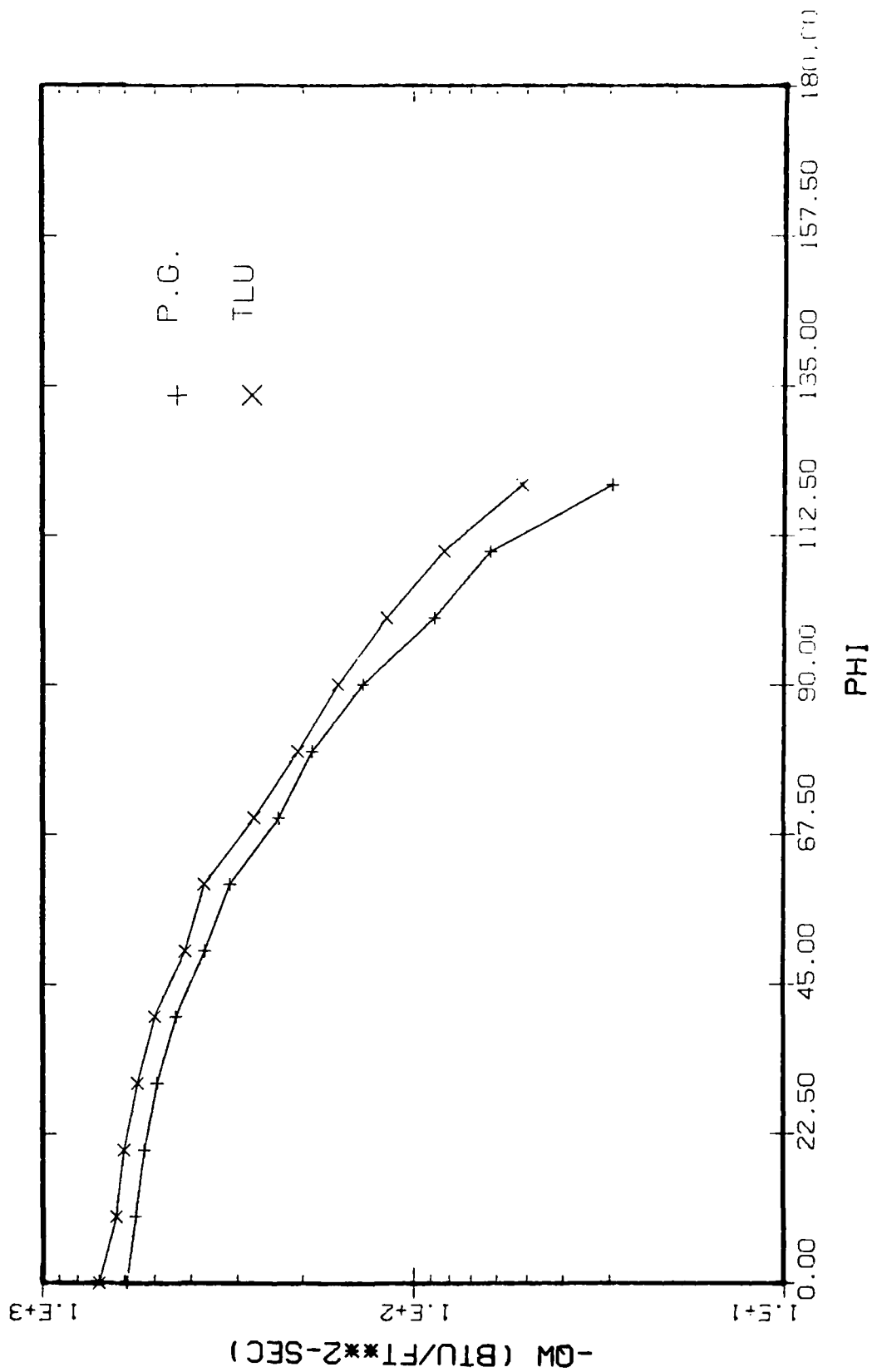
Figure 20. Transverse Variation of Wall Heat-Transfer Rate at S/R = 20
(Case D, α = 20 deg, Alt = 80,000 ft, T_w = 540R)
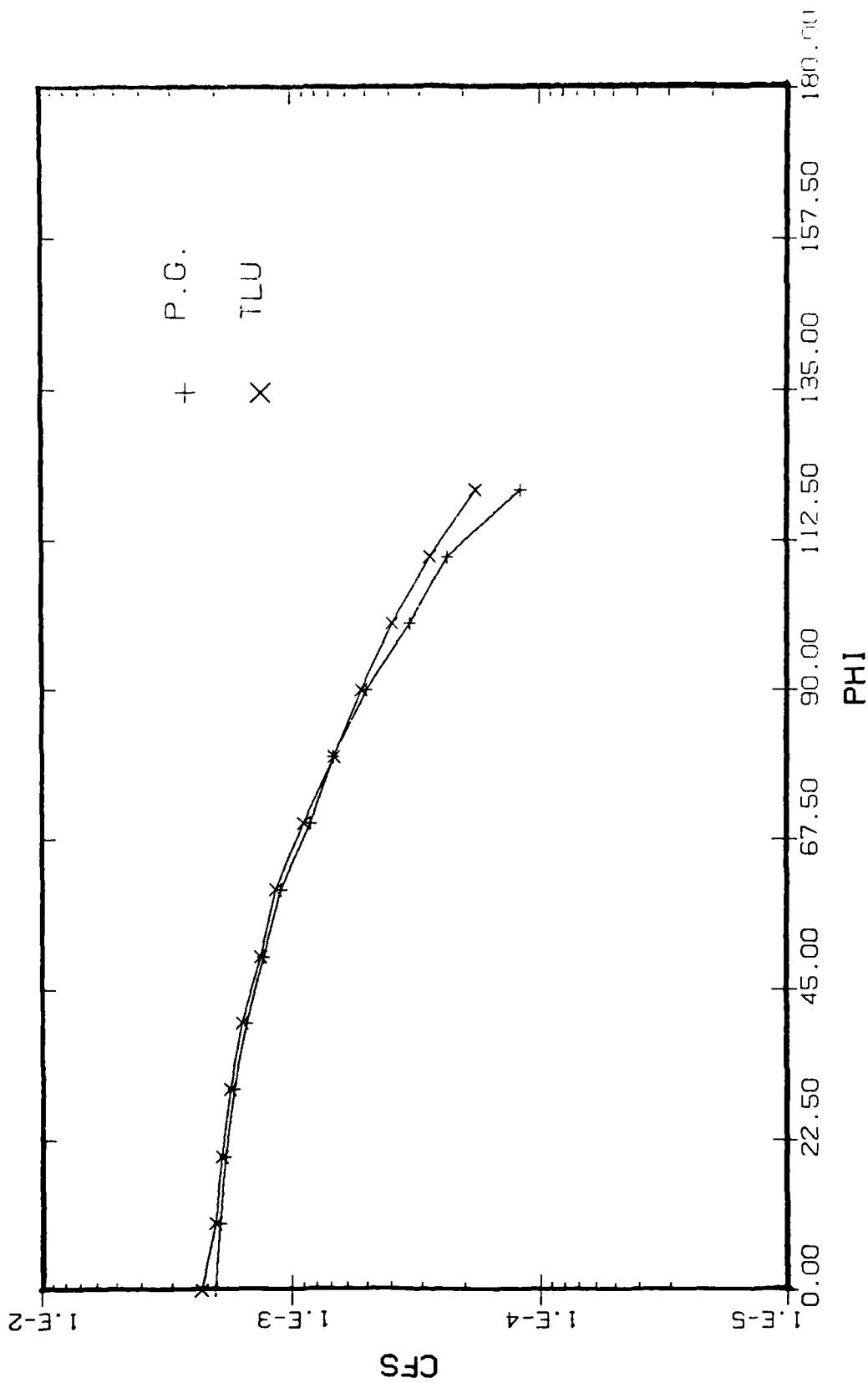
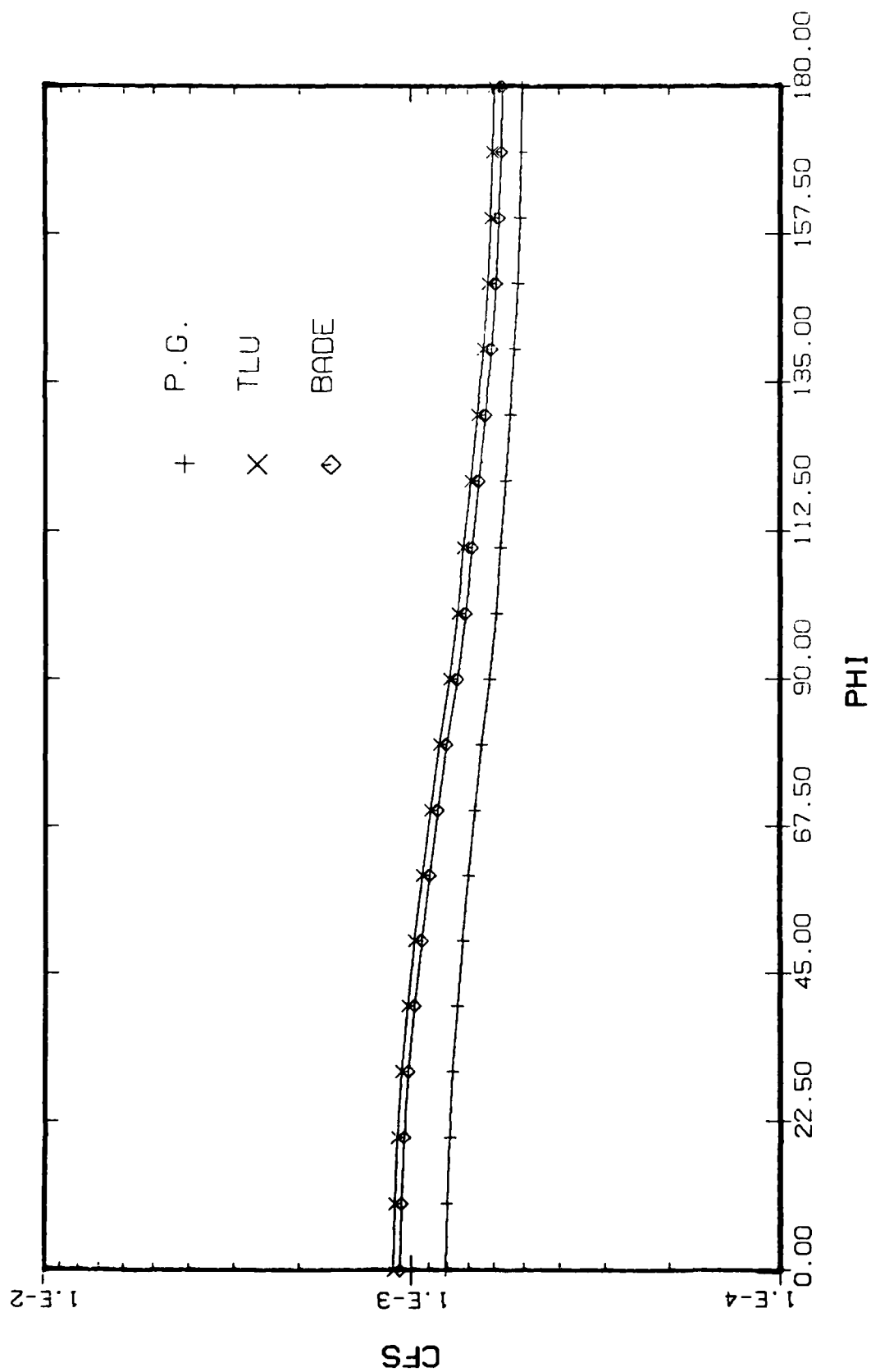Figure 21. Transverse Variation of C_{f_s} at $S/R = 20$
(Case D, $\alpha = 20$ deg, Alt = 80,000 ft, $T_w = 540R$)
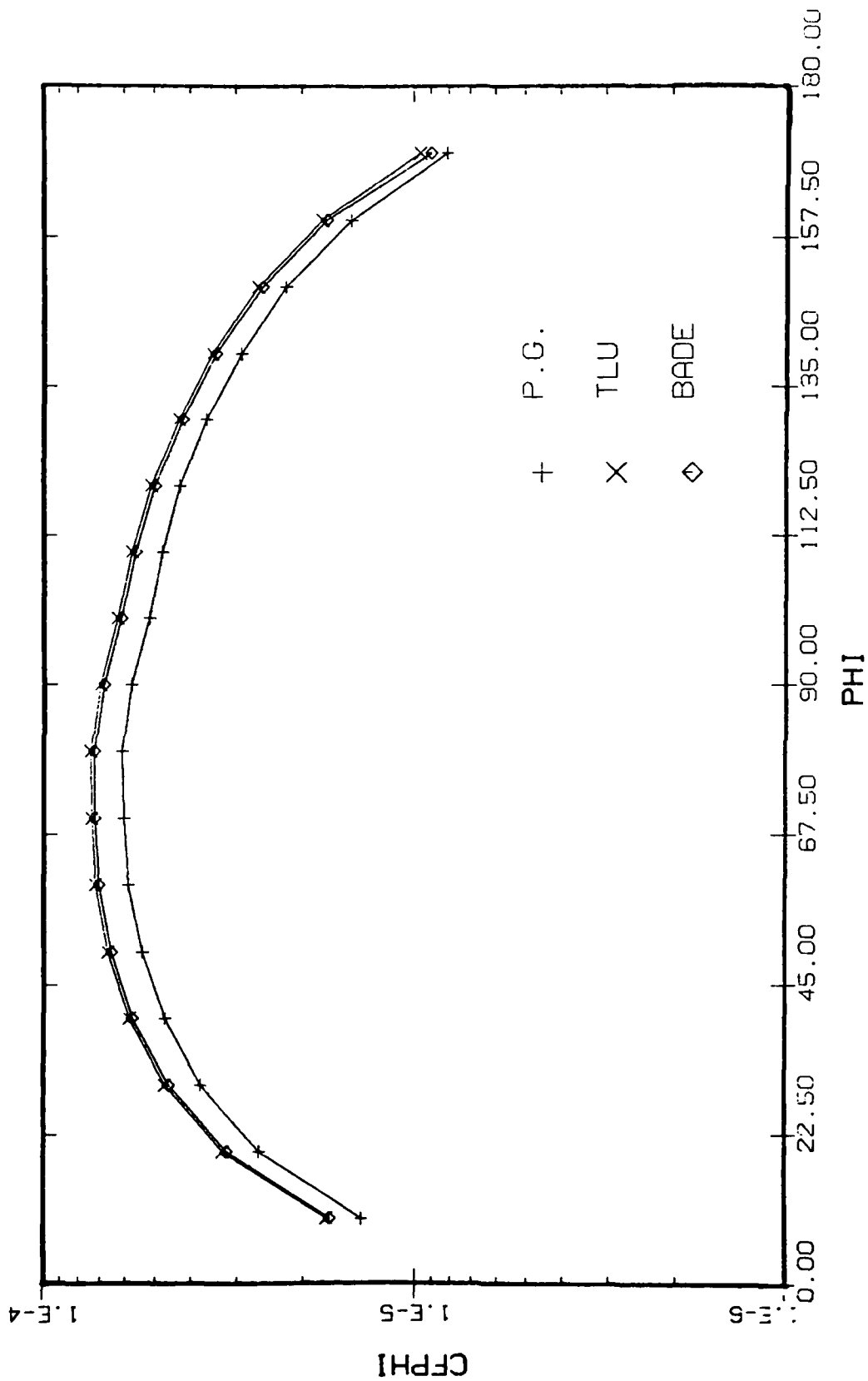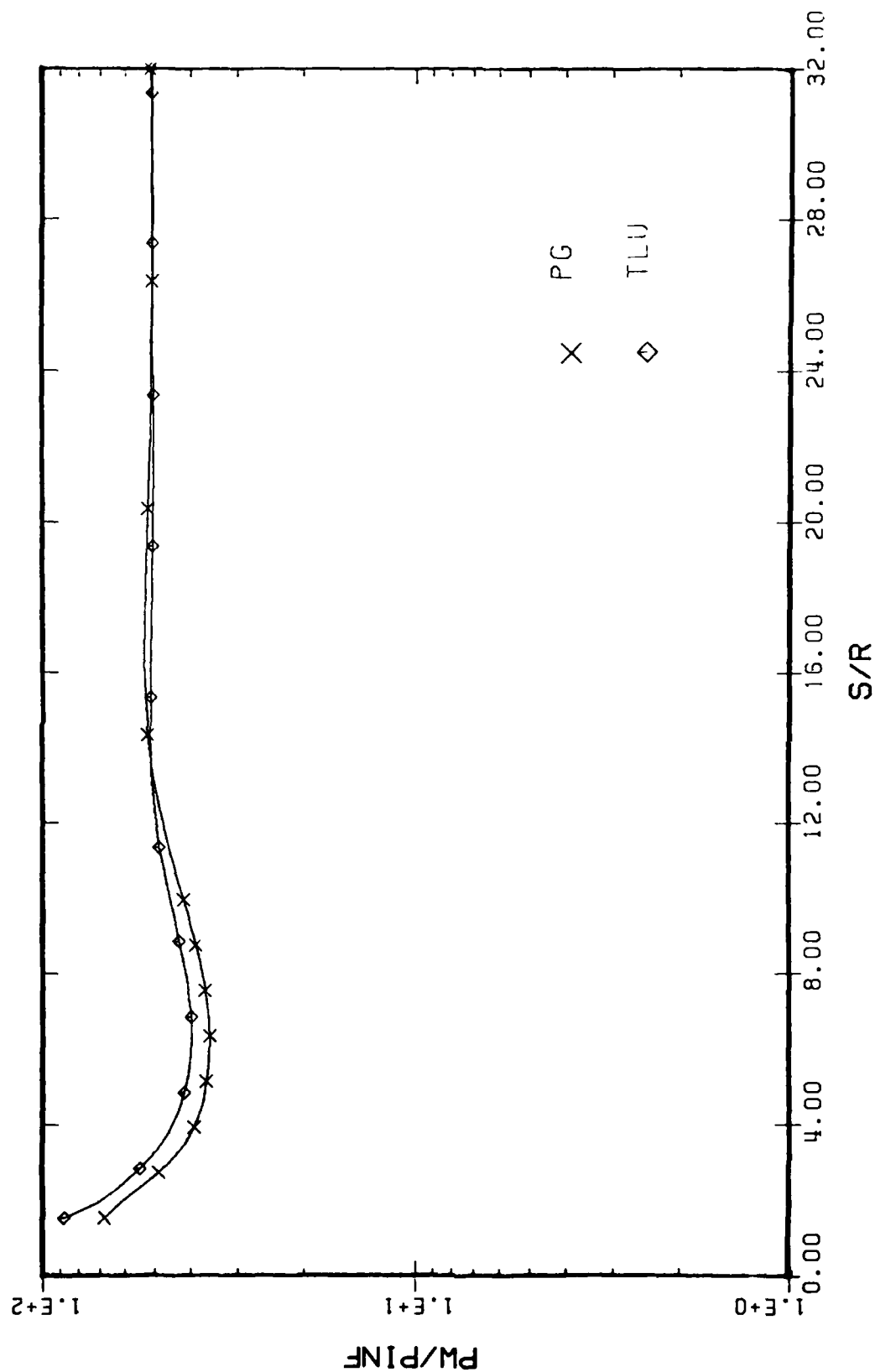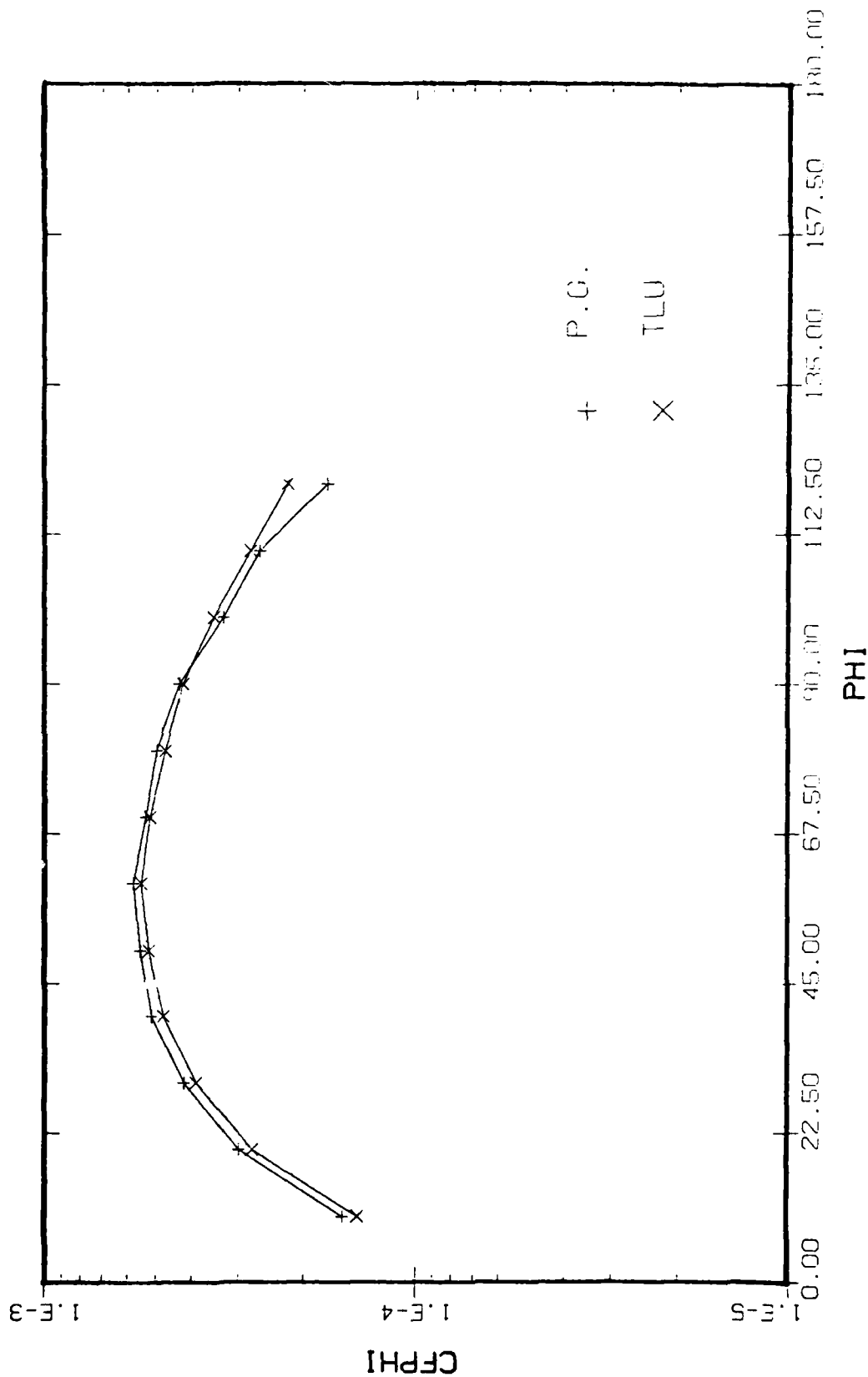
Figure 22. Transverse Variation of C_{f_ϕ} at S/R = 20

(Case D, α = 20 deg, Alt = 80,000 ft, T_w = 540R)

FURTHER DEVELOPMENT OF THE STREAMLINE METHOD FOR DETERMINATION OF THREE-DIMENSIONAL FLOW SEPARATION

Tsze C. Tai*

David Taylor Naval Ship Research and Development Center

Bethesda, Maryland, USA

Abstract

The streamline method for the determination of three-dimensional flow separation has been further exploited with emphasis on improving the friction model. Two approaches (numerical and analytical) for providing the required friction distribution are studied. The close agreement between the calculated line of separation based on numerical friction data and the original three-dimensional boundary-layer solution implies that the streamline method is a valid economical approach for determining the vortex-layer type flow separation if proper friction information is provided. The use of a simple analytical friction formula, on the other hand, only leads to qualitative results.

Introduction

A streamline approach for determining the free vortex-layer type, three-dimensional flow separation was developed recently.[1] This approach is based on the Maskell postulation about separation patterns in three dimensions. The line of separation is determined by the envelope of converging streamlines inside the viscous layer. To simulate the viscous effect, a friction model consisting of inertia terms multiplied by empirical parameters was proposed.

The method has been exploited further with emphasis on improving the friction model. As in the previous paper, a prolate spheroid in an incompressible flow at moderate angle of attack is considered as an illustration. An analytical friction formula as well as numerical friction data, have been employed in place of the previously proposed empirical model. Results of such uses on three-dimensional flow separation patterns over a prolate spheroid of $a/b = 6$ at $\alpha = 10$ deg are presented in the present paper.

Streamline Method

The streamline method for the determination of the vortex-layer type three-dimensional flow separation consists of three first-order ordinary differential equations. In particular, for the case of a prolate spheroid at an angle of attack, these equations take the axisymmetric form

$$\frac{D\Theta}{DS} = \frac{1}{\gamma M^2 P} \left[\left(\frac{\partial P}{\partial x} - \frac{\partial \tau_x}{\partial z} \right) \sin \Theta - \left(\frac{1}{f} \frac{\partial P}{\partial \phi} - \frac{\partial \tau_\phi}{\partial z} \right) \cos \Theta \right] - \frac{df}{dx} \frac{\sin \Theta}{f} \tag{1}$$

$$\frac{D\phi}{DS} = \frac{\sin \Theta}{f} \tag{2}$$

$$\frac{Dx}{DS} = \cos \Theta \tag{3}$$

where f = radial distance measured from the centerline

  S = the distance along a viscous streamline inside the boundary layer (see Fig. 1)

  x = the distance along the body surface of a constant ϕ plane

  Θ = the local streamline angle measured with respect to the x coordinate

  τ = shear stress

  ϕ = the azimuthal angle measured from the most windward line (see Fig. 2)

For a prolate spheroid, f is defined by

$$f = b \left[1 - (\frac{\bar{x}}{a} - 1)^2 \right]^{1/2} \tag{4}$$

Other symbols have their usual meaning.

For a prolate spheroid at incidence, values of pressure gradients are readily obtained by a closed-form potential-flow solution

$$P = P_\infty + \frac{\rho_\infty V_\infty^2}{2} \left[1 - \frac{u^2}{V_\infty^2} - \frac{v^2}{V_\infty^2} \right] \tag{5}$$

The pressure gradients are readily obtained using the relations[1]

$$\frac{\partial P}{\partial x} = -\rho_\infty V_\infty^2 \frac{u}{V_\infty} \left[\frac{2 \left(\frac{\bar{x}}{a}\right) - \left(\frac{\bar{x}}{a}\right)^2}{1 - e^2 \left(\frac{\bar{x}}{a} - 1\right)^2} \right]^{1/2} \frac{\partial}{\partial \bar{x}} \left(\frac{u}{V_\infty}\right) \tag{6}$$

$$\frac{\partial P}{\partial \phi} = -\rho_\infty V_\infty^2 \left[\frac{u}{V_\infty} \frac{\partial}{\partial \phi} \left(\frac{u}{V_\infty}\right) + \frac{v}{V_\infty} \frac{\partial}{\partial \phi} \left(\frac{v}{V_\infty}\right) \right] \tag{7}$$

where e is the eccentricity of the ellipsoid. Expressions for u/V_∞ and v/V_∞ given by Wang,[2] are also found in Ref. 1.

With these equations and with the knowledge of the friction distribution for $\partial\tau_x/\partial z$ and $\partial\tau_\phi/\partial z$, the viscous streamlines can be calculated inside the three-dimensional boundary layers. The flow separation line is then determined by tracing the envelope of converging viscous streamlines.[1]

Friction Distribution

The stumbling block in the problem lies, therefore, on the availability of the knowledge of the friction distribution without solving the complex three-dimensional boundary-layer equations. In addition to the earlier attempt,[1] a numerical approach and an analytical approach are used to provide the required friction information. The use of the numerical approach is solely as a check of the accuracy of the method, so that it should not be regarded as a normal course of computations.

Numerical Friction Data

The numerical friction data, provided by Cebeci, are based on the three-dimensional boundary-layer solution procedures described in Ref. 3. The distributions of shear stress and its normal derivative at the wall were computed for a prolate spheroid with body thickness ratio, $b/a = 1/6$, at an angle of attack $\alpha = 10$ deg. The Reynolds number was 7.2×10^6 based on a freestream velocity of 54 m/sec (177.17 ft/sec) and a total length of the body, $2a = 2$ m (6.56 ft).

To facilitate the numerical implementation, the friction data were curve fitted in accordance with the least squares method. Fourth-order polynominals were used for fitting the $\partial\tau_x/\partial z$ data and fifth-order polynominals for the $\partial\tau_\phi/\partial z$ data. Discontinuities of the numerical data that occur when $\tau_x \leq 0$ or $\tau_\phi \leq 0$ have been smoothed out by the curve fit. Plots of these curves are shown in Figs. 3 and 4.

Analytical Friction Formula

Attempts were also made to employ approximate analytical expressions for the friction model. As opposed to the balance-of-force type empirical form previously used in Ref. 1, a direct shear stress approach is undertaken in the present work. The shear stresses of interest are those in a surface above the wall where the viscous streamlines are to be calculated. In particular, the surface inside the boundary layer having a velocity $u = 0.707\ u_e$ is chosen for computing the viscous streamlines.

The shear stress for a two-dimensional turbulent boundary layer can be expressed approximately by taking over from the circular pipe equation, Eq. (20.12) of Ref. 4,

$$\tau = 0.0225\ \rho u^{7/4} \left(\frac{\nu}{z}\right)^{1/4} \tag{8}$$

This equation is valid for any wall distance z. Using the 1/10-th-power law velocity distribution (for high Reynolds number flows):

$$\frac{u}{u_e} = \left(\frac{z}{\delta}\right)^{1/10} \tag{9}$$

Equation (8) can be expressed in the form

$$\tau = 0.0225\ \rho u_e^{7/4}\ \delta^{-7/40}\ \nu^{1/4}\ z^{-3/40} \tag{10}$$

Differentiating Eq. (10) with respect to z yields the normal derivative of shear stress in the viscous layer having $u = 0.707\ u_e$

$$\frac{\partial \tau}{\partial z} = -0.075\ \frac{\tau}{z}$$

$$= -2.4\ \frac{\tau}{\delta} \tag{11}$$

where $z = 0.0312\ \delta$, which corresponds to $u = 0.707\ u_e$ in accordance with Eq. (9), has been used.

The boundary-layer thickness δ is obtained using the flat plate solution with the aid of 1/10-th-power law velocity distribution

$$\delta = 0.453 \ (x) \ (\frac{\nu}{u_e x})^{1/5} \tag{12}$$

The shear stress at $z = 0.0312 \ \delta$ is

$$\tau = 0.0292 \ \rho u_e^2 \ (\frac{\nu}{u_e \delta})^{1/4} \tag{13}$$

It is assumed that the crossflow is small so that Eq. (11) may be valid in the streamwise direction. Substituting the streamline distance for x and the overall velocity at the edge of boundary layer for u_e, $\partial \tau / \partial z$ will be valid along a streamline. Its components are

$$\frac{\partial \tau_x}{\partial z} = \frac{\partial \tau}{\partial z} \cos \Theta \tag{14}$$

$$\frac{\partial \tau_\phi}{\partial z} = \frac{\partial \tau}{\partial z} \sin \Theta \tag{15}$$

The plots of these components for the case of a prolate spheroid of thickness ratio b/a = 1/6 at α = 10 deg and $V_\infty \approx$ 54 m/sec (177.17 ft/sec) are shown in

Figs. 5 and 6. These conditions are chosen to be exactly the same as for numerical friction data so that a direct comparison can be made.

The small-crossflow assumption that restricts the validity of Eqs. (14) and (15) to bodies at small angle of attack almost prevents the consideration of most flow separation problems. Nevertheless, it is of interest to see how far a simple analytical friction formula can be of use in the subject problem.

Results and Discussion

Results of three-dimensional flow separation over a prolate spheroid with body thickness ratio 1/6 at α = 10 deg are presented using: (a) numerical friction data, (b) an analytical friction formula, or (c) zero friction (pure inviscid potential flow). For cases (a) and (b), the viscous streamlines were calculated inside the boundary layers at mean velocities about 0.707 of those at the edge of the boundary layer.

The results of case (a), that is, based on the numerical friction data, are shown in Fig. 7. The calculated line of separation by the present method coincides with the locus of flow separation corresponding to $\tau_x \leq 0$ in the original three-dimensional boundary-layer solution of Cebeci. The close agreement of the presently calculated result with the original solution implies that the streamline method is a valid economical approach for determining the line of separation, if proper friction information is provided. It also sheds some light on the formulation of the analytical friction model, on which the present method mainly relies.

The line of separation found by using the simple analytical form, case (b) on the other hand, lies further downstream; see Fig. 8. The length of the separation line is also reduced considerably. The difference is apparently caused by less severe variations of the shear stress derivatives from the analytical formula than from the numerical data. Particularly, the analytical $\partial\tau_\phi/\partial z$ does not exhibit any change from negative to positive values (see Fig. 6), which are the main driving forces for the flow separation. Therefore, the result can only be regarded as qualitatively correct.

The result is encouraging in the sense that there is plenty of room for improvement to the friction formula, and thus for the accuracy of the line of separation. In particular, the small crossflow assumption can be removed easily either by a correcting procedure or by a more realistic consideration of the crossflow theory.

Finally, for comparison purposes, the pure inviscid flow pattern, case (c), is depicted in Fig. 9. All of the streamlines merge to the rear stagnation point and leave the body surface. Since there is no friction, there is no separation. The curvatures of the inviscid streamlines are noticeably smaller than those of viscous streamlines, which are consistent with similar comparison observed by Han and Patel[5].

Concluding Remarks

The following are conclusions based on the present work

1. The streamline method is a valid economical approach for determining the vortex-layer type, three-dimensional flow separation if proper friction and pressure distributions are provided.

2. The use of a simple analytical friction formula in the streamline method produces only qualitatively correct results on the line of separation.

Acknowledgement

The author wishes to thank T. Cebeci of Douglas Aircraft Company for providing the numerical friction data.

References

1. Tai, T.C., "Determination of Three-Dimensional Flow Separation by a Streamline Method," AIAA Paper 80-1443, presented at AIAA 13th Fluid and Plasma Dynamics Conference, Snowmass, Colo., July 1980. To appear in AIAA Journal.

2. Wang, K.C., "Boundary Layer over a Blunt Body at High Incidence with an Open-Type of Separation," Proceeding of the Royal Society of London, A 340, pp. 35-55, 1974.

3. Cebeci, T., Khattab, A.A., and Stewartson, K., "Studies on Three-Dimensional Boundary Layers on Bodies of Revolution II, Three-Dimensional Laminar Boundary Layers and the OK of Accessibility," Douglas Aircraft Company, Report MDC J8716, April 1980.

4. Schlichting, H., Boundary Layer Theory, Fourth English Edition, McGraw-Hill, New York, 1960, p. 508 and pp. 536-537.

5. Han, T. and Patel, V.C., "Flow Separation on a Spheroid at Incidence," J. Fluid Mechanics, Vol. 92, Part 4, pp. 643-657, 1979.
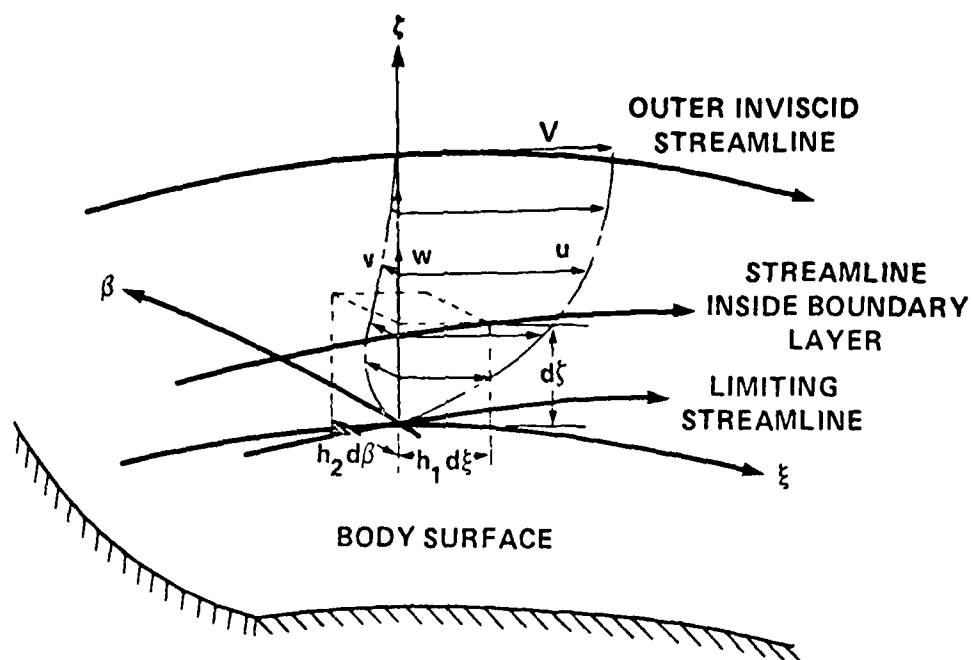
Fig. 1 – Streamline in a Boundary Layer
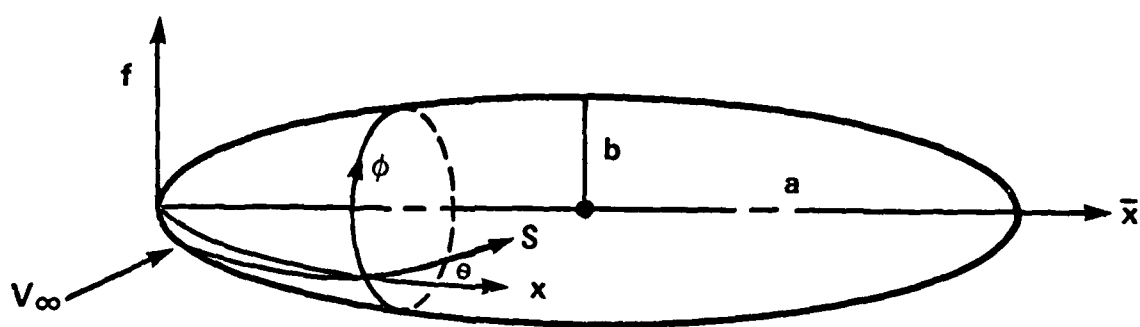
Fig. 2 – Coordinate System for a Prolate Spheroid
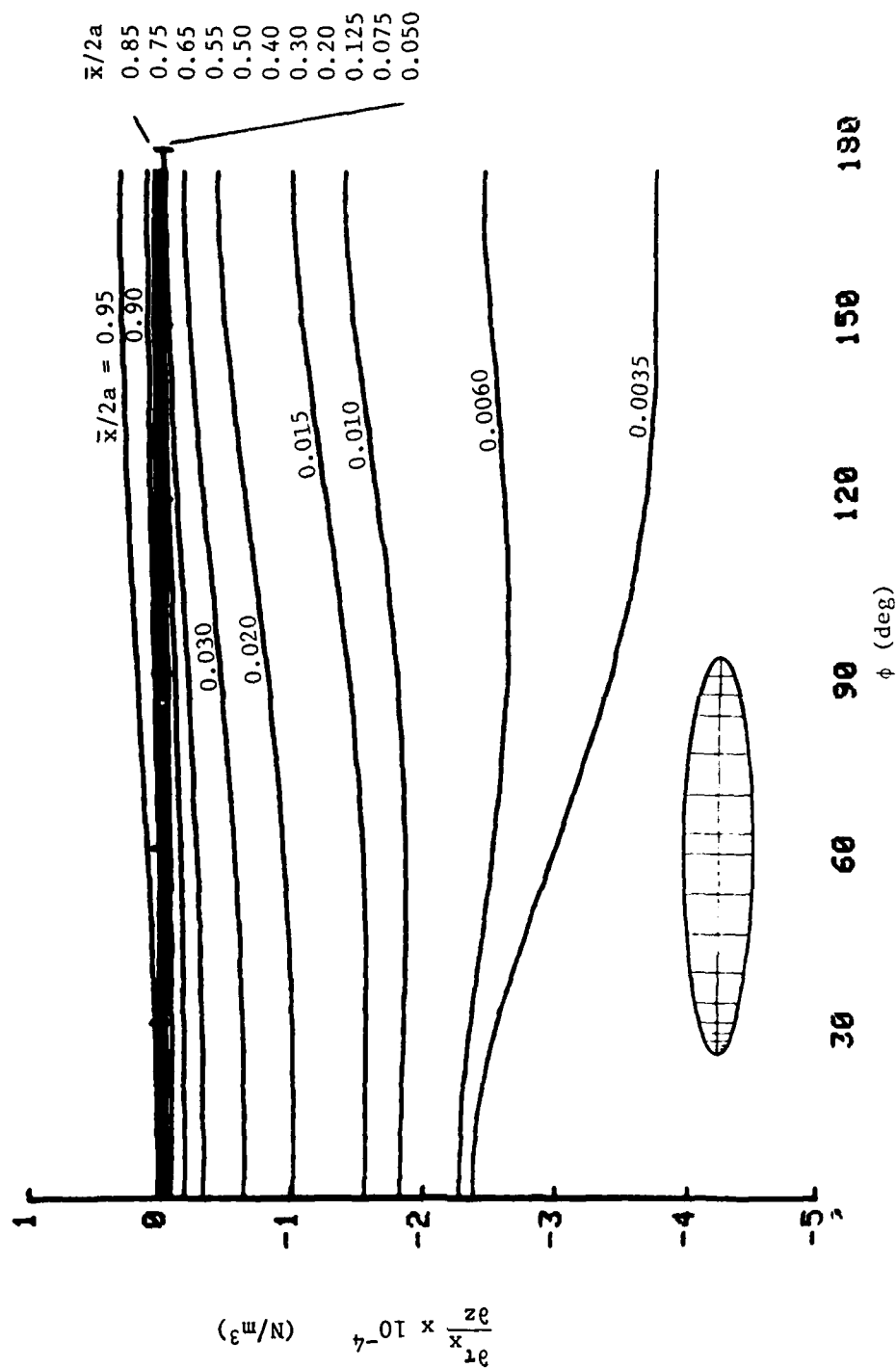
Fig. 3 - Least Squares Fit of Numerical Normal Derivatives of Longitudinal Shear Stress over a Prolate (a/b = 6, α = 10 deg, and Re = 7.2 x 10^6)
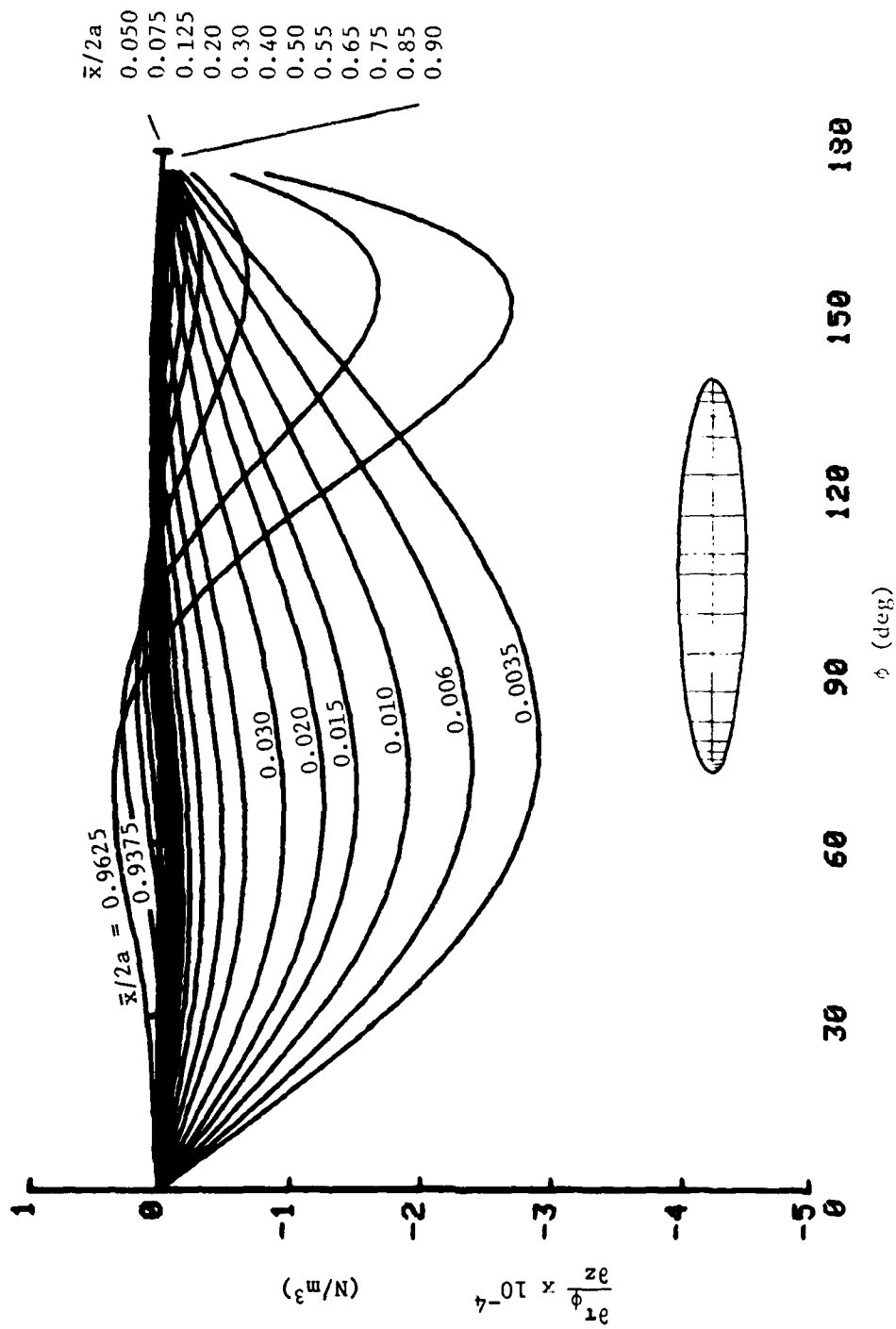
Fig. 4 - Least Squares Fit of Numerical Normal Derivatives of
Transverse Shear Stress over a Prolate Spheroid
($a/b = 6$, $\alpha = 10$ deg, and $Re = 7.2 \times 10^6$)
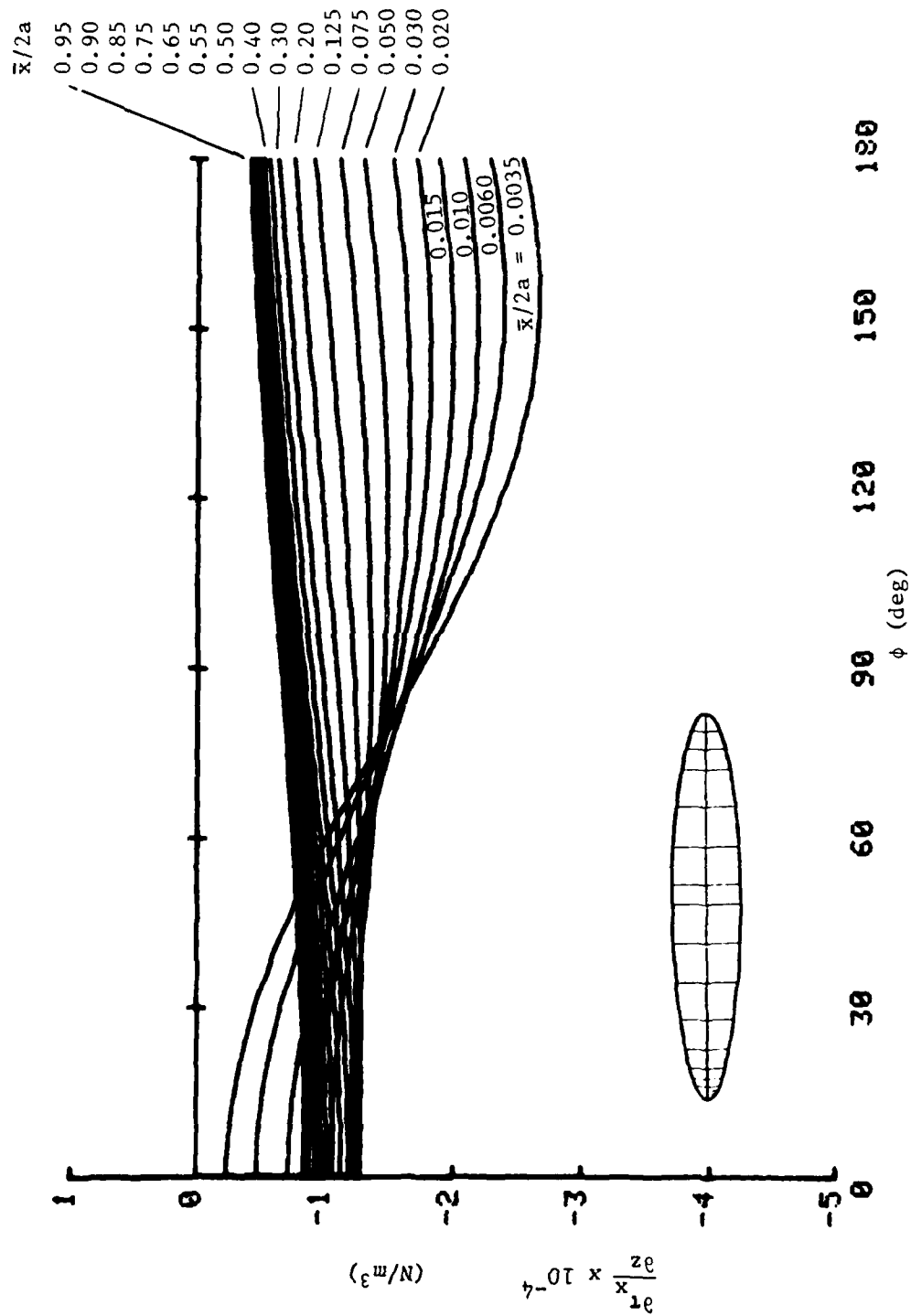
Fig. 5 - Analytical Normal Derivatives of Longitudinal Shear Stress over a Prolate Spheroid ($a/b = 6$, $\alpha = 10$ deg, and $Re = 7.2 \times 10^6$)
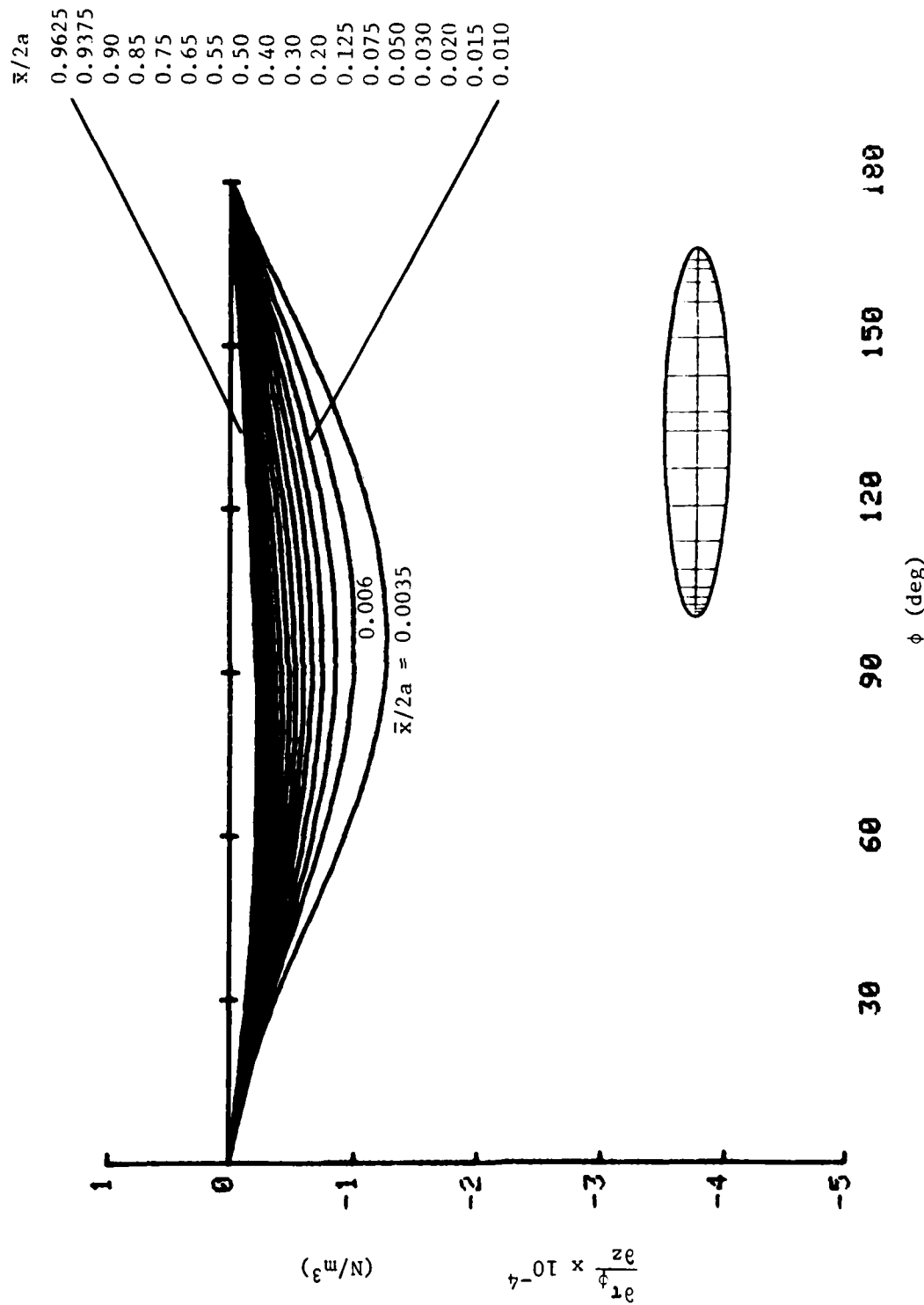
Fig. 6 – Analytical Normal Derivatives of Transverse
Shear Stress over a Prolate Spheroid
($a/b = 6$, $\alpha = 10$ deg, and $Re = 7.2 \times 10^6$)
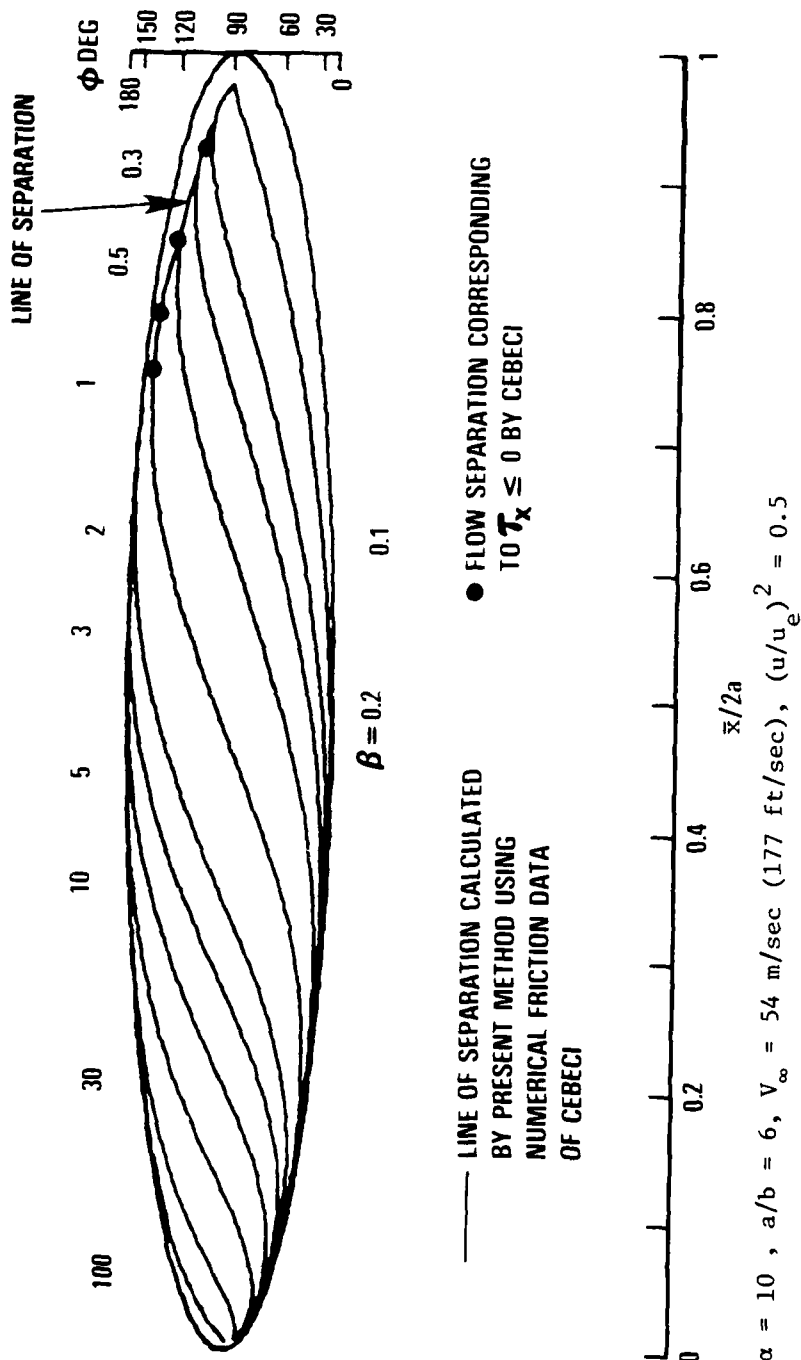
Fig. 7 - Line of Separation Obtained Using Numerical
Friction Data in the Streamline Method
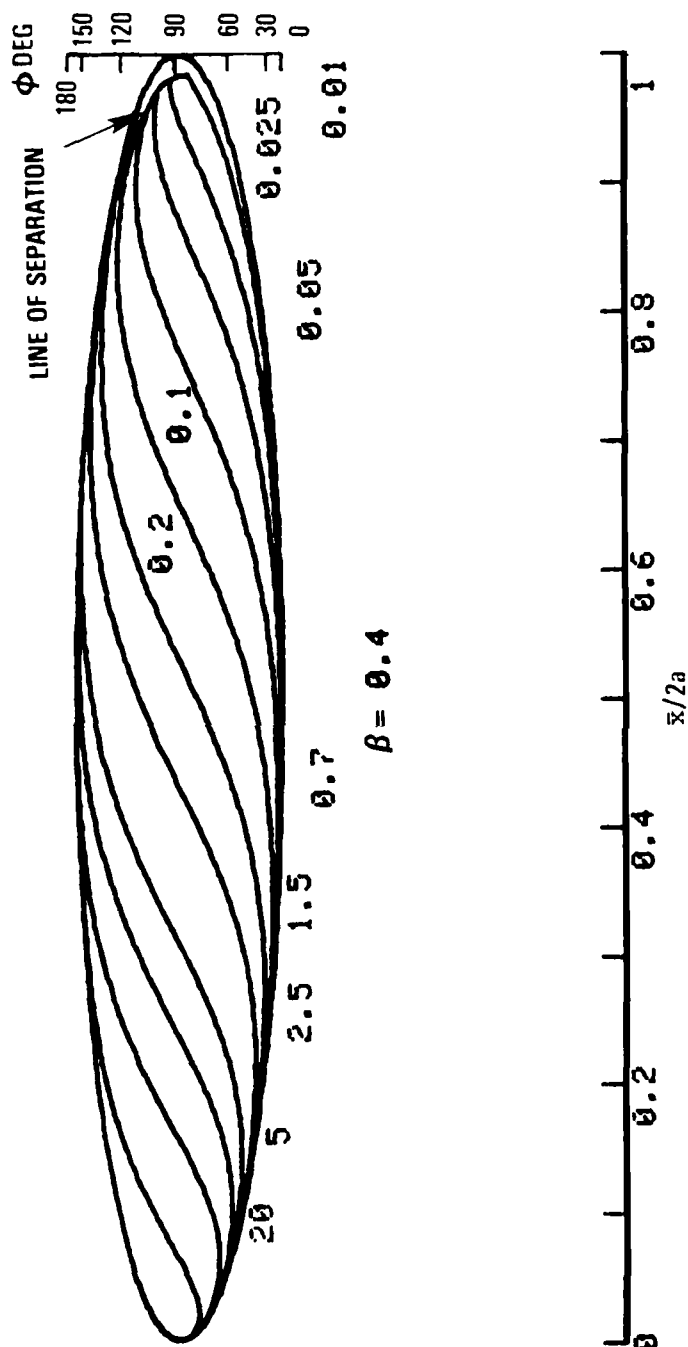
$\alpha = 10$, a/b = 6, V_∞ = 54 m/sec (177 ft/sec), $(u/u_e)^2$ = 0.5

Fig. 8 – Line of Separation Obtained Using Analytical
Friction Formula in the Streamline Method

$\alpha = 10$, $a/b = 6$, $V_\infty = 54$ m/sec (177 ft/sec), $(u/u_e)^2 = 0.5$
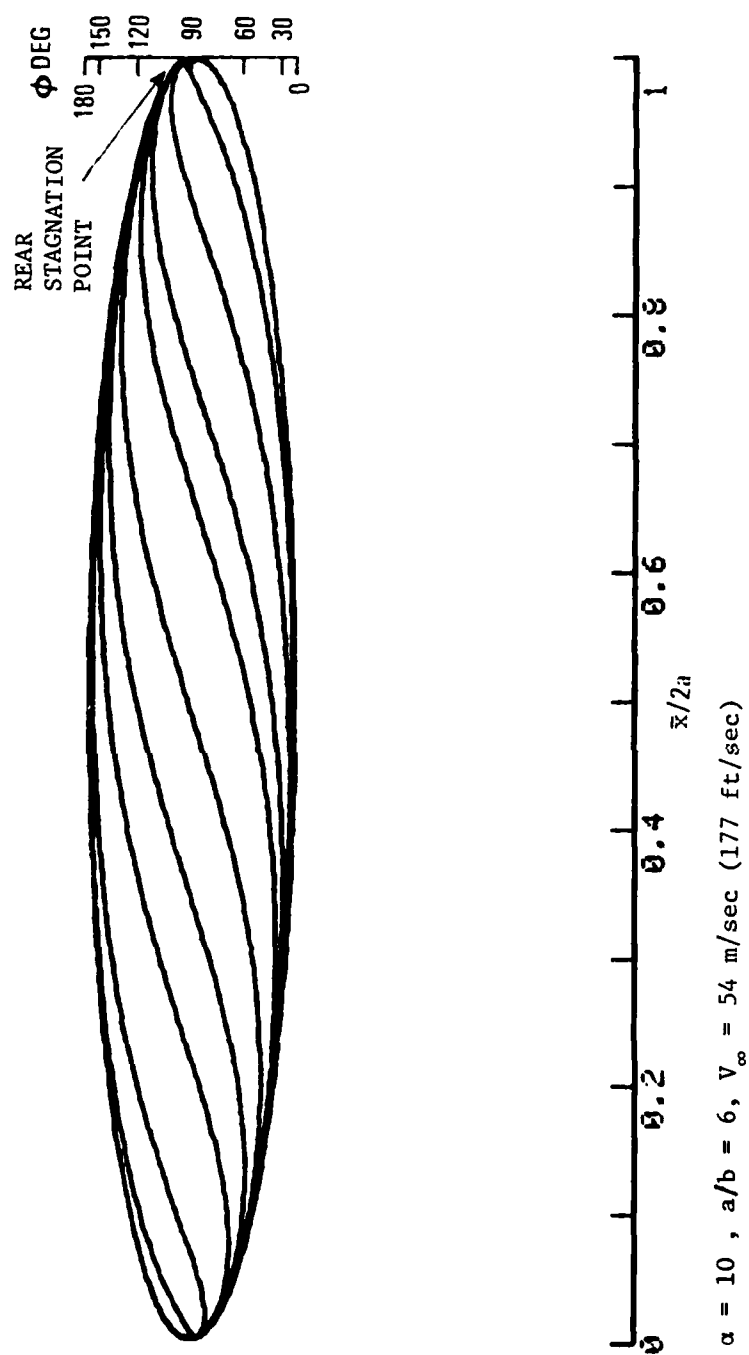
Fig. 9 – Inviscid Flow Pattern

$\alpha = 10$, $a/b = 6$, $V_\infty = 54$ m/sec (177 ft/sec)

COMPARISON OF NUMERICAL RESULTS AND MEASURED DATA FOR
SMOOTH AND INDENTED NOSETIPS

Tsuying Hsieh
Naval Surface Weapons Center, White Oak, Maryland

ABSTRACT

Numerical calculations, using an unsteady implicit numerical algorithm which solves either the inviscid or the thin-layer Navier-Stokes equations, were performed for smooth and severely indented nosetips at hypersonic speed and zero angle of attack. The computed results of inviscid and laminar flowfield are compared to wind tunnel measured data for surface pressure, shock location, heat transfer and density distribution in the shock layer. Good agreements between the calculated and measured flowfield are obtained for smooth nosetip without flow separation. Difficulties in the simulation of severely indented nosetips with large separation bubble or sharp corner are discussed.

NOMENCLATURE

C_p = Pressure coefficient, $p-p_\infty/\frac{1}{2}\ \rho_\infty\ U_\infty^{\ 2}$

J,K = Index of grid in the streamwise and body-to-shock direction respectively

L = Reference length, 2.56 cm (1 in.)

M = Mach number

n = normal direction

p = pressure

Pr = Prandtl number

R = Radius of circular arc

Re = Unit Reynolds number, U_∞/ν

Rs = Radius of sphere

S = Arc length

St = Stanton number = $\dfrac{(\mu_\ell + \mu_t)/\mu_\infty}{R_{e_\infty}\ (P_{r_\ell} + P_{r_t})} \left[\dfrac{T_o}{T_\infty} - \dfrac{T_w}{T_\infty}\right]^{-1} \dfrac{\partial(T/T_\infty)}{\partial(n/L)}$

t = time

T = temperature

U = Velocity

X,Y = Axial and radial coordinates respect-
ively

ρ = Density

ϵ_E = Coefficient for explicit dissipation

ϵ_I = Coefficient for implicit dissipation

ν = Kinematic viscosity of fluid

Subscript

∞ = free stream

ℓ = laminar flow

o = stagnation point

t = turbulent flow

w = wall

INTRODUCTION

Because of ablation, the nosetip of a spherical body undergoes continuous
change during re-entry. The shape of the nosetip has a great influence on
the flowfield over the entire body, i.e., the nose region and thus the
afterbody. In order to understand the flowfield about indented nosetip shapes
that are likely to occur during the re-entry process, considerable effort has
been expended both experimentally and theoretically.[1-4] (also see references
listed in Ref. 1 and 2).

Among the experimental work, Refs. 3 and 4 provide a comprehensive set of
measurements for a systematic change of nosetip shapes. This includes
surface pressures, heating rates, flowfield pictures using electro-optical
techniques and velocity mapping using Laser Doppler Velocimeter. These
experiments are intended to provide basic information about the important flow
features to be expected in the flowfield and also serve as a useful data
base for the development of a numerical code to predict the flowfield.

Among the many numerical schemes intended for indented nosetip calculation,
a promising and versatile one seems to be due to Kutler et al.[1] As described
in Ref. 1, Kutler et al solved the unsteady Navier-Stokes equations with the
"thin-layer" approximation for nosetip of arbitrary shapes at zero indicence
using the implicit factored numerical algorithm of Warming and Beam.[5] The
steady solution is obtained asymptotically in time and both viscous and
inviscid flowfields can be computed using the same computer program, refered
to as K-C-L code in this paper. As described in Ref. 2, when the inviscid
portion of the K-C-L code was applied to the nosetip shapes reported in
Ref. 3 and 4 surmountable difficulties were encountered during the course of
calculation because of the presence of small radius expansion corners and a

concave compression turn in these nosetips. It was later found that a special calculation procedure is required in order to obtain reasonable solutions.

For the details of the numerical procedure used in the K-C-L code and the special calculation procedure for the indented nosetip computation, the readers should consult to Ref. 1 and 2 and will not be repeated in this paper. The same calculation procedure has since been applied to compute viscous flow over smooth and indented nosetips and several typical results will be described and compared to measured data.

II.   RESULTS AND DISCUSSION

A.   Smooth Nosetips

The comparison of inviscid results for surface pressure and density distribution over a sphere is reproduced here from Ref. 2 as shown in Fig. 1. The grid used in the computation is $J = 32$ (along body surface) x $K = 12$ (across the shock layer) and the total number of time steps used is 600 (with a courant number of 2.5). This requires about 2 minutes CPU time in CDC-7600 computer. The surface pressure is compared to the work of Inouye and Lomax[6] and the measured data of Baer[7] as shown in Fig. 1a. The density distribution in the shock layer is compared to the measured data of Sedney and Kahl[8] as shown in Fig. 1b. The agreement are seen to be very good.

Viscous flow calculations based on the thin-layer approximation of Navier-Stokes equations, were performed for a hemisphere-cone under the following flow condition: $M_\infty = 5.92$, $Re_\infty = 5.5 \times 10^6/ft$ and $Tw/T_\infty = 4.78$.   A grid of 28x32 was used. For laminar calculation, 400 time steps with a Courant number (CN) of 75 can be considered as the final solution (the nondimensional shock speed is in the order of 10^{-3} and the CPU time is about 5 min). As shown in Fig. 2 the calculated results for heat transfer in term of Stanton number over the surface is compared to the measured data reported in Ref. 7. Also plotted in Fig. 2 is the boundary layer calculation using Cebeci-Smith's boundary layer code as given in Ref. 7. It is seen that the agreement is satisfactory. It should be noted that for hemisphere-cone, the flow is fully attached. The surface pressure agrees well among the inviscid and laminar calculation as well as the measured data. Therefore, the good agreement in heat transfer between the boundary layer and the thin layer N-S calculation is to be expected.

In the numerical procedure, there are two kinds of dissipation used for stability purpose, i.e., the explicit and implicit dissipation terms with coefficients of ϵ_E and ϵ_I respectively. For inviscid and laminar calculation, solution can be obtained without the implicit dissipation. For turbulent calculation, it was found that the implicit dissipation must be added in order to have a converged solution. Since the implicit dissipation terms have no effect on the solution as the steady state is approached, it is therefore used in both laminar and turbulent calculation. The explicit dissipation terms, on the other hand, will always present. In viscous flow calculation, it is desirable that the explicit dissipation coefficient be kept minimum so that the real viscous effects can be simulated. From the experience for indented nosetip calculation, the value of ϵ_E cannot be too small in order to have a smooth bow shock (no wiggling) where the flow can essentially be assumed to be inviscid. Therefore, the ϵ_E value in the η direction is linearly reduced to one tenth of the input

value toward the wall in order to minimize its effects there. This devise also consistent with the thin-layer approximation. When ϵ_E is linearly reduced, it is denoted by $\epsilon_E{}'$ to distinguish from the uniform one. As shown in Fig. 2, the effects of $\epsilon_E{}'$ are seen to be insignificant in the heat transfer results for hemisphere-cone with $\epsilon_E{}'$ varies from 0.1 to 0.02 and $\epsilon_I = 3 \, \epsilon_E{}'$. This is not so for indented nosetip calculation.

In the simulation of turbulent flow, the turbulence model of Baldwin and Lomax[9] was used. The final laminar solution with $\epsilon_E = 0.1$ was used as the initial flowfield for turbulent calculation. A turbulent solution was produced in 200 time steps with the nondimensional shock speed in the order of 10^{-3}. As shown in Fig. 2, the Stanton number increase significantly for turbulent flow as compared to the laminar flow one (no measured data for comparison). It should be pointed out that the surface pressure obtained from the laminar and turbulent solution agree to two digits.

B. Indented Nosetips

The special calculation procedure for inviscid flow over indented nosetips as described in Ref. 2 was applied to calculate viscous flow over indented nosetips. Model 1 and 4 as described in Ref. 2 were chosen for this investigation. The simulation of viscous turbulent flow over indented nosetips has not been very successful as described in the following paragraphs.

Laminar flow over Model 4 was first calculated. The calculation started with a grid of 24 x 32 (CN = 150, $\epsilon_E = 0.4$, $\epsilon_I = 0$) for 400 time steps to obtain a laminar solution over a sphere at $M_\infty = 5.0$, Re = 8 x 10^6/FT and $T_w/T_\infty = 5.4$. The sphere was then deformed to the shape of Model 4 in 1800 time steps. The grid was then increased to: (!) 58 x 32 and (B) 56 x 48 in another 1600 time steps each with the final values of CN = 50, $\epsilon_E = 0.1$ for (A) and $\epsilon_E{}' = 0.3$ for (B). The calculated surface pressure and shock locations from these two solutions are close (results not shown). This provides a self verification of the results. Since grid (B) contains more points in the η direction, its solution resolves the flow field better and is used for comparison as shown in Fig. 3 and 4.

Unlike the hemisphere-cone, the turbulent calculations for Model 4 encountered serious difficulties. Large amplitude oscillation of pressure in the flowfield quickly interrupted the computation. The value of CN was gradually reduced and the value of ϵ_I was increased ($\epsilon_E{}' = 0.3$ was maintained). At CN = 2 and $\epsilon_I = 6$, it was possible to run for 200 time steps with the non-dimensional shock speed coverging to a value of 0.04. The shock speed is then started to increase slowly but steadily. A further increase of ϵ_I up to 12 would not help to obtain a converged solution. Thus, the solution before the shock speed started to increase is shown in Fig. 3 and 4 for comparison. It is understood that the turbulent solution shown in Fig. 3 and 4 is not the converged solution.

Fig. 3 shows the comparison of shock location between calculations and experiments. The inviscid shock layer is thinner around the indented region as expected. The laminar and turbulent solutions for shock location are almost coincide and fall in between the inviscid solution and the measured data. The primary separation bubble indicated by the laminar solution is

smaller than observed experimentally. The laminar separation point of the primary separation bubble is at the downstream end of the expansion corner, but the flow picture (Fig. 8a of Ref. 2) shows that the flow separates immediately at the beginning of the expansion corner. In general, the effects of turbulence is to move the separation point toward downstream and the separation bubble will be smaller. This fact suggests that the discrepancy is not because of turbulence effects but from some other sources which are not captured in the numerical solution. Also the laminar solution indicates that there is a secondary separation bubble within the primary separation bubble as sketched in Fig. 3. The secondary separation bubble was not reported in Ref. 4.

In Fig. 4, the surface pressure distribution obtained from the inviscid, laminar and turbulent solution are compared to the measured data. It is noted that the viscous solutions compare better with the measured data than the inviscid curve. The region around the expansion corner $S/L \sim 0.26 - 0.7$ where the inviscid and viscous solutions are seen to agree well (i.e., no flow separation) but are lower than the measured data. The dip in the pressure curve in the region $S/L \sim 2.5$ (where the secondary separation bubble starts) is not shown by the measured data. A calculation was made with the complete Navier-Stokes equation for laminar flow with the same grid distribution as used in the thin-layer approximation calculation and the results for surface pressure agree up to two digits.

For Model 1, there is a sharp expansion corner with a radius of 0.062 inch. Three grid points were used to cover the corner as was done for the inviscid calculation reported in Ref. 2 and a total grid points of 33x32 were used for the viscous calculation. Only laminar solution can be obtained. As shown in Fig 5 and 6, the inviscid solution agrees reasonably well with the measured data for both the shock location and the surface pressure because the separation bubble is small as indicated by the flow picture (Fig. 5a of Ref. 2). In contrast to the result of Model 4, however, the laminar solution indicates that the flow separates immediately after the corner and form a large primary separation bubble as shown in Fig. 5. Within the primary separation bubble, there is also a secondary separation bubble around the location of compression turn. As a result of the primary separation bubble, the laminar shock layer becomes thicker near the separation bubble and thinner afterwards as compared to the measured data. Also the surface pressure obtained from the laminar solution looks entirely wrong.

It was not possible to obtain a turbulent solution for Model 1, not even one like that of Model 4. The obvious reason is that the laminar solution is too far off from the measured data, which is assumed to be close to the turbulent solution, therefore the starting flowfield is too poor to carry through the calculation.

From the above comparison of results, it is concluded that the numerical code works well for smooth nosetips. For those indented nosetips investigated in this paper, the code fail to give a satisfactory solution. Possible reasons for the failure of the code to obtain a solution and for the discrepancy between the viscous calculation and the experimental data are suggested as follows: (1) The turbulence model used is inadequate. (2) The first-order-accurate numerical procedure is not sufficient to simulate the complicated flowfield. (3) The grid points and their distribution are insufficient to resolve the viscous effects. (4) The sharp corner as described in Model 1 requires special treatment to avoid flow separation introduced from sources other than the viscous effects. (5) Because of the prevailing of a large separation bubble, the thin-layer approximation may lead to wrong solution, i.e., for a significant portion of the flowfield, the viscous terms in both the ξ and η directions should be kept.

REFERENCES

1. Kutler, P., Chakravarthy, S. R. and C. P. Lombard "Supersonic Flow Over Ablated Nosetips Using an Unsteady Implicit Numerical Procedure" AIAA Paper 78-213, Jan 16-18, 1978.

2. Hsieh, T., "Numerical Investigation of Flowfield About a Series of Indented Nosetips," AIAA Paper No. 81-0077, Jan. 1981.

3. Ragsdale, W. C. and Morrison, A. M., "IAP 202 Heat Transfer and Pressure Tests in the NSWC/WOL Hypersonic Tunnel," NSWC/WOL MP 78-18, October 27, 1978.

4. Yanta, W. J., "Indented Nose Flowfield Tests," WTR 1329, Naval Surface Weapons Center, White Oak, MD., July 1980.

5. Warming, K. F. and Beam, R., "On the Construction and Application of Implicit Factored Schemes for Conservation Laws," SIAM, ATNS Proceedings, Vol. 11, 1978, pp. 85-129.

6. Inouye, M. and Lomax, H., "Comparison of Experimental and Numerical Results for the Flow of a Perfect Gas About Blunt-Nosed Bodies," NASA TN D-1426, Sept 1962.

7. Baer, A. L., "Pressure Distribution on a Hemisphere Cylinder at Supersonic and Hypersonic Mach Numbers," AEDC TN-61-96, Arnold Engineering Development Center, 1961.

8. Sedney, R. and Kahl, G. D., "Interferometric Study of the Blunt Body Problem," Ballistic Research Laboratory Report No. 1100, 1960.

9. Baldwin, B. S. and Lomax, H. "Thin Layer Approximation and Algebraic Model for Separated Turbulent Flow" AIAA Paper 78-257, 1978.

Figure 1   Comparison of Surface Pressure and Density Field
Between Calculation and Experiment
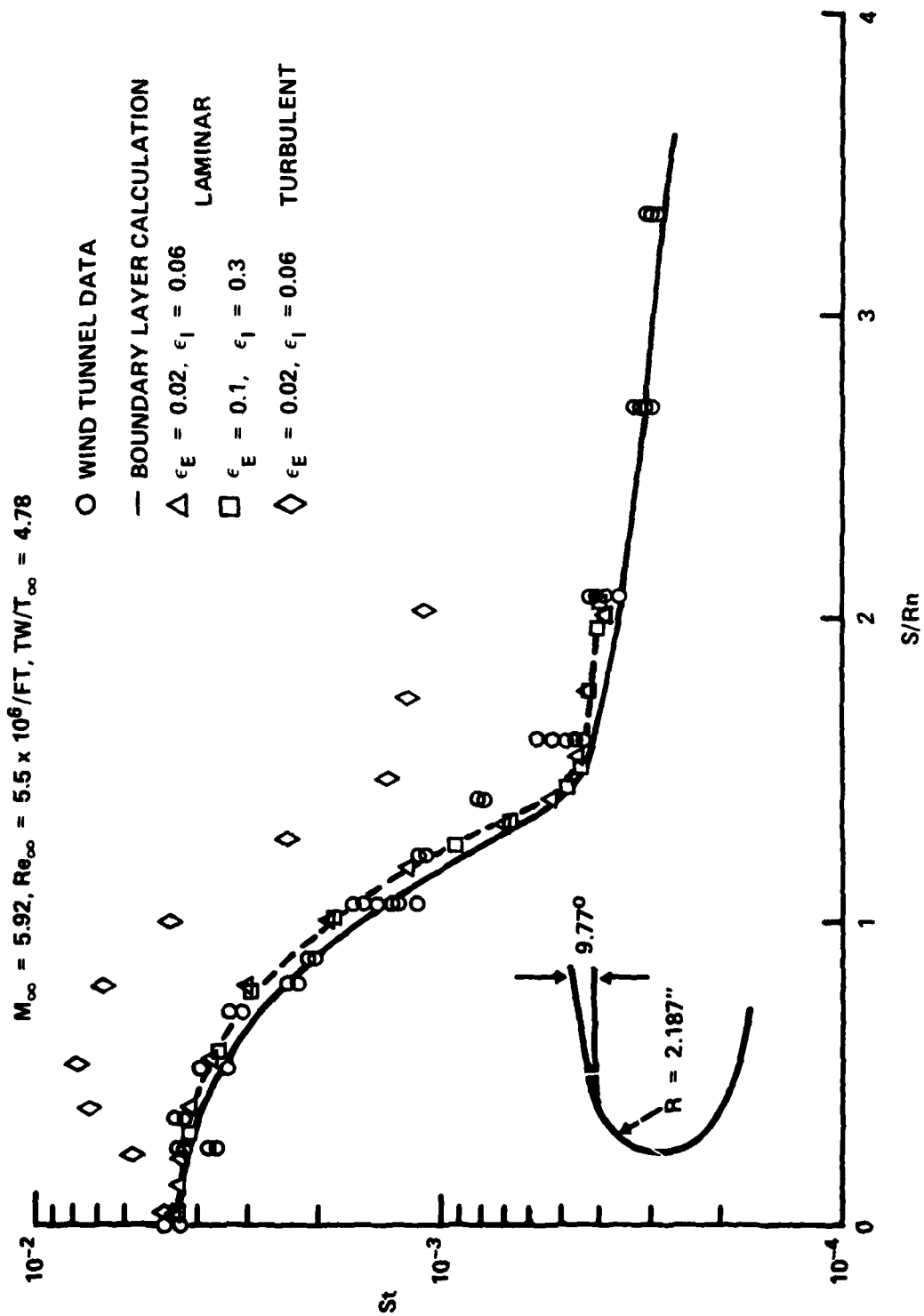
FIGURE 2 COMPARISON OF HEAT TRANSFER MEASUREMENTS ON A HEMISPHERE CONE

$M_\infty = 5.92$, $Re_\infty = 5.5 \times 10^6$/FT, $TW/T_\infty = 4.78$

○ WIND TUNNEL DATA

— BOUNDARY LAYER CALCULATION

△ $\epsilon_E = 0.02$, $\epsilon_I = 0.06$ LAMINAR

□ $\epsilon_E = 0.1$, $\epsilon_I = 0.3$

◇ $\epsilon_E = 0.02$, $\epsilon_I = 0.06$ TURBULENT

9.77°

$R = 2.187''$

St

S/Rn
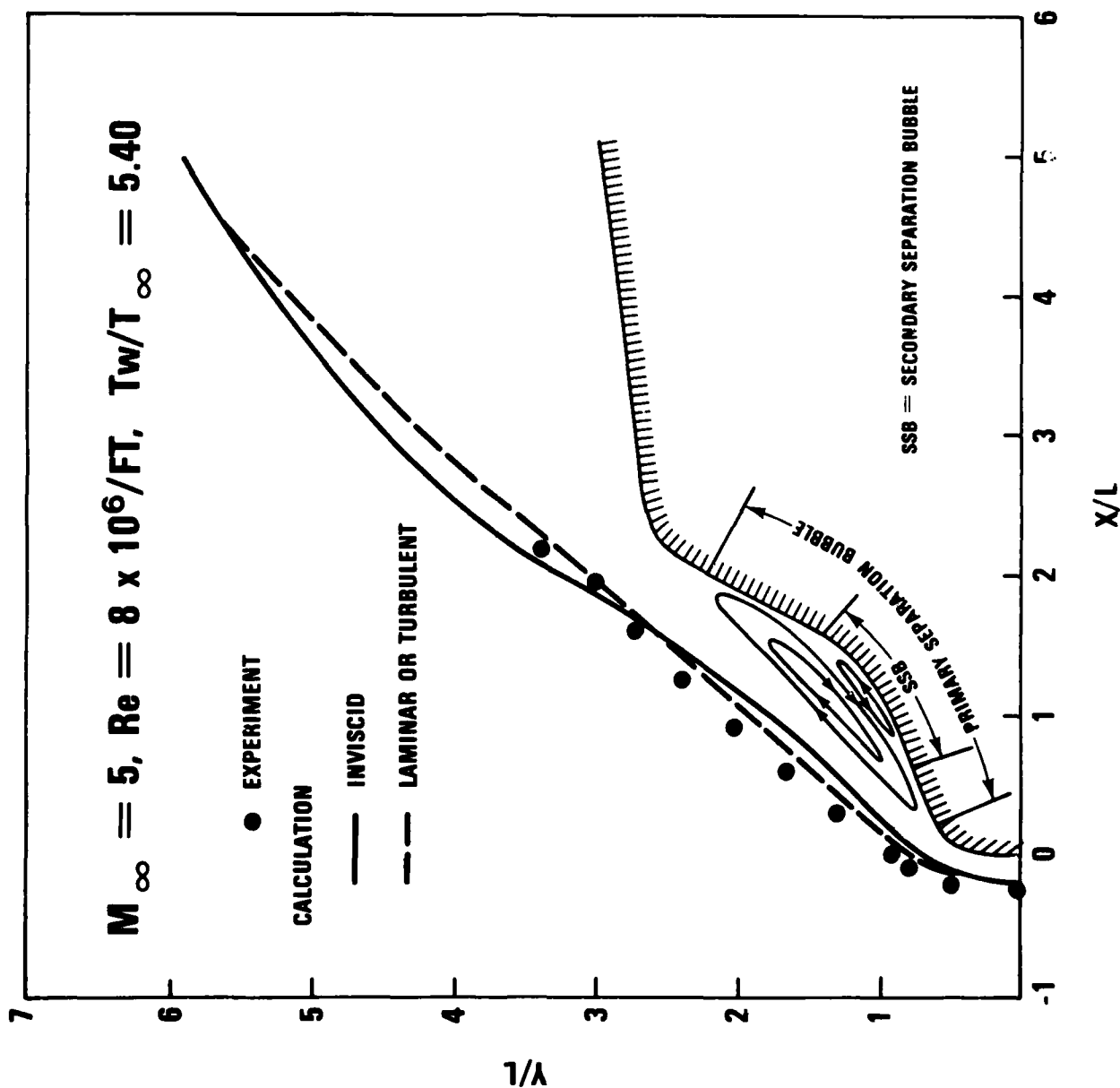
Figure 3   Comparison of Shock Location Between Calculation and Experiment for Model 4

1.0

1.1

1.25   1.4   1.6

2.8   2.5

3.2   2.2

3.6

4.0   2.0

1.8

45
50

MICROCOPY RESOLUTION TEST CHART
NATIONAL BUREAU OF STANDARDS-1963-A
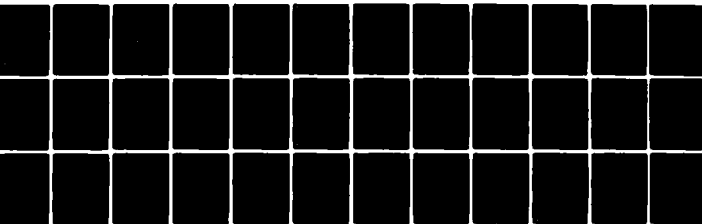
Figure 4   Comparison of Surface Pressure Between Calculation
and Experiment for Model 4

Figure 5   Comparison of Shock Location Between Calculation and Experiment for Model 1
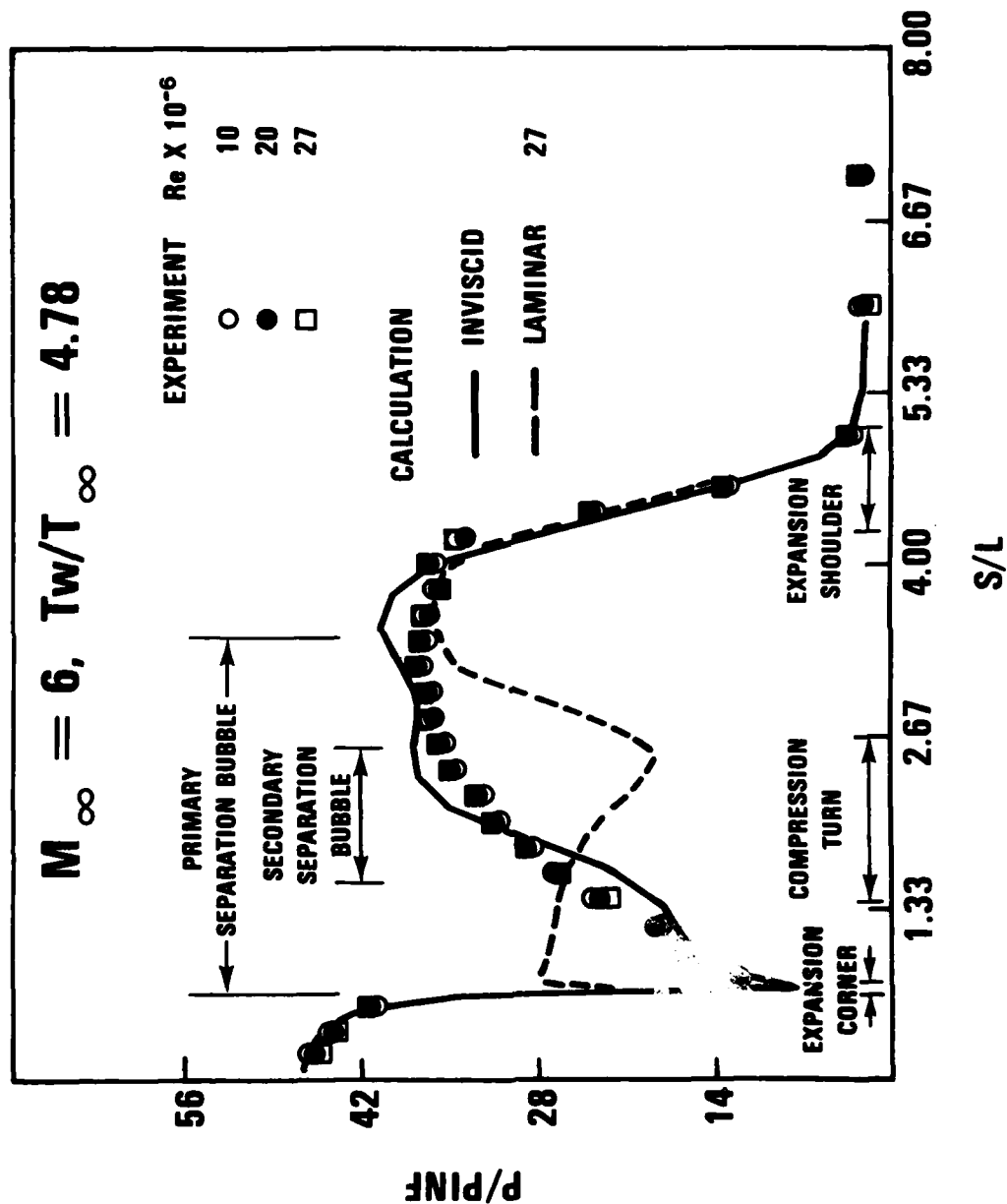
Figure 6   Comparison of Surface Pressure Between Calculation
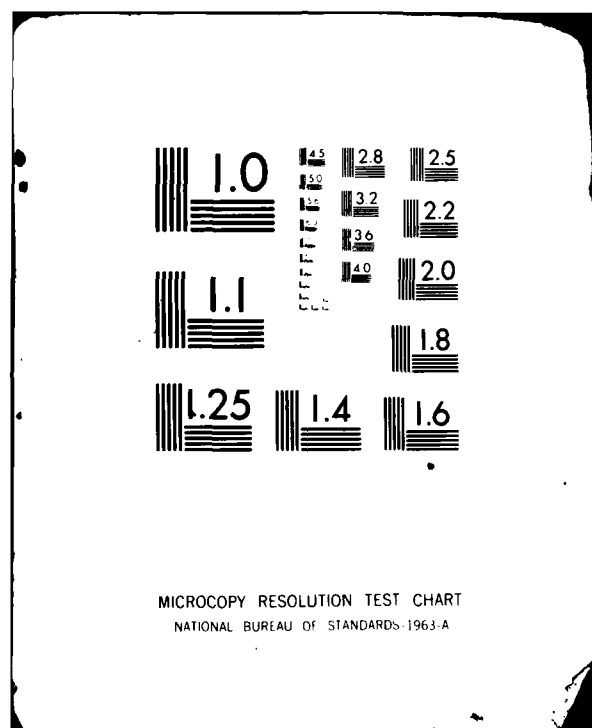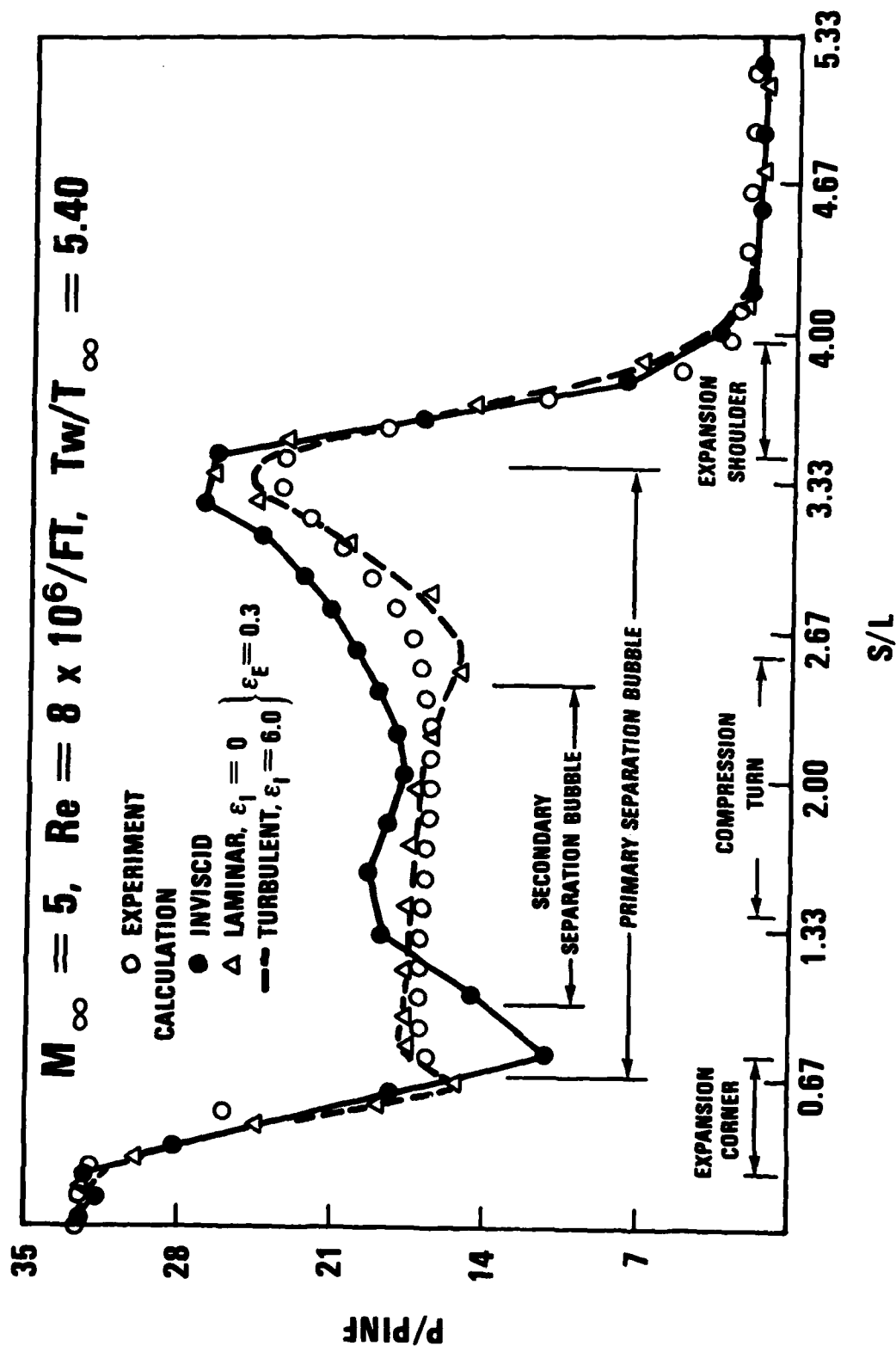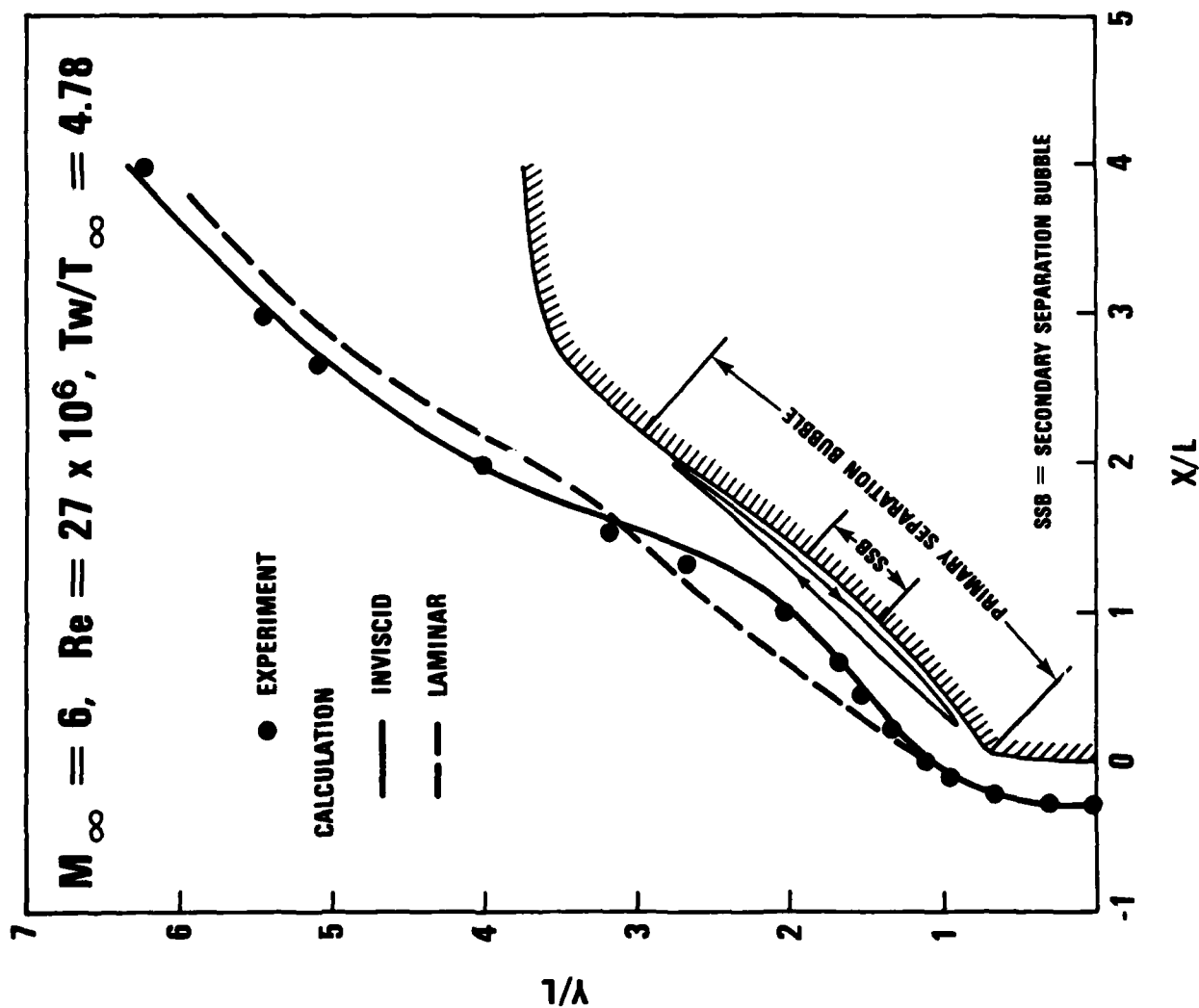and Experiment for Model 1

STRUCTURAL AND ELECTRICAL PERFORMANCE
CONSIDERATIONS IN THE DESIGN OF
MULTIBAND RADOMES

G. Dailey and R. C. Mallalieu
The Johns Hopkins University Applied Physics Laboratory
Laurel Maryland

ABSTRACT

Multimode guidance capability is a requirement for missiles that will satisfy the Navy's near- and far-term area defense needs, which implies the use of thin walled radomes on missiles that will operate at speeds up to M8. Structural analyses were conducted to determine the minimum wall thicknesses that are required to carry the aerodynamic loadings during sea level flight at speeds from M2 to M6 undergoing a 30g maneuver. In this paper the results of the parametric loads and stress investigation are discussed. Also covered are the results of an investigation into the electrical performance of three different wall configurations for use with dual-band guidance at 3 and 5 GHz.

INTRODUCTION

Three radome shapes were investigated, von Karman with length-to-diameter ratios (ℓ/d) of 2.1 and 3.0, and a hemispherical ℓ/d of 0.5. Of interest were base diameters of 7.5, 13,5, and 19.5 in. and flight Mach numbers of 2, 4, and 6. The materials of interest were Pyroceram 9606, reaction-sintered silicon nitride (RSSN), hot-pressed silicon nitride (HPSN), slip-cast fused silica (SCFS), and quartz polyimide (QPI). Thus there were three ℓ/d's, three diameters, three Mach numbers, and five materials, total of 135 cases.

Calculations of aerodynamic loads and centers of pressure were made (Reference 1) and used to define minimum wall thicknesses to carry the bending moments resulting from these loads. Also, using the HIMACH code (Reference 2) at NSWC/Dahlgren, pressure distributions were computed on several radomes at various angles of attack. After programming the von Karman radome geometry for the SATANS computer code (Reference 3), some of these cases were explored to determine the wall thicknesses required to prevent buckling. The mechanical analysis indicated that relatively thin ceramic radomes can withstand the assumed flight environments and that structural failure may be due to either buckling or excessive stress at the base of the radome.

In the electrical performance investigation a dual-band missile allowing 3 GHz passive guidance combined with 35 GHz terminal homing was assumed. For this concept an 0.078 inch halfwave Pyroceram radome was compared to fullwave and half-sandwich designs. The halfwave radome is sturdy enough to survive a variety of missions, but it is considered too fragile to survive the stresses of fabrication and military handling. However, the electrical evaluation showed that the performance of the halfwave radome far exceeded that of the thicker alternatives. Its bandwidth was about 5% at 35 GHz compared to 2% for the others. Even within their passbands, the boresight errors of the fullwave and half-sandwich will probably be twice those of the halfwave. If high frequency systems are to be utilized, methods must be found to allow the fabrication and handling of thin ceramic radomes.

LOADS AND STRESS ANALYSIS OF RADOME BASE

The aerodynamic loads on a missile are schematically shown in Figure 1, where N is the normal force, D is the drag force, and $\bar{x}$ and $\bar{y}$ give the location of the center of messure. The missile was assumed to be undergoing a sea level 30 g maneuver in order to get the maximum aerodynamic loads on the radome. The angles of attack necessary to pull the 30 g maneuver and the resulting aerodynamic loads were computed using standard missile weights and aerodynamics by Marley (Reference 1). It is assumed that the distance $\bar{y}$ is small and that the contribution to the moment at the base from drag is small. The inertial loads are also assumed to be small and are neglected.

The stress at the base of the radome due to bending moment and axial drag loading is therefore (Reference 4)

$$\sigma = \pm \frac{M_B}{\pi R^2 t} - \frac{D}{2\pi RT} \tag{1}$$

where σ is the stress, M_B the bending moment at the base ($N\bar{x}$), R the base radius, and t the radome thickness. To determine the strength requirement for a radome it has been found convenient to express the above in a more generalized parametric form given below:

$$\frac{\sigma_u}{R} = \frac{FS}{\pi R^2} \left[\pm \frac{M_B}{\pi R} - \frac{D}{2} \right] \tag{2}$$

where σ_u is the ultimate strength of the radome material and FS is the ultimate factor of safety.

The required values of $\frac{\sigma_u t}{R}$ as calculated from equation (1) are given in Table 1 with a factor of safety of 1.25 and are plotted versus Mach number in Figures 2 and 3 for all the different configurations. If the angle of attack is independent of diameter then the curves of Figures 2 and 3 reduce to a single curve for each value of ℓ/d. These results are expressed in general terms and are dependent upon the radome's material properties.

For thin-walled radomes under aerodynamic loads, failure due to buckling must be considered. Although a radome made of a brittle material will not buckle in the classic sense, impending buckling will cause stress failures. In order to study buckling of thin-walled radomes, the SATANS computer program (Reference 3) was used. The SATANS program solves geometrically nonlinear, arbitrarily loaded shells of revolution. It uses finite differences in the meridional coordinate and a Fourier expansion in the circumferential coordinate. In the linear case, the total solution is the sum of the solutions for the circumferential modes, but, for the nonlinear case, coupling occurs between the fourier modes. The SATANS program solves the geometrical nonlinear equilibrium problem rather than the eigenvalue problem. For a perfect shell subject to a perfectly symmetrical load, there is no coupling between Fourier modes and buckling will not occur. The method used to obtain buckling loads is to introduce an imperfection in the load of the form

$$\epsilon C_0 \cos n\theta, \tag{3}$$

where ϵ is a small number, C_0 is the Fourier coefficient for the zeroth mode, and n is the mode number for which the buckling load is wanted.

The aerodynamic loads were calculated using the HIMACH code (Reference 2) at NSWC. This code calculates the pressure coefficient, C_p, over the entire radome. The pressure coefficient is calculated as a three-term Fourier series,

$$C_p (X, \theta) = C_0(X) + C_1 (X) \cos \theta + C_2(X) \cos 2\theta.$$

The three functions, $C_0(X)$, $C_1(X)$, and $C_2(X)$, are read into the SATANS program and used to define the loading distribution. For most of the SATANS runs, four circumferential modes were used:

0, 1, 2, n,

where the load on mode n is defined by Equation 3.

The equations defining the geometry of the von Karman radome have been derived in the Appendix of Reference 5. These equations defining radius, radii of curvature, etc. have been programmed into the SATANS code.

For the base bending stress case, the important generalized parameter was $\sigma_u t/R$; however, for the buckling case it is Et^3/R^3 (the bending stiffness of the shell divided by R^3). The reason for dividing by R^3 is that for shells of the same shape but different size subject to similar loads, if the value of Et^3/R^3 is the same, the buckling load will be the same. From the results from the SATANS code, this generalized buckling parameter (Et^3/R^3) and a parameter referred to as the load factor are plotted in Figure 4 for the lowest buckling modes. The load factor is defined as the ratio of the applied load to the nominal load. Therefore, since a factor of safety of 1.25 is assumed to be the design requirement, the value of Et^3/R^3 at a load factor of 1.25 is used to calculate the required wall thickness for each material.

In Figure 4 note that all but one of the SATANS runs were made with a diameter of 19.5 in. This was done as an economy move to keep the number of runs to a minimum. It has been assumed that the effect of angles of attack is small and that the critical load versus Et^3/R^3 is independent of size. One run was made to check this assumption. The results for the 7.5 in. diameter radome do fall

on the curve for the 19.5 in. diameter radome. The required values of Et^3/R^3 for a load factor of 1.25 have been included in Table I. In this table only the $\ell/d = 3.0$ von Karman radome has a full set of values and no values are present for the hemispherical radome.

In Figure 5 the modal deflection curves for a typical SATANS run at Mach 6 are shown. Note that the curve for mode 4 becomes flat before the SATANS run stops. Near the buckling load the deflection for mode 4 changes a lot for a very small change in load.

CALCULATION OF MINIMUM WALL THICKNESS

The generalized results of the analyses are summarized in Table 1. Here the generalized parameters are $\sigma_u t/R$ for base bending stress and Et^3/R^3 for buckling. The radomes are assumed to have reached equilibrium temperatures at the time the loads are applied. For the five materials considered in this study, the ultimate stress in both tension and compression and the modulus of elasticity at the approximate equilibrium temperature are considered. Using the material property data of Table 2 and the generalized parameters from Table 1, the minimum wall thickness were calculated. The resultant wall thicknesses are shown in Table 3, and for Pyroceram 9606 they are shown in Figure 6.

ELECTRICAL CONSIDERATIONS FOR A HIGH-FREQUENCY CERAMIC RADOME

One attractive combination of guidance modes is passive guidance at frequencies on the order of 3 GHz followed by active guidance (transmitter and receiver on the missile) at a much higher frequency, perhaps 35 GHz. The most stringent requirements for the dual-band radome are at the high terminal frequency. There are:

1) Low insertion loss to allow timely detection.

2) Low radome refraction (boresight errors) to prevent steering instabilities.

3) Transmission relatively independent of changes in incident polarization.

The first requirement means that the radome wall structure must be designed to minimize microwave reflections since these are far more significant than material resistive heating. For a single layer radome, this restricts operation to passbands about the thin wall, halfwave, or multiple halfwave modes. Within these passbands, the other design objectives are primarily determined by the type of radome wall and the dielectric constant (ε) of the material.

The solid wall halfwave radome is by far the most attractive for single-band operation. Although its bandwidth is only 5%, its high transparency, low refraction, and favorable polarization properties make it a useful standard of comparison for other radome designs. The thinwall radome operates as a low-pass filter. Thus, a single layer radome could operate as a halfwave radome over a 5% band at 35 GHz and as a thin wall at frequencies up to one-tenth that or 3.5 GHz. This would appear to be an optimum choice for the dual-band radome.

Unfortunately, a ceramic radome is exceedingly thin at 35 GHz. For a radome operating in the N-halfwave mode and at a design angle of incidence θ, the thickness is:

$$t = \frac{Nc}{2f\sqrt{\varepsilon - \sin^2\theta}}$$

The design angle must be chosen to allow transmission over the near grazing angles encountered within a streamlined radome. For Pyroceram 9606 ($\varepsilon= 5.53$) and $\theta = 73^o$, panel thickness is only 0.078 inches. While the first portion of this study has indicated that such a radome could survive the flight stresses of many of the cases described, it is considered by some to be too thin to allow commercial fabrication and military handling. Its electrical performance should be evaluated and compared to the alternatives. If the performance penalty for the alternate designs is excessive, perhaps techniques may be devised to overcome the problems of manufacturing and handling such a radome.

The halfwave Pyroceram radome is evaluated in comparison to a fullwave of the same material and also to a half-sandwich design. The latter consists of an outer layer of Pyroceram backed up by a sufficient thickness of ceramic foam to maximize transmission. The thickness of the outer layer was set to 0.100 inches, the minimum considered allowable for fabrication and handling considerations. All radomes were designed for maximum transmission at 35 GHz and 73°.

The relative quality of these radome walls may be evaluated by the calculated loss and insertion phase delay (IPD) of large flat panels. Loss should remain low for angles of incidence between 40 and 80 degrees. Radome refraction, or boresight error, is primarily caused by the slope of the (IPD) characteristic with angle of incidence. This deflects the beam in a similar fashion to the bending of light by a prism. The third design objective, insensitivity to polarization, depends upon the spread between the transmission characteristics for parallel and perpendicular polarization.

Figure 7 shows the transmission of a 0.078 inch halfwave panel of Pyroceram 9606 at the design frequency and at $\pm5\%$ offsets. The center figure, at the design frequency, serves as the standard of comparison. As required, loss remains low over the critical high angles of incidence. The slope of the IPD curves is acceptable according to the low levels of boresight error associated with halfwave radomes. Both loss and IPD curves track as a function of polarization.

Figure 7's two outer diagrams show the detuning of the panel with frequency. These 5% frequency offsets are excessive for a halfwave radome, in which total bandwidth is about 5%. These offsets were chosen to emphasize changes in transmission with frequency. Loss increases for the perpendicular component, and the curves no longer track with polarization.

Figure 8 shows the transmission of a 0.157 inch fullwave panel of Pyroceram 9606. It also was designed for 35 GHz and 73°. At 35 GHz, insertion loss is significantly higher than the halfwave except in the vicinity of the design angle. The slopes of the IPD curves are twice those of the halfwave. Even at the design frequency, the resulting boresight errors would be about twice those of the half-wave. The outer diagrams of Figure 8 show a severe detuning for 5% frequency offsets.

Figure 9 represents the half-sandwich with a 0.100 outer layer of Pyroceram and an inner layer of ceramic foam (ϵ = 3.0, tan δ = 0.01) in which the 0.076 inch foam thickness was adjusted to maximize transmission at 35 GHz and 73°. A comparison of Figure 9 and Figure 8 shows that the transmission of this half-sandwich approximates that of the fullwave. The only noticeable exception is the higher loss of the parallel polarization component. This is due to the relatively high loss tangent assumed for the foam layer.

The two-layer half-sandwich has sometimes been called a "broadband" radome. In comparison to typical broadband panels, the thinwall, the A-sandwich and the C-sandwich, which offer broadband transmission for relatively low angles of incidence, Figure 9 shows that the half-sandwich approximates the relatively narrow-band performance of the fullwave. What then are its advantages? As a general rule, the presence of the foam layer behind a relatively thin outer layer of higher ϵ material makes the panel operate like the next higher N-halfwave wall. This may be advantageous in the following situations:

1) If the hard outer layer is made of a material which is expensive, a minimally thick outer wall may be combined with a less expensive inner layer.

2) The passband is somewhat great than that of the N-halfwave because of the decrease in average dielectric constant, but the mid-band performance will be slightly inferior to that of the N-halfwave panel. However, the half-sandwich is not a broadband radome.

The bandwidth of the halfwave, fullwave and half-sandwich panels are compared in Table 4. The phasor sum of the complex transmission coefficients for ten representative rays was calculated. These are parallel and perpendicular polarized rays at angles of incidence of 60, 65, 70, 75 and 80 degrees. At 3 GHz, all three panels would be satisfactory since insertion loss is not critical for passive guidance. According to loss considerations, the 35 GHz bandwidth of the halfwave radome is much wider than that of either of the alternatives. Since IPD slope variations would reduce bandwidth still further, the total bandwidth of the fullwave and the pseudo fullwave half-sandwich will only be about 2%, compared to the typical halfwave radome bandwidth of 5%.

DISCUSSION AND CONCLUSIONS

It is apparent from the results in Table 2 that, in general, both buckling and base bending stress should be considered in designing thin-walled radomes. The results do not vary much from configuration to configuration, and the conclusions reached regarding the importance of base stress versus buckling are independent of the configuration.

Several of the materials considered cannot withstand the equilibrium temperatures associated with the higher sea-level Mach numbers. The QPI cannot operate at equilibrium temperatures associated with Mach 4 and 6 and is buckling limited at Mach 2. The SCFS cannot operate at the Mach 6 equilibrium temperature and is stress-limited at Mach 2 and 4. Pyroceram 9606, RSSN, and HPSN all have the same characteristics - buckling controls the design at Mach 2, stress controls the design at Mach 6, and either may control at Mach 4. Thus, for these three materials, both failure modes must be considered.

If radome fragility during fabrication and handling is used to establish the minimum practical thickness for ceramic radomes, the performance penalty during active homing at 35 GHz could be quite high. The electrical performance of the fullwave and half-sandwich radomes are far inferior to that of the 0.078 inch halfwave. For a fixed diameter seeker, boresight errors and slopes appear to decrease somewhat with large increases in frequency for systems which use halfwave radomes. Thus, for a relatively large missile, the higher IPD slopes of the fullwave and half-sandwich radomes may be tolerable. The restricted bandwidth still remains, however, and this may make the system more vulnerable to secondary effects such as radome de-tuning due to aerodynamic heating.

References

1. E. T. Marley, "Calculation of Aerodynamic Loads and Centers of Pressure on a Series of Designated Radomes", JHU/APL BFD-EM-986, March 1980.

2. J. Sun, "User's Guide and Assessment of the NCSU Body Alone High Mach Code", NSEC K21 No. 2/79, November 1978.

3. R. E. Ball, "A Geometrically Nonlinear Analysis of Arbitrarily Loaded Shells of Revolution", NASA CR-909, January 1968.

4. G. Dailey, "Structural Analysis of Thin Walled Radomes", JHU/APL EM-4943, May 1980.

5. G. Dailey, "Structural Analysis of Three Postulated Radomes for the SS-N-3a Cruise Missile", APL/JHU EM-4567. June, 1974.

Table 1

Summary of Material Strength and Stiffness Requirements for
30 g Sea-Level Maneuver

Case	ℓ/d	d	M	Strength Requirement $\sigma_u t/R$		Stiffness Requirement Et^3/R^3
				Tension	Compression	
Spherical						
1	0.5	7.5	2		25.45	
2	0.5	7.5	4		99.84	
3	0.5	7.5	6		225.75	
4	0.5	13.5	2		25.51	
5	0.5	13.5	4		102.84	
6	0.5	13.5	6		228.18	
7	0.5	19.5	2		25.80	
8	0.5	19.5	4		102.07	
9	0.5	19.5	6		224.76	
Von Karman						
10	2.1	7.5	2	63.50	70.92	
11	2.1	7.5	4	75.80	97.67	
12	2.1	7.5	6	98.19	156.53	3.40
13	2.1	13.5	2	74.46	81.66	
14	2.1	13.5	4	96.72	117.99	
15	2.1	13.5	6	109.05	156.58	3.40
16	2.1	19.5	2	72.29	79.53	
17	2.1	19.5	4	87.97	109.20	
18	2.1	19.5	6	98.20	156.40	3.40
19	3.0	7.5	2	109.44	113.46	7.00
20	3.0	7.5	4	132.17	148.44	2.10
21	3.0	7.5	6	142.30	173.34	3.00
22	3.0	13.5	2	126.13	129.94	7.00
23	3.0	13.5	4	162.82	179.48	2.10
24	3.0	13.5	6	160.72	191.72	3.00
25	3.0	19.5	2	119.50	123.35	7.00
26	3.0	19.5	4	153.81	170.44	2.10
27	3.0	19.5	6	160.52	191.47	3.00

Table 2

Material Properties of Radome Materials at Equilibrium Temperatures

Ultimate Stress in Tension (psi)

M	T ($^{\circ}$F)	9606	RSSN	HPSN	SCFS	QPI
2	400	22 K	20 K	50 K	5 K	45 K
4	1400	12 K	20 K	50 K	5 K	-
6	3000	4.8 K	9.8 K	9 K	-	-

Ultimate Stress in Compression (psi)

M	T ($^{\circ}$F)	9606	RSSN	HPSN	SCFS	QPI
2	400	115 K	200 K	200 K	50 K	20 K
4	1400	115 K	200 K	200 K	80 K	-
6	3000	20 K	200 K	200 K	-	-

Modulus of Elasticity (psi)

M	T ($^{\circ}$F)	9606	RSSN	HPSN	SCFS	QPI
2	400	16.7×10^6	15×10^6	40×10^6	5×10^6	2×10^6
4	1400	16.7×10^6	15×10^6	35×10^6	5×10^6	-
6	3000	$.9 \times 10^6$	8×10^6	8.6×10^6	-	-

Table 3

Required Wall Thickness for Radomes Subject to Aerodynamic Loads

Case*	9606		RSSN		HPSN		SCFS		QPI	
	TS	TB	TS	TB	TS	TB	TS	TB	TS	TB
1	0.0008		0.0005		0.0005		0.0019		0.0048	
2	0.0033		0.0019		0.0019		0.0047			
3	0.0423		0.0042		0.0042					
4	0.0015		0.0009		0.0009		0.0034		0.0086	
5	0.0060		0.0035		0.0035		0.0087			
6	0.0770		0.0077		0.0077					
7	0.0022		0.0013		0.0013		0.0050		0.0126	
8	0.0087		0.0050		0.0050		0.0124			
9	0.1096		0.0110		0.0110					
10	0.0108		0.0119		0.0048		0.0476		0.0133	
11	0.0237		0.0142		0.0057		0.0568			
12	0.0767	0.0584	0.0376	0.0282	0.0409	0.0275				
13	0.0228		0.0251		0.0101		0.1005		0.0276	
14	0.0544		0.0326		0.0131		0.1306			
15	0.1534	0.1051	0.0751	0.0507	0.0818	0.0495				
16	0.0320		0.0352		0.0141		0.1410		0.0388	
17	0.0715		0.1429		0.0172		0.1715			
18	0.1995	0.1519	0.0977	0.0733	0.1064	0.0716				
19	0.0187	0.0281	0.0205	0.0291	0.0082	0.0210	0.0821	0.0420	0.0213	0.0569
20	0.0413	0.0188	0.0248	0.0195	0.0099	0.0147	0.0991	0.0281		
21	0.1112	0.0560	0.0545	0.0270	0.0593	0.0264				
22	0.0387	0.0505	0.0426	0.0524	0.0170	0.0378	0.1703	0.0755	0.0439	0.1025
23	0.0916	0.0338	0.0550	0.0350	0.0220	0.0264	0.2198	0.0505		
24	0.2260	0.1008	0.1107	0.0487	0.1205	0.0475				
25	0.0530	0.0730	0.0583	0.0756	0.0233	0.0545	0.2330	0.1091	0.0501	0.1480
26	0.1250	0.0488	0.0750	0.0506	0.0300	0.0382	0.2999	0.0730		
27	0.3261	0.1456	0.1597	0.0703	0.1739	0.0686				

*Specifications from Table 1

TS = Thickness required to satisfy the base bending stress (compressive stress limited for all spherical radomes and von Karman radome of QPI; all other von Karman radomes are tensile stress limited).

TB = Thickness required to satisfy buckling.

Table 4

Approximate Radome Insertion Loss (One-Way)

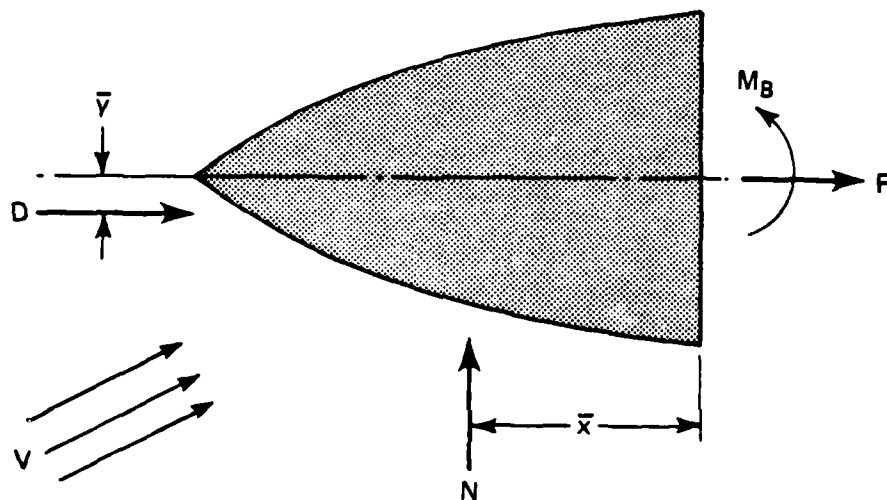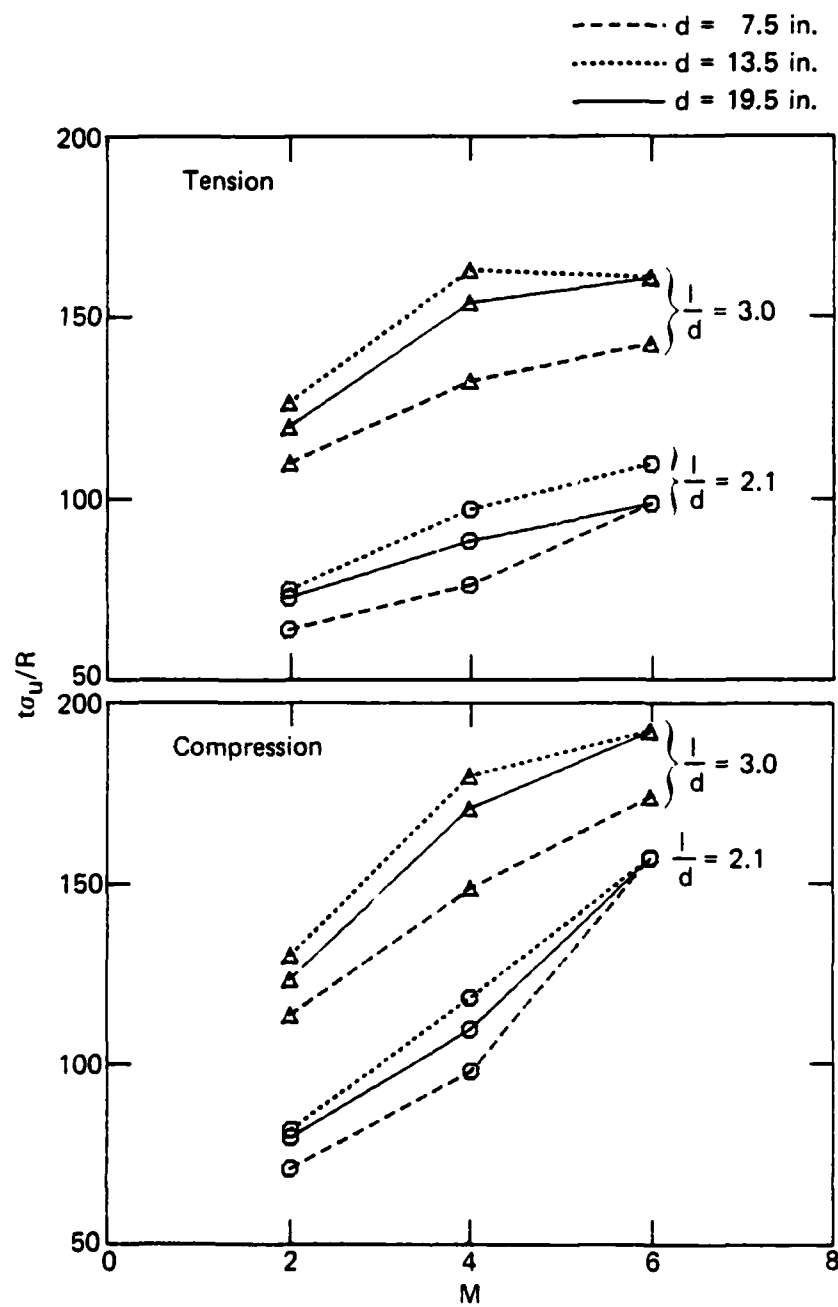| Type	3 GHz	33.25 GHz	35.00 GHz	36.75 GHz
Halfwave	1.6 dB	0.7 dB	0.1 dB	1.0 dB
Fullwave	2.9	1.8	0.3	2.5
Half-Sandwich	2.6	1.7	0.9	2.4

Figure 1   Aerodynamic loads on a radome.

Figure 2   Required wall thickness for stress at base of Von Karman radome.
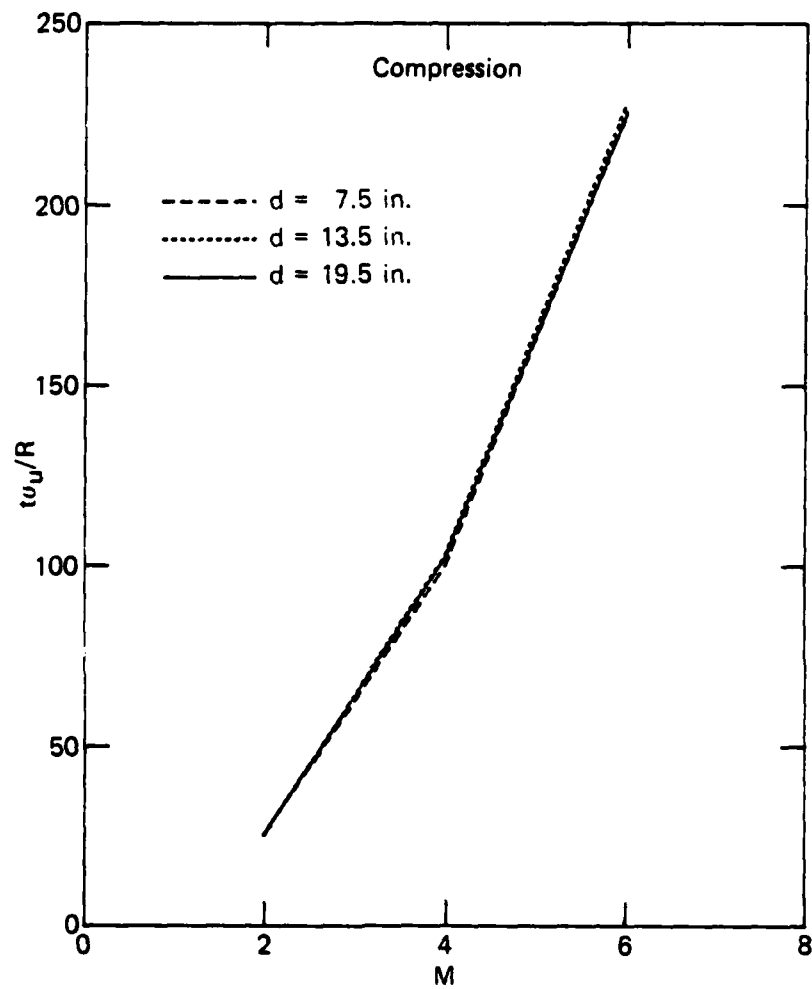
Figure 3   Required wall thickness for stress at base of hemispherical radome.

Figure 4   Load factor needed to buckle versus Et^3/R^3 for Von Karman radomes.

Figure 5 Load versus deflection for different circumferential modes of a Von Karman radome at Mach 6.

Figure 6   Required wall thicknesses for Pyroceram 9606 radome subject to
aerodynamic loads.

Figure 7   Transmission of halfwave panel.

II–327

Figure 8   Transmission of fullwave panel.

Figure 9   Transmission of halfsandwich panel.

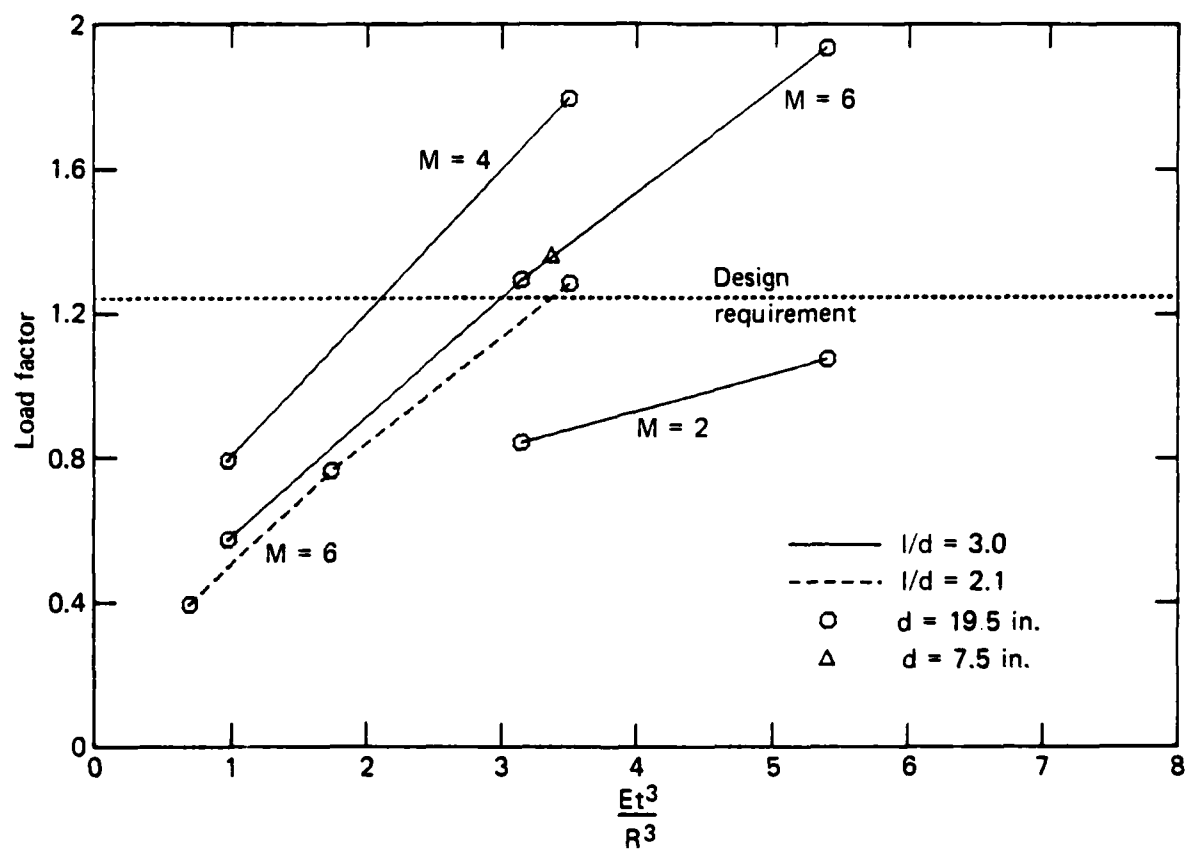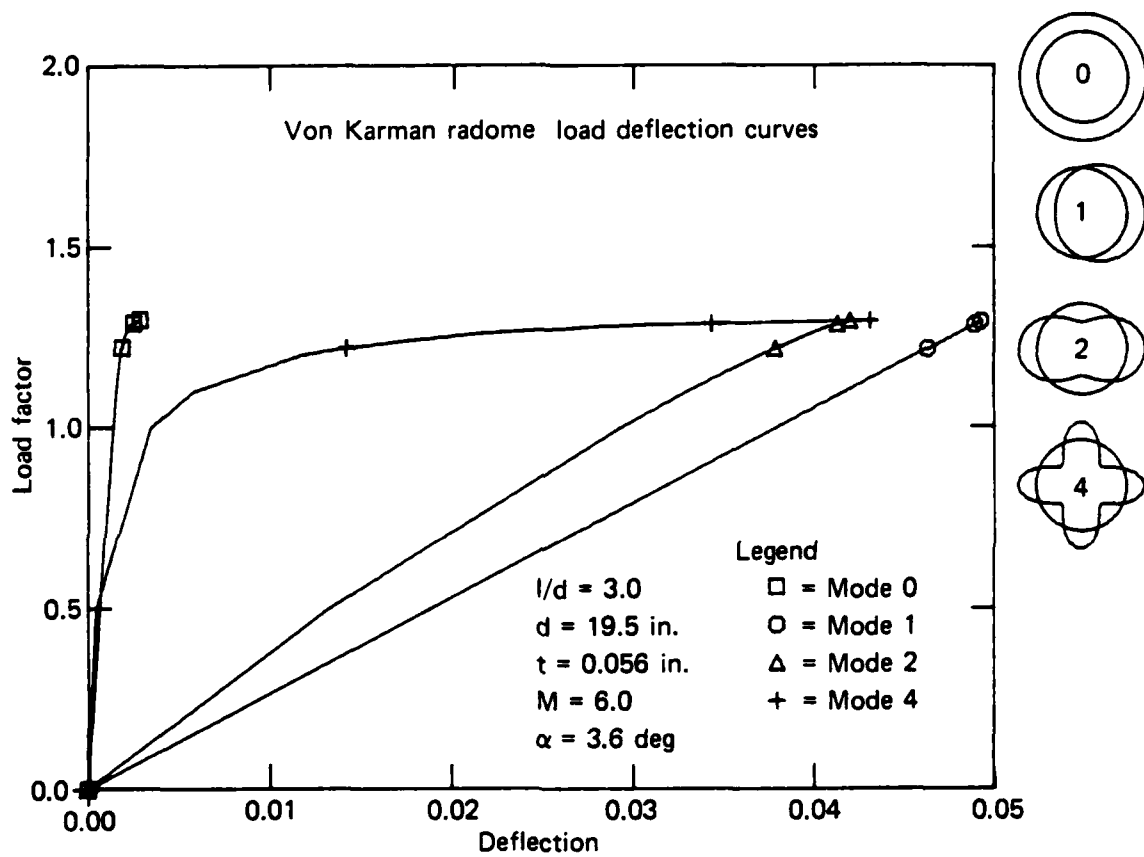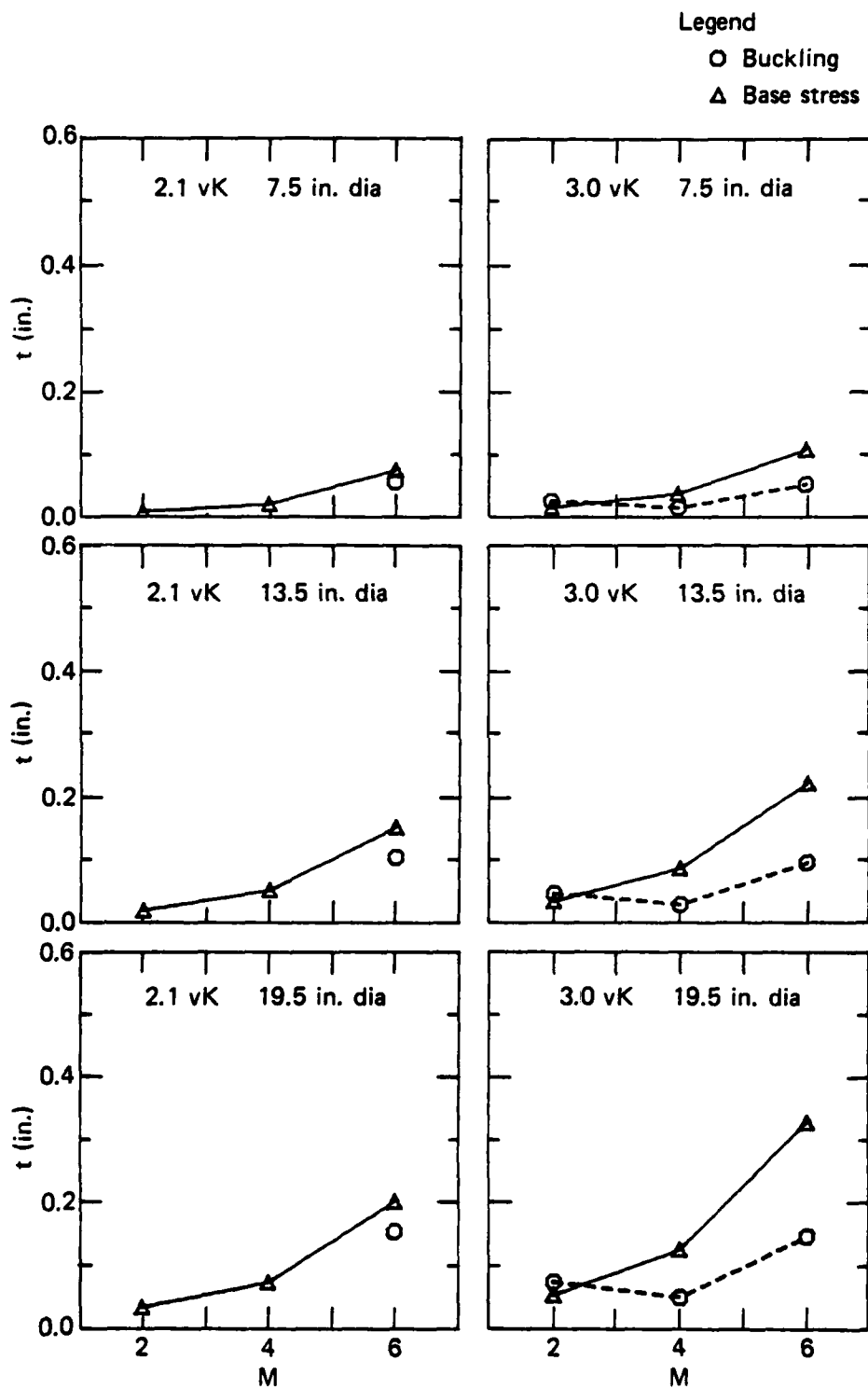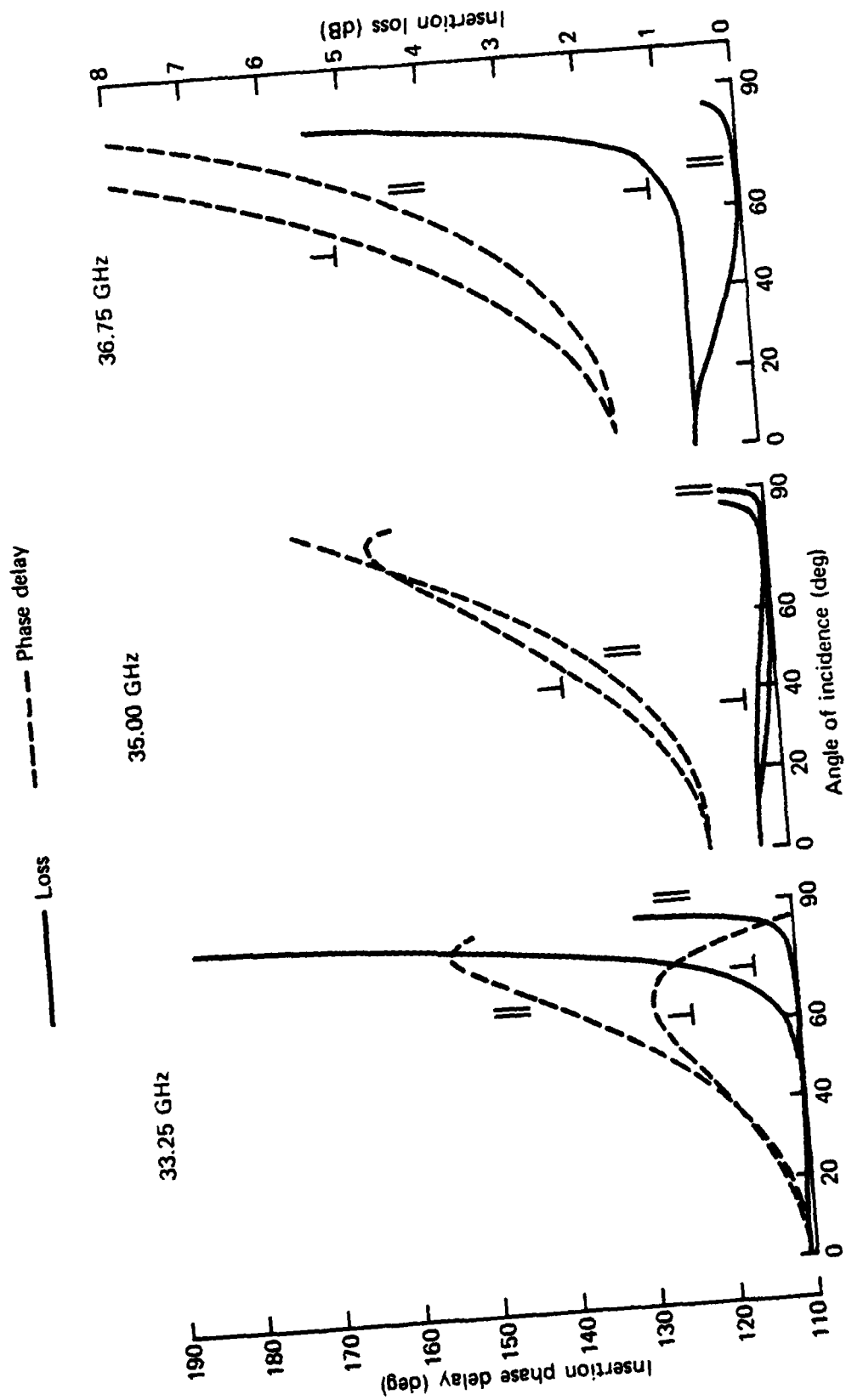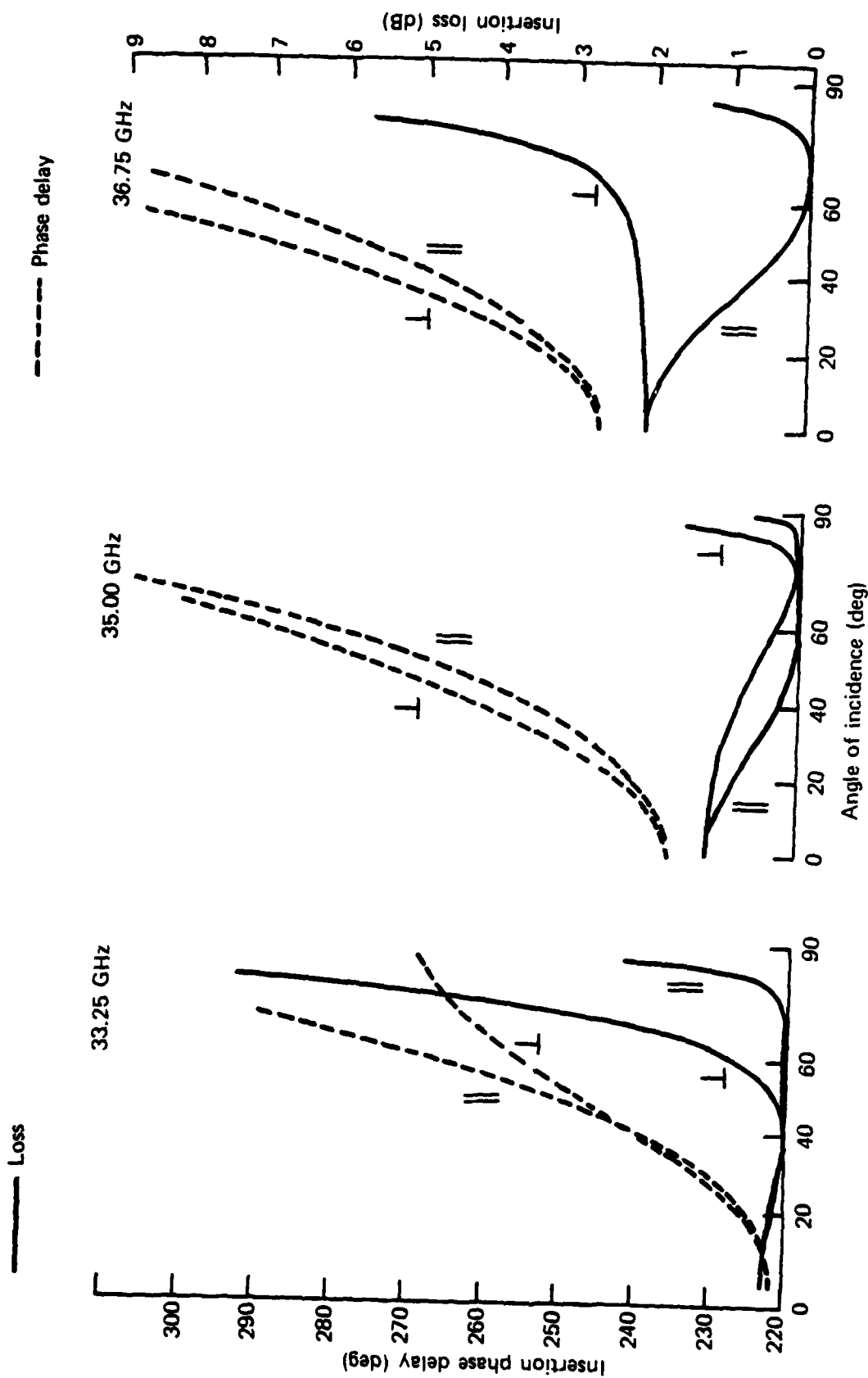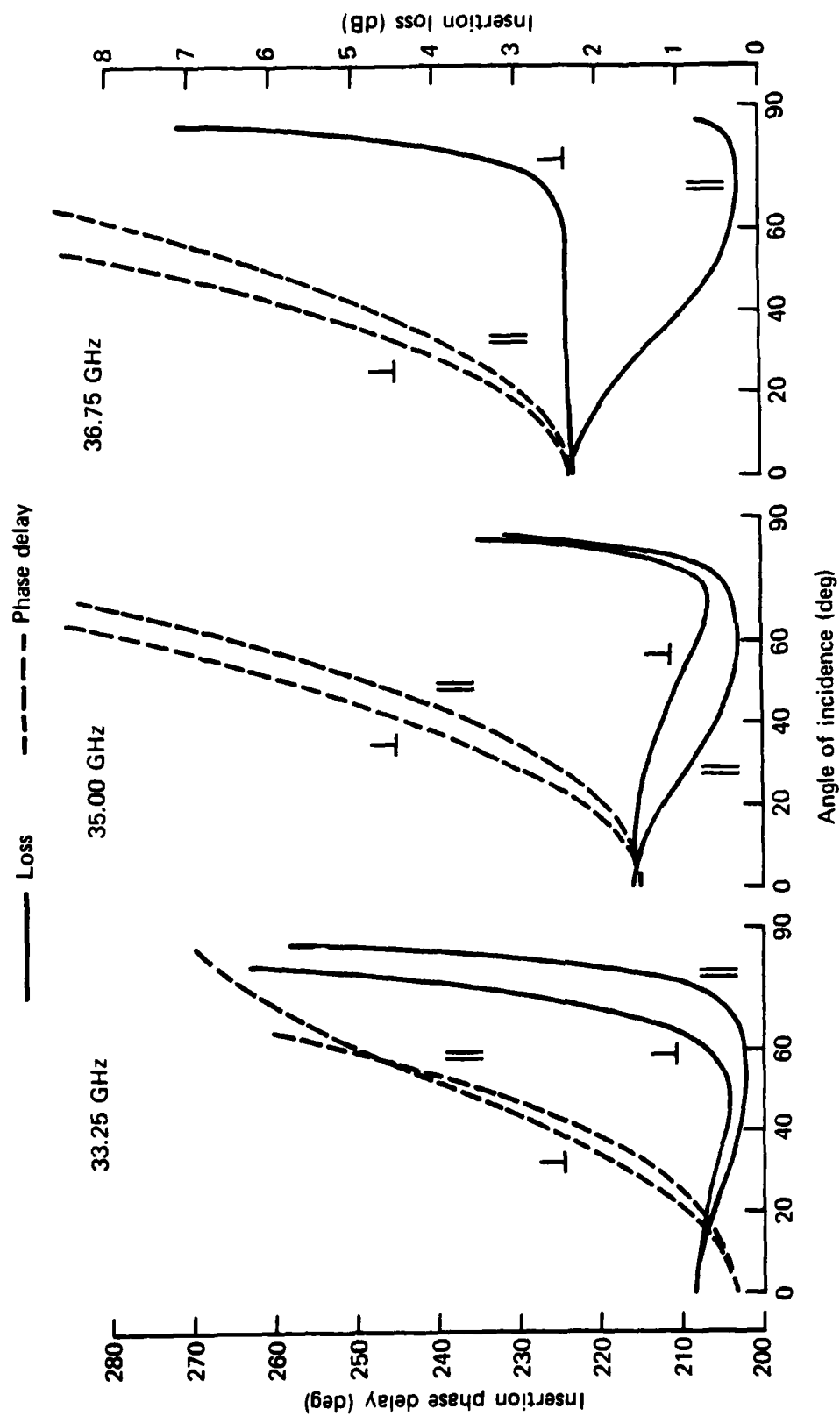STRUCTURAL CONSIDERATIONS FOR THE RECOVERY OF

AIR-TO-AIR MISSILES

Arvid A. Anderson
Pacific Missile Test Center
Point Mugu, California

ABSTRACT

The recovery of air-to-air missiles for training and evaluation is a cost and asset saving technique for consideration of the missile community. Cost, environmental, logistic, and physical constraints require decisions that complicate the structural designers task. Some considerations for design are discussed. An example showing possible trade-offs is given. A discussion of structural considerations is then followed by concluding statements.

INTRODUCTION

The recovery and reuse of air-to-air missiles, expended in testing and training environments, has long appeared to be a cost effective means for training capability and utilization of the weapon as well as providing the potential to accurately determine the causes of missile in-flight failures. Many studies have been conducted to analyse the technical feasibility and cost effectiveness of recovering missiles for reuse (references 1-2). The AIM-7 and AIM-54 missiles have been considered as prime candidates for consideration.

Many technical problems have been defined in considering the addition of recovery capability to an existing missile. Cost of course, is the limiting factor.   Issues driving technical considerations include: (1) land/water/mid-air recovery, (2) anticompromise, (3) full vs partial missile recovery, (4) water integrity, and (5) use envelope of launches.

STATEMENT OF INITIAL CONDITIONS

For this paper the purpose for a paracnute recovery system can be defined as: "a capability to reduce the velocity of a post-intercept missile to some acceptable amount low enough to allow retrieval of it for reuse."

Before a recovery system for a missile can be postulated, it is necessary to determine a use envelope of launches for both training and test and evaluation shots. Within that envelope an acceptable scenario can be generated for both training and test and evaluation. This has an important limiting effect on the design. Realistic decisions by the "user" can allow the designer sufficient flexibility to produce a more efficient/cost-effective product. For instance: if for training purposes a significant number of missiles, say 80-90 percent are to be fired at a mid-altitude, mid-range, mid-speed condition, then this should be specified. Design compromises are therefore more realistically made. An appropriate method for interpreting a given aircraft/missile launch envelope is to generate a scenario of launch geometries suitable for

training and/or RDT&E missions.

In order to construct a scenario of recoverable launch geometries for future Fleet training exercises and future T&E launches, a study of expected Fleet threats and a review of all past T&E launches should be made. Future Fleet training launch geometries must be designed around probable enemy threats. Air Test and Evaluation Squadron Four (VX-4) can supply data pertaining to expected enemy threats to the Fleet and beach head defense situations and has compiled this data in their report "FPX-2E". This classified report describes the threats as single bombers, multiple bombers, air-to-surface missiles (ASM) air launched, ASM surface launched, overland fighters, manuevering targets and the high altitude, high Mach threat. Target altitudes can be broken down into general categories; low (1,000 feet), medium (5,000 to 30,000 feet), and high (above 35,000 feet). Target speed and maneuvers can also be defined. Using the above criteria and prioritization criteria such as might come from the Ault Report (reference 7), threat profiles can be established against which future Fleet training launches can be designed.

Given a list of profiles, a table of launch geometries can be compiled and submitted to aerodynamists for post intercept parameter calculations. From the post intercept parameter calculations, worst case recovery conditions can be determined. To determine the worst-case recovery conditions, that is the geometry which would cause the most stress to the deploying parachutes, the post intercept parameters can be used to calculate the dynamic pressures (q) of individual geometries as follows:

dynamic pressure (q) = $1/2 \ P \ V^2$

P = air density at recovery altitude

V = missile velocity at recovery (ft/sec)

Given the initial loading conditions at intercept, the design problem of a recovery system can be addressed. This entails the designing of a parachute system to fit those load conditions and the load conditions at impact (water or land). The missiles structural integrity and its components resistence to shock and vibration are a limiting input to the parachute system design at this point.

CONSIDERATIONS OF POSSIBLE SOLUTIONS:

One of the first problems to be considered in the design of a recovery system is the question of a need to recover over both land and water. If over land, the missile terminal velocity and attitude at touchdown can be critically limiting to the design. If over water, terminal velocity and attitude are less critical but salt water integrity is required for most of the internal parts of a missile. One solution to both land and water recovery problems is MARS, a mid air recovery system. This is a complicated and costly solution. The logistics and expense of mid-air retrieval usually procludes its use except for unusual circunstances.

For over-land recovery, a very low terminal velocity or a cushioning device will probably be required. The TOMAHAWK missile solved this problem for recovery of test and evaluation shots by use of an inflatable air bag below a horizontally suspended airframe.

For over-water recovery, a flotation device must be incoporated to insure that a retrieval attempt can be made. Also required would be a device to insure that the floating missile would sink after some predetermined time because of security considerations. If the missile is suspended vertically by the parachute lines to enter the water nose first, a high terminal velocity could allow the missile to penetrate the water to below its crush depth.

Another problem to consider for a recovery system is whether the whole missile need be retrieved. The usual method for packing a recovery system in a missile is as a replacement for the warhead section. If only the empty motor, skin and wings are aft of the warhead section it would probably not be economic to recover the entire missile. Parachute deployment becomes simpler with this condition.

Still another problem to consider is the possibility of a slow down maneuver by directing the missile to climb to bleed off speed. The state-of-the-art of parachute design is limited in the supersonic region. Also, very low altitude recovery may require this maneuver because of a lack of time to impact for a recovery system to deploy.

Postulation of a Recovery System

A recovery system for a specific missile, such as the PHOENIX AIM-54, could probably be limited to over-water recovery since most testing and training shots occur over the ocean and most likely at a sea test range for control and data retrieval purposes. Consider the size, strength and volume of the recovery systems required to decelerate either the forward section of the PHOENIX or the total PHOENIX missile. The forward section includes the radome, the seeker, and the guidance section, and part of the warhead section. The total missile includes, in addition to the forward section, the spent motor section, the control section, and part of the warhead section.

To determine if both PHOENIX configurations can be recovered, consideration must be given to the total parachute systems. Deployment reliability, volume required for ejection mechanisms, volume required for the parachute and deployment complications associated with recovering the entire missile, all influence a decision as to recoverability. Factors to consider are: (1) recovering the forward section only allows for a traditional, unobstructed rear streaming flow of the parachute. Loads are longitudinal and do not impart pitching or tumbling motions to the missile (figure 1); (2) to recover the entire missile, the parachute system is more complicated (figure 2). First, dual drogue chutes are required to prevent the missile tumbling motion which would be induced if only one drogue were used. Then a large section of the missile's skin must be cut and removed to allow the main parachute deployment bag to exit. At least one-half the circumference of the body skin would need to be removed which would seriously weaken the fuselage. Structural failure could result when the main chute opening force is applied. When recovering only the forward section, danger of rotation or tumbling of the missile; thereby fouling the parachute, is removed. Tumbling will not be induced since the deployment force is along the missile's longitudinal axis, which ensures a stable deployment.

Regardless of which configuration is selected for recovery, the volume available for the parachute system is the same. Approximately 1,475 cubic inches are available for the parachutes, the mortars, the timers, the flotation gear, and the locator beacons. The defined terminal rate of descent is 65 ft/sec
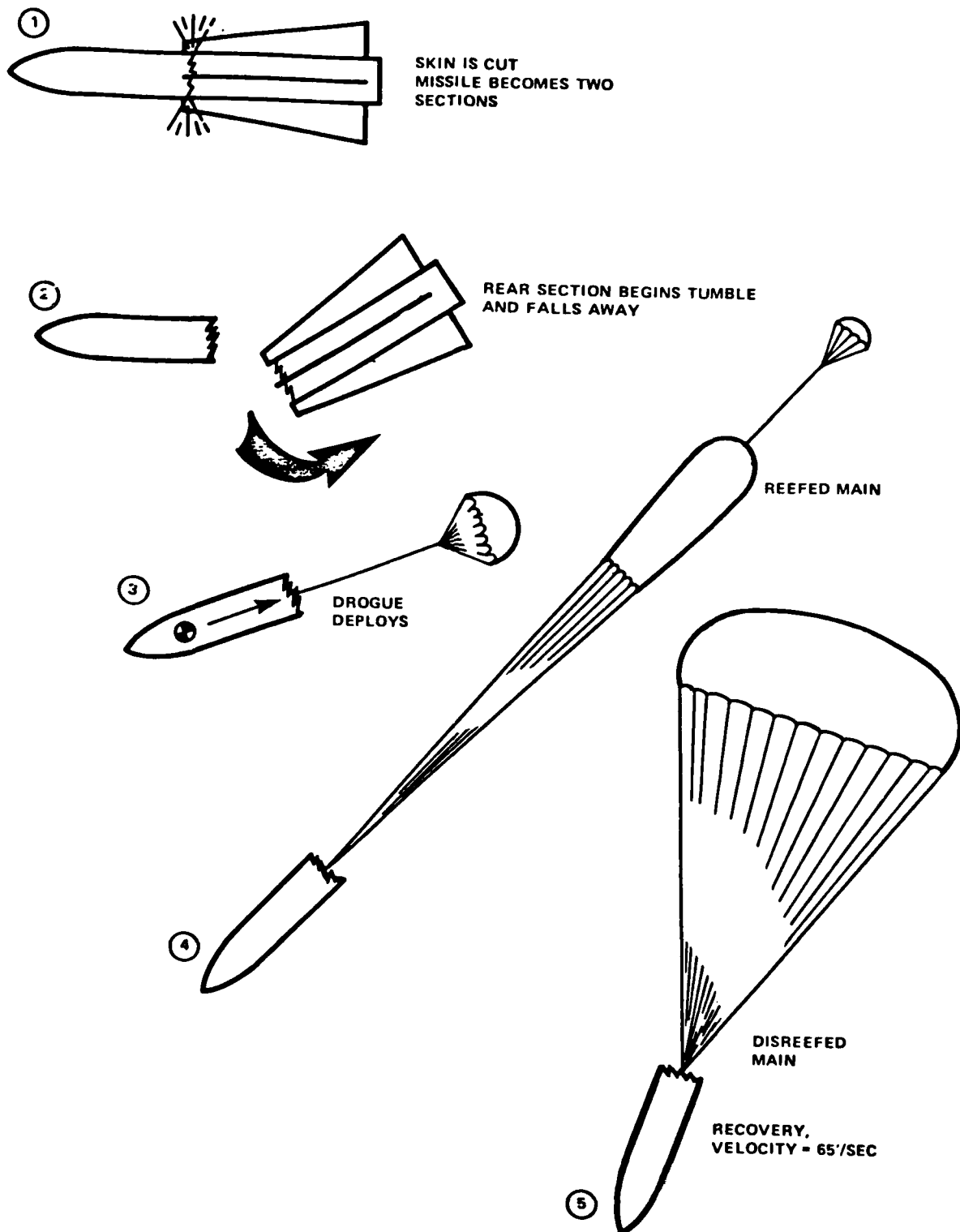
II-333

1. SKIN IS CUT
MISSILE BECOMES TWO
SECTIONS

2. REAR SECTION BEGINS TUMBLE
AND FALLS AWAY

3. DROGUE
DEPLOYS

REEFED MAIN

4.

DISREEFED
MAIN

RECOVERY,
VELOCITY = 65'/SEC

5.

Figure 1. Parachute Deployment Sequence (Forward Section).

DUAL DROGUES MORTERED OUT

DROGUE SLUGS

SKIN CUT, EXTRACTION CHUTE
DEPLOYES MAIN AFTER EJECTION
FROM MISSILE.

REEFED MAIN DEPLOYED SNATCH
FORCE MAY FRACTURE MISSILE

TUMBLING
MOMENT
INDUCED

DISREEFED MAIN
RECOVERY VELOCITY = 50'/SEC

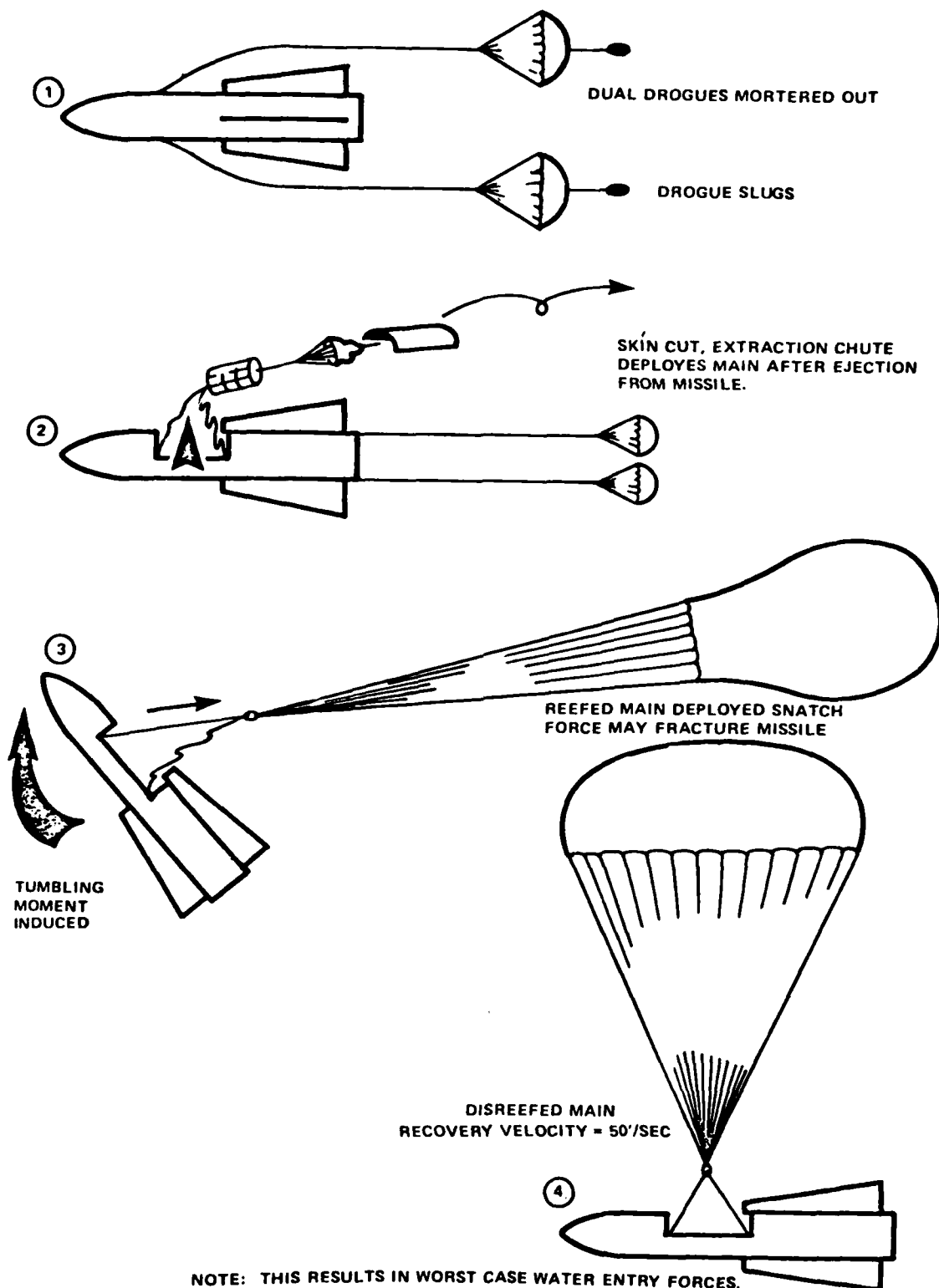NOTE: THIS RESULTS IN WORST CASE WATER ENTRY FORCES.

Figure 2. Parachute Deployment Sequence (Full Missile).

II-335

for either system. The forward section weighs 290 pounds while the entire
missile weighs 545 pounds at recovery. A larger diameter parachute constructed
of stronger material is required to lower 545 pounds at 65 ft/sec than to lower
the 290 pounds at the same rate of descent. There would be sufficient volume
to containe the parachute for the full missile recovery system but not the
space to also include the drogue mortars and flotation gear. These details
must be considered when making a decision as to which configuration is to be
recovered.

A parachute recovery system could be designed for both missile configura-
tions. The designs would be based on standard parachute design practices as
described in the handbook (reference 4). Basic calculation methods since
that date have not changed.

In order to calculate parachute size and strength, some assumptions have to
be made. The assumptions are consistent between systems and would include
the following:

Recovery velocity
Recovery altitude
Initial missile pitch angle
Recovery dynamic pressure
Maximum terminal velocity
Weight of forward section
Weight of entire missile

The basic equation used in calculating a theoretical parachute size and
force is:

$$F = q \, C_{D_o} \, S$$

where:
F = force or the weight recovered in pounds

q = dynamic pressure (lbs/sq.ft)

C_{D_o} = drag coefficient of the parachute type (.75 for a solid flat canopy)

S = the parachute area (usually flat canopy size) in sq.ft

Using equation (1), the parachute diameter required for the 65 ft/sec
terminal velocity rate of descent in recovering the front section only can be
calculated.

The drogue chute selected would be a ribless guide surface design of small
diameter.

Initial force calculations could indicate that an unreefed main opening
would exert excessive force on the parachute mounting points as well as damaging
components in the missile. Therefore, the main canopy could be reefed to an
effective diameter for a required time period. This reefing (restricting the
full open diameter of the main chute by lacing a constricting line through the
skirt) will allow a reduction of velocity while a smaller drag area is exposed
to the higher "q" conditions. The force is directly proportional to the velocity
and the drag area. By adjusting the reefing line length, a balance of forces

can be achieved between reefed open (smaller drag area) and full open; thus allowing the missile and parachute structure to see a lower peak force. The three stage recovery system for the forward section is defined as:

1. The drogue chute
2. The reefed main
3. The disreefed main

The force/time history of the deployment might be such as shown in figure 3. The curves connecting the inflection points are estimated shapes as there is no program available to derive exact force or time values during inflation periods and deceleration to equilibrium velocities. In order to determine the forces during the various sequences of deployment, it would be necessary to know the system velocity, altitude, and pitch angle at the appropriate events. To assist in these calculations, a set of parametric trajectory curves and nomographs can be used. They can be found in ASD-TR-61-579 (reference 4). By knowing the initial velocity (V_o) and pitch angle (0_o) and the required equilibrium velocity (V_{eo}), the following values may be found graphically: system velocity at a delta time after initialization (V), altitude loss (H), range (R), and a new pitch angle after delta time (t). By obtaining the velocities (V) and new altitudes at each deployment event, the force can be calculated using equation (1). With these data, a force/time histograph can be made.

The method of calculating the required data for the total missile recovery is the same as defined above. A typical force time histograph is included as figure 4.

With the above information as postulated it would now be possible to evaluate the structural integrity of a recovered missile (either the full missile or the partial front end section).

DISCUSSION OF STRUCTURAL CONSIDERATIONS

The structural integrity can be determined for the two critical events in the recovery sequence, the deployment shock and the water entry forces as compared to the missiles capability to resist those loads.

For the deployment shock a preliminary analysis of loading conditions can be investigated for the recovery. Two main concerns are:

1. Structural integrity of the parachute attachment design; and,

2. Responses of the guidance section to the loadings.

A structural model such as the Hughes Aircraft Company finite element model (reference 5) of the missiles' two forward sections can be used for this analysis. In order to have the proper weight and load path, the model would include the guidance section skin, bulkheads at both ends, radome and parachute installation container. Figure 5 shows the general arrangement of the recovery system. Figure 6 depicts the structural model.

The model has 74 beams and 411 plate elements. The Guidance section skin can be simulated by a beam connecting two nodes representing the bulkheads. Seeker and radome can be lumped as a single mass cantilevered from the bulkhead.
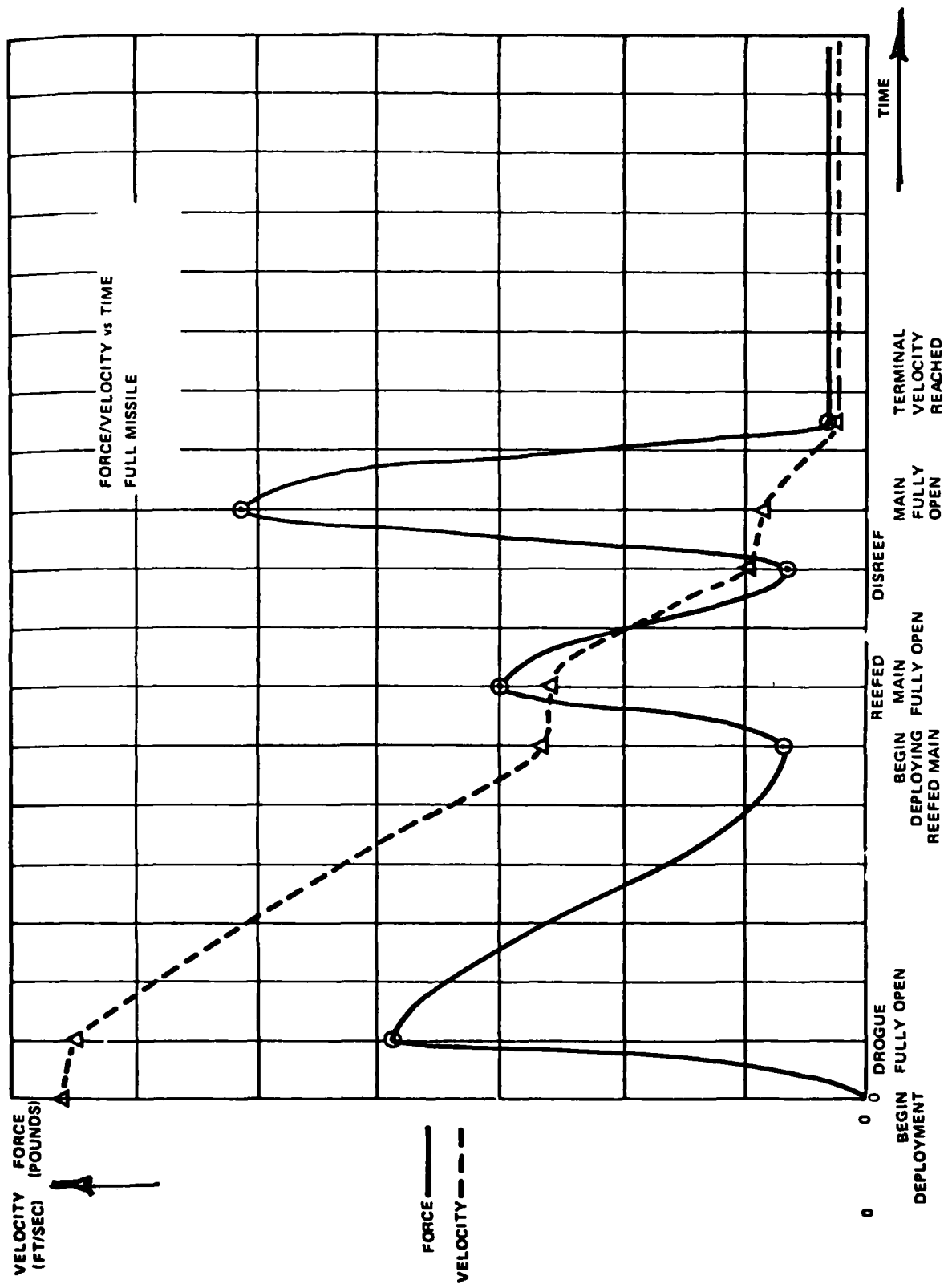
Figure 3. Guidance Section Force/Velocity vs Time.

II-338

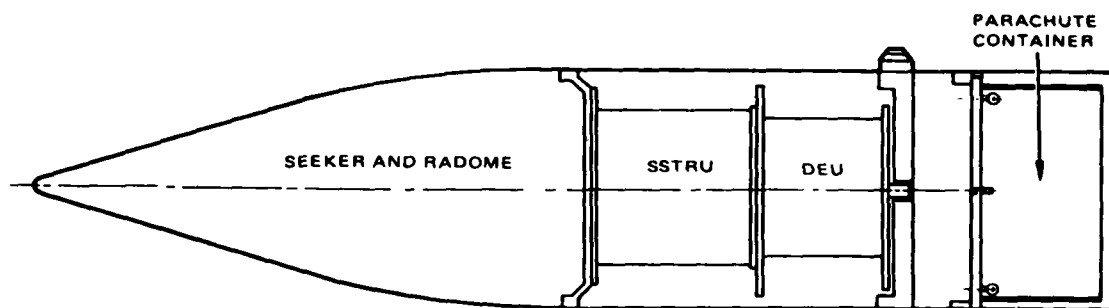Figure 4. Full Missile Force/Velocity vs Time.

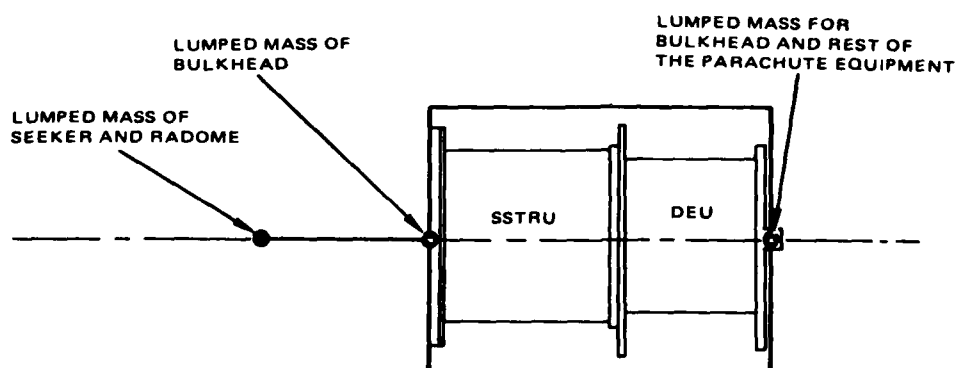II-339

Figure 5.   Recovery System

Figure 6.   Model for Response Study

Parachute opening loads are applied at the rear end, while water entry loads are at front end of the section or at bot'. ∩ids when there is a lateral component. The proper loading orientations are s..wn in figure 7. Figures 8 and 9 are typical time-acceleration histories of the parachute opening and of a 20 degree water entry impact.

Parachute opening shock is critical for the parachute supporting bracket (see figure 10). If four brackets are considered to carry the total load and a 1.5 factor is a shock factor, then the strenth of each spot weld tying the bracket to the skin can now be found. Assuming an even loads distribution, the number of welds needed for each bracket can be determined.

The missiles can be evaluated for structural integrity with water entry at 20° or less from the vertical. The missile responses to the two shock inputs (both parachute opening and water entry) can thus be studied. A similar investigation can be performed for the full missile recovery situation.

After water entry, the guidance section attached to a parachute, will descend into the ocean. Analyses can be performed to determine the deceleration, velocity, depth and pressure experienced by the guidance section during penetration. The effect of orientation on penetration can also be examined.

Typical forces acting on the guidance section after water entry are shown in figure 11. The resulting equations of motion are:

$$M\ddot{X} + Mg - F_B - F_H = 0 \quad (1)$$

$$F_H = C_D \; 1/2 \; P\dot{X}^2 A \quad (2)$$

where M = guidance section mass

$\quad\quad\quad F_B$ = buoyant force

$\quad\quad\quad X$ = penetration depth

$\quad\quad\quad F_H$ = hydraulic forces retarding motion

$\quad\quad\quad C_D$ = drag coefficient

$\quad\quad\quad P$ = density of water

$\quad\quad\quad A$ = cross section area

The equations were solved for X (and its derivatives) using a quasi-static approach, i.e.

$$\ddot{X}_j = \frac{C_D \; pA \; \dot{X}^2_{j-1}}{2M} + \frac{F_{Bj-1}}{M} - g$$

$$\dot{X}_j = \dot{X}_{j-1} + \ddot{X}_J \; t$$

WATER ENTRY
VERTICAL

WATER ENTRY
20° ANGLE

WATER ENTRY
LATERAL

PARACHUTE
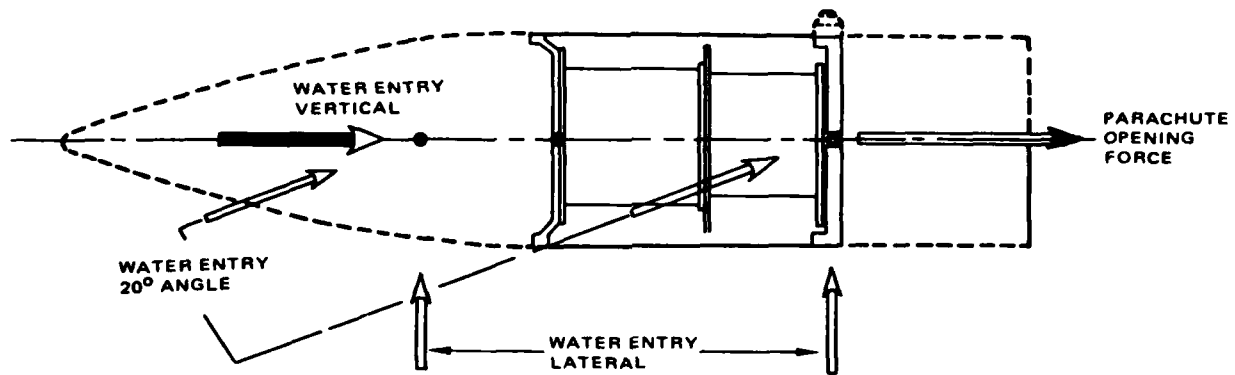OPENING
FORCE

Figure 7.   Loading Convention of the System
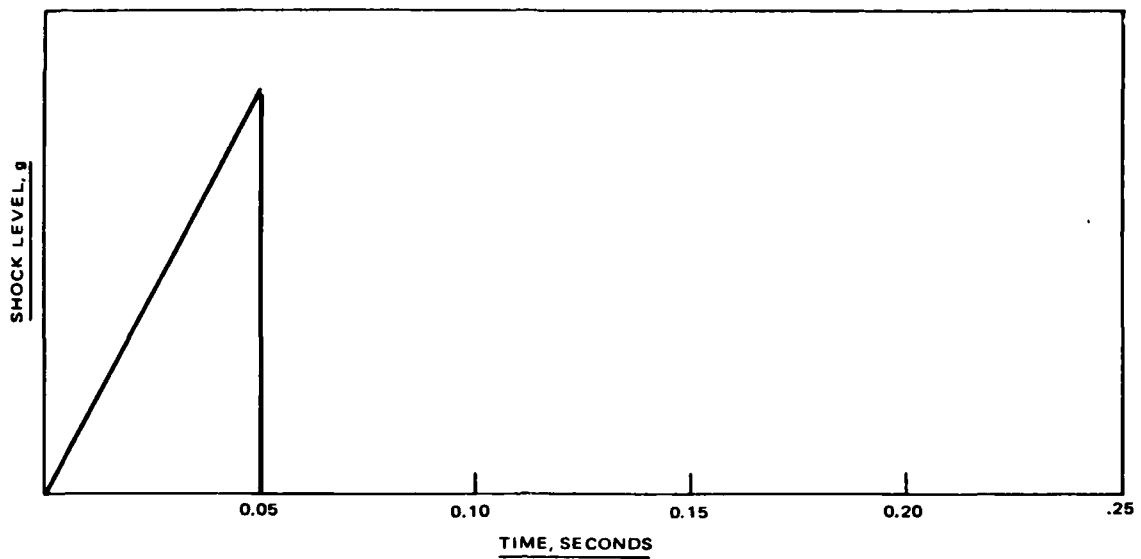
Figure 8.   Parachute Opening Shock
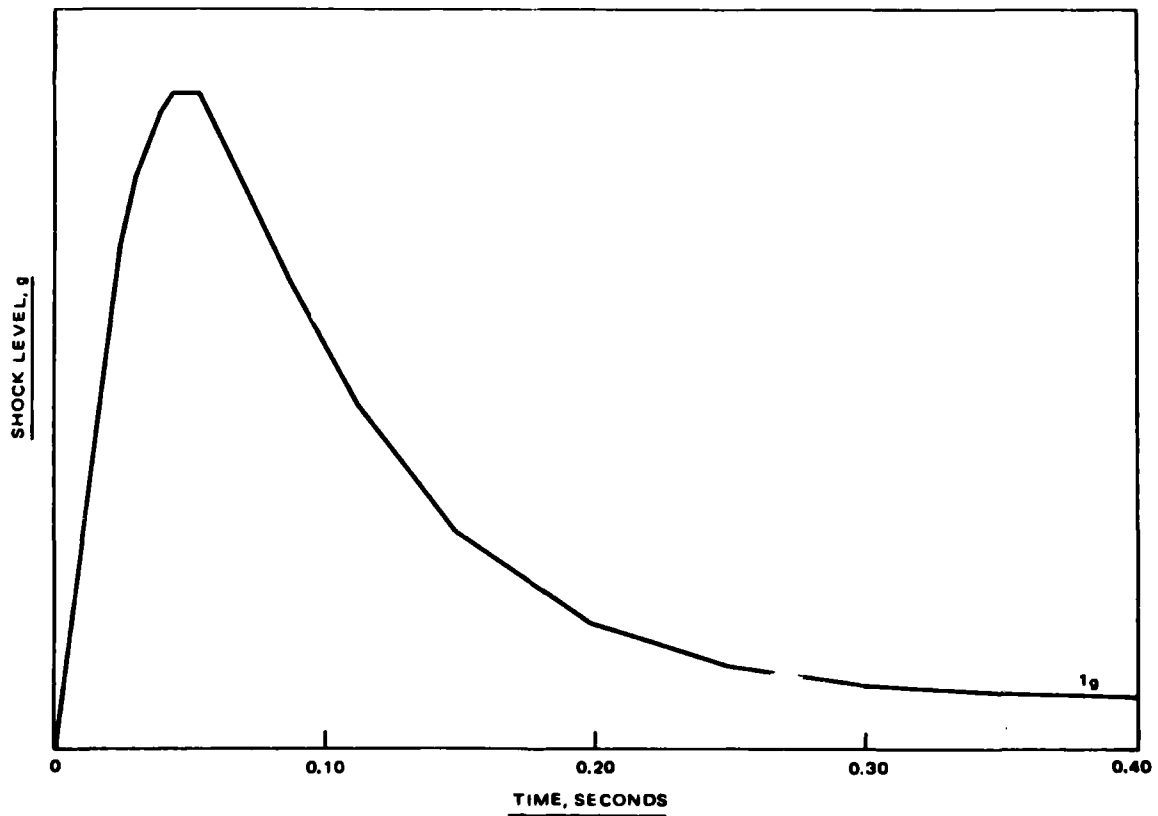
Figure 9.   Water Entry Shock, 20 degree Angle

RECOVERY SYSTEM
CONTAINER

SPOT WELDS ——— 0.072"

ATTACH
BRACKET

4 LOCATIONS
90° APART
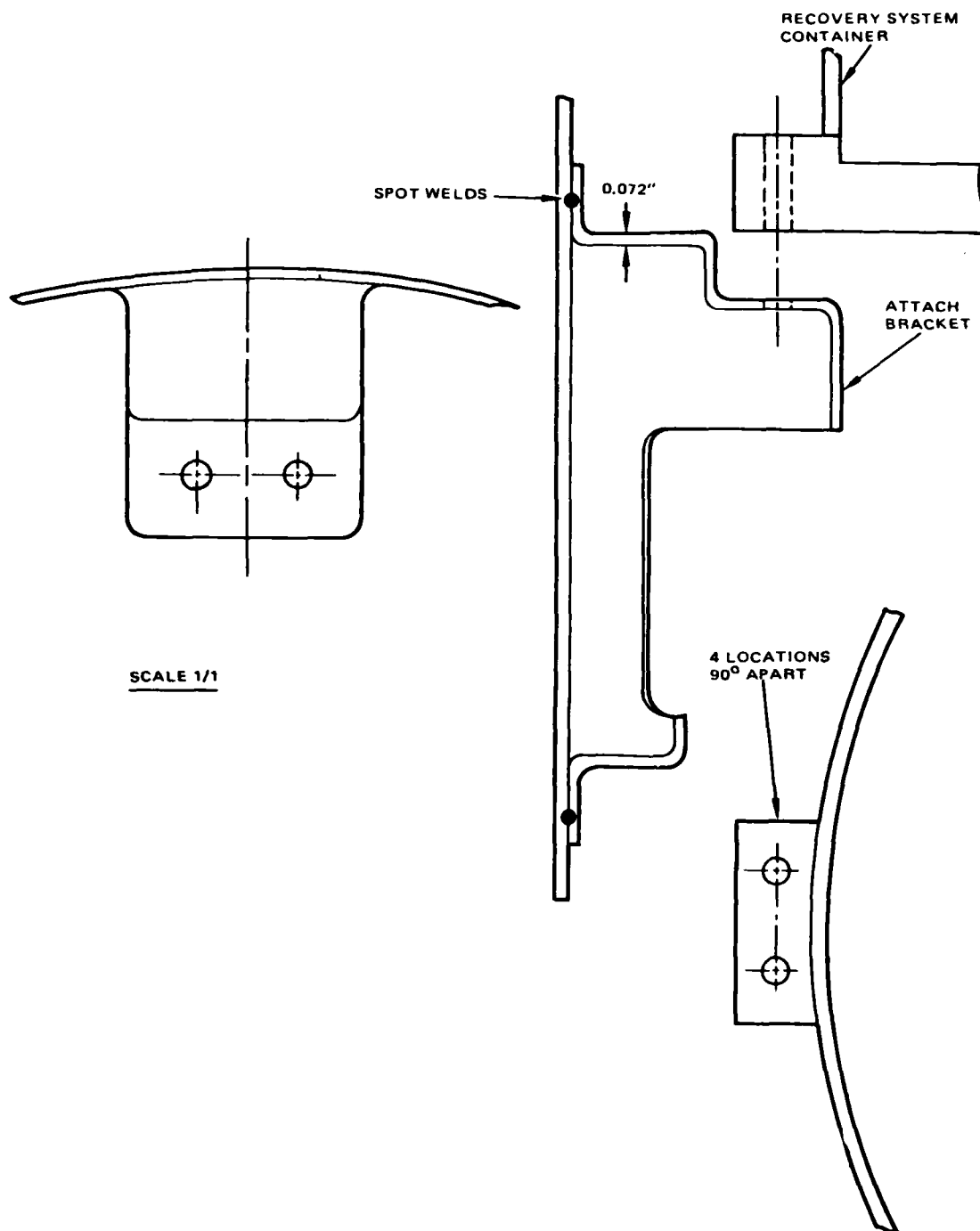
SCALE 1/1

Figure 10. Installation of Recovery System

$$X_j = X_{j-1} + \dot{X}_j \quad t$$

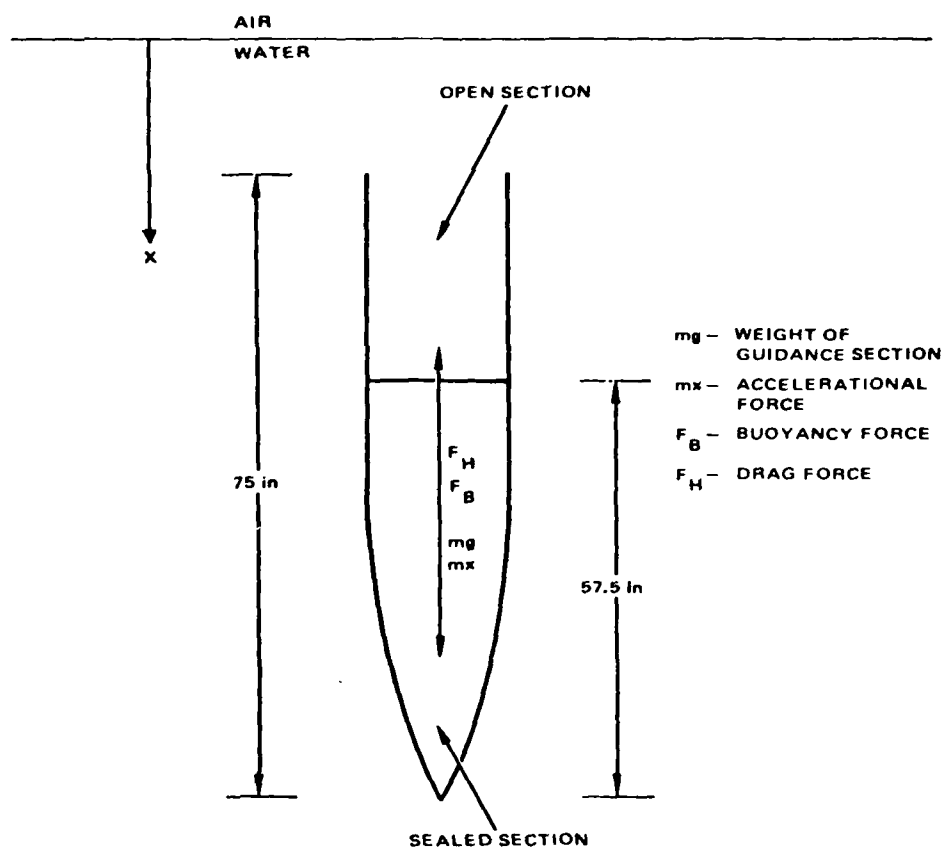j = current time step

t = time increment

Figure 11   Guidance Section and Partial Armament Section

The guidance section and partial armament section is composed of a sealed section and an open section. During penetration, the buoyancy force increases as the unit submerges and reaches a maximum value just prior to complete submergence. Upon complete submergence, buoyancy decreases to that of the sealed section as water fills the open section. Conservative values for penetration depths can be obtained by using buoyancy forces associated with the sealed section alone. Conservative deceleration values can be obtained by using the buoyancy of the entire unit.

Winds acting on the unit during descent may cause the guidance section to strike the water at an angle. Significant increases in deceleration can be expected from such penetrations. Therefore, analyses which considered orientation angles such as 20 and 90 degrees (measured from vertical) can be performed to determine the effect of orientation on deceleration. In an analysis, orientation manifests itself in the drag coefficient; the cross sectional area used in determining drag force, and the manner in which buoyancy force is computed as the body is entering the water. Orientation angles can be kept constant during the entire penetration calculation.

In an analysis considering 20 and 90 degree orientations, hydraulic forces are linearly increased to their full value as the unit enteres the water. Buoyancy forces for a 20 degrees orientation are similarly increased. However, for a horizontal penetration a function relating volume displaced by a cylinder should be used to determine buoyant forces. The forces on the missile can thus be calculated and compared to its skin's capability to resist these crushing forces.

CONCLUSIONS

The structural adequacy of a missile, redesigned to be recovered after launch, can be determined on a case by case basis using the existing structural analysis techniques.

REFERENCES

1.   PHOENIX Missile Recovery System, A Value Engineering Analysis by
R.L. Connors; 12 June 1972; Naval Missiles Center, Point Mugu, CA.

2.   NAVMISCEN TM/75-20 of Mar 1975; Subj: Moisture Intrusion from the
Water Recovery of Air-Launcher Missiles.

3.   NAVAIR Ltr. 0001: 4 May 1969, "Air-to-Air Weapon System Capability
Review," W.F. Ault, CAPT, USN.

4.   Tech Report ASD-TR-61-579, "Performance of and Design Criteria for
Deployable Aerodynamic Decelerations," published in December 1963 at
Wright-Patterson Air Force Base, Ohio.

5.   HAC "Structural Analysis of the Improved PHOENIX DEU/SSTRU Structure,"
IDC 5651/367, by C.Y. Chu, 27 Feb 1979.